



Doctoral Program in Physiology

Faculty of Medicine and Odontology

Polymer Therapeutics Laboratory

DEVELOPMENT OF MITOCHONDRIA METABOLOMIC ANALYSIS FOR THE PRECLINICAL CHARACTERIZATION OF THE IMPACT OF NEW ANTITUMORAL THERAPIES

Inés Domingo Ortí

Doctoral Thesis - University of Valencia

November 2023

Thesis directors: **Dr. María Jesús Vicent Docón, Dr. Martina Palomino Schätzlein** and **Dr. Antonio Pineda Lucena**

Thesis tutor: Dr. Federico Vicente Pallardó Calatayud





Dr. María J. Vicent Docón, Ph.D. in Chemistry and Head of the Polymer Therapeutics
Laboratory at the Centro de Investigación Príncipe Felipe (Valencia, Spain), Dr. Martina
Palomino Schäztlein, Ph.D. in Chemistry and Senior Researcher at ProtQSAR (Valencia, Spain),
and Dr. Antonio Pineda Lucena, Ph.D. in Chemical Sciences and Scientific Director at Center for
Applied Medical Research (CIMA, Navarra, Spain).

CERTIFY, that the work

"DEVELOPMENT OF MITOCHONDRIA METABOLOMIC ANALYSIS FOR THE PRECLINICAL CHARACTERIZATION OF THE IMPACT OF NEW ANTITUMORAL THERAPIES"

has been developed by Inés Domingo Ortí under their supervision in the Centro de Investigación Príncipe Felipe in Valencia, as a thesis project to obtain a Ph.D. degree in Physiology from the University of Valencia, Faculty of Medicine and Odontology.

Valencia, 22nd November 2023

Dr. María Jesús Vicent Docón

Dr. Martina Palomino Schätzlein

Dr. Antonio Pineda Lucena

A mis padres A Laia, Elia y Pau A Albert

ACKNOWLEDGMENTS

Esta tesis ha sido un recorrido largo, con cambios a los que me he tenido que adaptar y de aprendizaje en lo personal y en lo profesional. Durante el camino me he cruzado con muchas personas y, cada una de ellas me ha ayudado a que esta tesis saliera adelante.

En primer lugar, me gustaría agradecer a mis directores de tesis, Antonio, María Jesús y Martina. Antonio, gracias por creer en mí desde el primer minuto que me conociste durante las prácticas de la carrera y volver a abrirme la puerta de tu laboratorio para realizar la tesis. María Jesús, gracias por dejarme formar parte de tu laboratorio cuando ya había empezado el proyecto y por adaptarlo lo mejor posible a tu línea de investigación. Martina, has sido mi guía y apoyo en el día a día, tanto los primeros años de la tesis como en los últimos en la distancia. Gracias por enseñarme tanto de metabolómica, por siempre ver las cosas buenas, por tus consejos y por motivarme con tus palabras.

También me gustaría darle las gracias a Leo, por preguntarme cómo iba la tesis cada vez que iba al IIS La Fe y ofrecerme ayuda en lo que necesitara. I would like to thank Nils J. Færgeman and his team, to give me the opportunity to perform a short stay in his laboratory, for teaching me MS metabolomics and metabolism and for the help during my stay in Denmark. I felt at home.

Gracias a todos los compañeros que han pasado por el laboratorio de Polímeros Terapéuticos y servicio de RMN en el CIPF y por la Unidad de Descubrimiento de Fármacos en el IIS La Fe. No voy a nombrar a todo el mundo, porque la lista sería interminable. En primer lugar, darle las gracias a Pepe, por acompañarme en los primeros meses de la tesis, por dejarme aprender contigo y por las risas. Me acuerdo mucho de ti cuando dudo si he hecho algo mal; tu siempre me decías "confía en la Inés del pasado". Paz, desde que te conocí, hemos ido de la mano. Empezamos la tesis más o menos a la vez, pero cada una en su laboratorio, nos conocimos, empezamos a hacer mil planes juntas, hemos vivido y pasado una pandemia juntas, coincidimos en el mismo lab (y me has ayudado mucho cuando he tenido dudas), hemos hecho la estancia a la vez y, ahora, las dos estamos acabando la tesis (creo que el final es menos duro cuando tienes una persona cerca que está pasando por el mismo proceso). Aunque hemos tenido nuestros más y nuestros menos, has sido indispensable durante estos años. Toni, muchas gracias por tu apoyo, admiro la forma en la que llevas las cosas, con tranquilidad. Te queda el tramo final de la tesis, pero estoy segura de que lo llevarás bien. Esther Martínez, gracias por tu ayuda el lab y los ratitos de charlas durante las comidas. Ana, gracias por tus consejos para los estudios de cultivos y western blots. Esther Masiá, Paula, David y María Helena por hacer que el laboratorio funcione y por vuestra ayuda cuando la he necesitado. Inma, María Medel, Tetiana y Snežana, gracias por vuestra ayuda con la síntesis química, los cálculos, la caracterización y por vuestros consejos. Camilla (mi compi de Seahorse y del team mitocondria), Amina y María Ibáñez, mucha suerte y ánimo para lo que os queda, ha sido un placer coincidir con vosotras. Stuart, thank you for your patience and help during the writing part of thesis. We are lucky to have you in the laboratory.

Del servicio de RMN me gustaría darle las gracias a Rubén por tu dedicación al servicio y tu ayuda en el proyecto de eritrocitos. Y, a Patri, fuiste una estudiante ejemplar. Gracias por estar siempre dispuesta y ayudar en todo.

Del IIS La Fe, a Leti, Ayelén, Arturo, y en especial a Nuria y Marta. Nuria, siempre has estado dispuesta a ayudarme (cada vez que me iba del laboratorio, repetías la misma frase "si necesitas algo, me dices") y, aunque un poco en la distancia, nos hemos acompañado en el proceso. Marta, no hemos coincidido mucho tiempo juntas en el lab pero mi sentimiento es diferente. Puede que fuera corto pero intenso, siempre que te veo parece que hayamos compartido miles de momentos.

A mis amigos de toda la vida (Cris, Patri, Laia, Marga, Néstor, Marina, Sandra, Núria) y a los más recientes (Raquel, María, Chiara, Yaiza, Sonia, Carla y Lorena) porque, aunque no os vea mucho (sobre todo últimamente), os habéis preocupado por mí y animado cuando lo he necesitado. Núria, sempre tens paraules per animar-me i motivar-me. Ja t'he dit moltes vegades lo molt que t'admiro. A tu també et queda poc per convertir-te en una súper pediatra. Raquel, hem compartit molts moments (de risses i de patiments) durant la carrera i ara, encara que no ens vegem molt, sé que sempre estàs al meu costat. Yaiza, la casualidad nos llevó a vivir juntas y conocernos, no sabes cuanto me alegro. Eres una de las mejores coses que me llevo de estos años.

Mil gracias a toda mi família, que siempre ha creído en mi. Mama y papa, mil gracias por confiar tanto en mí, por apoyarme durante todos mis estudios, por animarme en los momentos duros y por ofrecerme otra visión de las cosas. A mis abuelos, por cada vez que iba su casa y me preguntaban "com van els estudis?, ja acabes?". A mis hermanas y mi sobrino, Elia, Laia y Pau, gracias por preocuparos por cómo estoy, aguantar mis días malos y darme tanto cariño. Gràcies Miriam, per ser com una tercera germana per a mi, per escoltar-me i compartir alegries i preocupacions. No me puedo dejar a él, Coco, porque es parte de la familia y, aunque no hable, no le hace falta decir palabra para demostrar su cariño. Mientras escribo estas palabras, él está acostado a mi lado y eso ha sido suficiente para hacerme sentir acompañada durante este proceso.

Albert, no tinc paraules per agrair-te tota la teua ajuda durant este procés, sobretot durant la última etapa. Mil gràcies per la teu paciència, comprensió, ànims, per donar-me la visió positiva de les coses, per aguantar-me ni quan jo mateixa ho feia, per aguantar els meus canvis d'estat d'ànim i intentar sempre fer els dies més divertits. Saps que sense tu, haguera sigut molt difícil arribar fins aquí.

TABLE OF CONTENTS

ABBI	REVIATIO	ONS	17
ABST	TRACT		25
RESU	JMEN		27
OBJE	CTIVES		29
СНА	PTER I.		31
INTI	RODUC	CTION AND BACKGROUND	31
1.:	1. MIT	TOCHONDRIA AND BREAST CANCER	32
	1.1.1.	Mitochondrial Function and Metabolism	32
	1.1.2.	Mitochondrial Diseases	37
	1.1.3.	Breast Cancer	38
	1.1.3.2	.1. Breast Cancer Definition, Prevalence, and Molecular Subtypes	38
	1.1.3.2	.2. Triple Negative Breast Cancer	40
	1.1.3.3	.3. Breast Cancer Metastasis	41
	1.1.3.4	.4. Current Breast Cancer Treatment	43
	1.1.	L.3.4.1. Triple Negative Breast Cancer Treatment	44
	1.1.4.	Alteration in Breast Cancer Metabolism: A Focus on Mitochondria	46
	1.1.5.	Mitochondrial Modulation in Breast Cancer Treatment	50
1.	2. DES	SIGNING POLYMER THERAPEUTICS FOR BREAST CANCER TREATMENT	51
	1.2.1.	Polymer Therapeutics as Nanomedicines	51
	1.2.1.2	.1. Polymer-Drug Conjugates	53
	1.2.1.2 Site	.2. Polymer-drug conjugates: from Patient Administration to the Fin	_
	1.2.2.	Polymer-drug Conjugates for Breast Cancer Treatment	58
	1.2.3.	Mitochondrially-targeted Therapies	58
	1.2.3.2	.1. Mitochondrially-targeted Breast Cancer Therapies	60
1.	3. ME	ETABOLOMICS: A FOCUS ON BREAST CANCER AND MITOCHONDRIA	61

	1.3.1.	Metabolomics	61
	1.3.2.	Breast Cancer Metabolomics	65
	1.3.3.	Metabolomics Methods to Assess Mitochondrial Metabolism	66
	1.3.4.	Pharmacometabolomics	71
C	HAPTER I	l	75
0	PTIMIZAT	TION OF NMR-BASED METABOLOMIC ANALYSIS OF MITO	CHONDRIA
IS	OLATED	FROM TRIPLE NEGATIVE BREAST CANCER CELL	75
	2.1. INTRO	DDUCTION	76
	2.2. RESUL	TS AND DISCUSSION	76
	2.2.1. M	litochondrial Isolation from Triple Negative Breast Cancer Cells	76
	2.2.2. M	letabolite Extraction from Mitochondrial Extracts	80
		letabolomic Profiling of Mitochondria Isolated from Triple Negative B ing NMR Spectroscopy	
	2.2.3.	1. A Comparison of the Metabolomic Profiles of Isolated Mitochondri	a and Whole
	Triple	Negative Breast Cancer Cells	90
	2.3. CONC	LUSIONS	94
	2.4. MATE	RIALS AND METHODS	95
	2.4.1. M	laterials	95
	2.4.2. Ce	ell Culture	95
	2.4.3. Bı	reast Cancer Cell Collection for Whole-cell Analysis	96
	2.4.4. M	litochondrial Isolation from Triple Negative Breast Cancer Cells	96
	2.4.5. As	ssays Used from the Optimization of Mitochondrial Isolation	97
	2.4.5.	1. Measurement of Cell Lysis by Cell Counting	97
	2.4.5.	2. Measurement of Lactate Dehydrogenase Activity	97
	2.4.5.	3. Measurement of Succinate Dehydrogenase Activity	98
	2.4.5.	4. Western Blotting	99
	2.4.6. M	letabolite Extraction Procedures and NMR Sample Preparation	100
	2.4.6.	1. Metabolite Extraction from Triple Negative Breast Cancer Cells (Fo	lch Method)
			100

2.4.6.2. Metabolite Extraction from Isolated Mitochondria from Triple Negative Breas
Cancer Cells
2.4.7. Metabolomic Analysis by NMR Spectroscopy
2.4.7.1. NMR Spectra Acquisition
2.4.7.2. NMR Data Processing
2.4.7.3. Metabolite Identification and Quantification
2.4.7.4. Univariate Analysis
CHAPTER III
EVALUATING THE IMPACT OF FREE DRUGS AND POLYMER-DRUG CONJUGATES
ON THE METABOLISM OF TRIPLE NEGATIVE BREAST CANCER CELLS 103
3.1. INTRODUCTION
3.2. RESULTS AND DISCUSSION
3.2.1. Synthesis and Characterization of StPGA-SS-palbociclib
3.2.1.1. Synthesis of StPGA-SS-palbociclib10
3.2.1.2. Physico-chemical Characterization of StPGA-SS-palbociclib108
3.2.2. Biological Evaluation of Palbociclib and StPGA-SS-palbociclib in Triple Negative Breas Cancer Cells
3.2.2.1. Cell Viability Assay of Palbociclib and StPGA-SS-palbociclib
3.2.2.2. Assessment of Mitochondrial Respiration After Palbociclib and StPGA-SS palbociclib Treatment
3.2.2.3. Analysis of the Metabolome and Lipidome of Isolated Mitochondria and Triple Negative Breast Cancer Cells After Treatment with Free Palbociclib and with StPGA-SS palbociclib
3.2.2.3.1. NMR Metabolomics Analysis of Mitochondria and Triple Negative Breas Cancer Cells After Treatment with Free Palbociclib and StPGA-SS-palbociclib 11
3.2.2.3.2. MS Metabolomics Analysis of Mitochondria and Triple Negative Breas Cancer Cells After Treatment with Free Palbociclib and StPGA-SS-palbociclib 128
3.2.2.3.3. MS Lipidomic Analysis of Mitochondria and Triple Negative Breast Cance Cells After Treatment with Free Palbociclib and StPGA-SS-palbociclib
3.2.2.4. Fluxomics Analysis of Triple Negative Breast Cancer Cells After Treatment with Free Palbociclib and StPGA-SS-palbociclib

3.2.2.4.1. Optimization of the Isotope-Labeling Experiments in Whole-Cells	146
3.2.2.4.2. MS Fluxomics Analysis in Whole-Cells After Treatment with Free Palk and StPGA-SS-palbociclib	
3.3. CONCLUSIONS	159
3.4. MATERIALS AND METHODS	164
3.4.1. Materials	164
3.4.2. Synthesis of StPGA-SS-palbociclib	165
3.4.3. Physico-chemical Characterization of StPGA-SS-Palbociclib	167
3.4.3.1. NMR Spectra Acquisition	167
3.4.3.2. Drug Loading Determination by UV-Vis Spectroscopy	167
3.4.3.3. Size Determination by Bayesian DOSY Transform	168
3.4.3.4. Zeta Potential Measurement by Dynamic Light Scattering	168
3.4.3.5. Secondary Structure Determination by Circular Dichroism	168
3.4.3.6. Release kinetics	168
3.4.4. Biological evaluation	170
3.4.4.1. Cell Culture	170
3.4.4.2. Cell Viability Studies	170
3.4.4.3. Evaluation of Mitochondrial Respiration of Treated Triple Negative Breast Cells	
3.4.4.4. Triple Negative Breast Cancer Cell Collection for Whole-Cell Metab	
3.4.4.5. Mitochondrial Isolation from Triple Negative Breast Cancer Ce	
3.4.4.6. Isotope Labeling of Triple Negative Breast Cancer Cells for NMR Metab	olomi
Analysis	172
3.4.4.7. Isotope Labeling of Triple Negative Breast Cancer Cells for LC-MS Metab	
3.4.4.8. Metabolite Extraction Methods and Sample Preparation for Metab	
3 4 4 8 1. Metabolite Extraction Protocols for NMR Metabolomic Analysis	173

3.4.4.8.2. Metabolite Extraction Protocols for LC-MS Metabolomic Analysis	174
3.4.4.9. Metabolomic Analysis by NMR Spectroscopy	175
3.4.4.9.1. NMR Spectra Acquisition	175
3.4.4.9.2. NMR Data Processing	176
3.4.4.9.3. Metabolite Identification and Quantification	176
3.4.4.10. Metabolomic Analysis by LC-MS	177
3.4.4.10.1. LC-MS Spectra Acquisition	177
3.4.4.10.2. MS Data Processing and Metabolite Annotation	177
3.4.4.11. Multivariate and Univariate Statistical Analysis	178
CHAPTER IV	179
METABOLOMIC ANALYSES OF MITOCHONDRIA ISOLATED FROM HEALTH	IY AND
PRIMARY AND METASTATIC TISSUES OF A TRIPLE NEGATIVE BREAST C	ANCER
MOUSE MODEL	179
4.1. INTRODUCTION	180
4.2. RESULTS AND DISCUSSION	181
4.2.1. Optimization of NMR-based Metabolomic Analysis of Mitochondria Isolat Triple Negative Breast Cancer Tumor and Healthy Liver, Kidneys, Lungs and Brain .	
4.2.1.1. Mitochondria Isolation from Tissues	181
4.2.1.2. Metabolite Extraction from Mitochondria Isolated from Tissues	188
4.2.1.3. NMR Metabolomic Profiling of Mitochondria Isolated from Tissues	190
4.2.2. Comparing Metabolomic Fingerprints of Whole-Cells and Mitochondrial Isolated from Breast Tumor, Liver, Kidney, Lungs, and Brain	
4.2.3. Metabolic Evaluation of Metastasis in Lungs, Liver, and Kidney of a Triple Breast Cancer Mouse Model	-
4.3. CONCLUSIONS	203
4.4. MATERIALS AND METHODS	204
4.4.1. Materials	204
4.4.2. Biological material	204
4.4.3. Mitochondrial isolation from tissues	205
4.4.4. Western Blotting for the confirmation of mitochondria isolation from tissue	s 206

4.4.5. Metabolite extraction procedure and NMR sample preparation	207
4.4.5.1. Metabolite extraction from tissues	207
4.4.5.2. Metabolite extraction from mitochondria isolated from tissues	208
4.4.6. Metabolomic analysis by NMR spectroscopy	208
4.4.6.1. NMR spectra acquisition	208
4.4.6.2. NMR data processing	209
4.4.6.3. Metabolite identification and quantification	209
4.4.6.4. Multivariate and univariate analysis	209
GENERAL DISCUSSION	211
FINAL CONCLUSIONS	227
MEMORIA DE LA TESIS	231
REFERENCES	253
ANNEX I	277
SUPPORTING INFORMATION	277
ANNEX II	323
PUBLICATIONS	323

ABBREVIATIONS

α-CD α-cyclodextrin α-KG α -ketoglutarate 1D One-dimensional 1-methylguanosine 1-MG 2D Two-dimensional A.U Arbitrary units AcAc Acetoacetate Ace Acetate

AceAsp N-acetylaspartate

AceGlu N-acetylglutamate

AceLS N-acetyl-D-lactosamine

AcN Acetonitrile
Ade Adenosine

ADP Adenosine diphosphate

AKT Protein kinase B

Ala Alanine

AMP Adenosine monophosphate

Anh Anhydrous

ANOVA Analysis of variance
AR Androgen receptor

ArabfurUMP 1-β-D-arabinofuranosyluracil 5-monophosphate

Arg Arginine
Asc Ascorbate
Asn Asparagine
Asp Aspartate

ATP Adenosine triphosphate

BACH1 Transcriptional repressor BTB and CNC homology 1

Bax Bcl-2-associated X protein

Bcl-2 B-cell lymphoma 2

BCSCs Breast cancer stem cells

BGly N-butyrylglycine

BL Basal-like

BMP Bismonoacylglycerophosphates

BMRB Biological magnetic resonance data bank
BRCA1/2 Breast cancer type 1/2 susceptibility protein

BSA Bovine serum albumin

ButGly N-butyrylglycine

cAMP Cyclic adenosine monophosphate
CCT Choline phosphate cytidylyltransferase

CD Circular dichroism
CDCl3 Deuterated chloroform

CDK4/6 Cyclin-dependent kinase 4 and 6

CDP Cytidine diphosphate

CE Cholesterol ester

Cer Ceramide
CHCI3 Chloroform
Chi Chitosan
CHK Choline kinase

CHK1 Checkpoint kinase 1

Cho Choline

CHPT1 Choline phosphotransferase 1

Cit Citrate
CL Cardiolipin

CLSM Confocal laser scanning microscopy

CMP Cytidine monophosphate

CoA Coenzyme A
CoQ Coenzyme Q₁₀

CPMG Carr Purcell Meiboom Gil
CPPs Cell-penetrating peptides

Cps Counts per second

Cre Creatine

CS Citrate synthase

CT Control

CTL1 Choline transporter-like protein 1
CTLA-4 Cytotoxic T lymphocyte protein-4

CTP Cytidine triphosphate

CV Cross validated

Cys Cysteine
Cyt c Cytochrome c
D1 Relaxation delay

DA Dimethylmaleic anhydride
DAD Photodiode array detector
DAS N1,N8-diacetylspermidine
DC Differential centrifugation
d-DMSO Deuterated dimethyl sulfoxide

Deoxfruc 1-Deoxy-1-fructosyl

Der Derivative

DFT N-(1-deoxy-1-fructosyl)threonine

DG Diacylglycerol

DGC Density gradient centrifugation
DHODH Dihydroorotate dehydrogenase
DIEA N, N-Diisopropylethylamine

DMA Dimethylamine

DMEM Dulbecco's modified eagle media

DMSO Dimethyl sulfoxide

DMTMM 4-(4,6-dimethoxy-1,3,5-triazin-2-yl)-4-methylmorpholinium

DOSY Diffusion-ordered NMR spectroscopy

DOX Doxorubicin

DPBS Dulbecco's phosphate-buffered saline
DQAsomes Dequalinium-based liposome-like vesicles
DSS Sodium trimethylsilylpropanesulfonate

DTT Dithiothreitol

dTTP Deoxythymidine triphosphate
ECAR Extracellular acidification rate
EDTA Ethylenediaminetetraacetic acid
EGFR Epidermal growth factor receptor
EMT Epithelial mesenchymal transition

EPR Enhanced permeability and retention effect

ER Estrogen receptor

ERK1/2 Extracellular signal-regulated kinase 1

ETC Electron transport chain

FA Fatty acid

FAD Flavin adenine dinucleotide

FAHFA Fatty acyl ester of hydroxy fatty acids

FBS Fetal bovine serum

FC Fold change

FCCP Carbonyl cyanide-p-trifluoromethoxyphenylhydrazone

FD Free drug

FDA Food and Drug Administration

FID Free induction decay

For Formate

F-1,6-BP Fructose-1,6-biphosphate

FVPR Functional Validation and Preclinical Research

G-6-P Glucose-6-phosphate

GAPDH Glyceraldehyde-3-phosphate dehydrogenase

GC Gas chromatography
GDP Guanosine diphosphate
GHP y-glutamylhydroxyproline

GL Glycerolipid

GLA Alpha-galactosidase A

GlcA Glucuronate

GlcA-6-P Glucosamine-6-phosphate

Gln Glutamine
GLS Glutaminase
Glu Glutamate
Gluc Glucose

GLUT1/2 Glucose transporter 1/2

Gly Glycine

Gly-3-P Glyceraldehyde-3-phosphate
GMP Guanosine monophosphate

GNAc-SiRNA N-acetylgalactosamine short-interfering RNA

GPC Glycerophosphocholine GPL Glycerophospholipid GSH Glutathione

GTP Guanosine triphosphate

h Hour

HBMP Hemibismonoacylglycerophosphates

HER2 Human epidermal growth factor receptor 2

HexCer Hexosylceramide

HIF1 Hypoxia-inducible factor 1

His Histidine
HK2 Hexokinase 2

HMDB Human metabolome database

HPLC High-performance liquid chromatography
HPMA N-(2-hydroxypropyl) methacrylamide
HR-MAS High-resolution sample spinning

HSP90 Heat shock protein 90

HSQC Heteronuclear Single Quantum Correlation

HydPro Hydroxyproline

IC₃₀
 IC₅₀
 IC₅₀
 Insulin-like growth factor

Ile Isoleucine

IM Immunomodulatory

IMM Inner mitochondrial membrane

IMP Inosine monophosphate
IMS Intermembrane space

Ino Inosine

INT p-iodonitrotetrazolium violet

IS Internal standard

KkDaKilodaltonKi67Antigen Kiel 67KOKnockdownLacLactate

LactoylLeu N-lactoylleucine

LactoylPhe N-lactoylphenylalanine
LAR Luminal androgen receptor
LC Liquid chromatography
LCFA Long chain fatty acids
LDH Lactate dehydrogenase

Leu Leucine

LNAPE Lyso-N-acyl-phosphatidylethanolamine

LPC Lysophosphatidylcholine

LPE Lysophosphatidylethanolamine

LPG Lysophosphatidylglycerol
LPI Lysophosphatidylinositols

Lys Lysine

M Mesenchymal

M+X Metabolite mass plus number of labeled carbons MACS Anti-TOM22 magnetically activated cell sorting

Mal Maltose

MCT1/4 Monocarboxylate transporter 1/4 MDPs Mitochondria-derived peptides

MeOH Methanol Met Methionine

MetSP Methionine salvage pathway
MGDG Monogalactosyldiacylglycerols
MID Mass isotopomer distribution

min Minutes

MMC O-methylmalonyl-L-carnitine

MMP Mitochondrial membrane potential

MMP2 Metalloproteinase-2

MoNA MassBank of North America

mPTP Mitochondrial permeability transition pore

MS Mass spectrometry
MSL Mesenchymal stem-like
mtDNA Mitochondrial DNA

mTOR Mammalian target of rapamycin

MTS 3-(4,5-dimethylthiazol-2-yl)-5-(3-carboxymethoxyphenyl)-2-(4-sulfophenyl)-2H-

tetrazolium salt

Mw Molecular weight
Myo Myo-inositol

Naa N-acetylaspartate

NAD⁺ Nicotinamide adenine dinucleotide

NADP⁺ Nicotinamide adenine dinucleotide phosphate

NAG N-acetylglucosamine

nDNA Nuclear DNA

NDUFB8 NADH: Ubiquinone Oxidoreductase Subunit B8

NCEs New chemical entities

Nia Niacinamide Nic Nicotinurate Nira Niraparib

NIST17 National Institute of Standards and Technology 17

NMR Nuclear magnetic resonance

NO Nitric oxide

NOESY Nuclear overhauser effect spectroscopy

norLeu Norleucine NP40 Nonidet P-40

ns Not statistically significant
OCR Oxygen consumption rate
OMM Outer mitochondrial membrane

OPLS-DA Orthogonal partial least squares discriminant analysis

Orn Ornithine ov Overlapping

OXPHOS Oxidative phosphorylation
P/S Penicillin/streptomycin
P4P Pantetheine 4 -phosphate

Palbo Palbociclib

PAMAM Polyamidoamine

PARP Poly (ADP-ribose) polymerase

PC Phosphatidylcholine

PCA Principal component analysis

P-choline Phosphocholine
Pcre Phosphocreatine
PD Phosphatidylserine

PD-1 Programmed cell death protein 1

PDCs Polymer-drug conjugates

PDE Phosphodiesterase

PDH Pyruvate dehydrogenase

PD-L1 Programmed cell death protein 1 ligand

PE Phosphatidylethanolamine

PEG Polyethylene glycol PEP Phosphoenolpyruvate

PEPCK Phosphoenolpyruvate carboxykinase

PFK Phosphofructokinase
PG Phosphatidylglycerol
PGA Poly-L-glutamic acid

PGC-1α Peroxisome proliferator-activated receptor gamma coactivator-1 alpha

PGM Phosphoglucomutase

Phe Phenylalanine

PI Phosphatidylinositol

PI3K Phosphatidylinositol-4,5-bisphosphate 3-kinase

PI3KCA Phosphatidylinositol-4,5-bisphosphate 3-kinase catalytic subunit alpha

PKM Pyruvate kinase muscle isozyme
PLGA Poly(lactic-co-glycolic acid)
PMS Phenazine methosulfate

ppm Parts per million

PR Progesterone receptor

Pro Proline
PTX Paclitaxel
Pyr Pyridine

PyroGlu Pyroglutamate QC Quality control

Rh Hydrodynamic radius

Rib Ribose

Ribulose-5-P Ribulose-5-phosphate

RIPA Radioimmunoprecipitation assay buffer

ROS Reactive oxygen species RSA Relative specific activity

SCL1A45 Solute carrier family 1 member 5

SD Standard deviation

SDH Succinate dehydrogenase

SDHB Succinate dehydrogenase protein complex

SDS Sodium dodecyl sulfate
SEM Standard error of the mean

Ser Serine
SIRT6 Sirtuin 6
SL Sphingolipid

SLC1A5 Solute carrier family 1 member 5 SLC25A12/13 Solute carrier family 25 member 12/13

SM Sphingomyelin Sper Spermidine SS Disulfide linker

STAT Signal transducer and activator of transcription

STL Sterol lipid

StPGA 3-arm star-shaped poly-L-glutamic acid

Suc Succinate
Tau Taurine

TCA Tricarboxylic acid
TDL Total drug loading

TEM Transmission electron microscopy

Temp Temperature
TG Triacylglycerol
Thr Threonine

TLC Thin-layer chromatography
TNBC Triple negative breast cancer

TOM/TIM IMM translocase/OMM translocase

TP53 Tumor protein p53
TPP Triphenylphosphonium

t_R Retention time

Tris Base 2-amino-2-(hydroxymethyl)-1,3-propanediol

Tris-HCl Tris(hydroxymethyl)aminomethane hydrochloride

tRNA Transfer RNA
Trp Tryptophan

TSP 3-(trimethylsilyl) propionic acid d4 sodium salt

Tyr Tyrosine

U Uniformly labeled
UC Ultracentrifugation
UDP Uridine diphosphate
UMP Uridine monophosphate

UPLC Ultrahigh-performance liquid chromatography

Ura Uracil

Uri Uridine

UTP Uridine triphosphate

UV Ultraviolet

v/v Volume/volume percentage

Val Valine

VDAC Voltage-dependent anion channel VEGF Vascular endothelial growth factor

VEGFR Vascular endothelial growth factor receptor

VIP Variable importance plot

Vis Visible

w/v Weight/volume percentage

WB Western blotting

WT Wild type
wt weight
Z pot Z potential

ABSTRACT

Mitochondrial metabolism has attracted increasing attention from the scientific community due to its essential role in modifying cell function and its ability to adapt to the cell state. In cancer, mitochondria modulate their metabolism according to the cell characteristics and demands; for instance, they promote aggressiveness and invasiveness in response to an energy demand or compensate for the impairment of other cellular metabolic pathways¹. The essential role of mitochondria in cancer cell progression² and the unique characteristics of mitochondria in cancer cells (e.g., mitochondrial membrane depolarization, high reactive oxygen species levels)³ makes mitochondria an attractive target for new cancer therapeutic approaches.

In this context, mitochondrial evaluations remain essential to understanding their function and adaptation during cancer progression and after cancer treatment, which requires methods that allow the specific evaluation of mitochondria. Mitochondrial respiration (comprising oxygen consumption, reactive oxygen species levels, and mitochondrial membrane potential)^{4,5} represents the most common mitochondrial function studied by researchers; however, mitochondrial metabolism, closely related to mitochondrial respiration functioning, remains poorly assessed.

The research developed in this thesis focuses on developing an NMR-based metabolomic methodology for the specific evaluation of mitochondrial metabolism in preclinical triple negative breast cancer models. We applied the optimized methodology to *in vitro* evaluate mitochondrial modulation after treatment with free palbociclib and a polypeptide-based palbociclib conjugate. We confirmed and complemented NMR metabolomic outcomes with mass spectrometry metabolomics and lipidomics and NMR and mass spectrometry fluxomics. Finally, we applied the developed metabolomics methodology to obtain the mitochondrial metabolic signature of *in vivo* breast tumors and assess mitochondrial metabolic modulation in metastatic tissues.

RESUMEN

En los últimos años el metabolismo mitocondrial ha llamado la atención de la comunidad científica debido a su papel fundamental para el correcto funcionamiento celular y a su capacidad de adaptarse al estado de la célula. En cáncer, las mitocondrias modulan su metabolismo de acuerdo a las características y demandas celulares, por ejemplo, para promover la agresividad e invasividad, en respuesta a una demanda energética o para compensar la disfunción de otras rutas metabólicas¹. El papel esencial que juega la mitocondria en la progresión del cáncer² y sus características únicas en las células tumorales (p.ej., despolarización de la membrana mitocondrial, elevados niveles de especies reactivas de oxígeno)³ han convertido a este orgánulo en una atractiva diana terapéutica para el tratamiento del cáncer.

En este contexto, la evaluación de las mitocondrias es esencial para comprender su funcionamientos y adaptación durante el desarrollo del cáncer y tras el tratamiento, por lo cual necesitamos métodos que nos permitan evalúan específicamente las mitocondrias. En general, los estudios mitocondriales suelen centrarse en la evaluación de la respiración mitocondrial (p.ej., consumo de oxígeno, niveles de especies reactivas de oxígeno y potencial de la membrana mitocondria)^{4,5}; sin embargo, el metabolismo mitocondrial, el cual está muy relacionado con el funcionamiento de la respiración mitocondrial, apenas se ha estudiado.

La investigación de esta tesis incluye el desarrollo de una metodología metabolómica mediante resonancia magnética nuclear (NMR) para el estudio específico del metabolismo mitocondrial en modelos preclínicos de cáncer de mama triple negativo. *In vitro*, aplicamos la metodología optimizada para estudiar la modulación del metabolismo mitocondrial tras el tratamiento con palbociclib y con un conjugado polipéptido-palbociclib. Además, los resultados del estudio por RMN fueron confirmados y complementados utilizando metabolómica y lipidómica mediante espectrometría de masas (MS) y estudios fluxómicas mediante NMR y MS. *In vivo*, aplicamos el método desarrollado para obtener el perfil metabolómico mitocondrial de los tumores de cáncer de mama y la modulación metabólica mitocondrial en tejidos metastásicos.

OBJECTIVES

The main aim of this thesis involves the development of an NMR-based metabolomic methodology for the specific evaluation of mitochondrial metabolism in cell and tissue samples. The specific objectives include:

- Objective 1. Optimization of a specific NMR mitochondrial metabolomic methodology in triple negative breast cancer cells comprising three steps (mitochondrial isolation, metabolite extraction, and NMR analysis) to support the comparative analysis of whole-cell and isolated mitochondrial metabolomic profiles
- Objective 2. Selection of pharmacological therapies (both free drugs and nanomedicinal formulations) to modulate mitochondria function and validate the developed NMR methodology, which also involves the synthesis and characterization of a star-shaped poly L-glutamic acid (StPGA)-based conjugate
- Objective 3. Biological evaluation of palbociclib and StPGA-based palbociclib conjugates and
 their impact on the mitochondrial metabolism of triple negative breast cancer cells using
 the previously optimized NMR methodology, whose results will be confirmed and
 complemented by mass spectrometry metabolomics and lipidomics and NMR and mass
 spectrometry fluxomics studies
- Objective 4. Optimization of the NMR mitochondrial metabolomic methodology in healthy
 and tumorigenic mouse tissues, which also involves a comparative analysis of the
 metabolomic profiles of whole-cell and isolated mitochondria samples
- Objective 5. Evaluation of metabolic alterations in the mitochondria isolated from metastatic triple negative breast cancer mouse model when compared to a healthy mouse model using the optimized methodology

CHAPTER I

INTRODUCTION AND BACKGROUND

1.1. MITOCHONDRIA AND BREAST CANCER

1.1.1. Mitochondrial Function and Metabolism

Mitochondria – the membrane-bound organelles found in most eukaryotic cells – are known as the powerhouse of the cell⁶. A double mitochondria membrane comprising inner (IMM) and outer (OMM) mitochondrial membranes and the intermembrane space (IMS) surrounds a mitochondria matrix containing mitochondrial DNA, ribosomes, enzymes, and small molecules where a vast range of cellular processes take place. The IMM forms dynamic membrane invaginations known as cristae, where the primary mitochondrial process - oxidative phosphorylation or OXPHOS - takes place (**Figure 1.1**)⁶.

Dynamic alterations to mitochondrial morphology due to fusion and fission processes strongly associate with bioenergetics and mitochondrial function and respond to energetic demands and alterations in metabolic flux^{7,8}. Mitochondrial biogenesis and fusion occur when cells suffer an increased need for energy, whereas fission and mitophagy occur when such a demand decreases⁹. These processes occur thanks to a nuclear-mitochondria crosstalk mechanism that allows the nucleus to receive the mitochondrial stress signals and generate nuclear stress responses. Overall, the mitochondrial takes on a wide range of morphologies- from small spheres with short tubules to more oval shapes with long tubules - depending on the cell type and the metabolic and energetic state. For example, mitochondria present as interconnected tubular networks in endothelial cells, long filaments in fibroblasts, and uniform spheres in hepatocytes¹⁰. Consequently, their size varies between cell types within a range of 0.5-3 μ m. The number of mitochondria also depends on cell type⁶ and cell state¹¹; for example, hepatocytes possess a relatively high number of mitochondria (1,000-4,000 per cell)¹² whereas cells in tissues with lower energy demand (e.g., the lungs) possess fewer mitochondria¹³.

Mitochondria play critical roles in various cellular processes, including OXPHOS, fatty acid oxidation, the urea and tricarboxylic acid (TCA) cycles, gluconeogenesis, and ketogenesis¹⁴. While adenosine triphosphate (ATP) generation by OXPHOS represents the primary function of mitochondria, they also provide building blocks for cell replication, control redox balance, participate in apoptosis and function as a signaling platform¹⁴. Therefore, normal cellular physiological function requires critical control of mitochondrial-associated activities. Mitochondria also participate in additional cellular processes, such as amino acid and lipid metabolism, calcium homeostasis, and thermogenesis¹⁴. **Figure 1.1** summarizes the cellular functions of mitochondria.

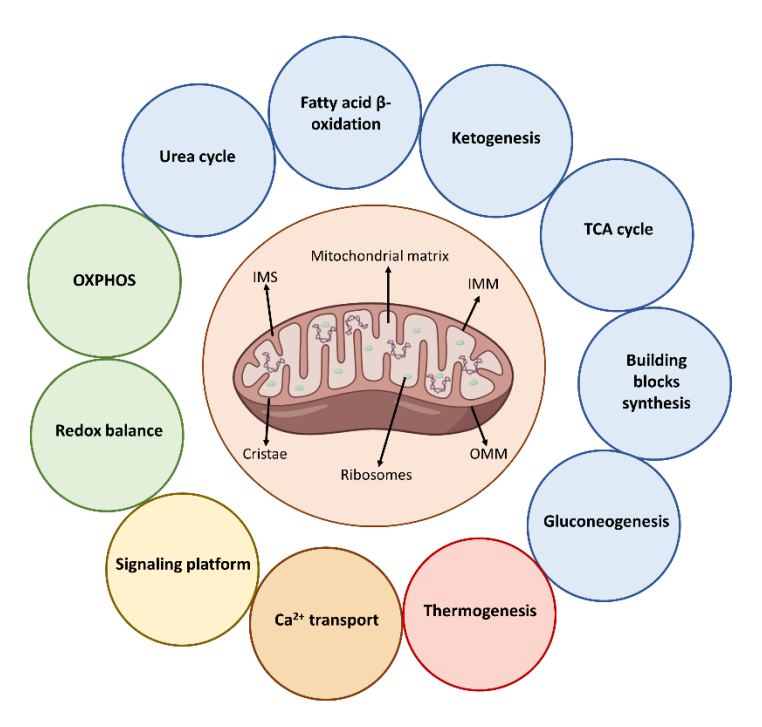


Figure 1.1. Structure and cellular functions of mitochondria. IMM = inner mitochondrial membrane; IMS = intermembrane space; OMM = outer mitochondrial membrane; OXPHOS = oxidative phosphorylation; TCA = tricarboxylic acid.

The generation of ATP by OXPHOS through the electron transport chain (ETC) provides the energy required for almost all cellular processes. Mitochondrial substrates such as pyruvate, amino acids, and products of the oxidation of fatty acids enter the TCA cycle and maintain the reduced state of the NADH/NAD+ and FADH2/FAD. Electrons from NADH and FADH2 become transferred to an electron acceptor until they reach an oxygen molecule, the most electronegative and final acceptor in the chain. This electron transport generates energy that triggers a protein gradient across the mitochondrial membrane, resulting in the electrical polarization of the mitochondrial membrane - the mitochondrial membrane potential (MMP that powers complex V (ATP synthase) to catalyze ATP formation¹⁵. These processes - known as OXPHOS in eukaryotes - involve a family of five protein complexes (Complex I-V) and two electron carriers (coenzyme Q₁₀ and cytochrome c)^{15,16}. OXPHOS displays greater efficiency than glycolysis (the other primary energy production approach in cells), with OXPHOS producing thirty-six ATP molecules and glycolysis producing only two¹⁷. Notably, glycolysis more rapidly generates ATP than OXPHOS; therefore, cancer cells stimulate glycolysis to support their rapid growth/proliferation, although OXPHOS produces metabolites required for tumor progression $^{17}.\,$ Cells prioritize glycolysis or OXPHOS for energy production depending on cell subtype, healthy/pathologic status, and energetic demands.

The mitochondrial respiration chain inevitably generates unpaired electrons from complexes I, II, and III that interact with oxygen to form reactive oxygen species (ROS) in the IMM. The superoxide anion (O_2^{-1}) - the primary ROS in mitochondria – reacts with protons to form hydroxide peroxide (H_2O_2) or hydroxyl radicals $(OH^{-1})^{18}$. Mitochondria represent the primary source of ROS in cells, which, at lower levels, act as signaling molecules (Figure 1.2).

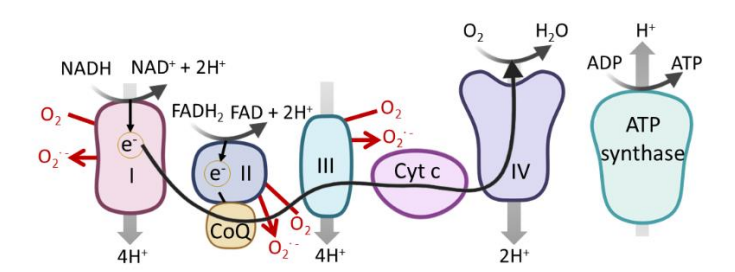


Figure 1.2. The mitochondrial respiration chain comprises complexes I-V, coenzyme Q_{10} (CoQ), and cytochrome c (Cyt c). ADP = adenosine diphosphate; ATP = adenosine triphosphate; NAD⁺ = nicotinamide adenine dinucleotide; FAD = flavin adenine dinucleotide. Adapted from Gorman et al., 2016¹⁶.

The TCA cycle, which involves a set of reactions supporting energy production, represents the main pathway within mitochondria. The oxidative decarboxylation of pyruvate, which derives from the β -oxidation of fatty acids or the catabolism of amino acids such as tyrosine, phenylalanine, leucine, and tryptophan, generates acetyl-coenzyme A (acetyl-CoA) as the primary substrate of the TCA cycle²⁰. Acetyl-CoA becomes converted into citrate, which initiates the TCA cycle and generates TCA cycle intermediates - aconitate, isocitrate, α-ketoglutarate, succinyl-CoA, succinate, fumarate, and malate²¹ (Figure 1.3). These intermediates feed other metabolic pathways or participate in the synthesis of macromolecules in a process called cataplerosis²². For example, citrate represents the carbon source for fatty acids, cholesterol, and ketone bodies, while α -ketoglutarate becomes converted into glutamate for the synthesis of amino acids and nucleotides, and oxaloacetate becomes converted to i) aspartate to serve as a substrate for the urea cycle and protein and nucleotide biosynthesis^{21,22} or ii) phosphoenolpyruvate (PEP) for transport to the cytosol and use in gluconeogenesis²². Reactions that generate TCA cycle intermediates occur during anaplerosis to maintain TCA cycle activity, while cataplerotic reactions occur. Pyruvate undergoes carboxylation to form oxaloacetate; glutamate (and arginine, histidine, and proline) undergo conversion into α -ketoglutarate; valine, leucine, isoleucine, and methionine participate in succinyl-CoA synthesis; aspartate undergoes conversion into oxaloacetate or fumarate; while phenylalanine and tyrosine undergo conversion into fumarate^{21,23}. Regarding the signaling functions of mitochondria, TCA cycle intermediates control DNA methylation, chromatin modifications, and post-translational protein modifications²⁴; moreover, the TCA cycle also provides NADH and FADH₂ for mitochondrial

respiration¹⁶.

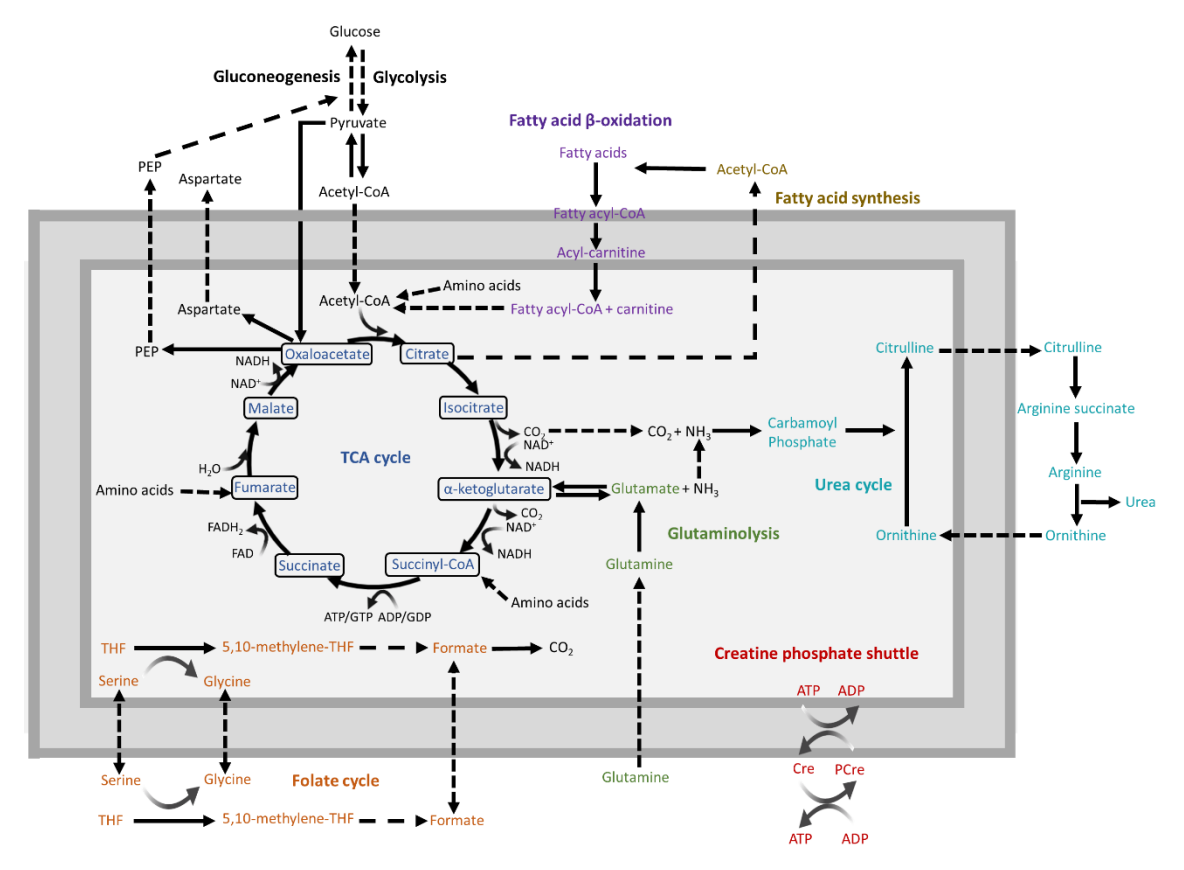


Figure 1.3. Representation of the central mitochondrial metabolic pathways that include the TCA cycle, glutaminolysis, folate cycle, urea cycle, fatty acid synthesis, β-oxidation of fatty acids, and the creatine phosphate shuttle. ADP = adenosine diphosphate; ATP = adenosine triphosphate; Cre = creatine; CoA = coenzyme A; FAD = flavin adenine dinucleotide; GDP = guanosine diphosphate; GTP = guanosine triphosphate; NAD⁺ = nicotinamide adenine dinucleotide; PCre = phosphocreatine; PEP = phosphoenolpyruvate; THF = tetrahydrofolate.

Glutaminolysis, which involves the conversion of glutamine to glutamate (with the release of ammonia release), also occurs in mitochondria (**Figure 1.3**). Glutamine becomes transported from the cytosol through the IMM using the SLC1A5 (Solute Carrier Family 1, member 5) neutral amino acid transporter, with the formed glutamate becoming a substrate for mitochondrial anaplerosis²⁵. Upregulated glutaminolysis occurs in many cancer types, which provides a nitrogen source to proliferating cells for amino acid synthesis and favors reductive carboxylation for lipid production²⁶. The formed ammonia can react with carbon dioxide to form carbamoyl phosphate, which allows the conversion of ornithine to citrulline in mitochondria²⁷. Citrulline then becomes transported to the cytosol to complete the urea cycle (**Figure 1.3**).

The creatine phosphate shuttle, which takes place inside and outside mitochondria, acts as an energy transporter from the mitochondria to the cytosol (Figure 1.3). The ATP synthesized

within mitochondria donates a phosphate group to creatine to form phosphocreatine, which then undergoes conversion to creatine while generating ATP in the cytosol²⁸.

The folate cycle involves the activation and transference of one-carbon units to support biological processes that occur partially in mitochondria (**Figure 1.3**). The folate cycle pathway remains critical for purine and thymidine monophosphate biosynthesis for methionine regeneration and mitochondrial protein translation²⁹. One-carbon donors include serine, glycine, and choline degradation products (dimethylglycine and methylglycine). Initially, serine undergoes conversion into glycine, transferring a one-carbon unit to mitochondrial tetrahydrofolate (THF) and forming 5,10-methylene-THF. This compound plays a crucial role in mitochondrial translation. Subsequently, 5,10-methylene-THF transforms into 10-formyl-THF within the mitochondria, initiating mitochondrial translation through the synthesis of formyl-methionine tRNA. Finally, 10-formyl-THF undergoes hydrolysis, producing formate. This formate can be transported back to the cytosol or undergo complete oxidation to CO₂ for elimination ²⁹.

Mitochondria also support the synthesis and β -oxidation of fatty acids (**Figure 1.3**). Citrate, generated in the TCA cycle, becomes transported to the cytosol or formed from cytosolic α -ketoglutarate and converted to acetyl-CoA, a substrate for *de novo* fatty acid synthesis³⁰. While studies have reported fatty acid synthesis inside mitochondria^{31–33}, this remains poorly characterized. Levels of some lipids become determined by the activity of the fatty acid β -oxidation³³, and β -oxidation functions seem determinant for ETC activity³².

 β -oxidation of fatty acids begins with fatty acid activation by acyl-CoA synthases in the OMM to form fatty acyl-CoA, which becomes transported to the mitochondrial matrix thanks to carnitine²⁰. Acyl-CoA reacts with carnitine in the IMS to form acyl-carnitines that undergo transport through carnitine acyltransferases to the mitochondrial matrix, where fatty acyl-CoA becomes released from carnitine ready for β -oxidation. Acyl-CoA is oxidized at the β -carbon to form acetyl-CoA, which is then used, in mitochondria, as a TCA cycle substrate and, in the cytosol, for the formation of ketone bodies and cholesterol.

Apart from generating energy for the cell, mitochondria play additional roles, such as the Ca²⁺ transport, achieved with the Na⁺/Ca²⁺ exchanger thanks to the generated proton gradient³⁴. The intramitochondrial Ca²⁺ concentration controls the cellular metabolic rate, as Ca²⁺ regulates some TCA cycle dehydrogenases by controlling activity rates³⁵. The mitochondria respiratory chain also participates in signaling events required for the correct functioning of cells. For example, cytochrome c becomes released from mitochondria upon activation of the caspase-

dependent apoptotic pathway while released ROS participates in protein thiol oxidation to induce gene expression²⁴.

The multifunctional nature of mitochondria, as the primary cell energy producer, a relevant metabolic hub, and the crosstalk between mitochondria and the nucleus and cytosol, makes mitochondria a determining factor in cell fate and function.

1.1.2. Mitochondrial Diseases

Mitochondria dysfunction relates to an impairment in OXPHOS caused by mutations in mitochondrial proteins encoded in both mtDNA (mitochondrial DNA) and nDNA (nuclear DNA) or other acquired defects, such as a caloric deficiency, dysfunction of the TCA cycle and folate cycle, lack of intermediates, and the accumulation of toxic substances^{16,36}.

Impaired mitochondrial respiration leads to mitochondrial depolarization, decreased ATP production³⁷, and increased ROS levels that lead to an altered redox state¹⁹. Increased ROS production occurs in the presence of an elevated proton motive force due to low ATP production, highly reduced coenzyme Q₁₀ levels, or a high NADH/NAD⁺ ratio¹⁹. Therefore, alterations to the MMP and ROS levels closely relate, associate with mitochondrial damage, and often precede cell death. Elevated ROS production results in irreversible damage to lipid membranes, nucleic acids, and proteins, leading to defects in mitochondria and the cell, thus triggering mitochondrial disease¹⁶. Fortunately, mitochondria possess robust antioxidant mechanisms to remove ROS and prevent mitochondrial damage to mtDNA, proteins, and lipids³⁸. These mechanisms include a significant amount of glutathione (GSH) and antioxidants to control oxidative stress and maintain cell homeostasis³⁹.

As MMP represents the driving force for Ca²⁺ transport, mitochondria depolarization leads to Ca²⁺ accumulation within the organelle³⁵. Ca²⁺ accumulation leads to the activation of the mitochondrial permeability transition pore (mPTP) in the IMM, the swelling of mitochondria, and the release of mitochondrial contents into the cytosol (e.g., cytochrome c), which then activates the caspase pathway and prompts the apoptotic cell death. mPTP opening allows the release of TCA cycle intermediates from dysfunctional mitochondria, which then may find use in other cellular processes, causing an imbalance in cellular metabolic routes⁴⁰. Moreover, increasing evidence has revealed that TCA cycle metabolites regulate immune responses⁴⁰.

To summarize, alterations to mitochondrial function and structure lead to decreased ATP production, an altered redox state due to increased ROS generation, Ca²⁺ accumulation, and mPTP collapse, leading to cell death.

Mitochondrial diseases represent a group of heterogeneous pathologies that can affect any tissue/organ during a person's lifetime. The most energy-dependent tissues fail when energy production decreases, resulting in degenerative diseases of the nervous system, heart, kidney, and muscles³⁶. Moreover, the abnormal caloric metabolism in the mitochondria leads to metabolic and endocrine deregulation and diseases such as diabetes, obesity, and cardiovascular disease³⁶. A range of studies have linked mitochondrial dysfunction to neurodegenerative diseases (Alzheimer's, Parkinson's, and Huntington's diseases)⁴¹, sclerosis³⁴, cardiomyopathy⁴², and multi-organ failure in sepsis⁴³. The accumulation of mtDNA mutations, which cause impairments to the respiratory chain and increased ROS production, has been linked to the aging process and age-related diseases^{44,45}.

Mitochondrial dysfunction also occurs in cancer cells⁴⁶. Indeed, Otto Warburg reported the "Warburg effect" in the 1930s, which describes how cancer cells obtain energy through anaerobic glycolysis due to low oxygen levels, which cause an impairment to the mitochondrial respiratory chain⁴⁷. Moreover, membrane depolarization also represents another characteristic of cancer cell mitochondria⁴⁶.

The clinical heterogeneity observed in mitochondrial diseases derives from the different ratios of mutations in mtDNA and nDNA, the tissues/organs where mitochondria dysfunction appears, and the age at onset³⁶, and hinders diagnosis and disease management. Therefore, studying the mechanisms underlying mitochondrial disease represents a critical means of improving diagnosis and developing new mitochondrial-targeting therapies. In this context, this thesis aims to contribute to the development of new tools that support the evaluation of those mitochondrial mechanisms underpinning disease development and treatment response with a specific focus on breast cancer.

1.1.3. Breast Cancer

1.1.3.1. Breast Cancer Definition, Prevalence, and Molecular Subtypes

Breast cancer represents a group of diseases involving the development of malignant tumors within breast tissue that have the potential to metastasize and invade other tissues⁴⁸. While the appearance of new lumps in the mammary glands represents the most common breast cancer symptom, other symptoms include breast swelling, skin dimpling, and nipple retraction or discharge⁴⁹. Progression of breast cancer can lead to metastasis, which presents with symptoms such as bone pain, lymph node swelling, and yellow skin.

Breast cancer is the most frequently diagnosed tumor and the leading cause of cancer deaths in women worldwide⁵⁰. The year 2020 saw an estimated 2.3 million new cases of breast cancer (11.7% of all cases), with 685,000 deaths worldwide⁵⁰, and while advances in population screening, early treatment, and novel therapies have supported a steady decrease in breast cancer mortality^{51,52}, breast cancer cases continue to rise each year⁵³.

Breast cancer screening currently relies on mammography, a non-invasive strategy primarily performed in women between 50 and 69 years of age that has prompted a reduction in breast cancer mortality⁵⁴. Nevertheless, this approach suffers from several limitations, including false-positive reporting and overdiagnosis^{55,56}. Ultrasound, magnetic resonance imaging, and computed tomography can overcome these problems thanks to their high sensitivity; however, the elevated costs associated with these tools make this approach less accessible.

Tumor size, location, lymph node involvement, and metastasis progression define different stages of breast cancer development (**Table 1.1**)⁵⁷. The breast cancer stage at disease diagnosis and the patient's health status will determine the breast cancer outcome.

Table 1.1. Description of the breast cancer development stages according to tumor size (T), lymph nodes spread (N), and metastasis (M).

T1	<2 cm	T2	2-5 cm	Т3	>5 cm	T4	Tumor extends to the skin/chest wall
NO	No spread to lymph nodes	N1	Spread to one to three axillary lymph nodes/ cancer found in internal mammary lymph nodes	N2	Spread to four to nine axillary lymph nodes/ cancer enlarges the internal mammary lymph nodes	N3	Spread to ten or more axillary lymph nodes/ infraclavicular or supraclavicular nodes/ any axillary lymph node and internal mammary lymph nodes
MO	No distant	M1	Distant metastasis				

Adapted from the American Cancer Society⁵⁷

Former classifications of breast cancer tumors employed tumor size, histological grade, immunohistochemistry of estrogen and progesterone receptors (ER/PR) status, amplification of human epidermal growth factor receptor 2 (HER2), and status of Kiel 67 (Ki67) proliferation marker⁵⁸. The addition of gene expression profiling (to detect mutations in oncogenes such as PI3KCA (phosphatidylinositol-4,5-bisphosphate 3-kinase catalytic subunit alpha) and HER2 or a loss of function mutations in tumor suppressor genes such as BRCA1/2 (breast cancer type 1/2 susceptibility protein)) added to these molecular features has resulted in the current classification⁵⁹. Five clinical subtypes have been accepted for patient stratification (**Figure 1.4**).

• Luminal A - this most frequent breast cancer subtype (60-70%) is defined by high ER and PR and low HER2 and Ki67 expression; patients have a good prognosis due to the low growth rate and favorable treatment response.

- Luminal B characterized by ER, PR, and Ki67 expression with or without HER2 expression (HER2+ or HER2-); mainly affects younger patients and suffers from more rapid tumor growth.
- HER2-enriched defined by high HER2 and Ki67 expression and the lack of ER and PR expression; characterized by more aggressive progression and a poorer prognosis than the Luminal A and B subtypes.
- Triple negative breast cancer (TNBC) characterized by the absence of ER, PR, and HER2 expression with high Ki67 expression; a less frequent subtype (10-15%) with the poorest prognosis due to high tumor growth rate, aggressive behavior, and capacity to metastasize.

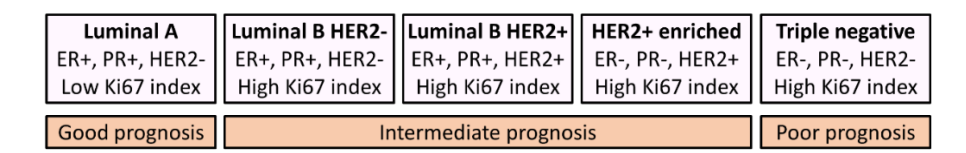


Figure 1.4. Breast cancer subtypes. Adapted from Boix et al., 2021⁵⁹.

While each breast cancer subtype possesses a characteristic biological profile, prognosis, and treatment strategy^{60,61}, current diagnostic systems do not accurately reflect breast cancer subtype heterogeneity among patients⁶². Thus, enormous efforts have been devoted to classifying heterogeneous breast subtypes into molecular subtypes that guide treatment decisions^{63–65}. In this context, multi-omics approaches (genomics, transcriptomics, proteomics, and metabolomics) have provided a more accurate understanding of breast cancer and its subclassification^{66,67}.

1.1.3.2. Triple Negative Breast Cancer

Disease aggressiveness, tumor heterogeneity, molecular complexity, and the low detection rate make TNBC the breast cancer subtype with the worst prognosis⁶⁸. TNBC typically affects young patients (<50 years old) and has more prevalence in the African American population, with most TNBC tumors originating in the milk ducts and developing metastasis^{68,69}.

Several prognostic markers help predict disease outcomes, classify TNBC into further subtypes, and select the most suitable therapeutic approach. Prognostic markers include Ki67 status, mutations in *TP53* (tumor protein p53) and BRCA1/2 (breast cancer susceptibility genes ½), androgen receptor (AR) status, cathepsin D level, number of tumor-infiltrating lymphocytes, and the expression of epidermal growth factor receptor (EGFR) and vascular endothelial growth factor (VEGF)⁷⁰.

The molecular heterogeneity observed in TNBC patients prompted the clinical classification of TNBC into six transcriptional subtypes: basal-like 1 and 2 (BL1 and BL2), immunomodulatory (IM), Luminal androgen receptor (LAR), mesenchymal (M), and mesenchymal stem-like (MSL)⁶³. **Table 1.2** summarizes the main characteristics of each TNBC subtype.

Table 1.2. TNBC subtypes and their main characteristics

TNBC subtype	Involved pathways					
BL1	Cell proliferation, cell cycle, and DNA repair					
BL2	Growth factor signaling, glycolysis, and gluconeogenesis					
IM	Best prognosis Immune cell signaling and STAT* transcription factor-mediated pathways					
LAR	Hormonally regulated pathways (steroid synthesis, porphyrin metabolism, and androgen/estrogen metabolism)					
М	Epithelial-mesenchymal transition, cell motility and differentiation, and extracellular receptor interactions					
MSL	M subtype with the addition of growth factor signaling pathways					

^{*}STAT = Signal transducer and activator of transcription. Adapted from Lehman et al., 2016⁶³

Although several studies have employed this TNBC classification, Lehmann et al. discovered that tumor-infiltrating lymphocytes and tumor-associated stromal cells contributed to the immunomodulatory (IM) and mesenchymal stem-like (MSL) subtypes⁶³; therefore, they redefined TNBC into only four subtypes (BL1, BL2, LAR, and M).

This work uses the MDA-MB-231 cell line, corresponding to a mesenchymal TNBC subtype.

1.1.3.3. Breast Cancer Metastasis

Breast cancer cells can spread to other sites in the body and develop metastasis, the primary breast cancer complication and the major cause of breast cancer death. Breast cancer metastatic sites include lymph nodes, bone, liver, lungs, brain, and peritoneum⁷¹; however, each breast cancer subtype possesses preferential colonization sites - Luminal A and B subtypes tend to metastasize to the bone, while visceral metastasis (lungs, brain, and liver) predominate in TNBC and HER2-enriched subtypes^{63,72}. In TNBC, the survival rate in patients correlates with the primary metastatic site, with distant brain metastasis the poorest survival indicator, followed by liver, pleura, bone, and lung⁷³.

The metastatic process involves several steps - invasion, intravasation to the lymphatic nodes/blood, circulation, extravasation, and colonization (**Figure 1.5**) - that can recommence from the secondary tumor site to reach other tissues and develop a secondary metastatic site.

Invasion begins with the expression of epithelial-mesenchymal transition (EMT)-inducing transcriptional factors in epithelial cells that cause loss of cell adhesion and cell depolarization,

basement membrane degradation, and cell motility and invasive capabilities (mesenchymal characteristics)⁷⁴. To highlight, TNBC presents enhanced EMT compared to other breast cancer subtypes, which drives early and distant metastasis⁶³.

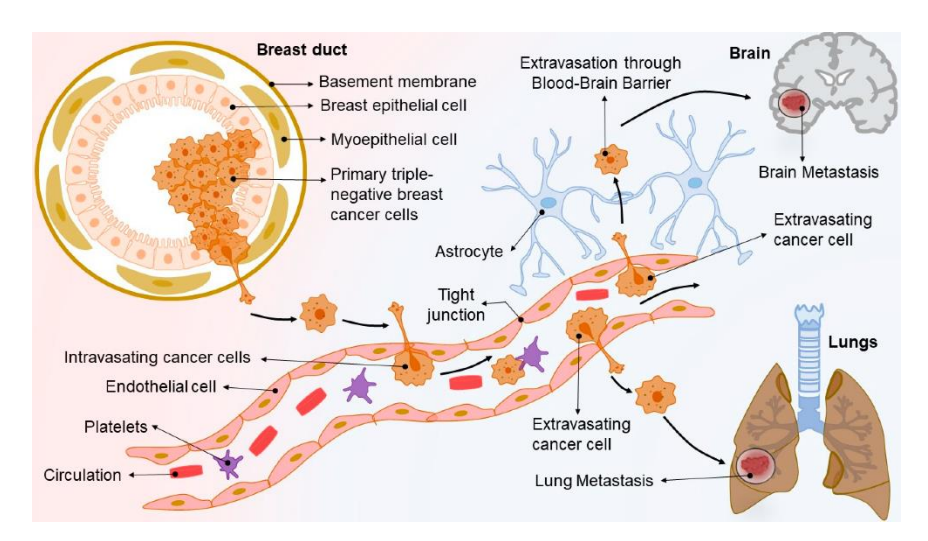


Figure 1.5. Schematic representation of TNBC metastasis spread to brain and lungs. Adapted from Chaudhuri et al., 2022⁷⁵

During intravasation into the lymph nodes (lymphatic intravasation) and blood vessels (hematogenous intravasation), cells acquire migrative capacities by extending cell membrane protrusions that allow single or collective cell migration⁷⁶. In the case of lymphatic intravasation, lymph nodes eventually drain to blood vessels, allowing tumor cells to reach blood circulation⁷⁷.

In the blood, circulating tumor cells face multiple challenges (e.g., immune system attack and mechanical injuries due to hemodynamic shear forces) to survive, which may stop them from reaching their final destination⁷⁸. The surviving circulating tumor cells become deposited in low-flow blood vessel regions, where they interact with the epithelium by weak interactions⁷⁹. Endothelial cells express selectins in response to leukocytes and cytokines secreted by cancer cells, which creates a bridge between tumor cells and endothelial cells. The expression of adhesion proteins by tumor cells allows stable adhesion to the endothelium and enables the extravasation of tumor cells across the endothelium (transendothelial migration).

Colonization - the final step of metastasis - involves adapting extravasated tumor cells to the new environment and forming a secondary tumor⁸⁰. Tumor cells remain attached to the abluminal side of the capillary after extravasation, ensuring a blood supply and inducing the formation of micrometastasis^{80,81}. At this stage, cancer cells can enter dormancy due to i) the presence of antiproliferative signals/lack of proliferative signals in the host tissue (cellular dormancy), ii) an immune system response to cancer cells (immune-mediated dormancy), or iii) new blood vessel formation that supports tumor cell migration (angiogenic dormancy)⁸⁰. The

dormant state can last for short or extended periods (depending on the cell type) before cancer cells proliferate again. Authors have reported that activation of dormant cancer cells takes place thanks to the downregulated expression of immune cell-recognized molecules and the favorable host microenvironment thanks to the expression of pro-metastatic signaling molecules (e.g., extracellular signal-regulated kinase 1 (ERK1/2))⁸⁰.

1.1.3.4. Current Breast Cancer Treatment

Breast cancer subtype and disease stage dictate the therapeutic strategy employed for each patient. Generally, patients with non-metastatic breast tumors receive total mastectomy or resection of the breast tumor, together with postoperative radiation and removal of the axillary lymph nodes⁸². Moreover, patients are typically prescribed neoadjuvant therapy for tumor reduction before surgery or adjuvant therapy for elevated risk of recurrence after surgery. Treatment approaches for metastatic breast cancer have the aim of symptom palliation (surgery and radiation), although no treatment strategy can currently overcome metastasis⁸².

Therapeutic approaches for Luminal A and B subtypes include endocrine therapies, which inhibit the activation of estrogen-dependent signaling pathways that promote cell proliferation⁸². The ER inhibitor tamoxifen represents the primary endocrine treatment, which is typically combined with aromatase inhibitors to reduce estrogen levels in post-menopausal women and gonadotropin-releasing hormone analogs to reduce sex hormone production in pre-menopausal women^{71,82}. In metastatic stages, the removal of ovaries significantly reduces estrogen levels in pre-menopausal women; moreover, the treatment also involves endocrine therapy, including non-steroidal aromatase inhibitors (letrozole and anastrozole). Other treatments include steroidal aromatase inhibitors (e.g., exemestane), cyclin-dependent kinase 4 and 6 (CDK4/6) inhibitors (e.g., palbociclib) combined ER dimerization inhibitors (e.g., fulvestrant), and mTOR inhibitors (e.g., everolimus) combined with exemestane or fulvestrant^{71,82}. Treatment of the Luminal B subtype with high HER2 expression combines endocrine therapy and chemotherapy with HER2-targeted therapy⁷¹.

Trastuzumab (a recombinant humanized monoclonal antibody targeting HER2) combined with chemotherapeutic treatment (taxanes) represents the primary therapy used to treat the HER2+ subtype⁸³. Treatment in metastatic stages includes trastuzumab with pertuzumab (another humanized monoclonal antibody targeting the HER2) and chemotherapy. Alternatively, trastuzumab emtansine (an antibody-drug conjugate) and combinations of trastuzumab and HER2 tyrosine kinase inhibitors (e.g., lapatinib, neratinib) can be applied to treat the metastatic HER2+ subtype⁸⁴.

1.1.3.4.1. Triple Negative Breast Cancer Treatment

The therapeutic approaches used for TNBC treatment involve conventional chemotherapeutics due to the absence of ER, PR, and HER2 expression. In the early stages of development, TNBC treatment involves surgical removal followed by radiation and adjuvant chemotherapy; however, the treatment of larger tumors involves neoadjuvant chemotherapy before surgery⁸⁵. In addition to conventional chemotherapy, therapeutic options based on targeted treatment (poly (ADP-ribose) polymerase (PARP) inhibitors, AR inhibitors, EGFR inhibitors, and VEGF inhibitors) and immunotherapy (immune checkpoint inhibitors, antibody-drug conjugates, and phosphatidylinositol-4,5-bisphosphate 3-kinase/protein kinase B/mammalian target of rapamycin (PI3K/AKT/mTOR) inhibitors) have been evaluated⁷⁰.

Chemotherapy used for TNBC treatment typically includes anthracyclines and taxanes. Anthracyclines such as doxorubicin (DOX), epirubicin, and idarubicin⁷⁰ disrupt DNA repair, which induces cancer cell death and activates the immune system. Taxanes such as paclitaxel, docetaxel, and cabazitaxel disrupt the mitotic spindle and slippage and inhibit angiogenesis. While docetaxel represents the most used taxane for cancer treatment⁸⁶, paclitaxel use is widespread due to specific, saturable, and reversible binding to microtubules, inhibiting mitosis. Platinum salts represent additional chemotherapeutic agents employed to treat TNBC via the induction of DNA damage; therefore, these therapeutic approaches represent important strategies in cancer subtypes with impaired DNA repair mechanisms, such as TNBC, especially those with germline BRCA mutations⁷⁰. The combination of platinum-based drugs with anthracyclines and taxanes improves the pathological response but at the cost of increased off-target toxic effects.

PARP inhibitors have found use in patients with BRCA mutations. PARP catalyzes the transfer of ADP-ribose from NAD⁺ to proteins and participates in DNA repair; PARP inhibition causes double-strand breaks, which can undergo repair by homologous recombinant repair. As BRCA1/2 genes participate in homologous recombinant repair, mutations in BRCA 1/2 make PARP inhibition a robust approach to inducing cancer cell death⁷⁰. The United States Food and Drug Administration (FDA)-approved PARP inhibitors include olaparib, niraparib, rucaparib, veliparib, and talazoparib.

While lacking ER, PR, and HER2, TNBC cells still express hormone receptors such as AR, which represent nuclear hormone transcription factors that participate in cell proliferation, invasion, migration, and apoptosis in TNBC⁸⁷; therefore, **AR inhibitors** may represent an efficient therapeutic approach for AR-expressing TNBC patients. AR inhibitors have been assessed in

phase II clinical trials; for example, abiraterone acetate combined with prednisone⁸⁸ and enzalutamide⁸⁹ demonstrated effectiveness in AR-expressing TNBC patients.

High expression levels of EGFR - a tyrosine kinase receptor that regulates proliferation, differentiation, invasion, angiogenesis, and apoptosis - associates with poor prognosis in breast cancer⁹⁰; furthermore, *EGFR* overexpression occurs in TNBC⁷⁰. While **inhibiting EGFR** activity can occur via small interfering RNA (siRNA)-mediated downregulation of gene expression, poor penetrative abilities and instability in the blood led researchers to develop novel nanomedicine-based siRNA delivery strategies⁹¹. The EGFR inhibitor cetuximab combined with gefitinib and erlotinib represents another potent means of inhibiting tumor growth⁷⁰.

The tyrosine kinase receptor VEGFR induces cancer cell proliferation and the formation of new blood vessels during tumor formation. High VEGFR levels associate with poor prognosis in TNBC⁹²; thus, **VEGFR inhibitors** represent a potentially effective TNBC therapeutic approach. Bevacizumab - a monoclonal antibody that binds to VEGFR - has been approved by the FDA for TNBC treatment⁷⁰.

TNBC-associated alterations in the PI3K/AKT/mTOR pathway have prompted researchers to consider PI3K, AKT, and mTOR inhibition as a potential therapeutic strategy. For example, the AKT inhibitor ipatasertib in combination with paclitaxel can improve TNBC outcomes⁹³; the mTOR inhibitor everolimus represents a potential TNBC treatment⁹⁴; while other inhibitors of the PI3K/AKT/mTOR pathway, such as bupalisib (PI3K inhibitor), capivarsertib (AKT inhibitor), and temsirolimus (mTOR inhibitor), have been studied concerning TNBC treatment⁷⁰.

The elevated number of tumor-infiltrating lymphocytes, expression of programmed cell death protein 1 ligand (PD-L1), and genomic instability that increases the production of tumor-specific neoantigens recognized by the immune system make **immune checkpoint inhibitors** a robust choice for TNBC treatment⁹⁵. Antibodies that target PD-L1 include durvalumab, avelumab, and aterolizumab⁷⁰. PD-L1 interacts with programmed cell death protein 1 (PD-1) expressed by T-cells to inhibit immune responses; therefore, PD-1 inhibitors have been explored as a TNBC treatment⁹⁶. Monoclonal antibodies bind to PD-1, inhibit interaction with PD-L1, and promote immune responses that kill cancer cells⁷⁰. The PD-1 inhibitors nivolumab and pembrolizumab are currently under study for TNBC treatment^{18,97}. An additional T cell regulatory pathway involves cytotoxic T lymphocyte protein-4 (CTLA-4), which becomes upregulated during T cell activation and competes with the CD80/CD86 gene to inhibit the T cell activation pathway; therefore, CTLA-4 inhibition improves T cell activation and the immune responses to dispose of

cancer cells⁷⁰. Although CTLA-4 has been targeted as a therapeutic strategy for other cancer types⁹⁸, we currently lack approved CTLA-4 inhibitors for TNBC treatment.

Currently approved **nanomedicines** for breast cancer treatment include Doxil®, Myocet®, and Lipidox® (liposomal DOX), Abraxane® (albumin-bound paclitaxel), Lipusu® (liposomal paclitaxel) and Kadcyla® (antibody-trastuzumab conjugate). The paclitaxel-based micelles Nanoxel® (2006) and Genexol® (2007) also received FDA approval for metastatic breast cancer treatment. Also, the polymeric conjugate Neulasta® (PEGylated granulocyte colony-stimulating factor) is used to prevent chemotherapy-induced neutropenia^{99–101}. Specifically, for TNBC treatment, **antibody-drug conjugates** – a monoclonal antibody used to deliver drugs to a specific target - represent an additional promising tool. Antibody-drug conjugates can be administered alone or in combination, forming a component of more extensive nanomedicine alternatives such as micelles or liposomes⁷⁰. The FDA approved Sacituzumab govitecan (Trodelvy®), which combines the anti-Trop-2 antibody and the chemotherapeutic drug SN-38, an irinotecan metabolite, for metastatic TNBC in patients previously treated with other therapies¹⁰².

1.1.4. Alteration in Breast Cancer Metabolism: A Focus on Mitochondria

High energy demand for cell growth and proliferation characterize cancer cells; in this context, alterations to metabolic pathways such as glycolysis, glutaminolysis, and fatty acids synthesis supply this demand through a process known as metabolic reprogramming¹⁰³.

Even given the presence of tumor heterogeneity, malignancy involves standard features that promote metabolic reprogramming: stimulation of signaling pathways (e.g., PI3K/AKT/mTOR pathway), loss of tumor suppressors, and oncogene activation promotes cell proliferation and metabolic alterations¹⁰⁴.

Focusing on breast cancer, metabolic regulators include PI3K, MYC, ER, BRCA1, and TP53, in addition to other extrinsic regulators such as oxygen and nutrient availability, acidosis, and tumor interactions with the microenvironment¹⁰⁵.

Healthy cells oxidize glucose to produce pyruvate, which enters the TCA cycle and generates energetic molecules by OXPHOS. Glucose undergoes incomplete oxidation under hypoxic conditions, which favors lactate production, thereby avoiding mitochondrial respiration and producing less energy. Despite the low-efficiency energy production of this mechanism, cancer cells can produce lactate from glucose metabolism even in high oxygen conditions¹⁰⁶. The reliance on glycolysis instead of OXPHOS for energy production may relate to the influence of OXPHOS on activating the Bax and Bak apoptosis regulators¹⁰⁷. Therefore, cancer cells may

protect themselves from apoptotic cell death following the loss of OXPHOS activity. Moreover, cancer cells may use glycolysis to generate intermediates for other metabolic pathways that favor cell proliferation and tumor progression¹⁰³. For example, the NAD+ required in glycolysis for energy generation is produced during pyruvate-lactate conversion¹⁰⁸. Additionally, several cancer types display the upregulated expression of pyruvate kinase muscle isozyme (PKM2), which catalyzes the formation of pyruvate from PEP¹. PKM2 is a spliced formed of pyruvate kinase and possesses lower enzymatic capacity; therefore, PEP and other glycolytic intermediates may accumulate and find use in alternative anabolic pathways in cancer cells (e.g., glycogen, nucleotides, or amino acid synthesis). The pentose phosphate pathway, which involves nicotinamide adenine dinucleotide phosphate (NADPH) production to combat cancer cell oxidative stress, represents an alternative pathway for metabolizing glucose¹.

Despite the general belief that cancer cells switch their metabolic flux to a more glycolytic-dependent metabolism due to impaired mitochondrial respiration, many studies have reported that specific breast cancer subtypes rely on OXPHOS for energy production^{109,110}. Indeed, Shiratori et al. demonstrated the importance of OXPHOS in cancer cell growth and tumor progression¹⁷; however, the formation of the metabolites required for tumor progression (instead of ATP production) may represent the primary function of OXPHOS in cancer cells. For example, aspartate produced by the TCA cycle aids purine and pyrimidine synthesis. In a 4T1 breast cancer mouse model, Bajzikova et al. demonstrated the essential nature of pyrimidine synthesis – but not ATP generation - for tumor growth¹¹¹. Overall, tumor metabolic heterogeneity occurs between breast cancer subtypes (inter-tumor) or cell populations within the same tumor (intra-tumor)¹¹².

As another example, Lunetti et al. reported metabolic heterogeneity when studying Luminal A (MCF-7 cell line) and TNBC subtypes (MDA-MB-231 cell line)¹⁰⁹ (**Figure 1.6**). The authors discovered that MCF-7 cells depended more on mitochondrial respiration, while MDA-MB-231 cells mainly relied on glycolysis for energy production¹⁰⁹. MCF-7 cells displayed increased monocarboxylate transporter 1 (MCT1) levels to import lactate from the tumor microenvironment due to low lactate production (reduced lactate dehydrogenase (LDH) expression) and increased expression of OXPHOS complexes (complex I, II, V) compared to MDA-MB-231 cells. Meanwhile, MDA-MB-231 cells displayed elevated levels of NADH, which may inhibit the activity of pyruvate dehydrogenase (PDH). PDH catalyzes the conversion of pyruvate to acetyl-CoA; therefore, MDA-MB-231 cells convert pyruvate to lactate (increased LDH activity) instead of entering the TCA cycle. Lactate then undergoes transport out of the cell by monocarboxylate transporter 4 (MCT4), which MCF-7 cells do not express. Finally, the authors

observed an increased mitochondrial/glycolytic ATP ratio in MCF-7 cells compared to MDA-MB-231 cells.

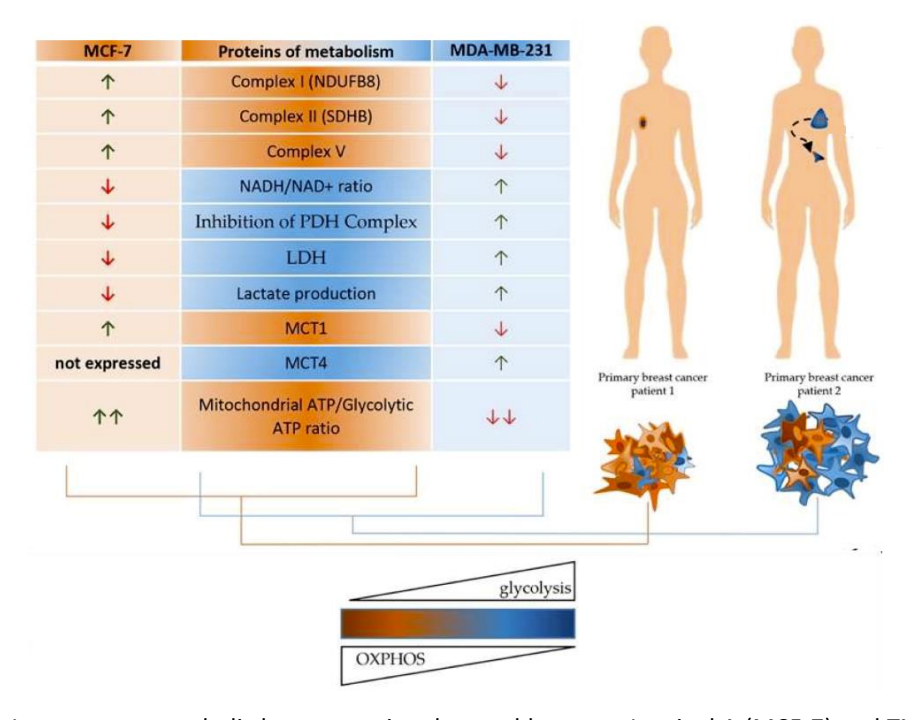


Figure 1.6. Intra-tumor metabolic heterogeneity observed between Luminal A (MCF-7) and TNBC (MDA-MB-231) subtypes. ATP = adenosine triphosphate; LDH = lactate dehydrogenase; NAD+ = nicotinamide adenine diphosphate; NDUFB8 = NADH:Ubiquinone Oxidoreductase Subunit B8; MCT1/4 = monocarboxylate transporter ¼; OXPHOS = oxidative phosphorylation; PDH = pyruvate dehydrogenase; SDHB = succinate dehydrogenase protein complex. Adapted from Lunetti et al., 2019 and Avagliano et al., 2019^{109,112}.

Related to this, Lyons et al. demonstrated that, in MCF-7 cells, the insulin-like growth factor (IGF)/PI3K pathway increased mitochondrial biogenesis by increasing the mitochondrial pool and OXPHOS activity while degrading damaged mitochondria¹¹³.

While distinct metabolic phenotypes may occur in each breast cancer subtype, the role of mitochondrial metabolism in breast cancer invasion remains controversial. A metabolomic study in a non-metastatic breast cancer mouse model (4T1) reported increased levels of glycolysis intermediates compared to healthy mice¹¹⁴; however, a 4T1 metastatic breast cancer mouse model reported increased mitochondrial activity, demonstrated by increased production of mitochondrial ATP mediated by the overexpression of peroxisome proliferator-activated receptor gamma coactivator-1 alpha (PGC-1 α)¹¹⁵. In breast cancer cells, high PGC-1 α expression has been correlated to lung and bone metastasis¹¹⁶, while enhanced glycolytic activity and decreased OXPHOS and glutaminolysis have been observed in liver metastatic breast cancer cells¹¹⁷.

Interestingly, breast cancer stem cells (BCSCs) have a higher dependence on mitochondrial function (high cell mitochondrial content and high mitochondrial ATP content) than glycolytic activity (low lactate production)¹¹⁸; furthermore, BCSCs also use more glucose than more differentiated progenitor cells, probably to supply other metabolic pathways and continue proliferating.

Glycolysis may be the primary choice for tumor progression in TNBC cells; however, they may rely on mitochondrial respiration to promote migration, invasion, and metastasis¹¹². In *in vivo* models, the considerable heterogeneity observed in tumor metabolism among breast cancer subtypes depending on the invasive capacity may derive from factors present in the tumor microenvironment. Overall, nutrient and oxygen availability may dictate the metabolic requirements of breast tumors¹¹². For example, in tumors that lie close to blood vessels with high oxygen supply, ATP can be produced via OXPHOS, and anabolic reactions may occur for substrate production¹¹². Moreover, collagen, the most abundant protein in the tumor microenvironment, modulates mitochondrial metabolic reprogramming in tumor cells¹¹⁹. 4T1 breast cancer cells grown in high-content collagen matrices displayed low glycolytic activity, decreased oxygen consumption, and preferred glutaminolysis as an energy supply mechanism¹¹⁹.

Therefore, glutamine represents an alternative source of energy for cancer cells. Glutamine becomes converted to glutamate and then to α -ketoglutarate in the TCA cycle and represents the primary source of anaplerotic carbon for TCA cycle reactions²¹. The expression of glutaminases, the enzymes that catalyze the conversion of glutamine to glutamate, has been correlated to tumor growth in xenograft models¹²⁰. In breast cancer, TP53 expression induces glutaminase-2 (GLS2) expression, which leads to increased α -ketoglutarate levels, TCA cycle activity, and mitochondrial respiration¹²¹. Wang et al. also reported increased glutamine metabolism in MCF-7 and 4T1 cells cultured under hypoxic conditions, ¹²². Moreover, reductive carboxylation of glutamine (citrate formation from α -ketoglutarate) represents the primary lipid synthesis route employed by many cancers, including breast cancer¹²³.

Min et al. reported that genes encoding for TCA cycle-associated enzymes contain mutations in several cancer types, which contributes to mitochondrial disruption¹. Disruption of the TCA cycle provokes acetyl-CoA accumulation, which becomes transported to the cytosol to synthesize fatty acids and cholesterol¹. Additionally, the authors reported the upregulated expression of fatty acid synthase in breast cancer¹.

Several studies have reported that fatty acids, as substrates for ATP and NADPH synthesis, represent the primary energy source in TNBC cells 124,125 ; however, this remains controversial as Wang et al. reported stimulated lipid metabolism in the HER2+ subtype when compared to the TNBC subtype, where glucose metabolism represented the primary source of energy 126 . The aim of fatty acid metabolism also depends on the breast cancer cell line. Balaban et al. reported that MCF-7 cells use fatty acids for β -oxidation, which generates acetyl-CoA to stimulate TCA cycle and, therefore, OXPHOS; however, triacyl glyceride synthesis represents the primary function of fatty acids in MDA-MB-231 cells 127 .

Changes to mitochondrial morphology also relate to metabolic alterations¹¹²; for example, mitochondrial fusion relates to increased ATP levels, while the absence of fusion processes causes OXPHOS disruption, ROS generation, and mtDNA depletion¹²⁸. In another study, Humphries et al. reported that mitochondrial fission inhibited migration, invasion, and metastasis in TNBC, while activation of fusion proteins overcame the fission-induced inhibition¹²⁹. Li et al. proved that fusion and fission processes depend on nutrient availability and metabolic demands in MDA-MB-231 and MCF-7 cells, which displayed mitochondrial elongation upon glucose deprivation¹³⁰. Cell metabolism adapted and switched from glycolysis to OXPHOS in these conditions to support cell survival.

Overall and independently of the breast cancer subtype, mitochondria metabolism remains essential for whole-cell metabolic reprogramming to allow adaptation to new stimuli and surroundings and continued proliferation and invasion. **Section 1.3.2** discusses further metabolic alterations in breast cancer detected by metabolomics.

1.1.5. Mitochondrial Modulation in Breast Cancer Treatment

Breast cancer treatment may involve induced alterations in mitochondria, such as morphological changes (fission and fusion processes), that trigger signaling pathways and alterations in mitochondrial metabolism. Mitochondrial modulation may be caused by mitochondrially-targeted therapeutics but also treatment approaches targeting other cell compartments, whose effects principally impact mitochondria.

Treatment of MDA-MB-231 TNBC cells with simvastatin, which targets cholesterol synthesis, decreased the expression of the B-cell lymphoma 2 (Bcl-2) antiapoptotic protein present in the OMM and increased caspase expression, indicating the activation of the mitochondrial apoptotic pathway¹³¹. Of note, many therapeutic strategies used to treat breast cancer cause cell death by mitochondrially-mediated apoptosis. Yuan et al. described mitochondrially-mediated apoptosis through decreased Bcl-2 and cytochrome c levels in mitochondria (with cytochrome c released

to the cytosol upon apoptosis activation) and increased Bcl-2-associated X (Bax) protein expression (which translocates to mitochondria from the cytosol)¹³². These protein alterations indicate mitochondrial apoptotic pathway activation, which is linked to apoptotic caspase pathway activation.

Mitochondria morphology also changes after breast cancer treatment; for example, Chen et al. demonstrated that the morphology of MCF7/ADR cell mitochondria – typically an ellipse shape, the characteristic cristae structure, and condensed matrix content – significantly altered (swelling and overall loss of typical morphology) upon treatment with mitochondrially-targeted hyaluronic acid protective shells encapsulating DOX and gold nanoparticles¹³³. In a recent study, Baek et al. reported that treatment of TNBC cells with DNA-damaging agents (DOX and carboplatin) caused increased mitochondrial content and elongation and glucose flux through the TCA cycle and OXPHOS, while taxanes (paclitaxel and docetaxel) decreased OXPHOS and mitochondrial elongation¹³⁴.

Focusing on mitochondrial OXPHOS and metabolic alterations, the treatment of PGC-1α-expressing breast cancer cells with an inhibitor of mitochondrial complex I (metformin) induced a metabolic switch by stimulating glycolysis for ATP production and using mitochondrial metabolites for anabolic reactions¹¹⁶. Lucantoni et al. observed decreased ATP levels and bioenergetics in the mitochondria of MCF-7 cells treated with a mitochondrial fission and complex I inhibitor (MDIVI-1)¹³⁵. Treatment of MCF-7 cells with free DOX and DOX conjugated to an N-(2-hydroxypropyl) methacrylamide (HPMA) copolymer showed decreased glycolysis and increased mitochondrial energy production compared to untreated cells¹³⁶. Interestingly, BT20 TNBC cells treated with palbociclib (10⁻⁷ M for 72 h) revealed significantly increased MMP and increased ROS levels¹³⁷, which provides evidence of mitochondrial alterations.

Given the vital role of mitochondria in cells, mitochondria typically display alterations after cell treatment; therefore, evaluating said mitochondrial alterations in treated cells may help to understand mechanisms of action with regard to cell death.

1.2. DESIGNING POLYMER THERAPEUTICS FOR BREAST CANCER TREATMENT

1.2.1. Polymer Therapeutics as Nanomedicines

The term Polymer therapeutics was coined by Prof Ruth Duncan in the 90's to define one of the first families of nanomedicines showing clinical benefit^{138,139}. These nano-sized medicines (5-100 nm in diameter) are considered as new chemical entities (NCEs) from an industrial standpoint, whose versatility in the synthetic chemistry used, the possibility of addition of biomimetic

features, and even the addition of bioresponsive units, make them one of the most versatile nanotechnologies currently available. Polymer therapeutics use water-soluble polymers that act as carriers for bioactive agents and/or can be considered as bioactive agents themselves¹³⁸. Therefore, this family encompasses polymeric drugs (polymers with inherent biological activity), polymer-drug conjugates, polymer-protein conjugates, polymeric micelles (with the active compound covalently linked to the polymer), and polyplexes (multi-component non-viral vectors for gene delivery)¹³⁹. The concept behind this group of polymeric nanosystems is evolving and new hybrid nanoconstructs formed by self-assembling strategies recently became part of the polymer therapeutics "family" of nanomedicines¹⁴⁰.

Polymer therapeutics have been approved by the FDA for the management of a number of distinct pathologies (**Table 1.3**), highlighting their already demonstrated clinical benefit with two of them being considered within the Top 10 US selling drugs, Copaxone® and Neulasta®141. There are a growing number of marketed products, in particular PEGylated and polymeric drugs, and the first generic products are also emerging, such as Copaxone®. However, only one polymer-drug conjugate has reached approval, and block copolymer micelle products (as covalent conjugates) have yet to enter routine clinical use¹⁴². Therefore, there are still room for improvements and much research is devoted towards it. Currently, polymer therapeutics represent 20% of FDA-approved nanomedicines, and many can be found in clinical phases¹⁴³.

Table 1.3. Clinically approved Polymer Therapeutics up to 2023^{99–101,144}

Name and approval year	Description	Application		
Adagen®, 1990	PEGylated* adenosine deaminase	Severe combined immunodeficiency		
SMANCS®, 1993	Styrene-co-maleic anhydride-neocarzinostatin conjugate	Hepatocellular carcinoma (Only approved in Japan)		
Oncaspar®, 1994	PEGylated L-asparagine amidohydrolase	Acute leukemia		
Copaxone®, 1996	Polypeptides of L-glutamic acid, L-alanine. L-tyrosine and L-lysine	Relapsing-remitting multiple sclerosis		
Renagel®, 1998	Phosphate binding drug	Hyperphosphatemia in chronic kidney disease		
PegIntron®, 2001 PEGylated interferon alpha-2b		Chronic hepatitis C		
Neulasta®, 2002	PEGylated granulocyte colony-stimulating factor	Neutropenia induced by chemotherapy		
Pegasys®, 2002	PEGylated interferon 2-a	Chronic hepatitis C		
Somavert®, 2003	PEGylated growth hormone receptor antagonist	Acromegaly		
Macugen®, 2004	PEGylated aptamer acting as a VEGF antagonist	Neovascular form of age-related macular degeneration		
Mircera®, 2007	PEGylated epoetin beta	Anemia in chronic renal disease		
Cimzia®, 2008	PEGylated monoclonal antibody against tumor necrosis factor-alpha	Crohn's disease		
Cholestagel®, 2009	Bile acid sequestrant	Hypercholesterolemia		
Krystexxa®, 2010	PEGylated uricase	Chronic gout		

Lonquex®, 2012	PEGylated granulocyte colony-stimulating factor	Neutropenia induced by chemotherapy
Lymphoseek®, 2013	Diethylenetriaminepentaacetic acid and mannose covalently linked to dextran	Radioactive diagnostic agent
Plegridy®, 2014	PEGylated interferon beta-1a	Multiple sclerosis
Movantik®, 2014	PEGylated naloxol	Opioid-induced constipation
Adynovate®, 2015	PEGylated coagulation factor VIII	Hemophilia A
Veltasa®, 2015	Cation-exchange polymer	Hyperkalemia
Peigebin®, 2016	PEGylated interferon beta-1a	Hemophilia B
Rebinyn®, 2017	Glyco-PEGylated coagulation factor IX	Hemophilia B
Zilretta®, 2017	PLGA hydrogel with triamcinolone acetonide	Knee osteoarthritis
Palynziq [®] , 2018	PEGylated phenylalanine ammonia-lyase	Phenylketonuria
Revcovi®, 2018	PEGylated adenosine deaminase	Severe combined immunodeficiency
Jivi®, 2018	PEGylated coagulation factor VIII	Hemophilia A
Asparlas®, 2018	PEGylated L-asparaginase isoenzyme II	Acute lymphocytic leukemia
Givosiran®, 2019	GNAc-siRNA* conjugate	Acute hepatic porphyria
Fulaimei®, 2019	PEGylated loxenatide	Diabetes type II
Ziextenzo®, 2019	PEGylated granulocyte colony-stimulating factor	Infection during chemotherapy
Esperoct®, 2019	PEGylated recombinant antihemophilic factor	Hemophilia A
Nyvepria®, 2020	PEGylated granulocyte colony-stimulating factor	Neutropenia associated with chemotherapy
Empaveli®, 2021	PEGylated pentadecapeptide	Paroxysmal nocturnal hemoglobinuria
Skytrofa®, 2021	PEGylated human growth hormone	Growth hormone deficiency
Besremi®, 2021	PEGylated interferon	Polycythemia vera
Fylnetra®, 2022	PEGylated granulocyte colony-stimulating factor	Neutropenia
Rolvedon®, 2022	PEGylated granulocyte colony-stimulating factor	Febrile neutropenia
SYFOVRE®, 2023	PEGylated pentadecapeptide	Geographic atrophy
Elfabrio®, 2023	PEGylated recombinant human GLA* enzyme	Fabry disease
Izervay®, 2023	PEGylated ribonucleic acid aptamer	Geographic atrophy

^{*}GLA = alpha-galactosidase A; GNAc-SiRNA = *N*-acetylgalactosamine short-interfering RNA; PEG = polyethylene glycol; PLGA = poly(lactic-co-glycolic acid)

Within the Polymer Therapeutics family in this thesis, we have focused on the use of Polymerdrug conjugates implementing a rational design towards the design of effective TNBC treatments and trying to understanding the differential features that triggers a greater pharmacological effect through mitochondrial metabolome modulation.

1.2.1.1. Polymer-Drug Conjugates

Therapeutic strategies based on the use of small drugs present with significant limitations such as poor water-solubility, side effects due to the use of non-targeted treatments, short circulation

times due to degradation and rapid clearance (renal excretion), and drug resistance development¹⁴⁵; however, conjugation of drugs to water-soluble polymers using bioresponsive linkers can overcome these limitations (**Figure 1.7**).

The rational design of a polymer-drug conjugate for systemic administration following Ringsdorf's traditional model¹⁴⁶, is based on a three component design: a water-soluble polymer, a bioresponsive linker and a bioactive agent. Nonetheless, due to polymer multivalency more than one compound can easily be introduced into the polymer main chain allowing a range of possibilities, including the incorporation of one or more bioactive agents at different loadings (polymer-based combination conjugates)¹⁴⁷, the use of bio-responsive linkers for the controlled release of the bioactive agent to specific tissues, and the possibility of adding imaging agents and targeting moieties for the controlled drug delivery in specific sites of cells¹³⁹.

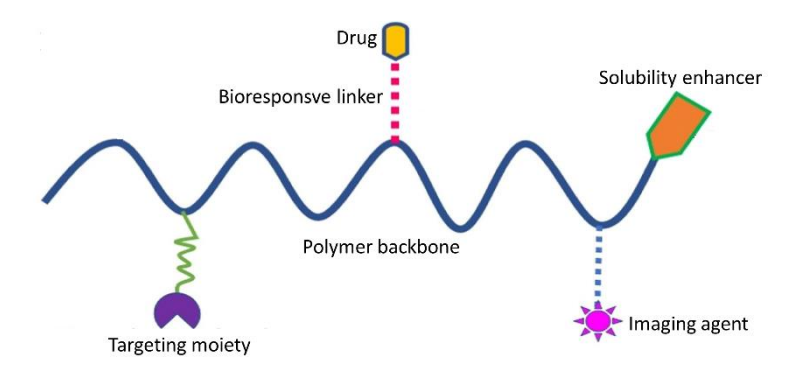


Figure 1.7. Basic polymer-drug conjugate composition defined by Ringsdorf in 1975. Adapted from Ringsdorf., 1975¹⁴⁶.

Polymer-drug conjugates modify the physicochemical properties and more importantly, the pharmacokinetics of small drugs once conjugated t a selected polymeric carrier, at cellular level as well as the whole organism level, in summary:

- Longer circulation times in bloodstream in comparison with parent small Mw drug^{142,148,149}
- ii) At whole organism level after systemic administration, passive targeting and accumulation in damaged tissues due to the enhanced permeability and retention effect (EPR) can be achieved 150,151
- iii) Enhanced treatment efficacy at the target site and non-toxic effects in off-target sites¹⁴⁹ due to the presence of bioresponsive linkers¹⁵² that allow specific drug release to the target site
- iv) Tailored drug loading and the possibility to conjugate synergistic drug combinations due to polymeric carrier multivalency¹⁴⁸

- v) Modified drug pharmacokinetic profiles, which enhance the drug therapeutic index and can bypass resistance mechanisms due to a lysosomotropic intracellular drug release mechanism after being uptaken by endocytosis^{148,149}
- vi) Controlled drug release at the target site in response to physiological conditions or specific stimulus due to engineered bioresponsive polymer-drug linkers¹⁴²
- vii) Enhanced therapeutic efficacy in several pathologies, including cancer as consequence for an improved pharmacokinetics in comparison with the free parent drug¹⁵³

1.2.1.2. Polymer-drug conjugates: from Patient Administration to the Final Target Site

Intravenous **administration** represents the preferred administration route for polymer-drug conjugates if systemic administration is seek, thereby avoiding crossing significant barriers to reach the bloodstream that could cause a reduction in blood bioavailability (as in the case of oral administration)^{154,155}. Alternative routes for polymer-drug conjugate treatment include intranasal, subcutaneous, and intraperitoneal administration¹⁵⁵.

After intravenous administration, the polymer-drug conjugate must display stability during blood **circulation**, **hemocompatibility** and absence of **immunogenicity** to ensure the adequate arrival of the conjugated drug to the target site, avoiding early recognition and destruction by the immune system¹⁵⁶. Polymer-drug conjugates must bypass the reticuloendothelial system (i.e., phagocytic cells in charge of eliminating foreign particles from the bloodstream and tissues). Indeed, positively charged particles can bind to negatively charged phagocytic cell surfaces and be removed from circulation; therefore, synthesizing polymer-drug conjugates with negatively charged surfaces is generally preferred¹⁵¹. Size also represents another crucial factor when designing a polymer-drug conjugate; a particle size below the renal filtration threshold (6-8 nm) ensures the elimination of non-degradable polymers by glomerular filtration¹⁵⁷. Polymer-drug conjugates with sizes above this threshold show prolonged circulation times¹⁵⁸, allowing fewer dose administrations. Therefore, biodegradable, biocompatible polymers such as polypeptides are preferred for designing polymer-drug conjugates with greater size that yield to longer circulation times in a stealth manner. This allows enhanced accumulation in the pathological site due to the EPR effect.

The EPR effect, first described by Maeda and colleagues¹⁵⁹, relies on the high permeability of the tumor-associated vasculature and impaired lymphatic drainage of tumor tissues, which allows polymer-drug conjugates to selectively **extravasate to the tumor tissue**¹⁵⁰. Small drugs can indistinctly diffuse from normal blood vessels or from fenestrated blood vessels to tumor tissues; however, polymer-drug conjugates can only diffuse from fenestrated blood vessels to

tumor tissues, passively accumulating in tumors and prolonging retention in tumor tissues (Figure 1.8).

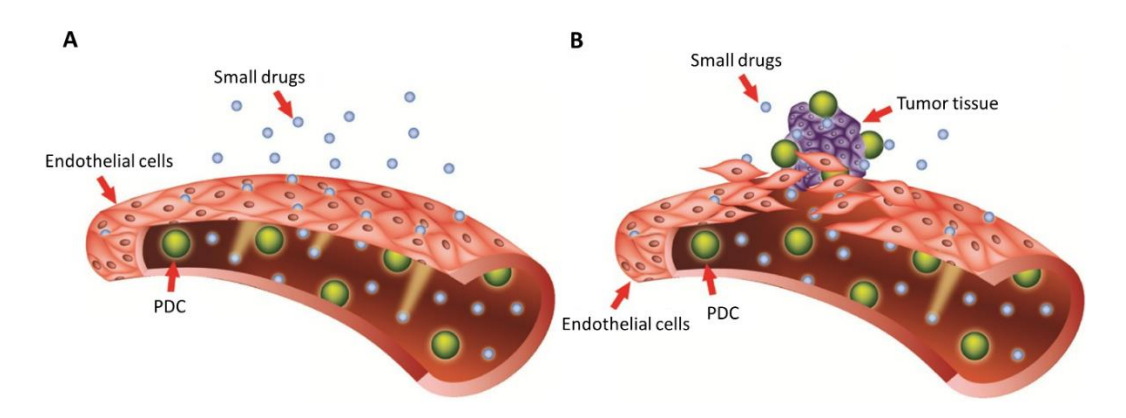


Figure 1.8. Representation of small drug and polymer-drug conjugates extravasation in normal and fenestrated blood vessels. **A)** Representation of normal blood vessels. Small drugs can diffuse through tightly joined endothelial cells, while polymer-drug conjugates (PDCs) cannot. **B)** Representation of blood vessels close to tumor tissues. The higher permeability allows the diffusion of both small drugs and PDCs. Adapted from Bozzuto et al., 2015¹⁶⁰.

After reaching the tumor, polymer-drug conjugates enter the cell via endocytosis, macropinocytosis, or phagocytosis due to their size and hydrophilic nature¹⁵² (Figure 1.9). First, polymer-drug conjugates interact with the cell surface and become engulfed within fluid-filled vesicles¹⁶¹. These vesicles maintain a similar pH of the extracellular space (pH 7.4); however, these vesicles rapidly fuse with early endosomes and acidify to a pH 6.3. The formed endosomes can be recycled back to the cell membrane or continue maturation and acidification to form late endosomes and multivesicular bodies before fusion with lysosomes. The acidic environment (pH 4.7) and the high hydrolase content (e.g., proteases, nucleases, esterases, and lipases) of lysosomes may prompt drug release when using polymer-drug conjugates with stimuliresponsive linkers or biodegradable polymers¹⁶¹. For example, cathepsin B cleavable peptides represent commonly employed polymer-drug linkers in conjugates given the tumor-specific overexpression of the serine-protease cathepsin B in tumors¹⁶²; moreover, Singer et al. demonstrated the degradation of the polymeric carrier polyglutamic acid (PGA) by cathepsin B in a study of PGA-paclitaxel conjugates 163. In this thesis, PGA will the carrier of the synthesized polymer-drug conjugate due to the intrinsic properties of polypeptides, in particular polyglutamates (multivalency, biocompatibility and biodegradability)¹⁵⁵.

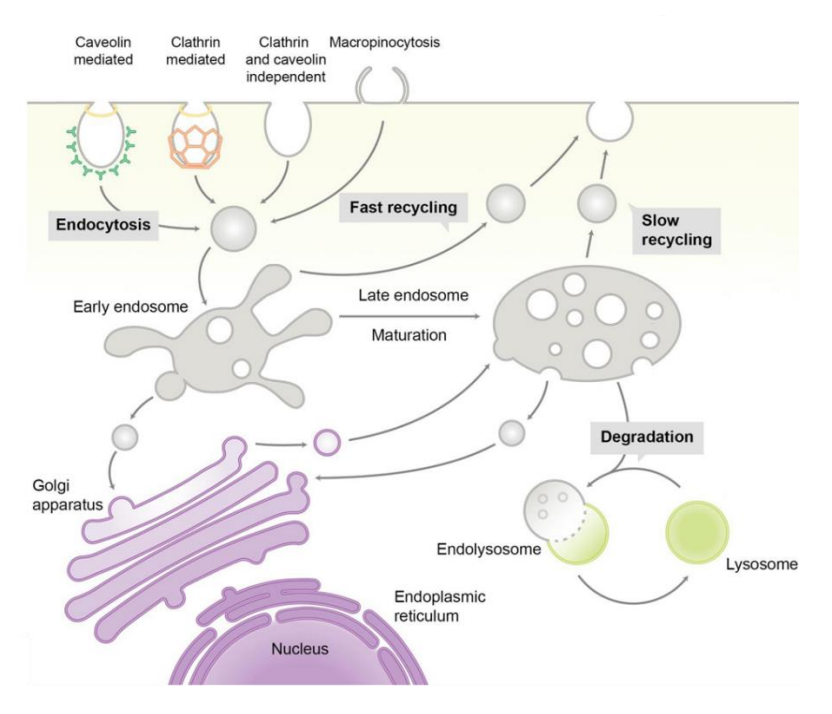


Figure 1.9. Polymer-drug conjugate internalization mechanisms. Adapted from Patel et al., 2019¹⁶⁴.

Redox-sensitive linkers have also seen widespread use in polymer-drug conjugates for cancer treatment. GSH is an essential regulator of the cellular redox state, which protects cells from oxidative stress by removing excessive ROS¹⁶⁵. The cytosol of cancer cells contains higher concentrations of GSH (1-10 mM) than the extracellular space (1-6 μM in plasma)¹⁶⁶, although the GSH concentration varies on the cancer subtype and the invasive status of cells¹⁶⁷. Taking advantage of increased GSH concentrations in tumor cells, redox-responsive linkers support selective drug release inside cancer cells and confer plasma stability to the polymer-drug conjugate. In this sense, disulfide linkers represent the most commonly employed redox-sensitive linkers^{153,168}; elevated levels of GSH in the cytosol of cancer cells reduces the disulfide linker, permitting the drug release. We will employ such linkers in this project to synthesize a PGA-based polymer-drug conjugate.

Apart from endocytic internalization mechanisms, direct cytoplasmic delivery of polymer-drug conjugates could be alternatively achieved by a strategy known as direct penetration. For example, cell-penetrating peptides (CPPs) attached to the nanoconjugate surface represent a primary strategy for achieving direct membrane penetration¹⁶⁹.

Once the drug enters the cytosol (either by direct cell permeation or after lysosomotropic delivery), specific trafficking to appropriate organelles, such as mitochondria, can enhance therapeutic output via targeting strategies.

Section 1.2.5 contains additional details regarding mitochondrial-targeting strategies.

1.2.2. Polymer-drug Conjugates for Breast Cancer Treatment

As mentioned above, the application of polymer therapeutics, and in particular polymer-drug conjugates, for the treatment of breast cancer can overcome the limitations of conventional treatments (such as drug resistance and side effects) due to the high blood circulation time, higher tumor accumulation, and controlled drug release¹⁴⁵.

Some polymer-drug conjugates have entered clinical trials for breast cancer treatment¹⁷⁰. For example, HPMA copolymer-DOX conjugate (PK1, FCE 28068), developed by Kopecek and Duncan that was the first anticancer drug conjugate to be clinically evaluated in 1994 and demonstrated effect in multidrug resistance breast cancer tumors in Phase I/II trials¹⁷¹; ENZ-2008 (PEGylated SN38 conjugated to a copolymer of PEG and poly(N6-carbobenzyloxy-L-lysine)–poly(β-benzyl-L-aspartate)) completed a phase II clinical trial (NCT01036113) for the treatment of breast cancer¹⁷². Xyotax®, also known as Opaxio®, a PGA-paclitaxel conjugate, completed a phase II clinical trial (NCT00148707) for the treatment of metastatic breast cancer¹⁶³. CRLX101, a camptothecin-polymer conjugate with a cyclodextrin-based polymer, completed the phase II clinical trial (NCT00333502) to treat advanced solid tumors, including breast cancer¹⁷³. However, none of them have reach approval yet for different reasons and research continues being very strong in this area.

Many examples can be found at preclinical level^{136,170,174,175} and Kaur et al. recently reported detailed information regarding patents, clinical trials, and approved polymeric therapies¹⁷⁶.

1.2.3. Mitochondrially-targeted Therapies

As described in **Section 1.1**, mitochondria are indispensable organelles for correct cell functioning, and their impairment relates to several pathological processes; therefore, mitochondria represent an attractive target for therapeutic approaches in diseases such as cancer¹⁷⁷. Mitochondria of cancer cells present unique features (e.g., altered MMP, mtDNA mutations, alterations in the energy production pathways) that differ from other organelles and, thus, can be exploited for specific targeting.

The MMP represents the main mitochondrial property employed for targeting, as molecules exhibiting a positive charge become attracted to mitochondria due to the highly negative mitochondria membrane potential. In this context, **delocalized lipophilic cations** represented the first developed "mitochondriotropic" compounds (display a high affinity for mitochondria), which move easily through mitochondrial membranes without a specific import mechanism and accumulate in the mitochondrial matrix¹⁷⁸. Cancer cells characterized by mitochondrial

depolarization demonstrate a more significant accumulation of delocalized lipophilic cations than normal cells, leading to more significant mitochondrial toxicity and selective killing. Triphenylphosphonium (TPP), a positively charged phosphorus ion linked to three phenyl groups and derivatives, represents the most widely used delocalized lipophilic cation¹⁷⁹. Additionally, cationic lipophilic dyes exhibit inherent mitochondria-penetrating ability¹⁷⁷; for example, rhodamine, pyridinium, and cyanine derivatives are used as staining agents, mitochondrial fluorescent probes, and imaging agents.

The IMM translocase/OMM translocase (TOM/TIM) complex, used by most mitochondrial proteins for translocation from the cytosol to the IMM, represents another unique property that can be targeted. The application of amphiphilic α -helix **mitochondrial-targeting sequences** represents a commonly employed strategy to target this protein transporter complex.

Mitochondria also exhibit exclusive structural features that affinity-driven molecules can target. Cardiolipin (CL) is a unique phospholipid of mitochondrial membranes; therefore, using CL-targeting moieties allows selective binding to mitochondria. Szeto-Schiller (tetra)peptides (aromatic-cationic peptides) can permeate the plasma membrane and selectively accumulate in the IMM through interactions with CL¹⁸⁰. Szeto-Schiller peptides not only function as mitochondria-targeting molecules but also as bioactive compounds, as demonstrated by Birk et al., who revealed that the Szeto-Schiller peptide SS31 inhibited cytochrome c/CL complex peroxidase activity¹⁸¹.

Mitochondria-penetrating peptides represent synthetic compounds that include a positively charged moiety (e.g., arginine or lysine) to target the negative MMP and a lipophilic residue (e.g., cyclohexylalanine) to cross the highly hydrophobic IMM¹⁸². Mitochondria-penetrating peptides display biodegradability and can deliver small molecules for cancer therapy¹⁸³ or fluorescent dyes¹⁸⁴.

Also, **small drugs** can efficiently target mitochondrial proteins and metabolic pathways and inhibit their function; for example, α -tocopheryl succinate (a vitamin E analog) inhibits succinate dehydrogenase (complex II) and induces ROS accumulation and apoptosis¹⁷⁷. Additionally, lonidamine (a derivative of indazole-3-carboxylic acid) targets hexokinase II, inhibits glycolysis, and induces cell death via apoptosis¹⁸⁵.

Applying the described mitochondrial-targeting moieties to nanomedicines, such as polymer therapeutics, can create novel mitochondrially-targeted treatments; for example, Zhang *et al.* exploited the SS31 peptide for mitochondria targeting, which they conjugated to a chitosan main chain via a cross-linked ROS-sensitive thioketal crosslinker generating multifunctional

nanoparticles with ROS-responsiveness and mitochondrial-targeting properties for the treatment of ischemic stroke¹⁸⁶. In another study, Zhang et al. created DOX-loaded micelles by the self-assembly of TPP-grafted PEG-poly(D, L-lactide) copolymers using GSH-sensitive disulfide bonds as an intermediate linker for the treatment of hepatocellular carcinoma¹⁸⁷.

1.2.3.1. Mitochondrially-targeted Breast Cancer Therapies

As described in **Section 1.1.4**, the metabolic heterogeneity displayed in breast cancer cells is closely associated with the adaptation of mitochondria bioenergetics to the cell demand. Moreover, researchers have provided evidence that mitochondria are essential for breast cancer progression². In this context, mitochondria represent an attractive therapeutic target for breast cancer.

Small drugs with inherent mitochondrial targeting ability, such as resveratrol, lonidamine, and α -tocopheryl succinate, have been used in breast cancer treatment. Resveratrol acts on mitochondria by decreasing the expression of mitochondrial superoxide dismutase, which dampens ROS levels¹⁷⁷. Treatment of MCF-7 cells with resveratrol led to increased Ca²⁺ leakage and apoptosis via activation of the caspase pathway, while treatment of MDA-MB-231 cells prompted increased MMP and cytochrome c release¹⁸⁸. Lonidamine has been used alone¹⁸⁹ or in combination¹⁹⁰ for breast cancer treatment, while α -tocopheryl succinate reduces cell proliferation and induces apoptosis in breast cancer cell lines, and decreases tumor growth in breast cancer *in vivo* models¹⁹¹.

Several research teams have also reported the design of mitochondrially-targeted nanomedicines for breast cancer treatment. Ma *et al.* designed an innovative breast cancer treatment based on mitochondrially-targeted paclitaxel delivery through a TPP-polyamidoamine (PAMAM) dendrimer-paclitaxel nanoconjugate using an amide bond to link TPP to PAMAM and paclitaxel (PTX) to PAMAM using a disulfide bond¹⁹². The authors of this study also conjugated glucose-PEG moieties via a metalloproteinase-2 (MMP2)-responsive GPLGIAGQ peptide linker to support active targeting via Glucose Transporter 1 (GLUT1) protein overexpressed in MCF7/ADR cells. *In vivo* studies demonstrated a significant improvement in tumor growth inhibition compared to free paclitaxel.

Shi *et al.* prepared doxorubicin-loaded DQAsomes (dequalinium-based liposome-like vesicles) functionalized with a pH-sensitive PEG derivative (PEG2k-Schiff base bond-cholesterol) modified with an HER-2 to treat drug-resistant breast cancer¹⁹³. The authors reported recognition and internalization in HER-2-positive MCF-7/ADR cells, DOX delivery to mitochondria to trigger apoptotic, and enhanced anti-tumor activity compared to the free drug and empty DQAsomes.

Deng et al. prepared an α -cyclodextrin (α -CD) nanocarrier bearing DOX, nitric oxide (NO) conjugated as precursor S-nitrosothiol NO donors (support GSH-triggered NO release), and an acid-cleavable dimethylmaleic anhydride moiety-modified PEG conjugated to a mitochondrial-targeting peptide ((KLAKLAK)2CGKRK) to form α -CD-DOX-DA nanoparticles¹⁹⁴. The specific release of NO within the mitochondria significantly amplified the effect of the nanoparticles in 4T1 and drug-resistant MCF-7/DOX *in vivo* breast cancer models, facilitating more robust mitochondrial membrane permeabilization and downregulated ATP levels by inhibiting mitochondria respiration when compared to control nanoparticles.

PEG-fluorinated micelles with fluorocarbon segments (PEG2k-F7) colocalized with the mitochondria in a potential-independent manner due to the binding affinity for CL¹⁹⁵. PEG2k-F7 micelles loaded with the anti-cancer drug vitamin E succinate boosted drug effectivity even at low doses, inducing a significant reduction in tumor size after two weeks compared to the free drug in a 4T1 breast cancer mice model.

1.3. METABOLOMICS: A FOCUS ON BREAST CANCER AND MITOCHONDRIA

1.3.1. Metabolomics

Metabolomics encompasses the study of substrates, intermediates, and end-products of metabolic routes¹⁹⁶. Metabolism lies downstream of the biological processes (gene expression, transcription, and translation); therefore, the study of the metabolic processes offers an overview of the health status of an organism (**Figure 1.10**). Metabolites include amino acids, nucleotides, vitamins, organic acids, lipids, carbohydrates, antioxidants, and hormones.

Metabolomics has been widely applied in precision medicine to study disease diagnosis, discover early disease indicators, identify tumor biomarkers and markers of progression, and optimize new therapies¹⁹⁷. In this sense, metabolomics represents a non-invasive technique for the clinical evaluation of pathologies through the analysis of plasma, urine, feces, or saliva samples¹⁹⁸; however, biofluids do not display organ specificity, and the metabolomic profile obtained reflects the whole-body metabolism, which complicates biological interpretation¹⁹⁹. In this context, cells (2D and 3D models) and tissues allow the more direct evaluation of metabolic alterations, providing more reliable information. This project thesis will focus on cells (cellular and subcellular) and tissue metabolomics.

The metabolomic process involves six steps (Figure 1.10):

i) experimental design and sample collection

- ii) sample preparation and analysis
- iii) data processing
- iv) metabolite identification
- v) statistical analysis
- vi) biological interpretation

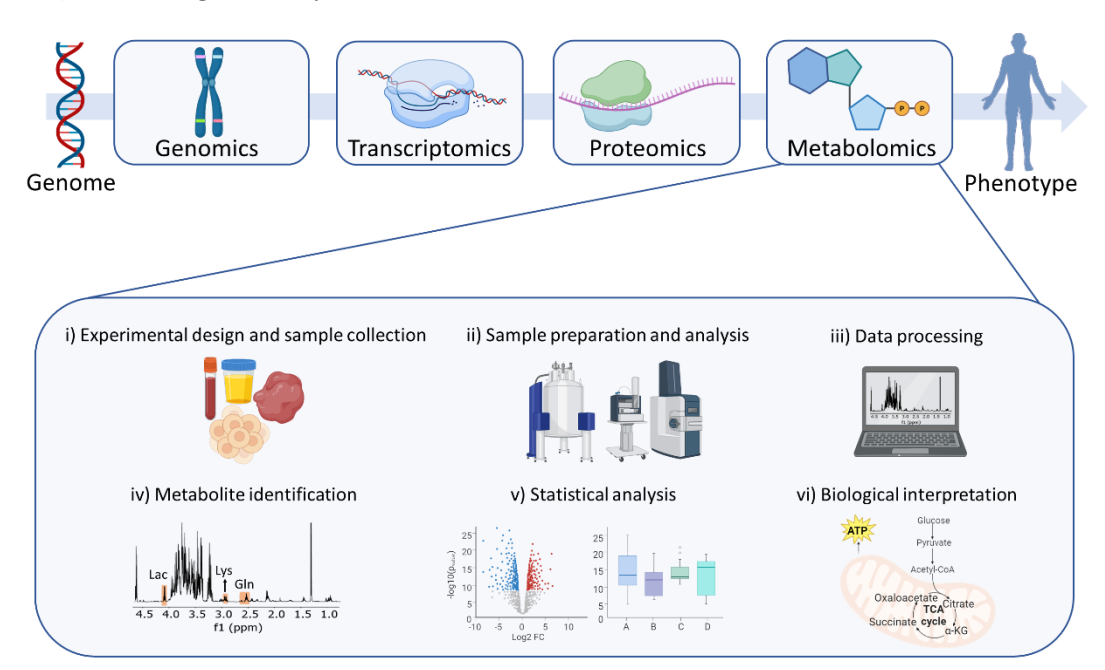


Figure 1.10. Overview of the omic sciences. Metabolomics is the omic approach that gets closer to the phenotype. Includes a schema describing the experimental workflow of metabolomic analysis. Adapted from Danzi et al., 2023²⁰⁰.

Sample preparation depends mainly on sample type and availability and the aim of the study. Avoiding solvents or additives that may overlap with metabolite signals and hamper identification is an important consideration when designing. Metabolite extraction from cell and tissue samples must take place before metabolomic analysis. **Sections 2.2.2** and **4.2.1.3** provide more details on metabolite extraction processes from cells and tissues.

Nuclear magnetic resonance (NMR) and mass spectrometry (MS) represent the main instruments used for metabolomic studies. The first reports of NMR technology in metabolomics studies came from studies in the 1970s that focused on the adrenal medulla²⁰¹. In 1984, Nicholson et al. applied metabolomics to serum, plasma, and urine samples of fasting and diabetic subjects²⁰². Since then, NMR has become one of the most used technologies for metabolomic studies. MS represents the other primary analytical tool for metabolomic studies, with a variety of separation methods and detectors: liquid chromatography coupled with MS (LC-MS²⁰³ or LC-MS/MS²⁰⁴), gas chromatography coupled to MS (GC-MS)²⁰⁵, and high or ultrahigh-performance liquid chromatography coupled to MS (HPLC/UPLC-MS)²⁰⁶. The platform

selection will depend on the study's focus, the samples' nature, and the cost and accessibility²⁰⁷. **Table 1.4** describes the main characteristics (strengths and weaknesses) of NMR and MS technologies for metabolomic studies. This thesis uses NMR (600Hz and 500 MHz) and MS technology (HPLC-MS).

Table 1.4. Characteristics of NMR and MS metabolomic studies

	NMR	MS		
Reproducibility	High	Less reproducible than NMR		
Sensitivity	Low but improves with longer experimental timeframes, cryoprobes, higher magnet field strength, and hyperpolarization methods	High sensitivity compared to NMR; detects metabolites at nanomolar concentrations		
Sample measurement	Relatively fast; all metabolites at a detectable concentration level measured in one analysis	Positive and negative ionization methods required to maximize the number of detected metabolites		
Sample preparation	Depends on sample type; biofluids require minimal sample preparation	Depends on sample type; requires sample derivatization for GC-MS		
Sample recovery	Non-destructive technique, one sample can be analyzed by different techniques	Destructive technique, the sample cannot be recovered; however, a low sample amount is required		
Quantitative analysis	Inherently quantitative, the signal intensity is proportional to the metabolite concentrations	Ionization efficiency represents a determining factor; the MS peak intensity is often not correlated with metabolite concentrations		
Tissue samples	Detects metabolites in intact tissues by high- resolution sample spinning (HR-MAS) NMR	Spatial metabolomics by MS imaging represents an innovative field in the study of intact tissue samples		
Number of detectable metabolites	Usually less than 200	Thousands of metabolites can be detected using different MS techniques		
Lipidomic analysis	Overlap of wide lipid signals difficult lipid identification	More specific for lipidomic analysis compared to NMR		
Targeted analysis	Used for both targeted and untargeted analysis but less used for targeted analysis	Superior for targeted analysis		
<i>In vivo</i> studies	In vivo analysis can be performed by magnetic resonance spectroscopy	Not used for <i>in vivo</i> studies		

Adapted from Emwas et al., 2019²⁰⁸

NMR spectra are processed by signal alignment, considering the internal standard and phase and baseline correction to obtain excellent quality spectra where peaks corresponding to the same metabolites are comparable in all spectra. MS spectra are first filtered to remove signals from blank samples and eliminate noise. Then, deconvolution is applied to define peaks, and finally, chromatograms of all the samples are aligned.

Identifying the metabolites present in the sample now represents a relatively straightforward thanks to public databases containing spectra of hundreds of known metabolites. Said databases include the Human Metabolome Database (HMDB)²⁰⁹ for both NMR and MS annotation, the

Biological Magnetic Resonance Data Bank (BMRB)²¹⁰, the NMRShiftDB2 database²¹¹ for NMR metabolite assignment and LipidBlast²¹², the NIST Mass Spectral Library (Bruker, Massachusetts, United States), and the MetaboBASE Personal Library (Bruker, Massachusetts, United States) for MS feature annotation.

Data normalization commonly occurs before statistical analysis to enable sample comparison, with the method used depending on the type of the analyzed sample. Normalization by total area sum is frequently applied for NMR data, although methods such as the probabilistic quotient normalization also exist²¹³. Several normalization methods exist for MS data; one of the most robust methods relies on using quality control (QC) samples included during the analysis between samples, which capture temporal signal drift trends²¹⁴. Then, the QC data can be used to apply computational correction to the entire dataset²¹⁴. Meanwhile, MS lipidomics data typically undergo normalization to the concentration of internal standards added to the sample.

Statistical analysis in NMR and MS metabolomics consists of multivariate and univariate analysis. Multivariate analysis (unsupervised and supervised) considers all the data features and allows the identification of relationships between samples. Unsupervised multivariate analysis detects sample patterns and outliers, while principal component analysis (PCA) is typically used for metabolic studies. Supervised multivariate analysis identifies correlations between the metabolic features and the phenotype of each group of samples. Orthogonal partial least squares discriminant analysis (OPLS-DA) is often used in metabolomic studies²¹⁵. Univariate analyses provide information regarding statistical differences between metabolite levels in different sample groups. The choice of univariate methods depends on the number of groups, the size of each group, and data distribution²¹⁶.

Biological interpretation represents the last step of a metabolomic analysis, where data integration provides information on the trends of metabolic pathways according to the metabolic alterations observed. Bibliographic research and available databases for biological interpretation such as MetaboAnalyst²¹⁷ are often used for this purpose.

Of note, fluxomics - an innovative omic field that studies the dynamics of metabolic fluxes²¹⁸ – represents a step beyond the standard analysis of metabolism in *in vitro* and *in vivo* models. Fluxomics employs isotope-labeled metabolites to live cells or animals and measures metabolic fluxes by the shift in metabolite levels. ¹³C-labeled metabolites represent commonly used analytes, although additional isotopes often involved include ¹⁵N, ¹⁸O, or ³¹P²¹⁸. While fluxomics analyses employ both NMR and MS, each technique presents specific advantages and limitations. Added to the advantages and limitations of NMR and MS (**Table 1.4**), isotope

mapping by NMR remains a more straightforward task than using MS, as NMR allows the identification of the exact labeled atoms within a molecule²¹⁸. Moreover, a combination of both metabolomics and fluxomics can provide valuable information on metabolic pathway alterations and more robust biological interpretations.

1.3.2. Breast Cancer Metabolomics

Metabolomics represented a revolutionary technique for cancer research by identifying cancer and tumor subtyping biomarkers, metabolic markers of tumor progression and metastasis, and metabolic responses to treatment²⁰⁰. Breast cancer has been widely studied by NMR and MS metabolomic analyses. Here, we summarize some relevant metabolomic contributions to breast cancer research.

Identification of breast cancer biomarkers by metabolomics has employed both preclinical (cells and mice tissues) and clinical samples (tissue, urine, blood). For example, a UPLC-MS/MS metabolomic study of human breast cancer tissues revealed an increase in membrane phospholipids compared to normal tissues²¹⁹. A multi-omic study (metabolomics and transcriptomics) of plasma, urine, and blood samples revealed that detecting alterations in taurine, alanine, aspartate, and glutamate metabolism could represent a critical step in early breast cancer diagnosis²²⁰.

Some studies identified specific metabolic profiles for each breast cancer subtype. For example, Willmann et al. reported a general decrease of amino acids in breast cancer cell lines (MDA-MB-231, MDA-MB-453, BT-474) compared to a non-tumorigenic breast cancer cell line (MCF-10A) by GC-MS metabolomics²²¹. Moreover, the authors observed robust discrimination between different breast cancer cell lines (e.g., increased glycolytic activity in TNBC cell lines compared to Luminal B subtype), which indicated specific metabolic profiles of each subtype (Luminal B, TNBC MSL, and TNBC LAR). Interestingly, Gong et al. identified three distinct metabolic-pathway subtypes in TNBC tissue samples with different prognoses by LC-MS/MS: a lipogenic subtype with upregulated lipid metabolism, a glycolytic subtype with upregulated carbohydrate and nucleotide metabolism, and a mixed subtype with partial pathway dysregulation²²².

An NMR-based metabolomic study of human TNBC tissues revealed metabolic differences between populations²²³. African-American women expressed higher levels of GSH, choline, and glutamine and suffered from decreased mitochondrial respiration and increased glycolytic activity; meanwhile, TNBC in Caucasian women associated with increased pyrimidine synthesis. This study further confirms the enormous heterogeneity in cancer, not only among cancer subtypes but also among populations.

Fluxomics analysis has been applied *in vitro* and *in vivo* in breast cancer research. For example, Lee et al. employed LC-MS/MS fluxomics analysis to demonstrate that increased transcriptional repressor BTB and CNC homology 1 (BACH1) in TNBC patients regulates mitochondrial metabolism (decreased glycolysis and TCA cycle intermediate and downregulated the expression of ETC genes)²²⁴. Christen et al. infused ¹³C-glucose in mice bearing a primary breast tumor and found that cancer cells from lung metastasis displayed increased pyruvate carboxylase-dependent anaplerosis by GC-MS fluxomics²²⁵.

More examples of breast cancer metabolomic studies can be found in Gómez et al., 2021¹⁹⁷, Silva et al., 2019¹⁶⁹, and Subrani et al., 2022²²⁶. **Section 1.3.4** describes breast cancer metabolomic studies focused on the therapeutic response.

1.3.3. Metabolomics Methods to Assess Mitochondrial Metabolism

The metabolic profiles associated with mitochondrial diseases have been evaluated by several authors^{227–229}; however, these studies used whole-cells or tissues to evaluate metabolic alterations, which provides the total metabolite pool of the sample. This analysis makes it challenging to quantify the levels of mitochondrial metabolites, as most localize to other cell compartments. Therefore, studying mitochondrial metabolism directly in the isolated organelle provides more mitochondrially-specific information than the whole-cell.

In this sense, mitochondrial metabolomics is a novel field, and few studies have directly studied metabolic alterations in mitochondria. Various studies have performed NMR-based metabolomic studies of isolated mitochondria in mouse brains^{230,231}, mouse quadriceps²³⁰, and in HCT116 cells²³²; meanwhile, MS-based mitochondrial metabolomic studies have employed various cell^{233–237} and tissue samples^{230,231,238–242} (**Table 1.5**). Most mitochondrial metabolomics studies have been performed by MS, while very few have been performed using NMR spectroscopy due mainly to the lower sensitivity for metabolite detection in small samples such as mitochondria.

Interestingly, mitochondrial fluxomics studies have recently reported a more specific evaluation of mitochondrial metabolic flux^{232,243–245}. For example, Gowda et al. isolated mitochondria from mouse skeletal myoblast cells and monitored mitochondrial metabolism by adding ¹³C-labelled pyruvate as a tracer substrate and using NMR spectroscopy²⁴⁴. Interestingly, they reported an increase in ¹³C-lactate levels, demonstrating that lactate synthesis can also occur inside the mitochondria. Similarly, Lee et al. analyzed the mitochondrial and cytosolic compartments of HeLa cells by MS fluxomics after feeding cells with ¹³C-glucose and ¹³C-glutamine²⁴⁵. Briefly, the authors revealed glutamine reduction to α -ketoglutarate as the primary source of cytosolic

citrate, which represented the major carbon contributor to the biosynthesis of fatty acids. Moreover, they reported oxaloacetate production in mitochondria by a reverse flux of citrate synthase to support the pyrimidine synthesis in defective succinate dehydrogenase cells.

 Table 1.5.
 Summary of reported metabolomics and fluxomics studies aimed to assess mitochondrial metabolism

Study	Sample type	Isolation method	Purity / Integrity	Technique Employed	Purpose of study
Seifert et al., 2010 ²⁴²	Skeletal muscle	DC*	-	GC-MS	Identification of metabolites within or effluxed from mitochondria that shifted with LCFA* oxidation
Roede et al., 2012 ²⁴¹	Mouse liver	DC	-	LC-MS	Described the metabolic phenotype based on gender and genotype
Go et al., 2014 ²⁴⁰	Mouse liver	DC	Activation of mitochondrial permeability transition	LC-MS	Distinguish mitochondrial metabolic differences based on sex and genotype
Fly et al., 2015 ²³⁹	Tissue	Non-aqueous fractionation	SDH* activity	GC-MS/LC-MS	Description of non-aqueous fractionation for metabolomic studies
Matuszczyk et al., 2015 ²³⁴	CHO cells	Digitonin-based buffer for cytosolic content removal	Levels of G-6-P*	LC-MS	Comparison of mitochondrial and cytosolic metabolite pools
Kappler et al., 2016 ²³⁶	HepG2 cells	DC, UC*, MACS*	Western Blot	UPLC-MS	Method optimization for lipidomic study
Nonnenmacher et al., 2017 ²⁴³	A549 cells	Digitonin-based buffer for cytosolic content removal	OCR, MMP*	NMR fluxomics	Experimental setup for ¹³ C-labeling studies on in situ mitochondria
Chen et al., 2017 ²³⁷	HEK293T cells	High-affinity magnetic immunopurification	Western Blot, CLSM	LC-MS	Protocol description for mitochondrial metabolite profiling
Bayraktar et al., 2018 ²³⁸	Mouse liver	High-affinity magnetic immunopurification	Western Blot, CLSM	LC-MS	Rapid mitochondria isolation for proteomic and metabolomic profiling through the generation of MITO-Tag Mice
Xu et al., 2018 ²³²	HCT-116 cells	Mitochondria isolation kit based on DC	Western Blot, TEM*, OCR*	NMR fluxomics	Real-time analysis of mitochondrial metabolic alterations
Lee et al., 2019 ²⁴⁵	HeLa cells	Digitonin-based buffer for cytosolic content removal	Western Blot, CLSM, CS* abundance	NMR fluxomics	Evaluation of reductive glutamine metabolism

Van der Walt et al., 2020 ²³¹	Mouse brain	MACS, DC	CS recovery, Western Blot	NMR, GC-MS	Optimization of mitochondria and cytosol purification for metabolomics studies
Long et al., 2020 ²³⁵	PANC1, A549, MDA-MB- 231 cells	DC	Western Blot, TEM	LC-MS	Optimization of mitochondria isolation from cells for metabolomic and lipidomic analysis
Van der Walt et al., 2021 ²³⁰	Mouse brain, quadricep muscle	MACS	-	NMR, LC-MS	Organelle-specific insight into Leight Syndrome
Nomiyama et al., 2022 ²³³	HEK293 cells	DC	Western Blot	LC-MS	Relation of mtDNA replication with mitochondrial metabolism
Gowda et al., 2023 ²⁴⁴	C2C12 cells	Mitochondria isolation kit based on DC	Western Blot, MMP, O ₂ levels	NMR fluxomics	Live mitochondrially metabolism in real-time

^{*}CLSM = confocal laser scanning microscopy; CS = citrate synthase; G-6-P = glucose-6-phosphate; DC = differential centrifugation; LCFA = long chain fatty acids; MACS = Anti-TOM22 magnetically activated cell sorting; MMP = mitochondrial membrane potential; OCR = oxygen consumption rate; SDH = succinate dehydrogenase; TEM = transmission electron microscopy; UC = ultracentrifugation.

In mitochondrial metabolomics, the procedure conducted for organelle isolation influences the metabolite content. Contaminants from the reagents or instruments used for isolation can be introduced into the sample, thereby distorting the mitochondrial metabolic profile. Consequently, selecting the correct method and reagent remains significant for metabolomics analysis. Mitochondrial isolation has been commonly performed by researchers using different procedures for the study of the content, structure, and functions of this organelle^{239,240,246}. The final aim of the study, such as intact and active mitochondria analysis and metabolite or protein quantification, also influences the selection of the method. The yield and purity of the isolated mitochondria will depend on the method used and the animal's age and physiological state²⁴⁷.

Mitochondria were first isolated in 1946 through the homogenization and differential centrifugation of liver samples²⁴⁸. The differential sedimentation properties of cell constituents allowed for the separation of mitochondria by centrifugation at various speeds, known as differential centrifugation (DC). Taking advantage of instrument and technique innovations and the research carried out to this day, some alternative methods have been developed to be used instead or with DC. Density gradient centrifugation (DGC) follows the same principle as DC adding increasingly dense media bands²⁴⁹; however, DGC is not suitable for metabolomic studies due to the addition of solutions such as Percoll that may interfere with metabolite signals. Affinity purification has also been used to obtain mitochondria of high quality from tissues and cells using antibody coupled-magnetic beads, where mitochondrial surface proteins adhere^{231,250}. Nonaqueous fractionation has been applied for mitochondria isolation for particle separation along a nonaqueous gradient, using solvents such as heptane and tetrachloroethylene²³⁹. An alternative method for mitochondria isolation consists of selectively permeabilizing the cytosolic membrane with digitonin to wash away cytosolic components and selectively extract mitochondrial metabolites^{234,243,245}. Microscale mitochondria isolation has been achieved using microfluidics and nanoprobes, providing a less damaging and more controlled method of sampling organelles²⁵¹.

Cell or tissue homogenization with Dounce tight or tissue blenders followed by traditional DC²⁴⁸ remains a typical choice for mitochondrial metabolomics (**Table 1.5**). The DC isolation buffer usually consists of a moderate ionic strength buffer such as 5-20 mM Tris at neutral pH containing iso-osmotic sucrose or mannitol²⁵². EDTA and bovine serum albumin (BSA) are commonly added to the buffer to chelate Ca²⁺ ions and stabilize the mitochondrial membrane, respectively^{253,254}.

The mitochondrial enrichment of the obtained fraction must be evaluated after isolation and before metabolomic analysis. This step evaluates mitochondrial proteins such as cytochrome c or citrate synthase through Western blotting or activity assays. Mitochondria integrity can be visualized by transmission electron microscopy (TEM) or confocal laser scanning microscopy (CLSM). Other parameter that can be assessed is mitochondrial functioning by evaluation of the MMP and the mitochondrial fraction's oxygen consumption rate (OCR) (Table 1.5).

Metabolite extraction of isolated mitochondria is generally performed using solvents (see **Sections 2.2.2** and **4.2.1.3** for more detail); however, no metabolite extraction procedure has been optimized for mitochondrial samples. Therefore, optimization of mitochondrial metabolite extraction represents one of the aims of this thesis.

1.3.4. Pharmacometabolomics

Metabolomics can be applied to assess the metabolic response to treatment – a field known as pharmacometabolomics²⁵⁵. An assessment of breast cancer metabolic alterations after treatment (breast cancer pharmacometabolomics) has been reported. For example, Cao et al. evaluated the metabolic response of chemotherapy (targretin or tamoxifen) in the serum of rats with ER+ breast tumors on a standard diet or a high-fat diet by LC-MS/MS and GC-MS²⁵⁶. The authors found chemotherapy-induced alterations in lipids, cofactors and vitamins, nucleotides, energy, and peptide pathways, while they found alterations in the urea cycle and benzoate metabolism associated with diet. Miolo et al. studied the metabolic response of HER-2-positive breast cancer patients to trastuzumab-paclitaxel neoadjuvant therapy through serum analysis by LC-MS²⁵⁷. They discovered increased spermidine and decreased tryptophan levels in patients who responded well to treatments compared to the poor responders. Therefore, these metabolites could represent potential biomarkers of the complete pathological response. Similarly, He et al. studied the relationship between the metabolic phenotype and chemotherapy sensitivity in serum samples of TNBC patients with poor, partial, and complete pathological responses by NMR metabolomics²⁵⁸. Briefly, the authors found that disturbed metabolic pathways associated with three metabolite groups (glycine, serine, and threonine; valine, leucine, and isoleucine; alanine, aspartate, and glutamate) could represent predictive models to distinguish the three TNBC patient groups.

In the nanomedicine field, pharmacometabolomics has been used to evaluate any impact on metabolic pathways (**pharmacometabolomics for nanomedicine impact evaluation**)^{259,260}. For example, Zhang et al. studied the effect of gold nanorods (AuNRs) on 16HBE human bronchial epithelial cells and in A595 cancer cells by ¹H NMR metabolomics²⁶¹. The authors found

decreased lactate levels and increased oxidative stress in both cell lines, downregulated nucleotides in the A595 cell line, and increased amino acids in healthy 16HBE cells. Interestingly, the authors reported that 16HBE cells upregulated the de novo synthesis of GSH to resist oxidative stress, which they did not observe in the A595 cancer cell line (leading to mitochondrial damage in these cells). Yaşacan et al. used MS metabolomics to assess the effect of L-carnitine-loaded liposomes (lipo-carnitine) and L-carnitine HCl–loaded poly(lactic-co-glycolic acid) (PLGA) nanoparticles (nano-carnitine) on the metabolism of cardiac fibroblasts²⁶². In general, both formulations caused alterations in amino acid, carbohydrate, and lipid metabolism; nano-carnitine increased the levels of TCA cycle intermediates, which the authors did not observe in cells treated with lipo-carnitine. Duarte et al. reported that silk fibroin nanoparticles induced an inflammatory response in macrophages and promoted increased glycolysis and alteration in the TCA cycle and the creatine phosphate shuttle (as observed by NMR metabolomics)²⁶³; however, PEGylation of silk fibroin nanoparticles reduced inflammatory and metabolic responses in treated macrophages.

Of note, fluxomics analysis can also be applied to evaluate metabolism response to treatment (fluxomics for treatment response evaluation). Schätzlein et al. employed NMR fluxomics using uniformly ¹³C-labeled glucose and glutamate to assess the impact of two gold nanoparticles (gold chitosan = AuChi and gold cerium oxide = AuCeO2) on HeLa cell metabolism²⁶⁴; overall, the authors reported increased levels of reduced GSH, which demonstrated the antioxidant capacity of the nanoparticles, and decreased levels of uridine diphosphate N-acetylglucosamine (UDP-NAG) after treatment with AuChi. Fluxomics analysis revealed that both GSH and UDP-NAG were synthesized from glucose, revealing an alteration in glucose metabolism. Moreover, the authors did not observe these alterations after treatment with AuCeO₂, which had a lesser impact on HeLa cell metabolism. Although Schätzlein and colleagues did not detect alterations in mitochondrial-related metabolites, they traced the ¹³C path to the mitochondria by detecting TCA intermediates.

Interestingly, Lee et al. assessed metabolic alterations in mitochondria (mitochondrial pharmacometabolomics) after treatment of SDH-knockout (KO) and SDH-wild type (WT) HeLa cells with dichloroacetate, which induced acetyl-CoA oxidation via citrate synthase²⁴⁵. The authors observed pyrimidine biosynthesis inhibition only in SDH-KO cells, as indicated by the decrease of malate, carbamoyl aspartate, uridine triphosphate (UTP), and deoxythymidine triphosphate (dTTP) in these cells. By adding ¹³C-glutamine to isolated mitochondria, they detected lower levels of the m + 3 (three labeled carbons) isotopologue of malate and carbamoyl

aspartate upon treatment in the SDH-KO cells, which suggested the role of reverse citrate synthase flux in their survival and growth.

CHAPTER II

OPTIMIZATION OF NMR-BASED METABOLOMIC ANALYSIS OF MITOCHONDRIA ISOLATED FROM TRIPLE NEGATIVE BREAST CANCER CELL

2.1. INTRODUCTION

Mitochondria are essential organelles of cells, which play a main role in energy production and participate in many other cellular functions (e.g., cell signaling, metabolite production and calcium transport)⁹. This central role of mitochondria for cell homeostasis makes mitochondria dysfunction lead to disease. Several pathologies have been closely associated with impaired mitochondrial function, including cancer⁴⁶.

Mitochondrial energy production and functioning are dependent on the mitochondrial metabolic pathways, which are adapted to the cellular needs²¹ (see **Section 1.1** for further details on mitochondrial functioning, impairment and metabolic modulation). In this context, researchers have started to shown awareness of the importance of studying mitochondrial metabolism to better understand mitochondrial modulation during disease and disease management.

To this end, some metabolomic methodologies have been implemented for the specific evaluation of mitochondrial metabolism^{233–235}. However, very few nuclear magnetic resonance (NMR) metabolomic studies in mitochondria isolated from cells have been reported, with few mitochondrial metabolites detected^{230,231}. The low NMR sensitivity hampers the detection of low metabolite pools such as in the mitochondria metabolome of cells. To overcome this problem, researchers have used isotopically labeled metabolites^{232,243–245}, an expensive approach by which only labeled metabolites can be detected.

In this chapter, we aim to develop an NMR metabolomic methodology to study the metabolome of mitochondria isolated from triple negative breast cancer (TNBC) cells. To accomplish this objective, our purpose is the development of a simply and cost-effective methodology focused on preventing sample losses that could affect the final metabolomic outcome.

2.2. RESULTS AND DISCUSSION

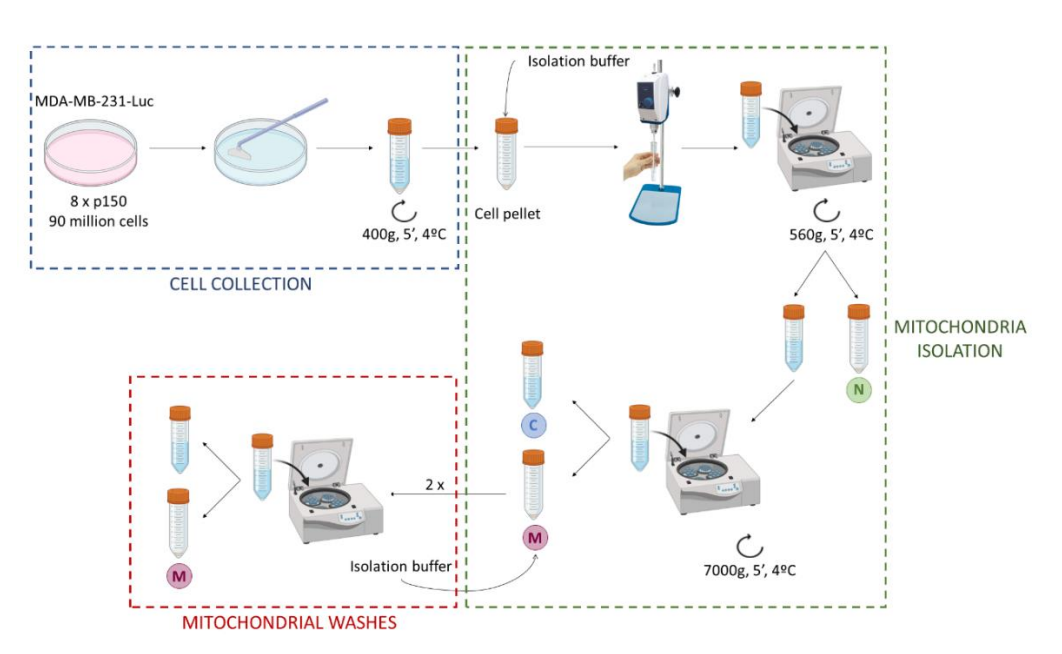
2.2.1. Mitochondrial Isolation from Triple Negative Breast Cancer Cells

Cell or tissue homogenization with Dounce tight or tissue blenders followed by traditional differential centrifugation (DF)²⁴⁸ remains a typical choice for mitochondrial metabolomics (**Table 1.5**); however, novel procedures, such as density gradient purification, non-aqueous fractionation, affinity purification, and permeabilization of the cytosolic membrane, have been described for mitochondria isolation from cell and tissue sample. A deeper description of this alternative mitochondrial isolation method is provided in **Chapter I Section 1.3.3**.

Despite the various available mitochondrial isolation approaches, we opted for the simplest method (homogenization of cells followed by DC) with the aim of developing a cost-effective and straightforward approach applicable to different laboratory settings.

Choosing an appropriate sample processing method is a crucial step in obtaining high-quality metabolomic analysis results. The reagents and processing strategy employed can influence the metabolic content of cell samples and potentially alter the final metabolomic profile. **Figure 2.1** depicts a schematic summary of the selected mitochondrial isolation protocol, consisting of the following main steps:

- i) Cell collection: we harvested approximately 90 million MDA-MB-231-Luc TNBC cells transfected with a luciferase transgene (cultured on eight 150 mm plates at 80-90% confluence).
- ii) Mitochondrial isolation: The cells were resuspended in an isolation buffer and subsequently homogenized using an electric glass homogenizer. Then, we performed low-speed centrifugation to separate the nuclear fraction (pellet), while the resulting supernatant containing low-weight organelles and the cytosolic fraction. Next, we isolated and centrifuged the supernatant at high-speed to obtain a mitochondrial pellet and a supernatant containing the cytosolic fraction.
- iii) Mitochondrial washing: Finally, we washed the mitochondrial pellet twice with an isolation buffer to remove organellar contamination.



M=mitochondrial fraction; N=nuclear fraction; C=cytosolic fraction

Isolation buffer: 220 mM mannitol, 70 mM sucrose, 10 mM Tris-HCl solution, and 0.5 mg/mL BSA in MilliQ water, pH 7.4

Figure 2.1. Schematic of the optimized methodology employed for metabolomic analysis for mitochondrial isolated from TNBC cells.

Several steps were further optimized to obtain a high quality metabolomic profile:

Isolation buffer: Typical isolation buffers contain a moderately ionic strength buffer, such as tris(hydroxymethyl)aminomethane (Tris), at a concentration of 5-20 mM and a neutral pH, along with iso-osmotic sucrose or mannitol²⁵². Common buffer additives include ethylenediaminetetraacetic acid (EDTA) and bovine serum albumin (BSA). EDTA chelates calcium ions to inactivate nucleases dependent on metal ions and prevent DNA and RNA degradation, while BSA helps maintain mitochondrial respiration^{253,254}. For our study, we selected an isolation buffer containing 220 mM mannitol and 70 mM sucrose as non-ionic osmotic supports, 10 mM tris(hydroxymethyl)aminomethane hydrochloride (Tris-HCl) at pH 7.4 to maintain physiological pH, and 0.5 mg/mL BSA to stabilize the mitochondrial membrane. We intentionally avoided the use of EDTA as a chelating agent to prevent overlap of EDTA-associated NMR signals with metabolite peaks. The combined use of sucrose and mannitol allowed us to work with lower sucrose concentration to avoid huge NMR signal overlapping with sucrose signals, as previously observed in our laboratory.

Cell disruption: To optimize cell homogenization, we initially assessed cell lysis by performing the trypan blue exclusion test to count non-disrupted cells. Additionally, we evaluated the lactate dehydrogenase (LDH) activity of the cell homogenate at different number of strokes with the electric glass homogenizer (10, 20, 30, 40, 50, and 60 strokes). The percentage of disrupted cells exhibited an increasing trend after 20 strokes compared to 10 strokes (p=0.051). However, we observed a significant increase in cell disruption after 30 strokes compared to 20 strokes (p=0.013). No significant increases in cell disruption were observed after 40, 50, or 60 strokes (**Figure 2.2.A**). LDH is an enzyme located in the cytosol that catalyzes the conversion of lactate to pyruvate, along with the reduction of nicotinamide adenine dinucleotide (NAD+) to NADH²⁶⁵. The measurement of NADH allows us to calculate LDH activity (see **Materials and Methods; Section 2.4.5.2**). Although we did not find any significant differences in LDH activity (**Figure 2.2.B**), we observed an increasing trend at 20 and 30 strokes, followed by a plateau at 40, 50, and 60 strokes. Considering the results of the cell disruption and LDH activity assays, we determined that 20 and 30 strokes with the electric glass homogenizer were optimal for cell homogenization.

<u>Mitochondrial purity evaluation:</u> To assess the purity of the mitochondrial fractions obtained with 20 and 30 strokes of the homogenizer, we measured the activity of succinate dehydrogenase (SDH), a mitochondrial enzyme (**Figure 2.2.C**). After 20 strokes, we did not observe significant differences in the

relative specific activity (RSA) for SDH among the nuclear, cytosolic, and mitochondrial fractions. However, after 30 strokes, we found a significantly higher RSA for SDH in the mitochondrial fraction compared to the nuclear (p=0.022) and cytosolic (p=0.007) fractions. This indicates that mitochondria are primarily present in the mitochondrial fraction, while the nuclear and cytosolic fractions contain minimal amounts of mitochondria following 30 strokes of cell homogenization.

Confirmation of the optimized mitochondrial isolation protocol was obtained through Western blotting of samples obtained after 30 strokes of the homogenizer (**Figure 2.2.D**). The mitochondrial marker voltage-dependent anion channel (VDAC) displayed significantly higher expression in the mitochondrial fraction compared to the cytosolic fraction (p=0.00005), while the cytosolic marker α -tubulin showed significantly higher expression in the cytosolic fraction compared to the mitochondrial fraction (p=0.017). These results confirm the enrichment of mitochondria in the mitochondrial fraction and the effectiveness of the optimized methodology. **Table 2.1** provides a summary of the data for all samples used in this section and the rest of **Chapter II**.

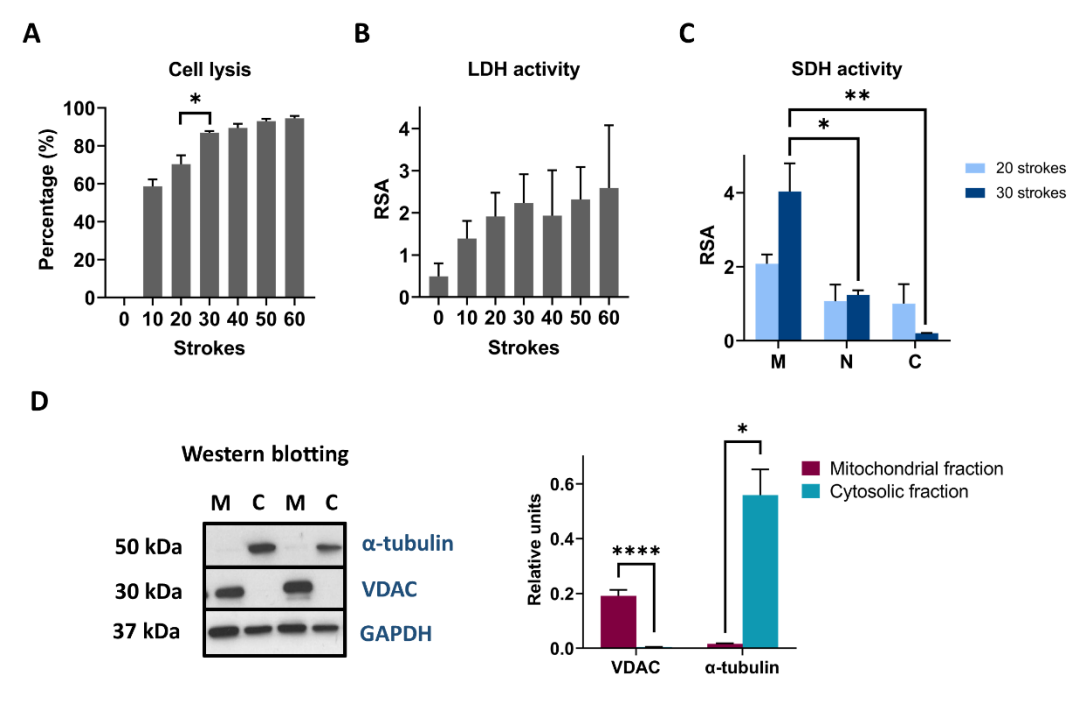


Figure 2.2. Optimizing mitochondrial isolation from TNBC cells for NMR-based metabolomic studies. **A)** Percentage of TNBC cell lysis after 0, 10, 20, 30, 40, 50, and 60 strokes with an electric homogenizer. **B)** RSA of LDH in TNBC cells after 0, 10, 20, 30, 40, 50, and 60 strokes with an electric homogenizer. **C)** RSA of succinate dehydrogenase (SDH) in the mitochondrial, nuclear, and cytosolic fractions after homogenization of cells with 0, 10, 20, 30, 40, 50, and 60 strokes with an electric homogenizer. C = cytosolic fraction; M = mitochondrial fraction; N = nuclear fraction. **D)** Representative Western blot (left panel) and quantitation of results by densitometry (right panel) for mitochondrial

and cytosolic markers from mitochondrial and cytosolic fractions obtained after 30 strokes with the homogenizer. VDAC (voltage-dependent anion channel): mitochondrial marker; α -tubulin: cytosolic marker; GAPDH (glyceraldehyde-3-phosphate dehydrogenase): loading control. Three independent experiments performed for all comparisons (n = 3). Data analysis used a T-test, with data presented as average \pm SEM; (* p-value < 0.05, ** p-value < 0.01, **** p-value < 0.0001).

Table 2.1. Data summary for samples used in Chapter II

Sample ID	Sample type	Purpose	P150 plates	Metabolite extraction
MITO036	Cell homogenate	LDH activity, Cell lysis	8	-
MITO037	Cell homogenate	LDH activity, Cell lysis	8	-
MITO038	Cell homogenate	LDH activity, Cell lysis	8	-
MITO040	Mitochondria	SDH activity	8	-
MIT0051	Mitochondria	SDH activity	8	-
MITO069	Mitochondria	SDH activity, WB	8	-
MITO070	Mitochondria	SDH activity, WB	8	-
MIT0071	Mitochondria	SDH activity, WB	8	-
MITO187	Mitochondria	Extraction optimization	8	Folch
MITO196	Mitochondria	Extraction optimization	8	Folch
MITO220	Mitochondria	Extraction optimization	8	Folch
MITO188	Mitochondria	Extraction optimization	8	Optimized
MITO197	Mitochondria	Extraction optimization	8	Optimized
MITO199	Mitochondria	Extraction optimization	8	Optimized
MITO108	Whole-cell	NMR metabolomics	1	Folch
MITO120	Whole-cell	NMR metabolomics	1	Folch
MITO126	Whole-cell	NMR metabolomics	1	Folch
MITO132	Whole-cell	NMR metabolomics	1	Folch
MITO111	Mitochondria	NMR metabolomics	8	Optimized
MITO123	Mitochondria	NMR metabolomics	8	Optimized
MITO129	Mitochondria	NMR metabolomics	8	Optimized
MITO135	Mitochondria	NMR metabolomics	8	Optimized

Our optimized methodology for isolating mitochondria from TNBC cells, based on mechanical homogenization and differential centrifugation, yielded an enriched mitochondrial fraction suitable for NMR-based metabolomic studies.

2.2.2. Metabolite Extraction from Mitochondrial Extracts

In order to perform a metabolomics analysis of the mitochondrial fraction, an extraction of the metabolites has to be performed, to avoid the interference of other cell components, such as membranes, proteins or DNA. The selection of a metabolite extraction procedure requires careful consideration of the class of metabolite, sample type, and analytical tool used to determine the metabolic profile. It is essential for the extraction procedure to exhibit reproducibility and accuracy while preventing metabolite degradation, ensuring the detection of alterations when comparing samples.

In 1956, Folch et al. published a metabolite extraction protocol for obtaining the lipid fraction from brain samples²⁶⁶. This method involved the addition of a chloroform/methanol mixture to extract lipids, and hydrophilic metabolites were separated by adding water to the sample. Modified Folch extraction methods and alternative solvent-based approaches (such as ethanol and dichloromethane) have since been developed for metabolite extraction^{267,268}. However, these methodologies typically involve solvent evaporation, which can result in metabolite loss.

To address this issue, some studies have employed NMR buffer instead of organic solvents for metabolite extraction. NMR buffer consists of a phosphate buffer at physiological pH (7.4) in D_2O . Sample sonication²⁶⁹ or quenching in liquid nitrogen²⁷⁰ has been utilized in combination with NMR buffer to prevent metabolite loss during solvent evaporation, especially for low-amount samples like mitochondria. Gomez et al. reported that sonication alone or in conjunction with ultrafiltration yields better quality spectra compared to the Folch extraction method²⁷⁰.

Based on these findings, we decided to compare the NMR outcome of the Folch protocol (Materials and Methods, Section 2.4.6.1) with an adapted version of the NMR buffer filtration protocol (Materials and Methods, Section 2.4.6.2; Figure 2.3). The resulting extracts were analyzed on a Bruker AVII-600MHz NMR spectrometer to obtain ¹H NMR spectra of each sample through Nuclear Overhauser Effect Spectroscopy (NOESY). To suppress the water signal, we employed presaturation²⁷¹ and applied a short mixing time (D8) to enhance the phase and baseline²⁷². These settings in the ¹H NOESY experiments resulted in spectra that exhibited the reproducibility and quantitative accuracy necessary for metabolomics²⁷³.

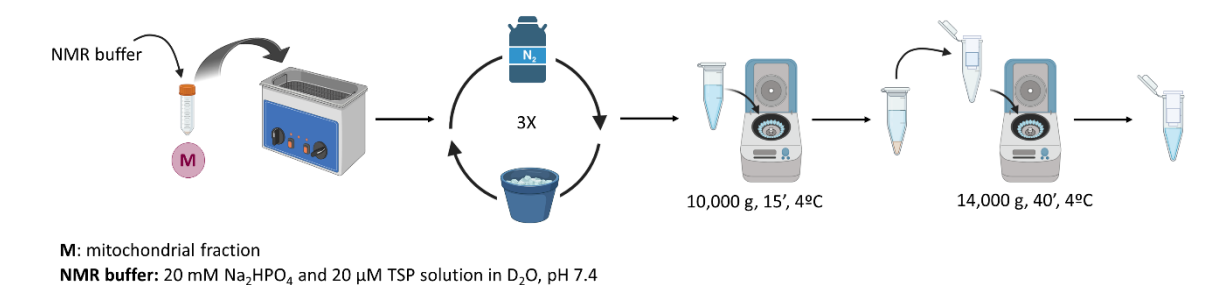


Figure 2.3. Optimized methodology for metabolite extraction of mitochondria isolated from TNBC cells.

When comparing the resulting spectra (**Figure 2.4A**), we observed a much higher recovery of mitochondrial metabolites with the "NOESY with filtration" method, likely due to the losses associated with solvent evaporation that occur in the "NOESY Folch extraction" method. For instance, in the "NOESY with filtration" spectrum, we detected isoleucine, valine, lactate, alanine, lysine, methionine, and glutamate (labeled in the top spectrum of **Figure 2.4A**), whereas these metabolites either showed no or low-intensity signals in the "NOESY Folch extraction" spectrum. The higher levels of acetate and dimethylamine (DMA) present in the "NOESY Folch extraction" spectrum (labeled in the bottom spectra of **Figure 2.4A**) could be attributed to impurities in the solvents used for metabolite extraction^{274,275}. **Table 2.2** provides the absolute quantification of metabolite levels for both methods, with three replicates per method. The assigned metabolites in the aliphatic part of the "NOESY with filtration" spectrum (**Figure 2.4A**) displayed significantly higher levels compared to the "NOESY Folch extraction" spectrum.

We further wanted to test if broad protein signals were best removed by physical filtration (centrifugal ultrafiltration) or by NMR based filtering using the Carr–Purcell–Meiboom–Gil (CPMG) method that employs a relaxation filter to minimize the intensity of any broad signals^{276,277}. To assess this, we compared the previously obtained "NOESY with filtration" spectra with a spectrum obtained after filtering out macromolecule signals using the CPMG method from an unfiltered sample ("CPMG without filtration") (Figure 2.4B). We also acquired a NOESY spectrum without filtration as reference ("NOESY without filtration"). The "NOESY without filtration" method resulted in the appearance of broad protein signals within the spectrum, which disrupted the baseline of the entire spectrum. In contrast, the "NOESY with filtration" method provided a higher-quality spectrum with reduced protein signals, facilitating accurate quantification of metabolite signals (e.g., lysine, the leftmost signal at 3 ppm). The "CPMG without filtration" method partially reduced the broad protein signals observed in specific spectra regions when using the "NOESY without filtration" method, resulting in cleaner metabolite signals. However, it also led to the loss of some metabolite signals, as indicated by the regions highlighted in red in Figure 2.4B, thereby decreasing the intensity of specific metabolites. The regions highlighted in grey represent the most

noticeable changes in protein signals among the three methods in **Figure 2.4B**. Based on these findings, we decided to employ the "NOESY with filtration" method for metabolite extraction and NMR measurements.

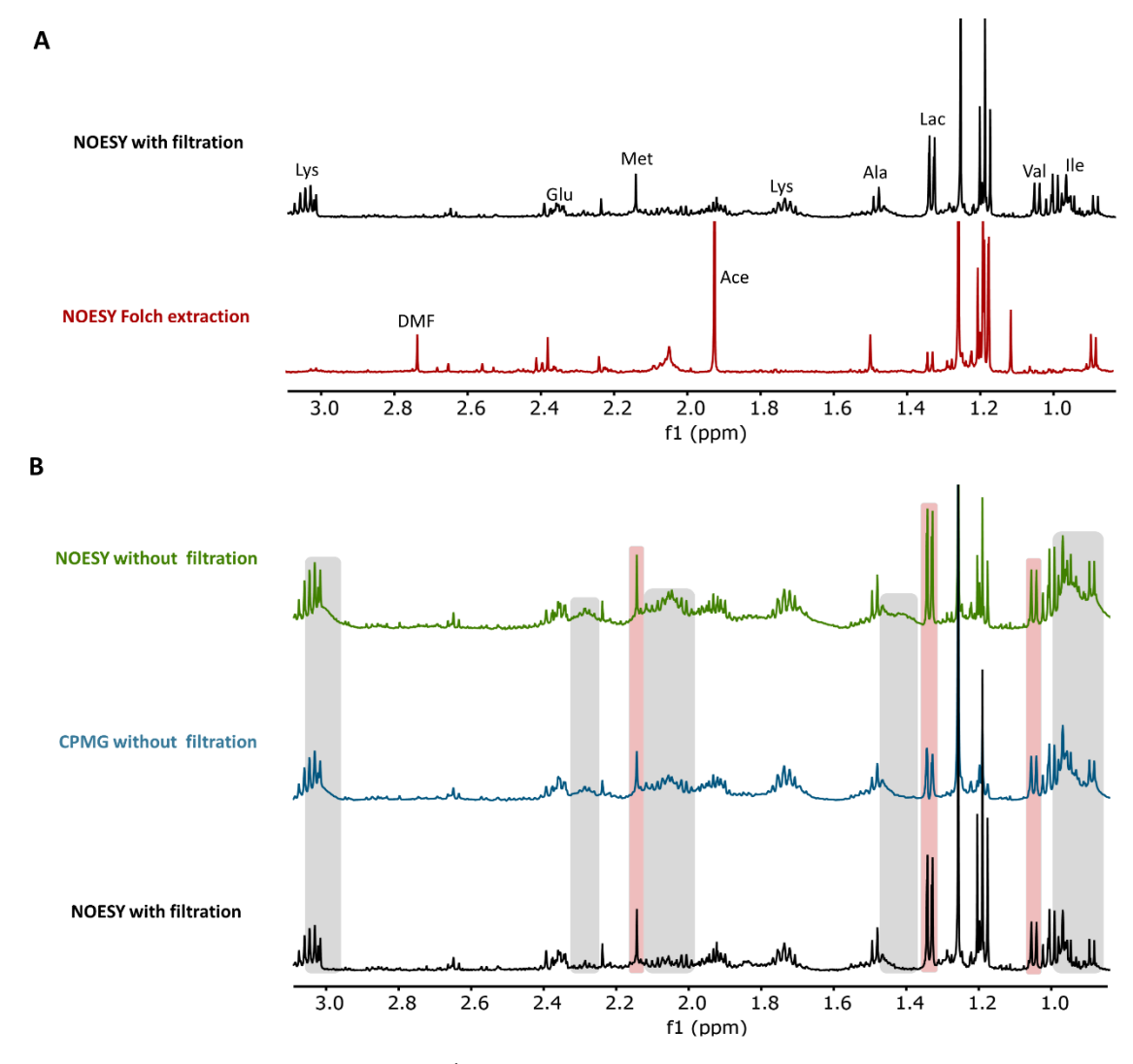


Figure 2.4. Representative aliphatic regions of ¹H NMR spectra acquired from mitochondrial extracts obtained using different extraction methods and NMR approaches. **A)** Comparison of spectra obtained after analyzing mitochondria isolated from TNBC cells using the optimized extraction method ("NOESY with filtration") and the traditional Folch method ("NOESY Folch extraction"). Ace = acetate; Ala = alanine; DMA = dimethylamine; Glu = glutamate; Ile = isoleucine; Lac = lactate; Leu = leucine; Lys = lysine; Met = methionine; Pro = proline; Val = valine. **B)** Spectra obtained after analyzing mitochondria isolated from TNBC cells using the optimized extraction method before ("NOESY without filtration") and after filtration ("NOESY with filtration") compared to the CPMG method used without filtration ("CPMG without filtration"). Regions highlighted in grey correspond with regions of the spectra where protein signal removal is noticeable, while regions highlighted in red correspond to metabolites that show lower levels in the "CPMG without filtration" spectrum.

Table 2.2. Quantification of ¹H-NMR spectra of mitochondria isolated from TNBC cells obtained following the optimized "NOESY with filtration" method and the traditional "Folch extraction" method.

			NOESY Folch extraction		NOESY with filtration		T-test
Metabolite	Right limit	Left limit	Mean (μM)	SEM	Mean (μM)	SEM	p-value
Valine	0.9848	1.0039	0.993	0.228	32.860	5.376	0.0042
Isoleucine	1.0037	1.0247	0.105	0.206	18.815	3.169	0.0074
Lactate	1.3217	1.3438	9.856	1.886	69.161	16.965	0.0324
Alanine	1.4725	1.4919	2.558	0.621	28.653	1.129	0.0003
Lysine	1.7002	1.7686	3.146	0.177	109.365	15.873	0.0052
Methionine	2.1385	2.1434	0.147	0.175	12.272	1.303	0.0021
Glutamate	2.3355	2.3738	6.249	2.265	57.793	5.952	0.0036
Tyrosine	6.8897	6.9246	0.254	0.169	16.542	1.135	0.0006
Histidine	7.0895	7.1032	0.068	0.115	5.777	0.862	0.0057
Phenylalanine	7.4106	7.4562	0.746	0.059	16.692	3.268	0.0100

The optimization steps undertaken in this study have contributed to the development of a robust methodology for obtaining the metabolomic profile of mitochondria isolated from TNBC cells using NMR spectroscopy. The utilization of NMR buffer during metabolite extraction, along with the implementation of quenching and protein filtration techniques, has proven effective in minimizing evaporation-associated losses and ensuring the acquisition of high-quality NOESY spectra.

2.2.3. Metabolomic Profiling of Mitochondria Isolated from Triple Negative Breast Cancer Cells Using NMR Spectroscopy

In general, there is a lack of studies that report the metabolomic profile of mitochondria isolated from cell lines using NMR spectroscopy. Previous NMR-based metabolomic studies on mitochondria isolated from mammalian cells^{232,244} have primarily utilized isotope labeling, as well as 2D and ¹³C spectra. However, the characterization of the ¹H NMR metabolomic profile of mitochondria isolated from mammalian cells remains unexplored. Therefore, our objective was to assess the metabolic content of mitochondria isolated from TNBC cells.

The optimized procedures for mitochondrial isolation, metabolite extraction, and NMR measurements outlined in **Sections 2.2.1** and **2.2.2** yielded spectra of high quality, effectively representing the metabolomic profile of mitochondria isolated from TNBC cells. **Figure 2.5** presents a representative spectrum illustrating the metabolomic profile of mitochondria, with assigned metabolites. The spectra exhibited an excellent signal-to-noise ratio, allowing us to identify a total of 33 metabolites (refer to **Table 2.3**).

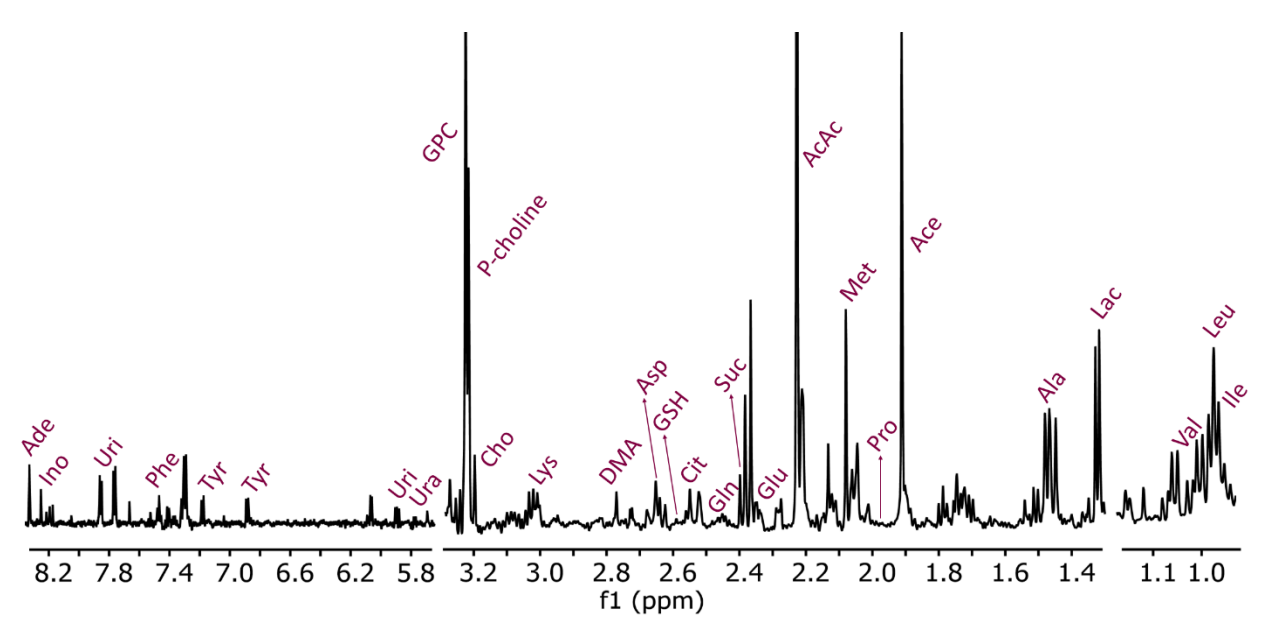


Figure 2.5. A representative spectrum reporting the mitochondria metabolites present in TNBC cells. Signals from solvents (water and ethanol) and the isolation buffer (sucrose and mannitol) have been excluded from the figure. AcAc = acetoacetate; Ace = acetate; Ade = adenosine; Ala = alanine; Asp = aspartate; Cho = choline; Cit = citrate; DMA = dimethylamine; Gln = glutamine; Glu = glutamate; GPC = glycerophosphocholine; GSH = glutathione; Ile = isoleucine; Ino = inosine; Lac = lactate; Leu = leucine; Lys = lysine; Met = methionine; P-choline = phosphocholine; Phe = phenylalanine; Pro = proline; Suc = succinate; Tyr = tyrosine; Ura = uracil; Uri = uridine; Val = valine.

Table 2.3. NMR signal assignment of the metabolome of TNBC cells and isolated mitochondria.

	Whole-cell		Mitochondria			
Metabolite	Right limit (ppm)	Left limit (ppm)	Metabolite	Right limit (ppm)	Left limit (ppm)	
Isoleucine	0.9275	0.9464	Isoleucine	0.9275	0.9464	
Leucine	0.9604	0.9815	Leucine	0.9604	0.9815	
Valine	0.9852	1.0036	Valine	0.9852	1.0036	
Isoleucine	1.0047	1.0237	Isoleucine	1.0047	1.0118	
Valine	1.0363	1.0544	Valine	1.0363	1.0544	
Lactate	1.3181	1.3423	Lactate	1.3212	1.339	
Alanine	1.4734	1.4816	Alanine	1.4734	1.4816	
Alanine	1.4819	1.4926	Alanine	1.4865	1.4926	
Acetate	1.9134	1.924	Acetate	1.9134	1.924	
Proline	1.9698	1.9895	Proline	1.9816	1.9875	
Proline	1.9896	2.0201	Proline	2.0044	2.0088	
UDP-NAG*	2.0808	2.0915				
Methionine	2.137	2.144	Methionine	2.137	2.144	
Acetoacetate	2.2292	2.239	Acetoacetate	2.2292	2.239	
Valine	2.2488	2.2842				
			Glutamate	2.3341	2.3698	
Succinate	2.4005	2.4079	Succinate	2.3995	2.4122	

Glutamine	2.435	2.4772	Glutamine	2.4361	2.4606
Citrate	2.5302	2.538	Citrate	2.5485	2.5641
Glutathione	2.5381	2.582	Glutathione	2.5646	2.5729
Aspartate	2.653	2.6666	Aspartate	2.653	2.6689
Aspartate	2.6762	2.6808			
Aspartate	2.6898	2.6962			
Dimethylamine	2.7257	2.736	Dimethylamine	2.7283	2.7323
Aspartate	2.7987	2.811			
Aspartate	2.8277	2.8402			
Glutathione	2.9075	2.9259			
Glutathione	2.9293	2.9727			
Glutathione	2.9827	2.9967			
Lysine	3.0112	3.0315	Lysine	3.0122	3.0455
Creatine	3.0355	3.0426			
P-creatine	3.0427	3.045			
Choline	3.2021	3.2093	Choline	3.198	3.2103
P-choline	3.2193	3.2284	P-choline	3.2193	3.2264
GPC*	3.2285	3.2366	GPC*	3.2265	3.2366
Taurine	3.2558	3.261			
Myo-inositol	3.2611	3.2661			
Taurine	3.2666	3.2722			
Myo-inositol	3.273	3.2825			
Myo-inositol	3.2903	3.2986			
Proline	3.3143	3.3443	Proline	3.3299	3.3424
Proline	3.3452	3.4076	Proline	3.3714	3.3872
Taurine	3.4077	3.4119			
Proline	3.4154	3.4191			
Taurine	3.4195	3.4236			
Taurine	3.4302	3.4342			
Proline	3.4348	3.4516			
Glucose	3.4574	3.4718			
Glucose	3.4761	3.5052			
Myo-inositol	3.5201	3.5488			
Glycine	3.554	3.5616			
			Threonine	3.5831	3.5965
P-choline	3.5848	3.5991			
Myo-inositol	3.6069	3.6297			
GPC*	3.6878	3.6959			
Glutamate	3.7518	3.7609			
Glutamate	3.7633	3.7714			
Glutathione	3.7755	3.7918			
Adenosine	3.8243	3.8388			
Creatine	3.9207	3.9292			
Serine	3.9703	3.9844	1		

Sorino	3.9927	4.0021	1		l
Serine					
Nucleotide	4.0356	4.0536			
Myo-inositol Lactate	4.0552 4.0898	4.0707	Lastata	4.006	4.1007
Lactate	4.0898	4.13	Lactate	4.086	4.1097
Thursday	4 2200	4.2220	Proline	4.1133	4.1465
Threonine	4.2289	4.2338			
Threonine	4.2379	4.2457			
Threonine	4.2487	4.2551			
Threonine	4.2573	4.263			
GPC*	4.315	4.347	n e de	4.25.42	4.260
Uridine	4.3468	4.3681	Uridine	4.3543	4.369
UDP-NAG*	4.3681	4.3843			
Glutathione	4.5541	4.5799		4.6270	4.6560
252*	5 4000	5.40	Glucose	4.6378	4.6568
PEP*	5.1808	5.19	PEP*	5.1808	5.19
PEP*	5.3569	5.3657			
UDP-NAG*	5.5072	5.5314			
			Glucose	5.1918	5.2073
UDP-glucose	5.5985	5.6083			
UDP-			UDP-der	5.6099	5.6371
glucuronate	5.6287	5.6406			
Uracil	5.7965	5.8145	Uracil	5.7965	5.8148
Uridine	5.8923	5.9251	Uridine	5.8923	5.9251
GTP*	5.9321	5.9523			
UDP-der	5.9664	6.0185			
NAD+*	6.0405	6.0567			
Adenosine	6.0743	6.0811			
Nucleotide	6.1045	6.1115			
ATP*	6.1438	6.164			
Fumarate	6.5163	6.5226	Fumarate	6.5163	6.5245
Tyrosine	6.8894	6.9166	Tyrosine	6.8861	6.9152
Hisitidine	7.0533	7.0641	Hisitidine	7.0533	7.0641
Tyrosine	7.1837	7.2127	Tyrosine	7.1837	7.2127
Phenylalanine	7.3239	7.3453	Phenylalanine	7.3239	7.3453
Phenylalanine	7.3587	7.4502	Phenylalanine	7.415	7.4502
Uracil	7.5286	7.5456	Uracil	7.5286	7.5456
Uridine	7.8627	7.8844	Uridine	7.8627	7.8844
GTP*	8.1441	8.1578			
Inosine	8.2294	8.2365	Inosine	8.2294	8.2365
Adenosine	8.2661	8.2705	Adenosine	8.2646	8.2734
ATP*	8.2707	8.2819			
Inosine	8.3371	8.3432	Inosine	8.3371	8.3432
Adenosine	8.3433	8.3499	Adenosine	8.3433	8.3499
NAD+/NADP+*	8.4333	8.4425			
•			•		

Formate	8.455	8.4631	Formate	8.455	8.4631
АТР	8.533	8.5559			
NAD+/NADP+*	8.8311	8.8545			
NAD+/NADP+*	9.1479	9.1695			
NAD+/NADP+*	9.3355	9.353			

*ATP = adenosine triphosphate; GTP = guanosine triphosphate; GPC = glycerophosphocholine; NAD+ = nicotinamide adenine dinucleotide; NADP+ = nicotinamide adenine dinucleotide phosphate; PEP = phosphoenolpyruvate; UDP-NAG = uridine diphosphate N-acetylglucosamine

Overall, our analysis revealed the presence of various metabolites in the mitochondria of TNBC cells, including amino acids, organic acids, nucleotides, sugars, and lipid-related metabolites (Figure 2.5, Table 2.3). Amino acids play essential roles in anaplerotic reactions to generate tricarboxylic acid (TCA) cycle intermediates²⁷⁸. They can be transported from the cytosol through specific carriers, synthesized within the mitochondria, or obtained through mitochondrial protein degradation^{279,280}. Branched-chain amino acids (leucine, isoleucine, and valine) along with lysine, tyrosine, phenylalanine, and threonine support the production of acetyl-CoA, a critical participant in the initial step of the TCA cycle^{279,281}. Additionally, we observed other essential (histidine) and non-essential amino acids (proline, aspartate, alanine, glutamine, and glutamate) as mitochondrial metabolites. Alanine and threonine catabolism generates pyruvate, which is then converted to acetyl-CoA^{281,282}. Isoleucine, valine, and methionine serve as precursors of succinyl-CoA, another component of the TCA cycle²⁸¹. Phenylalanine and tyrosine act as precursors of fumarate, while aspartate is involved in the production of oxaloacetate, both of which are TCA cycle intermediates. The production of glutamate requires histidine, proline, and glutamine, with glutamate being utilized to generate α -ketoglutarate, another TCA cycle intermediate, in a reversible reaction²⁸¹. Overall, amino acid metabolism is tightly interconnected with the TCA cycle within mitochondria.

Our NMR analysis also identified the presence of the antioxidant protein glutathione (GSH; gamma-glutamyl-cysteinyl-glycine) as the only peptide in the mitochondria of TNBC cells (**Figure 2.5**). After synthesis in the cytosol, GSH is transported to the mitochondria, where it plays a crucial role in maintaining cellular homeostasis by removing reactive oxygen species (ROS) generated during mitochondrial respiration²⁸³.

Furthermore, our analysis revealed the presence of several organic compounds in the mitochondria metabolome, including lactate, acetate, acetoacetate, dimethylamine, phosphoenolpyruvate, citrate, succinate, formate, and fumarate (Figure 2.5). Lactate, produced during anaerobic glycolysis in the cytosol, can diffuse into the mitochondria, where it is oxidized to pyruvate through the malate-aspartate

shuttle, generating NAD*²⁸⁴. Acetate, produced from pyruvate, enters the TCA cycle as acetyl-CoA through the action of acetyl-CoA synthetase-1 in the mitochondria and acetyl-CoA synthetase-2 in the cytosol²⁸⁵. Acetoacetate is formed within the mitochondria from two molecules of acetyl-CoA during ketogenesis and may serve as an alternative energy reservoir for cancer cells²⁸⁶. Acetyl-CoA synthetases have been implicated in breast cancer cell proliferation, as cancer cells utilize acetate to generate acetyl-CoA, supporting energy production through the TCA cycle²⁸⁷. Consequently, acetoacetate could serve as an alternative energy reservoir for cancer cells²⁸⁶. Interestingly, our NMR analysis revealed significantly elevated levels of acetate and acetoacetate in the mitochondria of TNBC cells. The presence of citrate, succinate, and fumarate in the mitochondria can be attributed to their role as intermediates of the TCA cycle²⁴, thus explaining their localization within this organelle. Formate in the mitochondria may result from its release during serine catabolism, an essential pathway for maintaining mitochondrial respiration²⁸⁸. Cytosolic phosphoenolpyruvate acts as an intermediate in glycolysis (prior to conversion to pyruvate), but it can also be synthesized within the mitochondria through the catalysis of mitochondrial phosphoenolpyruvate carboxykinase (PEPCK) from oxaloacetate²⁸⁹.

Although adenosine and inosine predominantly reside in the cytosol, we detected low levels of these nucleotides in the mitochondria of TNBC cells, potentially due to the elevated production of adenosine triphosphate (ATP) via the TCA cycle and oxidative phosphorylation²⁴. Additionally, we observed low levels of the nucleotides uridine and uracil in the mitochondria. While their synthesis occurs in the cytosol, uridine regulates the mitochondrial respiratory chain through dihydroorotate dehydrogenase (DHODH), which is present in the mitochondrial membrane²⁹⁰. Uridine degradation leads to the formation of uracil, one of the nucleotides comprising mitochondrial RNA²⁹⁰.

Glucose was the sole sugar detected in the metabolomic profile of the mitochondria from TNBC cells. Upon entering the cell, glucose undergoes rapid metabolism through glycolysis to produce energy²⁹¹. The observed glucose levels in the mitochondrial fraction may stem from the cleavage of the sucrose component in the isolation buffer²⁹².

Furthermore, we discovered metabolites associated with lipid metabolism, namely choline, phosphocholine, and glycerophosphocholine (GPC), which likely derive from phosphatidylcholine as a major component of the mitochondrial membrane. Phosphatidylcholine can enter the phosphatidylcholine cycle, leading to the formation of choline derivatives²⁹³. Elevated levels of phosphocholine and GPC were observed in the mitochondrial extract compared to other metabolites,

likely resulting from the cleavage of the mitochondrial membrane and subsequent release of phosphatidylcholine.

Applying an optimized methodology to isolate mitochondria from TNBC cells resulted in a metabolomic profile rich in amino acids, nucleotides, organic acids, and metabolites associated with lipid metabolism. This specific profiling of isolated mitochondria enables the precise quantification of metabolites within this organelle, making the described methodology applicable for studying mitochondrial diseases.

2.2.3.1. A Comparison of the Metabolomic Profiles of Isolated Mitochondria and Whole Triple Negative Breast Cancer Cells

We proceeded to compare the metabolomic profiles of isolated mitochondria from MDA-MB-231-Luc TNBC cells with the whole-cell metabolome, aiming to demonstrate that mitochondria offer additional information beyond the whole-cell analysis.

To obtain the metabolomic profile of whole-cells, we employed the traditional "NOESY Folch method," while we utilized the optimized "NOESY with filtration" methodology for the mitochondrial fractions. The assigned metabolites in the whole-cell and mitochondria samples are presented in **Table 2.3**.

Figure 2.6A illustrates the principal component analysis (PCA) score plot of all the samples, with four samples per group. No outlier samples were identified, and clear separation of the groups was observed. Robust discrimination was expected since several metabolites present in whole-cells (e.g., ATP, GTP, and creatine) were not detected in mitochondrial extracts. The non-detected metabolites in TNBC mitochondrial samples might either be absent in the organelle or present at such low levels that they remained undetected by NMR spectroscopy. Metabolites overlapping with sucrose and mannitol, components of the isolation buffer, were excluded from this analysis. Representative spectra of whole-cell (top, light color) and mitochondria (bottom, dark color) samples are depicted in Figure 2.6B, with labeled metabolites exhibiting increased levels in the corresponding sample type (e.g., lactate, creatine, fumarate, and GTP in whole-cell samples).

To assess the relative levels of each metabolite in whole-cell and mitochondrial samples, a univariate analysis and t-test were performed to compare the differences in metabolite contents. Figure 2.6C (low-intensity metabolites) and Figure 2.6D (high-intensity metabolites) present the relative levels of each metabolite in the whole-cell (light color) and mitochondrial (dark color) samples. Additionally, Figure 2.7 provides a schematic representation of relevant metabolic pathways occurring inside and outside

mitochondria, with metabolites displayed in green and red indicating higher and lower levels, respectively, in the mitochondria compared to the whole-cell.

Amino acids (leucine, p = 0.011; lysine, p = 0.005; valine, p = 0.011; and methionine, p = 0.014), citrate (p = 0.015), adenosine (p = 0.004), inosine (p = 0.033), and uridine (p = 0.024) exhibited significantly higher levels in the mitochondria than in whole-cells (Figure 2.6C and D). Leucine, valine, and lysine serve as precursors for acetyl-CoA, which enters the TCA cycle. Valine and methionine can be catabolized to succinyl-CoA, an intermediate of the TCA cycle. Citrate, an intermediate of the TCA cycle, can be transported to the cytosol via a citrate carrier, but its synthesis primarily occurs in the mitochondria²⁹⁴. The presence of adenosine, inosine, and uridine in mitochondrial samples may result from nucleotide cleavage for phosphate group donation to other molecules that need phosphorylation to enter pathways that promotes cancer cell proliferation²⁹⁵. Furthermore, mitochondrial ATP can be converted to adenosine, which can subsequently be converted to inosine²⁹⁶, while uridine monophosphate (UMP) may serve as the source of uridine 290 . In contrast, we observed significantly lower levels of lactate (p = 0.0003), GSH (p = 0.025), fumarate (p = 0.014), creatine (p = 0.005), phosphocreatine (p = 0.008), ATP (p = 0.0004), GTP (p = 0.02), NAD+/NADP+ (p = 0.013), and UDP-NAG (p = 0.0004) in the mitochondria compared to whole-cells (Figure 2.6C and D). The metabolism of most of these factors (lactate, GSH, creatine, phosphocreatine, and UDP-NAG) typically occurs in the cell cytosol^{291,297–299}, while others (ATP, GTP, NAD+, and NADP+) undergo continuous production and consumption both inside and outside the mitochondria³⁰⁰. ATP, NAD⁺, and NADP⁺ participate in numerous pathways, making it challenging to predict their specific levels in cell compartments. Lastly, fumarate, an intermediate of the TCA cycle, is also present in the cytosol as a byproduct of the urea cycle³⁰¹. The elevated levels of fumarate in the cytosol of cancer cells may result from the loss of cytosolic fumarate hydratase activity, which normally catalyzes the conversion of fumarate to malate, leading to the accumulation of cytosolic fumarate ³⁰². Fumarate accumulation has been associated with tumorigenesis and, more specifically, with epithelialmesenchymal transition³⁰³.

These findings suggest that the metabolomic profile of isolated mitochondria can provide additional, more specific information regarding mitochondrial metabolism compared to the analysis of whole-cell samples.

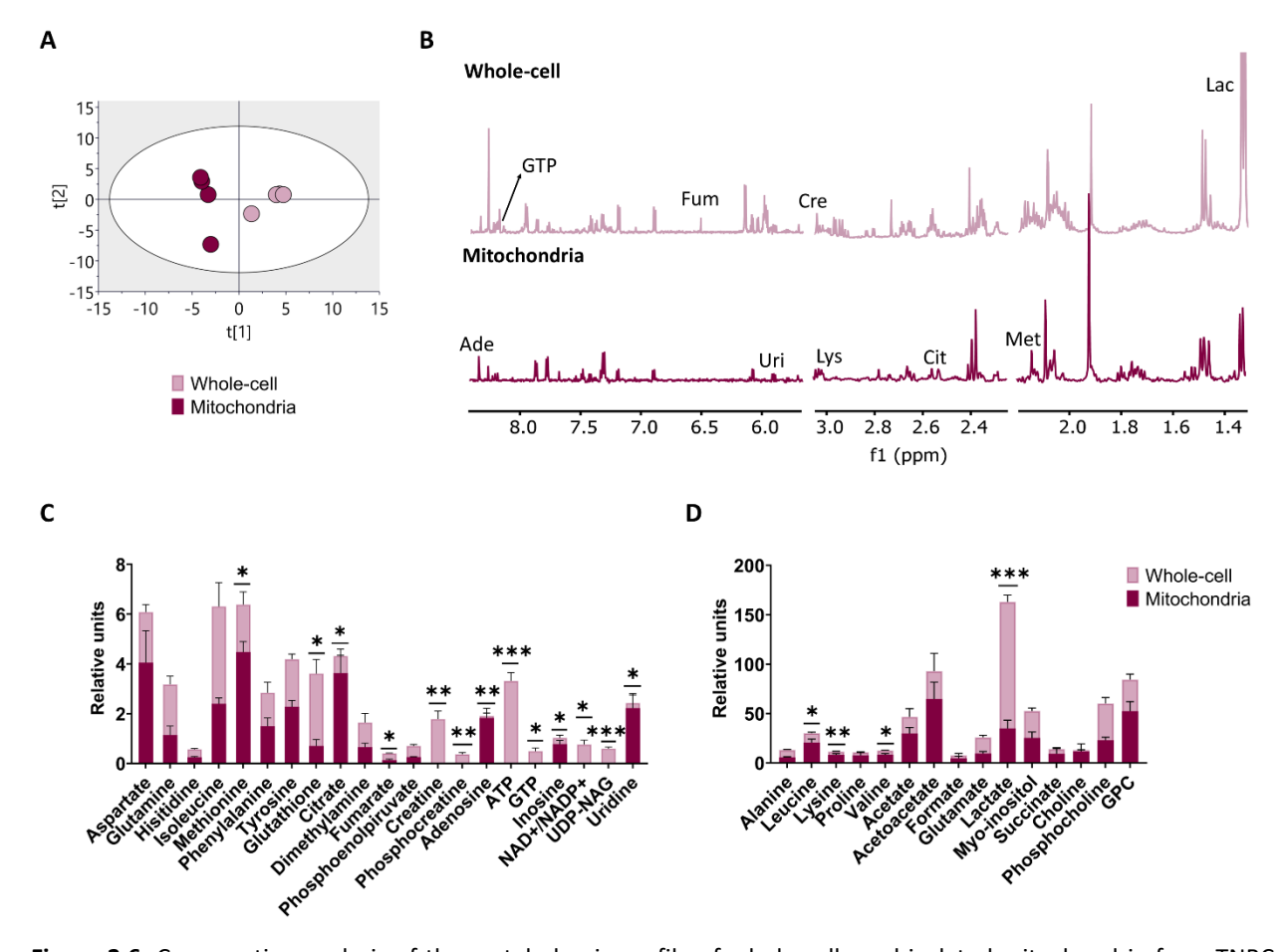


Figure 2.6. Comparative analysis of the metabolomic profile of whole-cells and isolated mitochondria from TNBC cells. **A)** PCA of all the samples (n = 4 per group; statistical algorithm: unit variance scaled). **B)** Representative spectra of the metabolomic profile of (top, light color) whole-cells and (bottom, dark color) isolated mitochondria. The labeled metabolites display significant differences between whole-cells and mitochondria. Ade = adenosine; Cit = citrate; Cre = creatine; Fum = fumarate; GTP = guanosine triphosphate; Lac = lactate; Lys = lysine; Met = methionine; Uri = uridine. **C** and **D)** Relative metabolite levels in the whole-cell (light color) and mitochondria (dark color). **C** depicts metabolites with low relative levels are, while **D** depicts metabolites with high relative levels. Data analysis used a T-test, with data presented as average ± SEM (n = 4); (* p-value < 0.05, ** p-value < 0.01, **** p-value < 0.0001). ATP = adenosine triphosphate; GPC = glycerophosphocholine; GTP = guanosine triphosphate; NAD⁺ = nicotinamide adenine dinucleotide; NADP⁺ = nicotinamide adenine dinucleotide phosphate.

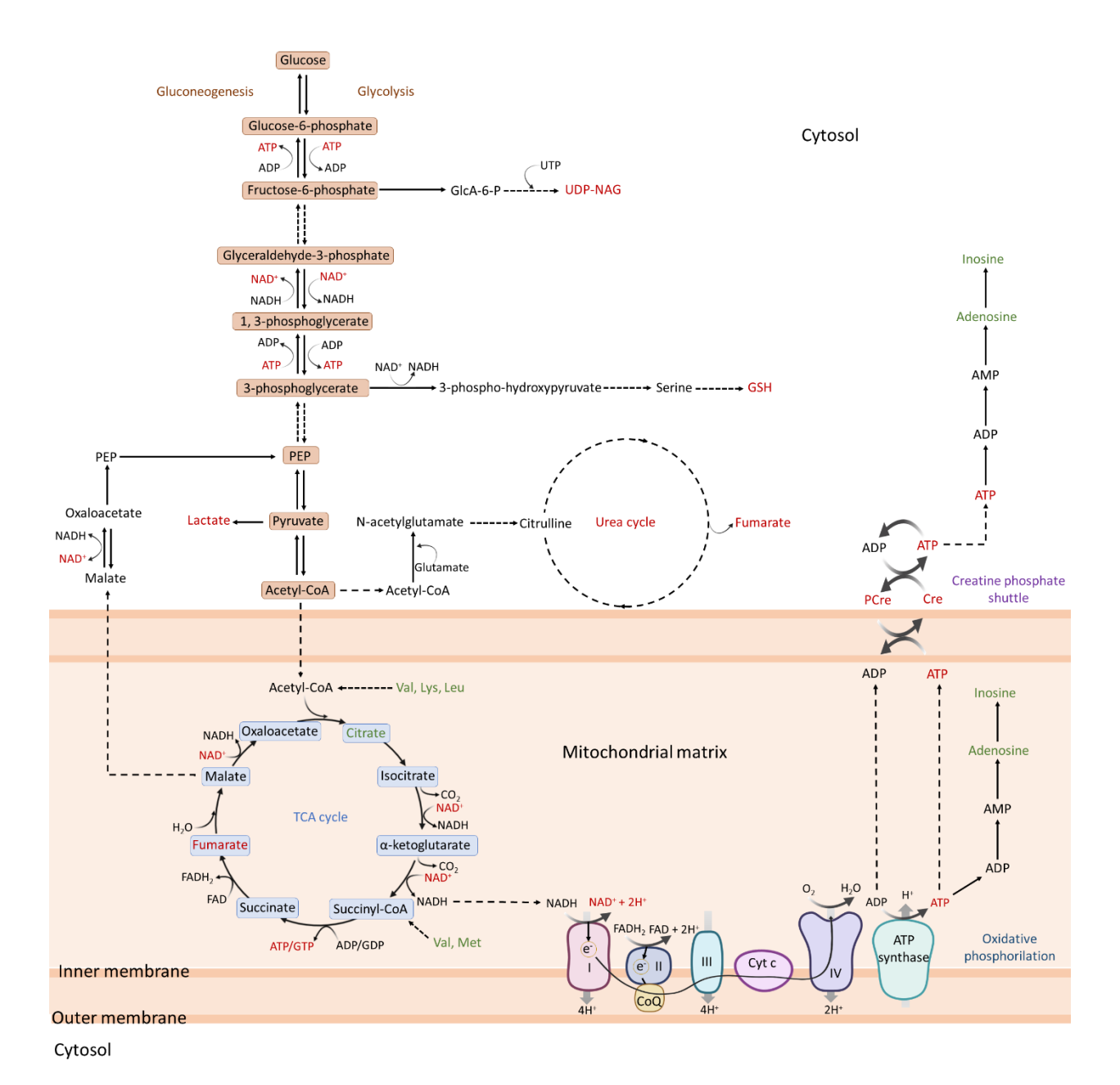


Figure 2.7. Summary of relevant metabolic pathways occurring in the mitochondria and the cytosol. Metabolites in green and in red showed increased and decreased levels, respectively, in the mitochondria analysis compared to the whole-cell analysis. ADP = adenosine diphosphate; AMP = adenosine monophosphate; ATP = adenosine triphosphate; CO_2 = carbon dioxide; COA = coenzyme A; COQ = coenzyme Q_{10} ; Cre = creatine; Cyt c = cytochrome c; CVE = flavin adenine dinucleotide; CEE = guanosine diphosphate; CEE = glucosamine-6-phosphate; CEE = glutathione; CEE = guanosine triphosphate; CEE = leucine; CEE = lysine; CEE = methionine; CEE = nicotinamide adenine dinucleotide; CEE = phosphocreatine; CEE = phosphoenolpyruvate; CEE = uridine diphosphate N-acetylglucosamine; CEE = uridine triphosphate; CEE = valine.

2.3. CONCLUSIONS

In this chapter, we optimized a methodology for analyzing the metabolomic profile of mitochondria isolated from mammalian cells using a TNBC cell line.

To establish the mitochondria isolation method, we employed cell homogenization and differential centrifugation. Cell pellets were homogenized using an electric glass homogenizer, and the disruption of cells was evaluated by measuring LDH activity and cell counting. The enrichment of mitochondria in the final mitochondrial fraction was confirmed through the SDH activity assay and Western blotting. It is crucial to obtain enriched mitochondrial pellets to detect mitochondrial metabolites using NMR spectroscopy.

Next, we optimized a metabolite extraction method suitable for samples with low metabolite levels, avoiding the use of solvents that require subsequent evaporation to prevent metabolite loss. We used an NMR buffer to resuspend the mitochondrial pellet, followed by sonication and quenching to break membranes and extract metabolites. The metabolite extraction process included a final filtration step to remove proteins from the sample, which can appear as broad signals in the NMR spectra and disrupt the baseline. The ¹H NOESY analysis of mitochondrial samples resulted in high-quality spectra. Compared to other methods, our optimized metabolite extraction provided the best spectra quality, a good signal-tonoise ratio, and many quantifiable NMR signals.

We successfully assigned thirty-three metabolites among various categories, including amino acids, organic acids, sugars, nucleotides, and lipids-related metabolites. Importantly, we observed significant differences in the levels of specific metabolites between the whole-cell and mitochondrial samples. Amino acids (leucine, lysine, valine, and methionine), the organic acid citrate, and nucleosides (adenosine, inosine, and uridine) all exhibited higher levels in the mitochondria compared to whole-cells. High mitochondrial amino acid levels are crucial as substrates for the TCA cycle in cancer cells, which may be stimulated for energy and substrate production for other reactions, as indicated by high levels of citrate. Indeed, high amount of mitochondrial metabolites in cancer cells, known as oncometabolites, may result from TCA cycle mutated enzymes. Therefore, researchers are developing anti-tumor therapies targeting mutated TCA cycle enzymes or the oncometabolite downstream pathways³⁰³. The elevated mitochondrial nucleoside pool could indicate stimulated nucleotide metabolism, which has been reported to occur in several cancers and has been considered as a potential target for the development of cancer therapies³⁰⁴. Different studies have reported that nucleotide metabolism targeting with nucleoside analogs enhances cancer immunotherapy³⁰⁵.

In conclusion, we have described, for the first time, an optimized methodology for obtaining the NMR metabolomic profile of mitochondria isolated from mammalian cells. Applying this methodology will facilitate the study of mitochondrial metabolism and provide complementary information to the analysis of whole-cells.

2.4. MATERIALS AND METHODS

2.4.1. Materials

GIBCO™ Dulbecco's Modified Eagle Media (DMEM), GIBCO™ penicillin/streptomycin (P/S), sodium dodecyl sulfate (SDS), Tween-20, and the Potter-Elvehjem Homogenizer were provided by ThermoFisher Scientific (Waltham, Massachusetts, United States). HyClone Dulbecco's phosphate-buffered saline (DPBS) was obtained from Cytiva UK Ltd. (Buckinghamshire, UK). Fetal bovine serum (FBS), sucrose, Tris-HCl, BSA, LDH activity assay kit, sodium succinate, sodium phosphate, p-iodonitrotetrazolium violet (INT), acetic acid, trichloroacetic acid, sodium deoxycholate, Nonidet P-40 (NP40), Bradford reagent, glycerol, bromophenol blue, dithiothreitol (DTT), α-tubulin antibody, secondary anti-rabbit and anti-mouse antibodies, methanol (MeOH) and chloroform (CHCl₃) were purchased from Sigma-Aldrich (St. Louis, Missouri, United States). The pillar drill for cell homogenization was obtained from Black and Becker (Towson, Maryland, United States). The Neubauer chamber was provided by Hirschmann Technicolor (Eberstadt, Germany). Mannitol, glycine, disodium hydrogen phosphate (Na₂HPO₄), Acrylamide/Bis-Acrylamide, and Amicon Ultra-0.5 mL 3 KDa centrifugal filters were obtained from Merck Millipore (Burlington, Massachusetts, United States). Absolute ethanol was purchased from Scharlab Chemicals (Barcelona, Spain). Sodium chloride (NaCl) was provided by VWR (Radnor, Pennsylvania, United States). The protease inhibitor cocktail was obtained from Roche (Basel, Switzerland). Skim milk was obtained from Midland Scientific (Omaha, Nebraska, United States). 150 mm cell culture plates were provided by Sarstedt (Nümbrecht, Germany). Amersham ECL™ Prime Western Blotting Detection Reagent, Amersham HypercassetteTM, Amersham HyperfilmTM, and Amersham full-range RainbowTM marker were purchased from ACEFESA (Gavà, Barcelona, Spain). VDAC (voltage-dependent anion channel) antibody was provided by Abcam (Cambridge, United Kingdom). The GAPDH (glyceraldehyde-3-phosphate dehydrogenase) antibody was obtained from Santa Cruz Biotechnology (Dallas, Texas, United States). D₂O, 3-(trimethylsilyl) propionic acid d4 sodium salt (TSP), and 5 mm NMR tubes and caps were purchased from Deutero GmbH (Kastellaun, Germany).

2.4.2. Cell Culture

The cell line chosen for this study was MDA-MB-231-Luc, which was obtained and characterized at the Functional Validation & Preclinical Research (FVPR) of CIBBIM-Nanomedicine, located at Unit 20 of the ICTS "NANBIOSIS" in Barcelona, Spain (http://www.nanbiosis.es/portfolio/u20-in-vivo-experimental-platform/). The MDA-MB-231-Luc cell line is a bioluminescent breast adenocarcinoma cell line widely used in TNBC research.

The cells were cultured at 37°C with 5% CO₂ in DMEM containing 4,500 mg glucose/L and 580 mg L-glutamine/L. The culture medium was supplemented with 10% inactivated FBS and 1% penicillin-streptomycin. The growth medium was refreshed every 3-4 days, and cell passages were performed when the cell confluence reached 80%.

2.4.3. Breast Cancer Cell Collection for Whole-cell Analysis

2.3 million MDA-MB-231-Luc cells were seeded onto a 150 mm cell culture plate. For each experiment, one plate was collected after four days when the cells reached 80-90% confluence. The collection procedure was performed at 4ºC. Initially, the medium was collected and centrifuged at 400 g for 5 minutes at 4ºC, and the supernatant was discarded. The cells were then collected using a scraper and resuspended in 2 mL of DPBS 1x. This cell suspension was combined with the cell pellet from the collected medium. Subsequently, the cells were washed three times with 2 mL of DPBS 1x. Finally, the resulting cell pellet was weighed and stored at -80°C.

2.4.4. Mitochondrial Isolation from Triple Negative Breast Cancer Cells

The isolation procedure, from cell collection to mitochondrial washes, was performed at 4°C. To obtain the mitochondrial fraction, 2.3 million cells were seeded onto 150 mm cell culture plates and allowed to grow for four days until reaching 80-90% confluence. For one replicate, eight plates (80-100 million cells) were collected following the same procedure described in Section 2.4.3.

The cell pellet was homogenized in an isolation buffer (2.5 times the weight of the cell pellet) consisting of 220 mM mannitol, 70 mM sucrose, 10 mM Tris-HCl solution, and 0.5 mg/mL BSA in MilliQ water at pH 7.4. Homogenization was achieved by subjecting the pellet to 30 strokes using an electric glass homogenizer. The resulting homogenate was then centrifuged at 560 g for 15 minutes at 4°C to obtain the nuclear fraction (pellet) and the soluble fraction (supernatant) containing mitochondria. The supernatant was further centrifuged at 7,000 g for 15 minutes at 4°C to isolate the mitochondrial fraction (pellet) and the cytosolic fraction (supernatant). The mitochondrial fraction was washed twice with the isolation buffer, and the final mitochondrial fraction was weighed and stored at -80°C.

2.4.5. Assays Used from the Optimization of Mitochondrial Isolation

2.4.5.1. Measurement of Cell Lysis by Cell Counting

Ten microliters (μ L) of homogenates obtained after 0, 10, 20, 30, 40, 50, and 60 strokes were combined with 10 μ L of 0.4% trypan blue solution. From this mixture, 10 μ L was loaded into a Neubauer chamber. Cell counting was performed in each quadrant of the chamber, and the following formula was used to calculate the number of cells per milliliter (mL) for each sample. The dilution factor was 2, and the chamber factor was 10,000 cells/mL:

$$Viable (cell/mL) = \frac{Counted \ cells}{Number \ of \ quadrants} \ x \ dilution \ factor \ x \ chamber \ factor$$

The percentage of cell lysis was determined after each number of strokes, taking into account 100% cells and 0% cell lysis before homogenization (0 strokes). The average percentage of cell lysis was plotted as mean ± standard error of the mean (SEM) with a sample size of n=4 using GraphPad Prism (version 9.5.0, GraphPad Software Inc., USA). Statistical significance was determined by comparing the data using a significance level of p<0.05.

2.4.5.2. Measurement of Lactate Dehydrogenase Activity

LDH activity was assessed using the LDH assay kit (Sigma Aldrich, MAK066). LDH reduces NAD⁺ to NADH, which is detected through a colorimetric assay. A standard curve for NADH concentration was prepared by adding 0, 2.5, 5, 7.5, 10, and 12.5 nmol/well in duplicate to a 96-well plate. Samples were prepared by centrifuging 20 μ L of homogenate at 10,000 g for 15 min at 4 $^{\circ}$ C. The supernatant was transferred to another tube, and dilutions were made based on the sample concentration (1:5-1:10) using the LDH assay buffer. For each sample, 1 μ L of diluted sample was added in duplicate to a 96-well plate, followed by 49 μ L of LDH assay buffer. Then, 50 μ L of Master Reaction Mix (48 μ L LDH assay buffer plus 2 μ L LDH substrate mix) was added to all wells, including standard curves and samples, and the contents were mixed by pipetting. Absorbance was measured at 450 nm at time 0 and every 5 min using a CLARIOstar Plus plate reader (BMG Labtech, Ortenberg, Germany). The measurement used for calculating LDH activity was the penultimate reading before the absorbance of the most active sample exceeded the last point of the standard curve. The standard curve was plotted to obtain the equation of the line. The mean absorbance of each sample was substituted into the equation to determine the amount of [NADH] converted by LDH in nmol. LDH activity was then calculated using the following formula:

$$LDH\ activity\ (nmol/\min/mL)\ = \frac{nmol\ NADH}{reaction\ time\ x\ Vsample}\ x\ Dilution\ factor$$

LDH activity was determined in triplicate for each number of strokes (0, 10, 20, 30, 40, 50, and 60) using the electric glass homogenizer. To obtain the relative LDH activity, the LDH activity of each sample was divided by the LDH activity of the sample before homogenization (0 strokes).

The RSA of LDH was plotted as the average \pm SEM (n=3) using GraphPad Prism (version 9.5.0, GraphPad Software Inc., USA). Statistical significance was determined by comparisons with p<0.05.

2.4.5.3. Measurement of Succinate Dehydrogenase Activity

SDH activity in the samples was determined by measuring the reduction of INT by SDH and quantifying the protein content of the mitochondrial, nuclear, and cytosolic fractions to calculate the RSA of the enzyme. The mitochondrial and nuclear pellets were divided into two parts for SDH activity measurement and protein quantification.

To measure SDH activity, a substrate medium containing 0.01 M sodium succinate in buffer (0.05 M sodium phosphate, pH 7.5) was prepared. A total of 300 μ L of the substrate medium was added to the mitochondrial pellet, the nuclear pellet, and 100 μ L of the cytosolic fraction, followed by incubation at 37°C for 10 min. The other half of the mitochondrial pellet was resuspended with 300 μ L of buffer as a control. Next, 100 μ L of acceptor INT (2.5 mg/mL) was added to each tube, and the tubes were incubated at 37°C for 10 min. The reaction was stopped using a solvent mixture of ethyl acetate, ethanol, and trichloroacetic acid (5:5:1). The tubes were then centrifuged at 10,000 g for 2 min to isolate any precipitate, and the absorbance was measured at 490 nm using a CLARIOstar plate reader. The percentage of SDH activity was calculated by dividing the absorbance of each subcellular compartment by the total absorbance of the three fractions (mitochondrial, nuclear, and cytosolic fractions).

Protein quantification was performed using Bradford assays. The mitochondria and nuclear pellets were resuspended in 100 μ L and 200 μ L, respectively, of radioimmunoprecipitation assay (RIPA) buffer (150 mM NaCl, 50 mM 2-Amino-2-(hydroxymethyl)-1,3-propanediol (Tris Base), 1% SDS, 5% sodium deoxycholate, 1% NP40) containing a 25x protease inhibitor cocktail. The samples were vortexed ten times and incubated on ice for 5 min. This process was repeated three times to ensure membrane breakage. Subsequently, the samples were centrifuged at 10,000 g for 15 min at 4 o C, and the supernatants were transferred to new tubes for protein quantification. The protein amount of the cytosolic fraction was determined by adding 4 μ L of protease inhibitor cocktail to 100 μ L of the cytosolic fraction. A standard

curve was prepared using BSA at concentrations of 0, 0.26, 0.43, 0.72, 1.2, and 2 mg/mL. The samples were diluted 1:1-1:30 in DPBS according to the sample concentration. Then, 5 μ L of each sample and the BSA dilutions were added in duplicate to a 96-well plate, followed by the addition of 200 μ L of Bradford reagent. The plate was incubated in darkness for 7 min, and the absorbance of each well was measured at 595 nm using a CLARIOstar Plus plate reader. Protein levels were determined by applying the regression equation and multiplying it by the volume used and the dilution factor. The percentage of protein content was calculated by dividing the protein amount of each subcellular compartment by the sum of the protein amounts of the three fractions (mitochondrial, nuclear, and cytosolic fractions).

The RSA was calculated using the following equation:

$$RSA = \frac{\% SDH \ activity}{\% \ protein \ amount}$$

The RSA was determined in triplicate for each subcellular fraction after 20 and 30 strokes using the electric glass homogenizer. The RSA of SDH was represented in GraphPad Prism (version 9.5.0, GraphPad Software Inc., USA) as the average \pm SEM (n=3), and comparisons with p<0.05 were considered statistically significant.

2.4.5.4. Western Blotting

Mitochondrial pellets were resuspended in 200 μL of RIPA buffer containing a 25x protease inhibitor cocktail, while 250 μL of the cytosolic fractions were supplemented with a 25x protease inhibitor cocktail. Thirty microliters of samples containing 20 μg protein were prepared with 4x loading buffer (130 mM Tris-HCl pH 8, 20% (v/v) glycerol, 4.6% (w/v) SDS, 0.02% bromophenol blue, 2% DTT) and MilliQ water. Proteins were denatured using a thermoblock at 95°C for 7 min, and samples were briefly spun down in a microcentrifuge at 13,000 rpm. Samples and 8 μL of protein marker were loaded into a 10-well, 1.5 mm-thick, 12% bis-Acrylamide (w/v) gel, and proteins were separated by electrophoresis in running buffer (25 mM Tris, 192 mM glycine, 20% (w/v) SDS) at 120 V. Subsequently, proteins were transferred to a nitrocellulose membrane at 400 mA for 2 h. The membrane was blocked with 5% (w/v) milk in DPBS-Tween 20 (0.05%, v/v) for 2 h. After removing the blocking solution, the membranes were incubated in 10 mL of primary antibody diluted in 5% (w/v) milk in DPBS-Tween 20 (0.05%, v/v) (Table 2.4) overnight at 4°C with agitation. The membranes were washed three times with 0.05% (v/v) DPBS-Tween 20 for 10 min at room temperature with agitation. Then, the membranes were incubated by shaking with secondary anti-rabbit or anti-mouse antibodies diluted in 5% (w/v) milk in DPBS-Tween 20 (Table 2.4) for 1 h at room

temperature. Following that, the membranes were washed three times with 0.05% (v/v) DPBS-Tween 20 for 10 min at room temperature with agitation. The ECLTM Prime Western Blotting Detection Reagent was used to detect protein signals. Substrates A and B were mixed in a 1:1 ratio and added to the membranes. Any excess mixture was removed, and the membranes were placed in an Amersham HypercassetteTM with an Amersham HyperfilmTM MP. An AGFA Curix 60 X-ray film processor was used to visualize the protein signals. Protein quantification (n=3) was performed by densitometry analysis using the ImageJ software, and a GAPDH loading control was used to normalize protein levels. The protein quantification graph was plotted in GraphPad Prism (version 9.5.0, GraphPad Software Inc., USA), and t-test analysis was performed in Excel. Comparisons with p<0.05 were considered statistically significant.

Table 2.4. Primary and secondary antibodies used for Western blotting

Antigen	Supplier	Host	Mw* (kDa)	Dilution	Subcellular location		
Primary antibodies							
α-tubulin	Sigma-Aldrich, T8203	Mouse	55	1:10,000	Cytoplasm		
VDAC	Abcam, ab15895	Rabbit	31	1:1,000	Mitochondria		
GAPDH	Santa Cruz Biotechnology, sc-32233	Mouse	37	1:6,000	Cytoplasm, nuclei, mitochondria		
	Secon	dary antibo	dies				
Anti-rabbit	Sigma-Aldrich, A6154	Goat	-	1:5,000	-		
Anti-mouse	Sigma-Aldrich, A9044	Rabbit	-	1:5,000- 1:20,000	-		

^{*}GAPDH = glyceraldehyde-3-phosphate dehydrogenase; Mw = molecular weight; VDAC = voltage-dependent anion channel

2.4.6. Metabolite Extraction Procedures and NMR Sample Preparation

2.4.6.1. Metabolite Extraction from Triple Negative Breast Cancer Cells (Folch Method)

Cell pellets (50-70 mg) were placed on ice and allowed to thaw for 5 min. To each sample, 320 μ L of methanol and 160 μ L of chloroform were added, and the tubes were incubated on ice for 5 min. Subsequently, the samples were vortexed, and cell membranes were disrupted by three freeze-thaw cycles (1 min in liquid nitrogen, 2 min on ice). Then, 250 μ L of MilliQ water and 250 μ L of chloroform were added to each sample, and the tubes were vortexed again. Samples were centrifuged at 10,000 g for 20 min at 4°C to separate the upper methanol/water phase from the lower chloroform phase. The aqueous and organic phases were carefully transferred to new tubes for solvent evaporation. Aqueous solvents were removed using a freeze dryer, while organic solvents were evaporated under a stream of nitrogen gas. The dried extracts were stored at -80°C until NMR analysis.

For NMR analysis, the aqueous phase was resuspended in 550 μ L of NMR buffer (20 mM Na₂HPO₄ pH 7.4, 20 μ M TSP in D₂O) and transferred to a 5 mm NMR tube.

To test the Folch metabolite extraction in mitochondrial samples, we resuspended the mitochondrial pellet in 320 μ L of methanol and 160 μ L of chloroform and continued metabolite extraction as in the previous **Section 2.4.6.1**.

2.4.6.2. Metabolite Extraction from Isolated Mitochondria from Triple Negative Breast Cancer Cells

In the case of metabolite extraction from isolated mitochondria from TNBC cells, mitochondrial pellets (70-100 mg) were placed on ice and allowed to thaw for 5 min. To the mitochondrial pellets, 700 μ L of NMR buffer (20 mM Na₂HPO₄ pH 7.4, 20 μ M TSP in D₂O) was added, followed by vortexing and incubation in an ultrasonic water bath at room temperature for 5 min. The samples were then subjected to a freeze-thaw cycle by incubating in liquid nitrogen for 1 min and thawing in a temperate water bath. This freeze-thaw cycle was repeated twice to disrupt membranes and facilitate metabolite extraction.

After centrifugation at 10,000 g for 20 min at 4° C, the supernatant was transferred to a new tube. To remove protein signals from the spectra, the samples were filtered using 3 kDa centrifugal filters. The filters were washed three times with 400 μ L of MilliQ water and once with 400 μ L of D₂O, followed by centrifugation at 14,000 g for 30 min to dry. Subsequently, the samples were filtered by centrifugation at 14,000 g for 45 min at 4°C, and the filtrate was transferred to a new tube for subsequent NMR analysis. For NMR analysis, 550 μ L of the filtered sample was transferred to a 5 mm NMR tube.

2.4.7. Metabolomic Analysis by NMR Spectroscopy

2.4.7.1. NMR Spectra Acquisition

NMR spectra were acquired using a Bruker AVII-600MHz NMR spectrometer equipped with a 5 mm TCI cryoprobe. The temperature was set to 300 K (27 $^{\circ}$ C), and a standard reference sample consisting of 2 mM sucrose, 0.5 mM sodium trimethylsilylpropanesulfonate (DSS), and 2 mM NaN₃ in H₂O/D₂O was used to ensure spectral resolution and water suppression.

¹H 1D spectra were obtained using the NOESY pulse sequence, with a 4 s relaxation delay between free induction decay (FID) readings and a water presaturation pulse of 25 Hz to minimize the water signal. For the whole-cell samples and for the optimization of the metabolite extraction method of mitochondrial samples, 256 scans (25 minutes) were acquired, while 2512 scans (4 hours) were performed for the analysis of final mitochondrial fractions. The difference in the number of scans is due to the low levels of metabolites in the mitochondria samples, which require more time to acquire high-quality spectra.

The CPMG experiment was conducted with a 4 second relaxation delay (D1) between free induction decay (FID) readings, 256 scans (31 minutes), 128 loops for filter T2 (L4), and a fixed echo time of 0.0003 s to eliminate J-modulation effects (D20).

2.4.7.2. NMR Data Processing

For data processing, FID values were multiplied by an exponential function with a 0.5 Hz line broadening factor and Fourier transformed in Topspin 3.2 (Bruker GmbH, Karlsruhe, Germany). Spectra were further processed in MestreNova (MestreLab Research, Santiago de Compostela, Spain). The spectra were referenced to the internal standard (TSP), and phase correction was performed manually. Baseline correction was applied using automatic Whittaker smoother correction for whole-cell samples, while manual optimization of the Whittaker smoother correction was applied for mitochondria spectra, taking into account significant sucrose and mannitol signals from the isolation buffer that can distort the baseline.

2.4.7.3. Metabolite Identification and Quantification

Metabolite signals were identified after processing the NMR spectra. An Excel file was created to assign the sample type (**Table 2.3**) using publicly available information from the Human Metabolome Database (HMDB) and the Chenomx profiler. The signals were integrated using the "Predefined sum" calculation method in MestreNova software, with the assignment table uploaded in text file format. The integral values were saved as 1D Integral Series (.txt) and opened in Excel.

Data were normalized using the total area method, where each integral value was divided by the sum of all integrals in the sample, excluding signals originating from the isolation buffer and the NMR buffer. This method preserved the relative intensities of the signals in each sample.

For the quantitative comparison of different procedures, a series of selected metabolites were integrated, and the integrals were quantified relative to the internal standard (TSP) to obtain absolute quantification.

2.4.7.4. Univariate Analysis

Univariate analysis was performed using t-tests in Excel to compare the relative intensities of metabolites in whole-cells and mitochondrial samples. Graphs were presented as average \pm SEM from three assays and plotted using GraphPad Prism (version 9.5.0, GraphPad Software Inc., USA). Comparisons with p < 0.05 were considered statistically significant.

CHAPTER III

EVALUATING THE IMPACT OF FREE DRUGS AND POLYMER-DRUG CONJUGATES ON THE METABOLISM OF TRIPLE NEGATIVE BREAST CANCER CELLS

3.1. INTRODUCTION

Triple negative breast cancer (TNBC) treatment involves the administration of chemotherapeutics until patients show maximal tolerance or maximal response; however, less than 30% of TNBC patients achieve a complete response, and recurrence and mortality rates remain higher than other breast cancer subtypes³⁰⁶. In this sense, developing advanced therapies, including nanomedicines, may help to improve outcomes in TNBC patients⁵⁹.

Chapter I (Section 1.2.1) described polymer therapeutics as a successful class of nanomedicines with demonstrated clinical benefit¹⁰¹. Within this family, polymer-drug conjugates – a water-soluble polymeric carrier conjugated to one or more small molecular-weight drugs through a bioresponsive linker – present with further advantages^{142,148} in addition to those already associated with nanomedicines (i.e., increased circulation times and higher tumor accumulation due to the enhanced permeability and retention [EPR] effect^{148,150}). These unique features mainly relate to the presence of a bioresponsive linker between the polymeric carrier and the drug(s) and include a modified drug pharmacokinetic profile and the possibility of site-specific controlled drug release kinetics that enhances treatment efficacy and reduces side effects^{142,148,149,151,155}. Moreover, the use of polypeptides such as poly-L-glutamic acid (PGA) as polymeric carriers adds more benefits when rationally designing polymer-drug conjugates due to their i) inherent biodegradability into endogenous metabolites and, therefore, biocompatibility, ii) structural versatility that can fine-tune whole body biodistribution, iii) cell uptake, and iv) multivalency, which allows high drug loading capacity and drug combination strategies¹⁵⁵.

The design of polymer-drug conjugates also supports the incorporation of targeting moieties for specific delivery at cellular or subcellular sites. Notably, certain polypeptidic systems also display inherent organ/organelle tropism (e.g., lymph nodes³⁰⁷; kidney³⁰⁸ or mitochondria^{309,310}). In this context, the unique features of cancer cells' mitochondria (e.g., mitochondrial membrane depolarization and metabolic reprogramming) make them an attractive target for cancer treatment⁴⁶. Indeed, the design of mitochondrially-targeted polymer therapeutics for cancer management represents a promising field^{170,309,310}.

Evaluations of mitochondrial membrane potential (MMP) ^{133,185}, oxidative phosphorylation (OXPHOS)^{311,312}, morphology¹³³, and protein expression³¹² can usually assess the impact of mitochondrially-targeted therapies; however, there exists a general lack of techniques for evaluating the impact of a given therapeutic on mitochondria metabolism.

In this chapter, we focus on the application of the mitochondrial metabolomics methodology described in **Chapter II** to evaluate the metabolic impact of the breast cancer chemotherapeutic drug palbociclib⁷¹ and a PGA-palbociclib conjugate¹⁵³ in the mitochondria of TNBC cells. Our optimized methodology could represent a valuable tool for evaluating mitochondrial metabolic response to any mitochondrial-affecting therapies ranging from small molecular weight drugs to advanced therapies.

3.2. RESULTS AND DISCUSSION

3.2.1. Synthesis and Characterization of StPGA-SS-palbociclib

3.2.1.1. Synthesis of StPGA-SS-palbociclib

We synthesized StPGA-SS-palbociclib as previously described in our laboratory ¹⁵³ (Materials and Methods 3.4.2) by conjugating palbociclib through a secondary amine to a 3-arm star-shaped poly-L-glutamic acid) (StPGA). We linked the StPGA and palbociclib using a redox-sensitive disulfide linker (SS) to achieve controlled drug release in the presence of glutathione (GSH). The higher levels of GSH levels in the cytosol of cells (1-10 μ M) compared to plasma (1-6 μ M)¹⁶⁶ ensure the stability of StPGA-SS-palbociclib in the blood and the intracellular linker cleavage and drug release. Figure 3.1 summarizes the complete synthetic procedure.

Figure 3.1. Schema of the procedure followed to synthesize StPGA-SS-palbociclib. i) palbociclib, TEA and CH₂Cl_{2anh}. ii) cysteamine hydrochloride, CH₂Cl₂:MeOH (1:1) iii) StPGA150, DMTMM·BF₄, DIEA, DMSO. Atoms colored in blue correspond to palbociclib, while atoms colored in orange correspond to StPGA.

The synthetic strategy comprised five steps (**Figure 3.1**), beginning with a thiol exchange reaction between 2,2-dithiodipyridine and mercaptoethanol, then coupling the palbociclib to the p-nitrophenyl chloroformate activated hydroxyl group to yield palbociclib-SS-pyridine (palbociclib-SS-Pyr; yield: 87.3%). After purification of palbociclib-SS-Pyr by column

chromatography, we confirmed identity by ¹H NMR spectroscopy (**Figure 3.2**). **Supporting Information 3.1 and 3.2** show the assigned ¹H NMR spectra of the disulfide linker (4-nitrophenyl (2-(pyridine-2-yldisulfaneyl)ethyl) carbonate) and palbociclib.

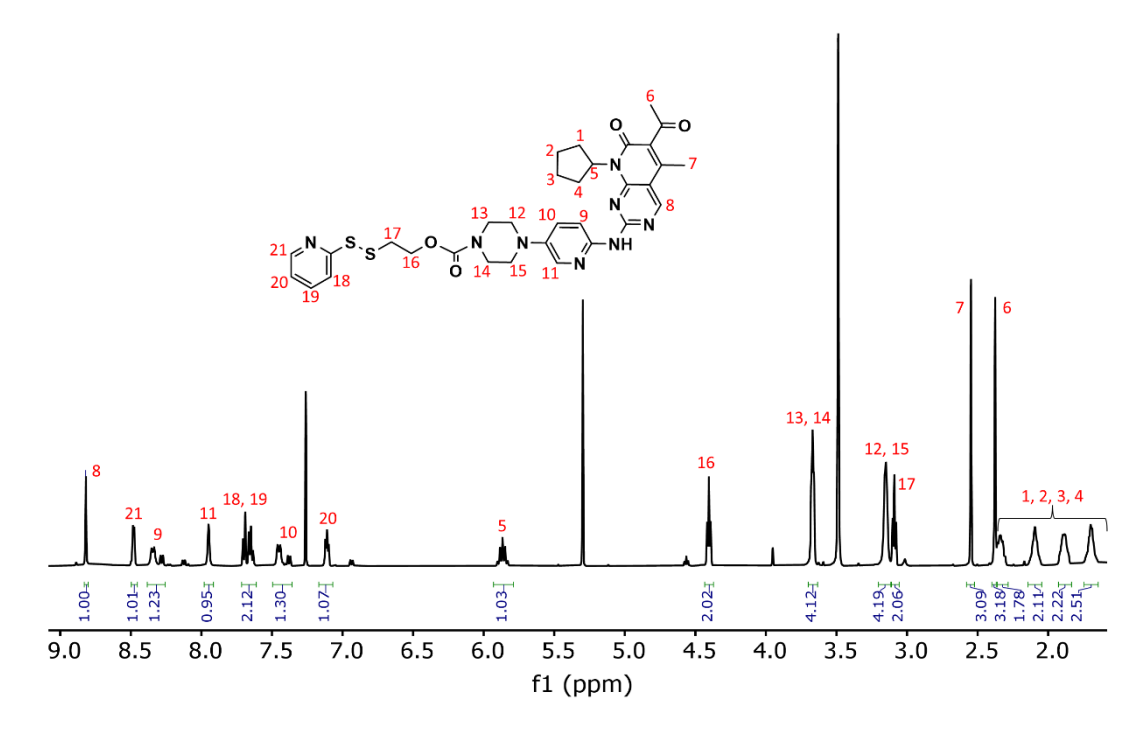


Figure 3.2. ¹H NMR spectra assignment of palbociclib-SS-Pyr. ¹H NMR chemical shifts (ppm) (500 MHz, CDCl₃): 1.70 (m, 2H), 1.88 (m, 2H), 2.08 (m, 2H), 2.33 (m, 2H), 2.37 (s, 3H), 2.54 (s, 3H), 3.09 (t, 2H), 3.14 (t, 4H), 3.66 (t, 4H), 4.40 (t, 2H), 5.86 (m, 1H), 7.10 (m, 1H), 7.40 (dd, 1H), 7.67 (m, 2H), 7.94 (s, 1H), 8.30 (dd, 1H), 8.47 (m, 1H), 8.81 (s, 1H).

The following reaction consisted of a second thiol exchange of the palbociclib-SS-Pyr with cysteamine hydrochloride to generate palbociclib-SS-NH₂ (yield: 81%). The reaction occurs due to the product's higher stability (palbociclib-SS-NH₂) than palbociclib-SS-Pyr. We then precipitated palbociclib-SS-NH₂ in ether to remove the remaining cysteamine hydrochloride and confirmed its identity by ¹H NMR spectroscopy (**Figure 3.3**).

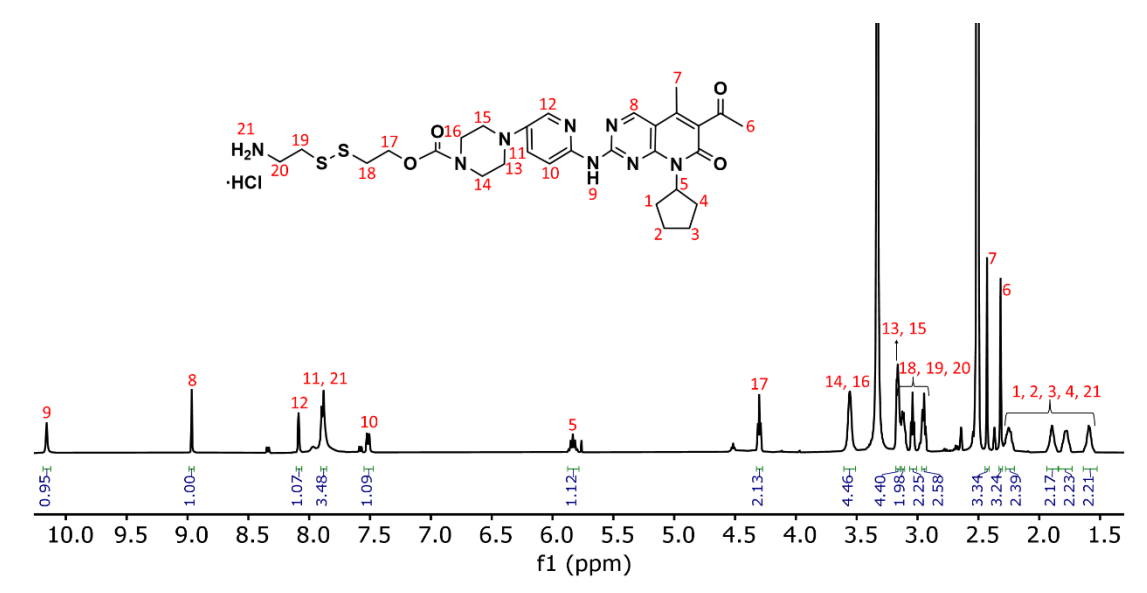


Figure 3.3. ¹H NMR spectra assignment of palbociclib-SS-NH₂. ¹H NMR chemical shifts (ppm) (500 MHz, d-DMSO): 1.58 (m, 2H), 1.77 (m, 2H), 1.88 (m,2H), 2.25 (m, 2H), 2.32 (s, 3H), 2.43 (s, 3H), 2.95 (t, 2H), 3.04 (t, 2H), 3.12 (m, 2H), 3.16 (t, 4H), 3.56 (t, 4H), 4.30 (t, 2H), 5.83 (m, 1H), 7.51 (dd, 1H), 7.88 (m + dd, 3H), 8.09 (s, 1H), 8.96 (s, 1H), 10.15 (s, 1H).

The final step involved conjugation of palbociclib-SS-NH₂ to St-PGA via amide coupling with the 4-(4,6-dimethoxy-1,3,5-triazin-2-yl)-4-methylmorpholinium tetrafluoroborate (DMTMM·BF₄) activator³¹³. We obtained the acid form of StPGA-SS-palbociclib at high purity after precipitation in diethyl ether, conversion into the salt form, and subsequent dialysis against Milli-Q water. In this particular case, we obtained a lower reaction yield than expected (Yield: 48%), perhaps due to a partial thiol exchange in the previous step and, therefore, the partial formation of palbociclib-SS-NH₂, which we observed in our laboratory during the synthesis optimization of similar conjugates^{153,168}. Despite the inefficiency of this reaction, we designed StPGA-SS-palbociclib with low drug loading, as previous studies in our laboratory reported an inverse correlation between drug loading and biological activity¹⁵³.

Finally, we purified the product by Sephadex column chromatography and confirmed the identity of StPGA-SS-palbociclib by ¹H NMR spectroscopy. PGA conjugation prompted band broadening; however, characteristic peaks of palbociclib in aromatic and aliphatic regions remained (**Figure 3.4 and Figure 3.5**). **Supporting Information, Section 3.3** reports the assigned ¹H NMR spectra of StPGA150 (starting polymeric carrier).

We next applied different characterization techniques to perform exhaustive physico-chemical characterization steps to determine conjugation efficiency.

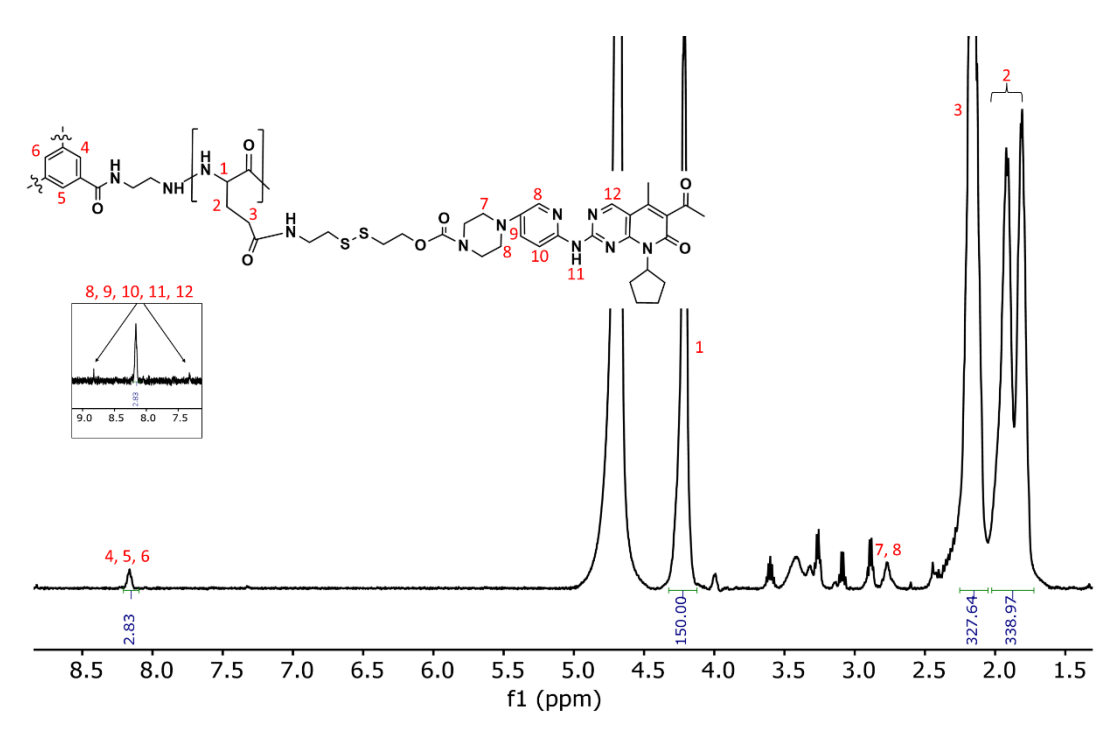


Figure 3.4. ¹H NMR spectra assignment of StPGA-SS-palbociclib. ¹H NMR chemical shifts of StPGA (ppm) (500 MHz, D₂O): 1.84 (m, 2H), 2.15 (m, 2H), 4.20 (m, 1H), 8.15 (s, 3H). Aliphatic (2.75 ppm) and aromatic (7.32, 8.81 ppm) of palbociclib were detected to confirm conjugation to StPGA.

3.2.1.2. Physico-chemical Characterization of StPGA-SS-palbociclib

The synthesis of any polymer-drug conjugate requires physico-chemical characterization to ensure identity and describe solution conformation properties to adequately correlate with therapeutic output¹⁵².

As mentioned in the previous section, we first monitored the synthesis of StPGA-SS-palbociclib by ¹H NMR spectroscopy. **Figure 3.5** reports the ¹H NMR spectra of all the precursors and products. We then determined conjugate total drug loading (TDL) by UV-Vis as 1.5 wt% palbociclib with a free drug content of 1.05 wt% compared to TDL as determined by liquid chromatography–mass spectrometry (LC–MS). In brief, we dissolved 3 mg of StPGA-SS-palbociclib in MeOH to selectively dissolve any remaining free palbociclib to identify free drug content. LC-MS analysis determined that the 1.05 wt% of the quantified loaded drug corresponded to free palbociclib.

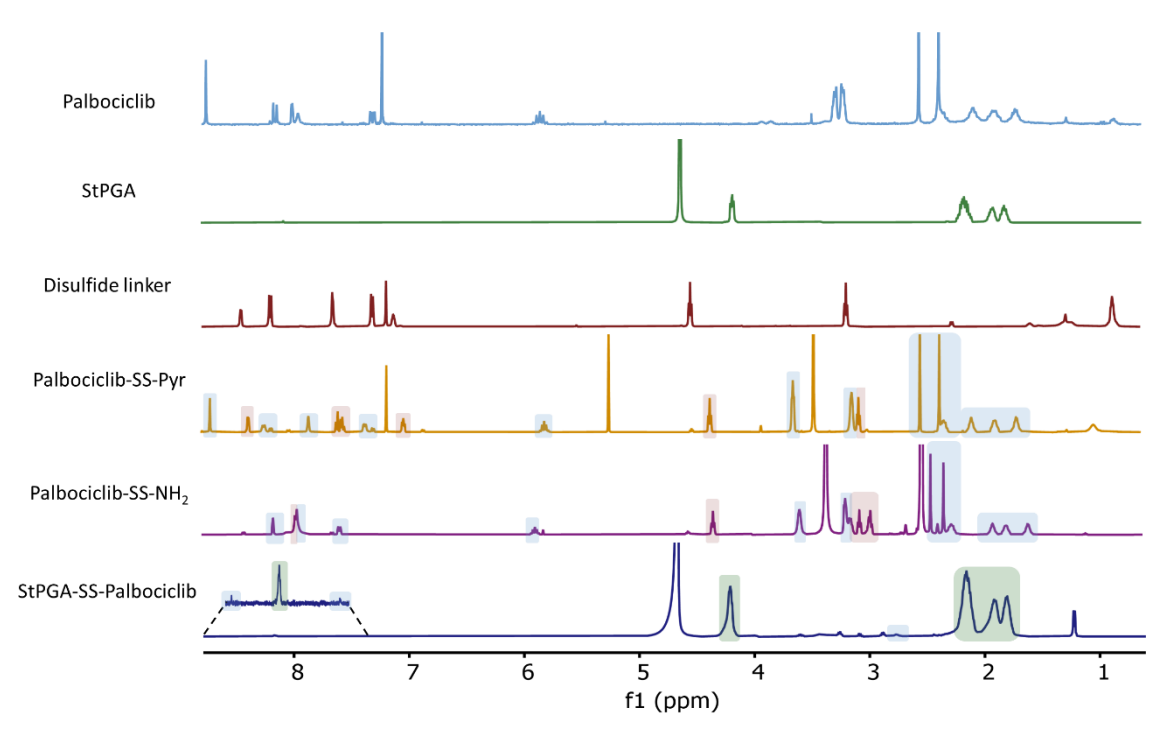


Figure 3.5. ¹H NMR spectra (500 MHz) of precursors (palbociclib, StPGA, and the disulfide linker) and products of each synthesis step (palbociclib-SS-Pyr, palbociclib-SS-NH₂ and StPGA-SS-palbociclib) with precursor signals highlighted in green (StPGA), blue (palbociclib), and red (disulfide linker).

We measured the hydrodynamic diameter of the conjugate by Bayesian diffusion-ordered NMR spectroscopy (DOSY) transform; we then substituted the obtained diffusion coefficient (3.2*10⁻¹¹ m²/s; **Figure 3.6**) into the Einstein-Strokes equation to determine the radius³¹⁴. We observed a hydrodynamic diameter of 11.56 nm, which agreed well with previous data¹⁵³ and lay within the size range (5-200 nm) suitable for biological application *in vivo*¹⁵².

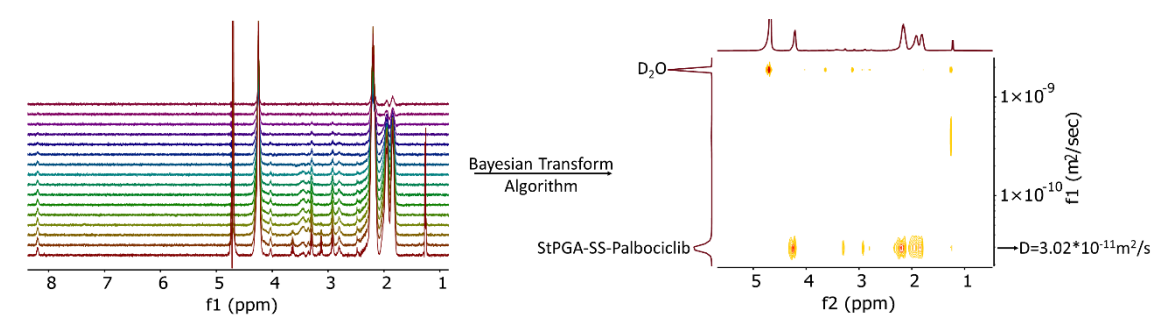


Figure 3.6. ¹H NMR diffusion spectra and 2D DOSY spectra (500 MHz, D₂O) of StPGA-SS-palbociclib after applying the Bayesian transform algorithm. D = diffusion coefficient obtained for StPGA-SS-palbociclib.

The zeta potential of StPGA-SS-palbociclib determined by a Malvern ZetasizerNano ZS instrument provided a negative value (-17 mV), as expected for conjugates with polyanionic PGA carriers.

Circular dichroism (CD) of StPGA-SS-palbociclib demonstrated a random coil conformation indicated by the negative peak at 200 nm (**Figure 3.7**). A random coil conformation has been previously observed for StPGA-palbociclib conjugates for low drug loadings, although it may suffer a transition to an α -helix conformation upon increasing the drug loading¹⁵³. **Table 3.1** summarizes the physico-chemical characteristics of StPGA-SS-palbociclib.

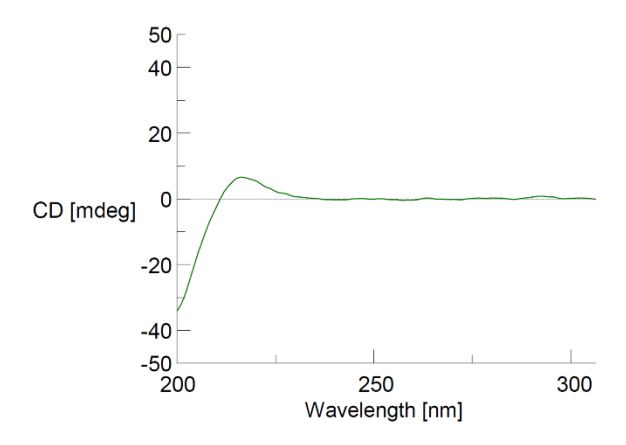


Figure 3.7. Circular dichroism (CD) spectra of StPGA-SS-palbociclib (0.25 mg/mL DPBS). Spectrum represents the result of three accumulated measurements.

Table 3.1. Summary of the physico-chemical characteristics of StPGA-SS-palbociclib

	TDL (wt %) ¹	TDL (mol %) ¹	Rh (nm)²	Z pot (mV) ³	Conformation ⁴	wt% FD toTDL⁵
StPGA-SS-palbociclib	1.46	0.5	11.56	-17.13	Random coil	1.05

¹UV-Visible spectroscopy; ²Bayesian Diffusion-Ordered NMR Spectroscopy Transform; ³Malvern ZetasizerNano ZS instrument; ⁴Circular Dichroism; ⁵Liquid chromatography-mass spectrometry/mass spectrometry. FD = free drug; Rh = hydrodynamic radius; TDL = total drug loading; wt = weight; Z pot = Z potential.

We then studied palbociclib release kinetics by exposing StPGA-SS-palbociclib to cytosolic (5 mM) and extracellular (10 µM) levels of dithiothreitol (DTT) as a trigger for linker self-immolation. We collected aliquots at different time points (0, 1, 2, 4, 6, 24, 48, and 72 h) to evaluate the drug release kinetics profile. Prior to the drug extraction step from each aliquot, we added niraparib as an internal standard (IS). Importantly, due to an error with the calculations of the IS volume, we could not perform an adequate determination of the palbociclib released by high-performance liquid chromatography (HPLC) coupled to a photodiode array detector (DAD) due to column oversaturation and an IS peak that masked any possible palbociclib signal (Figure 3.8A). HPLC only enabled the accurate detection of palbociclib and IS when we analyzed standard solutions (Figure 3.8B). Dilution of the samples by a factor that allowed the visualization of niraparib and palbociclib as separate peaks would have made palbociclib undetectable by HPLC; therefore, we sought an alternative analytical strategy using LC-MS/MS. As LC-MS/MS displays greater sensitivity than HPLC, we diluted samples to

adequately analyze palbociclib and IS (avoid peak tailing and splitting). We first diluted samples by the dilution factor required to obtain a symmetric chromatographic peak of palbociclib at a retention time (t_R) of 3.04 min (**Figure 3.9A**); then, we diluted the same samples to achieve 0.06 μ g/mL IS and obtain the symmetric peak at t_R = 2.96 min (**Figure 3.9B**). **Supporting Information 3.4** displays the MS spectrum and the MS fragmentation spectrum of a 2 μ g/mL palbociclib and 2 μ g/mL niraparib solution, where we detected the palbociclib (Palbo+1) and the niraparib (Nira+1) adducts at 448.2 Da and 321 Da, respectively.

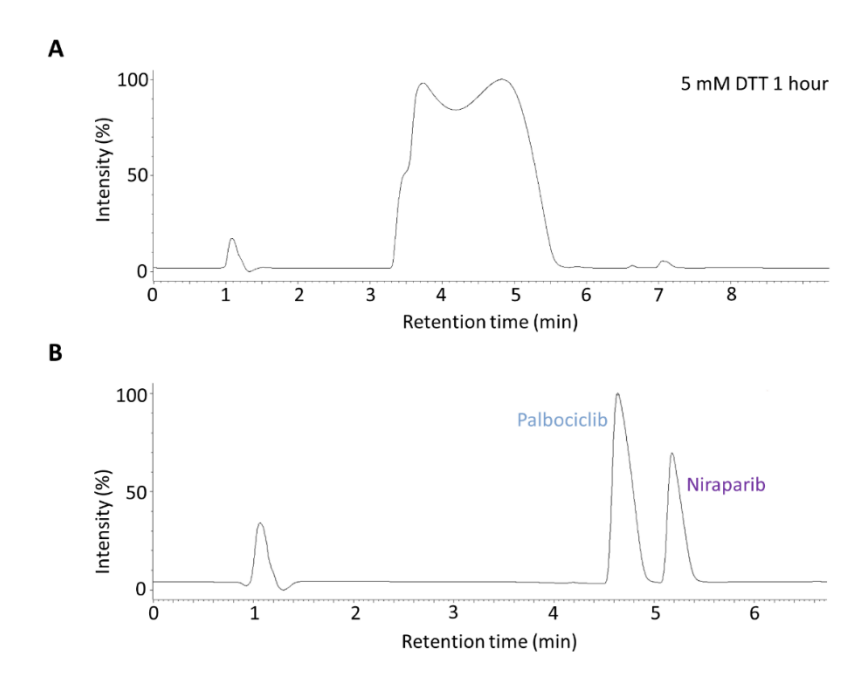


Figure 3.8. HPLC chromatograms of **A**) the released palbociclib from StPGA-SS-palbociclib and niraparib, as internal standard, after 1 h of incubation with 5 mM DTT samples and **B**) 5 μ g/mL palbociclib standard solution containing 1 μ g/mL niraparib as internal standard.

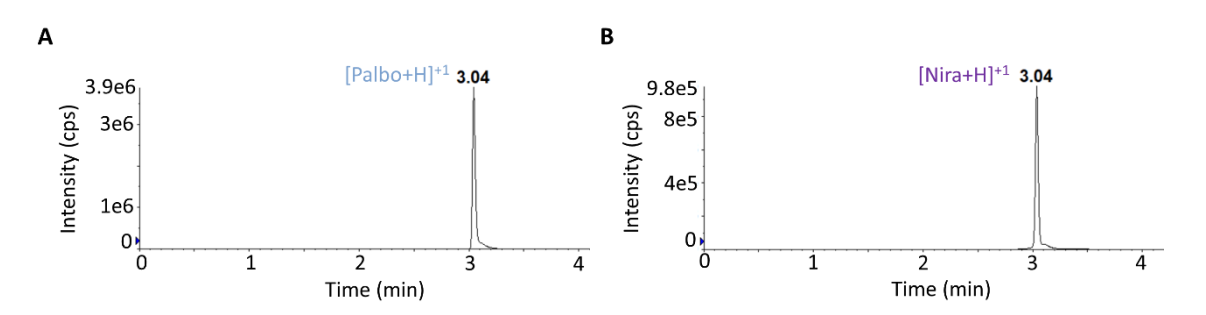


Figure 3.9. Representative LC-MS/MS chromatogram of **A**) released palbociclib (palbo) from StPGA-SS-palbociclib and **B**) the internal standard niraparib (nira) corresponding to a StPGA-SS-palbociclib sample incubated with 5 mM DTT for 1 h. cps = counts per second.

We observed 50% palbociclib released after 72 h when incubated with 5 mM DTT, while we only observed a 10% release under extracellular conditions (10 μ M DTT) (**Figure 3.10A**). Surprisingly, we observed 10% palbociclib release at extracellular conditions (10 μ m DTT) and 17% release at

intracellular conditions (5mM DTT); we detected only 1.05 wt% compared to TDL as free drug content in StPGA-SS-palbociclib. Overall, the matrix effect caused by high IS concentration influenced palbociclib analysis. As matrix effects enhance or suppress the response of the compound signal³¹⁵, minimizing matrix effects during sample preparation remains critical to obtaining a confident outcome. Considering this, we normalized the graph to zero at the starting time point; **Figure 3.10B** reports the resulting graph. We obtained 33.34% palbociclib released after 72 h under intracellular conditions, while we observed no significant release under extracellular conditions, confirming the disulfide linker's stability in extracellular conditions. Moreover, previous work in our laboratory demonstrated the stability of StPGA-SS-palbociclib in plasma, as less than 1% of palbociclib became released from the conjugates after seven days¹⁵³.

Due to time constraints, we could not repeat this experiment with the adequate concentration of niraparib as an internal standard; however, these experiments are ongoing, and data will be ready for future publication to corroborate preliminary results.

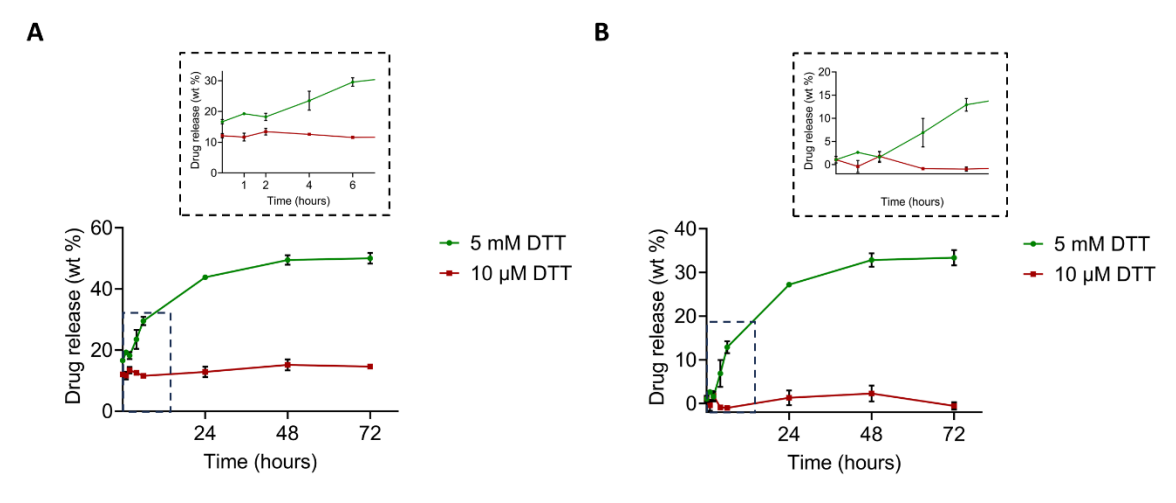


Figure 3.10. Drug release from StPGA-SS-palbociclib. **A)** Release of palbociclib from StPGA-SS-palbociclib under a reducing environment (5 mM dithiothreitol [DTT]) with 10 μ m DTT as a control sample (mimicking the extracellular environment) prior to the data normalization. **B)** Release of palbociclib from StPGA-SS-palbociclib under a reducing environment (5 mM DTT) with 10 μ m DTT as a control sample (mimicking the extracellular environment) after normalization of data to the amount of free drug at time zero. Data obtained from LC-MS/MS quantification of palbociclib and presented as mean \pm SD (n=3).

The physico-chemical characterization of StPGA-SS-palbociclib provided evidence of adequate conjugation efficiency though the disulfide linker. Previous studies in our laboratory reported higher biological activity of palbociclib conjugates with low drug loadings¹⁵³; therefore, we synthesized StPGA-SS-palbociclib with low drug loading (1.46% as determined by UV-Vis spectroscopy, from which the 1.05 wt% compared to TDL corresponded to free palbociclib). We

observed a random coil conformation by CD, with a negatively charged surface (Zetasizer) and a particle size around 10 nm (DOSY Bayesian transform). The release kinetics study revealed the stability of the StPGA-SS-palbociclib conjugate under extracellular conditions and 33% palbociclib release under intracellular conditions, confirming the stability conferred to palbociclib when conjugated to StPGA and the need for a reducing environment for drug release.

3.2.2. Biological Evaluation of Palbociclib and StPGA-SS-palbociclib in Triple Negative Breast Cancer Cells

3.2.2.1. Cell Viability Assay of Palbociclib and StPGA-SS-palbociclib

To evaluate the optimal concentration of palbociclib and StPGA-SS-palbociclib to study their effect on TNBC cell mitochondria, we performed a cell viability study using the MTS (3-(4,5-dimethylthiazol-2-yl)-5-(3-carboxymethoxyphenyl)-2-(4-sulfophenyl)-2H-tetrazolium salt) assay. This assay involves MTS reduction by metabolically active cells to form purple formazan crystals in phenazine methosulfate (PMS). NADPH-dependent dehydrogenases, which only display activity in viable cells, are responsible for this conversion. Therefore, the amount of formazan produced is directly proportional to the number of viable cells, allowing the calculation of the cell viability percentage. The colored formazan can be easily detected using a spectrophotometer³¹⁶.

We treated TNBC cells with palbociclib or StPGA-SS-palbociclib using a concentration range of 0.003-40 μ M (palbociclib equivalents) for 72 h and determined cell viability by MTS assay (**Figure 3.11**). We observed a higher cytotoxicity for free palbociclib (50% inhibitory concentration (IC₅₀) = 3.52 \pm 0.55 μ M, 30% inhibitory concentration (IC₃₀) = 0.77 \pm 0.12 μ M) than StPGA-SS-palbociclib (IC₅₀ = 43.26 \pm 3.57 μ M, IC₃₀ = 3.64 \pm 0.30 μ M). The lower cytotoxicity of StPGA-SS-palbociclib compared to free palbociclib may derived from the different internalization pathways employed; typically, small drugs enter cells by diffusion, reaching the cell target rapidly, while polymer-drug conjugates become internalized by endocytosis, which involves several steps and a longer process¹⁶¹. Therefore, at the same time point (72 h) and concentration (palbociclib equivalents), StPGA-SS-palbociclib displays less toxicity in TNBC cells than free palbociclib.

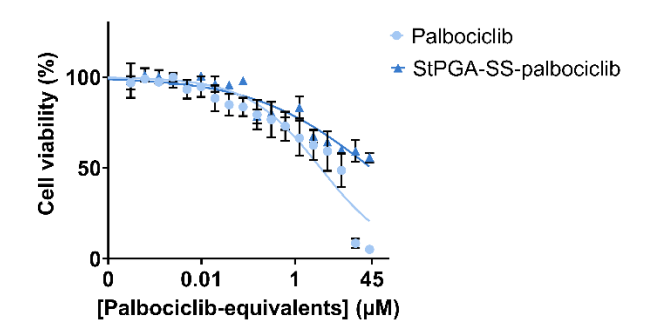


Figure 3.11. Cell viability study of palbociclib and StPGA-SS-palbociclib in TNBC cells. MTS assay measured cell viability at 72 h of treatment. Data represented in palbociclib equivalents as average \pm SEM (n = 3). IC₅₀ and IC₃₀ values shown in the table were obtained from the GraphPad Prism report and the GraphPad Prism Calculator, respectively.

Notably, the non-cytotoxic nature of naked StPGA (up to 0.5 mg/mL) in TNBC cells and a glioblastoma cell line has been previously reported^{153,158}, confirming the safety of StPGA and proving that the cytotoxic activity of StPGA-SS-palbociclib exclusively derived from the activity of the drug.

We employed IC₃₀ values to proceed with the metabolomic studies to assay mitochondria activity modulation; highly toxic concentrations should be avoided to secure the absence of any artifact derived from non-specific toxicities.

3.2.2.2. Assessment of Mitochondrial Respiration After Palbociclib and StPGA-SS-palbociclib Treatment

We assessed mitochondrial cell respiration to study the ability of palbociclib and StPGA-SS-palbociclib to impair mitochondria in TNBC cells. We selected the Agilent Seahorse XF Pro Analyzer (Santa Clara, California, United States) and the Agilent Seahorse XF Cell Mito Stress Test Kit to evaluate mitochondrial respiration. This combination of platform and kit supports the definition of oxygen consumption rate (OCR) and extracellular acidification rate (ECAR; proton concentration in assay media and measure of glycolytic rate) in cells to evaluate mitochondrial respiration and metabolic status, respectively^{317,318}. The Agilent Seahorse XF Cell Mito Stress Test Kit contains inhibitors that specifically target proteins involved in mitochondrial respiration to evaluate different parameters of mitochondrial respiration. Figure 3.12 displays a representative kinetic graph (OCR vs. time) in basal conditions and after the injection of the different inhibitors (oligomycin, carbonyl cyanide-p-trifluoromethoxyphenylhydrazone (FCCP), Antimycin A/Rotenone) and the different parameters (basal respiration, adenosine triphosphate (ATP)-coupled respiration, maximal respiration, non-mitochondrial respiration, spare capacity, and proton leak) that this assay evaluates.

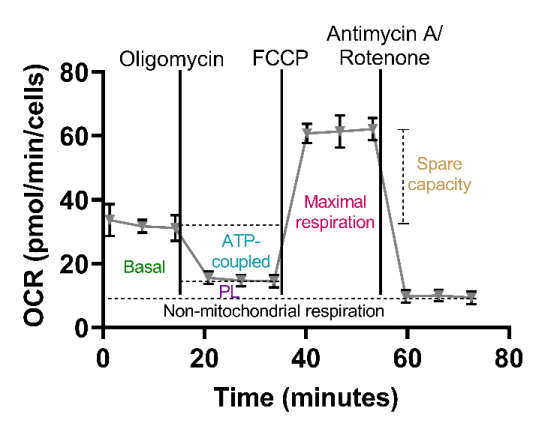


Figure 3.12. Schematic representation of a kinetic graph (OCR vs. time) obtained using the Agilent Seahorse XF Cell Mito Stress Test Kit. Oligomycin inhibits adenosine triphosphate (ATP) synthase to mitochondrial respiration **ATP** synthesis. determine and Carbonyl cyanide-ptrifluoromethoxyphenylhydrazone (FCCP), an ionophore that prompts the transport of protons across the inner mitochondrial membrane (IMM) and mitochondrial depolarization, mimics a physiological energy demand to estimate the maximal respiratory capacity of mitochondria. A mixture of Rotenone and Antimycin A inhibits respiratory complexes I and III, respectively, and inhibits the electron transport chain to allow an estimation of non-mitochondrial respiration carried out by other oxygen-consuming enzymes. Image and description adapted from Divakaruni et al., 2014³¹⁸. PL = proton leak.

Figure 3.13A depicts the OCR levels in TNBC cells following treatment with free palbociclib and StPGA-SS-palbociclib at the IC_{30} values compared to control untreated cells. Briefly, the kinetic graph revealed the maintenance of basal respiration (oxygen consumption associated with ATP synthesis and with other proton leak pathways³¹⁸) after free palbociclib treatment compared to control, while we observed a decline after StPGA-SS-palbociclib treatment compared to control and to free palbociclib. However, we observed a decrease in maximal respiration after treatment with palbociclib and StPGA-SS-palbociclib compared to control with a greater significant effect of StPGA-SS-palbociclib (**Figure 3.13A**).

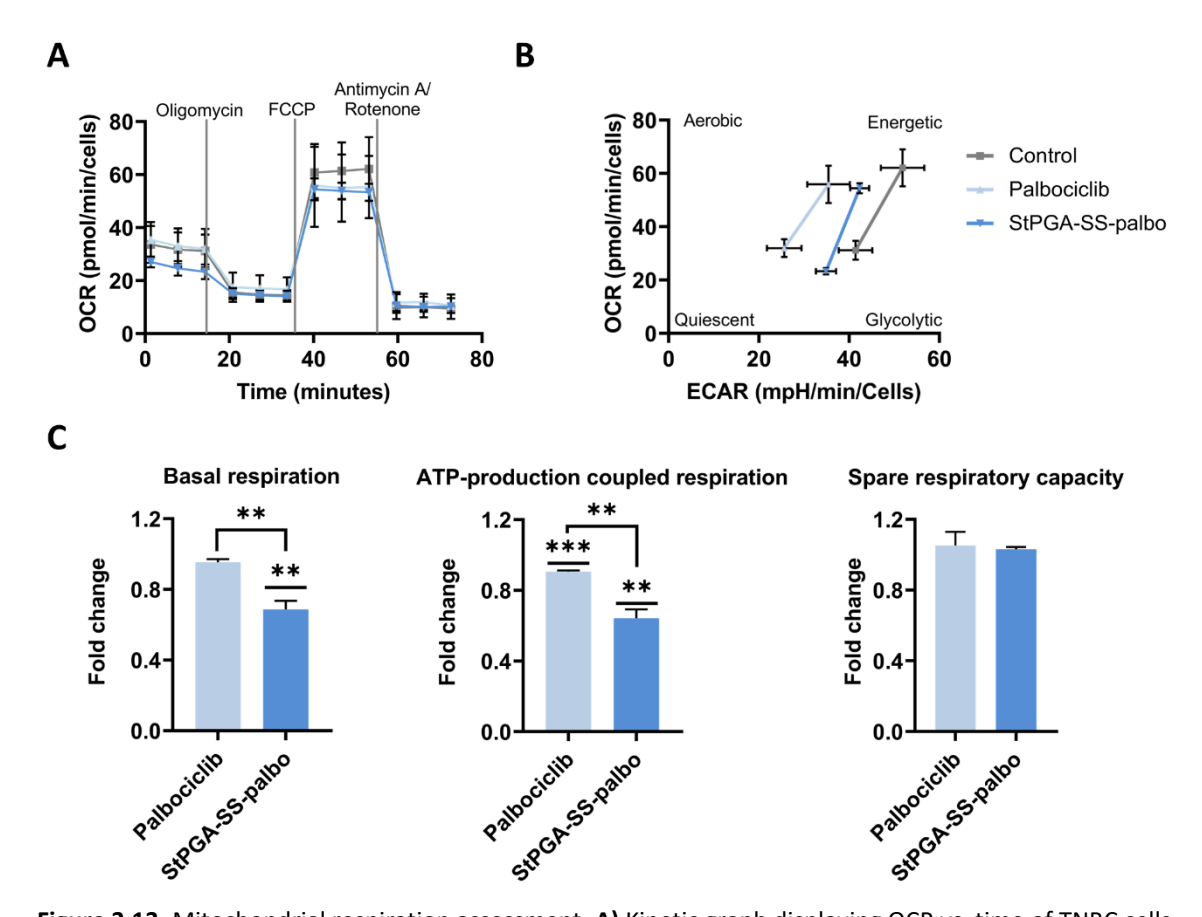


Figure 3.13. Mitochondrial respiration assessment. **A)** Kinetic graph displaying OCR vs. time of TNBC cells without (control) and after treatments with palbociclib and StPGA-SS-palbociclib (StPGA-SS-palbo) at the IC₃₀ concentrations for 72 h. **B)** Cell energy phenotype graph displaying OCR vs. ECAR of TNBC cells without (control) and after treatments with palbociclib and StPGA-SS-palbociclib (StPGA-SS-palbo) at the IC₃₀ concentrations for 72 h. **C)** Bar graphs displaying the fold change (over control cells = untreated) of basal respiration, ATP-production coupled respiration, and spare respiratory capacity in TNBC cells treated with palbociclib and StPGA-SS-palbociclib (StPGA-SS-palbo) at the IC₃₀ concentrations for 72 h. Data analysis used a T-test, with data presented as average \pm SEM; (** p-value < 0.01, *** p-value < 0.001).

Regarding the energy phenotype of treated cells (**Figure 3.13C**), we observed decreased ECAR values after treatment with palbociclib and StPGA-SS-palbociclib compared to control, reflecting a pH increase due to glycolysis impairment; therefore, both treatments impaired the glycolytic pathway and cell adaptation to a more quiescent phenotype, which follows the mechanism of action of palbociclib that induces cellular senescence³¹⁹.

The quantification of the mitochondrial respiration parameters revealed a significant decrease in basal respiration in TNBC cells treated with StPGA-SS-palbociclib compared to control cells and to cells treated with free palbociclib, while we observed no changes after treatment with free palbociclib compared to control cells after 72 h (Figure 3.13B). Nevertheless, ATP-

production coupled respiration became disrupted by both treatments compared to control cells and, to a greater extent, by StPGA-SS-palbociclib (Figure 3.13B). These results may reflect the different internalization pathways followed by each type of treatment: diffusion of the free drug and endocytosis of the conjugated drug¹⁶¹. Although both treatments are added to cells to cause the same percentage (30%) of cell death at 72 h, StPGA-SS-palbociclib triggers a more significant effect on mitochondrial respiration than free palbociclib. The free drug, internalized by diffusion, remains in the cytosol in a constant equilibrium with the extracellular medium, entering and exiting the cell and hindering mitochondrial disruption. StPGA-SS-palbociclib enters the cell by endocytosis, reaching the lysosomes where the drug undergoes controlled release, causing more significant mitochondrial damage. Exocytosis experiments are ongoing to ratify this hypothesis. Moreover, the lysosomal degradation of PGA¹⁶³ may increase the glutamic units in the cell, which could inhibit glutaminolysis and synergize with palbociclib to cause mitochondrial impairment. We will further discuss this hypothesis in the metabolomic analysis (Section **3.2.2.3**). Of note, the spare respiratory capacity of cells (the capability of the cell to respond to an energetic demand indicating cell fitness318) remained unaltered after both treatments, indicating that cells treated at the IC₃₀ concentration of treatments for 72 h responded to the energy demand (Figure 3.13B).

The evaluation of the mitochondrial impact of free palbociclib and StPGA-SS-palbociclib in TNBC cells revealed a decrease in ATP-production coupled respiration (with a more significant effect caused by StPGA-SS-palbociclib) linked to the downregulation of the glycolytic pathway in cells that respond to energy demand at the described time point (72 h after treatment at the IC₃₀ concentrations).

3.2.2.3. Analysis of the Metabolome and Lipidome of Isolated Mitochondria and Triple Negative Breast Cancer Cells After Treatment with Free Palbociclib and with StPGA-SS-palbociclib

3.2.2.3.1. NMR Metabolomics Analysis of Mitochondria and Triple Negative Breast Cancer Cells After Treatment with Free Palbociclib and StPGA-SS-palbociclib

We next performed an NMR metabolomic analysis of the isolated mitochondria (previously optimized in **Chapter II**) to better understand the obtained results regarding cell viability and respiration). We compared mitochondria isolated from untreated TNBC cells (control) to cells treated with free palbociclib or StPGA-SS-palbociclib at their IC₃₀ values for 72 h to assess effects on cell metabolism. We also completed our analysis with a metabolomic analysis of whole-cell samples.

Table 3.2 summarizes the data for all samples in the NMR metabolomic analysis (sample type, number of P150 plates, treatment, and type of metabolite extraction carried out).

Table 3.2. Data summary for samples in Section 3.2.2.3.1

Sample ID	Sample type	P150 plates	Treatment	Metabolite extraction
MITO108	Whole-cell	1	Control (untreated)	Folch
MITO109	Whole-cell	1	Palbociclib	Folch
MITO110	Whole-cell	1	StPGA-SS-palbociclib	Folch
MITO120	Whole-cell	1	Control (untreated)	Folch
MITO121	Whole-cell	1	Palbociclib	Folch
MITO122	Whole-cell	1	StPGA-SS-palbociclib	Folch
MITO126	Whole-cell	1	Control (untreated)	Folch
MITO127	Whole-cell	1	Palbociclib	Folch
MITO128	Whole-cell	1	StPGA-SS-palbociclib	Folch
MITO132	Whole-cell	1	Control (untreated)	Folch
MITO133	Whole-cell	1	Palbociclib	Folch
MITO134	Whole-cell	1	StPGA-SS-palbociclib	Folch
MITO189	Whole-cell	1	Control (untreated)	Folch
MITO190	Whole-cell	1	StPGA	Folch
MITO194	Whole-cell	1	Control (untreated)	Folch
MITO195	Whole-cell	1	StPGA	Folch
MITO200	Whole-cell	1	Control (untreated)	Folch
MITO201	Whole-cell	1	StPGA	Folch
MITO111	Mitochondria	8	Control (untreated)	Optimized
MITO112	Mitochondria	8	Palbociclib	Optimized
MITO113	Mitochondria	8	StPGA-SS-palbociclib	Optimized
MITO123	Mitochondria	8	Control (untreated)	Optimized
MITO124	Mitochondria	8	Palbociclib	Optimized
MITO125	Mitochondria	8	StPGA-SS-palbociclib	Optimized
MITO129	Mitochondria	8	Control (untreated)	Optimized
MITO130	Mitochondria	8	Palbociclib	Optimized
MITO131	Mitochondria	8	StPGA-SS-palbociclib	Optimized
MITO135	Mitochondria	8	Control (untreated)	Optimized
MITO136	Mitochondria	8	Palbociclib	Optimized
MITO137	Mitochondria	8	StPGA-SS-palbociclib	Optimized

Mitochondrial Metabolomic Alterations

The NMR metabolomic analysis, based on the previously optimized protocol, consisted of isolating the mitochondria from TNBC cells by differential centrifugation and protein removal by

centrifugal filtration and extracting the metabolites by adding NMR buffer and performing centrifugal filtration (Materials and Methods 3.4.4.5 and 3.4.4.8.1). We obtained NMR spectra of four mitochondrial samples for each treatment group with a 600 MHz spectrometer. We obtained good-quality spectra for the mitochondrial samples with the optimized NMR parameters. Figure 3.14 depicts representative spectra of mitochondria isolated from untreated cells (control) and cells treated with palbociclib and StPGA-SS-palbociclib. The qualitative analysis of the NMR spectra, prior to signal quantification, revealed alterations in metabolite signals in cells treated with free palbociclib and StPGA-SS-palbociclib (highlighted in Figure 3.14), suggesting that both treatments impacted cell metabolism upon treatment at the IC₃₀ values for 72 h.

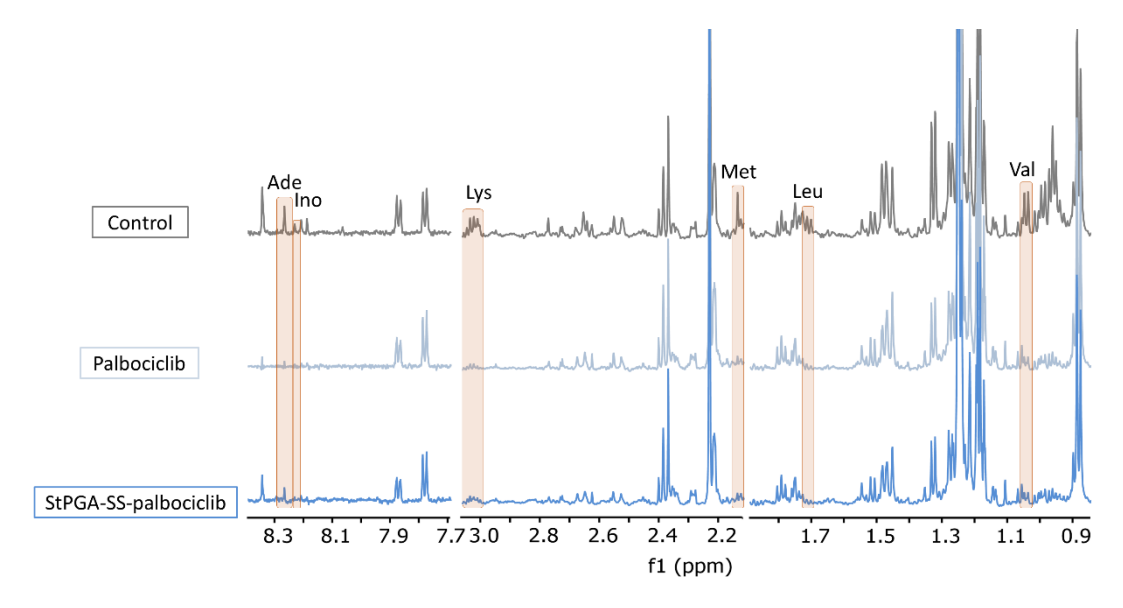


Figure 3.14. Representative spectra of mitochondria isolated from untreated TNBC cells (control), and cells treated with palbociclib and StPGA-SS-palbociclib. Treatments performed at the IC_{30} values for 72 h. Assigned metabolites displayed decreased levels after treatment. Ade = adenosine; Ino = inosine; Leu = leucine; Lys = lysine; Met = methionine; Val = valine.

After data processing, we performed principal component analysis (PCA) to visualize variations between samples and clustering tendencies. We excluded a control mitochondrial sample (MITO135) as an outlier due to two significant signals that may correspond to contaminations during sample processing. The PCA of the final samples revealed a noticeable separation of mitochondrial samples of untreated cells (controls) from treated cells (Figure 3.15A).

We plotted the logarithm-transformed p-values versus the fold change values in volcano plots to identify metabolites contributing to group discrimination. Colored points (green = increased in treated samples compared to control, red = decreased in treated samples compared to control) indicate the metabolites presenting p-values and fold changes above 0.05 and 1.2,

respectively. Mitochondrial samples displayed reduced levels of amino acids after treatment with free palbociclib and StPGA-SS-palbociclib compared to control (Figures 3.14 and 3.15B). Furthermore, free palbociclib also caused a decline in adenosine levels in the mitochondria of TNBC cells compared to mitochondria of control cells. However, we failed to observe any significant differences when comparing free palbociclib and StPGA-SS-palbociclib treatment (Figure 3.14 and 3.15B).

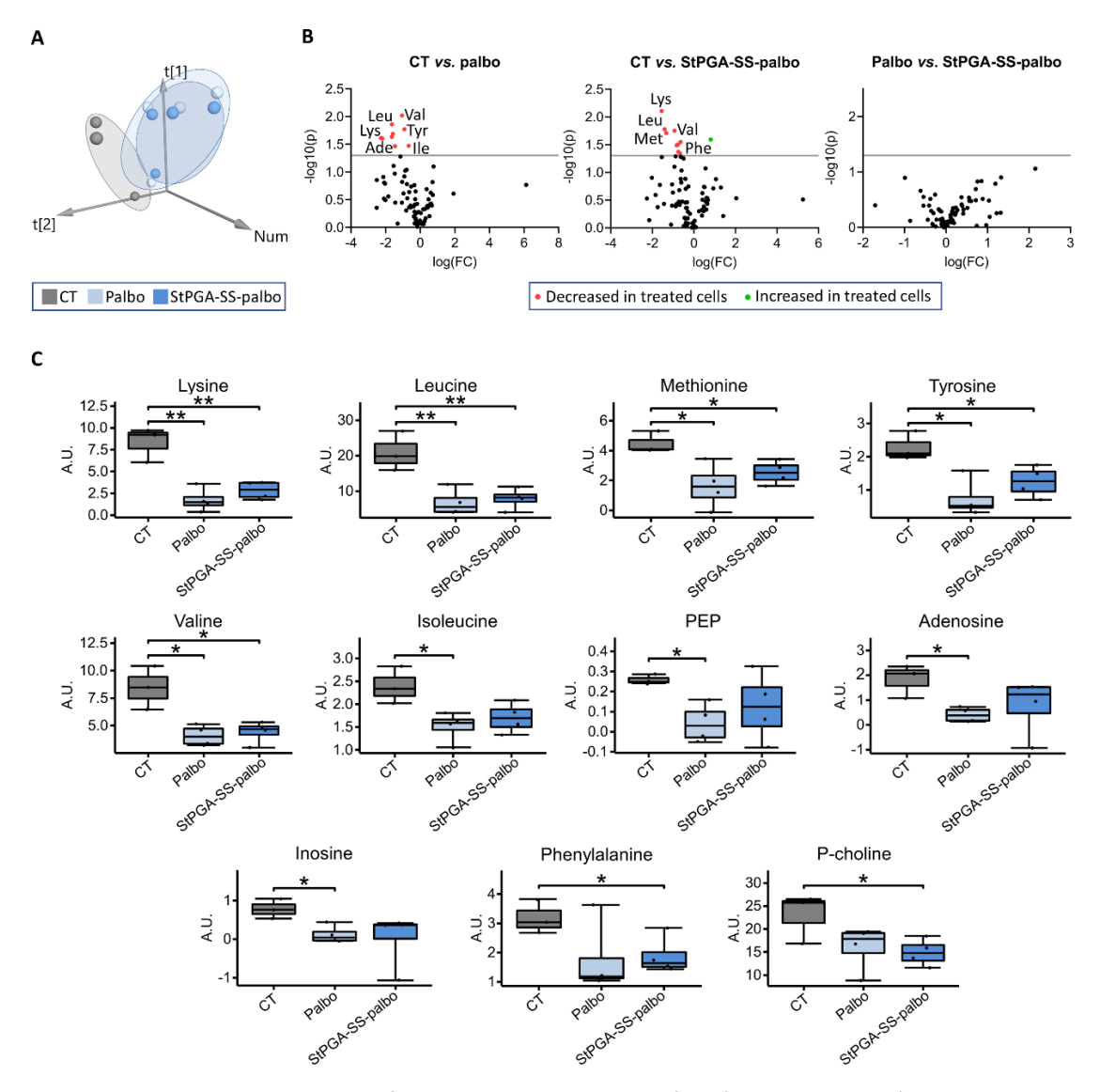


Figure 3.15. Comparative analysis of the NMR metabolomic profile of mitochondria. **A**) 3D PCA score plot of mitochondria isolated from untreated TNBC cells (CT = control) and from cells treated with free palbociclib (palbo) and StPGA-SS-palbo (StPGA-SS-palbociclib) (n = 4 per group, except for the control group where we excluded MITO135; statistical algorithm: unit variance scaled). **B**) Volcano plots of the three comparisons: control vs. free palbociclib, control vs. StPGA-SS-palbociclib, and free palbociclib vs. StPGA-SS-palbociclib. Colored points (green/red = increased/decreased in treated samples compared to control) indicate the metabolites presenting p-values and fold changes (FC) above 0.05 and 1.2, respectively. Ade = adenosine; A.U. = Arbitrary units; Ile = isoleucine; Leu = leucine; Lys = lysine; Met =

methionine; Phe = phenylalanine; Tyr = tyrosine; Val = valine. **C**) Boxplot of cellular metabolites displaying significant differences after treatment with free palbociclib or StPGA-SS-palbociclib compared to controls or after treatment with conjugated palbociclib compared to free palbociclib. Data analysis used a T-test, with data presented as average \pm SEM (n=3-4); (* p < 0.05, ** p < 0.01). PEP = phosphoenolpyruvate; P-choline = phosphocholine.

To better visualize mitochondrial alterations, we represented relevant metabolites (Supporting Information 3.5) as boxplots (Figure 3.15C). We observed a general and significant decrease in amino acids in mitochondria of cells treated with free palbociclib (lysine, leucine, methionine, tyrosine, valine, and isoleucine) and StPGA-SS-palbociclib (lysine, leucine, methionine, tyrosine, and valine) compared to control. Li et al. previously reported that a decrease in the level of amino acids in the mitochondria lowered MMP and altered mitochondrial respiration²⁷⁸ observed using the Seahorse Analyzer (Section 3.2.2.2). Moreover, a decreased amino acid pool means a decreased TCA cycle input, which suggests downregulation of the TCA cycle. We also observed a significant decrease in phosphoenolpyruvate (PEP - synthesized in the mitochondria from oxaloacetate²⁸⁹) in mitochondria of cells treated with free palbociclib compared to control cells, which could confirm a decreased activity of the TCA cycle. The nucleosides adenosine and inosine were also significantly reduced in mitochondria of cells treated with free palbociclib (although the same trend was observed in cells treated with StPGA-SS-palbociclib) compared to control cells (Figure 3.14 and 3.15C). TCA cycle downregulation and OXPHOS disruption may prompt lower levels of ATP generation, which would lead to reduced levels of adenosine and inosine in mitochondria. Phosphocholine displayed significantly lower levels in the mitochondria of cells treated with StPGA-SS-palbociclib compared to mitochondria of control cells (Figure 3.15C), which could derive from a decrease in the production of the ATP required to form phosphocholine from choline³²⁰.

Whole-cell Metabolomic Alterations

We next analyzed the metabolism of untreated and treated whole-cell samples to discover whether downregulated glycolysis caused TCA cycle downregulation and explore whole-cell metabolic alterations. We collected TNBC cells and employed the traditional Folch extraction method to extract metabolites for NMR analysis. We detected no outlier samples and observed clear differentiation of the three groups (control, palbociclib-treated, and StPGA-SS-palbociclib-treated) in the 3D PCA score plot (Figure 3.16A). In volcano plots, we observed a decrease in lactate, uridine diphosphate-N-acetylglucosamine (UDP-NAG), and ATP levels in whole-cells treated with free palbociclib and StPGA-SS-palbociclib compared to control (Figure 3.16B). Glutamine levels increased in whole-cells treated with palbociclib and StPGA-SS-palbociclib

treatment compared to control. Guanosine triphosphate (GTP) decreased and aspartate increased in whole-cells treated with free palbociclib compared to control. The comparison between free palbociclib and StPGA-SS-palbociclib revealed decreased levels of phosphocholine and increased levels of an overlapping glutamate NMR signal (Figure 3.16B).

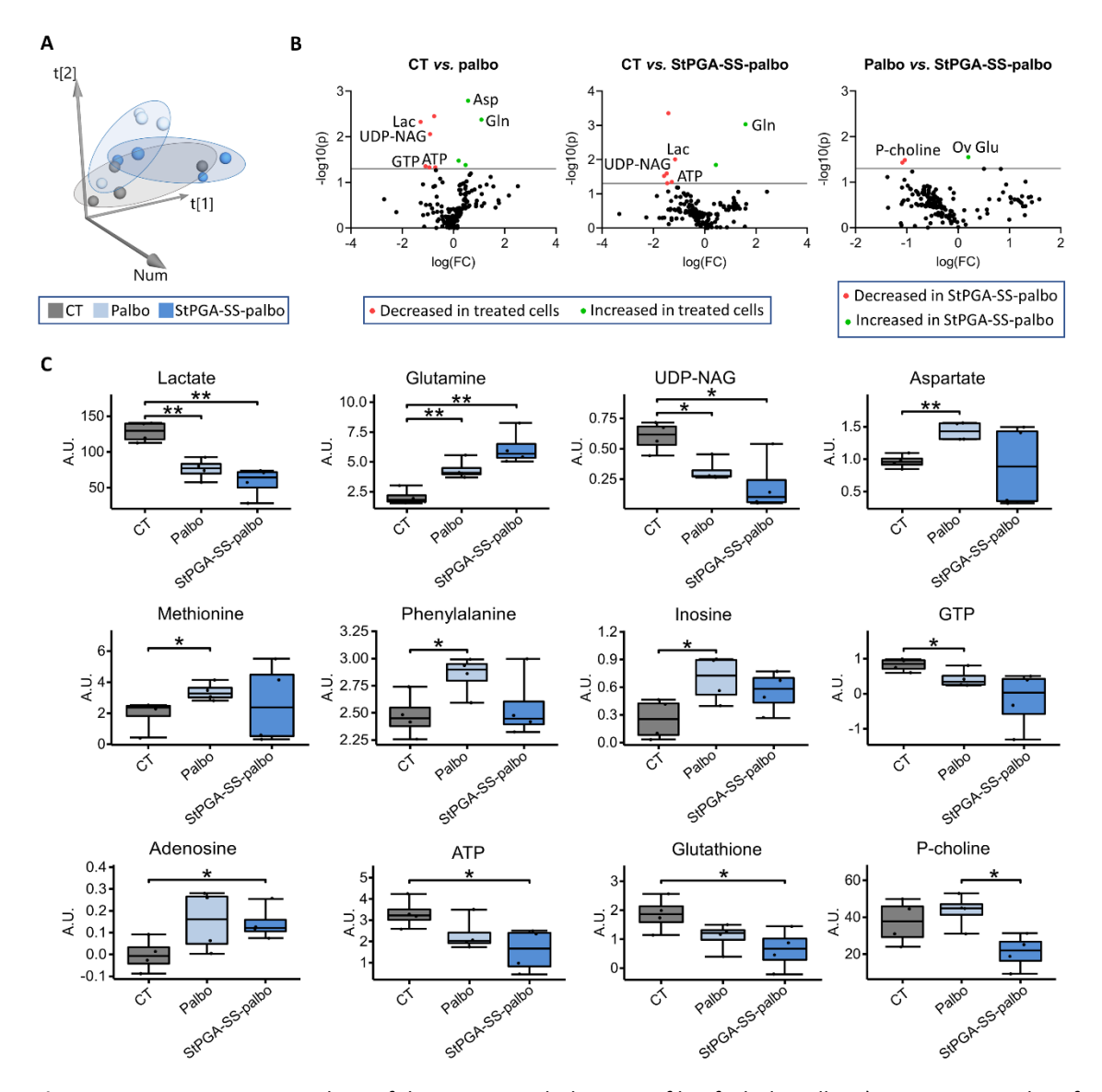


Figure 3.16. Comparative analysis of the NMR metabolomic profile of whole-cells. **A**) 3D PCA score plot of untreated whole-cells (CT = control) and after treatment with free palbociclib (palbo) and StPGA-SS-palbociclib (StPGA-SS-palbo) (n = 4 per group; statistical algorithm: unit variance scaled). **B**) Volcano plots of the three comparisons: control vs. free palbociclib, control vs. StPGA-SS-palbociclib, and free palbociclib vs. StPGA-SS-palbociclib. Colored points (green/red = increased/decreased in treated samples compared to control) indicate the metabolites presenting p-values and fold changes above 0.05 and 1.2, respectively. Asp = aspartate; ATP = adenosine triphosphate; Gln = glutamine; GTP = guanosine triphosphate; Lac = lactate; Ov Glu = overlapping glutamate; P-choline = phosphocholine; UDP-NAG = uridine diphosphate-N-acetylglucosamine. **C**) Boxplot of cellular metabolites displaying significant differences after treatment with free palbociclib or StPGA-SS-palbociclib compared to control or after treatment with StPGA-SS-

palbociclib compared to free palbociclib. Data analysis used a T-test, with data presented as average \pm SEM (n=4), (* < 0.05, ** p < 0.01). ATP = adenosine triphosphate; GTP = guanosine triphosphate; UDP-NAG = uridine diphosphate-N-acetylglucosamine.

Figure 3.16C depicts the boxplots of metabolites displaying significantly altered levels between treatment groups in whole-cell samples (Supporting Information 3.6 provides the mean and SEM of the metabolite relative amounts of each group and the p-values of the comparisons). As previously highlighted in Section 3.2.2.2, we confirmed the downregulation of the glycolytic pathway in whole-cells treated with palbociclib and StPGA-SS-palbociclib compared to control, as observed by significantly decreased lactate levels. Warth and colleagues also observed this phenomenon in MCF-7 cells treated with palbociclib³²¹. Glutamine levels significantly increased in whole-cells after free palbociclib and StPGA-SS-palbociclib treatment due to the downregulation of glutaminolysis. The slightly higher glutamine levels observed after StPGA-SSpalbociclib treatment compared to free palbociclib treatment may derive from the degradation of StPGA in the lysosomes³²², with the glutamic units converted to glutamine instead of α ketoglutarate. An analysis of cells treated with StPGA only revealed significantly increased glutamine levels (p = 0.016) in whole-cell samples compared to untreated cells, confirming the polymer's effect on the levels of this amino acid (Supporting Information 3.7). Moreover, we observed significantly different levels of glutamine between whole-cells treated with StPGA $(2.99 \pm 0.15 \text{ arbitrary units})$ and palbociclib $(4.34 \pm 0.41 \text{ arbitrary units}; p=0.043)$ and between whole-cells treated with StPGA (4.34 ± 0.41 arbitrary units) and StPGA-SS-palbociclib (6.15 ± 0.73 arbitrary units; p=0.001), which confirmed the effect of StPGA in glutamine levels. The conversion of glutamate to glutamine occurs in the mitochondria and the cytosol323; however, the mitochondrial analysis failed to reveal altered glutamine levels, while the whole-cell analysis revealed significantly increased levels after free palbociclib and StPGA-SS-palbociclib treatment. These results indicate that the glutamate-glutamine conversion mainly occurred in the cytosol and that the total glutamine levels of cells (including mitochondria) increased.

After treatment with free palbociclib, the whole-cell analysis revealed significantly increased levels of amino acids (aspartate, methionine, and phenylalanine). Unlike the mitochondrial analysis, which provides precise information regarding the decreased amino acid pool in mitochondria and TCA cycle downregulation, the whole-cell analysis failed to support these findings, as mitochondrial and cytosolic amino acids contribute to the whole-cell amino acid pool. Aspartate formation from oxaloacetate occurs within mitochondria, so we would expect decreased aspartate levels in the mitochondria as glycolysis and the TCA cycle become downregulated; however, aspartate becomes transported from the mitochondria to the cytosol

through the solute carrier family 25 member 12 (SLC25A12) or solute carrier family 25 member 13 (SLC25A13) transporters, with a counter-exchange of glutamate³²³. Therefore, increased aspartate levels in whole-cells treated with free palbociclib may indicate an increased activity of the transporters. Moreover, increased aspartate could explain the increase in methionine observed in free palbociclib-treated whole-cell samples, as methionine becomes synthesized from aspartate²⁸². The increase of phenylalanine could derive from elevated transport to the cytosol, reduced degradation to tyrosine, or higher synthesis from precursors^{282,324}.

In contrast to the mitochondrial analysis, where nucleotides remain undetectable, we detected alterations to the levels of certain nucleotide derivatives (UDP-NAG, GTP, and ATP) in the wholecell analysis (Figure 3.16C). Significantly decreased UDP-NAG levels in whole-cells treated with free palbociclib and StPGA-SS-palbociclib compared to control correlated with downregulated glycolysis, as UDP-NAG formation requires fructose-6-phosphate and acetyl-CoA³²⁵. UDP-NAG formation also requires glutamine³²⁵, so the decreased UDP-NAG synthesis may contribute to glutamine accumulation after free palbociclib and StPGA-SS-palbociclib treatment. The significantly reduced ATP levels observed in whole-cells treated with StPGA-SS-palbociclib treatment support the reduced ATP-coupled respiration observed when using the Seahorse XF Analyzer (Section 3.2.2.2). In this case, the whole-cell analysis provided complementary information to that provided by the mitochondrial study, revealing a reduction in the total ATP pool, which may derive from reduced mitochondrial respiration. Significantly decreased GTP levels in whole-cells treated with free palbociclib and StPGA-SS-palbociclib treatment compared to control could relate to the low ATP pool in whole-cells and using GTP as an alternative phosphate source. Contrary to the results of the mitochondrial analysis, inosine and adenosine levels significantly increased in whole-cells after free palbociclib and StPGA-SS-palbociclib treatment, respectively. The involvement of nucleotides and nucleosides in multiple pathways makes it challenging to understand the reason for these metabolic changes and demonstrates the importance of specifically analyzing mitochondrial metabolism. Of note, adenosine levels became significantly increased inn whole-cells after treatment with StPGA, probably responsible for the increased levels in whole-cells treated with StPGA-SS-palbociclib (Supporting Information 3.7 provides the results of the metabolomic analysis of whole-cells treated with StPGA).

Treatment with StPGA-SS-palbociclib led to significantly reduced GSH levels in the whole-cell samples, which agrees with the cleavage of the disulfide bond by GSH to release the drug from the polymer. Finally, StPGA-SS-palbociclib induced significantly lower phosphocholine levels in whole-cells compared to free palbociclib, following the same trend observed in mitochondria.

Analysis of whole-cell samples provided information about the effect of free palbociclib and StPGA-SS-palbociclib treatment on glycolysis, glutaminolysis, and energetic metabolites, which complements the analysis of the mitochondrial metabolome and helps to understand the metabolic fluxes inside the organelle.

Treatment with StPGA significantly decreased fumarate and NAD⁺/NADH levels in whole-cell samples (**Supporting Information 3.7**); however, these alterations were not reflected in the whole-cells treated with StPGA-SS-palbociclib.

Extracellular Medium Metabolomic Alterations

We completed our NMR-based metabolomics study with the analysis of the cell media to obtain information about the production and consumption of metabolites by cells. Table 3.3 summarizes the alteration of metabolites in cell media of control TNBC cells (untreated) and cells treated with free palbociclib and StPGA-SS-palbociclib. We observed significantly increased methionine in cell media after free palbociclib and StPGA-SS-palbociclib treatment (Table 3.3) (not significant for StPGA-SS-palbociclib in the previous whole-cell analysis (Figure 3.16)). We also observed significantly increased phenylalanine synthesis in cell media of cells treated with free palbociclib compared to control (Table 3.3), in agreement with the findings observed in the whole-cell analysis (Figure 3.16). Levels of glutamate, pyroglutamate, and glutamine significantly increased in the cell media after treatment with StPGA-SS-palbociclib compared to control (Table 3.3), supporting the theory that the increased glutamic units coming from StPGA were preferentially converted to glutamine rather than to α -ketoglutarate. After free palbociclib and StPGA-SS-palbociclib treatment, we detected significantly reduced levels of pyruvate and phosphoenolpyruvate in the cell media compared to control, confirming the downregulation of the glycolytic pathway (Table 3.3). Moreover, pyruvate decreased significantly more after treatment with StPGA-SS-palbociclib than free palbociclib, indicative of a more significant downregulation of the glycolytic pathway. We also observed significantly increased acetate in cell media after treatment with StPGA-SS-palbociclib compared to control (Table 3.3) which could reveal a more significant inhibition of the TCA cycle and, thus, acetate accumulation. We noted a more significant acetate accumulation after treatment with StPGA-SS-palbociclib than free palbociclib, which may indicate a more significant downregulation of the TCA cycle. Glycerophosphocholine (GPC) levels significantly increased in the media of cells treated with StPGA-SS-palbociclib compared to control (Table 3.3), which correlated to significantly decreased phosphocholine levels in whole-cells treated with StPGA-SS-palbociclib compared to free palbociclib (Figure 3.16). Additionally, GPC levels increased more significantly after treatment with StPGA-SS-palbociclib than free palbociclib, indicating a more substantial effect of the polymer-drug conjugate on lipid metabolism.

Alterations observed in the analysis of cell media that we did not observe by NMR metabolomics of whole-cell samples include significantly increased glycine levels after free palbociclib and StPGA-SS-palbociclib treatment compared to control, a significant increase of tyrosine after StPGA-SS-palbociclib treatment compared to control, and significantly increased tryptophan and formate and decreased fumarate after free palbociclib treatment compared to control (**Table 3.3**). The increase in formate levels may relate to the increased use of pyruvate to form formate and acetyl-CoA, while decreased fumarate may reflect the low activity of the TCA cycle. An increase in glycine may derive from the stimulation of the serine-glycine biosynthesis pathway to support one-carbon metabolism (folate cycle, methionine cycle, and trans-sulphuration pathway)³²⁵. Moreover, the serine-glycine branched glycolysis pathway uses 3-phosphoglycerate as a precursor for serine synthesis; therefore, glucose may find alternate uses in pathways other than glycolysis. Finally, elevated levels of tyrosine may reflect increased phenylalanine, the precursor of tyrosine, while increased tryptophan may relate to the increased levels of glutamine required for synthesis.

Overall, the study of the impact of free palbociclib and StPGA-SS-palbociclib by NMR metabolomic analysis of isolated mitochondria revealed a decrease in the amino acid pool linked to altered mitochondrial respiration. The reduced levels of the amino acids that serve as TCA cycle substrates and phosphoenolpyruvate indicate decreased pathway activity, which may directly relate to downregulated glycolytic activity, as we confirmed through an analysis of the metabolome of whole-cell and cell media samples. The analysis of the extracellular medium confirmed that non-consumed amino acids accumulated in cell media. Decreased levels of adenosine and inosine may indicate a reduction in ATP production within mitochondria due to the disruption of ATP-coupled respiration. Finally, analysis of whole-cell and cell media samples also provided evidence for the downregulation of glutaminolysis and the stimulation of the glycine-serine biosynthesis pathway as an alternative way to metabolize glucose. The metabolic alterations caused by StPGA-SS-palbociclib in mitochondria and in whole-cells generally were similar to the alterations caused by free palbociclib. However, only StPGA-SS-palbociclib induced a significant decline in phosphocholine levels, which we observed in the mitochondrial analysis (compared to control) and in the whole-cell analysis (compared to free palbociclib). This finding could indicate a more significant impact of StPGA-SS-palbociclib on lipid metabolism.

Table 3.3. Metabolomic profile of cell media in control cells (CT), cells treated with palbociclib (Palbo) and StPGA-SS-palbociclib (StPGA-SS-palbo)

	% Variation over clean media							p-value		Direction			
	СТ		Palb	0	StPGA-SS	6-palbo	CT Dalla	CT CADCA CCalla	Delha va CADCA CC velha	Dalla	S+DCA SS malha	C+DCA CC malba*	
Metabolite	Mean	SEM	Mean	SEM	Mean	SEM	CT vs. Palbo.	CT vs. StPGA-SS-palbo	Palbo vs. StPGA-SS-palbo	Palbo	StPGA-SS-palbo	StPGA-SS-palbo*	
Acetate	50.1	3.1	87.5	15.3	164.2	13.3	ns	0.002	0.019	-	↑	↑	
Methionine	-53.2	1.3	-39.1	2.4	-38.8	1.2	0.008	0.002	ns	↑	\uparrow	-	
Glutamate	111.5	1.6	169.7	27.3	191.9	13.8	ns	0.004	ns	-	\uparrow	-	
Pyruvate	-25.9	0.5	-61.1	0.8	-65.2	1.1	3E-05	3E-05	0.042	\downarrow	\downarrow	\downarrow	
Glutamine	-67.1	0.8	-63.1	2.0	-56.3	1.7	ns	0.006	ns	-	\uparrow	-	
PyroGlu	3.6	0.8	47.8	25.2	29.8	3.0	ns	0.001	ns	-	\uparrow	-	
Glycine	0.5	2.1	18.3	1.8	15.1	0.5	0.006	0.008	ns	↑	\uparrow	-	
GPC	-47.0	5.8	-16.5	42.0	1209.0	211.2	ns	0.004	0.005	-	\uparrow	↑	
PEP	-2791.6	78.8	-3926.3	87.3	-3595.0	222.8	0.001	0.032	ns	\downarrow	\downarrow	-	
Fumarate	265.1	14.6	186.7	17.4	192.1	26.8	0.028	ns	ns	\downarrow	-	-	
Tyrosine	-8.0	1.4	-1.3	1.6	-0.7	0.4	ns	0.043	ns	-	\uparrow	-	
Phe	-5.4	2.0	6.4	1.7	3.2	2.9	0.029	ns	ns	1	-	-	
Pyridoxine	10.6	2.0	-20.7	5.1	-8.8	5.5	0.007	0.040	ns	\downarrow	\downarrow	-	
Tryptophan	-4.1	2.9	24.0	0.8	20.6	5.5	0.019	ns	ns	↑	-	-	
Formate	612.4	14.0	858.4	56.4	838.9	28.5	0.014	0.002	ns	↑	\uparrow	-	

Mean and SEM of the variation percentages of metabolites over clean media in control cells, cells treated with palbociclib and StPGA-SS-palbociclib, p-values of the comparisons and direction of metabolite changes after each treatment over the control and of StPGA-SS-palbociclib over free palbociclib (StPGA-SS-palbo*). Green and red metabolites indicate increased and decreased levels. Data analysis used a T-test (n = 3). * GPC = glycerophosphocholine; ns = not statistically significant; PEP = phosphoenolpyruvate; Phe = phenylalanine; PyroGlu = pyroglutamate.

3.2.2.3.2. MS Metabolomics Analysis of Mitochondria and Triple Negative Breast Cancer Cells After Treatment with Free Palbociclib and StPGA-SS-palbociclib

We complemented the NMR metabolomic analysis with MS metabolomic and lipidomic studies (Section 3.2.2.3.3) performed during a short stay in the laboratory of Professor Nils J. Færgeman (Molecular Metabolism and Metabolomics laboratory, University of Southern Denmark). MS metabolomics provides greater sensitivity than NMR, allowing the detection of low amounts of metabolites and a large number of lipids undetectable by NMR²⁰⁸. As in the previous section, we performed the metabolomic study on i) isolated mitochondria and ii) whole-cell samples from TNBC cells treated with free palbociclib and StPGA-SS-palbociclib at their IC₃₀ values after a 72-h incubation to assess the effect of on cell metabolism by comparison to untreated control. We isolated mitochondria following the optimized method in **Chapter II** based on differential centrifugation and extracted metabolites using a modified Folch method based on the use of a CHCl₃:MeOH:H₂O mixture and a double aqueous phase extraction (Materials and Methods 3.4.4.8.2).

Table 3.4 summarizes the data for all samples for the MS metabolomic analysis of this section and the lipidomic analysis of **Section 3.2.2.4** (sample type, number of P150 plates, treatment, and type of metabolite extraction carried out).

Table 3.4. Data summary for samples in Sections 3.2.2.3.2 and 3.2.2.4

Sample ID	Sample type	P150 plates	Treatment	Metabolite extraction
CELLMS01	Whole-cell	1	Control (untreated)	Modified Folch
CELLMS02	Whole-cell	1	Control (untreated)	Modified Folch
CELLMS03	Whole-cell	1	Palbociclib	Modified Folch
CELLMS04	Whole-cell	1	Palbociclib	Modified Folch
CELLMS05	Whole-cell	1	StPGA-SS-palbociclib	Modified Folch
CELLMS06	Whole-cell	1	StPGA-SS-palbociclib	Modified Folch
CELLMS07	Whole-cell	1	Control (untreated)	Modified Folch
CELLMS08	Whole-cell	1	Control (untreated)	Modified Folch
CELLMS09	Whole-cell	1	Palbociclib	Modified Folch
CELLMS10	Whole-cell	1	Palbociclib	Modified Folch
CELLMS11	Whole-cell	1	StPGA-SS-palbociclib	Modified Folch
CELLMS12	Whole-cell	1	StPGA-SS-palbociclib	Modified Folch
MITMS01	Mitochondria	8	Control (untreated)	Modified Folch
MITMS02	Mitochondria	8	Control (untreated)	Modified Folch
MITMS03	Mitochondria	8	Palbociclib	Modified Folch
MITMS04	Mitochondria	8	Palbociclib	Modified Folch
MITMS05	Mitochondria	8	StPGA-SS-palbociclib	Modified Folch

MITMS06	Mitochondria		StPGA-SS-palbociclib	Modified Folch
MITMS07	Mitochondria	0	Control (untreated)	Modified Folch
MITMS08	Mitochondria	8	Control (untreated)	Modified Folch
MITMS09	Mitochondria	0	Palbociclib	Modified Folch
MITMS10	Mitochondria	8	Palbociclib	Modified Folch
MITMS11	Mitochondria	0	StPGA-SS-palbociclib	Modified Folch
MITMS12	Mitochondria	8	StPGA-SS-palbociclib	Modified Folch

We first performed a non-supervised PCA analysis and observed a clear discrimination between the control mitochondrial samples and the free palbociclib- and StPGA-SS-palbociclib-treated mitochondrial samples (Figure 3.17A). We identified an outlier sample (MITMS12) in the StPGA-SS-palbociclib group, which we removed from the study due to high levels of glucose-derivative metabolites that may derive from insufficient cell-washing to remove media. Our analysis revealed that multiple peptides displayed a decrease in levels after treatment with free palbociclib and StPGA-SS-palbociclib in isolated mitochondria, as depicted in the corresponding volcano plots (Figure 3.17B). We also detected increased levels of GPC after free palbociclib and StPGA-SS-palbociclib treatment and increases in deoxyguanosine and spermidine after treatment with free palbociclib and StPGA-SS-palbociclib, respectively. Interestingly, specific peptides displayed significantly differing levels in mitochondria isolated from StPGA-SS-palbociclib-treated cells compared to free palbociclib-treated cells (decreased: valine-serine-valine, isoleucine-glutamine-glutamate, and serine-valine-glutamate; Increased - tyrosine-glutamate and glycine-L-norleucine).

The PCA score plot of whole-cell samples (Figure 3.17C) also allowed a robust discrimination between the control and the free palbociclib- and StPGA-SS-palbociclib-treated samples, and we did not observe any abnormal samples. We observed decreased levels of glutamate and lactate derivatives and pantetheine 4'-phosphate and increased levels of nucleotides and N-(1-deoxy-1-fructosyl)threonine in whole-cells after free palbociclib and StPGA-SS-palbociclib treatment compared to control (Figure 3.17D). N1,N8-diacetylspermidine and isoleucine-aspartate peptide displayed decreased levels in whole-cells treated with free palbociclib compared to control, while aspartate-valine-leucine peptide, GPC, O-methylmalonyl-L-carnitine and N-acetyl-D-lactosamine showed increased levels (Figure 3.17D). Creatine became decreased in whole-cell samples following palbociclib treatment compared to control, while glycine-valine-arginine peptide was increased (Figure 3.17D). Meanwhile, specific metabolites (1-methylguanosine, a lactate derivative, and N-butyrylglycine) increased while creatine decreased in whole-cells treated with StPGA-SS-palbociclib compared to free palbociclib.

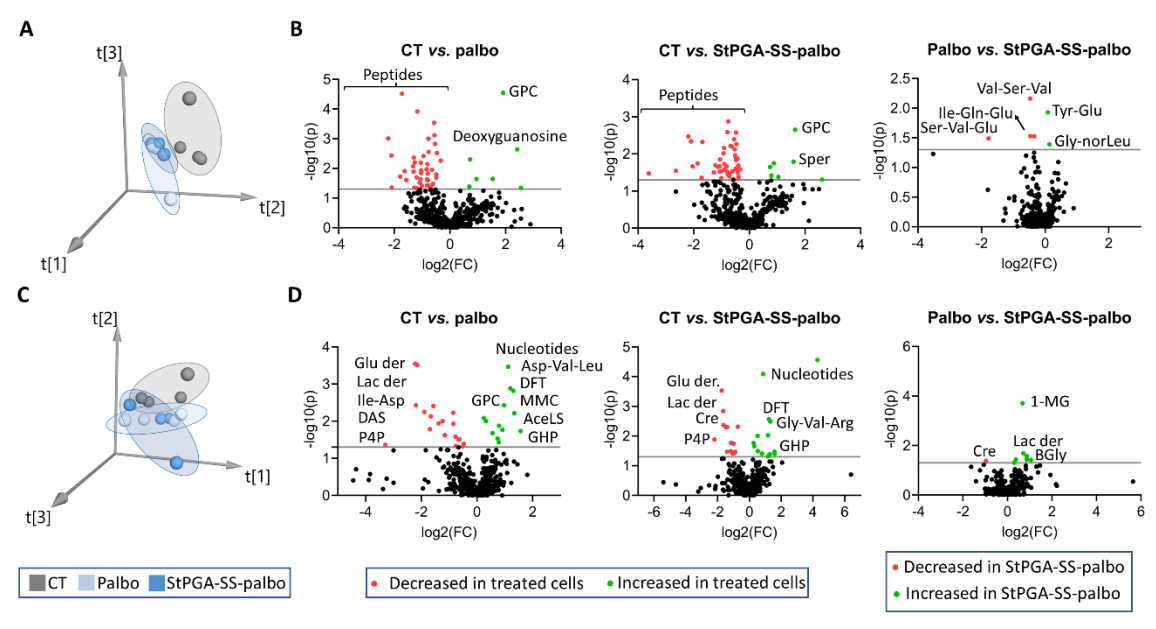


Figure 3.17. Comparative analysis of the MS metabolomic profile of whole-cells and mitochondria samples. A) 3D PCA score plot of mitochondria isolated from untreated TNBC cells (CT = control) and from cells treated with free palbociclib (palbo) and StPGA-SS-palbociclib (StPGA-SS-palbo) (n = 4 per group, except for the StPGA-SS-palbociclib group where MITMS12 was excluded; statistical algorithm: unit variance scaled). B) Volcano plots of the three comparisons in mitochondrial samples: control vs. free palbociclib, control vs. StPGA-SS-palbociclib, and free palbociclib vs. StPGA-SS-palbociclib. Gln = glutamine; Glu = glutamate; GPC = glycerophosphocholine; lle = isoleucine; norLeu = norleucine; Ser = serine; Tyr = tyrosine; Val = valine. C) 3D PCA score plot of untreated whole-cells (CT = control) and after treatment with free palbociclib (palbo) and StPGA-SS-palbociclib (StPGA-SS-palbo) (n = 4 per group; statistical algorithm: unit variance scaled). D) Volcano plots of the three comparisons in whole-cell samples: control vs. free palbociclib, control vs. StPGA-SS-palbociclib, and free palbociclib vs. StPGA-SSpalbociclib. Colored points (green/red = increased/decreased in treated samples compared to control) indicate the metabolites presenting p-values and fold changes above 0.05 and 1.2, respectively. 1-MG = 1-methylguanosine; AceLS = N-acetyl-D-lactosamine; Arg = arginine; Asp = Aspartate; BGly = Nbutyrylglycine; Cre = creatine; DAS = N1,N8-diacetylspermidine; der = derivatives; DFT = N-(1-deoxy-1fructosyl)threonine; GHP = γ-glutamylhydroxyproline; Gln = glutamine; Glu = glutamate; Gly = glycine; GPC = glycerophosphocholine; Ile = isoleucine; Lac = lactate; norLeu = norleucine; MMC = O-methylmalonyl-Lcarnitine; P4P = Pantetheine 4'-phosphate; Sper = spermidine; Tyr = tyrosine; Val = valine.

Table 3.5 summarizes the peptides and amino acid-related metabolites significantly altered levels in mitochondria and whole-cell samples after treatment with free palbociclib or StPGA-SS-palbociclib.

In **mitochondrial** samples, most peptides (twenty-six) displayed significantly reduced levels after free palbociclib and StPGA-SS-palbociclib treatment compared to control, while eight peptides displayed significantly reduced levels in mitochondria after free palbociclib treatment compared

to control and seven after StPGA-SS-palbociclib treatment compared to control. We only found two and three peptides significantly increased in isolated mitochondria from cells treated with free palbociclib and StPGA-SS-palbociclib, respectively, compared to control. Interestingly, two peptides (glutamate-valine-glutamate and valine-serine-valine) displayed significantly reduced levels and other two peptides (glycine-L-norleucine and tyrosine-glutamate) showed significantly increased levels in isolated mitochondria from cells treated with StPGA-SSpalbociclib compared to free palbociclib. Thirty-six of the peptides were dipeptides, while ten were tripeptides formed by essential (leucine, tryptophan, threonine, valine, histidine, isoleucine, lysine, methionine, phenylalanine) and non-essential amino acids (glycine, tyrosine, glutamate, alanine, aspartate, proline, arginine, serine). As described in Section 3.2.2.3.1, we already observed significantly reduced levels of amino acids in the mitochondria of cells treated with free palbociclib and StPGA-SS-palbociclib, which correlates with a considerable decrease in peptide levels observed by MS metabolomics. These peptides could represent mitochondriaderived peptides (MDPs), which have been associated with glucose, lipid, and nucleotide metabolism alterations and disrupted mitochondrial function, making them a potential therapeutic target of several diseases^{326,327}. Moreover, as explained in **Section 3.2.2.3.1**, decreased mitochondrial amino acids have been linked to decreased MMP and altered mitochondrial respiration²⁷⁸.

The **whole-cell** analysis revealed significant alterations in only eleven peptides (six decreased and five increased) after treatment with free palbociclib and ten peptides (six decreased and four increased) after treatment with StPGA-SS-palbociclib compared to control; however, we did not observe a notable reduction of peptides observed in the isolated mitochondrial sample analysis, supporting the need for a more specific analysis of mitochondrial samples. Of note, we detected significantly reduced levels of N-lactoyl-amino acids (N-lactoylleucine and N-lactoylphenylalanine) in whole-cells after treatment with free palbociclib and StPGA-SS-palbociclib compared to control, probably due to the decreased lactate related to reduced glycolysis in free palbociclib- and StPGA-SS-palbociclib-treated cells, as demonstrated by NMR metabolomics (Section 3.2.2.3.1).

Table 3.5. Amino acids and peptides displaying significant alterations in mitochondrial and whole-cell samples

Metabolite*	C	T	Palbo		StPGA-SS-palbo		P-value			Direction		
Metabolite	Mean	SEM	Mean	SEM	Mean	SEM	CT vs. palbo	CT vs. StPGA-SS-palbo	Palbo vs. StPGA-SS-palbo	Palbo	StPGA-SS-palbo	StPGA-SS-palbo*
Mitochondria												
Gly-L-norLeu	1.2048	0.0703	0.8736	0.0247	0.9585	0.0088	0.0044	0.0319	0.0373	\downarrow	\downarrow	\uparrow
Tyr-Glu	1.3684	0.0694	0.9210	0.0118	0.9782	0.0042	0.0007	0.0051	0.0107	\downarrow	\downarrow	\uparrow
Trp-Thr	1.3869	0.0683	0.9577	0.0428	0.9625	0.0675	0.0018	0.0077	ns*	\downarrow	\downarrow	-
Tyr-Ala	1.2024	0.1490	0.5866	0.0814	0.5789	0.0603	0.0110	0.0193	ns	\downarrow	\downarrow	-
Asp-Val	1.6602	0.1846	0.9685	0.2003	0.8710	0.0707	0.0441	0.0175	ns	\downarrow	\downarrow	-
Tyr-Val-Gly	2.4611	0.5536	0.5303	0.0469	0.5754	0.0623	0.0132	0.0350	ns	\downarrow	\downarrow	-
His-Leu	1.3064	0.0311	0.5808	0.0532	0.7722	0.0683	0.0000	0.0005	ns	\downarrow	\downarrow	-
Trp-Leu	1.4789	0.1504	0.6976	0.1619	0.8653	0.1575	0.0123	0.0393	ns	\downarrow	\downarrow	-
Val-Gly	1.5786	0.1821	0.8181	0.0516	0.8421	0.1101	0.0070	0.0256	ns	\downarrow	\downarrow	-
Val-Ile-Asp	1.3573	0.0698	1.0782	0.0172	0.9515	0.0791	0.0081	0.0122	ns	\downarrow	\downarrow	-
Val-Ile-Gly	1.3349	0.0559	0.9095	0.0414	0.9680	0.0528	0.0009	0.0058	ns	\downarrow	\downarrow	-
Val-Ile-Lys	1.3687	0.1204	0.6626	0.0984	0.7291	0.0784	0.0039	0.0095	ns	\downarrow	\downarrow	-
Val-Ala	1.3685	0.0651	0.7984	0.0612	0.9846	0.0775	0.0007	0.0125	ns	\downarrow	\downarrow	-
Arg-hydPro	1.8713	0.2946	0.9150	0.1317	0.8973	0.1698	0.0252	0.0490	ns	\downarrow	\downarrow	-
Asp-Tyr	1.4133	0.0794	0.9031	0.1169	0.9662	0.0463	0.0112	0.0070	ns	\downarrow	\downarrow	-
Asp-Ile	1.4826	0.1114	0.8527	0.1805	0.9598	0.0310	0.0250	0.0115	ns	\downarrow	\downarrow	-
Gly-Met	1.1308	0.1318	0.5462	0.1003	0.6400	0.0413	0.0124	0.0277	ns	\downarrow	\downarrow	-
Gly-Phe	1.1304	0.0596	0.8040	0.0806	0.8049	0.0625	0.0174	0.0139	ns	\downarrow	\downarrow	-
His-Ile	1.7683	0.2258	0.7369	0.1134	0.8415	0.1559	0.0065	0.0263	ns	\downarrow	\downarrow	-
Phe-His	1.2539	0.1663	0.7105	0.0627	0.6691	0.0385	0.0223	0.0326	ns	\downarrow	\downarrow	-
Pro-hydPro	2.0162	0.0440	0.6119	0.0685	0.6268	0.1799	2.4E-06	0.0003	ns	\downarrow	\downarrow	-
Trp-Glu	1.5106	0.0601	0.8840	0.0976	0.8713	0.0942	0.0016	0.0018	ns	V	\downarrow	-
Tyr-Ala	1.4908	0.2424	0.6489	0.1092	0.6813	0.0504	0.0194	0.0383	ns	V	\downarrow	-
Tyr-Asp	1.6125	0.1205	1.0010	0.2116	0.9234	0.2073	0.0458	0.0278	ns	V	\downarrow	-
Tyr-Thr	1.3275	0.1461	0.7657	0.0765	0.8882	0.0615	0.0144	0.0590	ns	V	\downarrow	-

Trp-Lys	1.5965	0.3852	0.4619	0.0545	0.4853	0.0400	0.0268	0.0593	ns	\downarrow	\downarrow	-	
Phe-Gly	1.4626	0.1785	0.8176	0.0848	0.8858	0.0909	0.0172	ns	ns	\downarrow	-	-	
Thr-Pro	1.4948	0.2910	0.6001	0.0543	0.6989	0.1323	0.0233	ns	ns	\downarrow	-	-	
Leu-Gly	1.7629	0.1006	1.1544	0.1743	1.2453	0.2464	0.0233	ns	ns	\downarrow	-	-	
Phe-Lys	1.3893	0.2729	0.4494	0.0674	0.5997	0.0787	0.0155	ns	ns	\downarrow	-	-	
Gly-Met	1.5017	0.3284	0.6177	0.1017	0.5326	0.1696	0.0423	ns	ns	\downarrow	-	-	
Gly-Pro	1.2445	0.2067	0.6124	0.0213	0.6577	0.1072	0.0227	ns	ns	\downarrow	-	-	
His-Met	1.3635	0.2085	0.7691	0.0620	0.8299	0.0323	0.0341	ns	ns	\downarrow	-	-	
His-Phe	1.4728	0.3421	0.5985	0.0907	0.6480	0.1033	0.0485	ns	ns	\downarrow	-	-	
Ser-Val-Glu	0.6611	0.0509	3.5416	1.0465	1.0289	0.2042	0.0333	ns	ns	\uparrow	-	-	
Val-Val-Val	0.9016	0.1077	1.7454	0.2574	1.2849	0.1947	0.0233	ns	ns	\uparrow	-	-	
Trp-Asp	1.3734	0.0808	0.9583	0.1582	0.9769	0.0927	ns	0.0234	ns	-	\downarrow	-	
Ile-Ala-Glu	1.2892	0.0594	1.1056	0.0666	0.9748	0.1161	ns	0.0470	ns	-	\downarrow	-	
Thr-Tyr	1.1029	0.0823	0.8239	0.0902	0.8187	0.0429	ns	0.0409	ns	-	\downarrow	-	
Leu-Glu-Thr	1.3679	0.0816	1.3386	0.0934	1.0439	0.0886	ns	0.0448	ns	-	\downarrow	-	
Phe-Asp	1.3298	0.0705	1.0944	0.1432	0.9549	0.0718	ns	0.0148	ns	-	\downarrow	-	
Ser-Val	0.5288	0.0786	0.8657	0.1293	0.9748	0.0937	ns	0.0145	ns	-	\uparrow	-	
N-AceAsp	0.8020	0.2484	2.3295	0.6389	2.4027	0.2298	ns	0.0061	ns	-	\uparrow	-	
HydPro-Met	0.4563	0.0130	2.6752	1.1313	0.7654	0.1373	ns	0.0445	ns	-	↑	-	
Glu-Val-Glu	1.2263	0.1404	1.1878	0.0490	0.8562	0.0598	ns	ns	0.0075	-	\downarrow	\downarrow	
Val-Ser-Val	1.4250	0.1813	1.3559	0.0511	1.0683	0.0846	ns	ns	0.0271	-	\downarrow	\downarrow	
							WI	nole-cell					
BGly	2.3631	0.3093	0.5061	0.0807	1.0590	0.2311	0.0011	0.0149	ns	\downarrow	\	-	
LactoylLeu	2.4444	0.3764	0.6611	0.1817	0.7808	0.1182	0.0053	0.0056	ns	\downarrow	\downarrow	-	
LactoylPhe	2.3902	0.2282	0.5401	0.0943	0.7166	0.0971	0.0003	0.0005	ns	\downarrow	\downarrow	-	
Glu-Glu	1.5613	0.2320	0.8695	0.0478	0.8217	0.1399	0.0266	0.0342	ns	\downarrow	\downarrow	-	
γ-Glu-hydPro	0.8641	0.0624	1.2753	0.1178	1.2527	0.1335	0.0216	0.0387	ns	\uparrow	\uparrow	-	
Ile-Gly-Glu	1.0127	0.0178	1.2697	0.0716	1.2544	0.0806	0.0131	0.0264	ns	↑	\uparrow	-	
(Deoxfruc)Thr	0.7975	0.2649	1.6625	0.1095	2.0777	0.3028	0.0235	0.0190	ns	\uparrow	\uparrow	-	

AceGlu	1.6669	0.3351	0.6428	0.1142	0.8983	0.0766	0.0276	ns	ns	\downarrow	-	-
Ile-Asp	1.2610	0.1263	0.8192	0.1003	0.9278	0.2213	0.0338	ns	ns	\downarrow	-	-
Asp-Val-Leu	0.9917	0.0355	1.1770	0.0308	1.1407	0.0813	0.0076	ns	ns	\uparrow	-	-
MetMalCarn	0.6433	0.0511	1.1135	0.1406	1.0685	0.2347	0.0200	ns	ns	\uparrow	-	-
(Deoxfruc)His	1.6267	0.2173	1.0796	0.1697	0.7528	0.1432	ns	0.0153	ns	-	\downarrow	-
Glu-Val	1.6710	0.1938	1.0400	0.4020	0.8083	0.2856	ns	0.0466	ns	-	\downarrow	-
Gly-Val-Arg	0.9417	0.0368	1.2514	0.1349	1.3509	0.1091	ns	0.0120	ns	-	\uparrow	-

Mean and SEM in untreated cells (CT) and in cells treated with free palbociclib (palbo) and with StPGA-SS-palbociclib (StPGA-SS-palbo). P-values of the comparisons between groups and directions of the metabolite changes. Data analysis used a T-test, with data presented as average ± SEM (n=4, except for the StPGA-SS-palbociclib group of mitochondrial samples where MITMS12 was excluded), (* p < 0.05, ** p < 0.01). *AceAsp = N-acetylaspartate; AceGlu = N-acetyl-L-glutamate; Ala = alanine; Arg = arginine; Asp = aspartate; BGly = N-butyrylglycine; Deoxfruc; = 1-Deoxy-1-fructosyl; Glu = glutamate; Gly = glycine; His = histidine; hydPro = hydroxyproline; lle = isoleucine; LactoylLeu = N-lactoylleucine; LactoylPhe = N-lactoylphenylalanine; Leu = leucine; Lys = lysine; Met = methionine; norLeu = norleucine; ns = not statistically significant; Phe = phenylalanine; Pro = proline; Ser = serine; Thr = threonine; Trp = tryptophan; Tyr = tyrosine; Val = valine.

We also detected alterations in nucleotide metabolism in whole-cell and mitochondrial samples by MS metabolomics, confirming the results from the NMR metabolomic analysis (Section 3.2.2.3.1). We generally observed a significant increase in several nucleotides and nucleosides after free palbociclib and StPGA-SS-palbociclib treatment in mitochondria and whole-cells (Figure 3.18 and Supporting Information 8). These changes may relate to the levels of ATP in treated cells. As observed in the whole-cell NMR metabolomic analysis, ATP levels decreased after treatment with StPGA-SS-palbociclib compared to control, and we observed the same trend of free palbociclib (Section 3.2.2.3.1). As ATP is needed as a phosphate donor, the reduced levels of ATP may lead to an increased synthesis of other nucleotides.

In the case of **mitochondria**, we observed a significant increase in the deoxyguanosine nucleotide after treatment with free palbociclib compared to control; however, the tendency for StPGA-SS-palbociclib remained similar. Deoxyguanosine -one deoxyribonucleoside that forms part of DNA- can convert to 8-hydroxy-deoxyguanosine, an indicator of mitochondrial DNA oxidative damage³²⁸.

For the **whole-cell** analysis, we detected significantly increased levels of cytidine 3-monophosphate (3-CMP) and, 1-β-D-arabinofuranosyluracil 5-monophosphate (ArabfurUMP) in whole-cells treated with free palbociclib and StPGA-SS-palbociclib compared to control. Guanosine 5-monophosphate (5-GMP) and, guanosine 5-diphosphate (5-GDP) became significantly increased in whole-cell samples following free palbociclib treatment compared to control (**Figure 3.18** and **Supporting Information 8**). While the alterations in nucleotide levels displayed a similar trend for free palbociclib and StPGA-SS-palbociclib treatment, 1-methylguanosine displayed significantly increased levels in whole-cells treated with StPGA-SS-palbociclib compared to free palbociclib. 1-methylguanosine, a post-transcriptional modification of transfer RNA (tRNA), can be detected upon tRNA degradation 329. Of note, 1-methylguanosine has been detected in urine of breast cancer patients 329. Therefore, increased levels of 1-methylguanosine may indicate a higher tRNA degradation in cells treated with StPGA-SS-palbociclib.

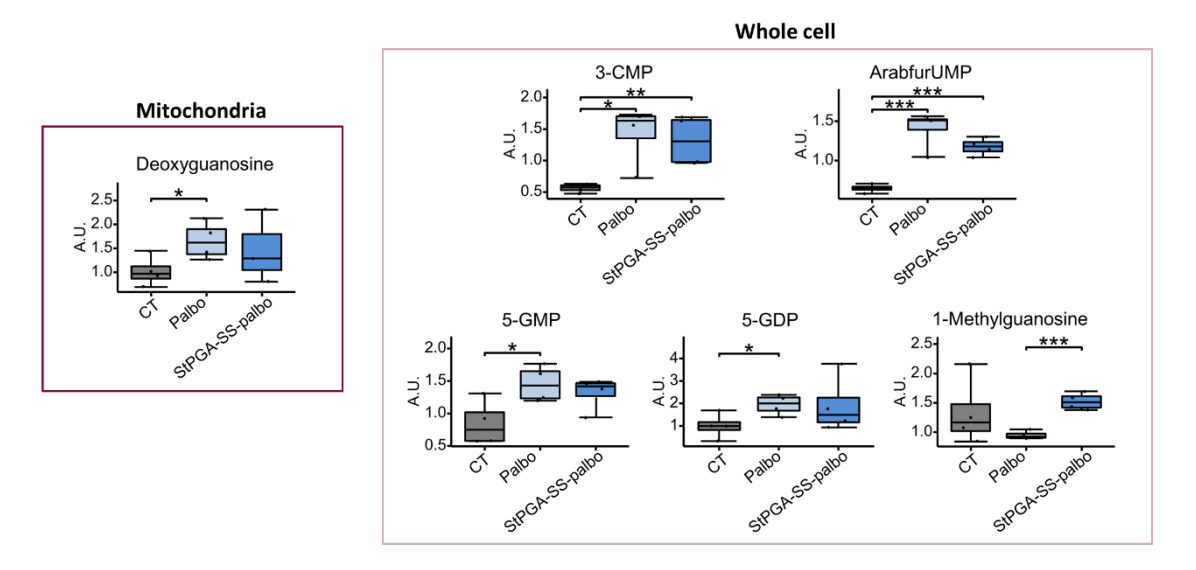


Figure 3.18. Alterations in nucleotide-related metabolites detected by MS metabolomics. Boxplot of the mitochondrial and whole-cell nucleotides displaying significant differences after treatment with free palbociclib (palbo) or StPGA-SS-palbociclib (StPGA-SS-palbo) compared to control (CT) or after treatment with StPGA-SS-palbociclib (StPGA-SS-palbo) compared to free palbociclib (palbo). Data analysis used a T-test, with data presented as average \pm SEM (n = 4, except for the conjugated Palbociclib group of the mitochondrial samples where MITMS12 was excluded). * p < 0.05, ** p < 0.01, *** p < 0.001. 3-CMP = Cytidine 3-monophosphate; 5-GDP = guanosine 5-diphophate; 5-GMP = guanosine 5-monophophate; ArabfurUMP = 1-β-D-Arabinofuranosyluracil 5-monophosphate.

In **mitochondria**, we found significantly elevated levels of GPC after treatment with free palbociclib and StPGA-SS-palbociclib compared to control (**Figure 3.19**), which we also observed in the cell media from cells treated with StPGA-SS-palbociclib by NMR metabolomics (**Section 3.2.2.3.1**). Increased GPC could correlate to the trend for decreased phosphocholine in isolated mitochondria of cells treated with free palbociclib and StPGA-SS-palbociclib observed by NMR metabolomics (**Section 3.2.2.3.1**) and, thus, to the lipidic composition of mitochondria. We also observed significantly increased spermidine levels in the isolated mitochondria of cells treated with StPGA-SS-palbociclib compared to control (**Figure 3.19**), which causes OXPHOS uncoupling in mitochondria³³⁰.

The **whole-cell** analysis (**Figure 3.19**) also revealed significantly increased GPC levels after free palbociclib treatment compared to control, and we observed the same trend in cells treated with StPGA-SS-palbociclib. We also detected significantly decreased pantetheine 4'-phosphate (P4P) levels in whole-cells treated with free palbociclib and StPGA-SS-palbociclib compared to control. P4P is an intermediate of coenzyme A (CoA) biosynthesis³³¹; therefore, reduced P4P levels could indicate reduced levels of CoA, which is necessary for the formation of acetyl-CoA for the TCA cycle. N-acetyl-D-lactosamine and N1,N8-diacetylspermidine presented significantly

increased and decreased levels in whole-cells treated with free palbociclib compared to control. N-acetyl-D-lactosamine is a monosaccharide derived from UDP-glucose³³²; thus, increased levels of glucose due to reduced glycolysis may lead to the use of other pathways such as N-acetyl-Dlactosamine formation. Although we observed significantly increased levels of spermidine in isolated mitochondria of cells treated with StPGA-SS-palbociclib, we detected significantly reduced levels of N1,N8-diacetylspermidine in the whole-cell analysis after treatment with free palbociclib compared to control and we observed the same trend for StPGA-SS-palbociclib. Hiramatsu et al. reported an increase in the levels of N1,N8-diacetylspermidine in the urine of patients with urogenital tumors and a decrease after patient treatment³³³, as we observed in our study. Creatine levels became significantly diminished after StPGA-SS-palbociclib treatment compared to control, which may relate to altered levels of glycine, arginine, and methionine, precursors of creatine³³⁴ or impairment on the creatine phosphate shuttle responsible for the maintenance of energy reservoir thanks to the transport of phosphates from mitochondria to the cytosol³³⁵. Finally, we observed significantly higher hydroxyphenyllactate levels in wholecells treated with StPGA-SS-palbociclib compared to free palbociclib. Hydroxyphenyllactate is a tyrosine-derived metabolite³³⁶; therefore, higher hydroxyphenyllactate levels after treatment with StPGA-SS-palbociclib could reflect the higher amount of substrate (tyrosine) for synthesis, as we observed increased tyrosine levels in the media of cells treated with StPGA-SS-palbociclib (Section 3.2.2.3.1).

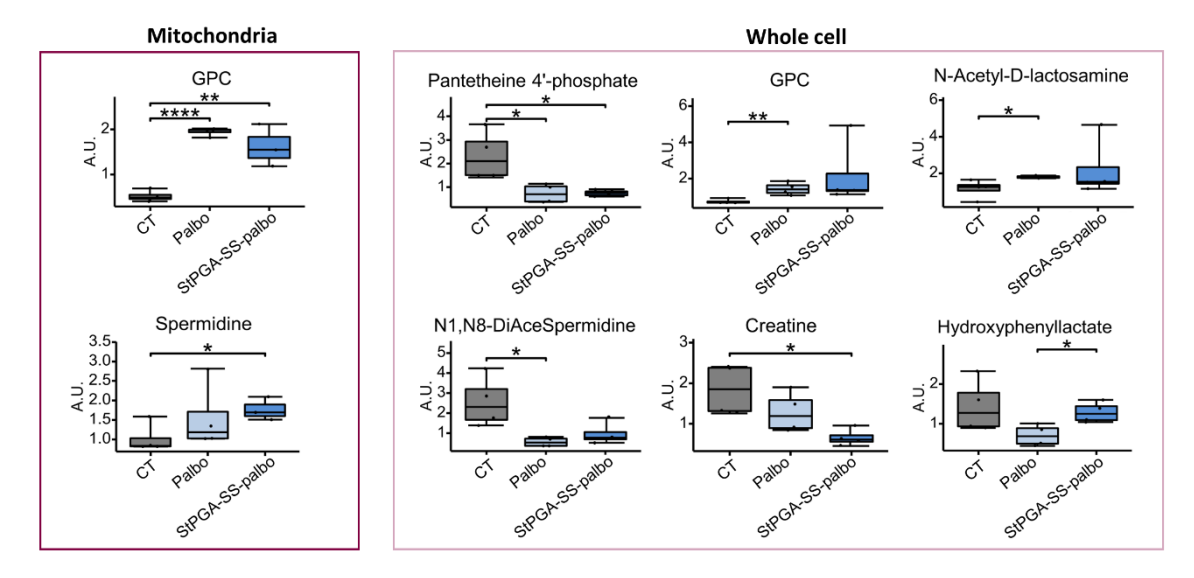


Figure 3.19. Metabolite alterations detected by MS metabolomics. Boxplots of mitochondrial and cellular metabolites displaying significant differences after treatment with free palbociclib (palbo) and StPGA-SS-palbociclib (StPGA-SS-palbo) compared to controls (CT) or after treatment with StPGA-SS-palbociclib (StPGA-SS-palbo) compared to free palbociclib (palbo). Data analysis used a T-test, with data presented as average ± SEM (n = 4, except for the StPGA-SS-palbociclib group of the mitochondrial samples where

MITMS12 was excluded). * p < 0.05, ** p < 0.01, **** p < 0.0001. GPC = glycerophosphocholine; N1,N8-DiAceSpermidine = N1,N8-Diacetylspermidine.

Analyzing the metabolomic profile of isolated mitochondria of cells treated with free palbociclib and StPGA-SS-palbociclib by MS provides complementary information to that obtained by NMR, providing a more detailed view of the effect of these treatments on mitochondrial metabolism. Overall, the MS metabolomic analysis of mitochondrial samples confirmed decreased peptide and amino acid levels after treatments in isolated mitochondria compared to control. The whole-cell analysis showed alterations in nucleotide metabolism and in lipid-related metabolites in whole-cells treated with free palbociclib and StPGA-SS-palbociclib compared to control. Moreover, the whole-cell analysis revealed the alteration of other mitochondrial-related metabolites such as creatine, not observed by NMR metabolomics. Of note, creatine levels significantly decreased in whole-cells treated with StPGA-SS-palbociclib compared to control. The creatine phosphate shuttle needs ATP for its functioning; therefore, this result may reflect the decreased ATP levels in whole-cells treated with StPGA-SS-palbociclib (Section 3.2.2.3.1) and the significant impact of StPGA-SS-palbociclib on mitochondrial respiration (Section 3.2.2.2). Use of the endocytic pathway may support the accumulation of StPGA-SS-palbociclib in cells compared to free palbociclib (enters and exits via diffusion), which makes StPGA-SS-palbociclib cause more significant damage in mitochondria. We also observed this effect in the significantly increased levels of hydroxyphenyllactate in whole-cells after StPGA-SS-palbociclib treatment compared to free palbociclib. The accumulation of tyrosine (observed in cell media; Section 3.2.2.3.1) - the substrate of hydroxyphenyllactate - due to the more significant impairment of the TCA cycle caused a significant increase in the synthesis of tyrosine-derivatives such as hydroxyphenyllactate. 1-methylguanosine also showed significantly increased levels in wholecells treated with StPGA-SS-palbociclib compared to whole-cells treated with free palbociclib. Again, the endocytic internalization pathway and the controlled drug release of StPGA-SSpalbociclib may support higher palbociclib levels within cells compared to free palbociclib, causing higher RNA damage and increased nucleoside formation.

3.2.2.3.3. MS Lipidomic Analysis of Mitochondria and Triple Negative Breast Cancer Cells After Treatment with Free Palbociclib and StPGA-SS-palbociclib

Through the analysis of the effect of free palbociclib and StPGA-SS-palbociclib on the mitochondrial and whole-cell metabolome by NMR and MS, we observed an impact of both treatments on lipid-related metabolites (phosphocholine and GPC); therefore, we took advantage of the ability of MS to perform lipidomic analyses and studied the lipidome of the samples used in the previous section (**Table 3.4**).

In the PCA score plot of the **mitochondrial** samples (**Figure 3.20A**), we observed a robust grouping with more pronounced discrimination than in the metabolomic analysis. The good differentiation between groups revealed a higher impact of treatments on the lipidome than on the metabolome of mitochondria and a different effect of each treatment on the lipidome of whole-cells. We then visualized the number of lipids contributing to the groupings by plotting them in volcano plots of the three comparisons: control vs. free palbociclib, control vs. StPGA-SS-palbociclib, and free palbociclib vs. StPGA-SS-palbociclib (**Figure 3.20B**). We detected many lipids that increased and decreased in isolated mitochondria from treated cells, and interestingly, we detected significant lipid changes in isolated mitochondria from cells treated with StPGA-SS-palbociclib compared to free palbociclib (**Figure 3.20B**). We did not see this effect for the metabolomic analysis, indicating that drug conjugation had a much more substantial impact on the mitochondrial lipidome than the metabolome.

The **whole-cell** lipidome also robustly discriminated the treatment groups (**Figure 3.20C**), similar to the mitochondrial samples grouping. We did observe an outlier sample (CELLMSO1) in the control group that we removed from the whole-cell analysis. The outlier sample presented many lipids with amounts three times the mean, which could be due to a greater amount of collected cells. The volcano plots of the whole-cell analysis (**Figure 3.20D**), revealed a moderate number of lipids that became altered after treatment with free palbociclib but a more significant amount for StPGA-SS-palbociclib compared to control. Interestingly, we also detected lipids that presented significantly different levels between free palbociclib- and StPGA-SS-palbociclib-treated cells.

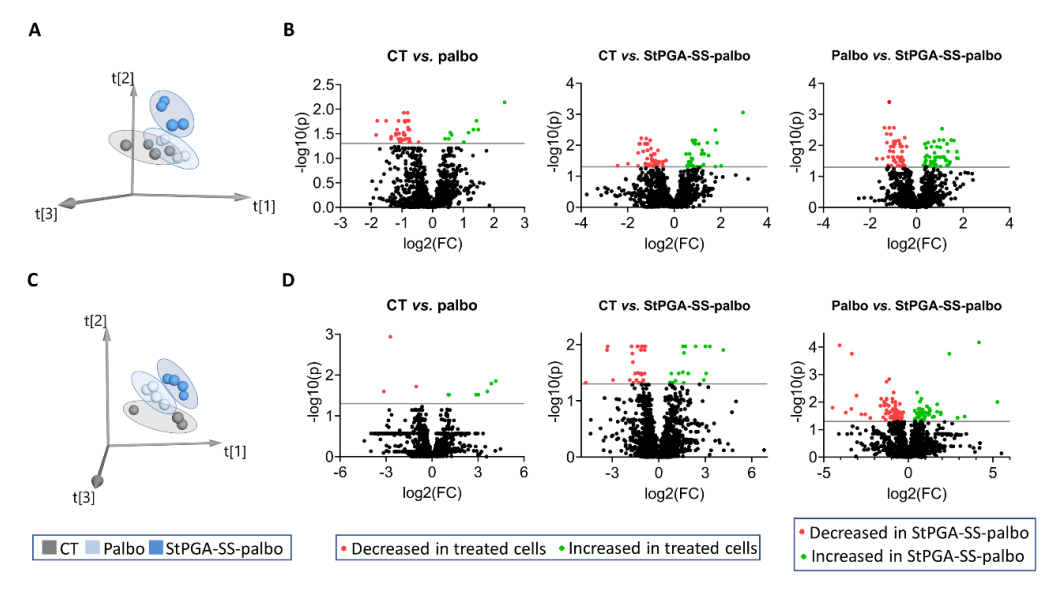


Figure 3.20. Comparative analysis of the MS lipidomic profile of whole-cells and mitochondria. **A)** 3D PCA score plot of mitochondria isolated from untreated TNBC cells (CT = control) and from cells treated with

free palbociclib (palbo) and StPGA-SS-palbociclib (StPGA-SS-palbo) (n = 4 per group; statistical algorithm: unit variance scaled). **B**) Volcano plots of the three comparisons in mitochondrial samples: control vs. free palbociclib, control vs. StPGA-SS-palbociclib, and free palbociclib vs. StPGA-SS-palbociclib. **C**) 3D PCA score plot of untreated whole-cells (CT = control) and after treatment with free palbociclib (palbo) and StPGA-SS-palbociclib (StPGA-SS-palbo) (n = 4 per group, except for the control group where we excluded CELLMS01; statistical algorithm: unit variance scaled). **D**) Volcano plots of the three comparisons in whole-cell samples: control vs. free palbociclib, control vs. StPGA-SS-palbociclib, and free palbociclib vs. StPGA-SS-palbociclib. Colored points (green/red = increased/decreased in treated samples compared to control or in the StPGA-SS-palbociclib group compared to free palbociclib group) indicate the metabolites presenting p-values and fold changes above 0.05 and 1.2, respectively.

Supporting Information 3.9 and **Supporting Information 3.10** report a complete list of all lipids that displayed significantly different levels in the three comparisons (control vs. free palbociclib; control vs. StPGA-SS-palbociclib; free palbociclib vs. StPGA-SS-palbociclib) for isolated mitochondria and whole-cell samples.

Mitochondrial Lipidomic Alterations

Forty-four lipids became significantly altered in isolated mitochondria of cells treated with free palbociclib compared to control, with thirty-four decreasing and ten increasing (Figure 3.21A). We found eighty-three lipid significant alterations in isolated mitochondria of cells treated with StPGA-SS-palbociclib compared to control, with forty-nine decreased and thirty-four increased (Figure 3.21A). Overall, these findings suggests a more significant impact of StPGA-SS-palbociclib on the mitochondrial lipidome than free palbociclib. The comparison of isolated mitochondria of cells treated with free palbociclib to StPGA-SS-palbociclib reflected these previous findings; overall, we found eighty-seven significant alterations to lipids (forty-two decreased and forty-five increased) in the StPGA-SS-palbociclib group in this comparison (Figure 3.21A).

When considering all significant changes from all comparisons in mitochondrial samples, 60-70% corresponded to glycerophospholipids, 25-33% to sphingolipids, and 4-5% to glycerolipids (Figure 3.21B); 80-86% corresponded to unsaturated fatty acids and 14-20% to saturated fatty acids (Figure 21C); and 95-98% corresponded to long-chain fatty acids (more than 12 carbons) and 2-5% of medium-chain fatty acids (7-12 carbons). Significantly altered glycerophospholipids in mitochondria included phosphatidylcholines (PC), lysophosphatidylcholines (LPC), phosphatidylethanolamines (PE), lysophosphatidylethanolamines (LPE), phosphatidylserines (PS), phosphatidylglycerols (PG), lysophosphatidylglycerols (LPG), phosphatidylinositols (PI), bismonoacylglycerophosphates (BMP) and hemibismonoacylglycerophosphates (HBMP) (Supporting Information 3.9); overall, being PC and PE the most abundant significantly altered

lipids. The high amount of altered glycerophospholipids correlates with glycerophospholipids being the main constituents of mitochondrial membranes (PC and PE comprising 30-40% of the total composition³³⁷). The noticeable alterations in PC and PE levels could relate to the disruption of energy production in mitochondria, as observed by Veen and colleagues³²⁰.

Significantly altered glycerolipids in mitochondria included diacylglycerols (DG) and monogalactosyldiacylglycerols (MGDG), while altered sphingolipids comprised sphingomyelins (SM), ceramides (Cer), and hexosylceramides (HexCer), with both, glycerolipids and sphingolipids, representing minor structural components of mitochondrial membranes³³⁷.

Most lipids that displayed significantly increased levels in mitochondria after treatment with free palbociclib and StPGA-SS-palbociclib compared to control were glycerophospholipids (80%). The remaining 20% consisted of sphingolipids in mitochondria from free palbociclib treated cells compared to controls and of sphingolipids (11%) and glycerolipids (9%) in the comparison of mitochondria from StPGA-SS-palbociclib treated cells compared to free palbociclib treated cells (Figure 3.21D). Interestingly, a higher number of sphingolipids (33%) presented with significantly increased levels in mitochondria isolated from cells treated with StPGA-SS-palbociclib compared to cells treated with free palbociclib, while 57% of increased lipids corresponded to glycerophospholipids and 11% to glycerolipids (Figure 3.21D). 58-59% of lipid species significantly decreased in mitochondria of cells treated with free palbociclib and StPGA-SS-palbociclib compared to control corresponded to glycerophospholipids, while 36%-39% were sphingolipids, and 2-6% corresponded to glycerolipids (Figure 3.21E).

Interestingly, we detected a high percentage of sphingolipids that displayed a significant decrease in level in mitochondria of cells treated with free palbociclib and StPGA-SS-palbociclib compared to control; however, we observed fewer significant decreases of sphingolipids (16%) in cells treated with StPGA-SS-palbociclib compared to cells treated with free palbociclib, while most corresponded to glycerophospholipids (84%) (**Figure 3.21E**).

Most PCs became significantly decreased in mitochondria after treatment with free palbociclib and StPGA-SS-palbociclib compared to control (**Supporting information 3.9**), confirming the alteration of the CDP-choline pathway, as previously observed by the NMR and MS metabolomic analysis (**Sections 3.2.2.3.1** and **3.2.2.3.2**). Among the altered sphingolipids, we observed that all SM and most Cer and HexCer became significantly decreased in mitochondria after treatment with free palbociclib and StPGA-SS-palbociclib compared to control (**Supporting Information 3.9**). Of note, PG and LPG, exclusively found in the mitochondrial membrane and precursors of the mitochondrial membrane lipid cardiolipins (CL)³³⁷, displayed significantly reduced levels in

Information 3.9). Interestingly, Claypool et al. reported that CL supported proteins involved in mitochondrial respiration³³⁸; thus, a decrease of PG and LPG could lead to decreased CL levels in mitochondria that could relate to the impairment in mitochondrial respiration observed in Section 3.2.2.2.

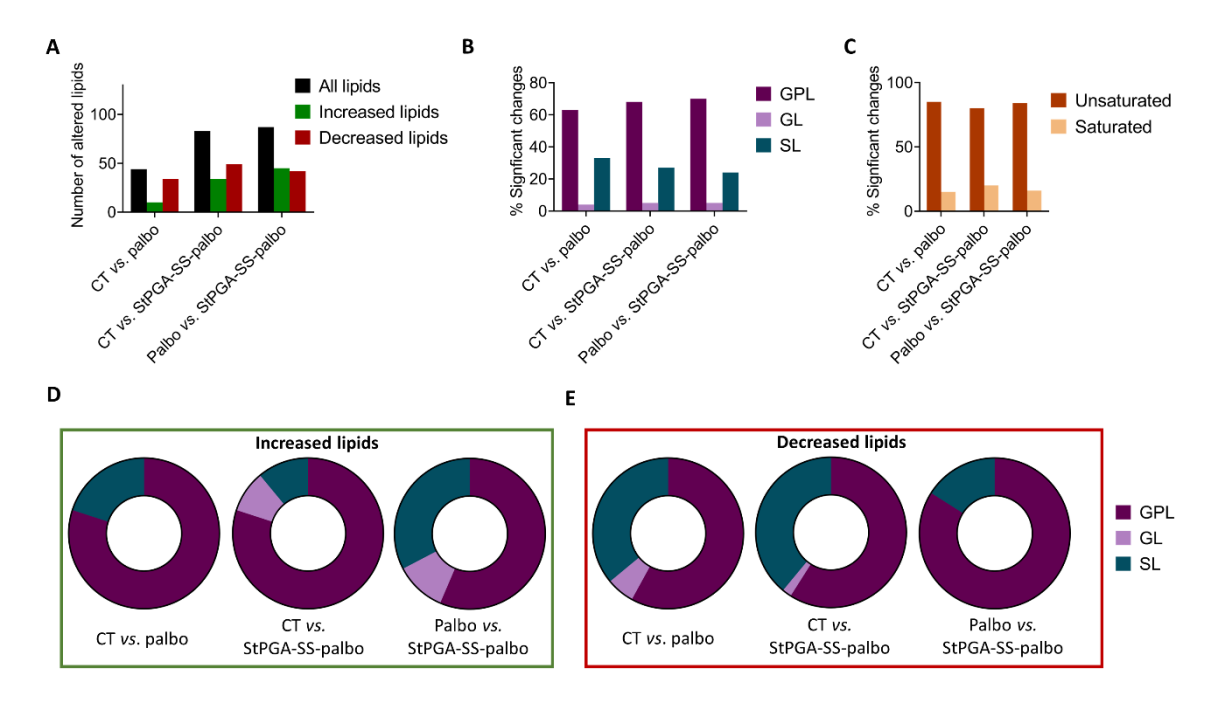


Figure 3.21. Summary of the mitochondrial lipid alterations. A) Total number of lipids significantly altered (black), number of significantly increased (green) and decreased (red) lipids in mitochondria of cells treated with free palbociclib (palbo) and StPGA-SS-palbociclib (StPGA-SS-palbo) compared to control (CT) and with StPGA-SS-palbociclib (StPGA-SS-palbo) compared to free palbociclib. B) Percentage of significant changes occurring in each class of lipids (GPL = glycerophospholipid (purple), GL = glycerolipid (pink) and SL = sphingolipid (blue)) in the three comparisons of mitochondrial sample groups (control vs. free palbociclib, control vs. StPGA-SS-palbociclib, and free palbociclib vs. StPGA-SS-palbociclib). C) Percentage of significant changes occurring in lipids regarding the presence (dark orange) or absence of unsaturated fatty acids (light orange) in the three comparisons of mitochondrial sample groups (control vs. free palbociclib, control vs. StPGA-SS-palbociclib, and free palbociclib vs. StPGA-SS-palbociclib). D) Percentage of each type of lipids that significantly increased in mitochondria of cells treated with free palbociclib compared to free palbociclib. E) The percentage of each type of lipids significantly decreased in mitochondria of cells treated with free palbociclib compared to control and in mitochondria of cells treated with free palbociclib compared to control and in mitochondria of cells treated with StPGA-SS-palbociclib compared to control and in mitochondria of cells treated with StPGA-SS-palbociclib compared to control and in mitochondria of cells treated with StPGA-SS-palbociclib compared to control and in mitochondria of cells treated with StPGA-SS-palbociclib compared to control and in mitochondria of cells treated with StPGA-SS-palbociclib compared to free palbociclib.

Whole-cell Lipidomic Alterations

The whole-cell lipidomic analysis provided additional and complementary information to that provided by the mitochondrial analysis. Interestingly, we detected fewer significant alterations in the whole-cell lipidome (10 and 37) than in the mitochondrial analysis (44 and 83) for free palbociclib and StPGA-SS-palbociclib treatment compared to control, respectively. Similar to mitochondrial analysis, we found fewer significant alterations in the lipidome of whole-cells treated with free palbociclib compared to control (10 - 3 decreased and 7 increased) than in whole-cells treated with StPGA-SS-palbociclib compared to control (37 - 29 decreased and 8 increased) (Figure 3.22A). Again, these findings indicate a more significant impact of StPGA-SS-palbociclib on the lipidome than free palbociclib. As observed in the study of the mitochondrial lipidome (87 lipids altered), we discovered many significant differences in lipid levels when comparing whole-cells treated with free palbociclib and StPGA-SS-palbociclib; of the 120 significantly altered lipids, 77 decreased and 42 increased in abundance (Figure 3.22A).

The majority of significant changes corresponded to glycerophospholipids (64-90%) and glycerolipid (9-10%); furthermore, we observed significant alterations in sphingolipids in wholecells after treatment with StPGA-SS-palbociclib (26% of total changes) compared to control cells (26%) and to free palbociclib (12%) (Figure 3.22B). Interestingly, we detected additional classes of significantly altered lipids in whole-cells treated with StPGA-SS-palbociclib compared to control and to free palbociclib. We discovered that 2% of significantly altered lipids in wholecells after treatment with StPGA-SS-palbociclib compared to control corresponded to fatty acids, and we found one sterol lipid (1%) with significantly different levels between whole-cells treated with free palbociclib and StPGA-SS-palbociclib (Figure 3.22B).

As in the lipidomic analysis of the isolated mitochondria, we found that most significantly altered lipids in all comparisons in whole-cells were unsaturated fatty acids (82-100%) and contained long-chain fatty acids (96-100%), while only 4% were medium-chain fatty acids in the whole-cell comparison of free palbociclib and StPGA-SS-palbociclib (**Figure 3.22C**).

In the whole-cell analysis, we observed significant alterations in practically the same glycerophospholipids as in the mitochondrial analysis (PC, LPC, PE, LPE, lyso-N-acyl-phosphatidylethanolamine [LNAPE], PS, PG, LPG, PI, lysophosphatidylinositols (LPI), BMP and HBMP), except for CL, whose alteration were exclusively observed in the whole-cell analysis (**Supporting Information 3.10**). Despite the detection of CL in the whole-cell analysis, it provides information on the mitochondrial lipidome, as CLs are exclusively found in the mitochondrial membranes³³⁷.

Similar to our previous findings in mitochondrial lipid alterations, significantly altered glycerolipids in whole-cells included DG, MGDG, and triacylglycerols (TG), while significantly altered sphingolipids in whole-cells consisted of SM, Cer, and HexCer. Of note, we found a significant alteration in a fatty acyl ester of hydroxy fatty acids (FAHFA; involved in glucose metabolism³³⁹) in whole-cells treated with StPGA-SS-palbociclib compared to control (**Supporting Information 3.10**). Moreover, a cholesterol ester (CE) became, involved in energy storage and maintaining cell membrane fluidity³⁴⁰, became significantly altered in whole-cells treated with StPGA-SS-palbociclib compared to free palbociclib (**Supporting Information 3.10**).

The percentage of significantly increased lipids in whole-cells after treatment with free palbociclib compared to control (90% glycerophospholipids, 10% sphingolipids) (Figure 3.22D) remained similar to the mitochondrial analysis (80% glycerophospholipids, 10% sphingolipids). However, a higher percentage of sphingolipids (47%) became increased in whole-cells after StPGA-SS-palbociclib treatment compared to control than in the mitochondrial analysis (11%), while 41% corresponded to glycerophospholipids and 12% to glycerolipids (Figure 3.22D). In difference to the mitochondrial analysis, we observed 2% of sterol lipids significantly increased in whole-cell samples from cells treated with StPGA-SS-palbociclib compared to free palbociclib, while we observed similar percentages of glycerophospholipids (74%), glycerophospholipids (9%) and sphingolipids (15%).

Similarly to mitochondrial lipidome alterations, significantly decreased lipids mainly corresponded to glycerophospholipids (77-100%) in whole-cells after treatment with free palbociclib and StPGA-SS-palbociclib compared to control cells. At the same time, we detected that 13% of sphingolipids, 7% of glycerolipids, and 3% of fatty acyls significantly decreased in whole-cells after treatment with StPGA-SS-palbociclib compared to control (Figure 3.22E). Moreover, in whole-cell samples, we detected 10% significantly decreased glycerolipids after StPGA-SS-palbociclib treatment compared to free palbociclib, which we did not detect in isolated mitochondria, and similar percentages of significantly decreased glycerophospholipids (80%) and sphingolipids (10%) (Figure 3.22E).

As indicated by analysis of isolated mitochondria, most PC became significantly decreased in whole-cells after treatment with free palbociclib and StPGA-SS-palbociclib compared to control and after treatment with StPGA-SS-palbociclib compared to free palbociclib (**Supporting information 3.10**). These findings again confirmed alterations in the CDP-choline pathway. We also observed a significant amount of PE and Cer/HexCer with significantly reduced levels in whole-cells after StPGA-SS-palbociclib treatment compared to free palbociclib treatment

(Supporting Information 3.10). This finding reveals the differential impact of treatments on the cell lipidome. Interestingly, we detected significantly decreased CL and PG/LPG (exclusively found in the mitochondrial membrane) in whole-cells treated with StPGA-SS-palbociclib compared to control and free palbociclib groups (Supporting Information 3.10), which confirms the previously mentioned hypothesis of decreased PG and LPG leading to decreased CL levels. This finding also supports the elevated level of mitochondrial disruption observed in cells treated with StPGA-SS-palbociclib and confirms that palbociclib conjugation to StPGA provides a modified pharmacokinetic profile to palbociclib that favors enhanced mitochondrial damage.

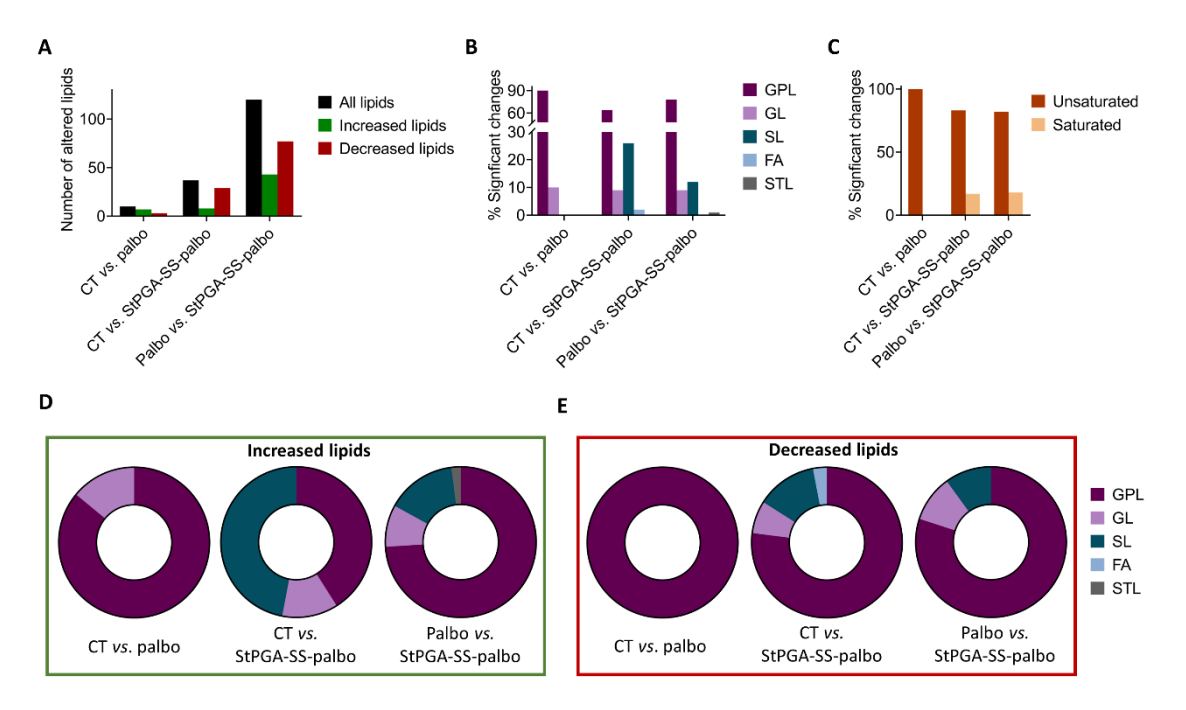


Figure 3.22. Summary of the whole-cell lipid alterations. A) Total number of lipids significantly altered (black), number of significantly increased (green) and decreased (red) lipids in whole-cells treated with free palbociclib (palbo) and StPGA-SS-palbociclib (StPGA-SS-palbo) compared to control (CT) and with StPGA-SS-palbociclib (StPGA-SS-palbo) compared to free palbociclib. B) Percentage of significant changes occurring in each class of lipids (GPL = glycerophospholipid (purple), GL = glycerolipid (pink), SL = sphingolipid (blue), FA = fatty acid (blue) and STL = sterol lipid (grey)) in the three comparisons of whole-cell sample groups (control vs. free palbociclib, control vs. StPGA-SS-palbociclib, and free palbociclib vs. StPGA-SS-palbociclib). C) Percentage of significant changes occurring in lipids regarding the presence (dark orange) or absence of unsaturated fatty acids (light orange) in the three comparisons of whole-cell sample groups (control vs. free palbociclib, control vs. StPGA-SS-palbociclib, and free palbociclib vs. StPGA-SS-palbociclib). D) Percentage of each type of lipids that significantly increased in whole-cells treated with free palbociclib compared to control and in whole-cells treated with StPGA-SS-palbociclib compared to free palbociclib compared to control and in whole-cells treated with free palbociclib and StPGA-SS-palbociclib compared to control and in whole-cells treated with StPGA-SS-palbociclib compared to free palbociclib compared to control and in whole-cells treated with StPGA-SS-palbociclib compared to free palbociclib compared to control and in whole-cells treated with StPGA-SS-palbociclib compared to free palbociclib compared to control and in whole-cells treated with StPGA-SS-palbociclib compared to free palbociclib compared to free palbociclib.

In conclusion, the analysis of mitochondria isolated from TNBC cells treated with palbociclib and StPGA-SS-palbociclib revealed an enormous impact on the lipidome; generally, we observed a more significant impact following StPGA-SS-palbociclib exposure. Interestingly, we discovered more significant alterations in the analysis of mitochondrial samples, which may derive from the different internalization mechanisms used for free and conjugated palbociclib (with endocytosis of StPGA-SS-palbociclib associated with membrane disruption and fusion). Among the altered lipids, we highlight the decrease of many PCs following treatment with palbociclib and StPGA-SS-palbociclib compared to control, which indicated an alteration in the CDP-choline pathway, as also suggested by the NMR and MS metabolomic results (Sections 3.2.2.3.1 and 3.2.2.3.2).

3.2.2.4. Fluxomics Analysis of Triple Negative Breast Cancer Cells After Treatment with Free Palbociclib and StPGA-SS-palbociclib

3.2.2.4.1. Optimization of the Isotope-Labeling Experiments in Whole-Cells

To complete the study of the impact of free palbociclib and StPGA-SS-palbociclib on the metabolism of isolated mitochondria and whole-cell samples of TNBC cells, we performed fluxomics analysis in whole-cells by both NMR and MS to gain insight into pathway dynamics. To this end, we employed ¹³C-glucose and ¹³C-glutamine in independent experiments to label downstream metabolites and trace their paths. First, we optimized the labeling time for each labeled substrate by LC-MS, taking advantage of its sensitivity. For this purpose, we incubated TNBC cells with media containing ¹³C-glucose or ¹³C-glutamine at different times and extracted metabolites using a mixture of MeOH:AcN:H₂O (AcN extraction). In this section, M+X represents a metabolite isotopologue (i.e., the mass of the metabolite (M) plus the number of labeled carbons (X)).

Table 3.6 summarizes the data for all samples used in the MS fluxomics analysis (**Sections 3.2.2.5.1** and **3.2.2.5.2**) (treatment, labeled metabolite, labeling time, and type of metabolite extraction carried out).

Table 3.6. Data summary for samples used in Section 3.2.2.5.1

Sample ID	Treatment*	Labeled metabolite	Labeling time (min)	Metabolite extraction
MITO293	Control (untreated)	¹³ C-glucose	15	AcN* extraction
MITO296	Control (untreated)	¹³ C-glucose	15	AcN extraction
MITO299	Control (untreated)	¹³ C-glucose	15	AcN extraction
MITO302	Control (untreated)	¹³ C-glucose	60	AcN extraction
MITO305	Control (untreated)	¹³ C-glucose	60	AcN extraction
MITO308	Control (untreated)	¹³ C-glucose	60	AcN extraction

MITO311	Control (untreated)	¹³ C-glucose	120	AcN extraction
MITO312	Palbociclib	¹³ C-glucose	120	AcN extraction
MITO313	StPGA-SS-palbociclib	¹³ C-glucose	120	AcN extraction
MITO314	Control (untreated)	¹³ C-glucose	120	AcN extraction
MITO315	Palbociclib	¹³ C-glucose	120	AcN extraction
MITO316	StPGA-SS-palbociclib	¹³ C-glucose	120	AcN extraction
MITO317	Control (untreated)	¹³ C-glucose	120	AcN extraction
MITO318	Palbociclib	¹³ C-glucose	120	AcN extraction
MITO319	StPGA-SS-palbociclib	¹³ C-glucose	120	AcN extraction
MITO320	Control (untreated)	¹³ C-glucose	180	AcN extraction
MITO323	Control (untreated)	¹³ C-glucose	180	AcN extraction
MITO326	Control (untreated)	¹³ C-glucose	180	AcN extraction
MITO266	Control (untreated)	¹³ C-glutamine	180	AcN extraction
MITO267	Palbociclib	¹³ C-glutamine	180	AcN extraction
MITO268	StPGA-SS-palbociclib	¹³ C-glutamine	180	AcN extraction
MITO269	Control (untreated)	¹³ C-glutamine	180	AcN extraction
MITO270	Palbociclib	¹³ C-glutamine	180	AcN extraction
MITO271	StPGA-SS-palbociclib	¹³ C-glutamine	180	AcN extraction
MITO272	Control (untreated)	¹³ C-glutamine	180	AcN extraction
MITO273	Palbociclib	¹³ C-glutamine	180	AcN extraction
MITO274	StPGA-SS-palbociclib	¹³ C-glutamine	180	AcN extraction
MITO275	Control (untreated)	¹³ C-glutamine	360	AcN extraction
MITO278	Control (untreated)	¹³ C-glutamine	360	AcN extraction
MITO281	Control (untreated)	¹³ C-glutamine	360	AcN extraction

^{*}AcN = acetonitrile

For the ¹³C-glucose labeling studies, we analyzed the mass isotopomer distribution (MID) of selected metabolites after four labeling times (15, 60, 120, and 180 min) in untreated TNBC cells. We observed ¹³C labeling of fructose-1,6-biphosphate (a glycolysis intermediate) after 15 min and no significant differences in MID after 60, 120, or 180 min (Figure 3.23A and Supporting Information 3.11), indicating that glucose became rapidly metabolized through the glycolytic pathway. In the TCA cycle intermediates, we observed significantly different MIDs between cells labeled for 15 min and 60 min and between cells labeled for 60 min and 120 min; however, we observed non-significant differences between 120 and 180 min of labeling. As expected, labeling TCA cycle intermediates required additional time compared to glycolysis intermediates; therefore, we incubated TNBC cells with ¹³C-glucose for 120 min (Figure 3.23A, red boxes).

We extended incubation times for the ¹³C-glutamine labeling analysis, as glutamine requires more time to metabolize and enter TCA cycle than glucose³⁴¹. We studied the MID of selected metabolites after incubating untreated TNBC cells with ¹³C-glutamine for 180 and 360 min. We

found non-significant differences in the MIDs for glutamate, the first metabolic product from glutamine, or for the TCA cycle intermediates between 180 and 360 min of labeling. Only citrate showed lower MID of the M+0 citrate, indicating relatively higher labeling after 360 min of incubation with ¹³C-glutamine (**Figure 3.23B** and **Supporting Information 3.12**). Given that most of the metabolites did not show significant differences between incubation of cells with ¹³C-glutamine for 180 min and for 360 min, we selected incubation for 180 min to perform ¹³C-glutamine labeling studies (**Figure 3.23B**, red box).

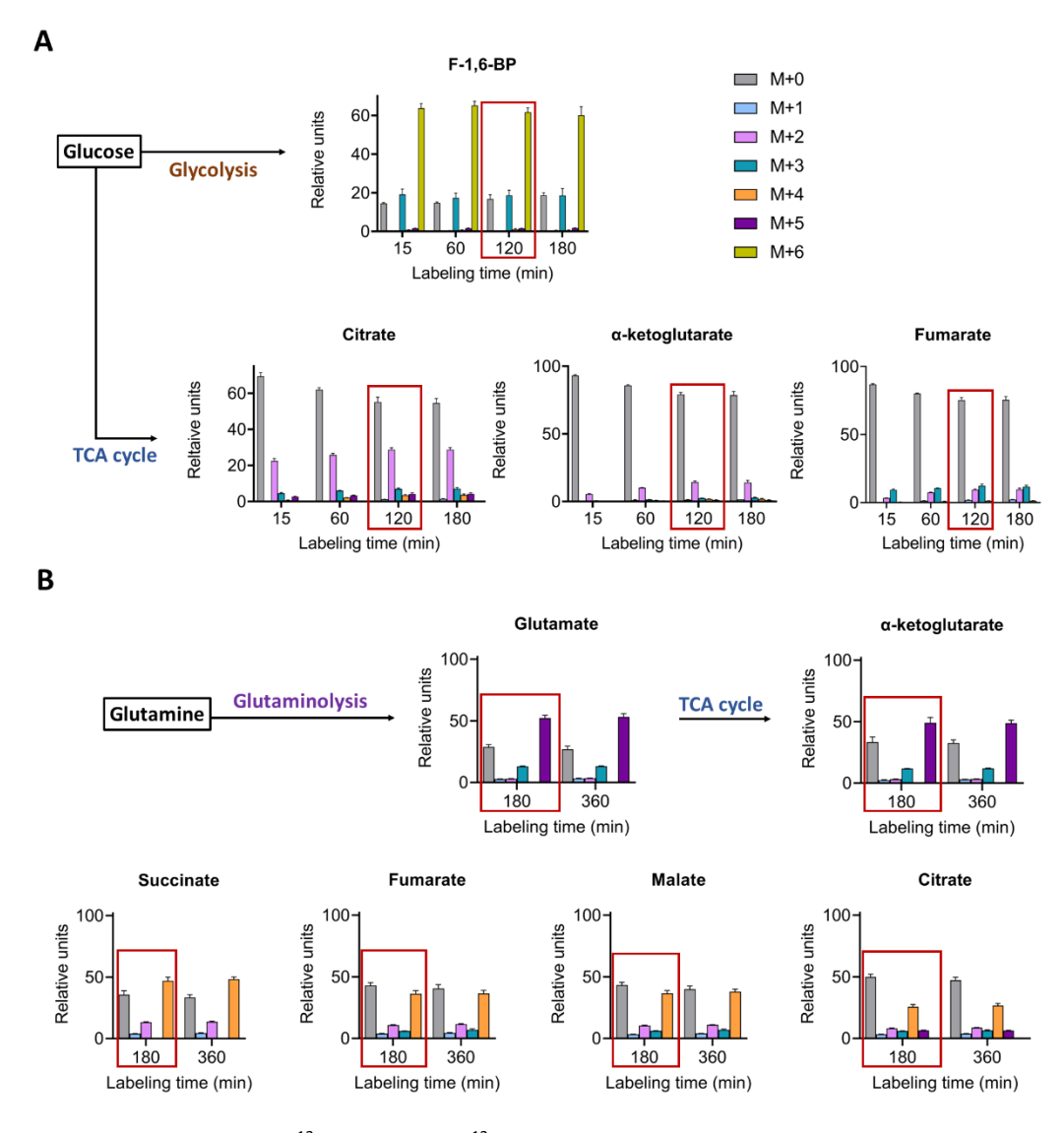


Figure 3.23. Optimization of 13 C-glucose and 13 C-glutamine labeling studies. Graphical representation of the relative amount of metabolite isotopologues in TNBC cells incubated with **A**) 13 C-glucose for 15, 60, 120, and 180 min or **B**) 13 C-glutamine for 180 and 360 min. Data presented as mean \pm SEM (n = 3). M+X represents the mass of the metabolites plus X labeled carbons, and red boxes indicate the selected labeling time. F-1,6-BP = fructose-1,6-biphosphate.

3.2.2.4.2. MS Fluxomics Analysis in Whole-Cells After Treatment with Free Palbociclib and StPGA-SS-palbociclib

After optimization, we evaluated the impact of free palbociclib and StPGA-SS-palbociclib on pathway dynamics by ¹³C-glucose and ¹³C-glutamine MS fluxomics analyses. **Figure 3.24** displays the most relevant ¹³C-labelled metabolites in untreated TNBC cells (CT) and after treatment with free palbociclib (palbo) and StPGA-SS-palbociclib (StPGA-SS-palbo).

¹³C-Glucose MS Fluxomics Analysis

Fructose-1,6-biphosphate M+0 showed significantly increased levels, while M+3 and M+6 isotopologues displayed significantly reduced levels after treatment with StPGA-SS-palbociclib compared to control cells, which indicated downregulation of glycolysis (**Figure 3.24A** and **Supporting 3.13**). However, we failed to detect MID alterations of the next glycolysis intermediate, glyceraldehyde-3-phosphate (**Figure 3.24A** and **Supporting 3.13**). ATP is needed for fructose-1,6-biphosphate synthesis but not for glyceraldehyde-3-phosphate synthesis³⁴²; therefore, StPGA-SS-palbociclib may cause higher glycolysis downregulation in the ATP-involving steps due to the previously observed decreased ATP levels in cells treated with StPGA-SS-palbociclib (detected by NMR metabolomics in **Section 3.2.2.3.1**).

UDP-glucuronate M+0 (UDP-GlcA; formed from UDP-glucose and glucose-6-phosphate³⁴³) displayed significantly reduced levels, while M+6 isotopologue significantly increased in cells treated with free palbociclib compared to control. Moreover, StPGA-SS-palbociclib caused a significant increase in M+10 and M+15 isotopologues compared to control (**Figure 3.24A** and **Supporting 3.13**). These findings indicated increased pathway flow to form UDP-GlcA after palbociclib and StPGA-SS-palbociclib treatment.

The synthesis of N-acetylneuraminate (formed in the hexosamine biosynthetic and sialic acid synthetic pathways from fructose-6-phosphate³⁴³) became downregulated after StPGA-SS-palbociclib treatment compared, as N-acetylneuraminate M+0 significantly increased and the M+2, M+3, M+5 M+8, M+9 and M+11 isotopologues significantly decreased compared to control (**Figure 3.24A** and **Supporting 3.13**). During N-acetylneuraminate synthesis from fructose-6-phosphate, the conversion of N-acetylmannosamine to N-acetylmannosamine-6-phopshate requires ATP³⁴⁴; therefore, the decreased ATP after StPGA-SS-palbociclib treatment (observed by NMR metabolomics in **Section 3.2.2.3.1**) may cause reduced N-acetylneuraminate synthesis.

Regarding TCA cycle intermediates, the ¹³C-glucose fluxomics study detected few alterations after treatment with free palbociclib and StPGA-SS-palbociclib. Citrate, the first intermediate of

the TCA cycle, displayed a significant increase of M+1 isotopologues after both treatments compared to control and significantly decreased M+2 isotopologue after StPGA-SS-palbociclib treatment compared to control (**Figure 3.24A** and **Supporting 3.13**). The M+1 citrate may derive from pyruvate carboxylation with ¹³C-CO₂ (formed in the decarboxylation process when glucose enters the pentose phosphate pathway) to form oxaloacetate, which converts to citrate³⁴⁵. The increased M+1 citrate could indicate the preference for pyruvate conversion to oxaloacetate rather than to acetyl-CoA in cells treated with free palbociclib and SPGA-SS-palbociclib. This finding was further supported by the significantly decreased citrate M+2 formed from ¹³C-acetyl-CoA after treatment with StPGA-SS-palbociclib compared to control.

α-ketoglutarate M+0, another TCA cycle intermediate, showed significantly reduced levels and M+1, M+2, M+3, M+4 and M+5 isotopologues displayed significantly increased levels in cells treated with free palbociclib compared to control (**Figure 3.24A** and **Supporting 3.13**), which may indicate stimulation of the TCA cycle for energy production when substrates come from the glycolytic pathway. Therefore, free palbociclib may induce increased TCA cycle activity, while StPGA-SS-palbociclib seems to slow the TCA flux when substrates for this pathway come from the glycolytic pathway.

Interestingly, we detected many changes in MID values for nucleotides after treatment with free palbociclib and StPGA-SS-palbociclib compared to control cells. Inosine monophosphate (IMP), which forms through the purine *de novo* synthesis pathway from phosphoribosyl pyrophosphate (PRPP) and the pentose phosphate pathway³⁴⁶, displayed significantly reduced levels of M+2 isotopologue after treatment with free palbociclib and StPGA-SS-palbociclib compared to control (**Figure 3.24A** and **Supporting 3.13**). Adenosine monophosphate (AMP), adenosine diphosphate (ADP), ATP, guanosine monophosphate (GMP), guanosine diphosphate (GDP), and GTP followed the same trend as IMP, as all them are synthesized from IMP through the purine *de novo* synthesis pathway. Nucleotides M+0 showed significantly increased levels, while M+2, M+3 and M+5 isotopologues were significantly reduced in cells treated with free palbociclib and StPGA-SS-palbociclib compared to control. (**Figure 3.24A** and **Supporting 3.13**). Overall, alterations in the MID of IMP, AMP, ADP, GMP, GDP, and GTP indicated the downregulation of the common purine *de novo* synthesis pathway after palbociclib and StPGA-SS-palbociclib treatment compared to control.

Interestingly, we found a significantly reduced MID for ADP-ribose M+0 and significantly increased M+13 isotopologue in cells treated with StPGA-SS-palbociclib compared to control (Figure 3.24A and Supporting 3.13). Moreover, we detected significantly increased M+13 and

M+15 isotopologues after treatment with free palbociclib compared to control cells. ADP-ribose forms poly(ADP-ribose), upon activation of the DNA repair mechanism, and, after repair, poly(ADP-ribose) undergoes degradation to ADP-ribose monomers³⁴⁷. Therefore, alterations to MIDs after free palbociclib and StPGA-SS-palbociclib treatments may indicate that DNA repair occurs in cells (probably due to the action of palbociclib, a CDK4/6 inhibitor³⁴⁸, on the cell cycle).

Treatment with free palbociclib and StPGA-SS-palbociclib seemed to have the opposite effect on uridine diphosphate (UDP) and uridine monophosphate (UMP) synthesis. UDP M+7 significantly decreased in cells treated with free palbociclib compared to control, while UDP M+9 significantly increased in cells treated with StPGA-SS-palbociclib compared to control. UMP M+0 significantly increased, and the M+2, M+3, and M+8 isotopologues significantly decreased in cells treated with free palbociclib compared to control. Of note, both UDP and UMP showed statistically significant differences regarding MIDs of some isotopologues (UDP M+5, UDP M+7 and UMP M+2) when comparing free palbociclib and StPGA-SS-palbociclib treatment (Figure 3.24A and Supporting 3.13), indicative of an opposite trend on the pyrimidine *de novo* synthesis pathway.

Finally, cytidine triphosphate M+0 (CTP - formed from uridine triphosphate (UTP)) demonstrated significantly decreased levels, while M+2 and M+7 isotopologues were significantly increased in cells treated with free palbociclib and StPGA-SS-palbociclib compared to control cells (**Figure 3.24A** and **Supporting 3.13**), which implies the upregulation of CTP synthesis after treatments. CTP is a high-energy molecule similar to ATP; therefore, increasing CTP could represent an alternative means of energy storage in cells with reduced ATP levels. Moreover, CTP remains essential for phospholipid synthesis (the main components of the cell membranes³⁴⁹); interestingly, we revealed that free palbociclib and StPGA-SS-palbociclib treatment altered phospholipid synthesis (**Section 3.2.2.3.3**).

In summary, labeling with ¹³C-glucose allowed the detection of flow alterations caused by free palbociclib and StPGA-SS-palbociclib in glycolysis, the hexosamine biosynthesis pathway, the pentose phosphate pathway, and *de novo* purine and pyrimidine synthesis. Interestingly, we observed some different trends between palbociclib and StPGA-SS-palbociclib treatment. StPGA-SS-palbociclib downregulated glycolysis and the TCA cycle, while free palbociclib stimulated the TCA cycle for energy production. Moreover, StPGA-SS-palbociclib downregulated N-acetylneuraminate synthesis, probably due to the reduced ATP required for synthesis, which we did not observe after free palbociclib treatment. Finally, while palbociclib and StPGA-SS-palbociclib impacted the purine *de novo* synthesis pathway in the same manner, we observed a

differential impact on the pyrimidine *de novo* synthesis pathway by each treatment (upregulated by StPGA-SS-palbociclib and downregulated by free palbociclib).

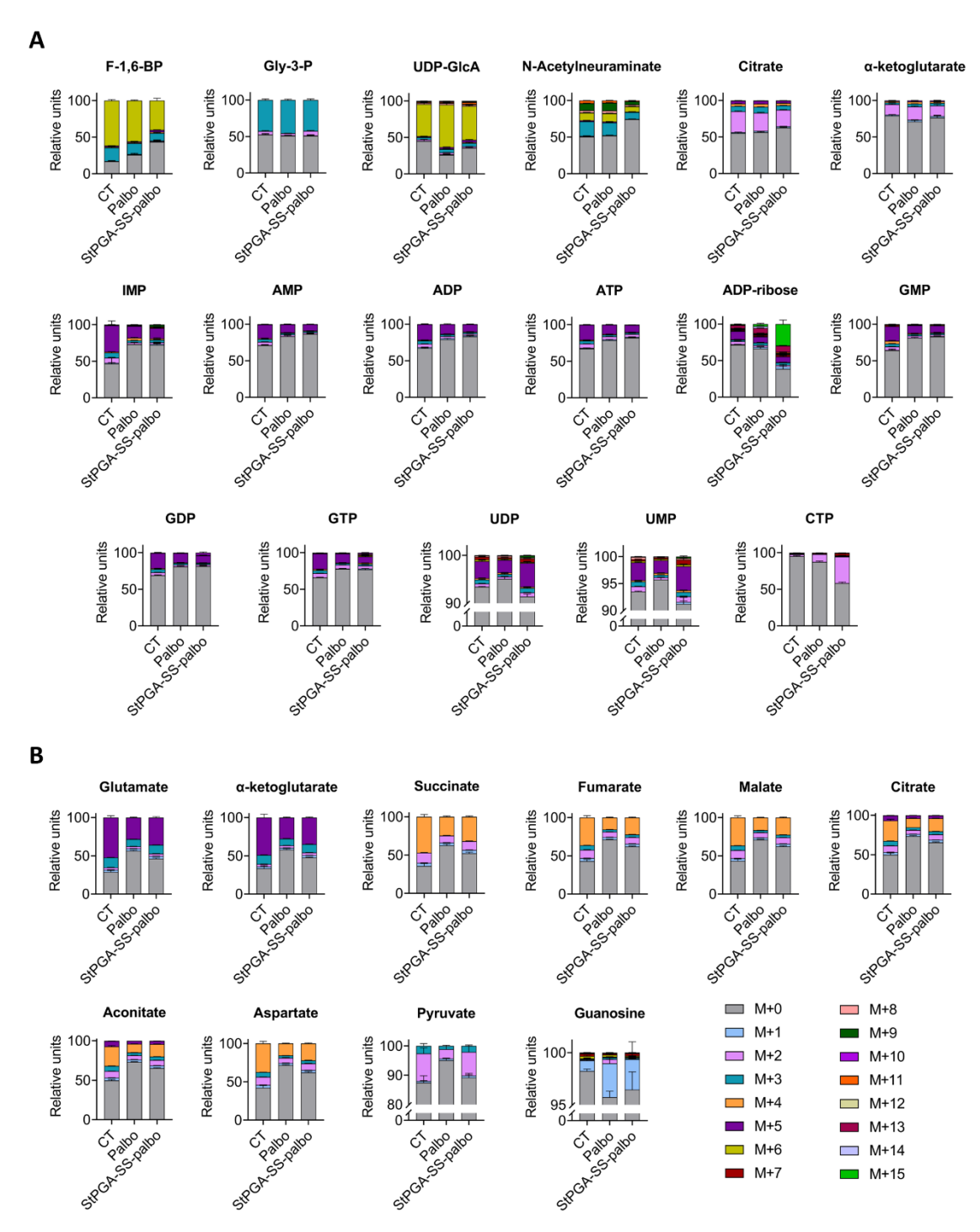


Figure 3.24. MS fluxomics analysis. **A)** Mass isotopomer distribution (MID) of ¹³C-labeled metabolites in untreated cells (CT) and in cells treated with free palbociclib (palbo) and StPGA-SS-palbociclib (StPGA-SS-palbo) after incubation with ¹³C-glucose for 120 min. ADP = adenosine diphosphate; AMP = adenosine monophosphate; ATP = Adenosine triphosphate; cAMP = cyclic adenosine monophosphate; CTP = cytidine triphosphate; F-1,6-BP = fructose-1,6-biphosphate; Gly-3-P = glyceraldehyde-3-phosphate; GMP = guanosine monophosphate; GDP = guanosine diphosphate; GTP = guanosine triphosphate; IMP = inosine

monophosphate; UDP = uridine diphosphate; UDP-GlcA = UDP-glucuronate; UMP = uridine monophosphate. **B**) MID of 13 C-labeled metabolites in untreated cells (CT) and in cells treated with free palbociclib (palbo) and StPGA-SS-palbociclib (StPGA-SS-palbo) after incubation with 13 C-glutamine for 120 min. Data represented as mean \pm SEM (n = 3).

¹³C-Glutamine MS Fluxomics Analysis

We completed the MS fluxomics study with labeling studies using ¹³C-glutamine to evaluate further alterations to glutaminolysis, the TCA cycle, and nucleotide-related metabolites. Glutamine first converts to glutamate through glutaminolysis³⁵⁰. Glutamate M+0 significantly increased, while M+3 and M+5 isotopologues significantly decreased in cells treated with free palbociclib and StPGA-SS-palbociclib treatment compared to control cells (**Figure 3.24B** and **Supporting Information 3.14**), which confirmed the downregulation of glutaminolysis observed by NMR and MS metabolomics (**Sections 3.2.2.3.1** and **3.2.2.3.2**)

Reduced glutaminolysis may lead to a reduced input of substrates to the TCA cycle and, thus, pathway downregulation, as indicated by significantly increased TCA cycle intermediates M+0 and a significant decrease in most isotopologues following treatment with free palbociclib and StPGA-SS-palbociclib compared to control cells (**Figure 3.24B** and **Supporting Information 3.14**). We detected citrate M+5 and aconitate M+5 (intermediate between isocitrate and α -ketoglutarate) (**Figure 3.24B** and **Supporting Information 3.14**), which indicated that part of α -ketoglutarate (produced from glutamate) followed reductive carboxylation or reverse TCA cycle to form citrate. Of note, this phenomenon occurs in cancer cells³⁵¹.

We also detected M+2 isotopologues of succinate, fumarate, malate, citrate, and aconitate (**Figure 3.24B** and **Supporting Information 3.14**), indicating citrate synthesis from ¹³C-acetyl-CoA. ¹³C-malate from the TCA cycle may form ¹³C-pyruvate, and this may be converted to ¹³C-acetyl-CoA³⁵².

We observed significantly increased pyruvate M+0 levels and significantly decreased pyruvate M+3 in cells treated with free palbociclib compared to control cells (**Figure 3.24B** and **Supporting Information 3.14**), demonstrating the significant effect of free palbociclib on the TCA cycle.

We also detected significantly increased aspartate M+0 and significantly decreased M+2, M+3, and M+4 isotopologues in cells treated with free palbociclib and StPGA-SS-palbociclib compared to control (**Figure 3.24B** and **Supporting Information 3.14**), indicating a reduction of aspartate synthesis. The MID indicates the synthesis of aspartate from two sources; M+2 and M+4 isotopologues demonstrated the formation of aspartate from oxaloacetate formed by oxidative

TCA cycle, while the M+3 isotopologue indicated the synthesis of aspartate through pyruvate carboxylation to oxaloacetate³⁵³.

Finally, the purine nucleoside guanosine demonstrated significantly reduced guanosine M+0 and significantly increased levels of the M+1 isotopologue in cells treated with free palbociclib compared to control (**Figure 3.24B** and **Supporting Information 3.14**), which revealed the formation of more significant levels of guanosine. Production of guanosine may occur through purine *de novo* synthesis, which requires glutamine³⁴⁶. An increase in guanosine may relate to guanosine-based nucleotide formation, as observed by the accumulation of GDP and GMP in cells treated with free palbociclib by the MS metabolomic analysis (**Section 3.2.2.3.2**).

The ¹³C-glutamine labeling study confirmed the downregulation of glutaminolysis and the TCA cycle after free palbociclib and StPGA-SS-palbociclib treatment compared to control. Interestingly, the disruption of these pathways seemed more robust in cells treated with free palbociclib than with StPGA-SS-palbociclib (**Figure 3.24B** and **Supporting Information 3.14**), which could derive from the delayed impact of palbociclib (after endocytosis, degradation, and release from StPGA-SS-palbociclib) on glutaminolysis and the TCA cycle (glutamine takes more time to undergo metabolization than glucose).

3.2.2.4.3. NMR Fluxomics Analysis in Whole-Cells After Treatment with Free Palbociclib and StPGA-SS-palbociclib

To confirm the results obtained by MS fluxomics and complement the labeling study of the impact of free palbociclib and StPGA-SS-palbociclib on metabolic pathway dynamics, we also performed an NMR fluxomics study of untreated (control) and treated TNBC cells. **Table 3.7** summarizes the data for all samples used in the NMR fluxomics analysis (treatment, labeled metabolite, labeling time, and type of metabolite extraction carried out).

Table 3.7. Data summary for samples used in Section 3.2.2.5.3

Sample ID	Treatment	Labeled metabolite	Labeling time (min)	Metabolite extraction
MITO184	Control (untreated)	¹³ C-glucose	120	Optimized
MITO185	Palbociclib	¹³ C-glucose	120	Optimized
MITO186	StPGA-SS-palbociclib	¹³ C-glucose	120	Optimized
MITO191	Control (untreated)	¹³ C-glucose	120	Optimized
MITO192	Palbociclib	¹³ C-glucose	120	Optimized
MITO193	StPGA-SS-palbociclib	¹³ C-glucose	120	Optimized
MITO202	Control (untreated)	¹³ C-glucose	120	Optimized
MITO203	Palbociclib	¹³ C-glucose	120	Optimized

MITO204	StPGA-SS-palbociclib	¹³ C-glucose	120	Optimized
MITO214	Control (untreated)	¹³ C-glucose	120	Optimized
MITO215	Palbociclib	¹³ C-glucose	120	Optimized
MITO216	StPGA-SS-palbociclib	¹³ C-glucose	120	Optimized
MITO205	Control (untreated)	¹³ C-glutamine	180	Optimized
MITO206	Palbociclib	¹³ C-glutamine	180	Optimized
MITO207	StPGA-SS-palbociclib	¹³ C-glutamine	180	Optimized
MITO208	Control (untreated)	¹³ C-glutamine	180	Optimized
MITO209	Palbociclib	¹³ C-glutamine	180	Optimized
MITO210	StPGA-SS-palbociclib	¹³ C-glutamine	180	Optimized
MITO211	Control (untreated)	¹³ C-glutamine	180	Optimized
MITO212	Palbociclib	¹³ C-glutamine	180	Optimized
MITO213	StPGA-SS-palbociclib	¹³ C-glutamine	180	Optimized
MITO217	Control (untreated)	¹³ C-glutamine	180	Optimized
MITO218	Palbociclib	¹³ C-glutamine	180	Optimized
MITO219	StPGA-SS-palbociclib	¹³ C-glutamine	180	Optimized

For NMR fluxomics, we incubated TNBC cells treated with free palbociclib and StPGA-SS-palbociclib with 13 C-glucose and 13 C-glutamine for previously optimized periods (120 and 180 min, respectively) and carried out cell extraction following the optimized method based on the use of the NMR buffer and centrifugal filtration. We acquired 13 C 1D and 1 H- 13 C 2D Heteronuclear Single Quantum Correlation (HSQC) spectra using a 600 MHz NMR spectrometer to detect 13 C-labeled metabolites. **Table 3.8** reports the assignment of the 1 H- 13 C 2D HSQC spectra of cells incubated with 13 C-glucose and 13 C-glutamine. Labeling with 13 C-glucose allowed the detection of 13 C-alanine and 13 C-lactate (both formed from pyruvate, the end-product of glycolysis 342), 13 C-UDP-GlcA (synthesized from fructose-6-phosphate, an intermediate of glycolysis 342), 13 C-glutamate (formed from α -ketoglutarate of the TCA cycle 354), and 13 C-glutamine (formed from labeled glutamate and phosphocholine, which may derive from citrate of the TCA cycle that undergoes transport to the cytosol for the fatty acid biosynthesis 30). Labeling with 13 C-glutamine allowed the detection of 13 C-glutamate formed from glutamine by glutaminolysis 350 and 13 C-phosphocholine and 13 C-GPC, most probably labeled from the citrate used for the fatty acid biosynthesis for lipid synthesis 30 .

Table 3.8. ¹H-¹³C 2D HSQC spectra assignments

	¹³ C-Glucose			¹³ C-Glutamine	
Metabolite	¹³ C chemical shift (ppm)	¹ H chemical shift (ppm)	Metabolite	¹³ C chemical shift (ppm)	¹ H chemical shift (ppm)
Alanine	16.54	1.49	Glutamate	33.63	2.67
Lactate	20.01	1.33	Glu + Gln*	26.93	2.16

Glutamate	22.18	2.06	Glu + Gln*	33.63	2.13
Glutamate	27	2.06	Glutamate	33.52	2.36
Glu + Gln*	26.77	2.13	Glutamate	26.88	2.31
Glutamate	33.52	2.35	Glutamate	26.9	3.37
Glutamate	33.17	2.4	P-choline*	54.11	3.2
P-choline	54.09	3.22	GPC*	54.11	3.24
Glutamate	54.93	3.77	Glutamate	54.66	3.77
Lactate	68.92	4.11			
UDP-GlcA*	97.4	5.62			

^{*}GIn = glutamine; Glu = glutamate; GPC = glycerophosphocholine; UDP-GIcA = uridine diphosphate glucuronate

The acquirement of the ¹³C 1D spectra helped the assignment of the ¹H-¹³C 2D HSQC spectra. **Figure 3.25** shows the signals that we assigned in the ¹³C 1D spectra obtained from TNBC cells incubated with ¹³C-glucose (**Figure 3.25A**) and ¹³C-glutamine (**Figure 3.25B**).

In the ¹³C 1D spectra of the ¹³C-glucose labeling studies, we detected ¹³C-alanine, ¹³C-lactate, ¹³C-glutamate, ¹³C-adenosine, and ¹³C-phosphoenolpyruvate (**Figure 3.25A**), while in the ¹³C 1D spectra of cells incubated with ¹³C-glutamine we detected ¹³C-glutamine, ¹³C-glutamate, ¹³C-phosphocholine and ¹³C-GPC (**Figure 3.25B**).

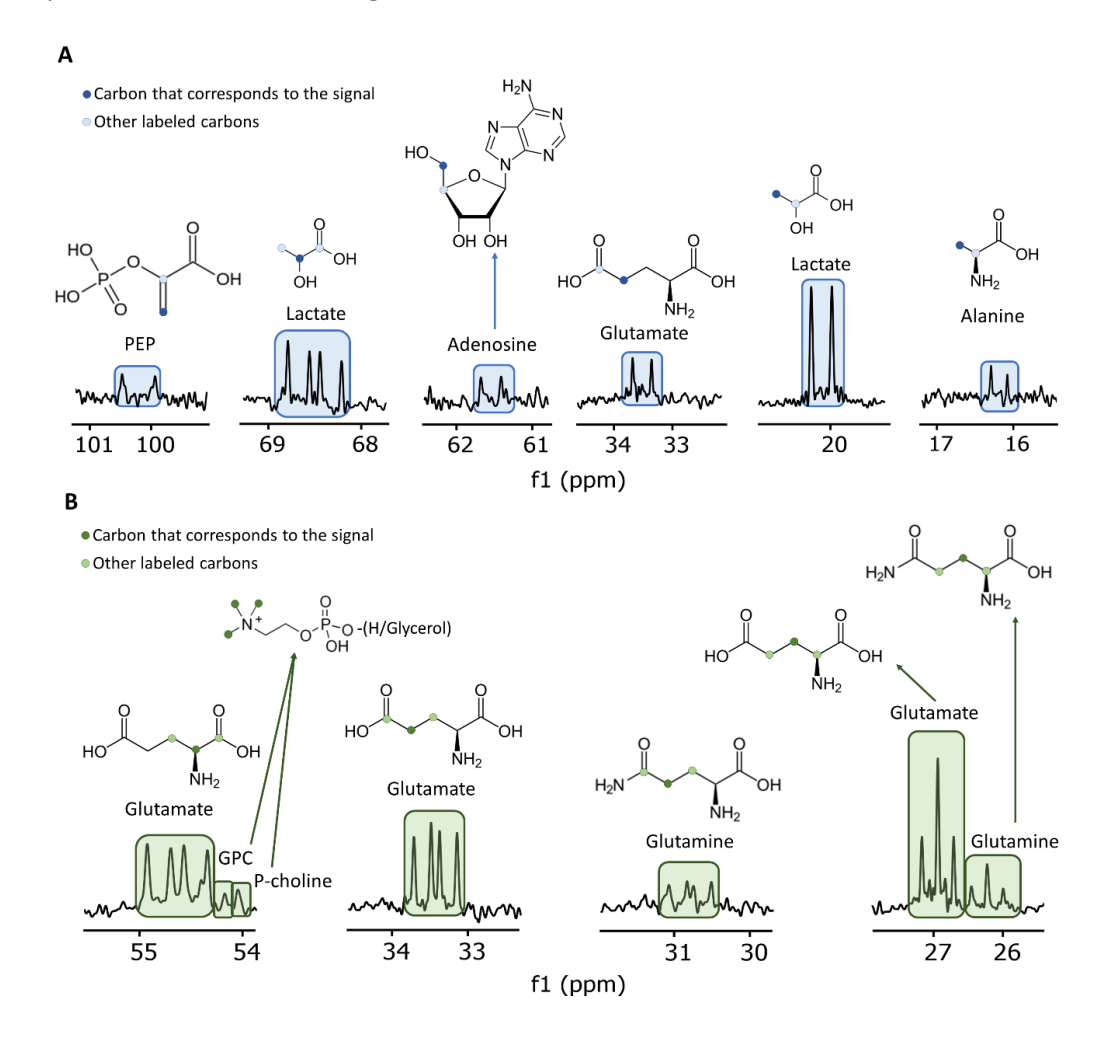


Figure 3.25. 13 C 1D spectra assignments. **A)** 13 C-labeled metabolites in TNBC cells incubated with 13 C-glucose for 120 min. PEP = phosphoenolpyruvate. **B)** 13 C-labeled metabolites in TNBC cells incubated with 13 C-glutamine for 180 min. Structure of the assigned metabolites are shown with the 13 C indicated by small circles (dark color for the carbon corresponding to the signal and light color for other labeled carbons that appear in the signal). GPC = glycerophosphocholine; P-choline = phosphocholine.

We next performed the relative quantification of ¹³C-labeled metabolites from the ¹H-¹³C 2D HSQC spectra of untreated TNBC cells (control) and cells treated with free palbociclib and StPGA-SS-palbociclib.

¹³C-Glucose NMR Fluxomics Analysis

By labeling metabolites with ¹³C-glucose, we detected a significant decrease of ¹³C-lactate synthesis following free palbociclib and StPGA-SS-palbociclib treatment compared to control (Figure 2.26A and Supporting Information 3.15), which demonstrated the downregulation of the glycolytic pathway (as previously indicated by the NMR and MS metabolomic analysis; Sections 3.2.2.3.1 and 3.2.2.3.2). Moreover, we also confirmed this finding by the detection of significantly decreased ¹³C-alanine synthesis in cells treated with free palbociclib compared to control (Figure 3.26A and Supporting Information 3.15). An overlapping signal of ¹³C-glutamine and ¹³C-glutamate indicated a significantly increased synthesis of some or both metabolites after StPGA-SS-palbociclib treatment compared to control (Figure 3.26A and Supporting Information 3.15). We already detected increased glutamine after StPGA-SS-palbociclib treatment by NMR metabolomics (Section 3.2.2.3.1), reduced glutamate-containing peptides by MS metabolomics (Section 3.2.2.3.2), and reduced glutaminolysis by MS labeling studies (Section 3.2.2.5.2). Therefore, we believe that the increase of the overlapping signal derived from increased glutamine levels, which balances the excess of glutamate from StPGA that cannot enter the TCA cycle (downregulated as confirmed by the MS labeling studies) and accumulates due to reduced glutaminolysis.

¹³C-Glutamine NMR Fluxomics Analysis

¹³C-glutamine labeling studies allowed the detection of alterations in the synthesis of GPC and glutamate. We detected significantly reduced glutamate formation in cells treated with free palbociclib and StPGA-SS-palbociclib compared to control, with a more significant effect for StPGA-SS-palbociclib (**Figure 3.26B** and **Supporting Information 3.16**). This finding confirmed the downregulation of glutaminolysis (as already described by MS fluxomics; **Section 3.2.2.5.2**). Furthermore, we found a significant increase in GPC synthesis in cells treated with free palbociclib and StPGA-SS-palbociclib treatment compared to control (**Figure 3.26B** and

Supporting Information 3.16). Of note, we already observed an increment of GPC levels in whole-cells treated with StPGA-SS-palbociclib compared to control in cell media by NMR metabolomics (Section 3.2.2.3.1) and in whole-cells treated with free palbociclib and StPGA-SSpalbociclib compared to control by MS metabolomics (Section 3.2.2.3.2). Furthermore, we observed decreased phosphocholine in mitochondria of cells treated with StPGA-SS-palbociclib compared to mitochondria of control cells, and in whole-cell samples treated with StPGA-SSpalbociclib compared to free palbociclib treatment by NMR metabolomics (Section 3.2.2.3.1). Therefore, the choline-related outcomes indicated an alteration in the CDP-choline pathway after treatment with StPGA-SS-palbociclib, while free palbociclib caused a milder effect on this pathway, which may reflect the different internalization mechanisms of each treatment. Choline metabolism becomes altered in cancer cells, and studies focusing on the impact of cancer cell treatments on cell metabolism have revealed a link between decreased phosphocholine and increased GPC²⁹³. Phosphocholine is a substrate for PC synthesis, and glycerophosphocholine is the product of PC degradation; decreased phosphocholine and increased GPC suggest a decrease in PC levels due to decreased synthesis and increased degradation. We detected a general decrease in PCs after free palbociclib and StPGA-SS-palbociclib treatment (Section 3.2.2.4), confirming this assumption. As phosphocholine levels associate with cell proliferation³⁵⁵, a decrease in phosphocholine and PCs may reflect the decreased cell growth caused by the cell cycle arrest induced by palbociclib.

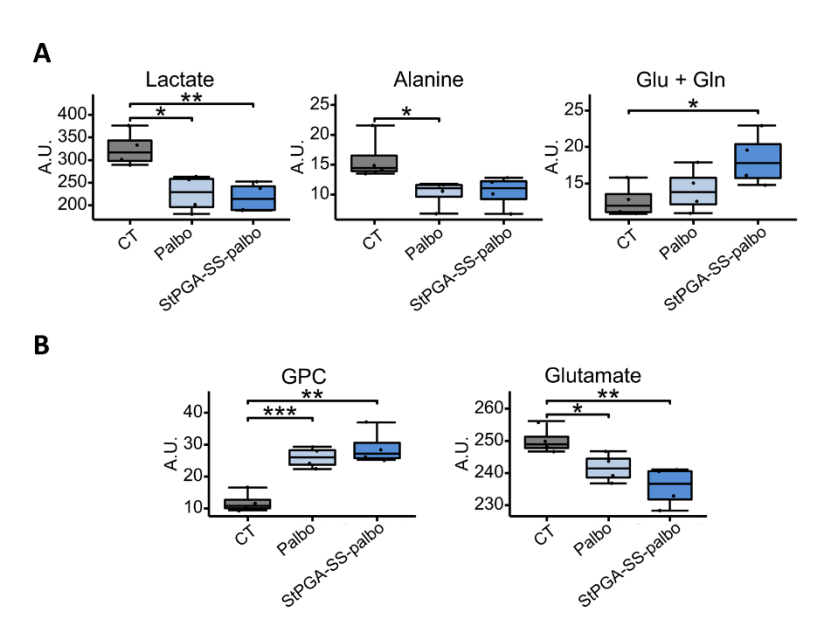


Figure 3.26. NMR fluxomics analysis. **A)** Boxplots of ¹³C-labeled metabolites in untreated cells (CT) and in cells treated with free palbociclib (palbo) and StPGA-SS-palbociclib (StPGA-SS-palbo) after incubation with ¹³C-glucose for 120 min. Gln = glutamine; Glu = glutamate. **B)** Boxplots of ¹³C-labeled metabolites in untreated cells (CT) and in cells treated with free palbociclib (palbo) and StPGA-SS-palbociclib (StPGA-SS-

palbo) after incubation with 13 C-glutamine for 180 min. Data analysis used a T-test, with data presented as average \pm SEM (n = 4); * p < 0.05, ** p < 0.01, *** p < 0.001. GPC = glycerophosphocholine.

In summary, the NMR fluxomics analysis of TNBC cells treated with free palbociclib and StPGA-SS-palbociclib confirmed certain previously described effects detected by MS in cell and mitochondrial metabolism, such as the downregulation of the glycolytic pathway and glutaminolysis. Moreover, NMR fluxomics has helped to understand how treatments affect lipid metabolism and revealed a slightly higher impact of StPGA-SS-palbociclib over free palbociclib on the CDP-choline pathway. Finally, the NMR fluxomics analysis complemented the MS fluxomics study by detecting additional labeled metabolites, such as lactate and alanine, through 13 C-glucose labeling and GPC through 13 C-glutamine labeling.

3.3. CONCLUSIONS

In this chapter, we analyzed the impact of free palbociclib and StPGA-SS-palbociclib on mitochondrial and whole-cell metabolism in a TNBC cell line by two analytical techniques (NMR and MS) and three different omic techniques (metabolomics, lipidomics, and fluxomics).

We first synthesized and characterized StPGA-SS-palbociclib by linking the StPGA polymer to palbociclib using a redox-responsive disulfide linker. Characterization of the StPGA-SS-palbociclib by NMR spectroscopy, UV-Vis spectroscopy, CD, and LC-MS confirmed the correct conjugation of the drug to the polypeptidic carrier and, in agreement with previously reported examples¹⁵³, revealed main characteristics: 1.5 wt% total drug loading with adequate free drug content, average size around 10 nm, negative net charge surface, a random coil conformation, and 33% drug release after 72 h incubation in the reductive intracellular conditions as determined by LC-MS/MS.

Then, we evaluated the impact of free palbociclib and StPGA-SS-palbociclib on TNBC cells. After cell viability studies, we identified the adequate concentration for mitochondrial metabolomic studies. We chose the IC_{30} values of free palbociclib (IC_{30} = 0.77 μ M) and StPGA-SS-palbociclib (IC_{30} = 3.64 μ M palbociclib-equiv.) for the evaluation of their impact on mitochondrial metabolism to avoid working with toxic conditions that could abolish metabolism.

We first employed the Seahorse Analytical platform to assess whether the free palbociclib and StPGA-SS-palbociclib impacted mitochondrial status. Free palbociclib and StPGA-SS-palbociclib disrupted ATP-production coupled respiration linked to the downregulation of the glycolytic pathway.

Figure 3.27 includes a summary of the metabolic alterations observed by all the techniques (NMR and MS metabolomics, MS lipidomics, and NMR and MS fluxomics) caused by free palbociclib and StPGA-SS-palbociclib exposure in TNBC cells. Colored metabolites indicate alterations in the metabolite levels, while colored arrows indicate alterations in the pathway flow observed by fluxomics studies (red = decreased in the free palbociclib and StPGA-SS-palbociclib groups; brown = decreased in the StPGA-SS-palbociclib group; orange = decreased in the free palbociclib group; dark green = increased in the free palbociclib and StPGA-SS-palbociclib groups; light green = increased in the StPGA-SS-palbociclib group; cyan = increased in the free palbociclib group).

We confirmed the downregulated **glycolysis** observed by the Seahorse XF Analyzer after both treatments (with a significantly higher effect of StPGA-SS-palbociclib) by i) the reduced levels of lactate in the whole-cell NMR metabolomic analysis and lactate-derivatives in the whole-cell MS metabolomic analysis, ii) the reduced pyruvate and PEP levels in cell media by NMR metabolomics, and iii) the ¹³C-glucose NMR (reduced lactate and alanine synthesis) and MS fluxomics analysis (reduced synthesis of glycolytic intermediates). Moreover, we discovered an alternative use of glucose (synthesis of N-acetyl-D-lactosamine) that increased in whole-cells treated with free palbociclib compared to control (observed by MS metabolomics). Similarly, MS fluxomics analysis revealed alternative use for glucose, such as forming UDP-GlcA.

We observed a reduction in **glutaminolysis** by NMR and MS metabolomics, as indicated by increased glutamine levels in whole-cell samples and cell media (NMR) and decreased glutamate derivatives (MS) in whole-cell samples. We confirmed these findings through the ¹³C-glutamine MS fluxomics study by the observation of reduced glutamate synthesis, with a more significant effect caused by free palbociclib, probably due to the slower internalization mechanism of the StPGA-SS-palbociclib added to slower glutamine metabolism compared to glucose.

In **mitochondria**, we observed a decreased **amino acid** pool by NMR and MS metabolomics after both treatments, which indicated the reduction of the TCA cycle activity. Reduced levels of PEP inside mitochondria detected by NMR metabolomics, which forms from oxaloacetate, also indicated the downregulation of this pathway. Through the ¹³C-glutamine MS fluxomics analysis, we demonstrated this finding by detecting decreased **TCA cycle** intermediates synthesis after both treatments, again with a more significant effect caused by free palbociclib, as observed for glutaminolysis.

The NMR metabolomic analysis of **whole-cells** revealed decreased ATP levels after treatment with StPGA-SS-palbociclib compared to control, which confirmed the disruption of

mitochondrial respiration observed by the Seahorse XF analyzer. Moreover, we observed reduced ATP in the cytosol thanks to the downregulation of the **purine** *de novo* **synthesis** pathway through the ¹³C-glucose MS fluxomics analysis. The ¹³C-glucose MS fluxomics analysis also revealed differential impacts of treatments on the **pyrimidine** *de novo* **synthesis** pathway (downregulated by free palbociclib and upregulated by StPGA-SS-palbociclib), which could indicate the greater need to generate CTP as an alternative energy source in cells treated with StPGA-SS-palbociclib.

Regarding lipid metabolism, we observed i) decreased phosphocholine, in isolated mitochondria and whole-cell samples from cells treated with StPGA-SS-palbociclib compared to control and to free palbociclib treatment, respectively, though the NMR metabolomic study, and ii) increased GPC synthesis in isolated mitochondria and whole-cell samples by MS metabolomics and ¹³C-glutamine NMR fluxomics analysis (also to a greater extent after StPGA-SS-palbociclib treatment as observed by increased GPC levels in cell media by NMR). These findings provided evidence for the alteration in lipid metabolism, confirmed by the MS lipidomic analysis. The lipidomic profiles for treated and untreated mitochondrial and whole-cell samples possessed significantly greater definitions compared to the metabolic profile, as observed by enhanced group discrimination in the PCA plot. This improvement indicated a significant and differential impact of palbociclib and StPGA-SS-palbociclib treatment on the lipidome than the metabolome. We observed a higher number of altered lipids following StPGA-SS-palbociclib than with free palbociclib, mainly in the whole-cell samples, and we observed significantly different levels of several lipids when comparing free palbociclib and StPGA-SS-palbociclib treatment (for both isolated mitochondria and whole-cell samples). Therefore, StPGA-SS-palbociclib caused a significant higher impact on the lipidome of TNBC cells. We also discovered a trend of decreasing PCs after treatment with free palbociclib and StPGA-SS-palbociclib compared to control in isolated mitochondria and whole-cell samples, which confirmed the alteration of the CDPcholine pathway (crucial for the mitochondrial and cell membrane maintenance).

In addition to the above-described pathway alterations, we detected specific metabolite alterations associated with additional pathways. For example, NMR metabolomics revealed decreased GSH levels following StPGA-SS-palbociclib treatment, which reflected the GSH use as a reductor of the disulfide linker for the drug release from the polymer. MS metabolomics of whole-cells revealed an impaired creatine phosphate shuttle after StPGA-SS-palbociclib, which could relate to decreased ATP synthesis in mitochondria.

In summary, the conjugation of palbociclib to a StPGA carrier provides differential mechanism of action that become reflected in whole-cell and mitochondrial metabolism. The different internalization and pharmacokinetic profile of StPGA-SS-palbociclib compared to free palbociclib induce higher mitochondrial impairment as observed by i) mitochondrial respiration, which reflected higher mitochondrial disruption, ii) metabolomics and fluxomics, which revealed decreased TCA cycle intermediates and ATP and, iii) lipidomics, which demonstrated alterations in mitochondria-specific lipids (CL and PG/LPG). Moreover, metabolomics, fluxomics, and lipidomics revealed the more significant impact of StPGA-SS-palbociclib on the CDP-choline pathway compared to free palbociclib, which may reflect the involvement of membranes (e.g., membrane invagination and fusion) in the endocytic internalization mechanism. Conjugation of palbociclib to StPGA also prompted the stimulation of pyrimidine nucleotide synthesis to a more significant degree than free palbociclib. Endocytosis is an energy-dependent process (while diffusion of small drugs is not); therefore, decreased levels of ATP due to mitochondrial impairment become compensated by the production of other energetic molecules, such as pyrimidine nucleotides.

We believe that NMR and MS represent complementary techniques for the study of isolated mitochondria or whole-cell samples. Each technique can detect alterations not observed by the other technique, while detection by both techniques acts to confirm findings. Moreover, MS provided considerably more information about lipidomic alterations occurring after treatment, which we could not detect by NMR lipidomics where wide lipid signals tended to overlap. Finally, both NMR and MS fluxomics provided valuable information about pathway dynamics to fully understand alterations in cell metabolism, specifically in the mitochondrial metabolome in cells treated with palbociclib and StPGA-SS-palbociclib.

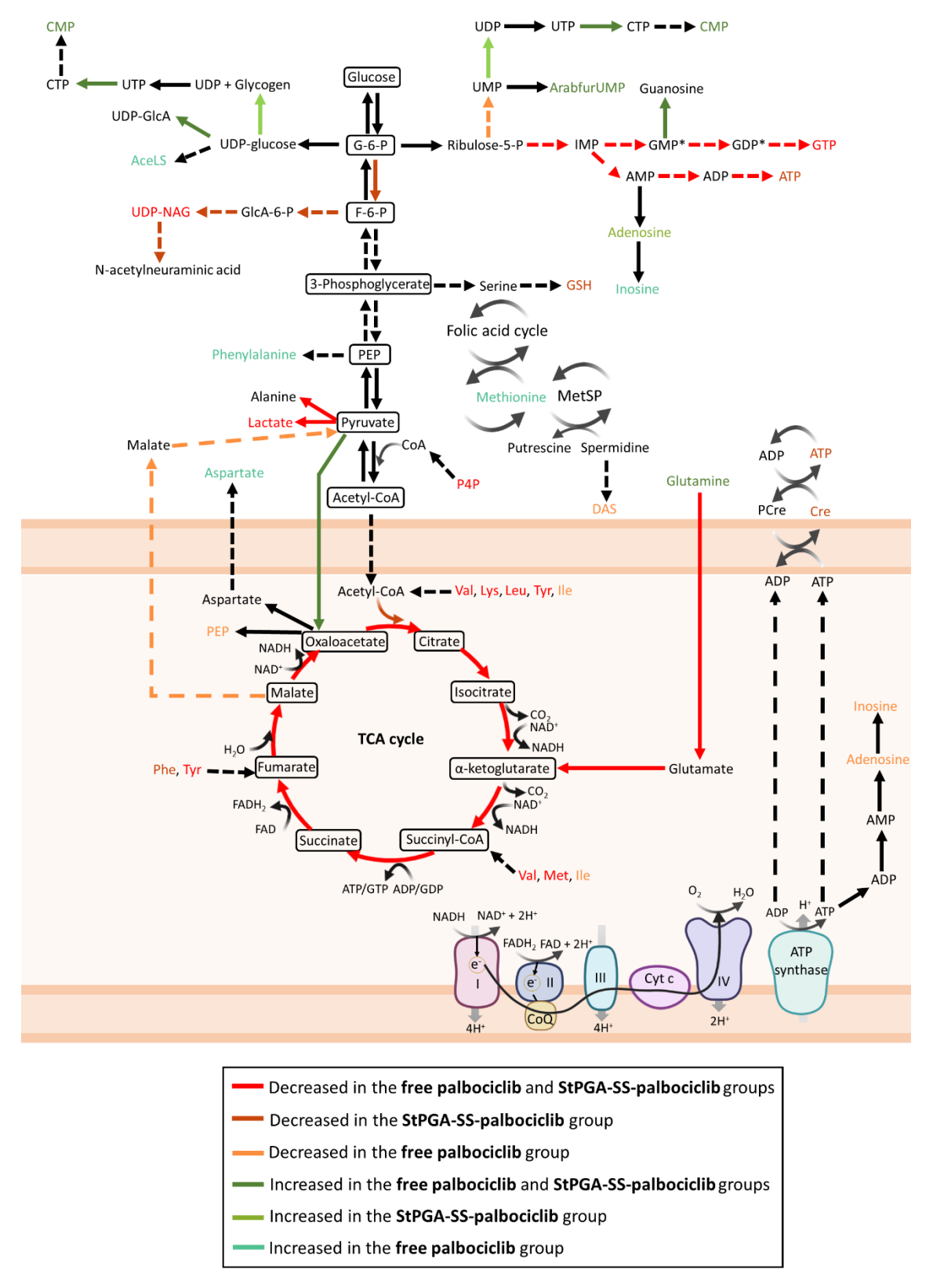


Figure 3.27. Summary of mitochondria and whole-cell alterations. Significant alterations in the pathway flow and in the metabolite levels in cells treated with free palbociclib and StPGA-SS-palbociclib are indicated by colored arrows and colored metabolites, respectively (red = decreased in the free palbociclib and StPGA-SS-palbociclib groups; brown = decreased in the StPGA-SS-palbociclib group; orange = decreased in the free palbociclib group; dark green = increased in the free palbociclib and StPGA-SS-palbociclib and StPGA-SS-palbociclib group; dark green = increased in the free palbociclib and StPGA-SS-palbociclib and StPGA-SS-palbociclib group; dark green = increased in the free palbociclib and StPGA-SS-palbociclib and StPGA-SS-palbociclib group; dark green = increased in the free palbociclib and StPGA-SS-palbociclib group; dark green = increased in the free palbociclib group; dark green = inc

palbociclib groups; light green = increased in the StPGA-SS-palbociclib group; cyan = increased in the free palbociclib group). *GDP and GMP showed increased levels after treatment with free palbociclib by MS metabolomics, while the MS fluxomics analysis showed the opposite trend. CoA = coenzyme A; AceLS = N-Acetyl-D-lactosamine; ADP = adenosine diphosphate; AMP = adenosine monophosphate; ArabfurUMP = 1-β-D-Arabinofuranosyluracil 5-monophosphate; ATP = Adenosine triphosphate; cAMP =cyclic adenosine monophosphate; CoQ = coenzyme Q₁₀; Cre = creatine; CTP = cytidine triphosphate; Cyt c = cytochrome c; DAS = N1,N8-Diacetylspermidine; FAD = flavin adenine dinucleotide; F-1,6-BP = fructose-1,6-biphosphate; GDP = guanosine diphosphate; GIcA-6-P = glucosamine-6-phosphate; G-6-P = glucose-6-phosphate; GMP = guanosine monophosphate; GSH = glutathione; GTP = guanosine triphosphate; Ile = Isoleucine; IMP = inosine monophosphate; Leu = Leucine; Lys = Iysine; NAD+ = nicotinamide adenine dinucleotide; MetSP = methionine salvage pathway; P4P = Pantetheine 4'-phosphate; PCre = phosphocreatine; Phe = phenylalanine; Ribusolose-5-P = ribulose-5-phopshate; Tyr = tyrosine; UDP = uridine diphosphate; UDP-GlcA = UDP-glucuronate; UDP-NAG = uridine diphosphate N-acetylglucosamine; UMP = uridine monophosphate; UTP = uridine triphosphate; Val = Valine.

3.4. MATERIALS AND METHODS

3.4.1. Materials

All solvents were of analytical grade and obtained from Scharlab (Barcelona, Spain), except chloroform and methanol, which were purchased from Sigma-Aldrich (St. Louis, Missouri, United States), and formic acid that was provided by ThermoFisher Scientific (Waltham, Massachusetts, United States). Deuterated solvents (d-DMSO, CDCl₃, and D₂O), 3-(trimethylsilyl) propionic acid d4 sodium salt (TSP), and 5 mm NMR tubes and caps were purchased from Deutero GmbH (Kastellaun, Germany). StPGA150 was provided by FluoroChem (Cork, Ireland). 4-nitrophenyl(2-(pyridin-2-yldisulfanyl)ethyl) carbonate was purchased from ChemoSapiens (Santiago de Compostela, Spain). Palbociclib was provided by LC Laboratories (Woburn, Massachusetts, United States). Palbociclib hydrochloride was purchased from MedChemExpress (South Brunswick Township, New Jersey, United States). Niraparib free base was provided by Medkoo Biosciences (Morrisville, United States). HyClone Dulbecco's phosphate-buffered saline (DPBS) was obtained from Cytiva UK Ltd. (Buckinghamshire, United Kingdom). GIBCO™ Dulbecco's modified Eagle Media (DMEM) and GIBCO[™] penicillin/streptomycin (P/S) were provided by ThermoFisher Scientific (Waltham, Massachusetts, United States). Ammonium acetate, ammonium formate, Hoechst 3342, sucrose, tris(hydroxymethyl)aminomethane hydrochloride (Tris-HCI), bovine serum albumin (BSA), cysteamine hydrochloride, potassium chloride and dithiothreitol (DTT), MTS and PMS were provided by Sigma-Aldrich (St. Louis, Missouri, United States). Mannitol, disodium hydrogen phosphate (Na₂HPO₄), and Amicon Ultra-0.5 mL 3 KDa centrifugal filters were obtained from Merck Millipore (Burlington, Massachusetts, United States). The plates, cartridges, and reagents used for the mitochondrial respiration analysis were provided by Agilent Technologies (Santa Clara, California, United States). Uniformly labeled ¹³C-glucose (U-¹³C-glucose) and U-¹³C-glutamine were purchased from Cambridge Isotope Laboratories (Tewksbury, Massachusetts, United States). Lipidomics Splashmix Mass Spec Standard was obtained from Avanti Polar Lipids (Snaith, United Kingdom).

3.4.2. Synthesis of StPGA-SS-palbociclib

The synthesis of StPGA-SS-palbociclib was performed following the procedure previously described by our group¹⁵³.

In a round bottom flask with a stirrer, 4-nitrophenyl (2-(pyridin-2-yldisulfanyl)ethyl) carbonate (229 mg, 0.65 mmol, Mw = 352.4 g/mol, 1.2 eq), palbociclib (247 mg, 0.54 mmol, Mw = 447.53 g/mol, 1 eq.) and TEA (56 μ L, 0.65 mmol, Mw = 101.1 g/mol, ρ = 0.726 g/mL, 1.4 eq) were placed in 60 mL of anhydrous CH₂Cl₂ (**Figure 3.28**). The reaction was left under agitation for 24 h at room temperature. Thin-layer chromatography (TLC) monitored the reaction with CH₂Cl₂:MeOH (9:1) as the mobile phase. The product (Palbociclib-SS-Pyr) was concentrated in the rotary evaporator and purified by column chromatography on silica gel using CH₂Cl₂:MeOH (9:1) as eluent. Fractions containing the Palbociclib-SS-Pyr were merged, and the product was concentrated in a rotary evaporator, followed by solvent evaporation in a freeze dryer to obtain a yellow oil. Product identity was evaluated by ¹H-NMR (Palbociclib-SS-Pyr in CDCl₃).

Figure 3.28. Synthesis of palbociclib-SS-Pyr. Coupling reaction of palbociclib to 4-nitrophenyl (2-(pyridine-2-yldisulfaneyl)ethyl) carbonate in CH₂Cl_{2anh} and TEA for 48h.

In a round bottom flask, palbociclib-SS-Pyr (319 mg, 0.48 mmol, Mw = 660.81 g/mol, 1 eq) and cysteamine hydrochloride (82 mg, 0.72 mmol, Mw = 113.61 g/mol, 1.5 eq) were added in 20 mL of CH_2Cl_2 :MeOH (1:1) (**Figure 3.29**). The mixture was stirred for 2 h at room temperature, and the reaction was monitored by TLC using CH_2Cl_2 :MeOH (9:1) as the mobile phase. The solvent was evaporated under vacuum, and the product was precipitated in cold diethyl ether four times

from methanol. The product (palbociclib-SS-NH₂) was dried under vacuum, giving rise to a yellow powder. Palbociclib-SS-NH₂ identity was confirmed by ¹H-NMR (Palbociclib-SS-NH₂ in d-DMSO).

Figure 3.29. Synthesis of palbociclib-SS-NH₂. Thiol exchange with cysteamine hydrochloride in CH₂Cl₂:MeOH (1:1) for 2 h.

In a round bottom flask, StPGA150 (720.2 mg, 5.57 mmol, Mw = 129.1 g/mol, 23 eq) and $DMTMM \cdot BF_4$ (158.4 mg, 0.48 mmol, Mw = 328.10 g/mol, 2 eq.) were placed in 24 mL of DMSO and the mixture was allowed to stir for 30 min to activate the carboxylic groups. Palbocilcib-SS- NH_2 (160.8 mg, 0.24 mmol, Mw = 663.25 g/mol, 1 eq.) was added to the flask, and the pH of the solution was adjusted to 8 with N, N-Diisopropylethylamine (DIEA). The reaction was stirred for 48 h at room temperature (Figure 3.30). To eliminate DMSO, 4 mL aliquots of the mixture were mixed with 40 mL of cold diethyl ether and centrifuged at high speed for 3 min. Diethyl ether was removed (above phase), while the bottom phase (DMSO and reaction mixture) was dissolved in 500 µL of MeOH. The mixture was again precipitated in cold diethyl ether and centrifugated for 3 to further eliminate DMSO. Then, three precipitation cycles were performed with cold diethyl ether and centrifuging for 10 min. The product (StPGA-SS-palbociclib) was dried under vacuum and, finally, with the freeze-drier. StPGA-SS-palbociclib was converted to its water-soluble sodium salt form, dissolving the product in NaHCO3 until pH 8. Once the product was dissolved, it was dialyzed against water (Cellulose ester membrane, cut off 500-1000Da) for 48 h, and the solution was freeze-dried. The ¹H-NMR spectrum of StPGA-SS-palbociclib in D₂O was obtained to evaluate the identity of the final product. The polymer-drug conjugate was dissolved in 300 μL of Milli-Q H₂O and purified in a PD-10 column with Sephadex G-25 as the stationary phase and Milli-Q H₂O as the mobile phase. Fractions containing the product were combined and lyophilized to obtain a yellow powder.

Figure 3.30. Synthesis of StPGA-SS-palbociclib. Conjugation of the drug-linker to StPGA via amide coupling with the DMTMM·BF₄ activator, DIEA, to remove HCl to allow the amide formation. The reaction took place in DMSO for 48 h and pH 8.

3.4.3. Physico-chemical Characterization of StPGA-SS-Palbociclib

3.4.3.1. NMR Spectra Acquisition

¹H-NMR spectra were obtained in an Avance III 500 MHz Bruker spectrometer (Billerica, Massachusetts, United States) at 25 °C and using a zg30 sequence with 128 scans. StPGA and palbociclib-SS-NH₂ were dissolved in d-DMSO, the linker (4-nitrophenyl (2-(pyridine-2-yldisulfaneyl)ethyl) carbonate), free palbociclib and palbociclib-SS-Pyr were measured in CDCl₃ and StPGA-SS-palbociclib was dissolved in D₂O. NMR spectra were processed and analyzed in MestreNova (MestreLab Research, Santiago de Compostela, Spain).

3.4.3.2. Drug Loading Determination by UV-Vis Spectroscopy

Drug loading of StPGA-SS-Palbociclib was determined by UV-Vis spectroscopy. A calibration curve was prepared by dissolving free palbociclib in water and measuring absorbance at 309 nm. The sample was prepared by dissolving StPGA-SS-Palbociclib in Milli-Q H_2O (2.23 mg/mL). StPGA was also dissolved in Milli-Q H_2O (2.23 mg/mL) to be used as the blank of the quantification. Six dilutions (1.12-0.62 mg/mL) of the StPGA-SS-palbociclib and the blank solutions were prepared, and absorbance was measured at 309 nm. UV-VIS absorbance spectra were obtained using the JASCO V-630 spectrophotometer (Jasco International Co., Ltd, Hachioji, Tokyo, Japan) at 25 $^{\circ}$ C with a 1.0 cm matched quartz cuvette recording three accumulations. Drug loading (wt %) of

StPGA-SS-palbociclib was determined by interpolating the absorbance value of three of the dilutions to the calibration curve of the free palbociclib.

Drug loading in mol % was obtained from the NMR spectra of StPGA-SS-palbociclib. The peak at 4.10 ppm corresponding to one hydrogen of StPGA and the peak at 8.13 ppm corresponding to four hydrogens of palbociclib were integrated. The intensity of the palbociclib signal was divided by the four hydrogens, obtaining the drug loading in mol %. The obtained value was confirmed by calculating the drug loading in wt% from the drug loading in mol %.

3.4.3.3. Size Determination by Bayesian DOSY Transform

StPGA-SS-palbociclib was dissolved in D_2O , and a 2D DOSY experiment was run in an Avance III 500 MHz Bruker spectrometer (Billerica, Massachusetts, United States) at 25 $^{\circ}$ C with 28 scans, p30 = 3000 μ s and D20 = 0.2 s. The 2D DOSY spectra were processed using the Bayesian Transformation in MestreNova (MestreLab Research, Santiago de Compostela, Spain), and the diffusion coefficient was obtained. Determining the size of StPGA-SS-Palbociclib used the Einstein-Strokes equation:

$$D = \frac{k_B T}{6 \pi \eta r}$$

D is the diffusion coefficient, k_B is the Boltzmann constant (1.38x10⁻²³ J/K), T is the temperature, η is the solvent's viscosity (1.25 mPa·s), and r is the hydrodynamic radius.

3.4.3.4. Zeta Potential Measurement by Dynamic Light Scattering

1 mg/mL StPGA-SS-palbociclib solution was prepared in filtered 1mM KCl, and zeta potential was measured in a Malvern Zetasizer nanoseries, nano ZS, ZEN3500 (Malvern Instruments, Malvern, UK) equipped with a 532 nm laser.

3.4.3.5. Secondary Structure Determination by Circular Dichroism

0.25 mg/mL StPGA-SS-palbociclib was prepared in DPBS, introduced in a quartz cuvette with 1 cm light path length, and measured in a J-1500 Circular Dichroism Spectropolarimeter (JASCO corporation, Easton, United States) under a nitrogen flow. The measured absorption of polarized light was an average of three cycles.

3.4.3.6. Release kinetics

The release kinetic studies of StPGA-SS-Palbociclib were performed in 5 mM DTT (intracellular reductive condition) and 10 μ M DTT as a control (extracellular reductive condition). For the study under intracellular reductive conditions, 3 mg of StPGA-SS-Palbociclib was dissolved in 733

 μ L of DPBS pH 5 followed by 267 μ L of 19.45 mM DTT, while, for the study under extracellular reductive conditions, 3 mg of StPGA-SS-Palbociclib were dissolved in 980 μ L of DPBS pH 5 followed by 20 μ L of 1 mM DTT. After vortexing, 100 μ L aliquots were collected from both solutions at different time points: 0, 1, 2, 4, 7, 24, 72, and 168 h. Immediately after the collection, 20 μ L or 40 μ L of 6 mg/mL niraparib was added to the 10 μ M DTT aliquots and 5 mM DTT aliquots, respectively, as internal standard. Then, the aliquots were immediately frozen and lyophilized. For the extraction of palbociclib and niraparib, 500 μ L of CH₂Cl₂ were added to the lyophilized aliquots, and samples were sonicated for 5 min and centrifuged at 11,000 g at room temperature for 5 min. The supernatants were transferred to new tubes, evaporating the solvent in a Speed Vacuum Concentrator.

For the HPLC analysis, 10 mM DTT samples were resuspended in 100 μ L of acidic water (1 mM ammonium formate and 0.2 % formic acid), while 5 mM DTT samples were resuspended in 200 μ L of acidic water. Then, samples were sonicated for 5 min and centrifuged at 11,000 g at room temperature for 5 min. Finally, 100 μ L of supernatants were transferred to 300 μ L vials and analyzed by HPLC/PAD. The HPLC system developed by Jasco (Madrid, Spain) was equipped with a Kinetex® 2.6 μ m Biphenyl 100 Å LC Column 100 x 3.0 mm operated at 25°C and coupled to a Photo Diode Array Detector (MD-4010). 50 μ L of sample were injected into the HPLC system, and analytes were eluted using a 0.5 mL/min flow rate. The mobile phase consisted of 0.2% formic acid in acetonitrile (A) and 1 mM ammonium formate, 0.2% formic acid in water (B). From 0 to 2 min, a gradient mode was used (20% A and 80% B to 30% A and 70% B). For the detection of palbociclib and the internal standard niraparib, the detector wavelength was set at 360 nm.

For LC-MS/MS analysis, the samples were diluted to detect first palbociclib (different dilution factors were applied depending on the drug concentration of the sample), and they were further diluted to detect niraparib. The LC-MS/MS analysis was performed using an ExionLC system comprising a pump, AC autosampler, AC Column oven, and AB Sciex QTRAP 4500 (all Sciex, Singapore). Eluent A was H_2O with 0.1 % FA, and eluent B was ACN. All runs were performed using a Kinetex Byphenyl column (100 mm × 3.0 mm, 2.6 μ m, 100 Å) (Phenomenex, USA) with a 20 μ L injection volume. The drugs were detected in positive electrospray mode with multiple reaction monitoring scans (448.3 m/z \rightarrow 380.1 m/z with collision energy 35 V for palbociclib; 321.1 m /z \rightarrow 304.1 m/z with collision energy 20 V for niraparib). The optimal starting LC conditions were eluent A 95 %, eluent B 5 %, flow rate 0.5 ml/min, and column temperature 40°C. The LC method was performed with a gradient from 5 % B to 100 % B during 4 min and kept constant for 2 min. Methanol with 0.1% FA was used as a blank control sample.

A calibration curve for palbociclib (0.1-1 μ g/mL) containing 0.6 μ g/mL niraparib was used to quantify the total palbociclib release from the StPGA-SS-Palbociclib.

3.4.4. Biological evaluation

3.4.4.1. Cell Culture

The cell line selected for this work was MDA-MB-231-Luc, which was obtained and characterized at the Functional Validation & Preclinical Research (FVPR) of CIBBIM-Nanomedicine working at Unit 20 of the ICTS "NANBIOSIS" (http://www.nanbiosis.es/portfolio/u20-in-vivo-experimental-platform/) (Barcelona, Spain). The MDA-MB-231-Luc cell line is a bioluminescence breast adenocarcinoma cell line and one of the most used for TNBC research.

Cells were maintained at 37°C and 5% CO₂ in DMEM with 4500 mg glucose/L and 580 mg L-glutamine/L supplemented with 10% inactivated FBS and 1% P/S. The growth medium was replaced every 3-4 days, and cell passages were performed at 80% cell confluence.

3.4.4.2. Cell Viability Studies

MDA-MB-231-Luc cells were seeded in sterile 96-well plates at a concentration of 5,000 cells/well in 50 μL. Moreover, they were maintained for 24 h at 37 C and 5% CO₂. For cell treatment, palbociclib hydrochloride was dissolved in MilliQ water, while StPGA-SS-palbociclib was dissolved directly in the cell media. Both treatments were filtered through a 0.22 μm Polyethersulfone filter, and serial dilutions of the treatment (50 μL) were added to the cells (three replicates for each treatment concentration). After incubation for 72 h, 10 μL of MTS/PMS (20:1) were added to each well and incubated for 3 h. The optical density of each well was measured at 490 nm on the CLARIOstar Plus plate reader (BMG Labtech, Ortenberg, Germany). The absorbance values obtained were represented as cell viability, where 100% corresponded to untreated cells. Data was log-transformed and fitted to a log (inhibitor) vs. normalized response-variable slope (four parameters) in GraphPad Prism (version 9.5.0, GraphPad Software Inc., USA); data was represented as average \pm SEM (n = 3). The IC₅₀ values were obtained from the GraphPad Prism report, which takes into consideration several aspects (e.g., fitting of data to the curve, top and bottom cell viability values), while IC₃₀ values were obtained in the GraphPad calculator (https://www.graphpad.com/quickcalcs/Ecanything1.cfm) from the IC50 value and the slope factor.

3.4.4.3. Evaluation of Mitochondrial Respiration of Treated Triple Negative Breast Cancer Cells

Mitochondrial respiration was assessed in the Agilent Seahorse XFe96 Analyzer using the Agilent Seahorse Cell Mito Stress Test kit (Santa Clara, California, United States).

5,000 MDA-MB-231-Luc cells were seeded in 80 μL of DMEM media in the Seahorse XF96 Cell Culture Microplates, and the plate was left 20 min in the biological safety cabinet to allow cells to settle in the well; five wells were seeded per condition. The plate was incubated for 24 h at 37ºC and 5% CO₂ before treatment. For cell treatment, palbociclib hydrochloride and StPGA-SSpalbociclib were prepared as explained in Section 3.4.4.2, and 80 µL was added to the cells to reach a final concentration corresponding to the IC30 values. Control cells (untreated) were maintained in the cell media. After incubation for 72h, cells were washed with Agilent Seahorse DMEM XF medium, first with 100 µL and the second time with 180 µL. With the last volume of media added, the plate was incubated at 37°C without CO₂ for 1 h. During this time, the Agilent Seahorse XF96 Sensor Cartridge, previously hydrated with 200 µL of the Agilent Seahorse XF Calibrant overnight, was loaded with the mitochondrial respiration inhibitors in the corresponding injection port: 20 μL of 1 μM Oligomycin in port A, 22 μL of 1 μM FCCP in port B, 24 μL of 0.5 μM Rotenone/Antimycin A in port C and 28 μL of Agilent Seahorse DMEM XF medium in port D. The loaded cartridge was then calibrated in the Agilent Seahorse XFe96 Analyzer and then, the cell plate was coupled to the cartridge and analyzed running the Mito Stress Kit protocol in the Seahorse Wave Software.

Cells were labeled with Hoechst 3342 to normalize the resulting data to the number of cells in each well. After analysis of the mitochondrial respiration, cell media was removed, and 50 µL of 1mg/mL Hoechst 3342 in DPBS were added to each well. After incubation for 20 min in darkness, absorbance was measured at 454 nm in the BioTek Synergy H1 Hybrid multi-detector microplate reader (Winooski, Vermont, United States). The data was normalized in the Seahorse Wave Software, and the results were analyzed on the Agilent Seahorse Analytics online platform (https://seahorseanalytics.agilent.com).

3.4.4.4. Triple Negative Breast Cancer Cell Collection for Whole-Cell Metabolomic Analysis

2.3 million MDA-MB-231-Luc cells were seeded in 15 mL of media on a 150 mm cell culture plate and incubated for 24 h at 37°C and 5% CO₂. Then, media was removed, and cells were treated with palbociclib hydrochloride or StPGA-SS-palbociclib in 15 mL at the IC₃₀ values. The compounds were prepared as explained in **Section 3.4.4.2**. Control cells (untreated) were maintained in the cell media. After 72 h of incubation, one plate was collected for control samples (untreated), while two plates were collected for treated samples. The collection

procedure was conducted at 4°C. First, the medium was collected and centrifuged at 400 g for 5 min at 4°C, and the supernatant was removed. Cells were collected in 2 mL DPBS 1x using a scraper and then added to the cell pellet from the medium. Then, cells were washed three times with 2 mL DPBS 1x, and the final cell pellet was weighed and stored at -80°C until metabolite extraction.

3.4.4.5. Mitochondrial Isolation from Triple Negative Breast Cancer Cells for Metabolomic analysis

The isolation procedure, from cell collection to mitochondrial washes, was conducted at 4°C. 2.3 million MDA-MB-231-Luc cells were seeded in 15 mL of media on a 150 mm cell culture plate and incubated for 24 h at 37°C and 5% CO₂ to obtain the mitochondrial fraction. Then, media was removed, and cells were treated with Palbociclib hydrochloride or StPGA-SS-Palbociclib in 15 mL at the IC₃₀ values. The compounds were prepared as explained in **Section 3.4.4**. Control cells (untreated) were maintained in the cell media. After 72 h of incubation, eight plates (80-100 million cells) were collected for each sample, following the same procedure as in **Section 3.4.4.4**.

The cell pellet was homogenized in isolation buffer (2.5X the weight of the cell pellet; 220 mM mannitol, 70 mM sucrose, 10 mM Tris-HCl solution, and 0.5 mg/mL BSA in MilliQ water, pH 7.4) after 30 strokes with an electric glass homogenizer. The homogenate was centrifuged at 560 g for 15 min at 4°C to obtain the nuclear fraction (pellet) and soluble fraction (supernatant) containing mitochondria. The supernatant was centrifuged at 7,000 g for 15 min at 4°C to obtain the mitochondrial fraction (pellet) and the cytosolic fraction (supernatant). The mitochondrial fraction was washed twice with the isolation buffer, and the final mitochondrial fraction was weighed and stored at -80°C until the metabolite extraction.

3.4.4.6. Isotope Labeling of Triple Negative Breast Cancer Cells for NMR Metabolomic Analysis

2.3 million MDA-MB-231-Luc cells were seeded in 15 mL of media on a 150 mm cell culture plate and incubated for 24 h at 37°C and 5% CO₂. Then, media was removed, and cells were treated with palbociclib hydrochloride or StPGA-SS-palbociclib in 15 mL at the IC₃₀ values. The compounds were prepared as explained in **Section 3.4.4.2**. Control cells (untreated) were maintained in the cell media. After 72 h of incubation, the media was replaced by DMEM with 4.5 g/L U-¹³C-glucose or 0.58 g/L U-¹³C-glutamine. After 120 min (for glucose) and 180 min (for glutamine) of incubation, two plates were collected for control samples (untreated), while three plates were collected for treated samples. Cell collection followed the same procedure as in **Section 3.4.4.4**, and cell pellets were stored at -80°C until the metabolite extraction.

3.4.4.7. Isotope Labeling of Triple Negative Breast Cancer Cells for LC-MS Metabolomic Analysis

150,000 MDA-MB-231-Luc cells were seeded in 1 mL of media on 6-well plates and incubated at 37 $^{\circ}$ C and 5% CO $_{2}$ for 24 h. Then, cells were treated with palbociclib hydrochloride or StPGA-SS-palbociclib in 1 mL at the IC $_{30}$ values. Treatments were prepared as explained in **Section 3.4.4.2**. Control cells (untreated) were maintained in the cell media. After 72 h of incubation, the media was replaced by DMEM with 4.5 g/L U- 13 C-glucose or 0.58 g/L U- 13 C-glutamine. After 120 min (for glucose) and 180 min (for glutamine) of incubation. One plate without cells followed the same treatments as blanks for the MS analysis. Before cell collection, 1 mL of media was collected from each well for further MS analysis. Then, cell media was removed, and cells were washed twice with cold 150 mM Ammonium acetate. 500 μ L of cold MeOH:AcN:H $_{2}$ O (50:30:20) were added to each well, and cells were collected with a cell scraper. The cell suspension was stored at -80 $^{\circ}$ C until further extraction.

3.4.4.8. Metabolite Extraction Methods and Sample Preparation for Metabolomic Analysis

3.4.4.8.1. Metabolite Extraction Protocols for NMR Metabolomic Analysis

Metabolite extraction from TNBC cells was performed following the traditional Folch method. Cell pellets (50-70 mg) were placed on ice and allowed to thaw for 5 min. 320 μ L methanol and 160 μ L chloroform were added to each sample, and the tubes were incubated on ice for 5 min. Samples were then vortexed, and cell membranes were broken by three freeze-thaw cycles (1 min in liquid nitrogen, 2 min in ice). 250 μ L MilliQ water and 250 μ L chloroform were added to each sample, and the tubes were vortexed. Samples were centrifuged at 10,000 g for 20 min at 4°C to separate the upper methanol/water and lower chloroform phases. The aqueous and organic phases were transferred to new tubes to evaporate solvents. Aqueous solvents were removed in a freeze-drier, while organic solvents were removed under a stream of nitrogen. The dried extracts were then stored at -80°C until their analysis. The aqueous phase was resuspended in 550 μ L NMR buffer (20 mM Na₂HPO₄ pH 7.4, 20 μ M TSP in D₂O) and transferred to a 5 mm NMR tube for NMR analysis.

Metabolite extraction from mitochondria samples and 13 C-labeled TNBC cells was performed following the extraction method optimized in **Chapter II**. Mitochondrial pellets (70-100 mg) and 13 C-labeled cells (40-140 mg) were placed on ice and thawed for 5 min. 700 μ L NMR buffer (20 mM Na₂HPO₄ pH 7.4, 20 μ M TSP in D₂O for mitochondrial samples and 100 mM Na₂HPO₄ pH 7.4, 200 μ M TSP in D₂O) was added to the pellets, vortexed, and incubated in an ultrasonic water bath at room temperature for 5 min. Samples were then incubated in liquid nitrogen for 1 min

and allowed to thaw in a temperate water bath. This cycle was repeated twice to break membranes and allow metabolite extraction. Samples were centrifuged at 10,000 g for 20 min at 4° C, the supernatant was transferred to a new tube, and the extraction pellet was stored at -80°C. Samples were filtered using 3kDa centrifugal filters to remove protein signals from the spectra, which were washed three times with 400 μ L MilliQ water and once with 400 μ L D₂O and then centrifuged at 14,000 g for 30 min to dry. Samples were filtered by centrifugation at 14,000g for 45 min at 4°C. 550 μ L of the filtered sample was transferred to a 5 mm NMR tube for subsequent NMR analysis.

For cell media, 100 μ L of NMR buffer (100 mM Na₂HPO₄ pH 7.4, 200 μ M TSP in D₂O) was added to 500 μ L of collected, vortexed, and transferred to a 5 mm NMR tube for subsequent NMR analysis.

3.4.4.8.2. Metabolite Extraction Protocols for LC-MS Metabolomic Analysis

Collected MDA-MB-231-Luc cell pellets and isolated mitochondria were divided into two technical replicates (20-45 mg). 1 mL of cold MeOH:CHCl₃ (1:2) containing 6 µL of Lipidomics Splashmix Mass Spec Standard/sample was added to each sample. The empty tubes followed the same procedure to serve as blanks. Then, 200 μL of MilliQ water was added to each sample, and samples were mixed in an Eppendorf Thermomixer (Hamburg, Germany) at 1,000 rpm for 30 min at 4ºC. Samples were centrifuged at 16,000 g for 10 min at 4ºC; the aqueous phase (upper) and the organic phase (lower) were transferred to newly labeled tubes, while the interphases remaining in the tube were saved at -20°C for protein quantification. The aqueous phase was re-extracted by adding 350 µL CHCl₃:MeOH:H₂O (86:14:1) and shaking at 1,000 rpm for 20 min at 4°C. After centrifugation of the samples at 16,000 g for 10 min at 4°C, the aqueous phases (upper) were transferred to new labeled tubes and lyophilized, while the organic phases (bottom) were transferred to the previous organic phase and dried under a stream of N₂. Samples were stored at -20°C until analysis. For LC-MS analysis, the aqueous and the organic extracts were resuspended in 20 μL of 0.1% formic acid or 20 μL of MeOH:CHCl₃ (1:1), respectively, centrifuged at 16,000 g for 5 min and transferred to labeled 9 mm, 2 mL LC-MS tubes with 0.1 mL inserts.

¹³C-labeled TNBC cells, previously collected in MeOH:AcN:H₂O (50:30:20), were shaken in an Eppendorf Thermomixer (Hamburg, Germany) at 1,400 rpm for 15 min at 4 $^{\circ}$ C and centrifuged at 16,000 g for 10 min at 4 $^{\circ}$ C. The supernatant was transferred to a new tube, lyophilized, and stored at -80 $^{\circ}$ C until the MS analysis. The protein pellet obtained from the centrifugation was also stored at -80 $^{\circ}$ C for protein quantification. Cell extracts were resuspended in 25 μL of 0.1%

formic acid for LC-MS analysis and centrifuged at 16,000 g for 5 min. Supernatants were transferred to labeled 9 mm, 2 mL LC-MS tubes with 0.1 mL inserts.

3.4.4.9. Metabolomic Analysis by NMR Spectroscopy

3.4.4.9.1. NMR Spectra Acquisition

NMR spectra of MDA-MB-231-Luc cells and mitochondrial samples were acquired in a Bruker AVII-600MHz NMR spectrometer (Billerica, Massachusetts, United States) with a 5 mm TCI cryoprobe. The temperature was set to 300 K (27°C), and a standard reference sample (2 mM sucrose, 0.5 mM sodium trimethylsilylpropanesulfonate (DSS), and 2 mM NaN3 in H₂O/D₂O) was used to ensure spectral resolution and water suppression. ¹H 1D spectra were obtained using the Nuclear Overhauser Effect Spectroscopy (NOESY) pulse sequence, a 4-s relaxation delay (D1) between free induction decay (FID) readings, and a water presaturation pulse of 25 Hz to minimize the water signal. 256 scans (25 min) were acquired for the whole-cell samples and the optimization of the metabolite extraction method of mitochondrial samples, while 2,512 scans (4 h) were run to analyze the final mitochondrial fractions. The difference in the number of scans is due to the low metabolite levels in the mitochondria samples, which need more time to acquire a good-quality spectrum. **Table 3.9** summarizes the NMR instrument and the parameters used for the NMR metabolomic analysis of this chapter's type of samples.

1D NMR ¹³C spectra and the 2D ¹H-¹³C spectra of ¹³C-labeled TNBC cells were acquired at 500K (27°C) in a Bruker AVANCE-TM 600 MHz NMR spectrometer (Billerica, Massachusetts, United States) with a 5mm BBI probe. The spectrometer was prepared as explained for the 600 MHz NMR spectrometer, and ¹H 1D spectra were obtained by applying the same parameters as for TNBC cells. ¹³C 1D spectra were acquired using a zgpg sequence, a 2-s relaxation delay between FID readings, and 32,000 scans (19 h). The ¹H-¹³C 2D spectra were obtained using an HSQC pulse sequence, a 2-s relaxation delay, and 156 scans (12 h).

Cell media spectra were acquired at 300 k (27°C) in an AV-III 500 MHz Bruker spectrometer (Billerica, Massachusetts, United States). ¹H ¹D NMR spectra were obtained using the NOESY pulse sequence, a 4-s relaxation delay FID readings, a water presaturation pulse of 25 Hz to minimize the water signal, and 128 scans (15 min).

Table 3.9. NMR spectrometer and parameters used for the metabolomic and fluxomics analysis of all the sample types used in **Chapter III**

	NMR spectrometer	Pulse sequence	Temp (K)*	Scans	D1 (s)*	Experiment duration
¹ H 1D cells	AVII-600 MHz	NOESY	300	256	4	25 min

¹ H 1D mitochondria	AVII-600 MHz	NOESY	300	2,512	4	4 h
¹H 1D media	AVIII-500 MHz	NOESY	300	128	4	15 min
¹ H 1D ¹³ C-labeled cells	600 MHz	NOESY	300	256	4	25 min
¹³ C 1D ¹³ C-labeled cells	600 MHz	zgpg	300	32,000	2	12 h
¹ H- ¹³ C 2D ¹³ C-labeled cells	600 MHz	HSQC	300	156	2	19 h

^{*}D1 = relaxation delay; HSQC = Heteronuclear Single Quantum Correlation; K = kelvin; NOESY = Nuclear Overhauser Effect Spectroscopy; Temp = temperature

3.4.4.9.2. NMR Data Processing

FID values were multiplied by an exponential function with a 0.5 Hz (¹H NOESY), 1 Hz (¹H CPMG), and 3 Hz (¹³C zgpg) line broadening factor, and Fourier transformed in Topspin 3.2 (Bruker GmbH, Karlsruhe, Germany). Spectra were processed in MestreNova (MestreLab Research, Santiago de Compostela, Spain). ¹H 1D NMR spectra were referenced to the internal standard (TSP), the phase was manually corrected, and the baseline was corrected using automatic Whittaker smoother correction for whole-cell samples and a manual optimization of the Whittaker smoother correction for mitochondria. ¹³C 1D NMR spectra were referenced to lactate (in ¹³C-labeled cells with ¹³C-glucose) and to glutamate (in ¹³C-labeled cells with ¹³C-glutamine), the phase was manually corrected, and the baseline was corrected using a manual optimization of the Whittaker smoother correction.

3.4.4.9.3. Metabolite Identification and Quantification

Metabolite signals were assigned after processing NMR spectra. An Excel file was prepared to assign sample type using publicly available information from the Human Metabolome Database (HMDB)²⁰⁹ and the Chenomx profiler (ChenomX Inc., Edmonton, Canada). The assignment of ¹H NMR spectra of TNBC cells and isolated mitochondria is presented in **Chapter II**. The assignment of ¹H-¹³C 2D HSQC spectra is presented in **Table 3.8**.

The signals were integrated using the "Predefined sum" calculation method in MestreNova software by uploading the assignment table in text file format. Signal integrals were saved as 1D Integral Series (.txt) or Script: Integral Table (.txt) for 2D spectra and opened in Excel.

Data were normalized by the total area method by dividing each integral value by the sum of all integrals in the sample, excluding signals coming from the isolation buffer and the NMR buffer. This method preserved the relative intensities of the signals in each sample.

Analysis of the metabolites in the cell media considered that commercial cell media already have their metabolome and depend on the cell number. First, the percentage change of each assigned

metabolite was calculated over the intensity of the same metabolite in clean cell media (media not added to the cells). Then, each percentage change was multiplied by a factor that equals the number of cells (1 for control cells and 1/0.7 = 1.42 for the treatments as treatment occurred at concentrations corresponding to the IC₃₀ values that maintain 70% of cells alive).

3.4.4.10. Metabolomic Analysis by LC-MS

3.4.4.10.1. LC-MS Spectra Acquisition

The LC-MS metabolomic and lipidomic analyses were performed in a ThermoFisher Scientific[™] Vanquish[™] Horizon UHPLC system (Waltham, Massachusetts, United States) equipped with a Waters ACQUITY Premier CSH (2.1 x 100mm, 1.7 μM) column (Milford, Massachusetts, United States) operated at 55°C and coupled to a Bruker TimsTOF FleX (Billerica, Massachusetts, United States) mass spectrometer. The running sequence of the samples was randomized before the LC-MS analysis. A quality control (QC) consisting of a pool of all the samples (5 μ L/sample) was run to generate fragments to identify the metabolites/lipids. 3 μL of the sample were injected into the UPLC, and analytes were eluted using a 400 μL/min flow rate. For the metabolomic analysis, the following composition of eluent A (0.1% formic acid in water) and eluent B (Isopropanol/acetonitrile (90:10), 0.1% formic acid in acetonitrile) was used: 3% of B from 0 to 1 min, 3-40% of B from 1 to 3 min, 40-95% of B from 3 to 5 min, 95 % of B from 5 to 7.6 min and 95 to 3% of B from 7.6 to 8 min before equilibration for 3.5 min with the initial conditions. For the lipidomic analysis, the following composition of eluent A (Acetonitrile/water (60:40), 10 mM ammonium formate, 0.1% formic acid) and eluent B (Isopropanol/acetonitrile (90:10), 10 mM ammonium formate, 0.1% formic acid) was used: 40% of B from 0 to 0.5 min, 40-43% of B from 0.5 to 0.7 min, 43-65% of B from 0.7 to 0.8 min, 65-70% of B from 0.8 to 2.3 min, 70-99% of B from 2.3 to 6 min, 99% of B from 6-6.8 min and 99-40% of B from 6.8-7 min before equilibration for 3 min with the initial conditions. The LC flow was coupled to the mass spectrometer scanning from a mass range of 40-1500 m/z (for metabolomics) or 100-1800 m/z (for lipidomics), operated in both positive and negative ion mode using trapped ion mobility spectrometry. A collision energy of 20 and 40 V was applied for the metabolomic studies, and, for lipidomics, a collision energy of 30 and 50 V was applied in positive and ion mode and 20 and 30 eV in negative ion mode. 13C-labeled samples were analyzed following the same protocol as for the metabolomic samples.

The total ion chromatograms and the extracted ion chromatograms of mass spectra were visualized on the Bruker Data Analysis software.

3.4.4.10.2. MS Data Processing and Metabolite Annotation

Spectra processing was performed in the Bruker MetaboScape software (Billerica, Massachusetts, United States). Data was filtered to remove the background and features in the blank; features were removed if their average signal was not > five times more abundant in the QC samples than blanks.

Lipid annotation was done using an in-build rule-based annotation approach and the LipidBlast MS2 library²¹². The signals were normalized to the internal standards in the SPLASH mix before correction for signal drift using statTarget³⁵⁶.

For the metabolomic analysis, feature annotation was done by first searching MS2 spectra against the following MSMS libraries: Bruker Metabobase, National Institute of Standards and Technology 17 (NIST17), and MassBank of North America (MoNA). Next, the not annotated compounds were annotated using Metfrag³⁵⁷ for in silico annotation. The features were corrected for signal drift using statTarget³⁵⁶.

Signals were normalized using the QC samples, log-transformed (base 10), and auto-scaled in Metaboanalyst²¹⁷.

Feature annotation of the ¹³C-labeling analysis was performed using the Bruker TASQ software (Billerica, Massachusetts, United States).

3.4.4.11. Multivariate and Univariate Statistical Analysis

PCAs were obtained using the SIMCA-P 17 software. Univariate analysis was carried out by p-value (t-test) and fold changes calculations performed in Excel and in MetaboAnalyst 5.0 web-based platform²¹⁷.

Rapid visualization of ¹³C-labeled data and data summary (mean and SEM) of each feature and their isotopologues were performed in the Metabolite Autoplotter application³⁵⁸.

Graphs were presented as average \pm SEM from three/four assays and plotted in GraphPad Prism (version 9.5.0, GraphPad Software Inc., USA). Boxplots were generated in RStudio 1.2.5033. Comparisons with p< 0.05 were considered statistically significant.

CHAPTER IV

METABOLOMIC ANALYSES OF MITOCHONDRIA ISOLATED FROM HEALTHY AND PRIMARY AND METASTATIC TISSUES OF A TRIPLE NEGATIVE BREAST CANCER MOUSE MODEL

4.1. INTRODUCTION

Generally, cancer cells obtain energy through anaerobic glycolysis due to low oxygen levels, which impairs mitochondrial respiration and increases cell acidity due to increased lactate production (the "Warburg effect")³⁵⁹. A higher mitochondrial membrane potential, reflecting the altered functional status of mitochondria, also characterizes tumorigenic development³⁶⁰. Mitochondrial dysfunction also triggers alterations to tumor cell energy production mechanisms (from OXPHOS to glycolysis), thus contributing to cancer progression⁴⁶. In this context, mitochondrial metabolism supports cancer cell adaptation, which promotes metastasis³⁶⁰. Furthermore, altered mitochondrial content supports additional facets of cancer aggressiveness³⁶¹.

A deeper understanding of disease-associated molecular mechanisms may help to develop better therapeutic approaches for aggressive metastatic cancers. In this context, developing specific methods to study mitochondrial metabolism may detect disease-associated alterations to inform on these mechanisms. Significantly, metabolomic data from tissue matrices reflect changes occurring at the origin of the disorder and provide relevant information regarding associated mechanisms³⁶².

Whole-tissue metabolomics has been widely applied in biomedical research for the diagnosis of pathological processes³⁶³, the discovery of early disease biomarkers³⁶⁴, optimization of therapies for various pathologies^{365,366}, the study of different disease rates between populations³⁶⁷, and identification of tumor characteristics and progression markers³⁶⁸. However, we lack protocols that support the metabolomic profiling of organelles, such as mitochondria. A more in-depth understanding of mitochondrial metabolomics could capture dynamic changes missed by "bulk" whole-cell profiling³⁶⁹. A more targeted approach could also represent a valuable tool in mitochondria-related disease research, helping to evaluate novel drugs (particularly those targeting mitochondria) and supporting the early identification of biomarkers in diseases with a known mitochondrial impact (e.g., Alzheimer's disease, Parkinson's disease, and diabetes³⁶).

While current mass spectrometry (MS)-based methods for quantifying the metabolite content of isolated mitochondria from tissues are very sensitive and suitable for the study of metabolic changes^{238,241,242,370}, the developed nuclear magnetic resonance (NMR)-based methods for metabolomic analysis of mitochondria isolated from tissues are scarce and result in a low number of detected metabolites^{230,231}. As an alternative strategy for mitochondrial metabolomics, we sought to develop a more straightforward, robust, nontargeted approach that generates a general mitochondrial metabolic fingerprint.

In this chapter, we describe the development of an optimized protocol for the NMR metabolomic analysis of mitochondria isolated from triple negative breast cancer (TNBC) mouse tumors and healthy mouse tissues (lungs, liver, bran and kidney). Moreover, we focus on the application of the mitochondrial metabolomics methodology to evaluate the mitochondrial metabolic modulation in metastatic tissues. The work presented in this chapter has been published in Domingo et al., 2023 (Annex II).

4.2. RESULTS AND DISCUSSION

4.2.1. Optimization of NMR-based Metabolomic Analysis of Mitochondria Isolated from Triple Negative Breast Cancer Tumor and Healthy Liver, Kidneys, Lungs and Brain

4.2.1.1. Mitochondria Isolation from Tissues

The procedure used for mitochondrial isolation from tissues depends on the final aim of the study and the grade of purity and activity of the isolated mitochondria required^{240,246}. As mentioned in **Chapter I Section 1.3.3**, several methodologies have been developed for mitochondria isolation. Specifically, mitochondria isolation from tissues has been achieved by differential centrifugation (DC)^{241,371}, density gradient centrifugation^{372,373}, by commercially available kits based on affinity purification^{230,231} or even by nanobiopsy using nanopipettes and electrowetting that allows aspiration of cell organelles in biopsies³⁷⁴. Despite the availability of several mitochondrial isolation approaches, we selected tissue homogenization followed by differential centrifugation as the most suitable method for mitochondria isolation from tissues to support the robust and reproducible acquisition of metabolomic profiles²⁴⁰. The simplicity and high recovery rate make this approach commonplace in organelle isolation protocols, with extensive applications in tissues such as the liver^{240,375}, heart³⁷⁵, musculoskeletal³⁷⁵, brain³⁷⁵, kidney²⁵⁴, and testes²⁵⁴. **Figure 4.1** depicts the optimized procedure (mitochondria isolation (**A**), metabolite extraction (**B**) and NMR analysis (**C**)) for the NMR metabolomic analysis of mitochondria isolated from tissues.

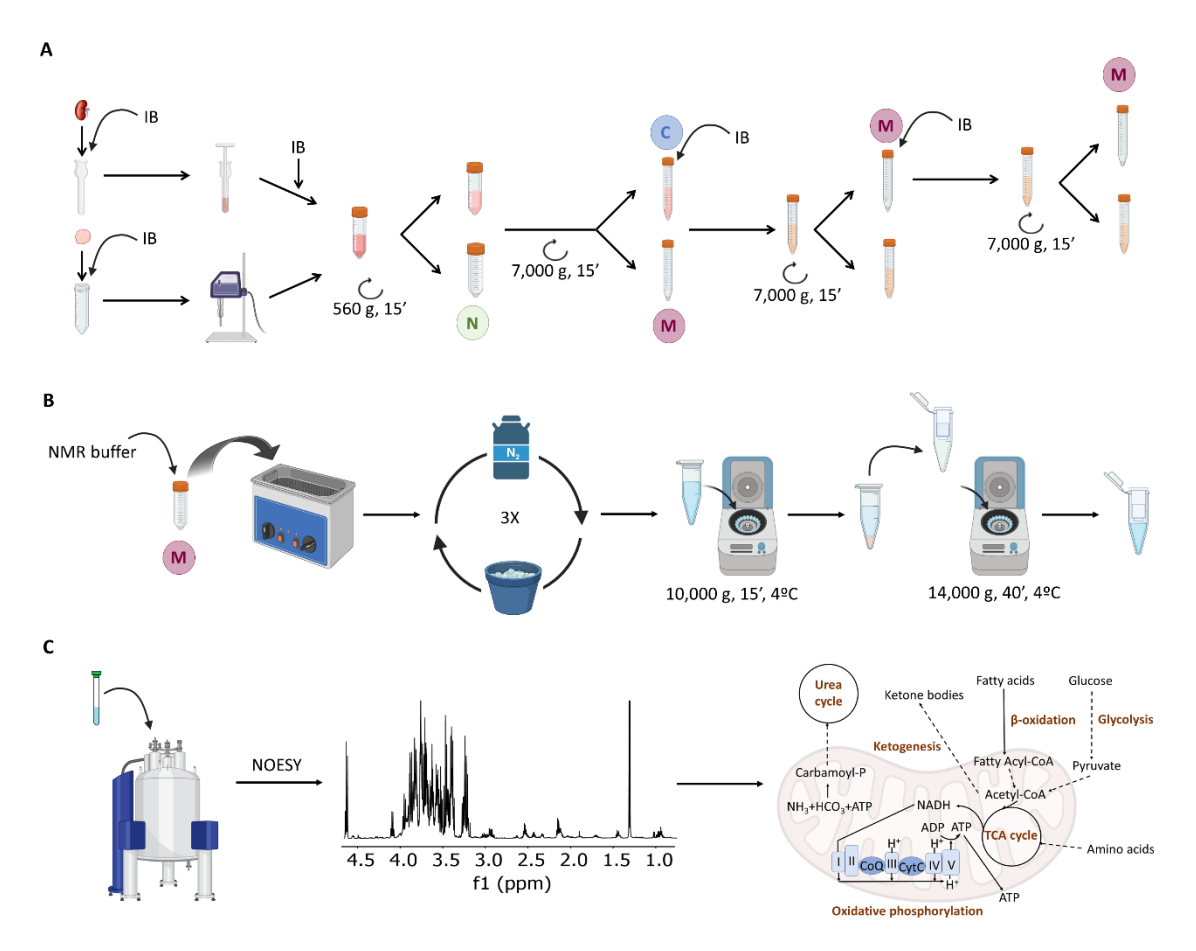


Figure 4.1. Schematic representation of the protocol used for (**A**) mitochondria isolation from tissues, (**B**) metabolite extraction and sample preparation, and (**C**) NMR analysis and biological interpretation. IB: isolation buffer (220 mM mannitol, 70 mM sucrose, 10 mM Tris-HCl solution, and 0.5 mg/mL bovine serum albumin (BSA) in MilliQ H2O, pH 7.4); NMR buffer (20 mM Na2HPO4 and 20 μM TSP solution in D₂O, pH 7.4), C = cytosol; M = mitochondria; N = nucleus.

Generally, two standard methods are available for tissue homogenization – manual Dounce or automatic Ultra-turrax approaches. We compared metabolite recovery using both homogenization methods for all tissues; only the TNBC tumors displayed a higher intensity in some NMR signals (e.g., acetate, creatine, and choline derivatives) after homogenization with Ultra-turrax compared to Dounce (**Figure 4.2**), probably due to its more compact nature (given the fibrous, muscular type of tissue). Therefore, we employed Ultra-turrax homogenization for TNBC tumors and Dounce homogenization for lungs, liver, brain and kidneys (**Table 4.1**).

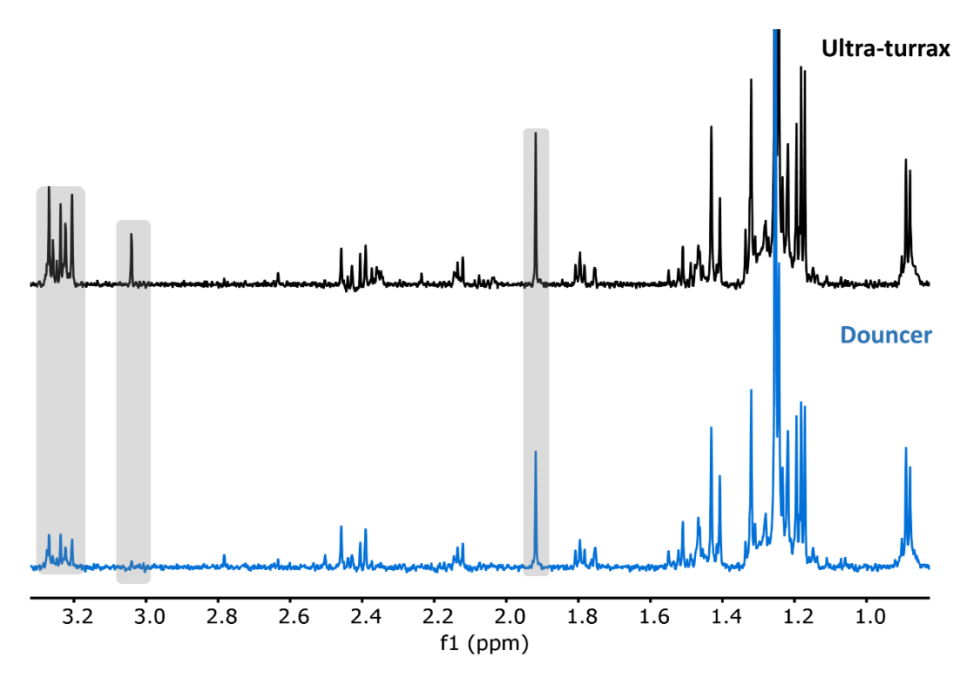


Figure 4.2. Aliphatic region of the ¹H-NMR spectra of tumor mitochondria samples obtained following Dounce or Ultra-turrax homogenization. Both methods employed the same tumor sample. The spectral regions experiencing the most significant changes are highlighted in grey.

Table 4.1. Parameters used for NMR analysis of mitochondrial samples isolated from different mouse tissues

Tissue	Homogenizer	Organ units	¹ H-NMR scans	Duration (minutes)
Breast tumor	Ultra-turrax	1/2	1280	125
Lung	Dounce	2	1280	125
Kidney	Dounce	2	640	61
Liver	Dounce	1	640	61
Brain	Dounce	1	640	61

We confirmed the isolation of mitochondria by Western blotting analysis of the mitochondrial and cytosolic fractions isolated from each tissue (**Figure 4.3**). We used cytochrome c and Heat Shock Protein 90 (HSP90) antibodies as mitochondrial and cytosolic markers, respectively, and β -actin, or VDAC as loading controls; in liver samples, we used β -actin for the cytosolic fractions and VDAC for the mitochondrial samples, due to the absence of β -actin in the mitochondria of healthy liver³⁷⁶. For all organs, we observed a significantly higher level of mitochondrial marker expression in mitochondrial fractions than in cytosolic fractions, thereby confirming the presence of mitochondria. The cytosolic fractions presented comparatively low levels of cytochrome c, further confirming the isolation of mitochondria from the cytosol (**Figure 4.3**). A quantitative analysis of several replicates (n=3-4) of the western blots showed higher

enrichment levels for brain, kidney, and liver samples (92-99%), while the enrichment was slightly lower for tumor and lung samples (75%) (**Table 4.2**).

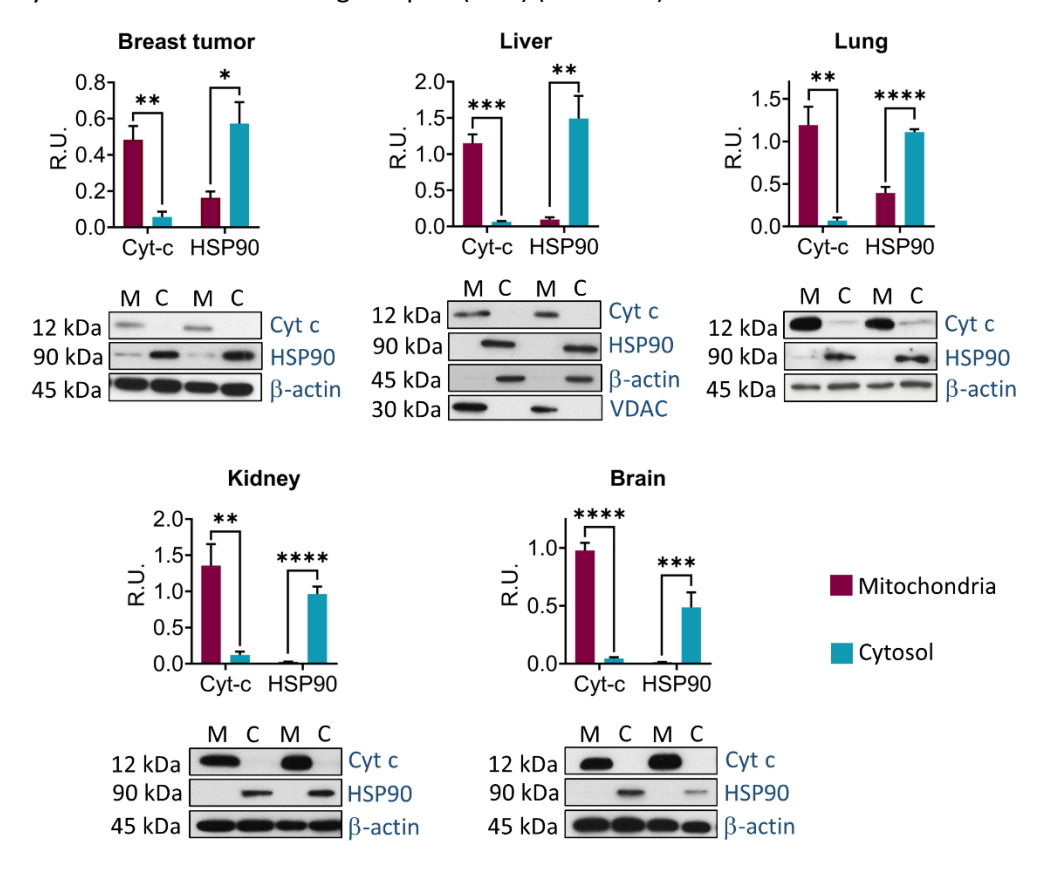


Figure 4.3. Representative Western blots and protein quantitation confirming mitochondrial isolation from tissues. Protein quantification was performed by densitometry analysis. Cytochrome c (Cyt c): mitochondrial marker; HSP90 (Heat shock protein 90): cytosolic marker; β-actin, and VDAC (voltage voltage-dependent anion channel): loading controls. M = mitochondria; C = cytosol. Three or four independent experiments performed for all comparisons (n = 3-4). Data analysis used a T-test, with data presented as average \pm SEM; (* p-value < 0.05, ** p-value < 0.01, *** p-value < 0.001, **** p-value < 0.001).

Table 4.2. Quantification of the Western blot bands (Mean and SEM), p-values of the comparison between mitochondrial samples and cytosolic samples and mitochondrial enrichment in the fractions obtained from the different organs calculated from the western blot analysis (cytochrome c intensity of mitochondrial samples divided by the sum of the cytochrome c and HSP90 intensities of mitochondrial samples). The displayed protein levels were already normalized with the loading controls.

Tissue	Protein	Fraction	Mean	SEM	P-value	Mitochondrial enrichment
	Cutachrama	Mitochondrial	0.483	0.076	0.006	
December 7	Cytochrome c	Cytosolic	0.058	0.029	0.006	750/
Breast Tumor	110000*	Mitochondrial	0.164	0.034	0.020	75%
	HSP90*	Cytosolic	0.573	0.118	0.029	
Liver	Cytochrome c	Mitochondrial	1.151	0.122	1E-04	92%

		Cytosolic	0.065	0.010		
	HSP90	Mitochondrial	0.095	0.033	0.004	
	ПЗРЭО	Cytosolic	1.492	0.315	0.004	
	Cytochrome c	Mitochondrial	1.191	0.216	0.002	
Lung	Cytochrome c	Cytosolic	0.070	0.034	0.002	75%
Lung	HSP90	Mitochondrial	0.395	0.071	0.000	75%
	пого	Cytosolic	1.110	0.033	0.000	
	Cytochrome c	Mitochondrial	1.357	0.297	0.006	
Kidney	Cytochrome c	Cytosolic	0.122	0.046	0.000	98%
Ridiley	HSP90	Mitochondrial	0.025	0.004	1E-04	96%
	H3P90	Cytosolic	0.887	0.095	16-04	
	Cytochrome c	Mitochondrial	0.979	0.065	8E-06	
Dunin	Cytochrome c	Cytosolic	0.045	0.011	8E-00	99%
Brain	HSP90	Mitochondrial	0.013	0.002	0.001	33%
	пэгэи	Cytosolic	0.487	0.078	0.001	

^{*}HSP90 = heat shock protein 90

Table 4.3 provides a summary of the data for all samples used in this section and the rest of **Chapter IV**.

Table 4.3. Data summary for samples used in Chapter IV

Sample ID	Tissue	Mouse	Sample type	Purpose	Metabolite extraction
MITE057	Breast tumor	NOD/SCID 231	Mitochondria	Homogenization, extraction optimization	Folch
MITE059	Breast tumor	NOD/SCID 231	Mitochondria	Homogenization, extraction optimization	Folch
MITE061	Breast tumor	NOD/SCID 231	Mitochondria	Homogenization, extraction optimization	Folch
MITE118	Breast tumor	NOD/SCID 231	Mitochondria	Homogenization optimization	Optimized
MITE119	Breast tumor	NOD/SCID 231	Mitochondria	Homogenization optimization, NMR* metabolomics	Optimized
MITE106	Liver	NOD/SCID	Mitochondria	Homogenization optimization	Optimized
MITE107	Liver	NOD/SCID	Mitochondria	Homogenization optimization	Optimized
MITE152	Lung	NOD/SCID	Mitochondria	Homogenization optimization	Optimized
MITE153	Lung	NOD/SCID	Mitochondria	Homogenization optimization	Optimized
MITE154	Kidney	NOD/SCID	Mitochondria	Homogenization optimization, NMR metabolomics	Optimized
MITE155	Kidney	NOD/SCID	Mitochondria	Homogenization optimization	Optimized
MITE158	Brain	NOD/SCID	Mitochondria	Homogenization optimization	Optimized
MITE159	Brain	NOD/SCID	Mitochondria	Homogenization optimization	Optimized
MITE113	Breast tumor	NOD/SCID 231	Mitochondria	WB*	-
MIET115	Breast tumor	NOD/SCID 231	Mitochondria	WB	-
MITE117	Breast tumor	NOD/SCID 231	Mitochondria	WB	-
MITE082	Liver	NOD/SCID	Mitochondria	WB	-
MITE083	Liver	NOD/SCID	Mitochondria	WB	-
MITE108	Liver	NOD/SCID	Mitochondria	WB	-

					,
MITE109	Liver	NOD/SCID	Mitochondria	WB	-
MITE088	Lung	NOD/SCID	Mitochondria	WB	-
MITE089	Lung	NOD/SCID	Mitochondria	WB	-
MITE090	Lung	NOD/SCID	Mitochondria	WB	-
MITE091	Lung	NOD/SCID	Mitochondria	WB	-
MITE094	Kidney	NOD/SCID	Mitochondria	WB	-
MITE095	Kidney	NOD/SCID	Mitochondria	WB	-
MITE096	Kidney	NOD/SCID	Mitochondria	WB	-
MITE097	Kidney	NOD/SCID	Mitochondria	WB	-
MITE098	Brain	NOD/SCID	Mitochondria	WB	-
MITE100	Brain	NOD/SCID	Mitochondria	WB	-
MITE102	Brain	NOD/SCID	Mitochondria	WB	-
MITE104	Brain	NOD/SCID	Mitochondria	WB	-
MITE025	Liver	NOD/SCID	Mitochondria	Extraction optimization	Folch
MITE026	Liver	NOD/SCID	Mitochondria	Extraction optimization	Folch
MITE027	Liver	NOD/SCID	Mitochondria	Extraction optimization	Folch
MITE172	Liver	NOD/SCID	Mitochondria	Extraction optimization, NMR metabolomics	Optimized
MITE173	Liver	NOD/SCID	Mitochondria	Extraction optimization, NMR metabolomics	Optimized
MITE197	Liver	NOD/SCID	Mitochondria	Extraction optimization, NMR metabolomics	Optimized
MITE165	Breast tumor	NOD/SCID 231	Mitochondria	Extraction optimization	Optimized
MITE167	Breast tumor	NOD/SCID 231	Mitochondria	Extraction optimization	Optimized
MITE168	Breast tumor	NOD/SCID 231	Mitochondria	Extraction optimization	Optimized
MITE163	Breast tumor	NOD/SCID 231	Mitochondria	NMR metabolomics	Optimized
MITE165	Breast tumor	NOD/SCID 231	Mitochondria	NMR metabolomics	Optimized
MITE167	Breast tumor	NOD/SCID 231	Mitochondria	NMR metabolomics	Optimized
MITE168	Breast tumor	NOD/SCID 231	Mitochondria	NMR metabolomics	Optimized
MITE180	Kidney	NOD/SCID	Mitochondria	NMR metabolomics	Optimized
MITE181	Kidney	NOD/SCID	Mitochondria	NMR metabolomics	Optimized
MITE182	Kidney	NOD/SCID	Mitochondria	NMR metabolomics	Optimized
MITE183	Kidney	NOD/SCID	Mitochondria	NMR metabolomics	Optimized
MITE174	Lung	NOD/SCID	Mitochondria	NMR metabolomics	Optimized
MITE175	Lung	NOD/SCID	Mitochondria	NMR metabolomics	Optimized
MITE233	Lung	NOD/SCID	Mitochondria	NMR metabolomics	Optimized
MITE234	Lung	NOD/SCID	Mitochondria	NMR metabolomics	Optimized
MITE176	Lung	NOD/SCID	Mitochondria	NMR metabolomics	Optimized
MITE131	Liver	NOD/SCID	Mitochondria	NMR metabolomics	Optimized
MITE170	Liver	NOD/SCID	Mitochondria	NMR metabolomics	Optimized
MITE158	Brain	NOD/SCID	Mitochondria	NMR metabolomics	Optimized
MITE160	Brain	NOD/SCID	Mitochondria	NMR metabolomics	Optimized
MITE177	Brain	NOD/SCID	Mitochondria	NMR metabolomics	Optimized

MITE178	Brain	NOD/SCID	Mitochondria	NMR metabolomics	Optimized
MITE179	Brain	NOD/SCID	Mitochondria	NMR metabolomics	Optimized
MITE133	Breast tumor	NOD/SCID 231	Whole-cell	NMR metabolomics	Optimized
MITE134	Breast tumor	NOD/SCID 231	Whole-cell	NMR metabolomics	Optimized
MITE135	Breast tumor	NOD/SCID 231	Whole-cell	NMR metabolomics	Optimized
MITE139	Lung	NOD/SCID	Whole-cell	NMR metabolomics	Optimized
MITE140	Lung	NOD/SCID	Whole-cell	NMR metabolomics	Optimized
MITE141	Lung	NOD/SCID	Whole-cell	NMR metabolomics	Optimized
MITE136	Liver	NOD/SCID	Whole-cell	NMR metabolomics	Optimized
MITE137	Liver	NOD/SCID	Whole-cell	NMR metabolomics	Optimized
MITE138	Liver	NOD/SCID	Whole-cell	NMR metabolomics	Optimized
MITE142	Kidney	NOD/SCID	Whole-cell	NMR metabolomics	Optimized
MITE143	Kidney	NOD/SCID	Whole-cell	NMR metabolomics	Optimized
MITE144	Kidney	NOD/SCID	Whole-cell	NMR metabolomics	Optimized
MITE145	Brain	NOD/SCID	Whole-cell	NMR metabolomics	Optimized
MITE146	Brain	NOD/SCID	Whole-cell	NMR metabolomics	Optimized
MITE147	Brain	NOD/SCID	Whole-cell	NMR metabolomics	Optimized
MITE196	Liver	NOD/SCID 231	Mitochondria	NMR metabolomics	Optimized
MITE202	Liver	NOD/SCID 231	Mitochondria	NMR metabolomics	Optimized
MITE206	Liver	NOD/SCID 231	Mitochondria	NMR metabolomics	Optimized
MITE224	Liver	NOD/SCID 231	Mitochondria	NMR metabolomics	Optimized
MITE225	Liver	NOD/SCID 231	Mitochondria	NMR metabolomics	Optimized
MITE192	Lung	NOD/SCID 231	Mitochondria	NMR metabolomics	Optimized
MITE193	Lung	NOD/SCID 231	Mitochondria	NMR metabolomics	Optimized
MITE211	Lung	NOD/SCID 231	Mitochondria	NMR metabolomics	Optimized
MITE212	Lung	NOD/SCID 231	Mitochondria	NMR metabolomics	Optimized
MITE213	Lung	NOD/SCID 231	Mitochondria	NMR metabolomics	Optimized
MITE199	Kidney	NOD/SCID 231	Mitochondria	NMR metabolomics	Optimized
MITE201	Kidney	NOD/SCID 231	Mitochondria	NMR metabolomics	Optimized
MITE205	Kidney	NOD/SCID 231	Mitochondria	NMR metabolomics	Optimized
MITE228	Kidney	NOD/SCID 231	Mitochondria	NMR metabolomics	Optimized
MITE229	Kidney	NOD/SCID 231	Mitochondria	NMR metabolomics	Optimized
MITE237	Liver	NOD/SCID 231	Whole-cell	NMR metabolomics	Optimized
MITE238	Liver	NOD/SCID 231	Whole-cell	NMR metabolomics	Optimized
MITE239	Liver	NOD/SCID 231	Whole-cell	NMR metabolomics	Optimized
MITE240	Kidney	NOD/SCID 231	Whole-cell	NMR metabolomics	Optimized
MITE241	Kidney	NOD/SCID 231	Whole-cell	NMR metabolomics	Optimized
MITE242	Kidney	NOD/SCID 231	Whole-cell	NMR metabolomics	Optimized
MITE243	Lung	NOD/SCID 231	Whole-cell	NMR metabolomics	Optimized
MITE244	Lung	NOD/SCID 231	Whole-cell	NMR metabolomics	Optimized
MITE245	Lung	NOD/SCID 231	Whole-cell	NMR metabolomics	Optimized

Our optimized methodology for isolating mitochondria from breast tumor, liver, lung, kidney and brain tissues based on mechanical homogenization and differential centrifugation, yielded an enriched mitochondrial fraction suitable for NMR-based metabolomic studies.

4.2.1.2. Metabolite Extraction from Mitochondria Isolated from Tissues

After organelle isolation, we explored the choice of metabolite extraction protocol. Analysis of intact mitochondria by high-resolution magic-angle spinning (HR-MAS) NMR provides lower resolution and sensitivity than a ¹H NOESY of a mitochondrial extract³⁷⁷, crucial parameters when working with small sample amounts (such as mitochondrial fractions, in our case). To our knowledge, no study has reported the specific optimization of a protocol for extracting mitochondrial metabolites; however, some protocols have been established for analyzing limited-quantity samples³⁷⁸. The commonly used Folch extraction method involves adding a chloroform/methanol/water mixture to simultaneously extract aqueous and hydrophobic metabolites²⁶⁶; however, alternative methods that avoid organic solvents may represent a more optimal choice for the analysis of small-quantity samples. The use of NMR buffer in place of organic solvents has been used in combination with sonication²⁶⁹ or quenching in liquid nitrogen²⁷⁰ to avoid metabolite loss during solvent evaporation. Moreover, sonication alone or combined with final sample ultrafiltration provides better quality spectra than the Folch method²⁷⁰. Given these data, we chose to resuspend mitochondrial extracts in NMR buffer, quench them in liquid nitrogen, and then carry out centrifugal ultrafiltration to extract the metabolites for the present study. We also introduced 3 KDa centrifugal filters to eliminate broad protein signals during centrifugal ultrafiltration. A schematic representation of the metabolite extraction protocol is shown in Figure 4.1B.

We first compared metabolite extraction carried out using two methods, namely the optimized ("NOESY with filtration") and the traditional extraction ("NOESY Folch extraction"), in liver and breast tumor mitochondria samples, which represent normal and diseased tissues, respectively (Figure 4.4A). A comparison of the obtained NMR spectra demonstrated a significantly higher metabolite recovery when using the "NOESY with filtration" method. This was further confirmed via the absolute quantification of a series of selected metabolites (valine, lactate, glutamate, glucose, fumarate, tyrosine, histidine, and phenylalanine) over the entire spectral range at different concentration levels (Table 4.4).

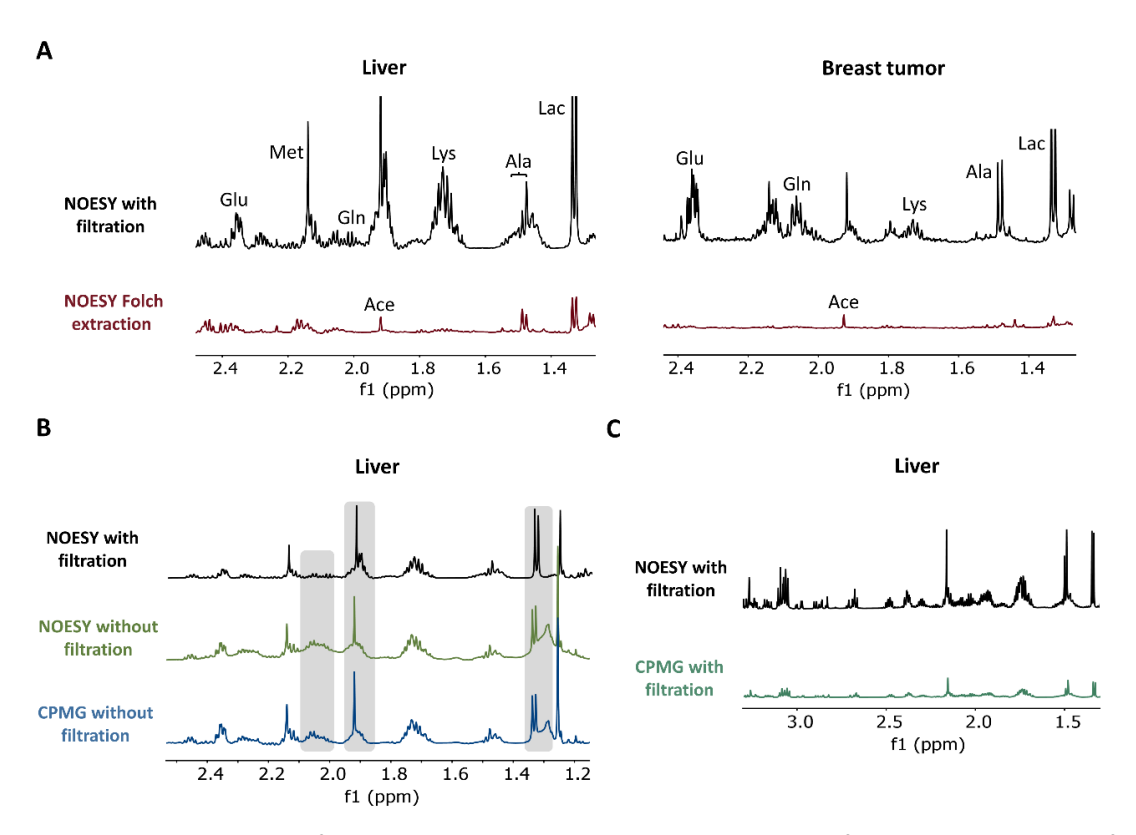


Figure 4.4. Optimization of the metabolite extraction and NMR analysis of mitochondria isolated from tissues. **A)** Aliphatic region of the ¹H-NMR spectra of liver and breast mitochondria obtained following metabolite extraction by the traditional method or the optimized protocol. Some signals could be assigned after the buffer plus filtration extraction while low signals detected by the traditional method. Glu = glutamate; Gln = glutamine; Met = methionine; Lys = lysine; Ala = alanine; Lac = lactate; Ace = acetate. **B)** Comparison between the aliphatic region of the NOESY spectra obtained with and without sample filtration and CPMG experiment without sample filtration. Those regions of the spectra experiencing the most significant changes are highlighted in grey. **C)** Comparison between the aliphatic region of the NOESY spectra obtained with filtration compared to CPMG with filtration.

Next, we evaluated the efficacy of our method to remove protein signals by comparing the obtained spectra with the NMR spectra resulting from a specific NMR experiment that filters out macromolecule signals (Carr–Purcell–Meiboom–Gil, CPMG method) from an unfiltered sample (Figure 4.4B). The CPMG method consists of a ¹H 1D NMR experiment using a relaxation filter that minimizes the intensity of broad signals^{276,277}. Therefore, we compared the CPMG analysis of unfiltered liver mitochondria samples ("CPMG without filtration") with NOESY analysis ("NOESY without filtration" and "NOESY with filtration") to choose the optimal method. The NOESY experiment without filtration showed broad protein signals, altering the baseline of the whole spectrum, while the CPMG analysis showed the partial deletion of these protein signals in specific spectra regions, leaving cleaner metabolite signals (Figure 4.4B). However, the NOESY experiment with filtration gave rise to better-quality spectra with further reduced protein

signals, enabling the correct relative quantification of the metabolite signals. Additionally, the "CPMG with filtration" analysis resulted in signals with lower intensity compared to the "NOESY with filtration" analysis (**Figure 4.4C**). Therefore, metabolite relative quantification relied on acquiring a 1D ¹H spectrum with water suppression by presaturation²⁷¹ and a short NOESY mixing time to improve phase and baseline²⁷². Spectra from ¹H NOESY experiments with the previous settings usually result in reproducible and quantitatively accurate data, which remains crucial for metabolomics analysis²⁷³.

Table 4.4. Quantification of ¹H-NMR spectra of liver and breast tumor mitochondria samples obtained following the optimized "NOESY with filtration" method and the traditional "NOESY Folch extraction" method.

				LIVER			E	BREAST 1	TUMOR	
				NOESY Folch NOESY with extraction filtration		NOESY Fo		NOESY w filtratio	-	
Metabolite	Right limit	Left limit	MEAN (A.U*)	SEM	MEAN (A.U.)	SEM	MEAN (A.U.)	SEM	MEAN (A.U)	SEM
Valine	0.98	1.00	1.941	0.293	7.527	3.113	0.000	0.000	0.806	0.216
Lactate	1.32	1.34	13.933	2.659	18.990	9.491	3.582	0.306	10.266	3.047
Glutamate	2.333	2.38	10.279	2.096	26.709	10.899	2.591	0.262	24.103	6.584
Glucose	5.22	5.25	74.884	29.784	126.480	57.763	0.227	0.079	1.342	0.266
Fumarate	6.52	6.523	0.306	0.088	0.931	0.683	0.055	0.023	0.125	0.039
Tyrosine	6.89	6.92	1.338	0.283	10.785	5.303	0.145	0.073	1.070	0.190
Histidine	7.05	7.07	0.536	0.068	3.955	1.696	0.045	0.032	0.401	0.116
Phenylalanine	7.41	7.45	0.928	0.125	6.282	2.767	0.000	0.000	0.627	0.194

^{*}A.U = arbitrary units

The optimized methodology for NMR analysis of mitochondria isolated from tissues consisted of tissue homogenization using Dounce or Ultra-turrax for soft and hard tissues, respectively, followed by differential centrifugation to obtain the mitochondrial fraction. Metabolite extraction from mitochondria involved dissolving the extract in the NMR buffer, quenching the samples, and filtering them to eliminate broad protein signals. Finally, NMR analysis of mitochondria was carried out using a ¹H NOESY experiment. The NMR spectra obtained from this procedure resulted in good-quality spectra, making this methodology suitable for studying metabolic alterations occurring in mitochondrial diseases.

4.2.1.3. NMR Metabolomic Profiling of Mitochondria Isolated from Tissues

Using mitochondria isolation through differential centrifugation, buffer plus filtration metabolite extraction, and NOESY NMR on healthy (liver, lung, kidney, and brain) and breast tumor tissues from a mouse model allowed us to obtain distinct mitochondrial metabolic profiles. **Figure 4.5** depicts the assigned ¹H-NOESY spectra of mitochondrial extracts isolated

from the various tissue types under investigation. We adjusted the number of required scans for each experiment based on the weight of the mitochondrial extract obtained from each tissue (**Table 4.1**). After carefully analyzing all the spectra, we identified 45 metabolites, including amino acids, organic acids, sugars, lipids, and nucleotides (**Supporting Information 4.1-4.5**). We observed high-quality spectra for breast tumors, kidney, and brain, and an excellent signal-to-noise ratio for the liver, perhaps due to the relatively high mitochondrial content of liver cells (1,000-4,000 per cell)¹². The signal-to-noise ratio was a bit lower for the spectra of lung mitochondria, which may be due to the relatively low mass of this organ³⁷⁹.

Further analysis of the spectra (**Figure 4.5**) provided evidence for the specificity of certain mitochondrial metabolites in specific tissues. For example, we only detected ornithine and maltose in the liver, betaine in the kidney, acetone in the lung, and nicotinurate, N-acetyl aspartate, and 4-aminobutyrate in the brain.

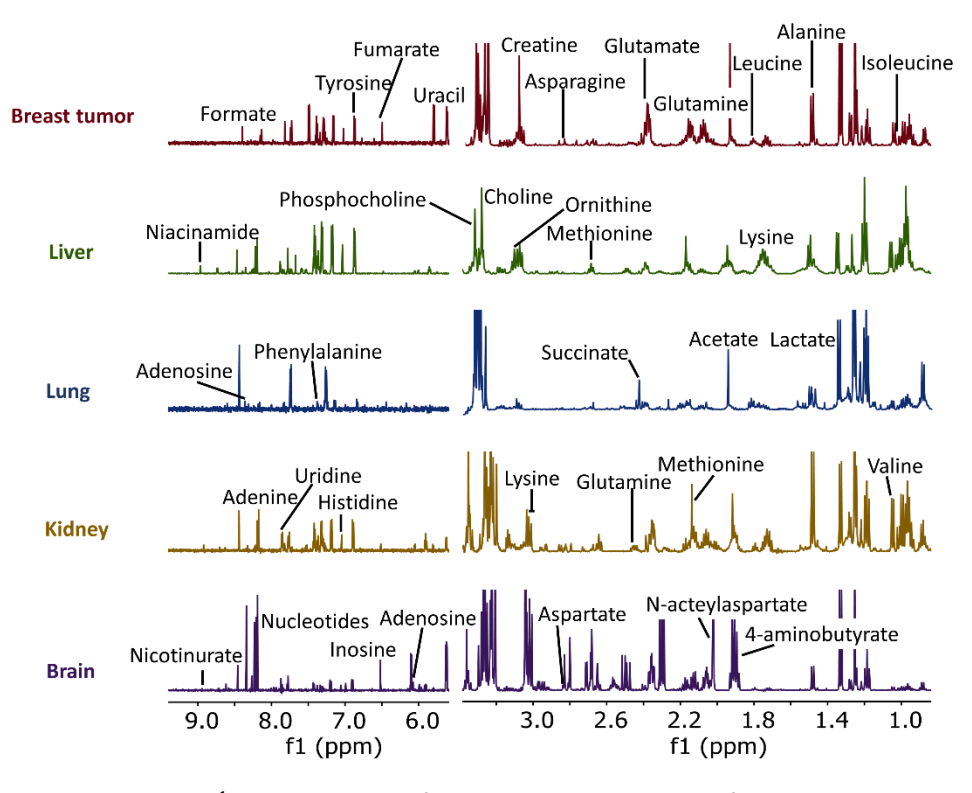


Figure 4.5. Representative ¹H-NOESY spectra from isolated mitochondria from healthy and tumorigenic tissues. The NMR region between 3.3 ppm and 6 ppm corresponding to water and sucrose/mannitol signals present in the isolation buffer were removed to facilitate visual inspection.

We next performed a principal component analysis (PCA) on mice from three independent litters to evaluate potential differences in the composition of tissue-specific mitochondrial metabolomic profiles (**Figure 4.6A**). The resulting score plot demonstrated that samples from the same tissues tended to cluster together, confirming that the mitochondrial metabolomic

profiles systematically differ between organs. Interestingly, the lung exhibited some compositional similarity to breast tumors, while brain and liver samples differed from the remaining tissues.

The loading plot obtained from this analysis (**Figure 4.6B**) facilitated the identification of the mitochondrial metabolites that supported the discrimination between tissues. Amino acids significantly contributed to the differentiation of liver and kidney samples, whereas nucleotides played a crucial role in discriminating brain tissue samples. Lipids and organic acids (such as lactate, citrate, and ascorbate) contributed to separating lung and breast tumor samples. We observed exceptionally high amounts of the organic acid succinate in lung samples, while breast tumor samples contained high amounts of creatine and acetate. Branched amino acids (such as valine, leucine, and isoleucine) and alanine characterized the kidney and breast tumors, while brain samples displayed high levels of aspartate. The non-essential amino acids glutamine and glutamate also contributed to separating breast tumor samples.

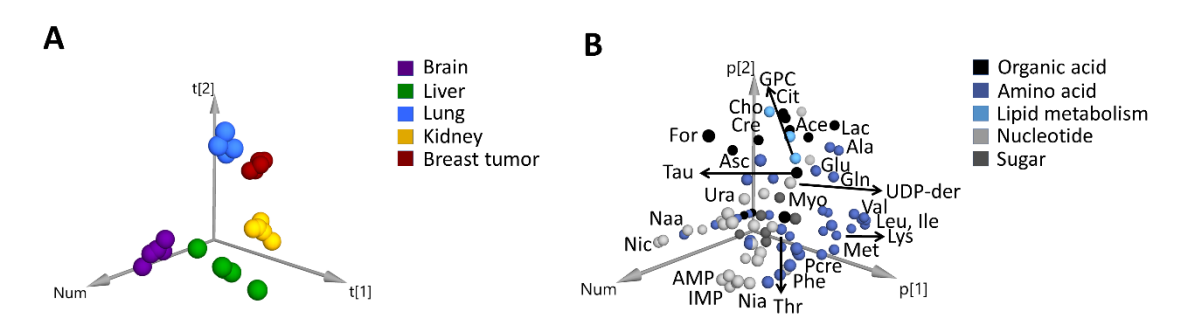


Figure 4.6. Principal component analysis (PCA) of mitochondrial metabolomic profiles obtained from healthy and tumorigenic tissues. **A**) PCA score plot. **B**) PCA loading plot colored according to metabolite chemical nature. Ace=acetate; Ala=alanine; AMP=adenosine monophosphate; Asc = ascorbate; Cre = creatine; Cho = choline; Cit = citrate; For = formate; Gln = glutamine; Glu = glutamate; GPC = glycerophosphocholine; Ile = isoleucine; IMP = inosine monophosphate; Lac = lactate; Leu = leucine; Lys = lysine; Met = methionine; Myo = myo-inositol; Naa = N-acetylaspartate; Nia = niacinamide; Nic = Nicotinurate; Phe = phenylalanine; PCre = phosphocreatine; Suc = succinate; Tau = taurine; Thr = threonine; UDP-der = UDP-derivative; Ura = uracil; Val = valine.

Overall, the application of our optimized methodology to breast tumors, liver, lung, kidney, and brain tissues resulted in a specific metabolic profile of mitochondria due to the differential content of amino acids, organic acids, lipids, sugars, and nucleotides.

4.2.2. Comparing Metabolomic Fingerprints of Whole-Cells and Mitochondrial Extracts Isolated from Breast Tumor, Liver, Kidney, Lungs, and Brain

We next performed a similar analysis using total tissue samples to evaluate the differences between the mitochondrial profile and the profile of the whole-cell (**Figure 4.7**). For that purpose, we followed a similar protocol consisting of tissue homogenization in the NMR buffer instead of the mitochondria isolation buffer, followed by the optimized metabolite extraction. The parameters used for the NMR analysis of whole-cell samples are shown in **Table 4.5**.

Table 4.5. Parameters (homogenizer used, organ units, number of scans for the ¹H-NMR experiment and duration of the ¹H-NMR analysis) for NMR analysis of whole-cells from the different tissues (breast tumor, lung, kidney, liver and brain).

Tissue	Homogenizer	Organ units	¹ H-NMR scans	Duration (minutes)
Breast tumor	Ultra-turrax	1/2	128	15
Lung	Dounce	1	128	15
Kidney	Dounce	1	128	15
Liver	Dounce	1/2	128	15
Brain	Dounce	1/2	128	15

PCA of whole-cell metabolomic profiles showed good separation between tissues (Figure 4.7A), with breast tumor and kidney samples closer than compared to the PCA for mitochondrial metabolomic profiles. The loading plot of whole-cell samples showed similarities to the mitochondrial samples (Figure 4.7B). Nucleotides again contributed to the separation of brain samples, while amino acids differentiated kidney and breast tumor samples from the remaining samples, and the lung displayed high choline content. In contrast to the mitochondrial analysis, several sugar metabolites, such as glucose, maltose, and ribose, separated liver samples from other tissues.

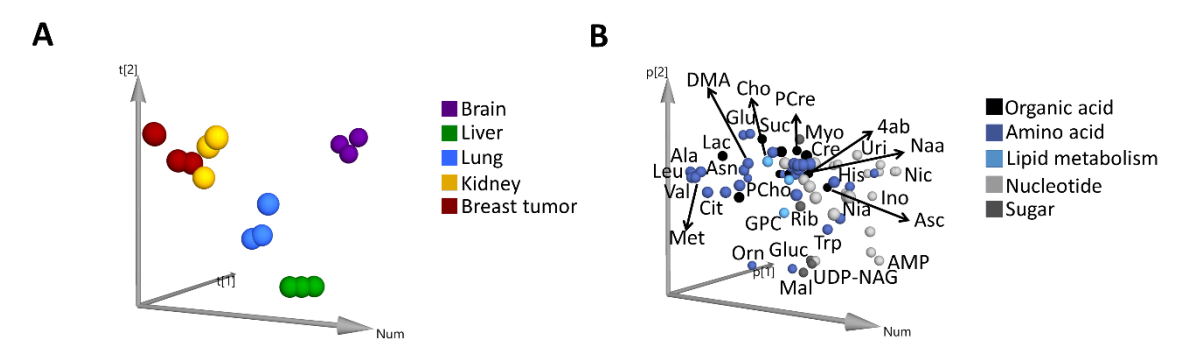


Figure 4.7. Principal component analysis (PCA) of whole-cell metabolomic profiles obtained from healthy and tumorigenic tissues. **A**) PCA score plot. **B**) PCA loading plot colored according to metabolite chemical nature. 4ab = 4-aminobutyrate; Ala = alanine; AMP = adenosine monophosphate; Asc = ascorbate; Asn = asparagine; Cre = creatine; Cho = choline; Cit = citrate; DMA = dimethylamine; Glu = glutamate; Gluc = glucose GPC = glycerophosphocholine; His = histidine; Ile = isoleucine; Ino = Inosine; Lac = lactate; Leu = leucine; Mal = maltose; Met = methionine; Myo = myo-inositol; Naa = N-acetylaspartate; Nia =

niacinamide; Nic = Nicotinurate; Orn = ornithine; Phe = phenylalanine; Pcre = phosphocreatine; Rib = ribose; Suc = succinate; Trp = tryptophan; UDP-NAG = UDP N-acetylglucosamine; Uri = uridine; Val = valine.

We performed a pairwise comparison (mitochondria vs. whole-cell; Supporting Information 4.1-4.5; Figure 4.8A) for each different organ by first generating a validated discriminating orthogonal partial least squares discriminant analysis (OPLS-DA) model and selecting metabolites with variable importance plot (VIP) values > 1, which were then subjected to univariate statistical analysis (Supporting Information 4.6-4.10). Figure 4.8A reports those metabolites displaying the most significant differences in intensity between isolated mitochondrial samples (bottom-dark colored bar) and whole-tissue samples (upper-light colored bar). In general, isolated mitochondria contained elevated levels of glycerophosphocholine (GPC), valine, leucine, isoleucine, lysine, and UDP-derivatives and decreased levels of phosphocreatine, glutamate, glutamine, glutathione (GSH), lactate, myoinositol, and taurine compared to the whole-cell samples (Figure 4.8A). These data agree with the distinct metabolic pathways that take place in the mitochondria and the cytosol (Figure **4.8B**). For example, amino acids can supply tricarboxylic acid (TCA) cycle intermediates in the mitochondria²⁴, while lactate, phosphocreatine, and myo-inositol mainly locate in the cytosol³⁸⁰ ³⁸². Metabolites such as GSH and taurine are synthesized in the cytosol and move into the mitochondria using specific carrier molecules^{383,384}, therefore their levels will change depending on the state of the cell.

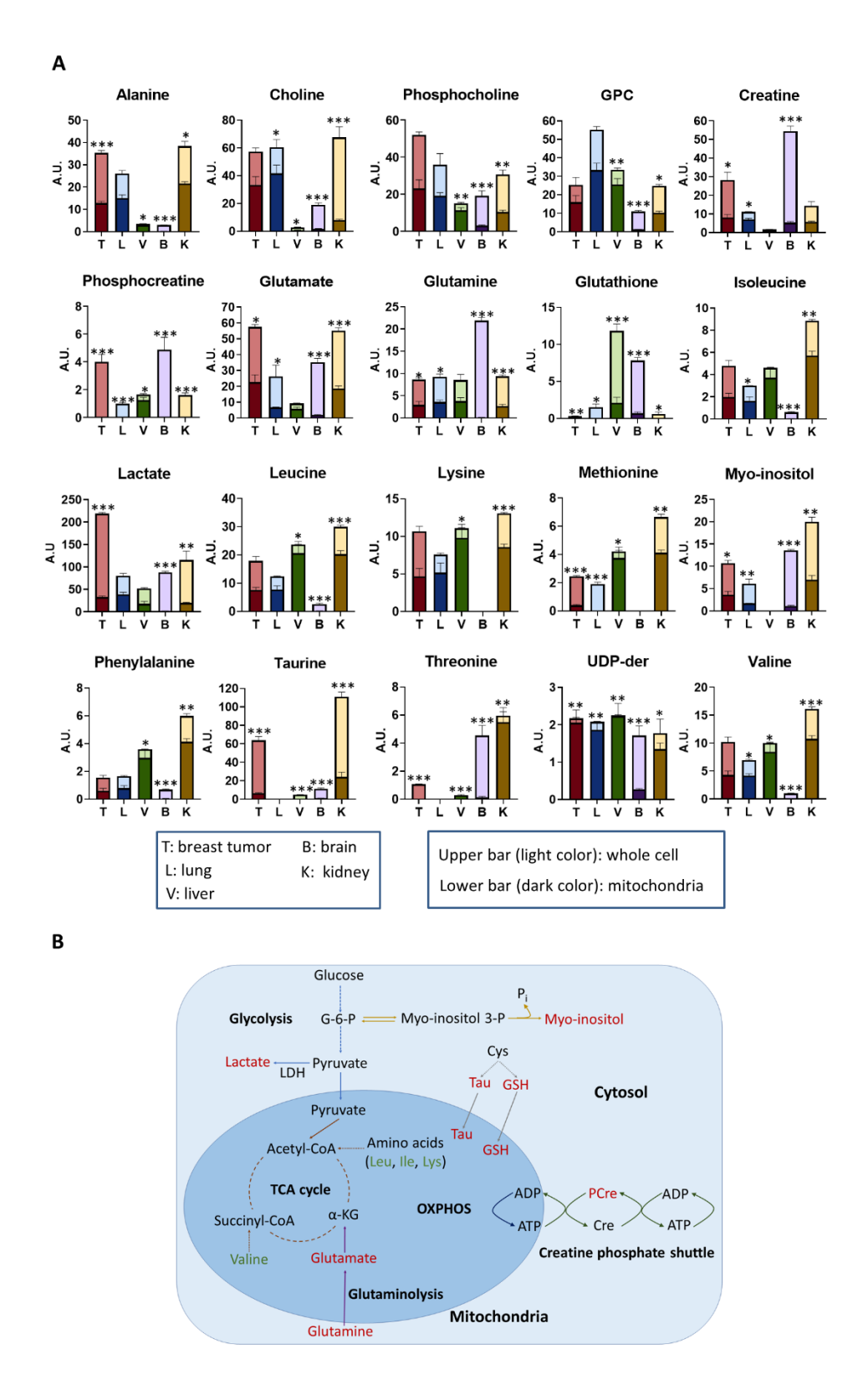


Figure 4.8. Comparative analysis of the metabolomic profile of whole-cells and isolated mitochondria from mouse tissues **A)** Bar graphs corresponding to significantly altered metabolites from whole-cells (top) and mitochondria (bottom) in healthy and tumorigenic tissues. Concentration values normalized to total intensity. Data analysis used a T-test, with data presented as average \pm SEM; * p < 0.05, ** p < 0.01, *** p < 0.001. T = breast tumor; L = lung; V = liver; B = brain; K = kidney; GPC = glycerophosphocholine;

UDP-der = UDP-derivative. **(B)** Summary of metabolic pathways in the mitochondria and cytosol and their interconnections. Mitochondrial metabolites in green are increased, and in red are decreased. α -KG = α -ketoglutarate; ADP = adenosine monophosphate; ATP = adenosine triphosphate; Cre = creatine; Cys = cysteine; G-6-P = glucose-6-phosphate; GSH = glutathione; Ile = Isoleucine; LDH = lactate dehydrogenase; Leu = leucine; Lys=lysine; myo-inositol 3-P = myo-inositol 3-phosphate; PCre = phosphocreatine; Tau = taurine.

Our analysis also supported the discovery that specific metabolites exhibited organ-specific changes. Tumor and brain samples possessed a higher proportion of most metabolites in whole-cells than mitochondria, whereas lung and liver exhibited higher relative quantities of most metabolites in mitochondria (Figure 4.8A). Kidney samples displayed different tendencies in metabolite levels; for example, we observed higher amounts of choline, P-choline, taurine, glutamate, myo-inositol, and lactate in whole-cells but higher amounts of the amino acids alanine, isoleucine, leucine, lysine, methionine, phenylalanine, threonine, and valine and a UDP-derivative in mitochondria (Figure 4.8A). Whole-cell samples from breast tumors showed significantly increased levels of lactate and P-choline compared to other organs (Figure 4.8A), which agrees with the metabolic reprogramming known to occur in tumor cells. Lactate levels tend to increase in tumor cells due to the Warburg effect, in which the final product of anaerobic glycolysis, pyruvate, becomes converted into lactate³⁸⁵. Additionally, choline metabolism also undergoes alterations in tumor cells, including breast cancer cells³⁸⁶.

We also performed an one-way analysis of variance (ANOVA) analysis on mitochondrial and whole-cell samples from all organs to obtain a more detailed description of any differences. The results demonstrated the alteration of 42 metabolites when comparing mitochondria isolated from distinct tissues but only 27 when performing the same analysis in whole-cell samples (**Table 4.6**).

Overall, these data confirm a significant contribution from organelle-specific metabolites and the relevance of the organelle-specific analysis.

Table 4.6. Altered metabolites obtained from ANOVA analysis of mitochondria and whole-cell samples from the different tissues

		Whole-cell			Mitochondria	
Metabolite	P-value	Fisher's LSD	Increased	P-value	Fisher's LSD	Increased
4-aminobutyrate	0.017	B* - K*; B – V*; B – L*; B – T*	В	5E-09	B - K; B - V; B - L; B - T	В
Acetone	-	-	-	2E-08	L - B; L - K; L - V; L - T	L
Alanine	-	-	-	8E-13	K - B; V - B; L - B; T - B; K - V; K - L; K - T; L - V; T - V	K>L>T>V>B
AMP*	0.001	V - B; V - K; V - L; V - T	V	5E-06	V - B; V - K; V - L; V - T	V
Arginine	-	-	-	0.002	K - B; K - V; K - L; K - T	К
Ascorbate	4E-04	B - K; B - V; B - L; B - T; L - K; L - V	B>L>T>V>K	2E-04	B - K; B - V; L - B; L - K; L - V; L - T	L>B>T
Asparagine	2E-04	K - B; K - V; K - L; K - T; L - V; T - V	K>T>L>B>V	4E-10	K - B; V - B; K - V; K - L; K - T; V - L; V - T	K>V>T>B>L
Aspartate	8E-07	B - K; B - V; B - L; B - T; K - V; L - K; L - V; T - V	B>L>T>K>V	0.001	B - V; B - L; K - V; K - L; T - V; T - L	K>B>T>L=V
Choline	0.001	K - B; K - V; K - L; K - T	K	1E-07	L - B; T - B; L - K; T - K; L - V; T - V	L>T>K>B>V
Citrate	1E-05	L - B; T - B; L - K; T - K; L - V; T - V	T>L>K>V=B	2E-06	L - B; T - B; L - K; T - K; L - V; T - V	L>T>K=B=V
Creatine	0.016	B - V; B - T; K - V; K - T; L - V	B>T>K>L>V	2E-04	B - V; T - B; K - V; L - V; T - V	T>L>K>B>V
Dimethylamine	4E-04	K - B; K - V; K - L; K - T	K	-	-	-
Formate	-	-	-	3E-11	K - B; L - B; T - B; L - K; L - V; L - T	L>T>K>V>B
Glucose	-	-	-	0.005	V - B; V - K; V - L; V - T	V
Glutamate	-	-	-	5E-06	K - B; T - B; K - V; K - L; T - V; T - L	T>K>L>V>B
Glutamine	0.004	K - B; V - B; L - B; T - B; K - V	B>K>T>L>V	0.001	K - B; V - B; L - B; T - B	V>L>T>K>B
GSH*	-	-	-	0.002	B - K; B - V; B - L; B - T	V>B>L>T>K
GPC*	-	-	-	5E-07	K - B; V - B; L - B; T - B; V - K; L - K; V - T; L - T	L>V>T>K>B
Histidine	0.012	T - B; T - K; T - V; T - L	T	1E-09	K - B; V - B; K - V; K - L; K - T; V - L; V - T	K>V>B>L=T
Inosine	0.000	B - K; B - V; B - L; B - T; K - V; K - L; K - T	B>K>V>T>L	0.034	K - T; V - T; L - T	L>K>V>B>T
Isoleucine	0.020	K - B; T - B; K - V; K - L	K>T>L>V>B	1E-06	K - B; V - B; L - B; T - B; K - V; K - L; K - T; V - L; V - T	K>V>T>L>B
Lactate	0.007	B - V; B - L; B - T; K - T	T>K>B>L>V	4E-06	K - B; V - B; L - B; T - B; L - K; T - K; L - V; T - V	L>T>K>V>B
Leucine	-	-	-	2E-06	K - B; V - B; L - B; T - B; K - L; K - T; V - L; V - T	V>K>L>T>B
Lysine	1E-06	K - B; L - B; T - B; K - V; K - L; T - K; L - V; T - V; T - L	T>K>L>V>B	5E-05	K - B; V - B; L - B; T - B; K - L; K - T; V - L; V - T	V>K>L>T>B
Maltose	-	-	-	0.002	V - B; V - K; V - L; V - T	V

3E-04	K - B; L - B; T - B; K - V; K - L; T - V; T - L	T>K>L>V>B	4E-08	K - B; V - B; K - L; K - T; V - L; V - T	K>V>L>T>B
1E-05	L - B; T - B; L - K; T - K; L - V; T - V; T - L	K>B>T>L>V	2E-07	K - B; T - B; K - V; K - L; K - T; T - V; T - L	K>T>L>B>V
2E-07	B - K; B - V; B - L; B - T	В	4E-11	B - K; B - V; B - L; B - T	В
1E-05	K - B; V - B; L - B; T - B; K - V; K - L; K - T; T - V	K>T>L>V>B	0.002	K - B; V - B; L - B; K - T; V - T; L - T	L>V>K>B=T
0.019	B - K; B - V; B - L; B - T	В	0.005	B - K; B - V; B - L; B - T	В
0.001	V - B; V - K; V - L; V - T	٧	3E-07	V - B; V - K; V - L; V - T	V
-	-	-	7E-06	K - B; V - B; T - B; K - L; K - T; V - L; V - T	K>V>T>L>B
-	-	-	5E-05	K - B; V - B; L - B; T - B; L - K; T - K; L - V; T - V	T>L>V>K>B
0.007	B - V; B - L; T - K; T - V; T - L	B>T>K>L>V	2E-08	V - B; V - K; V - L; V - T	V
0.003	B - V; B - L; K - V; K - L; T - V	B>K>T>L>V	6E-08	L - B; T - B; L - K; T - K; L - V; T - V; L - T	L>T>K>B>V
5E-07	K - B; B - V; B - L; T - B; K - V; K - L; K - T; T - V; T - L	K>T>B>L=V	4E-11	K - B; T - B; K - V; K - L; T - K; T - V; T - L	T>K>B>V=L
-	-	-	3E-10	K - B; K - V; K - L; K - T	K
-	-	-	2E-04	K - B; V - B; K - L; K - T; V - L; V - T	K>V>L=T=B
3E-04	K - B; T - B; K - V; K - L; T - V; T - L	T>K>L>B>V	3E-05	K - B; V - B; L - B; T - B; K - L; K - T; V - L; V - T	K>V>T>L>B
-	-	-	1E-04	K - B; V - B; L - B; T - B; V - K	V>T>L>K>B
-	-	-	0.001	K - B; T - B; K - L; T - V; T - L	T>K>V>B>L
0.006	B - V; B - L; K - V; K - L	K>B>T>V>L	2E-05	K - B; V - B; T - B; K - L; V - L; T - L	K>V>T>B>L
1E-05	K - B; L - B; T - B; K - V; K - L; T - V; T - L	T>K>L>V>B	5E-07	K - B; V - B; L - B; T - B; K - L; K - T; V - L; V - T	K>V>T>L>B
	1E-05 2E-07 1E-05 0.019 0.001 0.007 0.003 5E-07 - 3E-04 0.006	1E-05	1E-05 L-B; T-B; L-K; T-K; L-V; T-V; T-L K>B>T>L>V 2E-07 B-K; B-V; B-L; B-T B 1E-05 K-B; V-B; L-B; T-B; K-V; K-L; K-T; T-V K>T>L>V>B 0.019 B-K; B-V; B-L; B-T B 0.001 V-B; V-K; V-L; V-T V - - - 0.007 B-V; B-L; T-K; T-V; T-L B>T>K>L>V 0.003 B-V; B-L; K-V; K-L; T-V B>K>T>L>V 5E-07 K-B; B-V; B-L; T-B; K-V; K-L; K-T; T-V; T-L K>T>B>L=V - - - 3E-04 K-B; T-B; K-V; K-L; T-V; T-L T>K>L>B>V - - - 0.006 B-V; B-L; K-V; K-L K>B>T>V>L	1E-05 L-B; T-B; L-K; T-K; L-V; T-V; T-L K>B>T>L>V 2E-07 2E-07 B-K; B-V; B-L; B-T B 4E-11 1E-05 K-B; V-B; L-B; T-B; K-V; K-L; K-T; T-V K>T>L>V>B 0.002 0.019 B-K; B-V; B-L; B-T B 0.005 0.001 V-B; V-K; V-L; V-T V 3E-07 - - 7E-06 - - 5E-05 0.007 B-V; B-L; T-K; T-V; T-L B>T>K>L>V 2E-08 0.003 B-V; B-L; K-V; K-L; T-V B>K>T>L>V 6E-08 5E-07 K-B; B-V; B-L; T-B; K-V; K-L; K-T; T-V; T-L K>T>B>L=V 4E-11 - - 2E-04 3E-04 K-B; T-B; K-V; K-L; T-V; T-L T>K>L>B>V 3E-05 - - 1E-04 - - 0.001 0.006 B-V; B-L; K-V; K-L K>B>T>V>L 2E-05	1E-05 L - B; T - B; L - K; T - K; L - V; T - V; T - L K > B > T > L > V 2E-07 K - B; T - B; K - V; K - L; K - T; T - V; T - L 2E-07 K - B; T - B; K - V; K - L; K - T; T - V; T - L 2E-07 K - B; T - B; K - V; K - L; K - T; T - V; T - L 3E - K; B - V; B - L; B - T B 4E-11 B - K; B - V; B - L; B - T B - K; B - V; B - L; B - T 0.002 K - B; V - B; L - B; K - T; V - T; L - T C 0.001 B - K; B - V; B - L; B - T B - K; B - V; B - L; B - T 0.005 B - K; B - V; B - L; B - T 0.001 V - B; V - K; V - L; V - T V - B; V - K; V - L; V - T 0.001 V - B; V - K; V - L; V - T V - B; V - K; V - L; V - T 0.001 V - B; V - K; V - L; V - T 0.002 K - B; V - B; L - B; K - V; K - L; K - T; V - T; L - T 0.005 B - K; B - V; B - L; B - T 0.005 B - K; B - V; B - L; B - T 0.007 0.001 V - B; V - K; V - L; V - T 0.006 0.006 K - B; V - B; L - B; K - V; K - L; T - V; T - L 0.006 0.007 0.007 0.007 0.007 0.007 0.007 0.007 0.007 0.007 0.007 0.007 0.007 0.007 0.007 0.007 0.007 0.007 0.007 0.007 0.00

P-values, significant different pairwise comparisons obtained by the Fisher's least significant difference (LSD) test, and tissue showing increased levels are presented. *AMP=adenosine monophosphate; UDP-der=uridine diphosphate derivative; GPC=glycerophosphocholine; GSH = glutathione; T=breast tumor; L=lung; V=liver; K=kidney; B=brain

4.2.3. Metabolic Evaluation of Metastasis in Lungs, Liver, and Kidney of a Triple Negative Breast Cancer Mouse Model

We validated our mitochondrial metabolic profiling methodology by analyzing the impact of metastasis on mitochondrial metabolism in target and nontarget tissues using a mouse model of metastatic breast cancer. We induced MDA-MB-231-Luc tumors in five NOD/SCID mice, which we extracted after euthanizing them when tumors reached 1.0 cm³, approximately 42 days after inoculation. Previous work by our group revealed the complete invasion of the lungs at day 35, while the liver did not present signs of metastasis⁷². We compared the metabolic profiles of mitochondria isolated from a breast cancer-related metastatic site (lung) and nonmetastatic sites (liver and kidney) from healthy mice and TNBC model mice.

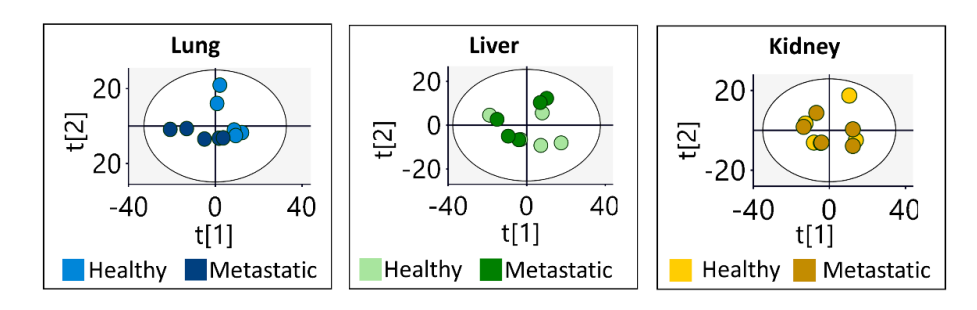


Figure 4.9. PCA score plots of the mitochondrial metabolomic profiles of mitochondria isolated from healthy and metastatic mouse models.

The PCA of mitochondria samples isolated from tissues from healthy and TNBC model mice revealed robust discrimination between healthy and breast cancer model mice for the lungs (metastatic site), a slight discrimination in the liver (nonmetastatic site), and a lack of separation in the kidney (nonmetastatic site) (**Figure 4.9**). The OPLS-DA model analysis of these data provided a similar outcome (**Table 4.7**), providing evidence for the significant impact of breast cancer metastasis on mitochondria in the lung. Notably, we failed to obtain an OPLS-DA model for liver and kidney mitochondria samples where metastasis does not tend to occur in this model. This result agrees with a previous study reporting that MDA-MB-231-Luc tumors produce multiple organ metastases, especially in the lung and axillary lymph nodes⁷². Overall, these data demonstrate the validity of the methodology for metabolic studies of mitochondria.

Table 4.7. Statistical values for the OPLS-DA models obtained from the comparison between mitochondria from healthy and TNBC mouse model tissues

	Lung	Liver	Kidney
R ² Y(cum)*	0.756	-	-
Q²(cum)*	0.614	-	-

CV-ANOVA p-value	0.0355	-	-
Intercept R ^{2*}	0.229	-	-
Intercept Q ² *	-0.652	-	-

*R²Y (cum): goodness of the fit; Q^2 (cum): goodness of the prediction. R^2 Y(cum) and Q^2 (cum) values closer to a value of 1 indicate a reliable model. Intercept R^2 and Q^2 : Cumulative R^2 and Q^2 values obtained from the permutation analysis of 200 permutation tests. Intercept R^2 below 0.3-0.4 and intercept Q^2 below zero demonstrates model validity. CV-ANOVA = cross validates analysis of variance.

We conducted a univariate statistical analysis on mitochondrial metabolites displaying VIP values of >1 in the OPLS-DA model when comparing healthy and metastatic tissues (Supporting Information 4.11). Figure 4.10A shows the boxplot of those mitochondrial metabolites exhibiting significant changes (p < 0.05, except alanine, whose p-value is 0.053) when comparing healthy and metastatic tissues and the corresponding NMR signal. Mitochondria from metastatic lung tissues had higher levels of eight metabolites when compared with healthy tissues (noted by black arrows in Figure 4.10B). Choline and phosphocholine, both exhibiting increased levels (known tumor-associated metabolic alterations³⁸⁶), were found in metastatic lung mitochondria. The RAS (rat sarcoma) oncogenic signaling pathway and the oncogenic transcription factor HIF1 (hypoxia-inducible factor 1) regulate the expression of the CHK1 (checkpoint kinase 1) and CTL1 (choline transporter-like protein 1) choline metabolismassociated enzymes, and their upregulation increases the total choline intracellular concentration³⁸⁷. We also observed an increase in glucose and lactate in metastatic lung mitochondria, which correlates with the impact of the Warburg effect on cancer cells¹⁰⁶. Many cancers, including breast cancer, are characterized by elevated lactate concentrations that can be explained by altered glucose metabolism by different tumor suppressor genes and oncoproteins³⁸⁸. HIF1 upregulates the expression of the GLUT1 (glucose transporter 1) and GLUT2 (glucose transporter 2), and the HK2 (hexokinase 2) that initiates glycolysis³⁸⁸. Despite the relevance of glucose and lactate in tumor cell metabolism, metastatic liver mitochondria did not display alterations to these metabolites, which may reflect this tissue's lower degree of metastasis. Creatine, whose level increases in metastatic lung mitochondria, plays an essential role in cancer cells by maintaining energy homeostasis. Furthermore, increased creatine kinase levels occur in distinct cancers³³⁵. Metastatic lung mitochondria also had increased levels of glutamate, alanine, and methionine, supporting the theory of dysregulated amino acid metabolism in cancer cells²⁷⁹. The increased levels of glutamate could also relate to tumorassociated increases in glutaminolysis³⁸⁹, which occurs when the MYC oncogene prompts the overexpression of the SLC1A5 (solute carrier family 1 member 5) glutamine transporter and upregulates the glutaminase enzyme (Figure 4.10B).

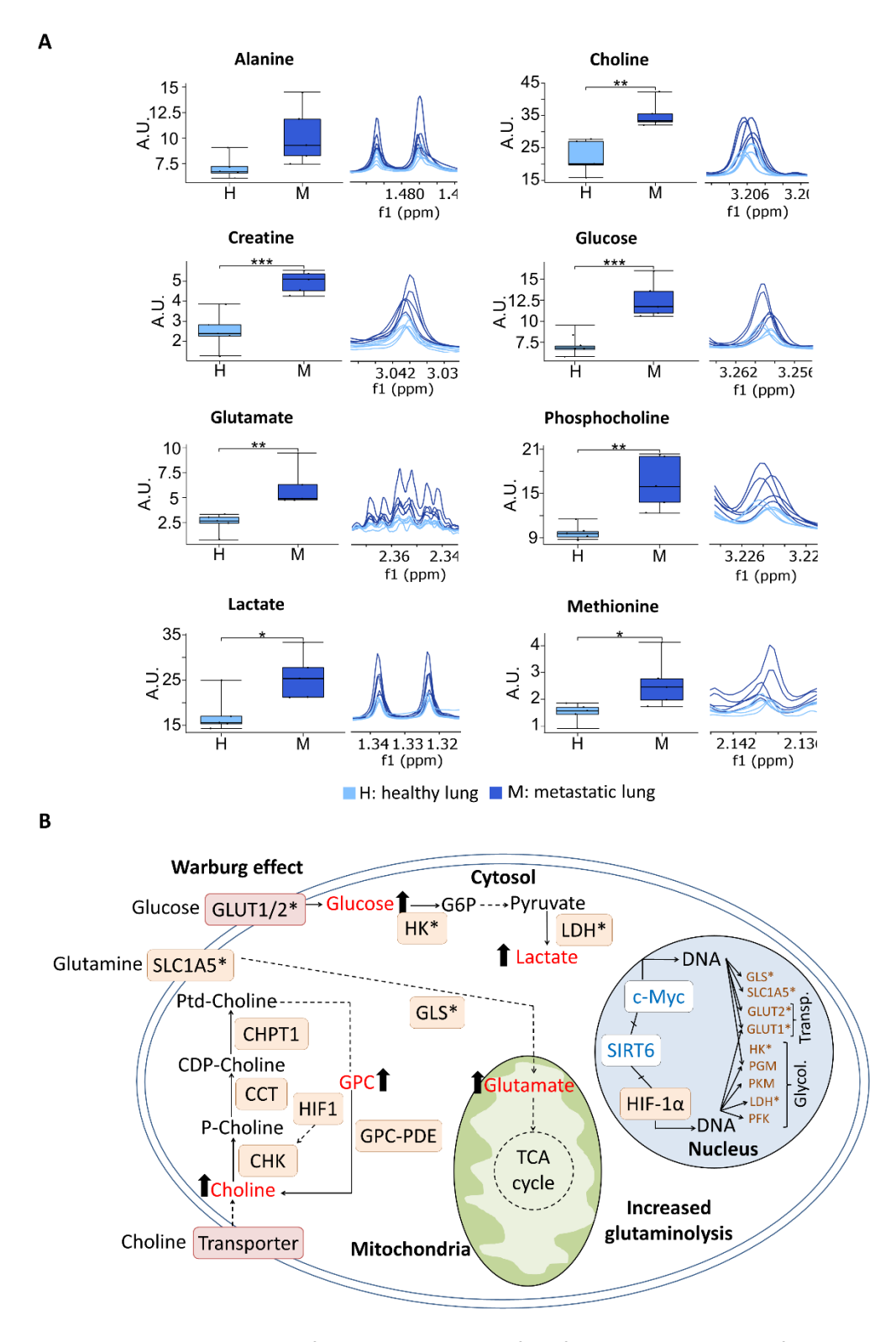


Figure 4.10. Comparative analysis of the metabolomic profile of mitochondria isolated from healthy and metastatic lungs. A) Mitochondrial metabolite signals and boxplots of relevant metabolites for group discrimination. Data analysis used a T-test, with data presented as average \pm SEM; *p < 0.05, **p < 0.01, ***p < 0.001. B) Choline and glutamine metabolic pathways and the Warburg effect in metastatic lungs. CHK = choline kinase; CHPT1 = choline phosphotransferase 1; GLS = glutaminase; GLUT1/2 = glucose transporter 1/2; GPC = glycerophosphocholine; HK = hexokinase; HIF1- α = hypoxia-inducible factor 1- α ;

LDH = lactate dehydrogenase; PDE = phosphodiesterase; PFK = phosphofructokinase; PGM = phosphoglucomutase; PKM = Pyruvate kinase isozymes M1/M2; SIRT6 = Sirtuin 6; SLC1A5 = solute carrier family 1 member 5

To further test the relevance of our method, we performed a similar comparison, assessing the whole-cell rather than mitochondria (**Table 4.8 and 4.9**). Interestingly, in this analysis, we failed to detect alterations in alanine, lactate, phosphocholine, and methionine in the metastatic lung. Choline and glutamate showed the same trend in both whole-cell and mitochondria of metastatic lung samples, while other metabolites (GPC, myo-inositol, leucine, lysine, and valine) displayed significant changes only in whole-cell analysis.

Table 4.8. Statistical values for the OPLS-DA models obtained from the comparison between whole-cells from healthy and TNBC mouse model tissues

	Lung	Liver	Kidney
R²Y(cum)*	0.934	0.853	0.973
Q²(cum)*	0.866	0.676	0.735
CV-ANOVA p-value	0.0014	0.444	0.370
Intercept R ² *	0.425	0.781	0.849
Intercept Q ^{2*}	-0.695	-0.148	-0.037

^{*}R²Y (cum): goodness of the fit; Q²(cum): goodness of the prediction. R²Y(cum) and \overline{Q}^2 (cum) values closer to a value of 1 indicate a reliable model. Intercept R² and Q²: Cumulative R² and Q² values obtained from the permutation analysis of 200 permutation tests. Intercept R² below 0.3-0.4 and intercept Q² below zero demonstrates model validity. CV-ANOVA = cross validates analysis of variance.

Table 4.9. Comparative analysis of the metabolomic profile of whole-cells from healthy and metastatic lungs

	Heal	thy	Metastatic		Healthy vs. Metastatic	
Metabolite	Mean	SEM	Mean	SEM	P-value	VIP value
GPC*	40.794	1.326	54.576	3.438	0.011	3.676
Glutamate	20.524	0.562	29.359	1.373	0.001	2.955
Creatine	13.013	1.053	6.609	0.079	8E-06	2.430
Choline	4.602	0.165	6.485	0.274	4E-04	1.409
Glucose	1.948	0.123	0.621	0.069	6E-07	1.167
Myo-inositol	3.975	0.138	5.244	0.158	2E-04	1.134
Leucine	5.803	0.222	4.492	0.119	1E-04	1.128
Lysine	4.875	0.206	3.765	0.184	0.002	1.008
Valine	3.983	0.149	2.960	0.106	1E-04	1.001

^{*}GPC=glycerophosphocholine

These findings support the hypothesis that mitochondrial and whole-cell metabolite analysis provides differing but complementary information, further evidence for the utility of organelle-specific analysis in exploring the mechanisms controlling metastasis.

4.3. CONCLUSIONS

In this chapter, we describe an optimized methodology to study the metabolomic profiles of mitochondria isolated from mouse tissues through NMR spectroscopy. The procedure involves (i) isolation of mitochondria through differential centrifugation, (ii) extraction of metabolites using an optimized protocol based on quenching, and (iii) NMR analysis. After confirming the presence of mitochondria in the isolated fractions by western blotting, we compared the metabolomic contents of whole-cells and mitochondria in healthy and tumorigenic mouse tissues. This comparison provided evidence of significant changes in the levels of many metabolites; furthermore, we observed specific changes occurring in the mitochondria that were not observed in the whole-cell analysis.

Our proposed methodology is relatively fast and straightforward, avoids solvent evaporation to prevent metabolite loss and degradation, and does not destroy samples, which allows further analysis with complementary analytical techniques (e.g., MS). Moreover, our methodology allows direct relative quantification of metabolite levels without a calibration curve. Overall, robust and reproducible metabolic data can be obtained in only a few hours.

Our methodology can also be applied to tissue samples obtained from animal models or human biopsies and could provide helpful information for clinical and preclinical research. Additionally, our methodology may find use in research projects focused on identifying biomarkers in diseases that impact mitochondrial metabolism, such as Alzheimer's disease, Parkinson's disease, or diabetes, using small muscle or fat biopsies before the manifestation of clinical symptoms.

Given the findings observed when comparing mitochondria isolated from tissues of healthy and metastatic breast cancer mouse models, we also hope that our methodology will play an essential role in cancer research. The increase in certain metabolite levels in lung mitochondria associated with tumorigenesis/metastasis suggests that components of the associated metabolic pathways could serve as therapeutic targets. Therefore, mitochondria constitute promising targets for developing novel anticancer agents, and this method could also provide critical information regarding the impact of novel anticancer drugs on mitochondrial metabolism.

4.4. MATERIALS AND METHODS

4.4.1. Materials

Bovine serum albumin (BSA) and tris(hydroxymethyl)aminomethane hydrochloride (Tris-HCl) were purchased from Sigma-Aldrich (St. Louis, USA). D-mannitol and sucrose were purchased from Merck Millipore (Burlington, USA). Deuterium oxide (D₂O) and 3-(trimethylsilyl) propionic acid d4 sodium salt (TSP) were obtained from Eurisotop (Tewksbury, USA). Monobasic sodium phosphate (NaH₂PO₄) was acquired from Acros Organics (Geel, Belgium). Milli-Q water was used for all experiments (Millipore; Burlington, USA). Radioimmunoprecipitation assay (RIPA) buffer was prepared by the authors. Immunodeficient NOD/SCID mice (NOD.CB17-Prkdc^{scid}/NCrHsd) were obtained from Envigo Laboratories Inc. (Spain).

A 15 mL Dounce tissue homogenizer and Ultra-turrax dispersing machine were purchased from Wheaton (Millville, USA) and IKA (Staufen, Germany), respectively. 3K centrifugal filters were acquired from Merck Millipore (Burlington, USA). 5 mm NMR tubes and 5 mm NMR tube caps for SampleJet were obtained from Deutero (Kastellaun, Germany) and Bruker (Billerica, USA), respectively.

4.4.2. Biological material

Immunodeficient NOD/SCID mice (NOD.CB17-Prkdc^{scid}/NCrHsd) were obtained from Envigo Laboratories Inc. (Spain), and sixteen female mice were used for this study. The animal experiments were performed following the European Communities Council Directive (86/609/ECC) guidelines and the Spanish Royal Decree 1201/2005, and the procedures were approved by the Institutional Animal Care and Use Committee. The mice were maintained in a specific pathogen-free facility under environmental control, and food pellets and water were provided *ad-libitum* during the experiment. The mice were evaluated twice a week to ensure their well-being.

Eight mice (four mice for whole-cell analysis and four mice for mitochondria analysis) were induced with MDA-MB-231-Luc tumors by subdermal inoculation of $3x10^6$ MDA-MB-231 TNBC cells transduced with a luciferase expression plasmid suspended in $100 \,\mu$ l of Matrigel (20%) into the second left mammary fat pad following inhalatory anesthesia (3% sevoflurane in 100% oxygen). Tumor development did not cause any significant animal weight loss or pain-related behavior, as shown in **Figure 4.11**.

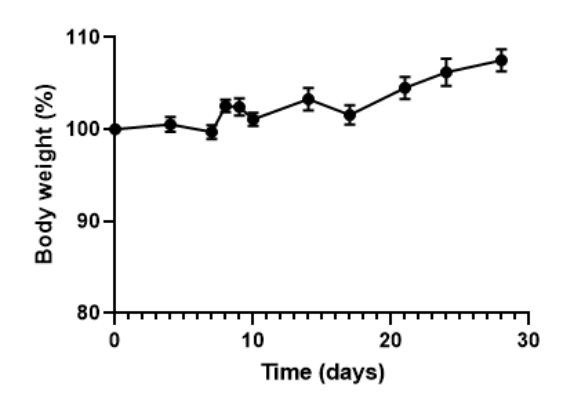


Figure 4.11. Percentage change in NOD/SCID mice body weight (%) following the induction of tumorigenesis. Tumors were induced via the inoculation of MDA-MB-231-Luc cells into the second left mammary fat pad. Data is represented as average ± SEM (n=3).

The mice were euthanized under a CO₂ atmosphere when tumors reached 1.0 cm³ (around 42 days after inoculation). The livers, lungs, kidneys, brains, and breast tumors were extracted, washed with 1X phosphate-buffered saline (PBS; 137 mM NaCl, 2.7 mM KCl, 10 mM Na₂HPO₄, 1.8 mM KH₂PO₄, pH 7.4), and snap-frozen in liquid nitrogen for subsequent metabolic analysis.

4.4.3. Mitochondrial isolation from tissues

The isolation procedure was performed at 4°C to preserve mitochondria and avoid significant metabolic alterations (see **Figure 4.1**). Organs were removed from storage at -80°C and kept on ice. After weighing each sample, the tissues were homogenized in Buffer 1 (220 mM mannitol, 70 mM sucrose, 10 mM Tris-HCl solution, and 0.5 mg/mL BSA in MilliQ water, pH 7.4) using a Dounce or Ultra-turrax homogenizer. The homogenization of soft tissues was performed using two volumes (1:2, tissue:buffer) of Buffer 1 and seventy strokes with a Dounce homogenizer. The homogenate was diluted to obtain a 10% (v/v) homogenate solution. Due to its fibrous nature, the breast tumor tissue was homogenized in twenty volumes (1:20, tissue:buffer) of Buffer 1 with the Ultra-turrax homogenizer used at 12,000 rpm for precisely 10 seconds. **Table 4.1** describes various parameters, including tissue type, amount of tissue used, the homogenizer used, and the number of scans and duration of the NMR experiment.

Each homogenate was centrifuged at 560g for 15 minutes at 4°C. Next, the supernatant containing mitochondria, cytosol, and membranes was transferred to a new tube while the nuclear pellet was stored at -80°C for further experiments. Critical step = As the nuclear pellet can easily become resuspended in the supernatant, sudden movements should be avoided, and the supernatant should be collected carefully. The supernatant was then centrifuged at 7,000g for 15 minutes at 4°C. An aliquot (1 mL) of the supernatant (cytosol and membranes) was stored

at -80°C for further experiments. The mitochondrial pellet was then washed twice with Buffer 1 (volume approximately equal to the weight of the initial tissue) and centrifuged at 7,000g for 15 minutes at 4°C. Mitochondrial pellets were then weighed and stored at -80°C.

4.4.4. Western Blotting for the confirmation of mitochondria isolation from tissues

The isolation of mitochondria was confirmed by Western blotting. Mitochondrial pellets were resuspended in RIPA buffer (25 μ L/10 mg; 150 mM NaCl, 50 mM 2-Amino-2-(hydroxymethyl)-1,3-propanediol (Tris Base), 1% sodium dodcyl sulfate (SDS), 0.5% sodium deoxycholate, and 1% Nonidet P-40 (NP40), pH 8) containing a protease inhibitor cocktail (25x). Cytosolic samples were prepared by adding 10 μ L of a protease inhibitor cocktail (25x) to 250 μ L of the cytosolic fraction. After vortexing, the samples were centrifuged at 13,200 rpm for 15 minutes at 4°C, and the supernatant was kept for protein quantification via the Bradford Assay. Twenty micrograms of protein extract were used to assess the expression of mitochondrial and cytosolic markers. **Table 4.12** reports the primary and secondary antibodies used.

Mitochondrial pellets were resuspended in RIPA buffer (25 μL/10 mg; 150 mM NaCl, 50 mM Tris Base, 1% SDS, 0.5% sodium deoxycholate, and 1% NP40, pH 8) containing a 25x protease inhibitor cocktail. Cytosolic samples were prepared by adding 10 μL of a protease inhibitor cocktail (25x) to 250 μL of the cytosolic fraction. Thirty microliters of samples containing 20 μg protein were prepared with 4x loading buffer (130 mM Tris-HCl pH 8, 20% (v/v) glycerol, 4.6% (w/v) SDS, 0.02% bromophenol blue, 2% DTT) and MilliQ water. Proteins were denatured using a thermoblock at 95°C for 7 min, and samples were briefly spun down in a microcentrifuge at 13,000 rpm. Samples and 8 μL of protein marker were loaded into a 10-well, 1.5 mm-thick, 12% bis-Acrylamide (w/v) gel, and proteins were separated by electrophoresis in running buffer (25 mM Tris, 192 mM glycine, 20% (w/v) SDS) at 120 V. Subsequently, proteins were transferred to a nitrocellulose membrane at 400 mA for 2 h. The membrane was blocked with 5% (w/v) milk in DPBS-Tween 20 (0.05%, v/v) for 2 h. After removing the blocking solution, the membranes were incubated in 10 mL of primary antibody diluted in 5% (w/v) milk in DPBS-Tween 20 (0.05%, v/v) (Table 4.12) overnight at 4ºC with agitation. The membranes were washed three times with 0.05% (v/v) DPBS-Tween 20 for 10 min at room temperature with agitation. Then, the membranes were incubated by shaking with secondary anti-rabbit or anti-mouse antibodies diluted in 5% (w/v) milk in DPBS-Tween 20 (Table 4.12) for 1 h at room temperature. Following that, the membranes were washed three times with 0.05% (v/v) DPBS-Tween 20 for 10 min at room temperature with agitation. The ECLTM Prime Western Blotting Detection Reagent was used to detect protein signals. Substrates A and B were mixed in a 1:1 ratio and added to the membranes. Any excess mixture was removed, and the membranes were placed in an Amersham HypercassetteTM with an Amersham HyperfilmTM MP. An AGFA Curix 60 X-ray film processor was used to visualize the protein signals. Protein quantification ($n\geq 3$) was performed by densitometry analysis using the ImageJ software, and a β -actin loading control was used to normalize protein levels, except for liver mitochondrial samples where VDAC was used as loading control. The protein quantification graph was plotted in GraphPad Prism (version 9.5.0, GraphPad Software Inc., USA), and t-test analysis was performed in Excel. Comparisons with p<0.05 were considered statistically significant.

Table 4.12. Primary and secondary antibodies used for Western blotting

Antigen	Supplier	Host	Mw (kDa)	Dilution	Subcellular location			
Primary antibodies								
Cytochrome c	Cell Sinaling, 4280	Rabbit	12	1:1,000	Mitochondria			
HSP90	Santa Cruz Biotechnology, sc-131119	Mouse	90	1:10,000	Cytoplasm			
β-actin	Santa Cruz Biotechnology, sc-8432	Mouse	42	1:10,000	Cytoplasm, mitochondria			
VDAC	Abcam, ab15895	Rabbit	31	1:1,000	Mitochondria			
Secondary antibodies								
Anti-rabbit	Sigma-Aldrich, A6154	Goat	-	1:3,000-1:5,000	-			
Anti-mouse	Sigma-Aldrich, A9044	Rabbit	-	1:5,000- 1:30,000	-			

^{*}HSP90 = Heat shock protein 90; Mw = molecular weight; VDAC = voltage-dependent anion channel

4.4.5. Metabolite extraction procedure and NMR sample preparation

4.4.5.1. Metabolite extraction from tissues

Tissue samples were placed on ice and allowed to thaw for 5 min. The amount of tissue used and the parameters used for the NMR analysis of whole-tissue samples are shown in **Table 4.5**. To the tissue samples, 700 μ L of NMR buffer (20 mM Na₂HPO₄ pH 7.4, 20 μ M TSP in D₂O) was added, followed by homogenization with Dounce/Ultra-turrax, vortexing and incubation in an ultrasonic water bath at room temperature for 5 min. The samples were then subjected to a freeze-thaw cycle by incubating in liquid nitrogen for 1 min and thawing in a temperate water bath. This freeze-thaw cycle was repeated twice to disrupt membranes and facilitate metabolite extraction.

After centrifugation at 10,000 g for 20 min at 4° C, the supernatant was transferred to a new tube. To remove protein signals from the spectra, the samples were filtered using 3 kDa centrifugal filters. The filters were washed three times with 400 μ L of MilliQ water and once with 400 μ L of D₂O, followed by centrifugation at 14,000 g for 30 min to dry. Subsequently, the samples were filtered by centrifugation at 14,000 g for 45 min at 4°C, and the filtrate was transferred to a new tube for subsequent NMR analysis.

For NMR analysis, 550 μL of the filtered sample was transferred to a 5 mm NMR tube.

4.4.5.2. Metabolite extraction from mitochondria isolated from tissues

Frozen mitochondrial pellets were placed on ice and allowed to thaw for 5 minutes. Then, 700 μL of Buffer 2 (20 mM Na₂HPO₄ and 20 μ M TSP [used as an internal standard for NMR analysis) in D₂O, pH 7.4) was added, and the suspension was homogenized with a vortex, resuspended with a pipette, and subjected to ultrasound by submerging the tubes in an ultrasonic bath for 5 minutes. Samples were placed in liquid nitrogen for 1 minute to break cell membranes and then allowed to thaw in a temperate water bath. This step was repeated two more times (three cycles in total). The suspension was centrifuged at 10,000 g for 15 minutes at 4°C, and the supernatant was transferred to 1.5 mL tubes.

Before NMR analysis, samples were passed through a 3 KDa centrifugal filter. The filter was washed three times with 400 μ L of Milli-Q water and once with 400 μ L of D2O by centrifuging at 14,000 g for 15 minutes at room temperature. Samples were then filtered by centrifugation at 14,000 g for 40 minutes at 4°C. Critical step=If the filter becomes clogged, transfer the sample to a fresh, washed filter. Finally, 550 μ L of the samples were transferred to a 5 mm NMR tube.

4.4.6. Metabolomic analysis by NMR spectroscopy

4.4.6.1. NMR spectra acquisition

NMR spectra were acquired using a Bruker AVII-600MHz NMR spectrometer equipped with a 5 mm TCI cryoprobe. The temperature was set to 300 K (27 $^{\circ}$ C), and a standard reference sample consisting of 2 mM sucrose, 0.5 mM sodium trimethylsilylpropanesulfonate (DSS), and 2 mM NaN₃ in H₂O/D₂O was used to ensure spectral resolution and water suppression.

¹H 1D spectra were obtained using the NOESY pulse sequence, with a 4 s relaxation delay between free induction decay (FID) readings and a water presaturation pulse of 25 Hz to minimize the water signal. For the whole-tissue samples, 128 scans (15 minutes) were acquired, while 640 scans (1 hour) were performed for the analysis of kidney, liver and brain mitochondrial fractions and 1280 scans (2 hours) for the analysis of breast tumor and lung mitochondrial samples. The difference in the number of scans is due to the low levels of metabolites in the mitochondria samples, which require more time to acquire high-quality spectra. Moreover, different scans were used for the analysis of mitochondrial samples isolated form the different tissues due to the different mitochondrial content of tissues.

The CPMG experiment was conducted with 256 scans, 128 loops for filter T2 (L4), and a fixed echo time of 0.0003 s to eliminate J - modulation effects (D20).

4.4.6.2. NMR data processing

For data processing, FID values were multiplied by an exponential function with a 0.5 Hz line broadening factor and Fourier transformed in Topspin 3.2 (Bruker GmbH, Karlsruhe, Germany). Spectra were further processed in MestreNova (MestreLab Research, Santiago de Compostela, Spain). The spectra were referenced to the internal standard (TSP), and phase correction was performed manually. Baseline correction was applied using automatic Whittaker smoother correction for whole-cell samples, while manual optimization of the Whittaker smoother correction was applied for mitochondria spectra, taking into account significant sucrose and mannitol signals from the isolation buffer that can distort the baseline.

4.4.6.3. Metabolite identification and quantification

Metabolite signals were identified after processing the NMR spectra. An Excel file was created to assign the sample type for each type of tissue (**Supporting Information 4.1-4.5**) using publicly available information from the Human Metabolome Database (HMDB)³⁹⁰ and the Chenomx profiler (Chenomx Inc. Edmonton, Canada), as well as information available regarding the metabolomic profile of the total tissue (liver³⁹¹, brain³⁹², lung³⁹³, kidney³⁹¹, breast tissue³⁹¹). The signals were integrated using the "Predefined sum" calculation method in MestreNova software, with the assignment table uploaded in text file format. The integral values were saved as 1D Integral Series (.txt) and opened in Excel.

Data were normalized using the total area method, where each integral value was divided by the sum of all integrals in the sample, excluding signals originating from the isolation buffer and the NMR buffer. This method preserved the relative intensities of the signals in each sample.

For the quantitative comparison of different procedures, a series of selected metabolites were integrated, and the integrals were quantified relative to the internal standard (TSP) to obtain absolute quantification.

4.4.6.4. Multivariate and univariate analysis

Statistical analyses followed standard methods for multivariate and univariate analysis of metabolomic data³⁹⁴. Unsupervised PCA and supervised OPLS-DA models were obtained using the SIMCA-P 16 software. Univariate analysis was performed using t-tests and ANOVA in Excel and the MetaboAnalyst 5.0 web-based platform²¹⁷. Graphs were presented as average ± SEM

from three-five assays and plotted using GraphPad Prism (version 9.5.0, GraphPad Software Inc., USA). Comparisons with p < 0.05 were considered statistically significant.

GENERAL DISCUSSION

Their inherent metabolic and energetic properties and crosstalk between the cytosol and nuclei make mitochondria a critical organelle regarding normal cell function⁹; therefore, the pathology of many diseases, including cancer, includes mitochondrial dysfunction⁴⁶. Researchers have taken advantage of unique features of cancer cell mitochondria, such as increased membrane potential and levels of reactive oxygen species (ROS), to develop targeted therapeutics¹⁷⁷. Many anticancer drugs specifically affect mitochondrial metabolism (such as palbociclib³⁹⁵ and methotrexate³⁹⁶) or inherently target mitochondria (such as lonidamine¹⁸⁵ and α -tocopherol¹⁷⁷). Furthermore, many nanomedicines that support the transport of small drugs, antibodies, or other bioactive agents into cancer cells specifically target the mitochondria^{177,397}.

Developing anti-tumor nanomedicines requires techniques that evaluate their impact on mitochondrial status. Alterations in mitochondrial bioenergetics and oxidative phosphorylation (OXPHOS) represent the most commonly analyzed parameters for evaluating the impact of mitochondrially targeted nanomedicine. Said alterations include mitochondrial respiration features (e.g., oxygen generation and consumption analysis, ROS production, and ATP synthesis)^{4,5} and mitochondrial membrane potential³⁷, while mitochondrial morphology⁸ and protein expression³⁹⁸ represent less often analyzed parameters. Surprisingly, the impact of cancer-targeted nanomedicines on mitochondrial metabolism remains mostly unassessed. Given the strong association of mitochondrial metabolism with mitochondrial respiration functioning and its crucial role in cell function²¹, evaluating mitochondrial metabolism could contribute to understanding a given nanomedicine's mechanism of action.

The scientific community has shown awareness of the importance of evaluating mitochondrial metabolism; recently, studies have implemented metabolomic methodologies to evaluate mitochondrial metabolism in cells/tissues. Mass spectrometry (MS) initially represented the preferred option for such analyses due to its high sensitivity; thus, several MS metabolomic methodologies have been applied to different research studies^{230,231,250,399,233,234,236,238–242}. NMR provides a valuable and complementary technique to MS due to robustness, non-destructive and rapid sample analysis, and the ability to detect all metabolites in a single spectrum, providing a reproducible fingerprint. Of note, the developed NMR-based approaches for mitochondrial analysis generally quantified a low number of metabolites^{230,231} or required expensive metabolic isotopes such as ¹³C-glucose and ¹³C-glutamine^{232,243–245}; therefore, the field requires novel NMR-based mitochondria metabolomic methods.

In the context of improving the design of mitochondrial-targeted nanomedicines and the need for tools to evaluate mitochondrial metabolism, we aimed to develop an NMR metabolomic methodology to evaluate the impact of mitochondrially-targeted nanomedicines on mitochondrial metabolism of cells/tissues. Given the low amount of mitochondrial content compared to whole-cell samples and low NMR sensitivity, a mitochondrial metabolomic methodology focused on obtaining enriched mitochondrial fractions and avoiding sample losses may help to improve NMR outcomes.

First, we optimized a mitochondrial metabolomic methodology in triple-negative breast cancer (TNBC) cells (**Chapter II**). While innovative methods for mitochondria isolation (e.g., density gradient centrifugation²⁴⁹, affinity purification^{231,237}, nonaqueous fractionation²³⁹) have been described, we selected cell homogenization followed by differential centrifugation as the isolation method for our mitochondrial metabolomic analysis. The method's simplicity, rapid isolation (1-1.5 h) of a highly enriched mitochondrial fraction, and the requirement for inexpensive material and equipment⁴⁰⁰ make differential centrifugation the preferred method in mitochondrial metabolomic studies.

Evaluation of lactate dehydrogenase (LDH) activity and the number of lysed cells in the cell homogenate helped to optimize the cell disruption protocol. Additionally, the assessment of the succinate dehydrogenase (SDH) activity and the expression of mitochondrial proteins by Western Blotting confirmed a suitable enrichment of the mitochondrial fraction after differential centrifugation, which remains critical to the specific analysis of the mitochondrial metabolomic profile.

Developing a suitable metabolite extraction method is crucial in avoiding metabolite loss in low-content samples such as mitochondria. Single-phase methods have advantages over biphasic methods⁴⁰¹ (e.g., Folch extraction²⁶⁶ and Bligh and Dyer extraction²⁶⁸). Folch and Bligh and Dyer extraction - based on the use of chloroform, methanol, and water to obtain aqueous and organic metabolite phases - requires phase separation, which can lead to metabolite loss and solvent evaporation, which can prompt volatile metabolite evaporation⁴⁰¹. Monophasic extraction can overcome these disadvantages, as they do not require phase separation, and the NMR-compatible buffers avoid metabolite loss; moreover, single-phase methods involve simpler, more rapid processes and less toxic chemicals⁴⁰¹.

Based on this rationale, we selected a monophasic extraction procedure using NMR buffer (phosphate buffer in D_2O), membrane disruption through liquid nitrogen quenching, and sonication for metabolite extraction from mitochondria. Sample sonication and quenching in liquid nitrogen provide reproducible membrane breakage and metabolite recovery^{269,270}, and we confirmed higher metabolite levels obtained through sonication compared to the traditional

Folch method. Proteins in samples appear in the NMR spectra as broad signals that overlap with the signals of interest and disrupt baseline⁴⁰²; their precipitation typically involves methanol/chloroform in conventional Folch²⁶⁶ and Bligh and Dyer extraction²⁶⁸ methods. Using aqueous extraction buffers instead makes protein ultrafiltration the unique method available for protein elimination⁴⁰². Our results demonstrated optimal NMR outcomes using protein elimination through physical ultrafiltration and nuclear overhauser effect spectroscopy (NOESY) but poorer results through NMR signal filtration using Carr-Purcell-Meiboom-Gill (CPMG) NMR^{276,277}. In agreement with a previous study using serum samples⁴⁰², CPMG efficiently removed protein signals but at the expense of metabolite signal disappearance and lower metabolite signal intensity; therefore, the optimized extraction method for mitochondrial samples relied on the use of the NMR buffer for mitochondrial pellet resuspension, sonication, and liquid nitrogen quenching and ultrafiltration for protein elimination as a rapid method that ensured no sample loss, important for the acquisition of good quality NMR spectra.

The optimized method allowed the detection of thirty-three metabolites in TNBC cells, more than previously reported NMR mitochondrial metabolomic studies^{230,231}. In the mitochondrial fraction we encountered i) tricarboxylic acid cycle (TCA) cycle intermediates, ii) amino acids used in anaplerotic reactions for the synthesis of TCA cycle intermediates²⁷⁸, iii) glutathione (GSH), for the elimination of ROS in cancer cells²⁸³, iv) acetoacetate, an energy reservoir for cancer cells²⁸⁶, v) nucleotides, vi) organic acids, and vii) high levels of choline-derivatives from mitochondrial membrane components.

Interestingly, we did not detect ATP in the TNBC cell mitochondria, which could relate to the high glycolytic phenotype of these cells reported by Lunetti et al. who reported that these cells relied more on glycolysis for energy production than mitochondrial OXPHOS¹¹². Thus, the primary function of mitochondrial bioenergetics in TNBC cells could be the production of metabolites required for tumor progression instead of ATP production, leading to low ATP levels undetectable by NMR.

To confirm this assumption, we evaluated the metabolite content of whole-cell samples; we found significantly higher relative ATP levels in whole-cell samples compared to isolated mitochondria, which confirmed higher ATP content in the cytosol obtained through glycolysis. These higher relative levels of amino acids in isolated mitochondria compared to whole-cell samples reflect the importance of anaplerotic reactions and TCA cycle function. Additionally, detected differences relied on cytosol-synthesized metabolites (e.g., glutathione, lactate, creatine, and phosphocreatine) which, as expected, showed decreased levels in isolated

mitochondria. Of note, these outcomes agree with an MS metabolomic study of isolated mitochondria and whole-cell samples from MDA-MB-231 cells performed by Long et al.²³⁵. Our results confirm that whole-cell sample analysis provides information about mitochondrial metabolites (e.g., TCA cycle intermediates, and amino acids); however, these metabolites can be transported to the cytosol and contribute to the total cellular metabolite pool, which involved the loss of information regarding mitochondrial metabolic. Thus, the different relative levels of metabolites in whole-cell and isolated mitochondria samples confirm the need for specific mitochondrial compartment analysis to evaluate mitochondrial metabolic pathways.

In order to validate the NMR metabolomic methodology just described, from a panel of FDA-approved drugs altering mitochondria function in TNBC, the CDK4/6 inhibitor senescence-inducer palbociclib was selected¹³⁷. Additionally, and moving a step further with our NMR metabolomic analysis tool, we characterized the mitochondrial metabolomic profile triggered by a nanomedicine containing palbociclib, specifically, a polymer-palbociclib conjugate¹³⁷ with improved pharmacological properties in comparison with the free parent drug (**Chapter III**). Polymer-drug conjugates have demonstrated extended circulation times and higher tumor accumulation than small drugs due to their intrinsic properties at the nanoscale, among them, the passive targeting effect by means of the enhanced permeability and retention (EPR) effect⁴⁰³ and the lysosomotropic delivery at cellular level after cell uptake by endocytosis¹⁰¹.

In the rational design of a polymer-drug conjugate, three key features should be taken into account: i) the polymeric carrier; ii) the bioresponsive polymer-drug linking strategy; iii) selection of drug and its loading155. As mentioned above, palbociclib was selected as drug due to its mitochondria modulatory effect. Regarding the polymeric carrier, the use of polypeptides, in particular poly-L-glutamic acid was a must, due to its multivalency, biodegradability and demonstrated biocompatibility¹⁵⁵. Based on previous work at the Polymeric Therapeutics Laboratory^{153,404}, the use of a three-arm star-shaped poly-L-glutamic acid (StPGA) was selected, and palbociclib was covalently linked through a redox-responsive self immolative linking strategy well-stablished in the laboratory 153,168. StPGA have shown increased cell uptake and blood circulation half-time in mice compared to linear PGA⁴⁰⁴. Importantly, StPGA as control carrier have demonstrated absence of toxicity in the MDA-MB-231-Luc cells¹⁵⁸. Lastly, the use of a bioresponsive linker is key for the design of cancer nanotherapeutics to ensure an endogenous site-specific drug release trigger that enhances treatment efficacy reducing side effects 155. The use of redox-responsive linking strategies is considered adequate due to the differential expression of intracellular glutathione in comparison with that in blood levels 166, which ensures intracellular drug release after nanoconjugate uptake via endocytosis. Therefore, a redoxresponsive self-immolative linker was used to conjugate palbociclib to StPGA yielding StPGA-SS-palbociclib conjugate with a low drug loading (1.5 wt%). Previous studies in our laboratory have shown that low drug loaded PGA-palbociclib conjugates present greater activity than a higher loaded analogue due to a more adequate drug release kinetics¹⁵³. StPGA-SS-palbociclib with high drug loading presents a more compact structure with restricted polypeptide chain motion, which hampers drug release. As expected, StPGA-SS-palbociclib - with a random coil conformation, a negatively charged surface, and a particle size around 10 nm - displayed lower toxicity in TNBC cells compared to free palbociclib due to the different cellular internalization mechanisms involved. Compared to the slower vesicular transport of polymer-drug conjugates during endocytosis, rapid uptake by diffusion makes small drugs more available in the cytosol at any time point⁴⁰⁵. Melnyk et al. observed similar differences in the biological activity of free palbociclib and StPGA-SS-palbociclib in glioblastoma cells¹⁵³.

Before acquiring the mitochondrial metabolomic profile of TNBC cells exposed to the free or conjugated forms of palbociclib, we first ensured partial mitochondrial impairment at the selected treatment concentration (IC₃₀) and time point (72 hours). Seahorse XF analysis revealed a more significant impairment of TNBC cells treated with StPGA-SS-palbociclib than free palbociclib. Two reasons may lie behind the differential mitochondrial impact of free palbociclib compared to StPGA-SS-palbociclib. First, free palbociclib may diffuse into and out of the cell in a constant equilibrium between the cytosol and the extracellular medium, hindering drug accumulation and mitochondrial disruption; meanwhile, StPGA-SS-palbociclib internalized by endocytosis through a lysosomotropic delivery, as demonstrated by the colocalization observed in the lysosomes¹⁵³ by confocal laser scanning microcopy. A greater palbociclib concentration could be found intracellularly upon nanoconjugate cell uptake as a controlled palbociclib release kinetics was observed, triggered by GSH overexpression in the lysosomes and causing greater mitochondrial respiration disruption due to prolonged exposure. A second hypothesis involved the synergism of palbociclib and StPGA to cause higher mitochondrial disruption. Singer et al. demonstrated PGA degradation in the lysosomes due to the presence of the endopeptidase cathepsin B¹⁶³; thus, glutamic acid or diglutamil unit from StPGA may increase the glutamate pool in cells. The mitochondria can use glutamate to synthesize the TCA cycle intermediate α ketoglutarate or convert glutamate to glutamine instead. The synergism of palbociclib with StPGA could be achieved in two scenarios. In the first, glutamate shifts the balance toward glutamine formation instead of α -ketoglutarate formation, lowering the amount of an essential intermediate of the TCA cycle. Increased glutamine would be used for alternative pathways, while lower TCA cycle activity would lead to decreased cell substrates, such as aspartate,

indispensable for cell cycle progression⁴⁰⁶. In the second scenario, glutamate accumulates in cells, causing a toxic effect. Increased glutamate levels inhibit glutathione synthesis, causing an increase in ROS levels and cell damage in neuronal cells^{407,408}; however, this has not been demonstrated in TNBC cells.

Further analysis of the mitochondrial metabolomic outcomes will provide clues about these assumptions. Interestingly, mitochondria responded to energy demands at the selected treatment conditions, indicating only partial mitochondrial disruption and ensuring the observation of mitochondrial metabolic modulation during treatment. Seahorse XF analysis also revealed decreased glycolysis, which could lead to decreased TCA cycle activity. Cretella et al. previously reported downregulated glucose uptake and metabolism and decreased expression of the GLUT-1 glucose transporter in MDA-MB-231 cells treated with palbociclib³⁹⁵. Moreover, this analysis revealed that palbociclib and StPGA-SS-palbociclib treatment caused the acquisition of a more quiescent cell phenotype, which correlates with the senescence induced by palbociclib in breast cancer cells³¹⁹.

We successfully applied the mitochondrial metabolomic methodology optimized in Chapter II to evaluate mitochondrial metabolism modulation in TNBC cells treated with free and conjugated palbociclib (StPGA-SS-palbociclib). Both treatments prompted a decreased amino acid pool compared to untreated cells, which indicated a downregulation of the TCA cycle, as previously hypothesized. Moreover, decreased levels of phosphoenolpyruvate (PEP) (synthesized in mitochondria from oxaloacetate) in mitochondria of cells treated with free palbociclib compared to control, supported the assumption of TCA cycle impairment after treatment. Warth and colleagues reported TCA cycle downregulation in MCF-7 breast cancer cells treated with palbociclib⁴⁰⁹; however, the modulation of the mitochondria in response to palbociclib could differ between different breast cancer subtypes due to metabolic heterogeneity²²¹. We failed to detect different metabolic responses in the isolated mitochondria of cells treated with free palbociclib and StPGA-SS-palbociclib, except in phosphocholine levels. StPGA-SS-palbociclib treatment caused a significant reduction of phosphocholine levels in isolated mitochondria compared to mitochondria from untreated cells. This data suggested that different mitochondrial metabolic modulation following free palbociclib and StPGA-SS-palbociclib treatment mainly rely on lipid-related metabolites.

To investigate this assumption further, we evaluated the mitochondrial metabolome and lipidome of cells treated with free palbociclib and StPGA-SS-palbociclib by MS technology during a short stay in the laboratory of Professor Nils J. Færgeman (Molecular Metabolism and

Metabolomics Laboratory, University of Southern Denmark). Taking advantage of the MS equipment and MS metabolomic expertise of this research group, we first analyzed the metabolomic profile of mitochondria to i) elucidate alterations induced by the treatment strategies under study that remained undetectable by NMR spectroscopy and ii) confirm the NMR metabolomic outcomes. Interestingly, many peptides presented low levels in mitochondria of cells treated with after free palbociclib and StPGA-SS-palbociclib compared to untreated cells, which correlates with the decreased amino acid levels detected by NMR. Decreased amino acid levels in mitochondria relate to mitochondrial respiration disruption and TCA cycle dysfunction²⁷⁸. Moreover, mitochondrial peptides could comprise the recently identified pool of mitochondrial-derived peptides, crucial mitochondrial components for correct organelle function³²⁶. Interestingly, the critical role of these peptides for mitochondrial homeostasis has now led to their investigation of a potential therapeutic target. MS sensitivity allowed the detection of significantly increased deoxyguanosine levels in isolated mitochondria following treatment with free palbociclib and StPGA-SS-palbociclib. Deoxyguanosine is a precursor of 8hydroxy-deoxyguanosine, an indicator of mitochondrial DNA damage³²⁸; therefore, free palbociclib and StPGA-SS-palbociclib may cause mitochondrial damage at the genetic level to induce the mitochondrial dysfunction observed (e.g., reduced nucleotide synthesis caused by TCA cycle downregulation may impair mitochondrial DNA replication). Increased spermidine levels in mitochondria of cells following StPGA-SS-palbociclib treatment correlated with more significant mitochondrial respiration impairment (as observed using the Seahorse analyzer), given that studies have reported that increased spermidine levels promote OXPHOS uncoupling³³⁰. Of note, increased glycerophosphocholine (GPC) levels in mitochondria of cells treated with free palbociclib and with StPGA-SS-palbociclib conjugate supported the hypothesis of a lipid metabolism alteration.

To confirm the assumption that palbociclib and StPGA-SS-palbociclib conjugate impact mitochondrial lipid metabolism and explore the potential for differential impacts, we performed an MS lipidomic analysis. MS detected a considerable amount of lipids that are challenging to detect by NMR spectroscopy due to overlapping lipid signals²⁰⁸. Interestingly, the lipidomic profile of mitochondria from TNBC cells treated with free palbociclib and StPGA-SS-palbociclib conjugate and the lipidomic profile of mitochondria from untreated cells differed. We detected more lipid alterations in mitochondria from cells following our StPGA-SS-palbociclib conjugate treatment compared to control than with free palbociclib, which indicated a more significant impact of StPGA-SS-palbociclib conjugate on the mitochondrial lipidome. Moreover, many lipids showed significantly different levels following palbociclib and StPGA-SS-palbociclib treatment,

confirming the higher impact of the latter on the mitochondrial lipidome of TNBC cells. A potential reason for these differences derives from cellular and subcellular membrane involvement during the endocytic internalization of StPGA-SS-palbociclib conjugate. The membrane invagination, fusion, and disruption taking place during this process may lead to membrane lipid alterations. To highlight, phosphatidylglycerols (exclusive mitochondrial lipids) decreased in the mitochondria of cells treated with StPGA-SS-palbociclib, while we observed no alterations after free palbociclib treatment, again supporting the higher impact of the conjugate on lipid metabolism in mitochondria. Moreover, many phosphatidylcholine species became decreased in mitochondria from treated cells in general compared to untreated cells. These data, together with the decreased phosphocholine levels (mainly after treatment with StPGA-SS-palbociclib conjugate) observed by NMR metabolomics and increased GPC levels observed by MS metabolomics, confirmed the impairment of the CDP-choline pathway. Decreased phosphocholine levels may lead to reduced phosphatidylcholine synthesis, while increased GPC levels may result from phosphatidylcholine degradation. Indeed, Sonkar et al. reported an association between decreased phosphocholine levels and increased GPC levels after doxorubicin treatment of breast cancer cells³⁸⁷. Moreover, Smith et al. linked phosphocholine to cell proliferation³⁵⁵; decreased phosphocholine levels may, therefore, reflect the loss of cell growth induced by palbociclib treatment.

The mitochondrial lipidomic study outcomes led to a further investigation of the origin of these alterations. Citrate (a TCA cycle intermediate) becomes transported to the cytosol for fatty acid biosynthesis^{30,350}; therefore, we hypothesized that reduced TCA cycle activity prompted reduced phosphatidylcholine levels and investigated this assumption by performing MS and NMR fluxomics analyses. Unlike metabolomics, fluxomics allows the measurement of intracellular flux rates, which allows us to trace the path of a metabolite using isotope-labeled metabolites²¹⁸. We used ¹³C-glucose to evaluate whether reduced fatty acid synthesis resulted from reduced glycolysis and, thus, reduced acetyl-CoA needed to synthesize fatty acids. An alternative hypothesis states that reduced glycolysis could lead to TCA cycle downregulation and, therefore, reduced levels of citrate, which can be transported to the cytosol for fatty acid synthesis. Additionally, we performed ¹³C-glutamine labeling studies to discover if reduced glutaminolysis could lead to decreased TCA cycle activity and, again, reduced citrate production for fatty acid synthesis.

The ¹³C-glucose MS fluxomics analysis indicated the downregulation of glycolysis following StPGA-SS-palbociclib treatment, which leads to a decreased TCA cycle (reduced M+2 citrate isotopologues). Surprisingly, free palbociclib did not downregulate the TCA cycle following the

downregulation of glycolysis. We observed increased 13 C-labeled α -ketoglutarate following free palbociclib treatment. We hypothesize that free palbociclib probably induced a milder effect on glycolysis than StPGA-SS-palbociclib conjugate due to the modified conjugate pharmacokinetic profile (greater intracellular palbociclib bioavailability due to a lysosomotropic controlled drug release mechanism). Interestingly, we also detected decreased purine synthesis (including reduced ATP synthesis) after palbociclib and StPGA-SS-palbociclib treatment, which indicated impairment of the pentose phosphate pathway (PPP) caused by reduced glycolysis or substrate production by the TCA cycle (e.g., aspartate remains crucial to nucleotide synthesis 406). Conroy et al. observed that palbociclib did not impact glycolysis in lung cells but reduced glucose metabolism through the PPP by reducing the activity of glucose-6-phosphate dehydrogenase⁴¹⁰. Moreover, palbociclib treatment of MCF-7 breast cancer cells also downregulated the PPP and the purine synthesis⁴⁰⁹, which supports our results. Meanwhile, increased pyrimidine synthesis following StPGA-SS-palbociclib treatment suggested that alternative phosphate source generation becomes stimulated to compensate for reduced ATP synthesis by glycolysis and the TCA cycle. Stimulation of pyrimidine synthesis could result from increased glutamine formation, as previously hypothesized in this section. Moreover, detecting high cytidine triphosphate (CTP) accumulation supported the hypothesis of reduced phosphatidylcholine synthesis (which requires CTP³⁴⁹).

The ¹³C-glutamine MS fluxomics analysis suggested the downregulation of glutaminolysis and TCA cycle following treatment with free palbociclib and StPGA-SS-palbociclib conjugate. Moreover, we detected significantly decreased aspartate synthesis in cells treated with free palbociclib and StPGA-SS-palbociclib compared to control, which supports the assumption of lower aspartate production as a nitrogen source for nucleotide synthesis and, thus, reduced purine *de novo* synthesis⁴⁰⁶. Glutamic acid units from StPGA lysosomal degradation could promote slightly higher TCA cycle activity; however, we did not observe significant differences between the impact of free palbociclib and StPGA-SS-palbociclib on glutaminolysis and TCA cycle activity. Therefore, the increased glutamate pool caused by StPGA degradation may find use for purposes other than TCA cycle incorporation. This outcome supports the hypothesis of glutamate conversion to glutamine and its use for alternative pathways; for example, pyrimidine synthesis increased following StPGA-SS-palbociclib treatment.

The ¹³C-glucose NMR fluxomics confirmed the downregulation of glycolysis in the downstream reactions (pyruvate conversion to lactate and alanine) in pathways after free palbociclib and StPGA-SS-palbociclib treatment. Interestingly, the ¹³C-glutamine NMR fluxomics analysis provided decisive information for our hypotheses. ¹³C-labeled glutamate levels increased after

free palbociclib treatment and, to a greater extent, StPGA-SS-palbociclib treatment, confirming the previously observed reduction in glutaminolysis. Moreover, the detection of increased levels of ¹³C-GPC after free and conjugated palbociclib treatment confirmed that reduced glutaminolysis led to reduced citrate production and, thus, reduced fatty acid synthesis for lipid production.

The whole-cell NMR and MS metabolomic study and the NMR analysis of the extracellular media helped us to understand overall mitochondrial metabolic modulation after free palbociclib and StPGA-SS-palbociclib treatment. Of note:

- i) StPGA-SS-palbociclib conjugate induced a more significant downregulation of glycolysis compared to free palbociclib, as observed by decreased lactate levels and decreased pyruvate and PEP levels in the extracellular medium
- ii) StPGA-SS-palbociclib conjugate prompted a more significant downregulation of the TCA cycle compared to free palbociclib (as suggested by the accumulation of acetate in the extracellular medium)
- iii) Free palbociclib and StPGA-SS-palbociclib conjugate prompted the downregulation of glutaminolysis (as observed by glutamine accumulation)
- StPGA degradation increased the glutamate pool (as observed by the increased levels of glutamate in the extracellular medium)
- v) StPGA-SS-palbociclib conjugate induced higher glutamine accumulation than StPGA control, suggesting the use of the increased glutamate pool for the synthesis of glutamine for use in other pathways (e.g., pyrimidine synthesis)
- vi) Glycolysis and mitochondrial respiration disruption in cells treated with StPGA-SSpalbociclib was confirmed by the detection of decreased ATP pool
- vii) Differentially, StPGA-SS-palbociclib conjugate but not palbociclib disrupted the creatine phosphate shuttle due to reduced mitochondrial ATP production
- viii) StPGA-SS-palbociclib had a more significant impact on the cell lipidome compared to free palbociclib (as observed by significantly lower levels of phosphocholine in whole-cells treated with StPGA-SS-palbociclib conjugate and the increased GPC levels encountered in the extracellular medium after StPGA-SS-palbociclib conjugate treatment compared to free palbociclib treatment)

Important to note that, the whole-cell MS lipidomic analysis also contributed to a more robust understanding of mitochondrial lipid alterations. The detection of decreased levels of cardiolipins and most phosphatidylglycerols (exclusive mitochondrial membrane lipids)

in cells treated with StPGA-SS-palbociclib conjugate confirmed a more significant level of mitochondrial damage induced by conjugated palbociclib compared to free palbociclib.

Overall, applying our mitochondrial metabolomic methodology for assessing the impact of free palbociclib and StPGA-SS-palbociclib allowed a detailed comparison of their metabolic impacts. Consequently, this study pointed out the importance of the use of nanomedicines and, even more, the need for a rational design in order to enhance the pharmacological activity of a given drug.

The analysis provided evidence of TCA cycle and lipid synthesis deregulation (to a greater extent after StPGA-SS-palbociclib treatment), which we confirmed using multiple omic techniques (NMR and MS metabolomics, MS lipidomics and NMR and MS fluxomics). Furthermore, the whole-cell analysis provided helpful information for the global understanding of metabolism modulation after free palbociclib and StPGA-SS-palbociclib treatment. Therefore, we believe integrating NMR spectroscopy with MS methods is crucial for obtaining more comprehensive results. Van der Walt and colleagues used an NMR and MS metabolomic approach to evaluate mitochondrial metabolism in tissues of a Leith Syndrome animal model²³⁰; however, to the best of our knowledge, we lack a mitochondrial metabolic multi-technique study that evaluated the impact of treatments of mitochondrial metabolism.

Therefore, the developed methodology herein presented represents a significant progress in the mitochondrial-targeting therapeutic field. The specific evaluation of mitochondrial metabolism can reduce/remove interference from other cell compartments and provide a more concrete view of how mitochondrially-targeted therapies act on mitochondrial metabolism. This will help to widen our understanding of their mechanism of action and optimize the design of new therapies directed to mitochondria.

Furthermore, we believe that our methodology will represent a valuable tool to assess the impact of mitochondria-targeted nanomedicines on mitochondrial metabolism. Currently, our laboratory is developing several mitochondria-targeted conjugates, and the present method will be applied to study their intracellular mechanism and determine the best treatment option for a given pathological problem.

Moving from cells to a more relevant preclinical scenario, thinking to take a step closer to clinical application, we adapted the NMR mitochondrial metabolomic analysis to mouse tissues: TNBC primary tumors, affected organs from TNBC metastasis (mainly lungs⁷²), and organs from healthy animals (lungs, liver, kidney, and brain) (**Chapter IV**). The optimization of the

methodology resulted in the use of the same experimental strategy to get mitochondria isolation, metabolite extraction, and NMR analysis methods from tissues than that developed for TNBC cells (Chapter II). Mitochondria isolation relies on tissue homogenization and differential centrifugation; however, certain factors must be considered for tissue homogenization. Compactness, solidity, and presence of filaments/fibers all impact correct tissue homogenization⁴¹¹. The optimization of the Homogenization of tissues suggested the use of manual Dounce homogenization for liver, lung, kidney, and brain samples but a more powerful homogenization method for the more compact and fibrous nature of breast tumor tissues, as indicated by Burden et al. for solid tissues⁴¹¹. Therefore, we used an electric homogenizer (Ultra-turrax disperser) for breast tumors to ensure complete tissue homogenization and provide better NMR spectra of isolated mitochondria. The Ultra Turrax disperser has been previously used to prepare tumor homogenates for several purposes⁴¹². We obtained mitochondrially-enriched fractions of each tissue by differential centrifugation and confirmed identity by Western Blotting analysis.

Based on the same rationale describer for the cells (Chapter II), metabolite extraction relied on the use of NMR buffer to avoid metabolite loss⁴⁰¹, sample sonication and quenching in liquid nitrogen to allow metabolite release from mitochondria^{269,270}, and protein ultrafiltration to avoid baseline alterations⁴¹³. The optimized methodology provided good-quality NMR spectra of the isolated mitochondria, which detected a total of forty-five metabolites; in comparison, previous NMR mitochondrial metabolomic studies only identified between six and fourteen metabolites^{230,231}. Interestingly, the metabolomic profile of each tissue displayed specificity (different metabolite intensities and metabolite content); for example, we only detected Nacetyl aspartate in brain samples, as reported by related mitochondrial metabolomic studies^{230,231}. An elevated number of amino acids generally characterized mitochondrial liver and kidney samples. The liver contains abundant amino acids as it participates in protein synthesis, degradation, and detoxification⁴¹⁴, while the kidneys represent crucial mediators of interorgan amino acid exchange 415. A high nucleotide content characterized the mitochondrial metabolome profile of brain tissues, which correlates with the reported role of nucleotides for neuronal functions such as cell-to-cell communication⁴¹⁶. A high lipid content characterized lung mitochondria, which agrees with the reported central role of lipids in lung physiology and pathology⁴¹⁷. Finally, high levels of organic acids (e.g., lactate and citrate), amino acids, and lipidrelated metabolites characterized breast tumor mitochondria, which may reflect the stimulation of glycolysis, the TCA cycle, and lipid synthesis to support tumor progression, as previously reported for the MDA-MB-231 breast cancer model^{72,112}. Interestingly, the profiling of the mitochondria metabolome also revealed specific signatures of each tissue, supporting the validity of the optimized methodology. For example, we exclusively found ornithine in mitochondria from liver tissues. Gamble et al. reported that, in mammalian liver, ornithine is transported to mitochondria, where conversion to citrulline takes place⁴¹⁸.

To ensure method validity, we next compared the metabolic content of isolated mitochondria with whole-cell samples taken from tissues. Previous studies compared the metabolic profile of isolated mitochondria with that of the cytosol^{230,231} instead of a whole-cell sample. While this methodology provided specific information on the metabolic alterations in the cytosol, we aimed to prove that the specific analysis of mitochondria provides specific metabolic signatures that whole-cell samples cannot. Overall, we encountered alterations in multiple metabolites when comparing whole-cell samples to isolate mitochondria in cells from distinct tissues, which supported this hypothesis. In general, MDA-MB-231-Luc TNBC tumors excised from mice at day 42 displayed higher relative levels of most metabolites in whole-cell samples (very high for lactate) when compared to isolated mitochondria, which supports the highly glycolytic phenotype for energy and substrate production of MDA-MB-231 cells¹¹². Nevertheless, we observed the elevated presence of choline derivatives in the isolated mitochondria of TNBC tumors, which remained similar to levels in the whole-cell samples. These results may reflect phosphatidylcholines' importance in maintaining cell and mitochondrial membranes³³⁷. Glunde et al. reported alterations in choline metabolism in breast cancer cells³⁸⁶, while Arroyo-Crespo et al. also noted increased GPC levels in the MDA-MB-231-Luc mouse model⁷².

We finally applied the described methodology to evaluate the modulation of mitochondrial metabolism upon breast cancer metastasis. We detected metabolic alterations in lung mitochondria isolated from a metastatic MDA-MB-231-Luc model⁷² compared to lung mitochondria isolated from healthy mice. Additionally, we observed few differences between the livers of healthy and metastatic mice, and we failed to detect mitochondrial alterations in kidney mitochondria from metastatic mice used as a negative control (our TNBC orthotopic model⁷² lacks kidney metastasis). These findings agree with a previous study reporting data showing that MDA-MB-231-Luc produced lung metastasis but no liver metastasis⁷². Eight metabolites (lactate, choline, phosphocholine, alanine, creatine, glucose, methionine, and glutamate) displayed increased levels in the mitochondria of metastatic lungs, which suggested increased glycolysis and increased amino acid, lipid, and creatine synthesis to supply cells with energy and metabolic substrates and continue tumor growth and invasion. Of note, Lebleu et al. reported increased mitochondrial activity in a 4T1 metastatic breast cancer mouse model with lung metastasis development¹¹⁵. In breast cancer cells, high mitochondrial activity has been

correlated to lung and bone metastasis¹¹⁶, while enhanced glycolytic activity and decreased OXPHOS and glutaminolysis have been observed in liver metastatic breast cancer cells¹¹⁷. Overall, **Chapter IV** data suggested that the described method, already validated in cells, has demonstrated validity for the metabolic studies of tissue mitochondria. The application of mitochondrial metabolomics in tissue samples to evaluate mitochondrial metabolic modulation after treatment with free drugs and nanomedicinal formulations represents a pending issue for future experiments.

Ultimately, our findings portray a validated method for the evaluation of metabolic mitochondrial alterations, which can be applied for several purposes, including the evaluation of the mitochondrial metabolic profile of different cancer subtypes at different disease stages and even the assessment of the mitochondrial impact induced by treatments and by mutations, knockdowns, or nutrient starvation.

Importantly, this thesis represents the first description of the impact of a polymer-drug conjugate on mitochondrial metabolism. Future application of this approach will provide researchers with a novel technique to specifically evaluate mitochondrial metabolism when evaluating mitochondrially-targeted therapies.

FINAL CONCLUSIONS

This thesis describes the implementation of an NMR-based mitochondria-specific approach to investigate alterations in mitochondrial metabolism following treatment with small molecular weight drugs and a nanomedicinal formulation in triple negative breast cancer (TNBC) cells and metastatic tissues. Our findings validated the developed methodology and underscored the significance of understanding mitochondrial metabolism. This understanding remains crucial to elucidate the distinct pharmacological outcomes of a given treatment and highlights the superior efficacy of rationally designed nanomedicines as anticancer therapies.

Based on our results, the main conclusions resulting from this thesis are:

- The developed NMR metabolomic protocol, applied to analyze isolated mitochondria in TNBC cells, healthy mouse tissues, and tissues from a TNBC mouse model, produced consistent and reproducible mitochondrial metabolic profiles. The methodology encompassed mitochondria isolation through differential centrifugation, monophase, and aqueous-based metabolite extraction, and the acquisition of nuclear overhauser effect spectroscopy NMR spectra.
- 2. We synthesized the StPGA-SS-palbociclib polypeptide-drug conjugate in a three-step procedure by conjugating palbociclib to the biodegradable StPGA polymer through a redox-responsive self-immolative disulfide linker (-SS-). StPGA-SS-palbociclib induced less cytotoxicity in TNBC cells compared to free palbociclib due to different internalization mechanisms. However, StPGA-SS-palbociclib triggered more significant mitochondrial respiration impairment due to synergism between glutamic acid units from StPGA degradation and palbociclib. This methodology also revealed the downregulation of glycolysis upon free palbociclib and StPGA-SS-palbociclib treatment.
- 3. The optimized mitochondrial NMR methodology allowed the determination of the metabolomic profile of mitochondria isolated from TNBC cells treated with free palbociclib and StPGA-SS-palbociclib conjugate. Palbociclib and StPGA-SS-palbociclib treatment downregulated TCA cycle activity, while StPGA-SS-palbociclib induced exclusive lipid alterations.
- 4. MS mitochondrial metabolomic analysis confirmed that free palbociclib and StPGA-SS-palbociclib treatment disrupted mitochondria from TNBC cells. Decreased peptide levels confirmed reduced TCA cycle activity, increased deoxyguanosine suggested mitochondrial DNA damage, and elevated glycerophosphocholine levels indicated lipid metabolism alteration. Increased spermidine levels in mitochondria evidenced the more

- significant disruption of oxidative phosphorylation induced by StPGA-SS-palbociclib treatment.
- 5. MS lipidomic analysis revealed a higher and more specific impact of free palbociclib and StPGA-SS-palbociclib treatment on the mitochondrial lipidome than on the mitochondrial metabolome in TNBC cells. StPGA-SS-palbociclib induced a more significant effect, with a notable decrease in phosphatidylcholines supporting the alteration of the CDP-choline pathway.
- 6. Whole-cell NMR and MS metabolomics analysis confirmed several key points: i) the disruption of glycolysis and mitochondrial respiration following StPGA-SS-palbociclib treatment; ii) a more significant effect of StPGA-SS-palbociclib compared to free palbociclib concerning the downregulation of TCA cycle activity; iii) the downregulation of glutaminolysis following free palbociclib and StPGA-SS-palbociclib treatment; and iv) a more significant impact of StPGA-SS-palbociclib treatment on the lipidome compared to free palbociclib.
- 7. NMR and MS fluxomics analysis confirmed the downregulation of glycolysis and the stimulation of pyrimidine synthesis following StPGA-SS-palbociclib treatment, while both free palbociclib and StPGA-SS-palbociclib treatments inhibited purine synthesis. These studies revealed downregulated glutaminolysis and TCA cycle activity following free palbociclib and StPGA-SS-palbociclib treatment at the mitochondrial level.
- 8. The optimized NMR methodology demonstrated its potential in preclinical *in vivo* studies by characterizing the mitochondrial metabolomic profile of cells from various tissues in healthy mice and in an orthotopic mouse model of metastatic TNBC. Distinct metabolic signatures were revealed in mitochondria from each tissue type. Notably, breast tumors exhibited increased levels of metabolites stimulating glucose metabolism, the TCA cycle, and lipid synthesis to support tumor progression.
- 9. The developed methodology was validated by comparing mitochondria-specific metabolomic modulation in tissues of healthy mice and those from an orthotopic mouse model of metastatic TNBC. Increased levels of metabolites in lung mitochondria suggested an adaptation of mitochondrial metabolism in TNBC metastatic cells to promote tumor growth and invasion.

MEMORIA DE LA TESIS

INTRODUCCIÓN Y CONTEXTO

Las mitocondrias son orgánulos centrales de las células dada su función como centro metabólico y fuente de energía, y su constante comunicación con el citosol y el núcleo⁹; por tanto, el desarrollo de muchas enfermedades, incluido el cáncer, están asociados a una disfunción mitocondrial⁴¹⁹. Durante el desarrollo del cáncer, las mitocondrias modulan su metabolismo para adaptarse a las nuevas demandas energéticas y de sustratos. Por ejemplo, las mitocondrias promueven la agresividad e invasión de las células tumorales en respuesta a una demanda de energía o aumentan su actividad para compensar el daño de otras vías metabólicas celulares¹.

Los investigadores han aprovechado las características únicas de las mitocondrias de las células cancerosas, como el aumento del potencial de membrana y los elevados niveles de especies reactivas de oxígeno (ROS), para desarrollar terapias dirigidas 177 . Muchas terapias anticancerígenas afectan específicamente el metabolismo mitocondrial (como palbociclib 395 y metotrexato 395) o se dirigen inherentemente a las mitocondrias (como lonidamina 185 y α -tocoferol 177). Además, muchas nanomedicinas que transportan pequeños fármacos, anticuerpos u otros agentes bioactivos al interior de las células cancerosas, son diseñadas para dirigirse específicamente a las mitocondrias 177,397 .

El desarrollo de nanomedicinas antitumorales requiere técnicas que evalúen su impacto en la función mitocondrial. Las alteraciones en la bioenergética mitocondrial y la fosforilación oxidativa (OXPHOS) representan los parámetros más comúnmente analizados para evaluar el impacto de la nanomedicina dirigida a las mitocondrias. Dichas alteraciones incluyen características de la respiración mitocondrial (p. ej., análisis de generación y consumo de oxígeno, producción de ROS y síntesis de adenosina trifosfato (ATP))^{4,5} y potencial de membrana mitocondrial³⁷, mientras que la morfología mitocondrial⁸ y la expresión de proteínas³⁹⁸ representan parámetros analizados con menos frecuencia. Sorprendentemente, el impacto de las nanomedicinas anticancerígenas en el metabolismo mitocondrial sigue sin evaluarse. Dada la fuerte asociación del metabolismo mitocondrial con el funcionamiento de la respiración mitocondrial y su papel crucial en la función celular²¹, la evaluación del metabolismo mitocondrial podría contribuir a comprender el mecanismo de acción de un determinado nanofármaco.

La comunidad científica ha mostrado conciencia sobre la importancia de evaluar el metabolismo mitocondrial; recientemente, los estudios mitocondriales han implementado metodologías metabolómicas para evaluar el metabolismo de estos orgánulos en células/tejidos. La espectrometría de masas (MS) representó inicialmente la técnica preferida para tales análisis

debido a su alta sensibilidad; por tanto, se han aplicado varias metodologías metabolómicas mediante MS a diferentes estudios de investigación^{230,231,250,399,233,234,236,238–242}. La resonancia magnética nuclear (NMR) proporciona una técnica valiosa y complementaria a la MS debido a su robustez, análisis de muestras rápido y no destructivo, y la capacidad de detectar todos los metabolitos en un solo espectro, proporcionando una huella digital reproducible. Las metodologías de NMR desarrolladas para el análisis mitocondrial generalmente cuantificaron una cantidad baja de metabolitos^{230,231} o requirieron isótopos metabólicos caros como ¹³C-glucosa y ¹³C-glutamina^{232,243–245}; por tanto, existe la necesidad de desarrollar nuevos métodos metabolómicos mitocondriales basados en NMR.

En el contexto de mejorar el diseño de nanofármacos dirigidos a mitocondrias y la necesidad de herramientas para evaluar el metabolismo mitocondrial, nuestro objetivo fue desarrollar una metodología metabolómica de NMR para evaluar la modulación mitocondrial durante el desarrollo del cáncer y el impacto de las nanomedicinas dirigidas a mitocondrias en el metabolismo mitocondrial de células/tejidos. Dada la baja cantidad de contenido mitocondrial en comparación con las muestras de células enteras y la baja sensibilidad de la NMR, el desarrollo de una metodología metabolómica mitocondrial centrada en obtener fracciones mitocondriales enriquecidas y evitar pérdidas de muestras puede ayudar a mejorar los resultados de la NMR.

OBJETIVOS

El objetivo principal de esta tesis implica el desarrollo de una metodología metabolómica basada en NMR para la evaluación específica del metabolismo mitocondrial en muestras de células y tejidos. Los objetivos específicos incluyen:

- **Objetivo 1**. Optimización de una metodología metabolómica mitocondrial de NMR específica en células de cáncer de mama triple negativo (TNBC; MDA-MB-231) que comprende tres pasos (aislamiento mitocondrial, extracción de metabolitos y análisis de NMR). Análisis comparativo de perfiles metabolómicos mitocondriales aislados y de células enteras.
- Objetivo 2. Selección de terapias farmacológicas (tanto fármacos libres como nanofármacos) para modular la función mitocondrial y validar la metodología de NMR desarrollada, lo cual también implica la síntesis y caracterización de un conjugado a base de ácido poli L-glutámico en forma de estrella (StPGA).
- **Objetivo 3**. Evaluación biológica de palbociclib y conjugados de palbociclib basados en StPGA y su impacto en el metabolismo mitocondrial de células de TNBC utilizando la metodología de

NMR previamente optimizada, cuyos resultados serán confirmados y complementados con estudios metabolómicos y lipidómicos mediante MS y estudios de fluxómica mediante NMR y MS.

- **Objetivo 4**. Optimización de la metodología metabolómica mitocondrial de NMR en tejidos de ratón sanos y tumorigénicos con TNBC. Análisis comparativo de los perfiles metabolómicos de muestras de células enteras y mitocondrias aisladas.
- **Objetivo 5**. Evaluación de alteraciones metabólicas en las mitocondrias aisladas de un modelo de ratón con TNBC metastásico en comparación con un modelo de ratón sano utilizando la metodología optimizada.

METODOLOGÍA Y RESULTADOS

 Optimización del Análisis Metabolómico Mitocondrial Mediante NMR de Mitocondrias Aisladas de Células de Cáncer de Mama Triple Negativo

En primer lugar, optimizamos una metodología metabolómica mitocondrial en células de TNBC mediante la optimización del aislamiento mitocondrial, la extracción de metabolitos y el análisis de NMR. Nuestro propósito fue el desarrollo de una metodología simple y económica enfocada a prevenir pérdidas de muestras que podrían afectar el resultado metabolómico final.

Aislamiento Mitocondrial

Si bien se han descrito métodos innovadores para el aislamiento de mitocondrias (p. ej., centrifugación en gradiente de densidad²⁴⁹, purificación por afinidad^{231,237}, fraccionamiento no acuoso²³⁹), seleccionamos la homogeneización celular seguida de centrifugación diferencial como método de aislamiento para nuestro análisis metabolómico mitocondrial. La simplicidad del método, el aislamiento rápido (1-1.5 h) de una fracción mitocondrial altamente enriquecida y la utilización de material y equipo económicos⁴⁰⁰ hacen que la centrifugación diferencial sea el método preferido en los estudios metabolómicos mitocondriales.

Concretamente, las células de TNBC se resuspendieron en el tampón de aislamiento (manitol 220 mM y sacarosa 70 mM como soportes osmóticos no iónicos, clorhidrato de tris(hidroximetil)aminometano (Tris-HCl) 10 mM a pH 7,4 para mantener el pH fisiológico y 0,5 mg/ml de BSA para estabilizar la membrana mitocondrial), y posteriormente se homogeneizaron utilizando un homogeneizador de vidrio eléctrico. La evaluación de la actividad del lactato deshidrogenasa (LDH) y el contaje de células lisadas en el homogeneizado celular ayudaron a optimizar el protocolo de rotura celular.

Seguidamente, realizamos una centrifugación a baja velocidad para separar la fracción nuclear (pellet), mientras que el sobrenadante resultante contenía orgánulos de bajo peso y la fracción citosólica. A continuación, centrifugamos el sobrenadante a alta velocidad para obtener la fracción mitocondrial (pellet) y el sobrenadante que contenía la fracción citosólica. Finalmente, lavamos la fracción mitocondrial dos veces con el tampón de aislamiento para eliminar posibles contaminaciones. La evaluación de la actividad succinato deshidrogenasa (SDH) y la expresión de proteínas mitocondriales mediante Western Blot en la fracción obtenida tras la centrifugación diferencial, confirmó el enriquecimiento de la fracción mitocondrial, fundamental para el análisis específico del perfil metabolómico mitocondrial.

Extracción de Metabolitos y Análisis Mediante NMR

Desarrollar un método de extracción de metabolitos adecuado es crucial para evitar la pérdida de metabolitos en muestras de bajo contenido, como las mitocondrias. Los métodos monofásicos tienen ventajas sobre los métodos bifásicos⁴⁰¹ (por ejemplo, la extracción de Folch²⁶⁶ y la extracción de Bligh y Dyer²⁶⁸). La extracción de Folch y Bligh y Dyer, basada en el uso de cloroformo, metanol y agua para obtener dos fases de metabolitos orgánicos y acuosos, requiere una separación de las fases. Esto puede provocar la pérdida de metabolitos al separar las fases y la evaporación de los metabolitos volátiles al evaporar el disolvente de cada fase⁴⁰¹. La extracción monofásica puede superar estas desventajas, ya que no requieren separación de fases y los tampones compatibles con NMR evitan la pérdida de metabolitos. Además, los métodos monofásicos implican procesos más simples y rápidos y el uso de productos químicos menos tóxicos⁴⁰¹.

En este contexto, seleccionamos un procedimiento de extracción monofásico utilizando el tampón de NMR (Na₂HPO₄ 100 mM pH 7.4, 200 μM 3-(trimethylsilyl) propionic acid d4 sodium salt (TSP) en D₂O), rotura de la membrana mediante ciclos de enfriamiento con nitrógeno líquido y sonicación para la extracción de metabolitos de las mitocondrias. La sonicación de la muestra y los ciclos de enfriamiento en nitrógeno líquido proporcionan una rotura de membrana reproducible y una buena recuperación de metabolitos^{269,270}. En nuestro estudio confirmamos niveles más altos de metabolitos obtenidos mediante sonicación en comparación con el método tradicional de Folch. Las proteínas de las muestras aparecen en los espectros de NMR como señales amplias que se superponen con las señales de interés y alteran la línea base⁴⁰²; su precipitación normalmente implica el uso de metanol/cloroformo en los métodos de extracción convencionales de Folch²⁶⁶ y Bligh y Dyer²⁶⁸. Sin embargo, el uso de tampones de extracción acuosos hace que la ultrafiltración de proteínas sea el único método disponible para la

eliminación de proteínas⁴⁰². En nuestro estudio demostramos que la eliminación de proteínas mediante ultrafiltración física seguido de la medición de las muestras mediante espectroscopia de efecto nuclear overhauser (NOESY) proporcionó resultados óptimos de NMR; sin embargo, obtuvimos peores resultados mediante la filtración de señales de proteínas utilizando el experimento de NMR Carr-Purcell-Meiboom-Gill (CPMG)^{276,277}. De acuerdo con un estudio previo que utilizó muestras de suero⁴⁰², el experimento CPMG eliminó eficientemente las señales de proteínas, pero a expensas de la desaparición o pérdida de intensidad de la señal de algunos metabolitos. Por tanto, el método de extracción optimizado para muestras mitocondriales se basó en el uso del tampón de NMR para la resuspensión del pellet mitocondrial, la sonicación y los ciclos de enfriamiento con nitrógeno líquido para romper las membranas y la ultrafiltración para la eliminación de proteínas como un método rápido que garantiza que no se pierdan muestras, muy importante para la adquisición de espectros de NMR de buena calidad.

Perfil Metabolómico de las Mitocondrias de Células de TNBC

El método optimizado permitió la detección de treinta y tres metabolitos en las mitocondrias de células de TNBC, más que los estudios metabolómicos mitocondriales de NMR publicados anteriormente^{230,231}. En la fracción mitocondrial encontramos i) intermediarios del ciclo del ácido tricarboxílico (TCA), ii) aminoácidos utilizados en reacciones anapleróticas para la síntesis de intermediarios del ciclo del TCA²⁷⁸, iii) glutatión (GSH), para la eliminación de ROS en células cancerosas²⁸³, iv) acetoacetato, un reservorio de energía para las células cancerosas²⁸⁶, v) nucleótidos, vi) ácidos orgánicos y vii) altos niveles de derivados de colina provenientes de los componentes lipídicos de la membrana mitocondrial.

Curiosamente, no detectamos ATP en las mitocondrias de las células de TNBC, lo que podría relacionarse con el fenotipo altamente glucolítico de estas células. Así lo informaron Lunetti et al., quienes mostraron que las células de TNBC MDA-MB-231 dependían más en la glucólisis para la producción de energía que en la OXPHOS mitocondrial¹¹². Por tanto, la función principal de la bioenergética mitocondrial en las células TNBC podría ser la producción de metabolitos necesarios para la progresión del tumor en lugar de la producción de ATP, lo que lleva a niveles bajos de ATP, indetectables mediante NMR.

Comparación del Perfil Metabolómico de las Mitocondrias y de las células de TNBC Completas

Para confirmar el fenotipo glucolítico de las células de TNBC, evaluamos el contenido de metabolitos de muestras de células completas. Encontramos niveles relativos de ATP significativamente más altos en muestras de células enteras en comparación con las

mitocondrias aisladas, lo que confirmó un mayor contenido de ATP en el citosol obtenido mediante glucólisis. También encontramos niveles relativos más altos de aminoácidos en mitocondrias aisladas en comparación con muestras de células completas, lo cual reflejó la importancia de las reacciones anapleróticas y la función del ciclo del TCA.

Además, las diferencias detectadas se basaron en metabolitos sintetizados en el citosol (p. ej., glutatión, lactato, creatina y fosfocreatina) que, como se esperaba, mostraron niveles reducidos en mitocondrias aisladas. Es de destacar que estos resultados concuerdan con un estudio metabolómico de MS de mitocondrias aisladas y muestras de células completas de células MDA-MB-231 realizado por Long et al²³⁵.

Nuestros resultados confirmaron que el análisis de muestras de células completas proporciona información sobre los metabolitos mitocondriales (p. ej., intermediarios del ciclo del TCA y aminoácidos); sin embargo, estos metabolitos pueden ser transportados al citosol y contribuir al cómputo total de metabolitos celulares, lo que implica la pérdida de información sobre el metabolismo mitocondrial. Por tanto, los diferentes niveles relativos de metabolitos en muestras de células enteras y de mitocondrias aisladas confirman la necesidad de un análisis del compartimento mitocondrial específico para evaluar las vías metabólicas mitocondriales.

Evaluación del Impacto de un Fármaco Libre y un Conjugado Polímero-Fármaco en el Metabolismo de Células de Cáncer de Mama Triple Negativo

Para validar la metodología metabolómica de NMR descrita en la sección anterior, estudiamos la modulación mitocondrial de células de TNBC en respuesta al tratamiento con diferentes aproximaciones terapéuticas.

Selección del Fármaco y Síntesis del Conjugado Polímero-Fármaco

De un panel de fármacos aprobados por la FDA que alteran la función de las mitocondrias en células de TNBC, se seleccionó el inhibidor de CDK4/6 inductor de senescencia palbociclib¹³⁷. Además, y avanzando un paso más con nuestra herramienta de análisis metabolómico de NMR, caracterizamos el perfil metabólico mitocondrial desencadenado por una nanomedicina que contiene palbociclib, específicamente, un conjugado polímero-palbociclib¹³⁷ con propiedades farmacológicas mejoradas en comparación con el fármaco original libre. Los conjugados polímero-fármaco han demostrado tiempos de circulación más largos y mayor acumulación tumoral que los fármacos pequeños debido a sus propiedades intrínsecas a nanoescala, entre ellas, el efecto de direccionamiento pasivo mediante el efecto de permeabilidad y retención

mejoradas $(EPR)^{403}$ y la administración lisosomotrópica a nivel celular tras la entrada celular mediante endocitosis¹⁰¹.

En el diseño racional de un conjugado polímero-fármaco, se deben tener en cuenta tres características clave: i) el portador polimérico; ii) la estrategia de unión polímero-fármaco mediante un enlace sensible a estímulos biológicos; iii) selección del fármaco y su carga¹⁵⁵. Como se mencionó anteriormente, se seleccionó palbociclib como fármaco debido a su efecto modulador de las mitocondrias. En cuanto al portador polimérico, el uso de polipéptidos, en particular ácido poli-L-glutámico, era imprescindible, debido a su multivalencia, biodegradabilidad y biocompatibilidad demostrada¹⁵⁵. Con base en trabajos previos del Laboratorio de Polimeros Terapéuticos^{153,404}, se seleccionó el uso del ácido poli-L-glutámico de tres brazos en forma de estrella (StPGA), y el palbociclib se unió covalentemente a través de una estrategia de enlace autoinmolativo con respuesta redox establecido en el laboratorio ^{153,168}. StPGA ha demostrado una mayor internalización celular y mayor tiempo medio de circulación sanguínea en ratones en comparación con PGA lineal⁴⁰⁴. Es importante destacar que el portador StPGA ha demostrado ausencia de toxicidad en las células MDA-MB-231-Luc¹⁵⁸.

El uso del enlace sensible a estímulos biológicos es clave para el diseño de nanomedicinas contra el cáncer para garantizar la liberación específica del fármaco en el sitio de acción que mejore la eficacia del tratamiento y reduzca los efectos secundarios¹⁵⁵. El uso de estrategias de enlace redox se considera adecuado debido a la diferente expresión del glutatión intracelular en comparación con la de los niveles sanguíneos¹⁶⁶, lo que asegura la liberación intracelular del fármaco después de la absorción del nanoconjugado mediante endocitosis. Por tanto, se utilizó un conector autoinmolativo sensible a redox (enlace disulfuro; -SS-) para conjugar el palbociclib al StPGA, lo cual resultó en el conjugado StPGA-SS-palbociclib.

La caracterización físico-química del conjugado StPGA-SS-palbociclib nos permitió conocer: i) la baja carga de fármaco en el conjugado (1,5% en peso; determinado mediante espectroscopía de Ultravioleta-Visible (UV-Vis)); ii) el 1,05% en peso de palbociclib libre comparado a la carga total de fármaco (determinado mediante cromatografía líquida-espectrometría de masas (LC-MS)); iii) la estabilidad del conjugado en condiciones extracelulares y la liberación de un 33% de palbociclib tras 72 horas en condiciones intracelulares (determinado mediante LC-MS); iv) la conformación con distribución aleatoria de los monómeros (determinada mediante dicroísmo circular); v) la superficie cargada negativamente (determinada mediante el instrumento Malvern ZetasizerNano ZS); vi) el tamaño de partícula de alrededor de 10 nm (determinado mediante espectroscopía de NMR con transformada bayesiana ordenada por difusión (DOSY)).

Ensayos de Toxicidad del Palbociclib y del Conjugado StPGA-SS-palbociclib en Células de TNBC

Estudios previos en nuestro laboratorio han demostrado que los conjugados PGA-palbociclib con baja carga de fármaco presentan una mayor actividad que un análogo con mayor carga debido a una cinética de liberación del fármaco más adecuada¹⁵³. StPGA-SS-palbociclib con alta carga de fármaco presenta una estructura más compacta con movimiento restringido de la cadena polipeptídica, lo que dificulta la liberación del fármaco. Como era de esperar, StPGA-SS-palbociclib mostró una menor toxicidad en las células de TNBC a 72 horas (IC₅₀ = 43.26 \pm 3.57 μ M) en comparación con el palbociclib libre (IC₅₀ = 3.52 \pm 0.55 μ M), debido a los diferentes mecanismos de internalización celular implicados. En comparación con el transporte vesicular más lento de los conjugados polímero-fármaco durante la endocitosis, la rápida absorción por difusión de los fármacos pequeños hace que estén más disponibles en el citosol en cualquier momento⁴⁰⁵. Melnyk et al. observaron diferencias similares en la actividad biológica de palbociclib libre y StPGA-SS-palbociclib en células de glioblastoma¹⁵³.

Para proceder con los estudios mitocondriales, seleccionamos las concentraciones correspondientes al IC₃₀ del palbociclib (IC₃₀ = 0.77 \pm 0.12 μ M) y del StPGA-SS-palbociclib (IC₃₀ = 3.64 \pm 0.30 μ M) para evitar concentraciones altamente tóxicas y asegurar la ausencia de cualquier artefacto derivado de toxicidades no específicas.

Evaluación de la Respiración Mitocondrial en Células de TNBC Tratadas con Palbociclib Libre y StPGA-SS-palbociclib

Antes de adquirir el perfil metabolómico mitocondrial de las células de TNBC expuestas al palbociclib libre y StPGA-SS-palbociclib, primero aseguramos que éstos provocaban un daño mitocondrial parcial a las concentraciones (IC₃₀) y tiempo de tratamiento seleccionadas (72 horas). El análisis de la respiración mitocondrial mediante el analizador Seahorse XF reveló una inhibición más significativa de las células TNBC tratadas con StPGA-SS-palbociclib que con palbociclib libre. El diferente impacto de los tratamientos en la respiración mitocondrial puede deberse a dos motivos. En primer lugar, el palbociclib libre puede entrar y salir de la célula mediante difusión en un equilibrio constante entre el citosol y el medio extracelular, lo que dificulta la acumulación del fármaco y la alteración mitocondrial; mientras tanto, StPGA-SS-palbociclib se internaliza por endocitosis a través de una administración lisosomotrópica, como lo demuestra la colocalización observada en los lisosomas¹⁵³ mediante microcopia confocal láser

de barrido. Se encontró una mayor concentración de palbociclib dentro de las células tras la internalización del nanoconjugado, ya que se observó una cinética de liberación controlada del palbociclib, desencadenada por la sobreexpresión de GSH en los lisosomas¹⁵³. Esta podría ser la razón por la cual observamos una mayor inhibición de la respiración mitocondrial debido a la exposición más prolongada al fármaco.

Una segunda hipótesis implicaba la sinergia de palbociclib y StPGA para provocar una mayor alteración mitocondrial. Singer e al. demostró la degradación de PGA en los lisosomas debido a la presencia de la endopeptidasa catepsina B163; por tanto, el ácido glutámico o la unidad de diglutamil de StPGA pueden aumentar la reserva de glutamato en las células. Las mitocondrias pueden usar glutamato para sintetizar el α -cetoglutarato intermediario del ciclo del TCA o convertir el glutamato en glutamina. La sinergia de palbociclib con StPGA podría lograrse de dos formas. Por una parte, el glutamato podría desplazar el equilibrio hacia la formación de glutamina en lugar de la formación de α -cetoglutarato, lo cual reduciría la cantidad de un intermediario esencial del ciclo del TCA. Un aumento de la glutamina se utilizaría para vías alternativas, mientras que una menor actividad del ciclo del TCA conduciría a una disminución de los sustratos celulares, como el aspartato, indispensable para la progresión del ciclo celular⁴⁰⁶. Por otra parte, el glutamato se podría acumular en las células provocando un efecto tóxico. Los niveles elevados de glutamato inhiben la síntesis de glutatión, provocando un aumento en los niveles de ROS y daño celular en las células neuronales 407,408; sin embargo, esto no se ha demostrado en células TNBC. Un análisis más detallado de los resultados metabolómicos mitocondriales proporcionará información relevante sobre estas suposiciones.

Curiosamente, las mitocondrias respondieron a las demandas de energía en las condiciones de tratamiento seleccionadas, lo que indica solo una alteración mitocondrial parcial y garantiza la observación de la modulación metabólica mitocondrial durante el tratamiento. El análisis de Seahorse XF también reveló una disminución de la glucólisis, lo que podría conducir a una disminución de la actividad del ciclo del TCA. Cretella et al. previamente observaron una menor absorción y metabolismo de la glucosa y una disminución de la expresión del transportador de glucosa GLUT-1 en células MDA-MB-231 tratadas con palbociclib³⁹⁵. Además, este análisis reveló que el tratamiento con palbociclib y StPGA-SS-palbociclib provocó la adquisición de un fenotipo celular más quiescente, que se correlaciona con la senescencia inducida por el palbociclib en las células de cáncer de mama³¹⁹.

Análisis Metobolómico Mitocondrial Mediante NMR de Células de TNBC Tratadas con Palbociclib y StPGA-SS-palbociclib

Aplicamos con éxito la metodología metabolómica mitocondrial optimizada en la sección 1 para evaluar la modulación del metabolismo mitocondrial en células TNBC tratadas con palbociclib libre y conjugado (StPGA-SS-palbociclib). Ambos tratamientos provocaron una disminución de aminoácidos en comparación con las células control (no tratadas), lo que indicó una pérdida de acitvidad del ciclo del TCA, como se había planteado anteriormente. Además, la disminución de los niveles de fosfoenolpiruvato (PEP; sintetizado en las mitocondrias a partir de oxalacetato) en células tratadas con palbociclib libre apoyó la suposición de la inhibición del ciclo del TCA. Warth et al. también observaron una menor actividad del ciclo del TCA en células de cáncer de mama MCF-7 tratadas con palbociclib⁴⁰⁹; sin embargo, la modulación de las mitocondrias en respuesta a palbociclib podría diferir entre los diferentes subtipos de cáncer de mama debido a la gran heterogeneidad metabólica²²¹. No pudimos detectar diferentes respuestas metabólicas en las mitocondrias aisladas de células tratadas con palbociclib libre y StPGA-SS-palbociclib, excepto en los niveles de fosfocolina. El tratamiento con StPGA-SS-palbociclib provocó una reducción significativa de los niveles de fosfocolina en mitocondrias aisladas en comparación con las mitocondrias de células no tratadas. Estos datos sugirieron que la diferente modulación metabólica mitocondrial después del tratamiento con palbociclib libre y StPGA-SS-palbociclib depende principalmente de metabolitos relacionados con los lípidos.

Análisis Metobolómico y Lipidómico Mitocondrial Mediante MS de Células de TNBC Tratadas con Palbociclib y StPGA-SS-palbociclib

Para investigar más a fondo el diferente impacto del fármaco libre y conjugado en el lipidoma mitocondrial, evaluamos el metaboloma y el lipidoma mitocondrial de las células tratadas con palbociclib libre y StPGA-SS-palbociclib mediante MS durante una breve estancia en el laboratorio del profesor Nils J. Færgeman (Laboratorio de Metabolismo Molecular y Metabolómica, Universidad de Dinamarca Meridional).

Aprovechando la disponibilidad del equipo de MS y la experiencia metabolómica de este grupo de investigación, primero analizamos el **perfil metabolómico** de las mitocondrias para i) dilucidar las alteraciones inducidas por el palbociclib libre y StPGA-SS-palbociclib que fueron indetectables mediante espectroscopia de NMR y ii) confirmar los resultados metabolómicos de NMR. Para ello, llevamos a cabo el aislamiento mitocondrial optimizado en la sección 1 y se llevó a cabo la extracción de metabolitos y extrajimos los metabolitos utilizando un método de Folch²⁶⁶ modificado basado en el uso de una mezcla de CHCl₃:MeOH:H₂O y una doble extracción de la fase acuosa.

Curiosamente, muchos péptidos presentaron niveles reducidos en las mitocondrias de las células tratadas con palbociclib libre y StPGA-SS-palbociclib en comparación con las células no tratadas, lo que se correlaciona con la disminución de los niveles de aminoácidos detectados por NMR. La disminución de los niveles de aminoácidos en las mitocondrias se ha asociado a una deficiencia en la respiración mitocondrial y a la disfunción del ciclo del TCA²⁷⁸. Además, los péptidos mitocondriales podrían formar parte de los recientemente identificados péptidos derivados de las mitocondrias, componentes mitocondriales cruciales para la función correcta de los orgánulos³²⁶. Curiosamente, el papel fundamental de estos péptidos para la homeostasis mitocondrial ha llevado a los investigadores a utilizarlos como dianas terapéuticas. La sensibilidad de la MS permitió la detección de niveles de desoxiguanosina significativamente aumentados en mitocondrias aisladas después del tratamiento con palbociclib libre y StPGA-SSpalbociclib. La desoxiguanosina es un precursor de la 8-hidroxidesoxiguanosina, un indicador del daño del ADN mitocondrial³²⁸; por tanto, EL palbociclib libre y StPGA-SS-palbociclib pueden causar daño mitocondrial a nivel genético para inducir la disfunción mitocondrial observada (p. ej., la síntesis reducida de nucleótidos causada por la inhibición del ciclo del TCA puede afectar a la replicación del ADN mitocondrial). También se detectaron niveles elevados de espermidina en las mitocondrias de las células después del tratamiento con StPGA-SS-palbociclib. Este aumento de espermidina se correlacionó con un deterioro más significativo de la respiración mitocondrial en células tratadas con StPGA-SS-palbociclib (como se observó utilizando el analizador Seahorse), dado que estudios publicados anteriormente han demostrado que los niveles elevados de espermidina promueven el desacoplamiento de la OXPHOS³³⁰. Es de destacar que se detectó un aumento de los niveles de glicerofosfocolina (GPC) en las mitocondrias de las células tratadas con palbociclib libre y con el conjugado StPGA-SSpalbociclib, lo cual apoyó la hipótesis de una alteración del metabolismo de los lípidos.

Para confirmar la suposición de que el palbociclib y el conjugado StPGA-SS-palbociclib impactan el metabolismo de los lípidos mitocondriales y para explorar el diferente impacto de cada tipo de tratamiento, realizamos un **análisis lipidómico** mediante MS. Para ello, analizamos el extracto orgánico tras la extracción de metabolitos utilizando el protocolo de extracción modificado de Folch.

Detectamos una cantidad considerable de lípidos que son difíciles de detectar mediante espectroscopia de NMR debido a la superposición de señales de lípidos²⁰⁸. Curiosamente, encontramos un perfil lipidómico diferente entre las mitocondrias de las células de TNBC tratadas con palbociclib libre y el conjugado StPGA-SS-palbociclib y las de las células no tratadas. Detectamos más alteraciones lipídicas en las mitocondrias de las células tratadas con el

conjugado StPGA-SS-palbociclib en comparación con el control que con palbociclib libre, lo cual indicó un impacto más significativo del conjugado StPGA-SS-palbociclib en el lipidoma mitocondrial. Además, muchos lípidos mostraron niveles significativamente diferentes después del tratamiento con palbociclib y StPGA-SS-palbociclib, lo que confirma el mayor impacto de este último en el lipidoma mitocondrial de las células de TNBC. Una posible razón de estas diferencias deriva de la implicación de las membranas celulares y subcelulares durante la internalización endocítica del conjugado StPGA-SS-palbociclib. La invaginación, fusión y disrupción de las membranas que tiene lugar durante este proceso, puede provocar alteraciones de los lípidos de la membrana. A destacar, los fosfatidilgliceroles (lípidos exclusivos de las mitocondrias) disminuyeron en las mitocondrias de las células tratadas con StPGA-SSpalbociclib, mientras que no observamos alteraciones después del tratamiento con palbociclib libre, lo cual respalda nuevamente el mayor impacto del conjugado en el metabolismo de los lípidos en las mitocondrias. Además, muchas especies de fosfatidilcolina disminuyeron en las mitocondrias de las células tratadas con palbociclib y StPGA-SS-palbociclib en comparación con las células no tratadas. Estos datos, junto con la disminución de los niveles de fosfocolina (principalmente después del tratamiento con el conjugado StPGA-SS-palbociclib) observada mediante la metabolómica de NMR y el aumento de los niveles de GPC observados mediante la metabolómica de MS, confirmaron el deterioro de la vía CDP-colina. La disminución de los niveles de fosfocolina puede conducir a una reducción de la síntesis de fosfatidilcolina, mientras que el aumento de los niveles de GPC puede resultar de la degradación de la fosfatidilcolina. De hecho, Sonkar et al. mostraron una asociación entre la disminución de los niveles de fosfocolina y el aumento de los niveles de GPC después del tratamiento con doxorrubicina en células de cáncer de mama³⁸⁷. Además, Smith et al. relacionó la fosfocolina con la proliferación celular³⁵⁵; por tanto, la disminución de los niveles de fosfocolina puede reflejar el arresto del crecimiento celular inducido por el tratamiento con palbociclib.

Análisis Fluxómico Mediante MS de Células de TNBC Tratadas con Palbociclib y StPGA-SS-palbociclib

Los resultados del estudio lipidómico mitocondrial nos llevó a estudiar el origen de estas alteraciones. El citrato (un intermedio del ciclo del TCA) se transporta al citosol para la biosíntesis de ácidos grasos^{30,350}; por tanto, planteamos la hipótesis de que la actividad reducida del ciclo del TCA provocó una reducción en los niveles de fosfatidilcolina e investigamos esta suposición realizando análisis fluxómicos mediante MS y NMR. A diferencia de la metabolómica, la fluxómica permite medir las tasas de flujo intracelular, lo que nos permite rastrear la ruta de un metabolito utilizando metabolitos marcados isotópicamente²¹⁸. Utilizamos ¹³C-glucosa para

evaluar si la síntesis reducida de ácidos grasos era el resultado de una glucólisis reducida y, por tanto, de una reducción del acetil-CoA necesario para sintetizar ácidos grasos. Una hipótesis alternativa podría ser que que la glucólisis reducida podría conducir a una reducción de la actividad del ciclo del TCA y, por tanto, a niveles reducidos de citrato, que puede transportarse al citosol para la síntesis de ácidos grasos. Además, realizamos estudios de marcaje con ¹³C-glutamina para descubrir si la glutaminolisis reducida podría conducir a una disminución de la actividad del ciclo del TCA y, nuevamente, a una reducción de la producción de citrato para la síntesis de ácidos grasos.

Para llevar a cabo los experimentos de fluxómica, optimizamos los tiempos de marcaje de los metabolitos. Tras el tratamiento de las células con palbociclib libre y StPGA-SS-palbociclib con las concentraciones correspondientes a los IC₃₀ durante 72 h, incubamos las células con medio con ¹³C-glucose durante 15, 60, 120 y 180 min o ¹³C-glutamine durante 180 y 360 min. Los resultados del análisis por MS de las células mostraron que el marcaje máximo de los metabolitos se alcanzó a los 120 min para la ¹³C-glucose y 180 min para la ¹³C-glutamine.

El análisis fluxómico mediante MS con 13C-glucosa indicó la inhibición de la glucólisis después del tratamiento con StPGA-SS-palbociclib, lo que condujo a una disminución de la actividad del ciclo del TCA (reducción del isotopólogo de citrato M+2). Sorprendentemente, el palbociclib libre no disminuyó la actividad del ciclo del TCA tras la inhibición de la glucólisis. Observamos un aumento del α-cetoglutarato marcado con ¹³C después del tratamiento con palbociclib libre. Nuestra hipótesis es que el palbociclib libre probablemente indujo un efecto más leve sobre la glucólisis que el conjugado StPGA-SS-palbociclib debido al perfil farmacocinético modificado del conjugado (mayor biodisponibilidad intracelular de palbociclib debido a un mecanismo lisosomotrópico de liberación controlada del fármaco). Curiosamente, también detectamos una disminución de la síntesis de purinas (incluida una reducción de la síntesis de ATP) después del tratamiento con palbociclib y StPGA-SS-palbociclib, lo que indicó un deterioro de la vía de las pentosas fosfato (PPP) causado por una reducción de la glucólisis o de la producción de sustratos por el ciclo del TCA (p. ej., el aspartato es crucial para la síntesis de nucleótidos⁴⁰⁶). Conroy et al. observaron que el tratamiento de células de pulmón con palbociclib no afectó a la glucólisis, pero redujo el metabolismo de la glucosa a través del PPP al reducir la actividad de la glucosa-6fosfato deshidrogenasa⁴¹⁰. Además, el tratamiento con palbociclib de las células de cáncer de mama MCF-7 también reguló negativamente la PPP y la síntesis de purinas⁴⁰⁹, lo cual respalda nuestros resultados. Sin embargo, observamos un aumento de la síntesis de pirimidina después del tratamiento con StPGA-SS-palbociclib, lo cual sugirió que se produce una estimulación de la generación de fuentes alternativas de fosfato para compensar la síntesis reducida de ATP mediante la glucólisis y el ciclo del TCA. La mayor síntesis de pirimidinas podría ser consecuencia de una mayor formación de glutamina, como se planteó anteriormente en esta sección. Además, detectamos una mayor acumulación de citidina trifosfato (CTP), lo cual apoyó la hipótesis de una menor síntesis de fosfatidilcolina (requiere CTP³⁴⁹).

El análisis fluxómico de MS de ¹³C-glutamina mostró la inhibición de la glutaminólisis y el ciclo del TCA después del tratamiento con palbociclib libre y el conjugado StPGA-SS-palbociclib. Además, detectamos una síntesis de aspartato significativamente menor en las células tratadas con palbociclib libre y StPGA-SS-palbociclib en comparación con el control, lo que apoya la suposición de una menor producción de aspartato como fuente de nitrógeno para la síntesis de nucleótidos y, por tanto, una reducción de la síntesis de purinas ⁴⁰⁶. Las unidades de ácido glutámico resultantes de la degradación lisosomal del StPGA podrían promover una mayor actividad del ciclo del TCA; sin embargo, no observamos diferencias significativas entre el impacto de palbociclib libre y StPGA-SS-palbociclib sobre la glutaminólisis y la actividad del ciclo del TCA. Por tanto, el aumento de la reserva de glutamato causado por la degradación de StPGA puede usarse para fines distintos a la incorporación del ciclo del TCA. Este resultado apoya la hipótesis de la conversión de glutamato a glutamina y su uso para vías alternativas; por ejemplo, para la síntesis de pirimidina, la cual aumentó después del tratamiento con StPGA-SS-palbociclib.

Análisis Fluxómico Mediante NMR de Células de TNBC Tratadas con Palbociclib y StPGA-SSpalbociclib

Siguiendo el mismo procedimiento que en la sección anterior, realizamos un análisis fluxómico mediante NMR de células tratadas con palbociclib y StPGA-SS-palbociclib. La **fluxómica de NMR con** ¹³**C-glucosa** confirmó la inhibición de la glucólisis en las últimas reacciones de la ruta metabólica (conversión de piruvato en lactato y alanina) después del tratamiento con palbociclib libre y StPGA-SS-palbociclib.

Curiosamente, el análisis fluxómico de NMR de ¹³C-glutamina</sup> proporcionó información relevante para nuestras hipótesis. Los niveles de ¹³C-glutamato aumentaron después del tratamiento con palbociclib libre y, en mayor medida, con el tratamiento con StPGA-SS-palbociclib, lo que confirma la reducción observada previamente en la glutaminólisis. Además, la detección de niveles elevados de ¹³C-GPC después del tratamiento con palbociclib libre y conjugado confirmó que la glutaminólisis reducida condujo a una producción reducida de citrato y, por tanto, a una reducción de la síntesis de ácidos grasos para la producción de lípidos.

Estudio Metabolómico y Lipidómico de Células Completas Tratadas con Palbociclib Libre y StPGA-SS-palbociclib

El estudio metabolómico de NMR y MS de células completas y el análisis de NMR del medio extracelular nos ayudaron a comprender mejor la modulación metabólica mitocondrial después del tratamiento con palbociclib libre y StPGA-SS-palbociclib.

Para ello, tras recoger las células, se llevó a cabo la extracción de metabolitos siguiendo el protocolo de Folch, basado en el uso de metanol, cloroformo y agua 266 . El análisis del medio extracelular mediante NMR se llevó a cabo añadiendo 100 μ L de buffer de NMR a 500 μ L de medio extracelular.

De estos análisis destacamos:

- i) El conjugado StPGA-SS-palbociclib indujo una inhibición más significativa de la glucólisis en comparación con el palbociclib libre, ya que observamos una disminución de los niveles de lactato en célula completa y una disminución de los niveles de piruvato y PEP en el medio extracelular
- ii) El conjugado StPGA-SS-palbociclib provocó una inhibición más significativa del ciclo del TCA en comparación con el palbociclib libre, ya que detectamos una acumulación de acetato en el medio extracelular
- iii) El palbociclib libre y el conjugado StPGA-SS-palbociclib provocaron la inhibición de la glutaminólisis, ya que observamos una acumulación de glutamina
- iv) La degradación de StPGA aumentó la reserva de glutamato, ya que detectamos un aumento de los niveles de glutamato en el medio extracelular
- v) El conjugado StPGA-SS-palbociclib produjo una mayor acumulación de glutamina que el control StPGA, lo cual sugirió el uso del exceso de glutamato para la síntesis de glutamina y su uso en otras vías (p. ej., síntesis de pirimidina)
- vi) La glucólisis y la alteración de la respiración mitocondrial en células tratadas con StPGA-SSpalbociclib se confirmaron mediante la detección de una disminución de la reserva de ATP
- vii) A diferencia del palbociclib, el conjugado StPGA-SS-palbociclib interrumpió la función de la fosfocreatina para transportar grupos fosfato al citosol de las células debido a la menor producción de ATP mitocondrial
- viii) StPGA-SS-palbociclib tuvo un impacto más significativo en el lipidoma celular en comparación con el palbociclib libre, ya que observamos niveles significativamente más bajos de fosfocolina en células completas tratadas con el conjugado StPGA-SS-palbociclib y niveles

elevados de GPC en el medio extracelular después del tratamiento con conjugado StPGA-SSpalbociclib en comparación con el tratamiento con palbociclib libre.

Es importante señalar que el análisis lipidómico mediante MS de células completas también contribuyó a una comprensión más sólida de las alteraciones de los lípidos mitocondriales. La detección de niveles reducidos de cardiolipinas y de la mayoría de los fosfatidilgliceroles (ambos lípidos exclusivos de la membrana mitocondrial) en células tratadas con el conjugado StPGA-SS-palbociclib confirmó un mayor daño mitocondrial inducido por palbociclib conjugado en comparación con el palbociclib libre.

3. Análisis Metabolómico de Mitocondria Aislada de Tejidos de Ratones Sanos y de un Modelo de Ratón con Cáncer de Mama Triple Negativo

Pensando en dar un paso más hacia la aplicación clínica, adaptamos el análisis metabolómico mitocondrial mediante NMR a tejidos de ratón: tumores primarios de TNBC, órganos afectados por metástasis (principalmente pulmones⁷²) y órganos de animales sanos (pulmones, hígado, riñón y cerebro).

Optimización del Análisis Metabolómico Mitocondrial Mediante NMR de Mitocondrias Aisladas de Tejidos Murinos

La optimización de la metodología resultó en el uso de la misma estrategia experimental para el aislamiento de mitocondrias, la extracción de metabolitos y el análisis de NMR que en las secciones 1 y 2 para células TNBC. El aislamiento de mitocondrias consistió en la homogeneización de tejidos y fraccionamiento mediante centrifugación diferencial; sin embargo, consideramos ciertos factores para la homogeneización del tejido. La densidad, la solidez y la presencia de filamentos/fibras influyen en la homogeneización del tejido⁴¹¹. Mediante la optimización de la homogeneización de tejidos seleccionamos el uso de la homogeneización manual con Dounce para muestras de hígado, pulmón, riñón y cerebro, y un método de homogeneización más potente para los tejidos de naturaleza más compacta y fibrosa como los tejidos tumorales de TNBC, como lo indican Burden et al. para tejidos sólidos⁴¹¹. Por tanto, utilizamos un homogeneización completa del tejido y proporcionar mejores espectros de NMR de mitocondrias aisladas. Obtuvimos fracciones enriquecidas en mitocondrias de cada tejido mediante centrifugación diferencial y confirmamos la identidad mediante análisis de Western Blot.

Siguiendo el mismo razonamiento que para las células (sección 1), la extracción de metabolitos se basó en el uso de tampón de NMR para evitar la pérdida de metabolitos⁴⁰¹, sonicación y enfriamiento de la muestra en nitrógeno líquido para permitir la liberación de los metabolitos de las mitocondrias^{269,270} y ultrafiltración de proteínas para evitar alteraciones en la línea base⁴¹³.

Perfil Metabolómico de las Mitocondrias de Tejidos Murinos

La metodología optimizada proporcionó espectros de NMR NOESY de buena calidad de las mitocondrias aisladas, a partir de los cuales identificamos un total de cuarenta y cinco metabolitos; en comparación, estudios metabolómicos mitocondriales de NMR anteriores solo identificaron entre seis y catorce metabolitos^{230,231}. Curiosamente, el perfil metabolómico de cada tejido mostró especificidad (diferentes intensidades de metabolitos y contenido de metabolitos); por ejemplo, solo detectamos N-acetil aspartato en muestras de cerebro, tal y como han mostrado otros estudios metabolómicos mitocondriales^{230,231}. Las muestras mitocondriales de hígado y riñón se caracterizaron por un número elevado de aminoácidos. El hígado contiene abundantes aminoácidos ya que participa en la síntesis, degradación y desintoxicación de proteínas⁴¹⁴, mientras que los riñones representan mediadores cruciales para el intercambio de aminoácidos entre órganos⁴¹⁵. El metaboloma mitocondrial de los tejidos cerebrales se caracterizó por un alto contenido de nucleótidos, lo cual se correlaciona con el papel esencial de los nucleótidos para diversas funciones neuronales como la comunicación entre células⁴¹⁶. Las mitocondrias de los pulmones mostraron un alto contenido de lípidos, lo que concuerda con el papel central de los lípidos en la fisiología y patología pulmonar⁴¹⁷. Finalmente, las mitocondrias del tumor de TNBC presentaron altos niveles de ácidos orgánicos (p. ej., lactato y citrato), aminoácidos y metabolitos relacionados con los lípidos, lo cual puede reflejar la estimulación de la glucólisis, el ciclo del TCA y la síntesis de lípidos para promover la progresión del tumor, como se ha descrito anteriormente para el modelo de TNBC MDA-MB-231^{72,112}. Curiosamente, el perfil metabolómico de las mitocondrias también reveló características específicas de cada tejido, lo cual respalda la validez de la metodología optimizada. Por ejemplo, encontramos ornitina exclusivamente en las mitocondrias del tejido hepático. Gamble et al. informaron que, en el hígado de los mamíferos, la ornitina se transporta a las mitocondrias, donde tiene lugar la conversión a citrulina⁴¹⁸.

Comparación del Perfil Metabolómico de las Mitocondrias y de las Células Completas de Tejidos Murinos

Para garantizar la validez del método, a continuación, comparamos el contenido metabolómico de las mitocondrias aisladas con muestras de células completas tomadas de los tejidos. Estudios anteriores compararon el perfil metabolómico de mitocondrias aisladas con el del citosol^{230,231}, en lugar de con muestras de células completas. Mediante esa metodología loas autores proporcionaron información específica sobre las alteraciones metabólicas en el citosol; sin embargo, nuestro objetivo fue demostrar que el análisis específico de las mitocondrias proporciona firmas metabolómicas específicas que las muestras de células completas no pueden. En general, encontramos alteraciones en múltiples metabolitos al comparar muestras de células completas con mitocondrias aisladas de células de distintos tejidos, lo cual respalda esta hipótesis.

En general, los tumores de TNBC MDA-MB-231-Luc extirpados de ratones tras 42 días desde la inducción, mostraron niveles relativos más altos de la mayoría de los metabolitos en muestras de células completas (muy altos para el lactato) en comparación con las mitocondrias aisladas. Esto resultados reflejan el fenotipo altamente glucolítico de las células MDA-MB-231 para producir sustratos y energía en forma de ATP¹¹². Sin embargo, observamos niveles elevados de derivados de colina en las mitocondrias aisladas de tumores de TNBC, que se mantuvieron similares a los niveles en las muestras de células completas. Estos resultados pueden reflejar la importancia de las fosfatidilcolinas en el mantenimiento de las membranas celulares y mitocondriales³³⁷. Glunde et al. mostraron alteraciones en el metabolismo de la colina en células de cáncer de mama³⁸⁶. Además, Arroyo-Crespo et al. también observaron elevados niveles de GPC en el modelo de ratón MDA-MB-231-Luc⁷².

Evaluación de la Modulación Metabólica Mitocondrial durante la Metástasis en Tejidos de un Modelo de Ratón con TNBC

Finalmente aplicamos la metodología descrita para evaluar la modulación del metabolismo mitocondrial en la metástasis del TNBC. Detectamos alteraciones metabólicas en las mitocondrias pulmonares aisladas de un modelo metastásico MDA-MB-231-Luc⁷² en comparación con las mitocondrias aisladas de pulmones de ratones sanos. Además, observamos pocas diferencias entre los hígados de ratones sanos y metastásicos, y no pudimos detectar alteraciones mitocondriales en las mitocondrias de los riñones de ratones metastásicos, los cuales utilizamos como control negativo (nuestro modelo ortotópico de TNBC⁷² carece de metástasis renal). Estos resultados concuerdan con un estudio anterior que muestra que el modelo de ratón MDA-MB-231-Luc produjo metástasis pulmonar pero no metástasis hepática⁷². Ocho metabolitos (lactato, colina, fosfocolina, alanina, creatina, glucosa, metionina y glutamato)

mostraron niveles elevados en las mitocondrias de los pulmones metastásicos. Estos hallazgos indicaron un aumento de la glucólisis y una mayor síntesis de aminoácidos, lípidos y creatina para suministrar energía y sustratos metabólicos a las células y promover el crecimiento y la invasión del tumor. Lebleu et al. mostraron un aumento de la actividad mitocondrial en un modelo de ratón con cáncer de mama 4T1 con desarrollo de metástasis pulmonar¹¹⁵. En las células de cáncer de mama, una alta actividad mitocondrial se ha correlacionado con el desarrollo de metástasis pulmonar y ósea¹¹⁶, mientras que en células de cáncer de mama metastásico hepático se ha observado una mayor actividad glucolítica y una disminución de la OXPHOS y la glutaminólisis¹¹⁷.

En general, los resultados de esta sección sugirieron que el método descrito, ya validado en células, demostró validez para los estudios metabólicos de las mitocondrias tisulares. La aplicación de metabolómica mitocondrial en muestras de tejido para evaluar la modulación metabólica mitocondrial tras el tratamiento con fármacos libres y formulaciones nanomedicinales representa un trabajo pendiente para futuros experimentos.

CONCLUSIONES

Esta tesis describe la implementación de una metodología metabolómica basada en NMR para el estudio específico de mitocondrias con el objetivo de investigar alteraciones en el metabolismo mitocondrial después del tratamiento con fármacos de pequeño peso molecular y un nanofármaco en células de TNBC y la modulación del metabolismo mitocondrial en tejidos metastásicos. Nuestros hallazgos validaron la metodología desarrollada y subrayaron la importancia de comprender el metabolismo mitocondrial. El estudio de las rutas metabólicas mitocondriales es crucial para dilucidar las distintas respuestas farmacológicas de un tratamiento determinado y destaca la eficacia superior de las nanomedicinas diseñadas racionalmente como terapias contra el cáncer.

En base a nuestros resultados, las principales conclusiones que se desprenden de esta tesis son:

- 1. El protocolo metabolómico de NMR desarrollado, aplicado para analizar mitocondrias aisladas en células TNBC, tejidos de ratón sanos y tejidos de un modelo de ratón TNBC, resultó en perfiles metabólicos mitocondriales consistentes y reproducibles. La metodología abarcó el aislamiento de mitocondrias mediante centrifugación diferencial, extracción de metabolitos monofásica y basada en el uso de disolventes acuosos, y la adquisición de espectros de NMR mediante NOESY.
- 2. Sintetizamos el conjugado polipéptido-fármaco StPGA-SS-palbociclib en un procedimiento de tres pasos conjugando palbociclib con el polímero biodegradable StPGA a través de un enlace

disulfuro autoinmolativo sensible a redox (-SS-). StPGA-SS-palbociclib indujo menos citotoxicidad en células TNBC en comparación con palbociclib libre debido a diferentes mecanismos de internalización. Sin embargo, StPGA-SS-palbociclib provocó un daño más significativo en la respiración mitocondrial debido al sinergismo entre las unidades de ácido glutámico de StPGA y palbociclib. Esta metodología también reveló una disminución en la actividad glucolítica tras el tratamiento con palbociclib libre y StPGA-SS-palbociclib.

- 3. La metodología optimizada de NMR mitocondrial permitió la determinación del perfil metabolómico de las mitocondrias aisladas de células de TNBC tratadas con palbociclib libre y conjugado StPGA-SS-palbociclib. El tratamiento con palbociclib y StPGA-SS-palbociclib disminuyó la actividad del ciclo del TCA, mientras que StPGA-SS-palbociclib indujo mayores alteraciones lipídicas.
- 4. El análisis metabolómico mitocondrial mediante MS confirmó que el tratamiento con palbociclib libre y StPGA-SS-palbociclib alteró las mitocondrias de las células de TNBC. La disminución de los niveles de péptidos confirmó una reducción de la actividad del ciclo del TCA, el aumento de la desoxiguanosina sugirió daño en el ADN mitocondrial y los niveles elevados de GPC indicaron una alteración del metabolismo de los lípidos. Los niveles elevados de espermidina en las mitocondrias demostraron una alteración más significativa de la OXPHOS inducida por el tratamiento con StPGA-SS-palbociclib.
- 5. El análisis lipidómico mediante MS reveló un impacto mayor y más específico del tratamiento con palbociclib libre y StPGA-SS-palbociclib en el lipidoma mitocondrial que en el metaboloma mitocondrial en las células de TNBC. StPGA-SS-palbociclib indujo un efecto más significativo, con una disminución notable de las fosfatidilcolinas que respalda la alteración de la vía CDP-colina.
- 6. El análisis metabolómico mediante NMR y MS de células completas confirmó varias teorías: i) la interrupción de la glucólisis y la respiración mitocondrial después del tratamiento con StPGA-SS-palbociclib; ii) un efecto más significativo de StPGA-SS-palbociclib en comparación con palbociclib libre en la reducción de la actividad del ciclo del TCA; iii) la inhibición de la glutaminólisis después del tratamiento con palbociclib libre y StPGA-SS-palbociclib; y iv) un impacto más significativo del tratamiento con StPGA-SS-palbociclib en el lipidoma comparado con el palbociclib libre.
- 7. El análisis de fluxómica mediante NMR y MS confirmó la inhibición de la glucólisis y la estimulación de la síntesis de pirimidina después del tratamiento con StPGA-SS-palbociclib, mientras que tanto el tratamiento con palbociclib libre como con StPGA-SS-palbociclib inhibieron la síntesis de purinas. A nivel mitocondrial, estos estudios revelaron una inhibición de

la glutaminólisis y de la actividad del ciclo del TCA después del tratamiento con palbociclib libre y StPGA-SS-palbociclib.

- 8. La metodología optimizada de NMR demostró su potencial en estudios preclínicos *in vivo* al caracterizar el perfil metabolómico mitocondrial de células de diversos tejidos en ratone sanos y en un modelo de ratón ortotópico de TNBC metastásico. El estudio reveló distintas firmas metabólicas en las mitocondrias de cada tipo de tejido. En particular, los tumores de mama exhibieron niveles elevados de metabolitos que estimulan el metabolismo de la glucosa, el ciclo del TCA y la síntesis de lípidos para apoyar la progresión del tumor.
- 9. La metodología desarrollada se validó comparando la modulación metabolómica específica de las mitocondrias en tejidos de ratones sanos y en los de un modelo de ratón ortotópico de TNBC metastásico. Los niveles elevados de metabolitos en las mitocondrias pulmonares sugirieron una adaptación del metabolismo mitocondrial en las células metastásicas del TNBC para promover el crecimiento y la invasión del tumor.

REFERENCES

- 1. Min, H. Y. & Lee, H. Y. Oncogene-driven metabolic alterations in cancer. *Biomol. Ther.* **26**, 45–56 (2018).
- 2. Wedam, R. *et al.* Targeting Mitochondria with ClpP Agonists as a Novel Therapeutic Opportunity in Breast Cancer. *Cancers (Basel).* **15**, (2023).
- 3. Gururaja Rao, S. Mitochondrial changes in cancer. in *Handbook of Experimental Pharmacology* (2017). doi:10.1007/164_2016_40.
- 4. Nakamura, H. & Takada, K. Reactive oxygen species in cancer: Current findings and future directions. *Cancer Sci.* **112**, 3945–3952 (2021).
- 5. Valenti, D. & Atlante, A. Mitochondrial Bioenergetics in Different Pathophysiological Conditions 2.0. *Int. J. Mol. Sci.* **23**, (2022).
- 6. Joubert, F. & Puff, N. Mitochondrial cristae architecture and functions: Lessons from minimal model systems. *Membranes (Basel).* **11**, 1–27 (2021).
- 7. Galloway, C. A., Lee, H. & Yoon, Y. Mitochondrial morphology Emerging role in bioenergetics. **53**, 1–23 (2013).
- 8. Chu, C. H., Tseng, W. W., Hsu, C. M. & Wei, A. C. Image Analysis of the Mitochondrial Network Morphology With Applications in Cancer Research. *Front. Phys.* **10**, 1–16 (2022).
- 9. Herst, P. M., Rowe, M. R., Carson, G. M. & Berridge, M. V. Functional mitochondria in health and disease. *Front. Endocrinol. (Lausanne).* **8**, (2017).
- 10. McCarron, J. G. *et al.* From structure to function: Mitochondrial morphology, motion and shaping in vascular smooth muscle. *J. Vasc. Res.* **50**, 357–371 (2013).
- 11. Cole, L. W. The evolution of per-cell organelle number. Front. Cell Dev. Biol. 4, 1–7 (2016).
- 12. Degli Esposti, D. *et al.* Mitochondrial roles and cytoprotection in chronic liver injury. *Biochem. Res. Int.* **2012**, (2012).
- 13. Osorio, D. & Cai, J. J. Systematic determination of the mitochondrial proportion in human and mice tissues for single-cell RNA-sequencing data quality control. *Bioinformatics* **37**, 963–967 (2021).
- 14. Chakrabarty, R. P. & Chandel, N. S. Beyond ATP, new roles of mitochondria. *Biochem.* (Lond). 44, 2–8 (2022).
- 15. Zorova, L. D. et al. Mitochondrial membrane potential. Anal. Biochem. **552**, 50–59 (2018).
- 16. Gorman, G. S. et al. Mitochondrial diseases. Nat. Rev. Dis. Prim. 2, 1–23 (2016).
- 17. Shiratori, R. *et al.* Glycolytic suppression dramatically changes the intracellular metabolic profile of multiple cancer cell lines in a mitochondrial metabolism-dependent manner. *Sci. Rep.* **9**, 1–15 (2019).
- 18. Adams, S. *et al.* Pembrolizumab monotherapy for previously treated metastatic triplenegative breast cancer: Cohort A of the phase II KEYNOTE-086 study. *Ann. Oncol.* **30**, 397–404 (2019).
- 19. Murphy, M. P. How mitochondria produce reactive oxygen species. *Biochem. J.* **417**, 1–13 (2009).

- 20. Bhagavan, N. V. & Ha, C.-E. Lipids I. *Essentials Med. Biochem.* 269–297 (2015) doi:10.1016/b978-0-12-416687-5.00016-6.
- 21. Spinelli, J. B. & Haigis, M. C. The multifaceted contributions of mitochondria to cellular metabolism. *Nat. Cell Biol.* **20**, 745–754 (2018).
- 22. Arnold, P. K. & Finley, L. W. S. Regulation and function of the mammalian tricarboxylic acid cycle. *J. Biol. Chem.* **299**, 102838 (2023).
- 23. Sherry, E. B., Lee, P. & Choi, I. Y. In Vivo NMR Studies of the Brain with Hereditary or Acquired Metabolic Disorders. *Neurochem. Res.* **40**, 2647–2685 (2015).
- 24. Martínez-Reyes, I. & Chandel, N. S. Mitochondrial TCA cycle metabolites control physiology and disease. *Nat. Commun.* **11**, 1–11 (2020).
- 25. Yoo, H. C., Yu, Y. C., Sung, Y. & Han, J. M. Glutamine reliance in cell metabolism. *Exp. Mol. Med.* **52**, 1496–1516 (2020).
- 26. Li, C., Zhang, G., Zhao, L., Ma, Z. & Chen, H. Metabolic reprogramming in cancer cells: Glycolysis, glutaminolysis, and Bcl-2 proteins as novel therapeutic targets for cancer. *World J. Surg. Oncol.* **14**, 1–7 (2016).
- 27. Haskins, N. *et al.* Mitochondrial Enzymes of the Urea Cycle Cluster at the Inner Mitochondrial Membrane. *Front. Physiol.* **11**, 1–17 (2021).
- 28. Wallimann, T., Tokarska-Schlattner, M. & Schlattner, U. The creatine kinase system and pleiotropic effects of creatine. *Amino Acids* **40**, 1271–1296 (2011).
- 29. Zarou, M. M., Vazquez, A. & Vignir Helgason, G. Folate metabolism: a re-emerging therapeutic target in haematological cancers. *Leukemia* **35**, 1539–1551 (2021).
- 30. Tumanov, S., Bulusu, V. & Kamphorst, J. J. *Analysis of Fatty Acid Metabolism Using Stable Isotope Tracers and Mass Spectrometry. Methods in Enzymology* vol. 561 (Elsevier Inc., 2015).
- 31. Nowinski, S. M., Van Vranken, J. G., Dove, K. K. & Rutter, J. Mitochondrial Fatty Acid Synthesis is the puppet master of mitochondrial biogenesis. *Curr. Biol.* **18**, 1212–1219 (2018).
- 32. Nowinski, S. M. *et al.* Mitochondrial fatty acid synthesis coordinates oxidative metabolism in mammalian mitochondria. *Elife* **9**, 1–35 (2020).
- 33. Clay, H. B. *et al.* Altering the mitochondrial fatty acid synthesis (mtFASII) pathway modulates cellular metabolic states and bioactive lipid profiles AS revealed by metabolomic profiling. *PLoS One* **11**, 1–23 (2016).
- 34. Duchen, M. R. Roles of Mitochondria in Health and Disease. *Diabetes* **53**, (2004).
- 35. Palty, R. & Sekler, I. The mitochondrial Na+/Ca2+ exchanger. Cell Calcium 52, 9–15 (2012).
- 36. Murphy, E. *et al.* Mitochondrial Function, Biology, and Role in Disease: A Scientific Statement from the American Heart Association. *Circ. Res.* **118**, 1960–1991 (2016).
- 37. Vasan, K. *et al.* Genes Involved in Maintaining Mitochondrial Membrane Potential Upon Electron Transport Chain Disruption. *Front. Cell Dev. Biol.* **10**, 1–6 (2022).
- 38. Chen, Y., Zhang, H., Jenny, H., Ji, W. & Min, W. Mitochondrial redox signaling and tumor progression. *Cancers (Basel).* **8**, 1–15 (2016).

- 39. Sheu, S. S., Nauduri, D. & Anders, M. W. Targeting antioxidants to mitochondria: A new therapeutic direction. *Biochim. Biophys. Acta Mol. Basis Dis.* **1762**, 256–265 (2006).
- 40. Choi, I., Son, H. & Baek, J. H. Tricarboxylic acid (Tca) cycle intermediates: Regulators of immune responses. *Life* **11**, 1–19 (2021).
- 41. Xu, S. *et al.* Role of Mitochondria in Neurodegenerative Diseases: From an Epigenetic Perspective. *Front. Cell Dev. Biol.* **9**, 1–16 (2021).
- 42. Zhang, D. *et al.* Mitochondrial DNA mutations activate the mitochondrial apoptotic pathway and cause dilated cardiomyopathy. *Cardiovasc. Res.* **57**, 147–157 (2003).
- 43. Cairns, C. B. Rude unhinging of the machinery of life: Metabolic approaches to hemorrhagic shock. *Curr. Opin. Crit. Care* **7**, 437–443 (2001).
- 44. Sun, N., Youle, R. J. & Finkel, T. The Mitochondrial Basis of Aging. *Mol. Cell* **61**, 654–666 (2016).
- 45. Hekimi, S. & Guarente, L. Genetics and the specificity of the aging process. *Science (80-.)*. **299**, 1351–1354 (2003).
- 46. Zong, W.-X., Rabinowitz, J. D. & White, E. Mitochondria and Cancer. *Mol. Cell* **61**, 667–676 (2016).
- 47. DeBerardinis, R. J. & Chandel, N. S. We need to talk about the Warburg effect. *Nat. Metab.* **2**, 127–129 (2020).
- 48. breastcancer.org. Breast Cancer Facts and Statistics. https://www.breastcancer.org/facts-statistics.
- 49. American Cancer Society. Breast Cancer Signs and Symptoms. https://www.cancer.org/cancer/types/breast-cancer/screening-tests-and-early-detection/breast-cancer-signs-and-symptoms.html (2022).
- 50. Sung, H. *et al.* Global Cancer Statistics 2020: GLOBOCAN Estimates of Incidence and Mortality Worldwide for 36 Cancers in 185 Countries. *CA. Cancer J. Clin.* **71**, 209–249 (2021).
- 51. Ye, F. *et al.* Advancements in clinical aspects of targeted therapy and immunotherapy in breast cancer. *Mol. Cancer* **22**, 1–40 (2023).
- 52. Plevritis, S. K. *et al.* Association of screening and treatment with breast cancer mortality by molecular subtype in US women, 2000-2012. *JAMA J. Am. Med. Assoc.* **319**, 154–164 (2018).
- 53. Siegel, R. L., Miller, K. D., Wagle, N. S. & Jemal, A. Cancer statistics, 2023. *CA. Cancer J. Clin.* **73**, 17–48 (2023).
- 54. Marmot, M. G. *et al.* The benefits and harms of breast cancer screening: An independent review. *Br. J. Cancer* **108**, 2205–2240 (2013).
- 55. Houssami, N. Overdiagnosis of breast cancer in population screening: does it make breast screening worthless? *Cancer Biol. Med.* **14**, 1–8 (2017).
- 56. Carter, J. L., Coletti, R. J. & Harris, R. P. Quantifying and monitoring overdiagnosis in cancer screening: A systematic review of methods. *BMJ* **350**, 1–18 (2015).
- 57. American Cancer Society. Breast Cancer Stages. https://www.cancer.org/cancer/types/breast-cancer/understanding-a-breast-cancer-

- diagnosis/stages-of-breast-cancer.html.
- 58. Brewer, H. R., Jones, M. E., Schoemaker, M. J., Ashworth, A. & Swerdlow, A. J. Family history and risk of breast cancer: an analysis accounting for family structure. *Breast Cancer Res. Treat.* **165**, 193–200 (2017).
- 59. Boix-Montesinos, P., Soriano-Teruel, P. M., Armiñán, A., Orzáez, M. & Vicent, M. J. The past, present, and future of breast cancer models for nanomedicine development. *Adv. Drug Deliv. Rev.* **173**, 306–330 (2021).
- 60. Rouzier, R. *et al.* Breast cancer molecular subtypes respond differently to preoperative chemotherapy. *Clin. Cancer Res.* **11**, 5678–5685 (2005).
- 61. Carey, L. A. *et al.* The triple negative paradox: Primary tumor chemosensitivity of breast cancer subtypes. *Clin. Cancer Res.* **13**, 2329–2334 (2007).
- 62. Phung, M. T., Tin Tin, S. & Elwood, J. M. Prognostic models for breast cancer: A systematic review. *BMC Cancer* **19**, 1–18 (2019).
- 63. Lehmann, B. D. *et al.* Refinement of triple-negative breast cancer molecular subtypes: Implications for neoadjuvant chemotherapy selection. *PLoS One* **11**, 1–22 (2016).
- 64. Jiang, Y. Z. *et al.* Genomic and Transcriptomic Landscape of Triple-Negative Breast Cancers: Subtypes and Treatment Strategies. *Cancer Cell* **35**, 428-440.e5 (2019).
- 65. Bareche, Y. *et al.* Unravelling triple-negative breast cancer molecular heterogeneity using an integrative multiomic analysis. *Ann. Oncol.* **29**, 895–902 (2018).
- 66. Borgan, E. *et al.* Merging transcriptomics and metabolomics advances in breast cancer profiling. *BMC Cancer* **10**, (2010).
- 67. Haukaas, T. H. *et al.* Metabolic clusters of breast cancer in relation to gene- and protein expression subtypes. *Cancer Metab.* **4**, 1–14 (2016).
- 68. Almansour, N. M. Triple-Negative Breast Cancer: A Brief Review About Epidemiology, Risk Factors, Signaling Pathways, Treatment and Role of Artificial Intelligence. *Front. Mol. Biosci.* **9**, 1–15 (2022).
- 69. Jitariu, A.-A., Cîmpean, A. M., Ribatti, D. & Raica, M. Triple negative breast cancer: the kiss of death THE EMERGING CONCEPT OF TRIPLE NEGATIVE BREAST CANCERJitariu, A.-A., Cîmpean, A. M., Ribatti, D., & Raica, M. (2017). Triple negative breast cancer: the kiss of death THE EMERGING CONCEPT OF TRIPLE NEGATIVE. **8**, 46652–46662 (2017).
- 70. Obidiro, O., Battogtokh, G. & Akala, E. O. Triple Negative Breast Cancer Treatment Options and Limitations: Future Outlook. *Pharmaceutics* **15**, (2023).
- 71. Harbeck, N. et al. Breast cancer. Nature Reviews Disease Primers vol. 5 (2019).
- 72. Arroyo-Crespo, J. J. *et al.* Characterization of triple-negative breast cancer preclinical models provides functional evidence of metastatic progression. *Int. J. Cancer* **145**, 2267–2281 (2019).
- 73. Tseng, L. M. *et al.* Distant metastasis in triple-negative breast cancer. *Neoplasma* **60**, 290–294 (2013).
- 74. Dongre, A. & Weinberg, R. A. New insights into the mechanisms of epithelial—mesenchymal transition and implications for cancer. *Nat. Rev. Mol. Cell Biol.* **20**, 69–84 (2019).

- 75. Chaudhuri, A. *et al.* Emergence of Nanotechnology as a Powerful Cavalry against Triple-Negative Breast Cancer (TNBC). *Pharmaceuticals* **15**, (2022).
- 76. Friedl, P. & Wolf, K. Tumour-cell invasion and migration: Diversity and escape mechanisms. *Nat. Rev. Cancer* **3**, 362–374 (2003).
- 77. Chiang, S. P. H., Cabrera, R. M. & Segall, J. E. Tumor cell intravasation. *Am. J. Physiol. Cell Physiol.* **311**, C1–C14 (2016).
- 78. Riggi, N., Aguet, M. & Stamenkovic, I. Cancer Metastasis: A Reappraisal of Its Underlying Mechanisms and Their Relevance to Treatment. *Annu. Rev. Pathol. Mech. Dis.* **13**, 117–140 (2018).
- 79. Cheng, X. & Cheng, K. Visualizing cancer extravasation: from mechanistic studies to drug development. *Cancer Metastasis Rev.* **40**, 71–88 (2021).
- 80. Fares, J., Fares, M. Y., Khachfe, H. H., Salhab, H. A. & Fares, Y. Molecular principles of metastasis: a hallmark of cancer revisited. *Signal Transduct. Target. Ther.* **5**, (2020).
- 81. Donnem, T. *et al.* Vessel co-option in primary human tumors and metastases: An obstacle to effective anti-angiogenic treatment? *Cancer Med.* **2**, 427–436 (2013).
- 82. Waks, A. G. & Winer, E. P. Breast Cancer Treatment: A Review. *JAMA J. Am. Med. Assoc.* **321**, 288–300 (2019).
- 83. Cardoso, F. *et al.* Early breast cancer: ESMO Clinical Practice Guidelines for diagnosis, treatment and follow-up. *Ann. Oncol.* **30**, 1194–1220 (2019).
- 84. Wu, X., Yang, H., Yu, X. & Qin, J. J. Drug-resistant HER2-positive breast cancer: Molecular mechanisms and overcoming strategies. *Front. Pharmacol.* **13**, 1–10 (2022).
- 85. American Cancer Society. Treatment of Triple-negative Breast Cancer. https://www.cancer.org/cancer/types/breast-cancer/treatment/treatment-of-triple-negative.html (2022).
- 86. Catalano, A. *et al.* New Achievements for the Treatment of Triple-Negative Breast Cancer. *Appl. Sci.* **12**, (2022).
- 87. Maqbool, M., Bekele, F. & Fekadu, G. Treatment Strategies Against Triple-Negative Breast Cancer: An Updated Review. *Breast Cancer Targets Ther.* **14**, 15–24 (2022).
- 88. Bonnefoi, H. *et al.* A phase II trial of abiraterone acetate plus prednisone in patients with triple-negative androgen receptor positive locally advanced or metastatic breast cancer (UCBG 12-1). *Ann. Oncol.* **27**, 812–818 (2016).
- 89. Traina, T. A. *et al.* Enzalutamide for the treatment of androgen receptor-expressing triplenegative breast cancer. *J. Clin. Oncol.* **36**, 884–890 (2018).
- 90. Masuda, H. *et al.* Role of epidermal growth factor receptor in breast cancer. *Breast Cancer Res. Treat.* **136**, 331–345 (2012).
- 91. Darvishi, B., Farahmand, L. & Majidzadeh-A, K. Stimuli-Responsive Mesoporous Silica NPs as Non-viral Dual siRNA/Chemotherapy Carriers for Triple Negative Breast Cancer. *Mol. Ther. Nucleic Acids* **7**, 164–180 (2017).
- 92. Yang, R. *et al.* Therapeutic progress and challenges for triple negative breast cancer: targeted therapy and immunotherapy. *Mol. Biomed.* **3**, (2022).
- 93. Kim, S. B. et al. Ipatasertib plus paclitaxel versus placebo plus paclitaxel as first-line

- therapy for metastatic triple-negative breast cancer (LOTUS): a multicentre, randomised, double-blind, placebo-controlled, phase 2 trial. *Lancet Oncol.* **18**, 1360–1372 (2017).
- 94. Stemline Therapeutics, I. Open-Label Umbrella Study To Evaluate Safety And Efficacy Of Elacestrant In Various Combination In Patients With Metastatic Breast Cancer. *Clinical Trial*NCT05563220
 https://clinicaltrials.gov/study/NCT05563220?term=NCT05563220&rank=1.
- 95. Keenan, T. E. & Tolaney, S. M. Role of immunotherapy in triple-negative breast cancer. *JNCCN J. Natl. Compr. Cancer Netw.* **18**, 479–489 (2020).
- 96. Han, Y., Liu, D. & Li, L. PD-1/PD-L1 pathway: current researches in cancer. *Am. J. Cancer Res.* **10**, 727–742 (2020).
- 97. Schmid, P. *et al.* Pembrolizumab plus chemotherapy as neoadjuvant treatment of highrisk, early-stage triple-negative breast cancer: results from the phase 1b open-label, multicohort KEYNOTE-173 study. *Ann. Oncol.* **31**, 569–581 (2020).
- 98. Yang, M., Li, J., Gu, P. & Fan, X. The application of nanoparticles in cancer immunotherapy: Targeting tumor microenvironment. *Bioact. Mater.* **6**, 1973–1987 (2021).
- 99. Younis, M. A., Tawfeek, H. M., Abdellatif, A. A. H., Abdel-Aleem, J. A. & Harashima, H. Clinical translation of nanomedicines: Challenges, opportunities, and keys. *Adv. Drug Deliv. Rev.* **181**, (2022).
- 100. Shan, X. et al. Current approaches of nanomedicines in the market and various stage of clinical translation. *Acta Pharm. Sin. B* **12**, 3028–3048 (2022).
- 101. Duncan, R. Polymer therapeutics at a crossroads? Finding the path for improved translation in the twenty-first century. *J. Drug Target.* **25**, 759–780 (2017).
- 102. Bardia, A. *et al.* Sacituzumab Govitecan-hziy in Refractory Metastatic Triple-Negative Breast Cancer. *N. Engl. J. Med.* **380**, 741–751 (2019).
- 103. Bartlome, S. & Berry, C. C. Recent insights into the effects of metabolism on breast cancer cell dormancy. *Br. J. Cancer* **127**, 1385–1393 (2022).
- 104. De Berardinis, R. J. & Chandel, N. S. Fundamentals of cancer metabolism. *Sci. Adv.* **2**, (2016).
- 105. Gandhi, N. & Das, G. M. Metabolic reprogramming in breast cancer and its therapeutic implications. *Cells* **8**, (2019).
- 106. Warburg, O., Wind, F. & Negelein, E. The metabolism of tumours in the body. *Br. Med. J.* **8**, 519–530 (1927).
- 107. Tomiyama, A. *et al.* Critical role for mitochondrial oxidative phosphorylation in the activation of tumor suppressors Bax and Bak. *J. Natl. Cancer Inst.* **98**, 1462–1473 (2006).
- 108. Hammoudi, N., Ahmed, K. B. R., Garcia-Prieto, C. & Huang, P. Metabolic alterations in cancer cells and therapeutic implications. *Chin. J. Cancer* **30**, 508–525 (2011).
- 109. Lunetti, P. *et al.* Metabolic reprogramming in breast cancer results in distinct mitochondrial bioenergetics between luminal and basal subtypes. *FEBS J.* **286**, 688–709 (2019).
- 110. Whitaker-Menezes, D. *et al.* Hyperactivation of oxidative mitochondrial metabolism in epithelial cancer cells in situ: Visualizing the therapeutic effects of metformin in tumor

- tissue. Cell Cycle 10, 4047-4064 (2011).
- 111. Bajzikova, M. *et al.* Reactivation of Dihydroorotate Dehydrogenase-Driven Pyrimidine Biosynthesis Restores Tumor Growth of Respiration-Deficient Cancer Cells. *Cell Metab.* **29**, 399-416.e10 (2019).
- 112. Avagliano, A. *et al.* Mitochondrial flexibility of breast cancers: A growth advantage and a therapeutic opportunity. *Cells* **8**, 1–30 (2019).
- 113. Lyons, A. *et al.* Insulin-like growth factor 1 signaling is essential for mitochondrial biogenesis and mitophagy in cancer cells. *J. Biol. Chem.* **292**, 16983–16998 (2017).
- 114. Lu, X., Bennet, B., Mu, E., Rabinowitz, J. & Kang, Y. Metabolomic changes accompanying transformation and acquisition of metastatic potential in a syngeneic mouse mammary tumor model. *J. Biol. Chem.* **285**, 9317–9321 (2010).
- 115. Lebleu, V. S. *et al.* PGC-1α mediates mitochondrial biogenesis and oxidative phosphorylation in cancer cells to promote metastasis. *Nat. Cell Biol.* **16**, 992–1003 (2014).
- 116. Andrzejewski, S. *et al.* PGC-1α Promotes Breast Cancer Metastasis and Confers Bioenergetic Flexibility against Metabolic Drugs. *Cell Metab.* **26**, 778-787.e5 (2017).
- 117. Dupuy, F. *et al.* PDK1-dependent metabolic reprogramming dictates metastatic potential in breast cancer. *Cell Metab.* **22**, 577–589 (2015).
- 118. Vlashi, E. *et al.* Metabolic differences in breast cancer stem cells and differentiated progeny. *Breast Cancer Res Treat* **146**, 525–534 (2014).
- 119. Morris, B. A. *et al.* Collagen Matrix Density Drives the Metabolic Shift in Breast Cancer Cells. *EBioMedicine* **13**, 146–156 (2016).
- 120. Lobo, C. *et al.* Inhibition of glutaminase expression by antisense mRNA decreases growth and tumourigenicity of tumour cells. *Biochem. J.* **348**, 257–261 (2000).
- 121. Moulder, D. E., Hatoum, D., Tay, E., Lin, Y. & McGowan, E. M. The roles of p53 in mitochondrial dynamics and cancer metabolism: The pendulum between survival and death in breast cancer? *Cancers (Basel)*. **10**, (2018).
- 122. Wang, Y. *et al.* Coordinative metabolism of glutamine carbon and nitrogen in proliferating cancer cells under hypoxia. *Nat. Commun.* **10**, (2019).
- 123. Metallo, C. M. *et al.* Reductive glutamine metabolism by IDH1 mediates lipogenesis under hypoxia. *Nature* **481**, 380–384 (2012).
- 124. Park, J. H. *et al.* Fatty Acid Oxidation-Driven Src Links Mitochondrial Energy Reprogramming and Oncogenic Properties in Triple-Negative Breast Cancer. *Cell Rep.* **14**, 2154–2165 (2016).
- 125. Camarda, R. *et al.* Inhibition of fatty acid oxidation as a therapy for MYC-overexpressing triple-negative breast cancer. *Nat. Med.* **22**, 427–432 (2016).
- 126. Wang, L., Zhang, S. & Wang, X. The Metabolic Mechanisms of Breast Cancer Metastasis. *Front. Oncol.* **10**, 1–21 (2021).
- 127. Balaban, S. *et al.* Adipocyte lipolysis links obesity to breast cancer growth: adipocyte-derived fatty acids drive breast cancer cell proliferation and migration. *Cancer Metab.* **5**, 1–14 (2017).

- 128. Wai, T. & Langer, T. Mitochondrial Dynamics and Metabolic Regulation. *Trends Endocrinol. Metab.* **27**, 105–117 (2016).
- 129. Humphries, B. A. *et al.* Enhanced mitochondrial fission suppresses signaling and metastasis in triple-negative breast cancer. *Breast Cancer Res.* **22**, 1–18 (2020).
- 130. Li, J. *et al.* Mitochondrial elongation-mediated glucose metabolism reprogramming is essential for tumour cell survival during energy stress. *Oncogene* **36**, 4901–4912 (2017).
- 131. Shen, Y. Y., Yuan, Y., Du, Y. Y. & Pan, Y. Y. Molecular mechanism underlying the anticancer effect of simvastatin on MDA-MB-231 human breast cancer cells. *Mol. Med. Rep.* **12**, 623–630 (2015).
- 132. Yuan, L. *et al.* Promoting Apoptosis, a Promising Way to Treat Breast Cancer With Natural Products: A Comprehensive Review. *Front. Pharmacol.* **12**, 1–45 (2022).
- 133. Chen, S. *et al.* Mitochondria-targeting "Nanoheater" for enhanced photothermal/chemotherapy. *Biomaterials* **117**, 92–104 (2017).
- 134. Baek, M. L. et al. Mitochondrial structure and function adaptation in residual triple negative breast cancer cells surviving chemotherapy treatment. Oncogene 42, 1117– 1131 (2023).
- 135. Lucantoni, F., Dussmann, H. & Prehn, J. H. M. Metabolic targeting of breast cancer cells with the 2-deoxy-D-glucose and the mitochondrial bioenergetics inhibitor MDIVI-1. *Front. Cell Dev. Biol.* **6**, 1–12 (2018).
- 136. Armiñán, A. *et al.* Metabolomics facilitates the discrimination of the specific anti-cancer effects of free- and polymer-conjugated doxorubicin in breast cancer models. *Biomaterials* **162**, 144–153 (2018).
- 137. Vanhevel, J. et al. The Combination of the CDK4/6 Inhibitor, Palbociclib, With the Vitamin D3 Analog, Inecalcitol, Has Potent In Vitro and In Vivo Anticancer Effects in Hormone-Sensitive Breast Cancer, But Has a More Limited Effect in Triple-Negative Breast Cancer. Front. Endocrinol. (Lausanne). 13, 1–17 (2022).
- 138. Duncan, R. The dawning era of polymer therapeutics. *Nat. Rev. Drug Discov.* **2**, 347–360 (2003).
- 139. Duncan, R. & Vicent, M. J. Polymer therapeutics-prospects for 21st century: The end of the beginning. *Adv. Drug Deliv. Rev.* **65**, 60–70 (2013).
- 140. Ashford, M. B., England, R. M. & Akhtar, N. Highway to Success—Developing Advanced Polymer Therapeutics. *Adv. Ther.* **4**, 1–27 (2021).
- 141. Duncan, R. Polymer therapeutics: Top 10 selling pharmaceuticals What next? *J. Control. Release* **190**, 371–380 (2014).
- 142. Ekladious, I., Colson, Y. L. & Grinstaff, M. W. Polymer–drug conjugate therapeutics: advances, insights and prospects. *Nat. Rev. Drug Discov.* **18**, 273–294 (2019).
- 143. Shan, X. *et al.* Current approaches of nanomedicines in the market and various stage of clinical translation. *Acta Pharm. Sin. B* **12**, 3028–3048 (2022).
- 144. Biopharma PEG. FDA Approved PEGylated Drugs By 2023. https://www.biochempeg.com/article/58.html (2023).
- 145. Alven, S., Nqoro, X., Buyana, B. & Aderibigbe, B. A. Polymer-drug conjugate, a potential therapeutic to combat breast and lung cancer. *Pharmaceutics* **12**, (2020).

- 146. Ringsdorf, H. Structure and Properties of Pharmacologically Active Polymers. *J Polym Sci Polym Symp* **153**, 135–153 (1975).
- 147. Greco, F. & Vicent, M. J. Combination therapy: Opportunities and challenges for polymer-drug conjugates as anticancer nanomedicines. *Adv. Drug Deliv. Rev.* **61**, 1203–1213 (2009).
- 148. Duro-Castano, A., Conejos-Sánchez, I. & Vicent, M. J. Peptide-based polymer therapeutics. *Polymers (Basel)*. **6**, 515–551 (2014).
- 149. Vicent, M. J. *et al.* Polymer therapeutics designed for a combination therapy of hormone-dependent cancer. *Angew. Chemie Int. Ed.* **44**, 4061–4066 (2005).
- 150. Sun, R. *et al.* The tumor EPR effect for cancer drug delivery: Current status, limitations, and alternatives. *Adv. Drug Deliv. Rev.* **191**, 114614 (2022).
- 151. Fang, J., Islam, W. & Maeda, H. Exploiting the dynamics of the EPR effect and strategies to improve the therapeutic effects of nanomedicines by using EPR effect enhancers. *Adv. Drug Deliv. Rev.* **157**, 142–160 (2020).
- 152. Zagorodko, O., Arroyo-Crespo, J. J., Nebot, V. J. & Vicent, M. J. Polypeptide-Based Conjugates as Therapeutics: Opportunities and Challenges. *Macromol. Biosci.* 17, 1–22 (2017).
- 153. Melnyk, T., Masiá, E., Zagorodko, O., Conejos-Sánchez, I. & Vicent, M. J. Rational design of poly-L-glutamic acid-palbociclib conjugates for pediatric glioma treatment. *J. Control. Release* **355**, 385–394 (2023).
- 154. Maheshwari, R. et al. Manipulation of Physiological Processes for Pharmaceutical Product Development. Dosage Form Design Considerations: Volume I (Elsevier Inc., 2018). doi:10.1016/B978-0-12-814423-7.00020-4.
- 155. Melnyk, T., Đorđević, S., Conejos-Sánchez, I. & Vicent, M. J. Therapeutic potential of polypeptide-based conjugates: Rational design and analytical tools that can boost clinical translation. *Adv. Drug Deliv. Rev.* **160**, 136–169 (2020).
- 156. Atkinson, S. P., Andreu, Z. & Vicent, M. J. Polymer therapeutics: Biomarkers and new approaches for personalized cancer treatment. *J. Pers. Med.* **8**, (2018).
- 157. Kopeček, J. & Yang, J. Polymer Nanomedicines. Adv. Drug Deliv. Rev. 156, 40–64 (2020).
- 158. Rodríguez Otormin, F. D. Design Of Novel Targeted Polymer Therapeutics As Combination Therapy For The Treatmeant Of Brain Metastasis Overcoming The Blood-Brain Barrier. (Univeritat de València, 2022).
- 159. Matsumura, Y. & Maeda, H. A new concept for macromolecular therapeutics in cancer chemotherapy: mechanism of tumoritropic accumulation of proteins and the antitumor agent smancs. *Cancer Res.* **46**, 6387–6392 (1986).
- 160. Bozzuto, G. & Molinari, A. Liposomes as nanomedical devices. *Int. J. Nanomedicine* **10**, 975–999 (2015).
- 161. Selby, L. I., Cortez-Jugo, C. M., Such, G. K. & Johnston, A. P. R. Nanoescapology: progress toward understanding the endosomal escape of polymeric nanoparticles. *Wiley Interdiscip. Rev. Nanomedicine Nanobiotechnology* **9**, (2017).
- 162. Dheer, D., Nicolas, J. & Shankar, R. Cathepsin-sensitive nanoscale drug delivery systems for cancer therapy and other diseases. *Adv. Drug Deliv. Rev.* **151–152**, 130–151 (2019).

- 163. Singer, J. W. *et al.* Poly-(L)-glutamic acid-paclitaxel (CT-2103) [XYOTAX[™]], a biodegradable polymeric drug conjugate: Characterization, preclinical pharmacology, and preliminary clinical data. *Adv. Exp. Med. Biol.* **519**, 81−99 (2003).
- 164. Patel, S. et al. Brief update on endocytosis of nanomedicines. Adv. Drug Deliv. Rev. **144**, 90–111 (2019).
- 165. Niu, B. *et al.* Application of glutathione depletion in cancer therapy: Enhanced ROS-based therapy, ferroptosis, and chemotherapy. *Biomaterials* **277**, 121110 (2021).
- 166. Hakuna, L., Doughan, B., Escobedo, J. O. & Strongin, R. M. A simple assay for glutathione in whole blood. *Analyst* **140**, 3339–3342 (2015).
- 167. Bansal, A. & Celeste Simon, M. Glutathione metabolism in cancer progression and treatment resistance. *J. Cell Biol.* **217**, 2291–2298 (2018).
- 168. Đorđević, S. *et al.* Critical Design Strategies Supporting Optimized Drug Release from Polymer–Drug Conjugates. *Small* (2023) doi:10.1002/smll.202303157.
- 169. Silva, S., Almeida, A. J. & Vale, N. Combination of cell-penetrating peptides with nanoparticles for therapeutic application: A review. *Biomolecules* **9**, (2019).
- 170. Akpa, P. A. *et al.* Nanotheranostics: Platforms, Current Applications, and Mechanisms of Targeting in Breast and Prostate Cancers. *J. Nanotheranostics* **4**, 346–383 (2023).
- 171. Vasey, P. A. et al. Phase I clinical and pharmacokinetic study of PK1 [N-(2-hydroxypropyl)methacrylamide copolymer doxorubicin]: First member of a new class of chemotherapeutic agents Drug-polymer conjugates. *Clin. Cancer Res.* **5**, 83–94 (1999).
- 172. Sapra, P. *et al.* Novel delivery of SN38 markedly inhibits tumor growth in xenografts, including a camptothecin-11-refractory model. *Clin. Cancer Res.* **14**, 1888–1896 (2008).
- 173. Schluep, T., Cheng, J., Khin, K. T. & Davis, M. E. Pharmacokinetics and biodistribution of the camptothecin-polymer conjugate IT-101 in rats and tumor-bearing mice. *Cancer Chemother. Pharmacol.* **57**, 654–662 (2006).
- 174. Arroyo-Crespo, J. J. *et al.* Anticancer Activity Driven by Drug Linker Modification in a Polyglutamic Acid-Based Combination-Drug Conjugate. *Adv. Funct. Mater.* **28**, (2018).
- 175. Arroyo-Crespo, J. J. *et al.* Tumor microenvironment-targeted poly-L-glutamic acid-based combination conjugate for enhanced triple negative breast cancer treatment. *Biomaterials* **186**, 8–21 (2018).
- 176. Grewal, I. K., Singh, S., Arora, S. & Sharma, N. Polymeric nanoparticles for breast cancer therapy: A comprehensive review. *Biointerface Res. Appl. Chem.* **11**, 11151–11171 (2021).
- 177. Jeena, M. T., Kim, S., Jin, S. & Ryu, J. H. Recent progress in mitochondria-targeted drug and drug-free agents for cancer therapy. *Cancers (Basel)*. **12**, (2020).
- 178. Ritchie, R. J. A critical assessment of the use of lipophilic cations as membrane potential probes. *Prog. Biophys. Mol. Biol.* **43**, 1–32 (1984).
- 179. Cheng, X. *et al.* Application Prospects of Triphenylphosphine-Based. *Cancers (Basel).* **15**, 666 (2023).
- 180. Szeto, H. H. First-in-class cardiolipin-protective compound as a therapeutic agent to restore mitochondrial bioenergetics. *Br. J. Pharmacol.* **171**, 2029–2050 (2014).

- 181. Birk, A. V., Chao, W. M., Bracken, C., Warren, J. D. & Szeto, H. H. Targeting mitochondrial cardiolipin and the cytochrome c/cardiolipin complex to promote electron transport and optimize mitochondrial ATP synthesis. *Br. J. Pharmacol.* **171**, 2017–2028 (2014).
- 182. Horton, K. L., Stewart, K. M., Fonseca, S. B., Guo, Q. & Kelley, S. O. Mitochondria-Penetrating Peptides. *Chem. Biol.* **15**, 375–382 (2008).
- 183. Fonseca, S. B. *et al.* Rerouting chlorambucil to mitochondria combats drug deactivation and resistance in cancer cells. *Chem. Biol.* **18**, 445–453 (2011).
- 184. Lei, E. K. & Kelley, S. O. Delivery and Release of Small-Molecule Probes in Mitochondria Using Traceless Linkers. *J. Am. Chem. Soc.* **139**, 9455–9458 (2017).
- 185. Liu, Y. *et al.* Mitochondrial-Targeting Lonidamine-Doxorubicin Nanoparticles for Synergistic Chemotherapy to Conquer Drug Resistance. *ACS Appl. Mater. Interfaces* **9**, 43498–43507 (2017).
- 186. Zhang, Y. *et al.* Mitochondrial-targeted and ROS-responsive nanocarrier via nose-to-brain pathway for ischemic stroke treatment. *Acta Pharm. Sin. B* (2023) doi:10.1016/j.apsb.2023.06.011.
- 187. Zhang, X. *et al.* Stepwise dual targeting and dual responsive polymer micelles for mitochondrion therapy. *J. Control. Release* **322**, 157–169 (2020).
- 188. Sinha, D., Sarkar, N., Biswas, J. & Bishayee, A. Resveratrol for breast cancer prevention and therapy: Preclinical evidence and molecular mechanisms. *Semin. Cancer Biol.* **40_41**, 209–232 (2016).
- 189. Pronzato, P. *et al.* Phase II study of lonidamine in metastatic breast cancer. *Br. J. Cancer* **59**, 251–253 (1989).
- 190. Pacini, P. *et al.* FEC (5-fluorouracil, epidoxorubicin and cyclophosphamide) versus EM (epidoxorubicin and mitomycin-C) with or without lonidamine as first-line treatment for advanced breast cancer. A multicentric randomised study. Final results. *Eur. J. Cancer* **36**, 966–975 (2000).
- 191. Smolarek, A. K. & Suh, N. Chemopreventive activity of vitamin e in breast cancer: A focus on γ and δ -tocopherol. *Nutrients* (2011) doi:10.3390/nu3110962.
- 192. Ma, P. et al. Overcoming Multidrug Resistance through the GLUT1-Mediated and Enzyme-Triggered Mitochondrial Targeting Conjugate with Redox-Sensitive Paclitaxel Release. ACS Appl. Mater. Interfaces 10, 12351–12363 (2018).
- 193. Shi, M. *et al.* Mitochondria-targeted delivery of doxorubicin to enhance antitumor activity with HER-2 peptide-mediated multifunctional pH-sensitive DQAsomes. *Int. J. Nanomedicine* **13**, 4209–4226 (2018).
- 194. Deng, Y., Jia, F., Chen, X., Jin, Q. & Ji, J. ATP Suppression by pH-Activated Mitochondria-Targeted Delivery of Nitric Oxide Nanoplatform for Drug Resistance Reversal and Metastasis Inhibition. *Small* **16**, 1–14 (2020).
- 195. Liu, Y., Zhang, J., Tu, Y. & Zhu, L. Potential-Independent Intracellular Drug Delivery and Mitochondrial Targeting. *ACS Nano* **16**, 1409–1420 (2022).
- 196. Clish, C. B. Metabolomics: an emerging but powerful tool for precision medicine. *Mol. Case Stud.* **1**, a000588 (2015).
- 197. Gómez-Cebrián, N. et al. Multi-omic approaches to breast cancer metabolic phenotyping:

- Applications in diagnosis, prognosis, and the development of novel treatments. *Cancers* (Basel). **13**, 1–22 (2021).
- 198. Martias, C. *et al.* Optimization of sample preparation for metabolomics exploration of urine, feces, blood and saliva in humans using combined nmr and uhplc-hrms platforms. *Molecules* **26**, (2021).
- 199. Saoi, M. & Britz-Mckibbin, P. New advances in tissue metabolomics: A review. *Metabolites* **11**, (2021).
- 200. Danzi, F. *et al.* To metabolomics and beyond: a technological portfolio to investigate cancer metabolism. *Signal Transduct. Target. Ther.* **8**, (2023).
- 201. Daniels, A., Williams, R. J. P. & Wright, P. E. Nuclear magnetic resonance studies of the adrenal gland and some other organs. *Nature* **261**, 321–323 (1976).
- 202. Nicholson, J. K. *et al.* Proton-nuclear-magnetic-resonance studies of serum, plasma and urine from fasting normal and diabetic subjects. *Biochem. J.* **217**, 365–375 (1984).
- 203. Fraisier-Vannier, O. et al. MS-CleanR: A Feature-Filtering Workflow for Untargeted LC-MS Based Metabolomics. Anal. Chem. 92, 9971–9981 (2020).
- 204. Manier, S. K., Keller, A., Schäper, J. & Meyer, M. R. Untargeted metabolomics by high resolution mass spectrometry coupled to normal and reversed phase liquid chromatography as a tool to study the in vitro biotransformation of new psychoactive substances. Sci. Rep. 9, 1–11 (2019).
- 205. Stettin, D., Poulin, R. X. & Pohnert, G. Metabolomics Benefits from Orbitrap GC MS Comparison of Low- and. *Metabolites* (2020).
- 206. Luo, X., Zhang, A., Wang, X. & Lu, H. UHPLC/MS based large-scale targeted metabolomics method for multiple-biological matrix assay. *bioRxiv* (2019).
- 207. Emwas, A. H. M. The strengths and weaknesses of NMR spectroscopy and mass spectrometry with particular focus on metabolomics research. Methods in Molecular Biology vol. 1277 (2015).
- 208. Emwas, A. H. et al. Nmr spectroscopy for metabolomics research. Metabolites 9, (2019).
- 209. Wishart, D. S. *et al.* HMDB 4.0: The human metabolome database for 2018. *Nucleic Acids Res.* **46**, D608–D617 (2018).
- 210. Ulrich, E. L. et al. BioMagResBank. Nucleic Acids Res. **36**, 402–408 (2008).
- 211. Kuhn, S. & Schlörer, N. E. Facilitating quality control for spectra assignments of small organic molecules: Nmrshiftdb2 A free in-house NMR database with integrated LIMS for academic service laboratories. *Magn. Reson. Chem.* **53**, 582–589 (2015).
- 212. Kind, T. *et al.* LipidBlast in silico tandem mass spectrometry database for lipid identification. *Nat. Methods* **10**, 755–758 (2013).
- 213. Hochrein, J. *et al.* Data Normalization of 1H NMR Metabolite Fingerprinting Data Sets in the Presence of Unbalanced Metabolite Regulation. *J. Proteome Res.* **14**, 3217–3228 (2015).
- 214. Rodriguez, J., Gomez-Cano, L., Grotewold, E. & de Leon, N. Normalizing and Correcting Variable and Complex LC–MS Metabolomic Data with the R Package pseudoDrift. *Metabolites* **12**, (2022).

- 215. Worley, B. & Powers, R. Multivariate Analysis in Metabolomics. *Curr. Metabolomics* **1**, 92–107 (2013).
- 216. Vinaixa, M. *et al.* A guideline to univariate statistical analysis for LC/MS-based untargeted metabolomics-derived data. *Metabolites* **2**, 775–795 (2012).
- 217. Pang, Z. *et al.* MetaboAnalyst 5.0: Narrowing the gap between raw spectra and functional insights. *Nucleic Acids Res.* **49**, W388–W396 (2021).
- 218. Emwas, A. H., Szczepski, K., Al-Younis, I., Lachowicz, J. I. & Jaremko, M. Fluxomics New Metabolomics Approaches to Monitor Metabolic Pathways. *Front. Pharmacol.* **13**, 1–13 (2022).
- 219. Hilvo, M. *et al.* Novel theranostic opportunities offered by characterization of altered membrane lipid metabolism in breast cancer progression. *Cancer Res.* **71**, 3236–3245 (2011).
- 220. Huang, S. *et al.* Novel personalized pathway-based metabolomics models reveal key metabolic pathways for breast cancer diagnosis. *Genome Med.* **8**, 1–14 (2016).
- 221. Willmann, L. *et al.* Metabolic profiling of breast cancer: Differences in central metabolism between subtypes of breast cancer cell lines. *J. Chromatogr. B Anal. Technol. Biomed. Life Sci.* **1000**, 95–104 (2015).
- 222. Gong, Y. *et al.* Metabolic-Pathway-Based Subtyping of Triple-Negative Breast Cancer Reveals Potential Therapeutic Targets. *Cell Metab.* **33**, 51-64.e9 (2021).
- 223. Tayyari, F. *et al.* Metabolic profiles of triple-negative and luminal A breast cancer subtypes in African-American identify key metabolic differences. *Oncotarget* **9**, 11677–11690 (2018).
- 224. Lee, J. et al. Effective breast cancer combination therapy targeting BACH1 and mitochondrial metabolism. *Nature* **568**, 254–258 (2019).
- 225. Christen, S. *et al.* Breast Cancer-Derived Lung Metastases Show Increased Pyruvate Carboxylase-Dependent Anaplerosis. *Cell Rep.* **17**, 837–848 (2016).
- 226. Subramani, R., Poudel, S., Smith, K. D., Estrada, A. & Lakshmanaswamy, R. Metabolomics of Breast Cancer: A Review. *Metabolites* **12**, (2022).
- 227. Legault, J. T. et al. through a Monogenic Form of Leigh Syndrome. 13, 981–989 (2015).
- 228. Buzkova, J. *et al.* Metabolomes of mitochondrial diseases and inclusion body myositis patients: treatment targets and biomarkers. *EMBO Mol. Med.* **10**, 1–15 (2018).
- 229. Boenzi, S. & Diodato, D. Biomarkers for mitochondrial energy metabolism diseases. *Essays Biochem.* **62**, 443–454 (2018).
- 230. van der Walt, G., Lindeque, J. Z., Mason, S. & Louw, R. Sub-cellular metabolomics contributes mitochondria-specific metabolic insights to a mouse model of leigh syndrome. *Metabolites* **11**, (2021).
- 231. van der Walt, G. & Louw, R. Novel mitochondrial and cytosolic purification pipeline for compartment-specific metabolomics in mammalian disease model tissues. *Metabolomics* **16**, 1–15 (2020).
- 232. Xu, W. J. *et al.* Observation of acetyl phosphate formation in mammalian mitochondria using real-time in-organelle NMR metabolomics. *Proc. Natl. Acad. Sci. U. S. A.* **115**, 4152–4157 (2018).

- 233. Nomiyama, T., Setoyama, D., Yasukawa, T. & Kang, D. Mitochondria metabolomics reveals a role of β -nicotinamide mononucleotide metabolism in mitochondrial DNA replication. *J. Biochem.* **171**, 325–338 (2022).
- 234. Matuszczyk, J. C., Teleki, A., Pfizenmaier, J. & Takors, R. Compartment-specific metabolomics for CHO reveals that ATP pools in mitochondria are much lower than in cytosol. *Biotechnol. J.* **10**, 1639–1650 (2015).
- 235. Long, N. P. *et al.* Isolation and metabolic assessment of cancer cell mitochondria. *ACS Omega* **5**, 27304–27313 (2020).
- 236. Kappler, L. *et al.* Purity matters: A workflow for the valid high-resolution lipid profiling of mitochondria from cell culture samples. *Sci. Rep.* **6**, 1–10 (2016).
- 237. Chen, W. W., Frenkman, E., Wang, T., Birsoy, K. & Sabatini, D. M. Absolute quantification of matrix metabolites reveals the dynamics of mitochondrial metabolism. *Cell* **166**, 1324–1337 (2016).
- 238. Bayraktar, E. C. *et al.* MITO-Tag Mice enable rapid isolation and multimodal profiling of mitochondria from specific cell types in vivo. *Proc. Natl. Acad. Sci. U. S. A.* **116**, 303–312 (2019).
- 239. Fly, R., Lloyd, J., Krueger, S., Fernie, A. & Merwe, M. J. van der. Improvements to Defi ne Mitochondrial Metabolomics Using Nonaqueous Fractionation. in *Plant Mitochondria: Methods and Protocols* vol. 1305 1–303 (2015).
- 240. Go, Y. M. *et al.* Mitochondrial metabolomics using high-resolution fourier-transform mass spectrometry. *Methods Mol. Biol.* **1198**, 43–73 (2014).
- 241. Roede, J. R., Park, Y., Li, S., Strobel, F. H. & Jones, D. P. Detailed mitochondrial phenotyping by high resolution metabolomics. *PLoS One* **7**, 1–8 (2012).
- 242. Seifert, E. L. *et al.* Long-chain fatty acid combustion rate is associated with unique metabolite profiles in skeletal muscle mitochondria. *PLoS One* **5**, (2010).
- 243. Nonnenmacher, Y. *et al.* Analysis of mitochondrial metabolism in situ: Combining stable isotope labeling with selective permeabilization. *Metab. Eng.* **43**, 147–155 (2017).
- 244. Nagana Gowda, G. A. *et al.* Monitoring live mitochondrial metabolism in real-time using NMR spectroscopy. *Magn. Reson. Chem.* 1–10 (2023) doi:10.1002/mrc.5341.
- 245. Lee, W. D., Mukha, D., Aizenshtein, E. & Shlomi, T. Spatial-fluxomics provides a subcellular-compartmentalized view of reductive glutamine metabolism in cancer cells. *Nat. Commun.* **10**, 1–14 (2019).
- 246. Barbieri, L., Luchinat, E. & Banci, L. Structural insights of proteins in sub-cellular compartments: In-mitochondria NMR. *Biochim. Biophys. Acta Mol. Cell Res.* **1843**, 2492–2496 (2014).
- 247. Clayton, D. A. & Shadel, G. S. Isolation of mitochondria from animal tissue. *Cold Spring Harb. Protoc.* **2014**, 1112–1114 (2014).
- 248. HOGEBOOM, G. H., SCHNEIDER, W. C. & PALLADE, G. E. Cytochemical studies of mammalian tissues; isolation of intact mitochondria from rat liver; some biochemical properties of mitochondria and submicroscopic particulate material. *J. Biol. Chem.* **172**, 619–635 (1948).
- 249. Liao, P. C., Bergamini, C., Fato, R., Pon, L. A. & Pallotti, F. Isolation of mitochondria from

- cells and tissues. Methods in Cell Biology vol. 155 (Elsevier Inc., 2020).
- 250. Chen, W. W., Freinkman, E. & Sabatini, D. M. Rapid immunopurification of mitochondria for metabolite profiling and absolute quantification of matrix metabolites. *Nat. Protoc.* **12**, 2215–2231 (2017).
- 251. Kang, W., L. McNaughton, R. & D. Espinosa, H. Micro- and Nano-scale Technologies for Delivery into Adherent Cells. *Trends Biotechnol.* **34**, 665–678 (2016).
- 252. Simpson, R. J. Homogenization of mammalian tissue. Cold Spring Harb. Protoc. 5, (2010).
- 253. Doliba, N. M., Babsky, A. M., Doliba, N. M., Wehrli, S. L. & Osbakken, M. D. AMP promotes oxygen consumption and ATP synthesis in heart mitochondria through the adenylate kinase reaction: An NMR spectroscopy and polarography study. *Cell Biochem. Funct.* 33, 67–72 (2015).
- 254. Pallotti, F. & Lenaz, G. Isolation and Subfractionation of Mitochondria from Animal Cells and Tissue Culture Lines. *Methods Cell Biol.* **80**, 3–44 (2007).
- 255. Beger, R. D., Schmidt, M. A. & Kaddurah-Daouk, R. Current concepts in pharmacometabolomics, biomarker discovery, and precision medicine. *Metabolites* **10**, (2020).
- 256. Cao, Z., Miller, M. S., Lubet, R. A., Grubbs, C. J. & Beger, R. D. Pharmacometabolomic pathway response of effective anticancer agents on different diets in rats with induced mammary tumors. *Metabolites* **9**, (2019).
- 257. Miolo, G. *et al.* Phamacometabolomics study identifies circulating spermidine and tryptophan as potential biomarkers associated with the complete pathological response to trastuzumab-paclitaxel neoadjuvant therapy in HER-2 positive breast cancer. *Oncotarget* **7**, 39809–39822 (2016).
- 258. He, X. et al. NMR-Based Metabolomics Analysis Predicts Response to Neoadjuvant Chemotherapy for Triple-Negative Breast Cancer. Front. Mol. Biosci. 8, 1–15 (2021).
- 259. Awashra, M. & Młynarz, P. The toxicity of nanoparticles and their interaction with cells: an in vitro metabolomic perspective. *Nanoscale Adv.* **5**, 2674–2723 (2023).
- 260. Duarte, I. F. Following dynamic biological processes through NMR-based metabonomics: A new tool in nanomedicine? *J. Control. Release* **153**, 34–39 (2011).
- 261. Zhang, L. *et al.* Selective metabolic effects of gold nanorods on normal and cancer cells and their application in anticancer drug screening. *Biomaterials* **34**, 7117–7126 (2013).
- 262. Yaşacan, M. *et al.* Polymeric Nanoparticle Versus Liposome Formulations: Comparative Physicochemical and Metabolomic Studies as I-Carnitine Delivery Systems. *AAPS PharmSciTech* (2020) doi:10.1208/s12249-020-01852-4.
- 263. Totten, J. D., Wongpinyochit, T., Carrola, J., Duarte, I. F. & Seib, F. P. PEGylation-Dependent Metabolic Rewiring of Macrophages with Silk Fibroin Nanoparticles. *ACS Appl. Mater. Interfaces* **11**, 14515–14525 (2019).
- 264. Schätzlein, M. P. *et al.* Rapid two-dimensional ALSOFAST-HSQC experiment for metabolomics and fluxomics studies: application to a 13C-enriched cancer cell model treated with gold nanoparticles. *Anal. Bioanal. Chem.* **410**, 2793–2804 (2018).
- 265. Farhana, A. & Lappin, S. L. Biochemistry, Lactate Dehydrogenase (LDH). StatPearls (2020).
- 266. Folch, J., Lees, M. & Sloane Stanley, G. . A simple method for the isolation and purification

- of total lipides from animal tissues. 226, 497–509 (1957).
- 267. Römisch-Margl, W. *et al.* Procedure for tissue sample preparation and metabolite extraction for high-throughput targeted metabolomics. *Metabolomics* **8**, 133–142 (2010).
- 268. Bligh, E.G. and Dyer, W. J. A rapid method of total lipid extraction and purification. *Can. J. Biochem. Physiol.* **37**, (1959).
- 269. Matheus, N. *et al.* An easy, convenient cell and tissue extraction protocol for nuclear magnetic resonance metabolomics. *Phytochem. Anal.* **25**, 342–349 (2014).
- 270. Gómez-Archila, L. G., Palomino-Schätzlein, M., Zapata-Builes, W. & Galeano, E. Development of an optimized method for processing peripheral blood mononuclear cells for 1H-nuclear magnetic resonancebased metabolomic profiling. *PLoS One* 16, 1–20 (2021).
- 271. Price, W. S. Water Signal Suppression in NMR Spectroscopy. Annual Reports on NMR Spectroscopy vol. 38 (1999).
- 272. Emwas, A. H. *et al.* Recommended strategies for spectral processing and post-processing of 1D 1 H-NMR data of biofluids with a particular focus on urine. *Metabolomics* **14**, 1–23 (2018).
- 273. Emwas, A. H. *et al.* Nmr spectroscopy for metabolomics research. *Metabolites* **9**, 123 (2019).
- 274. Heravi, M. M., Ghavidel, M. & Mohammadkhani, L. RSC Advances Beyond a solvent: triple roles of dimethylformamide in organic chemistry. 27832–27862 (2018) doi:10.1039/c8ra04985h.
- 275. Fulmer, G. R. *et al.* NMR Chemical Shifts of Trace Impurities: Common Laboratory Solvents, Organics, and Gases in Deuterated Solvents Relevant to the Organometallic Chemist. 2176–2179 (2010) doi:10.1021/om100106e.
- 276. Carr, H. Y. & Purcell, E. M. Effects of diffusion on free precession in nuclear magnetic resonance experiments. *Phys. Rev.* **94**, 630–638 (1954).
- 277. Meiboom, S. & Gill, D. Modified spin-echo method for measuring nuclear relaxation times. *Rev. Sci. Instrum.* **29**, 688–691 (1958).
- 278. Li, Q. & Hoppe, T. Role of amino acid metabolism in mitochondrial homeostasis. *Front. Cell Dev. Biol.* **11**, 1–8 (2023).
- 279. Lieu, E. L., Nguyen, T., Rhyne, S. & Kim, J. Amino acids in cancer. *Exp. Mol. Med.* **52**, 15–30 (2020).
- 280. Ross-Inta, C., Tsai, C.-Y. & Giulivi, C. The mitochondrial pool of free amino acids reflects the composition of mitochondrial-DNA encoded proteins. *Biosci. Rep.* **28**, 239–249 (2008).
- 281. Owen, O. E., Kalhan, S. C. & Hanson, R. W. The key role of anaplerosis and cataplerosis for citric acid cycle function. *J. Biol. Chem.* **277**, 30409–30412 (2002).
- 282. Hewton, K. G., Johal, A. S. & Parker, S. J. Transporters at the interface between cytosolic and mitochondrial amino acid metabolism. *Metabolites* **11**, 1–28 (2021).
- 283. Marí, M. *et al.* Mitochondrial glutathione: Recent insights and role in disease. *Antioxidants* **9**, 1–21 (2020).

- 284. Kane, D. A. Lactate oxidation at the mitochondria: A lactate-malate-aspartate shuttle at work. *Front. Neurosci.* **8**, 1–6 (2014).
- 285. Moffett, J. R., Puthillathu, N., Vengilote, R., Jaworski, D. M. & Namboodiri, A. M. Acetate Revisited: A Key Biomolecule at the Nexus of Metabolism, Epigenetics and Oncogenesis—Part 1: Acetyl-CoA, Acetogenesis and Acyl-CoA Short-Chain Synthetases. *Front. Physiol.* 11, 1–24 (2020).
- 286. Kolb, H. *et al.* Ketone bodies: from enemy to friend and guardian angel. *BMC Med.* **19**, 1–15 (2021).
- 287. Schug, Z. T., Vande Voorde, J. & Gottlieb, E. The metabolic fate of acetate in cancer. *Nat. Rev. Cancer* **16**, 708–717 (2016).
- 288. Meiser, J. *et al.* Serine one-carbon catabolism with formate overflow. *Sci. Adv.* **2**, 1–11 (2016).
- 289. Stark, R. & Kibbey, R. G. The mitochondrial isoform of phosphoenolpyruvate carboxykinase (PEPCK-M) and glucose homeostasis: Has it been overlooked? *Biochim. Biophys. Acta Gen. Subj.* **1840**, 1313–1330 (2014).
- 290. Zhang, Y., Guo, S., Xie, C. & Fang, J. Uridine Metabolism and Its Role in Glucose, Lipid, and Amino Acid Homeostasis. *Biomed Res. Int.* **2020**, 1–7 (2020).
- 291. Zhao, Y., Chard Dunmall, L. S., Cheng, Z., Wang, Y. & Si, L. Natural products targeting glycolysis in cancer. *Front. Pharmacol.* **13**, 1–18 (2022).
- 292. Singh, J., Her, C. & Krishnan, V. V. Enzymatic conversion of sucrose to glucose and its anomerization by quantitative NMR spectroscopy: Application of a simple consecutive reaction rates approach. *J. Mol. Struct.* **1153**, 187–191 (2018).
- 293. Saito, R. de F., Andrade, L. N. de S., Bustos, S. O. & Chammas, R. Phosphatidylcholine-Derived Lipid Mediators: The Crosstalk Between Cancer Cells and Immune Cells. *Front. Immunol.* **13**, 1–24 (2022).
- 294. Zara, V., Assalve, G. & Ferramosca, A. Multiple roles played by the mitochondrial citrate carrier in cellular metabolism and physiology. *Cell. Mol. Life Sci.* **79**, 1–12 (2022).
- 295. Pang, K. *et al.* Role of protein phosphorylation in cell signaling , disease , and the intervention therapy. 1–28 (2022) doi:10.1002/mco2.175.
- 296. Boison, D. & Yegutkin, G. G. Adenosine Metabolism: Emerging Concepts for Cancer Therapy. *Cancer Cell* **36**, 582–596 (2019).
- 297. Wu, G., Fang, Y. Z., Yang, S., Lupton, J. R. & Turner, N. D. Glutathione Metabolism and Its Implications for Health. *J. Nutr.* **134**, 489–492 (2004).
- 298. Moseley, H. N. B., Lane, A. N., Belshoff, A. C., Higashi, R. M. & Fan, T. W. M. A novel deconvolution method for modeling UDP-N-acetyl-D-glucosamine biosynthetic pathways based on 13C mass isotopologue profiles under non-steady-state conditions. *BMC Biol.* 9, (2011).
- 299. Bessman, S. P. The creatine phosphate energy shuttle-The molecular asymmetry of a "pool." *Anal. Biochem.* **161**, 519–523 (1987).
- 300. Wang, L. Mitochondrial purine and pyrimidine metabolism and beyond. *Nucleosides, Nucleotides and Nucleic Acids* **35**, 578–594 (2016).
- 301. Keshet, R., Szlosarek, P., Carracedo, A. & Erez, A. Rewiring urea cycle metabolism

- in cancer to support anabolism. Nat. Rev. Cancer 18, 634-645 (2018).
- 302. Adam, J. *et al.* A Role for Cytosolic Fumarate Hydratase in Urea Cycle Metabolism and Renal Neoplasia. *Cell Rep.* **3**, 1440–1448 (2013).
- 303. Janin, M. & Esteller, M. Previews Oncometabolite Accumulation and Epithelial-to-Mesenchymal Transition: The Turn of Fumarate. *Cell Metab.* **24**, 529–530 (2016).
- 304. Ma, J. *et al.* Emerging roles of nucleotide metabolism in cancer development : progress and prospect. **13**, 13349–13358 (2021).
- 305. Wu, H. *et al.* Targeting nucleotide metabolism: a promising approach to enhance cancer immunotherapy. *J. Hematol. Oncol.* 1–21 (2022) doi:10.1186/s13045-022-01263-x.
- 306. Li, Y. et al. Recent advances in therapeutic strategies for triple-negative breast cancer. J. Hematol. Oncol. 15, 1–30 (2022).
- 307. Duro-Castano, A. *et al.* Capturing "Extraordinary" Soft-Assembled Charge-Like Polypeptides as a Strategy for Nanocarrier Design. *Adv. Mater.* **29**, (2017).
- 308. Córdoba-David, G. *et al.* Effective Nephroprotection Against Acute Kidney Injury with a Star-Shaped Polyglutamate-Curcuminoid Conjugate. *Sci. Rep.* **10**, 1–15 (2020).
- 309. Polyproline-based block copolymers.
- 310. Kalafut, D., Anderson, T. N. & Chmielewski, J. Mitochondrial targeting of a cationic amphiphilic polyproline helix. *Bioorganic Med. Chem. Lett.* **22**, 561–563 (2012).
- 311. Marrache, S. & Dhar, S. The energy blocker inside the power house: Mitochondria targeted delivery of 3-bromopyruvate. *Chem. Sci.* **6**, 1832–1845 (2015).
- 312. Reddy, C. A. *et al.* Mitochondrial-targeted curcuminoids: A strategy to enhance bioavailability and anticancer efficacy of curcumin. *PLoS One* **9**, (2014).
- 313. Barz, M., Duro-Castano, A. & Vicent, M. J. A versatile post-polymerization modification method for polyglutamic acid: Synthesis of orthogonal reactive polyglutamates and their use in "click chemistry." *Polym. Chem.* **4**, 2989–2994 (2013).
- 314. Evans, R. The interpretation of small molecule diffusion coefficients: Quantitative use of diffusion-ordered NMR spectroscopy. *Prog. Nucl. Magn. Reson. Spectrosc.* **117**, 33–69 (2020).
- 315. Van De Steene, J. C. & Lambert, W. E. Comparison of Matrix Effects in HPLC-MS/MS and UPLC-MS/MS Analysis of Nine Basic Pharmaceuticals in Surface Waters. *J. Am. Soc. Mass Spectrom.* **19**, 713–718 (2008).
- 316. Berridge, M. V., Herst, P. M. & Tan, A. S. Tetrazolium dyes as tools in cell biology: New insights into their cellular reduction. *Biotechnol. Annu. Rev.* **11**, 127–152 (2005).
- 317. Gu, X., Ma, Y., Liu, Y. & Wan, Q. Measurement of mitochondrial respiration in adherent cells by Seahorse XF96 Cell Mito Stress Test. *STAR Protoc.* **2**, 100245 (2021).
- 318. Divakaruni, A. S., Paradyse, A., Ferrick, D. A., Murphy, A. N. & Jastroch, M. *Analysis and interpretation of microplate-based oxygen consumption and pH data. Methods in Enzymology* vol. 547 (Elsevier Inc., 2014).
- 319. Jost, T., Heinzerling, L., Fietkau, R., Hecht, M. & Distel, L. V. Palbociclib Induces Senescence in Melanoma and Breast Cancer Cells and Leads to Additive Growth Arrest in Combination With Irradiation. *Front. Oncol.* **11**, 1–10 (2021).

- 320. van der Veen, J. N. *et al.* The critical role of phosphatidylcholine and phosphatidylethanolamine metabolism in health and disease. *Biochim. Biophys. Acta Biomembr.* **1859**, 1558–1572 (2017).
- 321. Warth, B. *et al.* Metabolomics Reveals that Dietary Xenoestrogens Alter Cellular Metabolism Induced by Palbociclib/Letrozole Combination Cancer Therapy. *Cell Chem. Biol.* **25**, 291-300.e3 (2018).
- 322. Chiu, H. C., Kopečková, P., Deshmane, S. S. & Kopeček, J. Lysosomal degradability of poly(α-amino acids). *J. Biomed. Mater. Res.* **34**, 381–392 (1997).
- 323. Robinson, M. B., Lee, M. L. & DaSilva, S. Glutamate Transporters and Mitochondria: Signaling, Co-compartmentalization, Functional Coupling, and Future Directions. *Neurochem Res.* **45**, 526–540 (2020).
- 324. Guda, P., Guda, C. & Subramaniam, S. Reconstruction of Pathways Associated with Amino Acid Metabolism in Human Mitochondria. *Genomics, Proteomics Bioinforma*. **5**, 166–176 (2007).
- 325. Raimi, O. G. *et al.* A mechanism-inspired UDP-: N -acetylglucosamine pyrophosphorylase inhibitor. *RSC Chem. Biol.* **1**, 13–25 (2020).
- 326. Dabravolski, S. A., Nikiforov, N. G., Starodubova, A. V., Popkova, T. V. & Orekhov, A. N. The role of mitochondria-derived peptides in cardiovascular diseases and their potential as therapeutic targets. *Int. J. Mol. Sci.* **22**, (2021).
- 327. Kim, S. J. *et al.* Mitochondrial peptides modulate mitochondrial function during cellular senescence. **10**, 1239–1256 (2018).
- 328. Wang, X. Bin, Cui, N. H., Liu, X. & Liu, X. Mitochondrial 8-hydroxy-2'-deoxyguanosine and coronary artery disease in patients with type 2 diabetes mellitus. *Cardiovasc. Diabetol.* **19**, 1–15 (2020).
- 329. Liebich, H. M., Di Stefano, C., Wixforth, A. & Schmid, H. R. Quantitation of urinary nucleosides by high-performance liquid chromatography. *J. Chromatogr. A* **763**, 193–197 (1997).
- 330. Maccarrone, M. *et al.* Oxidation products of polyamines induce mitochondrial uncoupling and cytochrome c release. *FEBS Lett.* **507**, 30–34 (2001).
- 331. Leonardi, R., Zhang, Y. M., Rock, C. O. & Jackowski, S. Coenzyme A: Back in action. *Prog. Lipid Res.* **44**, 125–153 (2005).
- 332. Chen, J. K., Shen, C. R. & Liu, C. L. N-acetylglucosamine: Production and applications. *Mar. Drugs* **8**, 2493–2516 (2010).
- 333. Hiramatsu, K. *et al.* Diagnostic and prognostic usefulness of N1,N8-diacetylspermidine and N1,N2-diacetylspermine in urine as novel markers of malignancy. *J. Cancer Res. Clin. Oncol.* **123**, 539–545 (1997).
- 334. Joncquel-Chevalier Curt, M. *et al.* Creatine biosynthesis and transport in health and disease. *Biochimie* **119**, 146–165 (2015).
- 335. Kazak, L. & Cohen, P. Creatine metabolism: energy homeostasis, immunity and cancer biology. *Nat. Rev. Endocrinol.* **16**, 421–436 (2020).
- 336. Swamy, M. K., Sinniah, U. R. & Ghasemzadeh, A. Anticancer potential of rosmarinic acid and its improved production through biotechnological interventions and functional

- genomics. Appl. Microbiol. Biotechnol. 102, 7775-7793 (2018).
- 337. Schenkel, L. C. & Bakovic, M. Formation and regulation of mitochondrial membranes. *Int. J. Cell Biol.* **2014**, (2014).
- 338. Claypool, S. M., Oktay, Y., Boontheung, P., Loo, J. A. & Koehler, C. M. Cardiolipin defines the interactome of the major ADP/ATP carrier protein of the mitochondrial inner membrane. *J. Cell Biol.* **182**, 937–950 (2008).
- 339. Wood, P. L. Fatty acyl esters of hydroxy fatty acid (FAHFA) lipidreviewfamilies. *Metabolites* **10**, 1–8 (2020).
- 340. Dufourc, E. J. Sterols and membrane dynamics. J. Chem. Biol. 1, 63-77 (2008).
- 341. Woo Suk, A. & Antoniewicz, M. R. Parallel labeling experiments with [1,2-13C]glucose and [U-13C]glutamine provide new insights into CHO cell metabolism. *Metab. Eng.* **15**, 34–47 (2013).
- 342. Patil, N., Howe, O., Cahill, P. & Byrne, H. J. Monitoring and modelling the dynamics of the cellular glycolysis pathway: A review and future perspectives. *Mol. Metab.* **66**, 101635 (2022).
- 343. Mikkola, S. Nucleotide sugars in chemistry and biology. *Molecules* 25, (2020).
- 344. Schwarzkopf, M. *et al.* Sialylation is essential for early development in mice. *Proc. Natl. Acad. Sci. U. S. A.* **99**, 5267–5270 (2002).
- 345. Duan, L. *et al.* 13C tracer analysis suggests extensive recycling of endogenous CO2 in vivo. *Cancer Metab.* **10**, 1–15 (2022).
- 346. Pareek, V., Pedley, A. M. & Benkovic, S. J. Human de novo Purine Biosynthesis. *Crit Rev Biochem Mol Biol* **56**, 1–16 (2021).
- 347. Lambrecht, M. J. *et al.* Synthesis of Dimeric ADP-Ribose and Its Structure with Human Poly(ADP-ribose) Glycohydrolase. *J. Am. Chem. Soc.* **137**, 3558–3564 (2015).
- 348. Ehab, M. & Elbaz, M. Profile of palbociclib in the treatment of metastatic breast cancer. *Breast Cancer Targets Ther.* **8**, 83–91 (2016).
- 349. Cornell, R. B. & Ridgway, N. D. CTP:phosphocholine cytidylyltransferase: Function, regulation, and structure of an amphitropic enzyme required for membrane biogenesis. *Prog. Lipid Res.* **59**, 147–171 (2015).
- 350. Wang, Z. *et al.* Targeting Glutaminolysis: New Perspectives to Understand Cancer Development and Novel Strategies for Potential Target Therapies. *Front. Oncol.* **10**, 1–13 (2020).
- 351. Mullen, A. R. *et al.* Reductive carboxylation supports growth in tumour cells with defective mitochondria. *Nature* **481**, 385–388 (2012).
- 352. Antoniewicz, M. R. A guide to 13C metabolic flux analysis for the cancer biologist. *Exp. Mol. Med.* **50**, (2018).
- 353. Le, A. *et al.* Glucose-independent glutamine metabolism via TCA cycling for proliferation and survival in b cells. *Cell Metab.* **15**, 110–121 (2012).
- 354. Maus, A. & Peters, G. J. Glutamate and α -ketoglutarate: key players in glioma metabolism. *Amino Acids* **49**, 21–32 (2017).

- 355. Smith, T. A. D. *et al.* The phosphocholine and glycerophosphocholine content of an oestrogen- sensitive rat mammary tumour correlates strongly with growth rate. *Br. J. Cancer* **64**, 821–826 (1991).
- 356. Luan, H., Ji, F., Chen, Y. & Cai, Z. statTarget: A streamlined tool for signal drift correction and interpretations of quantitative mass spectrometry-based omics data. *Anal. Chim. Acta* **1036**, 66–72 (2018).
- 357. Ruttkies, C., Schymanski, E. L., Wolf, S., Hollender, J. & Neumann, S. MetFrag relaunched: Incorporating strategies beyond in silico fragmentation. *J. Cheminform.* **8**, 1–16 (2016).
- 358. Pietzke, M. & Vazquez, A. Metabolite AutoPlotter an application to process and visualise metabolite data in the web browser. *Cancer Metab.* **8**, 1–11 (2020).
- 359. Modica-Napolitano, J. S. & Singh, K. K. Mitochondrial dysfunction in cancer. *Mitochondrion* **4**, 755–762 (2004).
- 360. Scheid, A. D., Beadnell, T. C. & Welch, D. R. Roles of mitochondria in the hallmarks of metastasis. *Br. J. Cancer* **124**, 124–135 (2021).
- 361. Simonnet, H. *et al.* Low mitochondrial respiratory chain content correlates with tumor aggressiveness in renal cell carcinoma. *Carcinogenesis* **23**, 759–768 (2002).
- 362. Naz, S., Moreira Dos Santos, D. C., García, A. & Barbas, C. Analytical protocols based on LC-MS, GC-MS and CE-MS for nontargeted metabolomics of biological tissues. *Bioanalysis* **6**, 1657–1677 (2014).
- 363. Domingo-Ortí, I. *et al.* Metabolic footprint of aging and obesity in red blood cells. *Aging* (*Albany. NY*). **13**, 4850–4880 (2021).
- 364. Mayers, J. R. *et al.* Elevation of circulating branched-chain amino acids is an early event in human pancreatic adenocarcinoma development. *Nat. Med.* **20**, 1193–1198 (2014).
- 365. Armiñán, A. *et al.* Metabolomics facilitates the discrimination of the specific anti-cancer effects of free- and polymer-conjugated doxorubicin in breast cancer models. *Biomaterials* **162**, 144–153 (2018).
- 366. Kaddurah-Daouk, R., Kristal, B. S. & Weinshilboum, R. M. Metabolomics: A global biochemical approach to drug response and disease. *Annu. Rev. Pharmacol. Toxicol.* **48**, 653–683 (2008).
- 367. O'Keefe, S. J. D. *et al.* Fat, fibre and cancer risk in African Americans and rural Africans. *Nat. Commun.* **6**, (2015).
- 368. Chan, C. Y. E. *et al.* Metabolic profiling of human colorectal cancer using high-resolution magic angle spinning nuclear magnetic resonance (HR-MAS NMR) spectroscopy and gas chromatography mass spectrometry (GC/MS). *J. Proteome Res.* **8**, 352–361 (2009).
- 369. Pan, D., Lindau, C., Lagies, S., Wiedemann, N. & Kammerer, B. Metabolic profiling of isolated mitochondria and cytoplasm reveals compartment-specific metabolic responses. *Metabolomics* **14**, 1–12 (2018).
- 370. Go, Y. M., Roede, J. R., Orr, M., Liang, Y. & Jones, D. P. Integrated redox proteomics and metabolomics of mitochondria to identify mechanisms of Cd toxicity. *Toxicol. Sci.* **139**, 59–73 (2014).
- 371. Caldeira, D. de A. F. *et al.* Isolation of Mitochondria From Fresh Mice Lung Tissue. *Front. Physiol.* **12**, 1–13 (2021).

- 372. Schneider, A. *et al.* Single organelle analysis to characterize mitochondrial function and crosstalk during viral infection. *Sci. Rep.* **9**, 1–11 (2019).
- 373. Song, Y. *et al.* Sample preparation project for the subcellular proteome of mouse liver. *Proteomics* **6**, 5269–5277 (2006).
- 374. Bury, A. G., Vincent, A. E., Turnbull, D. M., Actis, P. & Hudson, G. Mitochondrial isolation: when size matters. *Wellcome Open Res.* **5**, 226 (2020).
- 375. Franko, A. *et al.* Efficient isolation of pure and functional mitochondria from mouse tissues using automated tissue disruption and enrichment with anti-TOM22 magnetic beads. *PLoS One* **8**, (2013).
- 376. Tang, H. L., Le, A. H. P. & Lung, H. L. The increase in mitochondrial association with actin precedes Bax translocation in apoptosis. *Biochem. J.* **396**, 1–5 (2006).
- 377. Gogiashvili, M. *et al.* HR-MAS NMR based quantitative metabolomics in breast cancer. *Metabolites* **9**, (2019).
- 378. Mason, S., Terburgh, K. & Louw, R. Miniaturized 1 H-NMR method for analyzing limited-quantity samples applied to a mouse model of Leigh disease. *Metabolomics* **14**, 74 (2018).
- 379. Bitar, A. *et al.* A voxel-based mouse for internal dose calculations using Monte Carlo simulations (MCNP). *Phys. Med. Biol.* **52**, 1013–1025 (2007).
- 380. Adeva-Andany, M. *et al.* Comprehensive review on lactate metabolism in human health. *Mitochondrion* **17**, 76–100 (2014).
- 381. Croze, M. L. & Soulage, C. O. Potential role and therapeutic interests of myo-inositol in metabolic diseases. *Biochimie* **95**, 1811–1827 (2013).
- 382. Schlattner, U., Tokarska-Schlattner, M. & Wallimann, T. Mitochondrial creatine kinase in human health and disease. *Biochim. Biophys. Acta Mol. Basis Dis.* **1762**, 164–180 (2006).
- 383. Marí, M., Morales, A., Colell, A., García-Ruiz, C. & Fernández-Checa, J. C. Mitochondrial glutathione, a key survival antioxidant. *Antioxidants Redox Signal.* **11**, 2685–2700 (2009).
- 384. Hansen, S. H., Andersen, M. L., Cornett, C., Gradinaru, R. & Grunnet, N. A role for taurine in mitochondrial function. *J. Biomed. Sci.* **17**, 1–8 (2010).
- 385. Warburg, O., Wind, F. & Negelein, E. The metabolism of tumours. *J. Gen. Physiol.* **8**, 519–530 (1927).
- 386. Glunde, K., Penet, M. F., Jiang, L., Jacobs, M. A. & Bhujwalla, Z. M. Choline metabolism-based molecular diagnosis of cancer: An update. *Expert Rev. Mol. Diagn.* **15**, 735–747 (2015).
- 387. Sonkar, K. *et al.* Focus on the glycerophosphocholine pathway in choline phospholipid metabolism of cancer. *NMR in Biomedicine* (2019) doi:10.1002/nbm.4112.
- 388. Hay, N. Reprogramming glucose metabolism in cancer: Can it be exploited for cancer therapy? *Nat. Rev. Cancer* **16**, 635–649 (2016).
- 389. Altman, B. J., Stine, Z. E. & Dang, C. V. From Krebs to clinic: Glutamine metabolism to cancer therapy. *Nat. Rev. Cancer* **16**, 619–634 (2016).
- 390. Wishart, D. S. *et al.* HMDB 5.0: The Human Metabolome Database for 2022. *Nucleic Acids Res.* **50**, D622–D631 (2022).

- 391. Carneiro, T. J. *et al.* Multi-organ NMR metabolomics to assess in vivo overall metabolic impact of cisplatin in mice. *Metabolites* **9**, 1–17 (2019).
- 392. Glinskikh, A. *et al.* The effect of blood contained in the samples on the metabolomic profile of mouse brain tissue: A study by NMR spectroscopy. *Molecules* **26**, (2021).
- 393. Ling, Y. S., Liang, H. J., Chung, M. H., Lin, M. H. & Lin, C. Y. NMR- and MS-based metabolomics: Various organ responses following naphthalene intervention. *Mol. Biosyst.* **10**, 1918–1931 (2014).
- 394. Puchades-Carrasco, L., Palomino-Schätzlein, M., Pérez-Rambla, C. & Pineda-Lucena, A. Bioinformatics tools for the analysis of NMR metabolomics studies focused on the identification of clinically relevant biomarkers. *Brief. Bioinform.* **17**, 541–552 (2016).
- 395. Cretella, D. *et al.* The anti-tumor efficacy of CDK4/6 inhibition is enhanced by the combination with PI3K/AKT/mTOR inhibitors through impairment of glucose metabolism in TNBC cells. *J. Exp. Clin. Cancer Res.* **37**, 1–12 (2018).
- 396. Al Maruf, A. *et al.* Methotrexate induced mitochondrial injury and cytochrome c release in rat liver hepatocytes. *Drug Chem. Toxicol.* **41**, 51–61 (2018).
- 397. Bottani, E. & Brunetti, D. Advances in Mitochondria-Targeted Drug Delivery. *Pharmaceutics* (2023) doi:10.3390/pharmaceutics15082089.
- 398. Pfanner, N., Warscheid, B. & Wiedemann, N. Mitochondrial proteins: from biogenesis to functional networks. *Nat. Rev. Mol. Cell Biol.* **20**, 267–284 (2019).
- 399. Yaşacan, M. et al. Polymeric Nanoparticle Versus Liposome Formulations: Comparative Physicochemical and Metabolomic Studies as L-Carnitine Delivery Systems. AAPS PharmSciTech 21, (2020).
- 400. Djafarzadeh, S. & Jakob, S. M. High-resolution respirometry to assess mitochondrial function in permeabilized and intact cells. *J. Vis. Exp.* **2017**, 1–11 (2017).
- 401. Kelly, P. E. *et al.* An Optimised Monophasic Faecal Extraction Method for LC-MS Analysis and Its Application in Gastrointestinal Disease. *Metabolites* **12**, (2022).
- 402. Nagana Gowda, G. A. & Raftery, D. NMR-Based Metabolomics. in *Advances in Experimental Medicine and Biology* (2021). doi:10.1007/978-3-030-51652-9_2.
- 403. Shi, Y., van der Meel, R., Chen, X. & Lammers, T. The EPR effect and beyond: Strategies to improve tumor targeting and cancer nanomedicine treatment efficacy. *Theranostics* **10**, 7921–7924 (2020).
- 404. Duro-Castano, A. *et al.* Well-defined star-shaped polyglutamates with improved pharmacokinetic profiles as excellent candidates for biomedical applications. *Mol. Pharm.* **12**, 3639–3649 (2015).
- 405. Rennick, J. J., Johnston, A. P. R. & Parton, R. G. Key principles and methods for studying the endocytosis of biological and nanoparticle therapeutics. *Nat. Nanotechnol.* **16**, 266–276 (2021).
- 406. Jin, J., Byun, J. K., Choi, Y. K. & Park, K. G. Targeting glutamine metabolism as a therapeutic strategy for cancer. *Exp. Mol. Med.* **55**, 706–715 (2023).
- 407. Kumari, S., Mehta, S. L. & Li, P. A. Glutamate induces mitochondrial dynamic imbalance and autophagy activation: Preventive effects of selenium. *PLoS One* **7**, (2012).
- 408. Tobaben, S. et al. Bid-mediated mitochondrial damage is a key mechanism in glutamate-

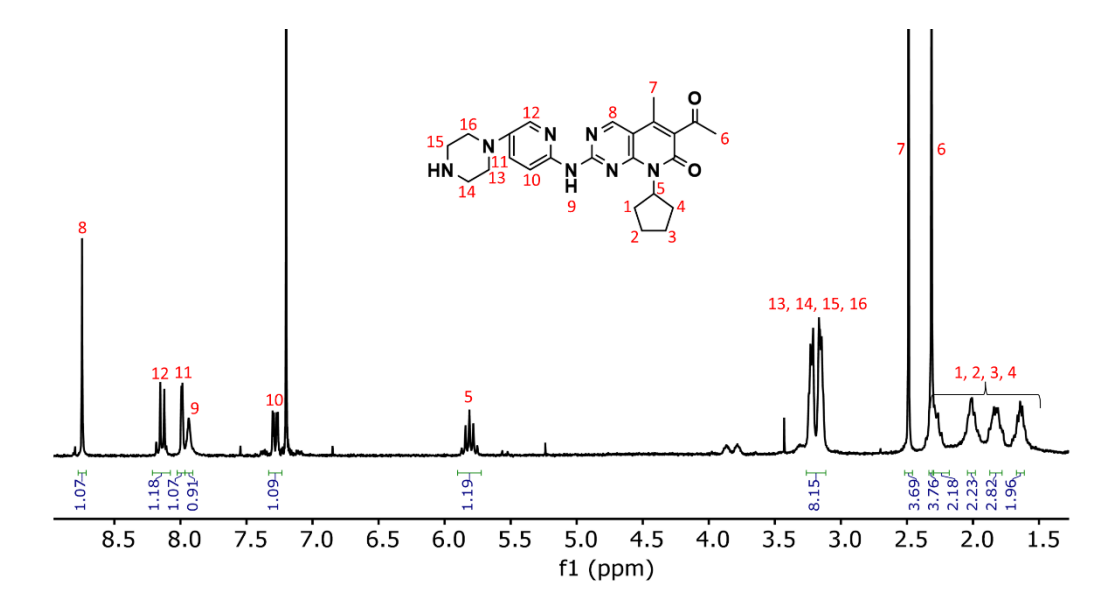
- induced oxidative stress and AIF-dependent cell death in immortalized HT-22 hippocampal neurons. *Cell Death Differ.* **18**, 282–292 (2011).
- 409. Warth, B. *et al.* Palbociclib and fulvestrant act in synergy to modulate central carbon metabolism in breast cancer cells. *Metabolites* **9**, 1–15 (2019).
- 410. Conroy, L. R. *et al.* Palbociclib treatment alters nucleotide biosynthesis and glutamine dependency in A549 cells. *Cancer Cell Int.* **20**, 1–12 (2020).
- 411. Burden, D. Guide to the homogenization of biological samples. Random Prim. (2008).
- 412. Robertson, N. & Leek, R. Preparation of tumor homogenates for subsequent preparation of cytosols, membrane fractions, RNA, and DNA. *Methods Mol. Med.* (2006) doi:10.1385/1-59259-969-9:51.
- 413. Gowda, G. A. N. & Raftery, D. NMR Based Metabolomics. **1280**, 19–37 (2021).
- 414. Lee, D.-Y. & Kim, E.-H. Therapeutic Effects of Amino Acids in Liver Diseases: Current Studies and Future Perspectives. *J. Cancer Prev.* **24**, 72–78 (2019).
- 415. Van De Poll, M. C. G., Soeters, P. B., Deutz, N. E. P., Fearon, K. C. H. & Dejong, C. H. C. Renal metabolism of amino acids: Its role in interorgan amino acid exchange. *Am. J. Clin. Nutr.* **79**, 185–197 (2004).
- 416. Inoue, K., Koizumi, S. & Tsuda, M. The role of nucleotides in the neuron-glia communication responsible for the brain functions. *J. Neurochem.* **102**, 1447–1458 (2007).
- 417. Zemski Berry, K. A., Murphy, R. C., Kosmider, B. & Mason, R. J. Lipidomic characterization and localization of phospholipids in the human lung. *J. Lipid Res.* **58**, 926–933 (2017).
- 418. Gamble, J. G. & Lehninger, A. L. Transport of ornithine and citrulline across the mitochondrial membrane. *J. Biol. Chem.* **248**, 610–618 (1973).
- 419. Zong, W.-X., Rabinowitz, J. D. & White, E. Mitochondria and Cancer. *Mol Cell* **61**, 667–676 (2016).

ANNEX I

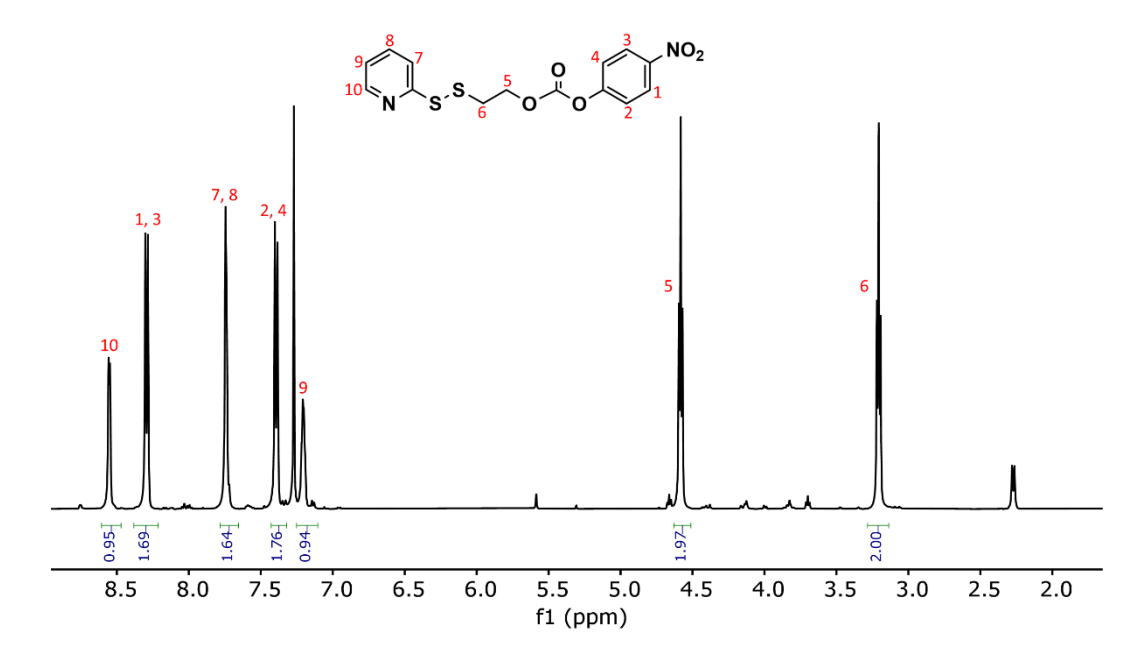
SUPPORTING INFORMATION

CHAPTER III

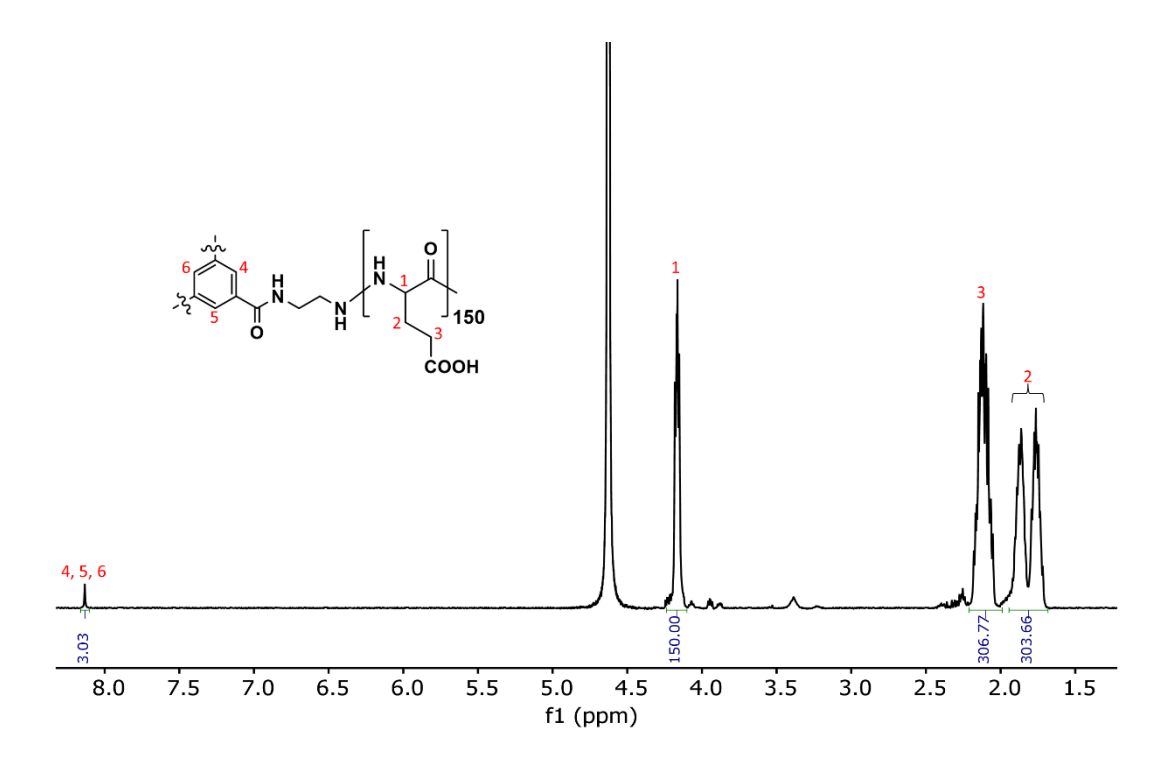
Supporting Information 3.1. 1 H NMR spectra assignment of palbociclib. 1 H NMR chemical shifts (ppm) (500 MHz, CDCl₃): 1.64 (m, 2H), 1.81 (m, 2H), 2.00 (m, 2H), 2.27 (m, 2H), 2.31 (s, 3H), 3.19 (t + t, 8H), 5.80 (m, 1H), 7.27 (d, 1H), 7.94 (s, 1H), 7.98 (d, 1H), 8.15 (s, 1H), 8.74 (s, 1H).



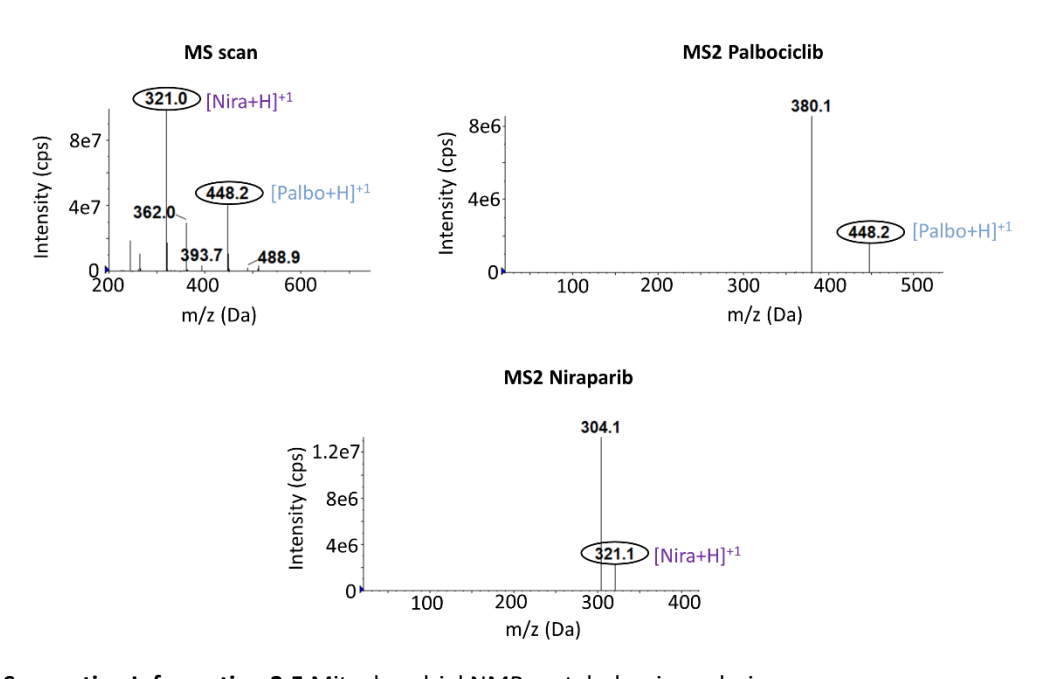
Supporting Information 3.2. ¹H NMR spectra assignment of the disulfide linker 4-nitrophenyl (2-(pyridin-2-yldisulfanyl)ethyl) carbonate. ¹H NMR chemical shifts (ppm) (500 MHz, CDCl₃): 3.20 (t, 2H), 4.57 (t, 2H), 7.21 (m, 1H), 7.39 (m, 2H), 7.64 (m, 2H), 8.29 (m, 2H), 8.55 (m, 1H).



Supporting Information 3.3. ¹H NMR spectra assignment of StPGA150. ¹H NMR chemical shifts (ppm) (500 MHz, D₂O): 1.81 (m, 300H), 2.11 (m, 300H), 4.17 (q, 150H), 8.13 (s, 3H).



Supporting Information 3.4. MS spectrum of a standard solution of 2 μ g/mL palbociclib (palbo) and Niraparib (nira) and MS fragmentation spectra of palbociclib and niraparib. Cps = counts per second.



Supporting Information 3.5 Mitochondrial NMR metabolomic analysis

	C	Т	Pa	lbo	StPGA-S	S-palbo		P-value
Metabolite	Mean	SEM	Mean	SEM	Mean	SEM	CT vs. Palbo	CT vs. StPGA-SS-palbo
Leucine	20.868	3.233	6.725	1.833	7.842	1.482	0.010	0.010
Valine	8.436	1.140	4.073	0.469	4.409	0.495	0.011	0.016
Methionine	4.479	0.415	1.614	0.746	2.519	0.393	0.029	0.020
Lysine	8.305	1.139	1.723	0.672	2.835	0.514	0.003	0.005
Tyrosine	2.281	0.248	0.731	0.282	1.238	0.235	0.011	0.030
Isoleucine	2.393	0.234	1.507	0.162	1.697	0.163	0.023	ns

PEP*	0.258	0.014	0.042	0.048	0.124	0.086	0.014	ns
Inosine	0.776	0.149	0.114	0.114	0.018	0.361	0.015	ns
Adenosine	1.826	0.386	0.399	0.145	0.761	0.582	0.011	ns
Phosphocholine	22.999	3.083	15.99 0	2.466	14.879	1.479	ns	0.048
Phenylalanine	3.175	0.340	1.748	0.620	1.881	0.324	ns	0.042

Mean and SEM of the metabolites showing significantly different levels in mitochondria of TNBC cells treated with free palbociclib (palbo) and StPGA-SS-palbociclib (StPGA-SS-palbo) compared to control (CT) cells by NMR metabolomics and p-values and direction changes of the comparisons. Data analysis used a T-test (n = 3-4). *ns = not statistically significant; PEP = phosphoenolpyruvate.

Supporting Information 3.6. Whole-cell NMR metabolomic analysis

	СТ		Pall	00	StPGA-S	S-palbo		P-value	
Metabolite	Mean	SEM	Mean	SEM	Mean	SEM	CT <i>vs</i> . Palbo	CT vs. StPGA- SS-palbo	Palbo vs StPGA- SS-palbo
Lactate	127.840	7.05	75.88	7.294	57.516	10.446	0.002	0.001	ns
Glutamine	2.036	0.336	4.338	0.409	6.153	0.725	0.005	0.002	ns
UDP-NAG*	0.597	0.061	0.317	0.046	0.199	0.116	0.010	0.023	ns
Methionine	1.904	0.508	3.369	0.288	2.636	1.292	0.046	ns	ns
Aspartate	0.962	0.052	1.429	0.071	0.894	0.322	0.002	ns	ns
GTP*	0.817	0.091	0.425	0.130	-0.190	0.419	0.048	ns	ns
Phenylalanine	2.473	0.100	2.844	0.088	2.553	0.151	0.032	ns	ns
Inosine	0.251	0.109	0.687	0.126	0.550	0.112	0.040	ns	ns
Glutathione	1.856	0.294	1.078	0.237	0.641	0.350	ns	0.038	ns
Adenosine	0.026	0.022	0.152	0.070	0.143	0.040	ns	0.037	ns
ATP*	3.847	0.448	2.391	0.518	1.398	0.591	ns	0.016	ns
P-choline	37.307	5.972	43.387	4.550	21.118	4.698	ns	ns	0.014

Mean and SEM of the metabolites showing significantly different levels in TNBC cells treated with free palbociclib (palbo) and StPGA-SS-palbociclib (StPGA-SS-palbo) compared to control (CT) cells by NMR metabolomics and p-values and direction changes of the comparisons. Data analysis used a T-test (n = 4). *ATP = adenosine triphosphate; GTP = guanosine triphosphate; ns = not statistically significant; P-choline = phosphcholine; UDP-NAG = uridine diphosphate N-acetylglucosamine.

Supporting Information 3.7. StPGA-induced metabolomic alterations.

	C	т	StP	GA	CT vs	. StPGA
Metabolite	Mean	SEM	Mean	SEM	P-value	Direction
Glutamine	1.657	0.297	2.994	0.152	0.016	↑
Adenosine	0.825	0.174	4.556	1.218	0.039	\uparrow
Fumarate	0.423	0.028	0.208	0.067	0.041	\downarrow
NAD+/NADP+*	1.422	0.079	1.008	0.102	0.032	\downarrow

Mean and SEM of the metabolites showing significantly different levels in TNBC cells treated with StPGA compared to control (CT) cells and p-values and direction changes of the comparisons. Data analysis used a T-test (n = 3). *NAD+/NADP+ = nicotinamide adenine dinucleotide/nicotinamide adenine dinucleotide phosphate.

Supporting Information 3.8. Mitochondrial and whole-cell MS metabolomic analysis

	C.	Т	Pal	bo	StPGA-	SS-palbo		P-value			Direction	
Metabolite	Mean	SEM	Mean	SEM	Mean	SEM	CT vs. Palbo	CT vs. StPGA-SS-palbo	Palbo vs StPGA-SS-palbo	Palbo	StPGA-SS-palbo	StPGA-SS-palbo*
								Mitochondria				
Deoxyguanosine	1.02	0.16	1.66	0.20	1.47	0.44	0.04	-	-	↑	-	-
GPC	0.52	0.06	1.95	0.05	1.61	0.27	2E-06	0.01	-	\uparrow	\uparrow	-
Spermidine	1.02	0.19	1.55	0.42	1.76	0.17	-	0.04	-	-	↑	-
								Whole-cell				
3-CMP	0.56	0.03	1.42	0.23	1.31	0.20	0.01	0.01	-	↑	↑	-
ArabfurUMP	0.65	0.03	1.40	0.12	1.17	0.06	9E-04	1E-04	-	\uparrow	\uparrow	-
5-GMP	0.84	0.17	1.45	0.14	1.31	0.13	0.03	-	-	\uparrow	-	-
5-GDP	1.00	0.28	1.94	0.23	1.92	0.64	0.04	-	-	\uparrow	-	-
1-methylguanosine	1.33	0.29	0.95	0.03	1.52	0.07	-	-	4E-04	-	-	\uparrow
P4P	2.34	0.52	0.72	0.20	0.75	0.07	0.03	0.02	-	\downarrow	\downarrow	-
GPC	0.73	0.06	1.43	0.17	2.20	0.91	0.01	-	-	\uparrow	-	-
AceLsm	1.14	0.26	1.79	0.03	2.21	0.82	0.05	-	-	\uparrow	-	-
DiAceSpe	2.55	0.64	0.56	0.11	0.97	0.29	0.02	-	-	\downarrow	-	-
Creatine	1.84	0.32	1.28	0.25	0.66	0.11	-	0.01	-	-	\downarrow	-
HPLac	1.44	0.34	0.70	0.13	1.28	0.13	-	-	0.02	-	-	↑

Mean and SEM of metabolites showing significantly different levels in mitochondria and whole-cells treated with free palbociclib (palbo) and StPGA-SS-palbociclib (StPGA-SS-palbo) compared to control (CT) cells by MS metabolomics, p-values and direction of the comparisons. Direction of StPGA-SS-palbociclib over free palbociclib is represented as StPGA-SS-palbo*. Data analysis used a T-test (n = 4, except for StPGA-SS-palbo group where MITMS12 was excluded).*1-methylGua = 1-methylguanosine; 3-CMP = cytidine 3'-monophosphate; 5-GDP = guanosine 5'-diphosphate; 5-GMP = guanosine 5-monophosphate; AceLsm = N-acetyl-D-lactosamine; ArabfurUMP = 1-β-D-Arabinofuranosyluracil 5-monophosphate; DeoxyGua = deoxyguanosine; DiAceSpe = N1,N8-Diacetylspermidine; GPC = glycerophosphocholine; HPLac = hydroxyphenyllactate; ns = not statistically significant; P4P = Pantetheine 4'-phosphate.

Supporting Information 3.9. Mitochondrial MS lipidomic analysis

		C	T.	Pa	lbo	StPGA-S	S-palbo		FDR			Directio	n
Lipid*	Group *	Mean	SEM	Mean	SEM	Mean	SEM	CT vs. Palbo	CT vs. StPGA-SS-palbo	Palbo vs. StPGA-SS-palbo	Palb o	StPGA-SS-palbo	StPGA-SS-palbo*
DG 18:0_19:1	GL	5.642	0.463	2.642	0.192	1.931	0.238	0.031	0.018	ns*	\downarrow	V	-
MGDG 16:0_26:0	GL	0.231	0.012	0.112	0.013	0.181	0.041	0.040	ns	ns	\downarrow	-	-
DG 16:0_26:0	GL	2.599	0.234	2.403	0.195	5.959	0.379	ns	0.015	0.009	-	\uparrow	↑
DG 15:0_18:1(d7)(is)	GL	1.783	0.170	1.941	0.174	4.365	0.390	ns	0.019	0.023	-	\uparrow	↑
DG 11:0_16:1	GL	0.373	0.024	0.442	0.037	0.893	0.115	ns	0.042	ns	-	\uparrow	-
DG 18:0_18:1	GL	2.240	0.243	1.551	0.172	3.949	0.349	ns	ns	0.016	-	-	\uparrow
DG 18:0_20:3	GL	1.804	0.225	1.077	0.112	2.351	0.185	ns	ns	0.023	-	-	\uparrow
DG 18:0_22:3	GL	1.404	0.126	1.139	0.114	2.318	0.237	ns	ns	0.048	-	-	\uparrow
PC 34:1	GPL	0.015	0.001	0.009	4E-04	0.007	0.001	0.040	0.021	0.016	\downarrow	\downarrow	\downarrow
PE O-34:2	GPL	0.053	0.002	0.039	0.002	0.024	0.002	0.047	0.009	0.033	\downarrow	\downarrow	\downarrow
PC O-40:6	GPL	0.222	0.020	0.118	0.005	0.099	0.010	0.033	0.027	ns	\downarrow	\downarrow	-
LPE O-18:2	GPL	3.221	0.262	1.896	0.091	1.523	0.194	0.047	0.041	ns	\downarrow	\downarrow	-
PS 42:1	GPL	0.292	0.014	0.170	0.006	0.180	0.006	0.017	0.015	ns	\downarrow	\downarrow	-
PS 42:2	GPL	1.391	0.059	0.726	0.027	0.605	0.031	0.012	0.006	ns	\downarrow	\downarrow	-
PC O-26:5	GPL	0.027	0.001	0.015	3E-04	0.032	0.002	0.012	ns	0.003	\downarrow	-	\uparrow
LPC 26:3	GPL	0.402	0.029	0.212	0.019	0.391	0.018	0.042	ns	0.023	\downarrow	-	\uparrow
LPE O-19:1	GPL	6.131	0.407	3.010	0.305	6.075	0.300	0.045	ns	0.024	\downarrow	-	\uparrow
LPE O-20:1	GPL	3.066	0.264	1.072	0.078	1.921	0.174	0.017	ns	0.045	\downarrow	-	\uparrow
PC 24:0_24:0	GPL	0.023	0.002	0.011	4E-04	0.015	0.002	0.017	ns	ns	\downarrow	-	-
PC O-42:0	GPL	0.243	0.022	0.134	0.006	0.151	0.018	0.040	ns	ns	\downarrow	-	-
PC 11:0_20:2	GPL	0.053	0.007	0.021	0.001	0.024	0.005	0.040	ns	ns	\downarrow	-	-
PC 22:0_24:4	GPL	0.793	0.063	0.381	0.041	0.592	0.138	0.047	ns	ns	\downarrow	-	-
PC 22:0_24:4	GPL	0.105	0.019	0.029	0.002	0.057	0.015	0.033	ns	ns	\downarrow	-	-
PC 44:2	GPL	0.089	0.009	0.039	0.002	0.039	0.016	0.031	ns	ns	\downarrow	-	-
PC O-41:6	GPL	0.343	0.045	0.134	0.012	0.203	0.049	0.040	ns	ns	\downarrow	-	-

PC O-42:5	GPL	0.136	0.017	0.039	0.002	0.057	0.013	0.017	ns	ns	\downarrow	-	-	
PC O-42:6	GPL	0.138	0.017	0.054	0.004	0.070	0.015	0.036	ns	ns	\downarrow	-	-	
LPC O-16:1	GPL	0.965	0.044	0.560	0.032	0.905	0.105	0.026	ns	ns	\downarrow	-	-	
PC O-44:1	GPL	0.065	0.008	0.132	0.009	0.114	0.002	0.047	0.047	ns	↑	\downarrow	-	
PC 18:1/18:1	GPL	0.512	0.024	0.740	0.032	0.961	0.033	0.040	0.007	0.044	↑	\uparrow	\uparrow	
PE O-36:5	GPL	0.026	0.001	0.035	0.001	0.045	0.002	0.040	0.007	0.003	↑	\uparrow	\uparrow	
PG 18:0_22:6	GPL	0.043	0.003	0.098	0.009	0.105	0.010	0.030	0.019	ns	↑	\uparrow	-	
PI 40:3	GPL	0.057	0.003	0.160	0.020	0.128	0.012	0.026	0.019	ns	↑	\uparrow	-	
PC O-32:0	GPL	0.021	0.001	0.032	0.002	0.030	0.004	0.030	ns	ns	↑	-	-	
PC O-42:0	GPL	0.034	0.002	0.052	0.001	0.041	0.003	0.033	ns	ns	↑	-	-	
PE O-32:2	GPL	0.211	0.020	0.533	0.039	0.399	0.041	0.026	ns	ns	↑	-	-	
PC 11:0_11:0	GPL	0.081	0.006	0.108	0.004	0.050	0.003	ns	0.040	0.004	-	\downarrow	\downarrow	
PC 42:0	GPL	0.033	0.003	0.034	0.002	0.017	0.001	ns	0.033	0.011	-	\downarrow	\downarrow	
PC 8:0_15:0	GPL	0.037	0.002	0.042	0.002	0.027	0.001	ns	0.050	0.026	-	\downarrow	\downarrow	
PC O-28:0	GPL	0.906	0.091	0.757	0.115	0.520	0.024	ns	0.047	0.023	-	\downarrow	\downarrow	
PC 17:0_16:2	GPL	0.226	0.012	0.218	0.014	0.111	0.004	ns	0.007	0.007	-	\downarrow	\downarrow	
PC 17:1_16:3	GPL	0.098	0.008	0.098	0.004	0.044	0.002	ns	0.009	0.003	-	\downarrow	\downarrow	
PC 18:0_18:1;O	GPL	0.485	0.035	0.555	0.026	0.213	0.010	ns	0.009	0.003	-	\downarrow	\downarrow	
PE O-36:3	GPL	0.758	0.054	0.641	0.019	0.284	0.004	ns	0.006	4Ens04	-	\downarrow	\downarrow	
PS 18:0_17:1	GPL	0.044	0.005	0.038	0.003	0.016	0.001	ns	0.009	0.008	-	\downarrow	\downarrow	
PC O-16:0_17:0	GPL	0.097	0.005	0.082	0.002	0.070	0.003	ns	0.049	ns	-	\downarrow	-	
PC O-38:0	GPL	0.186	0.010	0.127	0.013	0.078	0.006	ns	0.009	ns	-	\downarrow	-	
PC 16:0_18:1;O	GPL	0.318	0.026	0.362	0.031	0.163	0.011	ns	0.028	ns	-	\downarrow	-	
PC O-16:0_22:5	GPL	0.116	0.006	0.114	0.013	0.063	0.006	ns	0.032	ns	-	\downarrow	-	
PC O-36:3	GPL	1.155	0.081	0.916	0.073	0.708	0.042	ns	0.046	ns	-	\downarrow	-	
PC O-36:4	GPL	0.437	0.031	0.288	0.027	0.222	0.016	ns	0.021	ns	-	\downarrow	-	
PC O-38:3	GPL	0.950	0.069	0.565	0.060	0.335	0.027	ns	0.009	ns	-	\downarrow	-	
PC O-38:4	GPL	0.197	0.015	0.137	0.018	0.092	0.012	ns	0.047	ns	-	\downarrow	-	
LPG 18:1	GPL	0.054	0.006	0.039	0.004	0.023	0.002	ns	0.040	ns	-	\downarrow	-	

PS 44:1	GPL	0.833	0.061	0.568	0.039	0.531	0.010	ns	0.034	ns	-	\downarrow	-	
PS 9:0_24:1	GPL	2.101	0.206	1.344	0.028	1.089	0.059	ns	0.034	ns	-	\downarrow	-	
HBMP 18:1_22:0_12:0	GPL	0.130	0.004	0.106	0.007	0.103	0.002	ns	0.031	ns	-	\downarrow	-	
PC 16:0_18:1	GPL	0.090	0.004	0.100	0.003	0.148	0.011	ns	0.002	0.005	-	\uparrow	\uparrow	
PC 15:0_18:0	GPL	0.031	0.003	0.031	0.002	0.054	0.004	ns	0.049	0.030	-	\uparrow	\uparrow	
PC O-26:0	GPL	0.019	0.002	0.015	0.001	0.031	0.001	ns	0.041	0.012	-	\uparrow	\uparrow	
LPE 22:0	GPL	0.653	0.031	0.606	0.036	1.034	0.051	ns	0.019	0.017	-	\uparrow	\uparrow	
PC 15:0_18:1(d7)(is)	GPL	0.850	0.031	0.862	0.013	1.214	0.042	ns	0.019	0.008	-	\uparrow	\uparrow	
PC 38:2	GPL	0.175	0.012	0.206	0.004	0.280	0.011	ns	0.039	0.021	-	\uparrow	\uparrow	
PC 38:4	GPL	0.002	1E-04	0.002	2E-04	0.004	2E-04	ns	0.050	0.011	-	\uparrow	\uparrow	
PC O-19:3	GPL	0.004	4E-04	0.004	4E-04	0.013	0.001	ns	0.008	0.007	-	\uparrow	\uparrow	
PC O-24:2	GPL	0.037	0.002	0.042	0.004	0.128	0.007	ns	0.003	0.007	-	\uparrow	\uparrow	
PC O-25:1	GPL	0.117	0.009	0.103	0.006	0.202	0.009	ns	0.028	0.007	-	\uparrow	\uparrow	
PE 16:0_16:1	GPL	0.785	0.054	1.059	0.022	1.309	0.050	ns	0.026	0.044	-	\uparrow	\uparrow	
PC 13:0_14:0	GPL	0.158	0.022	0.160	0.027	0.314	0.014	ns	0.050	ns	-	\uparrow	-	
PC 14:0_15:0	GPL	0.472	0.026	0.550	0.049	0.729	0.042	ns	0.040	ns	-	\uparrow	-	
PC 9:0_32:2	GPL	0.015	0.002	0.018	0.004	0.043	0.003	ns	0.022	ns	-	\uparrow	-	
PC O-17:1	GPL	0.023	0.001	0.029	0.003	0.034	0.002	ns	0.049	ns	-	\uparrow	-	
PC O-20:5	GPL	0.046	0.002	0.054	0.001	0.082	0.009	ns	0.049	ns	-	\uparrow	-	
PC O-24:3	GPL	0.027	0.001	0.040	0.006	0.049	0.002	ns	0.008	ns	-	\uparrow	-	
LPC 22:5	GPL	0.266	0.012	0.305	0.027	0.433	0.032	ns	0.042	ns	-	\uparrow	-	
PE O-18:2_22:5	GPL	0.296	0.017	0.384	0.012	0.456	0.020	ns	0.034	ns	-	\uparrow	-	
PE O-38:6	GPL	1.438	0.073	1.250	0.178	0.605	0.094	ns	0.040	ns	-	\uparrow	-	
PE O-40:7	GPL	0.131	0.016	0.200	0.011	0.257	0.020	ns	0.050	ns	-	\uparrow	-	
LPE 18:1	GPL	0.348	0.005	0.489	0.046	0.652	0.044	ns	0.009	ns	-	\uparrow	-	
LPE 20:2	GPL	0.477	0.018	0.687	0.041	0.700	0.044	ns	0.046	ns	-	\uparrow	-	
PI 39:5	GPL	0.113	0.011	0.380	0.088	0.385	0.082	ns	0.049	ns	-	\uparrow	-	
PC 40:0	GPL	0.127	0.018	0.171	0.010	0.120	0.006	ns	ns	0.045	-	-	\downarrow	
PC 17:1_16:2	GPL	0.033	0.005	0.034	0.001	0.017	0.002	ns	ns	0.023	-	-	\downarrow	

PC 17:1_18:2	GPL	0.358	0.017	0.464	0.033	0.287	0.012	ns	ns	0.032	-	-	\downarrow	
PC 22:0_15:1	GPL	0.068	0.006	0.071	0.003	0.047	0.003	ns	ns	0.033	-	-	\downarrow	
PC 22:0_21:2	GPL	0.073	0.011	0.069	0.003	0.037	0.005	ns	ns	0.035	-	-	\downarrow	
PC 24:2_24:2	GPL	0.388	0.069	0.396	0.046	0.144	0.017	ns	ns	0.027	-	-	\downarrow	
PC 36:1	GPL	0.418	0.037	0.503	0.042	0.258	0.022	ns	ns	0.029	-	-	\downarrow	
PC 38:0_16:2	GPL	0.422	0.027	0.502	0.044	0.287	0.018	ns	ns	0.045	-	-	\downarrow	
PC 38:5	GPL	0.071	0.007	0.083	0.005	0.053	0.002	ns	ns	0.023	-	-	\downarrow	
PE 18:0_18:1	GPL	0.348	0.026	0.483	0.027	0.246	0.013	ns	ns	0.009	-	-	\downarrow	
PE 18:0_20:1	GPL	0.689	0.062	1.021	0.038	0.536	0.037	ns	ns	0.009	-	-	\downarrow	
PE 18:0_20:4	GPL	0.482	0.049	0.614	0.028	0.415	0.024	ns	ns	0.030	-	-	\downarrow	
PE 36:4	GPL	6.147	2.294	7.086	0.500	3.586	0.358	ns	ns	0.030	-	-	\downarrow	
PE 44:3	GPL	0.683	0.284	0.707	0.036	0.302	0.051	ns	ns	0.044	-	-	\downarrow	
PE O-18:1_16:0	GPL	16.89 4	6.338	13.94 7	1.706	6.616	0.631	ns	ns	0.045	-	-	\downarrow	
PE O-18:5_4:0	GPL	0.065	0.007	0.088	0.005	0.053	0.003	ns	ns	0.026	-	-	\downarrow	
PE O-22:1_22:5	GPL	0.877	0.139	1.154	0.038	0.749	0.032	ns	ns	0.011	-	-	\downarrow	
PE O-28:3_9:0	GPL	0.308	0.047	0.472	0.024	0.194	0.011	ns	ns	0.004	-	-	\downarrow	
PE O-38:7	GPL	0.254	0.024	0.264	0.012	0.161	0.005	ns	ns	0.009	-	-	\downarrow	
PG 16:0_22:6	GPL	0.382	0.056	0.522	0.026	0.261	0.023	ns	ns	0.016	-	-	\downarrow	
PG 16:1_18:1	GPL	0.609	0.057	0.707	0.019	0.413	0.044	ns	ns	0.044	-	-	\downarrow	
PG 16:2_22:6	GPL	0.354	0.112	0.557	0.024	0.317	0.027	ns	ns	0.023	-	-	\downarrow	
PG 18:1_22:5	GPL	0.061	0.007	0.077	0.004	0.033	0.005	ns	ns	0.024	-	-	\downarrow	
PI 38:2	GPL	0.027	0.003	0.038	0.005	0.012	0.002	ns	ns	0.027	-	-	\downarrow	
BMP 17:1_22:6	GPL	0.243	0.042	0.255	0.020	0.156	0.003	ns	ns	0.030	-	-	\downarrow	
PC O-34:0	GPL	1.654	0.154	1.612	0.061	1.977	0.030	ns	ns	0.044	-	-	\uparrow	
LPC 16:0	GPL	0.921	0.099	0.851	0.048	1.394	0.100	ns	ns	0.035	-	-	\uparrow	
PC 36:2	GPL	0.219	0.023	0.228	0.019	0.385	0.024	ns	ns	0.043	-	-	\uparrow	
PC O-16:1_16:1	GPL	0.121	0.016	0.123	0.007	0.181	0.003	ns	ns	0.023	-	-	\uparrow	
PC O-22:0_20:4	GPL	0.948	0.086	0.830	0.030	1.292	0.056	ns	ns	0.011	-	-	\uparrow	
PC O-28:1	GPL	0.066	0.007	0.051	0.004	0.094	0.002	ns	ns	0.011	-	-	\uparrow	

PC O-28:1	GPL	0.075	0.005	0.066	0.002	0.111	0.005	ns	ns	0.007	-	-	\uparrow	
PE O-18:1_22:2	GPL	0.537	0.411	1.284	0.210	3.357	0.340	ns	ns	0.041	-	-	\uparrow	
SM 34:0;O2	SL	2.173	0.140	1.171	0.045	1.284	0.116	0.018	0.049	ns	\downarrow	\downarrow	-	
Cer 18:1;O2/24:1	SL	8.198	0.713	4.389	0.147	4.886	0.251	0.033	0.049	ns	\downarrow	\downarrow	-	
Hex2Cer 18:1;20/22:0	SL	3.253	0.308	1.700	0.077	1.963	0.226	0.033	0.046	ns	\downarrow	\downarrow	-	
HexCer 18:1;O2/22:0	SL	34.32 0	3.937	15.00 1	1.159	18.024	1.190	0.034	0.046	ns	\downarrow	\downarrow	-	
HexCer 18:1;O2/22:1	SL	6.294	0.772	2.916	0.151	3.333	0.173	0.040	0.047	ns	\downarrow	\downarrow	-	
SM 30:1;O2	SL	0.053	0.001	0.028	0.002	0.029	0.003	0.018	0.019	ns	\downarrow	\downarrow	-	
SM 20:1;20/15:1	SL	0.539	0.031	0.288	0.012	0.955	0.173	0.017	ns	0.026	\downarrow	-	\uparrow	
Hex2Cer 18:1;20/26:0	SL	1.592	0.130	0.957	0.034	1.267	0.076	0.047	ns	ns	\downarrow	-	-	
SM 34:1;20(FA 16:0)	SL	0.940	0.118	0.446	0.016	0.430	0.092	0.045	ns	ns	\downarrow	-	-	
SM 34:1;20(FA 16:1)	SL	0.089	0.003	0.049	0.002	0.054	0.007	0.017	ns	ns	\downarrow	-	-	
SM 34:1;20(FA 17:0)	SL	0.408	0.024	0.235	0.009	0.329	0.026	0.024	ns	ns	\downarrow	-	-	
SM 34:1;O2	SL	1.258	0.110	0.654	0.019	0.854	0.111	0.030	ns	ns	\downarrow	-	-	
Cer 22:0;3O/20:0;(2OH)	SL	0.052	0.003	0.140	0.013	0.108	0.006	0.017	0.009	ns	\uparrow	\uparrow	-	
Cer 22:0;20/19:2	SL	0.055	0.002	0.279	0.030	0.425	0.037	0.007	0.001	ns	\uparrow	\uparrow	-	
HexCer 17:0;30/25:0	SL	0.063	0.005	0.054	0.001	0.025	0.002	ns	0.016	0.011	-	\downarrow	\downarrow	
SM 32:1;O3	SL	0.366	0.037	0.327	0.014	0.203	0.009	ns	0.036	0.011	-	\downarrow	\downarrow	
SM 34:1;O3	SL	0.494	0.049	0.451	0.018	0.266	0.009	ns	0.031	0.007	-	\downarrow	\downarrow	
SM 30:0;O2	SL	0.127	0.020	0.057	0.007	0.043	0.006	ns	0.047	ns	-	\downarrow	-	
SM 38:0;O2	SL	0.125	0.007	0.081	0.006	0.070	0.004	ns	0.019	ns	-	\downarrow	-	
SM 12:1;20/32:0	SL	1.602	0.077	1.208	0.069	0.924	0.083	ns	0.040	ns	-	\downarrow	-	
SM 19:1;20/24:1	SL	2.163	0.087	1.678	0.056	1.547	0.063	ns	0.034	ns	-	\downarrow	-	
SM 20:1;20/14:0	SL	1.208	0.205	0.554	0.049	0.304	0.054	ns	0.040	ns	-	\downarrow	-	
SM 33:2;30	SL	0.201	0.042	0.061	0.008	0.037	0.009	ns	0.046	ns	-	\downarrow	-	
SM 34:2;O2	SL	0.580	0.034	0.430	0.010	0.408	0.012	ns	0.040	ns	-	\downarrow	-	
SM 42:1;O2	SL	4.893	0.600	2.764	0.136	2.136	0.230	ns	0.046	ns	-	\downarrow	-	
SM 42:1;O2	SL	2.117	0.184	1.327	0.046	1.216	0.037	ns	0.031	ns	-	\downarrow	-	
HexCer 31:0;20/17:1	SL	0.004	3E-04	0.003	4E-04	0.002	2E-04	ns	0.046	ns	-	\downarrow	-	

Cer 15:0;20/26:1	SL	0.072	0.005	0.087	0.004	0.193	0.013	ns	0.008	0.007	-	\uparrow	↑
HexCer 38:0;20/3:0	SL	0.019	0.001	0.015	0.005	0.079	0.019	ns	0.047	ns	-	\uparrow	-
SM 20:1;20/21:0	SL	0.079	0.010	0.068	0.002	0.048	0.001	ns	ns	0.006	-	-	\downarrow
SM 60:5;30_	SL	0.138	0.018	0.174	0.004	0.093	0.006	ns	ns	0.007	-	-	\downarrow
SM 25:0;20/18:0	SM	0.350	0.047	0.288	0.017	0.182	0.014	ns	ns	0.048	-	-	\downarrow
SM 13:1;20/18:0	SL	0.120	0.008	0.082	0.006	0.142	0.008	ns	ns	0.024	-	-	↑
SM 15:1;20/28:1	SL	0.204	0.014	0.155	0.006	0.379	0.055	ns	ns	0.030	-	-	↑
SM 21:1;20/17:0	SL	0.128	0.009	0.117	0.006	0.279	0.039	ns	ns	0.030	-	-	↑
SM 32:1;20(FA 22:2)	SL	1.495	0.159	0.844	0.069	2.286	0.359	ns	ns	0.034	-	-	↑
SM 34:2;O3	SL	1.145	0.170	0.752	0.022	1.863	0.307	ns	ns	0.044	-	-	↑
SM 37:1;20(FA 20:1)	SL	1.666	0.225	1.165	0.044	3.865	0.607	ns	ns	0.016	-	-	↑
Cer 18:1;O2/16:0	SL	3.571	0.450	2.277	0.295	5.201	0.143	ns	ns	0.024	-	-	↑
Cer 18:1;O2/26:1	SL	2.958	0.317	3.060	0.063	4.042	0.181	ns	ns	0.030	-	-	↑
Hex3Cer 20:2;20/14:0	SL	0.340	0.027	0.268	0.005	0.358	0.012	ns	ns	0.012	-	-	↑
HexCer 16:2;20/42:0;0	SL	0.003	0.001	0.003	4E-04	0.009	0.001	ns	ns	0.026	-	-	↑
HexCer 18:1;O2/18:0	SL	32.02 0	2.825	20.86 6	1.351	31.867	1.573	ns	ns	0.033	-	-	↑
HexCer 18:1;O2/24:1	SL	0.388	0.048	0.256	0.004	0.328	0.008	ns	ns	0.009	-	-	↑
Hex3Cer 18:1;20/16:0	SL	0.460	0.045	0.426	0.025	0.650	0.037	ns	ns	0.039	-	-	↑

Mean and SEM of the relative levels of lipids in mitochondria of untreated TNBC cells (CT = control), cells treated with palbociclib (palbo) and StPGA-SS-palbociclib (StPGA-SS-palbo), adjusted p-values (FDR = false discovery rate) of the comparisons and direction of lipid changes after each treatment over the control and o StPGA-SS-palbociclib over free palbociclib (StPGA-SS-palbo*).

Data analysis used a FDR test (n = 4).*DG = Diacylglyceride; BMP = bis(monoacylglycerol)phosphate; Cer = ceramide; GL = glycerolipid; GPL = glycerophospholipid; HexCer = hexosylceramide;

HBMP = hemibis(monoacylglycero)phosphate; LPC = lyso-phosphatidylcholine; LPE = Lyso-Phosphatidylethanolamine; LPG = lyso-phosphatidylglycerol; MGDG = Monogalactosyldiacylglycerol;

ns = not statistically significant; PC = phosphatidylcholine; PE = phosphatidylethanolamine; PG = Phosphatidylglycerol; PI = Phosphatidylinositol; PS = phosphatidylserine; SL = sphingolipid; SM = sphingomyelin.

Supporting Information 3.10. Whole-cell MS lipidomic analysis

		C	T	Pa	lbo	StPGA-S	S-palbo		FDR			Directio	n
Lipid*	Group *	Mean	SEM	Mean	SEM	Mean	SEM	CT vs. Palbo	CT vs. StPGA-SS-palbo	Palbo vs. StPGA-SS-palbo	Palb o	StPGA-SS-palbo	StPGA-SS-palbo*
FAHFA 22:6/22:5	FA	5.964	0.081	3.311	0.225	2.939	0.273	ns*	0.048	ns	-	\downarrow	-
TG O-18:0_16:0_22:5	GL	0.033	0.007	0.588	0.029	0.035	0.003	0.014	ns	9Ens05	\uparrow	-	\downarrow
MGDG 16:0_18:0	GL	0.818	0.131	0.826	0.086	0.264	0.023	ns	0.048	0.014	-	\downarrow	\downarrow
TG 16:0_18:0_26:0	GL	0.009	0.001	0.016	0.003	0.034	0.003	ns	0.033	ns	-	\downarrow	-
TG O-18:0_18:1_22:6	GL	42.358	3.431	20.77 7	1.277	15.639	1.570	ns	0.043	ns	-	\downarrow	-
TG 16:0_22:5_22:5	GL	0.012	0.001	0.014	0.003	0.021	0.001	ns	0.033	ns	-	\uparrow	-
MGDG 16:0_26:0	GL	0.106	0.048	0.223	0.020	0.132	0.006	ns	ns	0.047	-	-	\downarrow
MGDG O-16:0_16:0	GL	0.234	0.039	0.272	0.014	0.193	0.004	ns	ns	0.025	-	-	\downarrow
DG 18:1/18:1	GL	0.018	0.006	0.010	0.001	0.004	0.001	ns	ns	0.044	-	-	\downarrow
TG O-16:0_16:0_18:1	GL	9.825	2.541	7.145	0.472	4.831	0.207	ns	ns	0.041	-	-	\downarrow
TG O-16:0_16:1_22:5	GL	8.976	2.011	5.660	0.238	4.190	0.098	ns	ns	0.025	-	-	\downarrow
TG O-18:0_16:0_18:1	GL	3.745	0.781	3.763	0.048	2.226	0.138	ns	ns	0.013	-	-	\downarrow
DG 16:0_18:0	GL	0.532	0.073	0.422	0.024	0.656	0.028	ns	ns	0.027	-	-	↑
DG 16:0_18:1	GL	0.037	0.003	0.038	0.002	0.062	0.002	ns	ns	0.010	-	-	↑
DG 18:0_26:1	GL	0.022	0.001	0.014	3E-04	0.020	4E-04	ns	ns	0.004	-	-	↑
TG O-18:1_14:0_16:0	GL	11.698	3.643	9.079	0.679	16.327	0.404	ns	ns	0.019	-	-	↑
PC O-34:3	GPL	34.417	0.953	16.87 0	0.660	15.481	0.860	0.019	0.013	ns	\downarrow	\downarrow	-
PC 17:2_17:2	GPL	1.180	0.041	0.180	0.008	0.966	0.051	0.001	ns	2Ens04	\downarrow	-	\uparrow
LNAPE 16:1/N-26:0	GPL	0.003	0.001	4E-04	2E-05	0.007	0.001	0.025	ns	7Ens05	\downarrow	-	\uparrow
PE O-17:1_20:4	GPL	0.564	0.037	1.179	0.043	0.635	0.048	0.030	ns	0.018	\uparrow	-	\downarrow
PC 16:0_19:1	GPL	0.094	0.020	0.766	0.072	0.345	0.248	0.030	ns	ns	\uparrow	-	-
PE O-36:5	GPL	0.012	0.002	0.174	0.011	0.049	0.036	0.016	ns	ns	\uparrow	-	-
PE O-36:7	GPL	0.244	0.019	0.531	0.016	0.243	0.043	0.030	ns	ns	\uparrow	-	-
BMP 20:3_22:6	GPL	0.005	0.001	0.063	0.006	0.047	0.011	0.025	ns	ns	\uparrow	-	-

								•					
HBMP 18:1_18:1_16:0	GPL	3.0E- 04	6E-05	0.002	2E-04	0.002	5E-04	0.030	ns	ns	↑	-	-
PC 24:0_24:0	GPL	0.283	0.036	0.162	0.011	0.110	0.003	ns	0.032	0.036	-	\downarrow	\downarrow
PC 20:0_21:0	GPL	0.183	0.013	0.145	0.010	0.084	0.006	ns	0.034	0.029	-	\downarrow	\downarrow
PC 16:0_24:0	GPL	0.490	0.054	0.488	0.018	0.223	0.007	ns	0.033	0.001	-	\downarrow	\downarrow
PC O-34:1	GPL	2.358	0.094	1.711	0.122	1.237	0.038	ns	0.011	0.042	-	\downarrow	\downarrow
PC 38:5	GPL	14.769	1.877	9.632	0.735	5.122	0.238	ns	0.033	0.020	-	\downarrow	\downarrow
PC 36:2	GPL	6.281	1.038	5.351	0.511	0.240	0.123	ns	0.048	0.016	-	\downarrow	\downarrow
PC 18:2/18:2	GPL	1.287	0.071	1.039	0.064	0.709	0.002	ns	0.011	0.025	-	\downarrow	\downarrow
PC 14:0_17:1	GPL	0.117	0.004	0.084	0.004	0.047	0.004	ns	0.032	0.028	-	\downarrow	\downarrow
PE 25:0_18:1	GPL	0.105	0.005	0.087	0.009	0.041	0.002	ns	0.011	0.023	-	\downarrow	\downarrow
PE 18:1_24:0	GPL	1.597	0.167	1.255	0.092	0.796	0.027	ns	0.043	0.034	-	\downarrow	\downarrow
PE 18:1_20:5	GPL	19.568	2.158	14.67 6	0.937	6.012	0.331	ns	0.014	0.008	-	\downarrow	\downarrow
PE 18:0_22:6	GPL	11.655	2.109	9.667	0.646	3.188	0.275	ns	0.043	0.008	-	\downarrow	\downarrow
PS 40:2	GPL	6.480	0.331	4.394	0.401	2.481	0.112	ns	0.011	0.034	-	\downarrow	\downarrow
LPG 22:6	GPL	0.246	0.020	0.219	0.009	0.130	0.005	ns	0.033	0.010	-	\downarrow	\downarrow
CL 16:1_16:1_18:1_18:1	GPL	0.933	0.104	0.745	0.071	0.276	0.009	ns	0.011	0.010	-	\downarrow	\downarrow
PC O-35:0	GPL	11.337	1.356	5.464	0.075	4.619	0.341	ns	0.048	ns	-	\downarrow	-
PC 26:0_26:1	GPL	0.414	0.049	0.256	0.026	0.183	0.003	ns	0.033	ns	-	\downarrow	-
PC 23:0_22:2	GPL	0.691	0.047	0.376	0.027	0.332	0.005	ns	0.011	ns	-	\downarrow	-
PS 18:1_18:1	GPL	1.107	0.077	0.769	0.060	0.523	0.044	ns	0.048	ns	-	\downarrow	-
PC 42:5	GPL	0.015	0.002	0.024	0.004	0.077	0.004	ns	0.011	0.022	-	\uparrow	\uparrow
PC 38:1	GPL	0.061	0.013	0.145	0.072	1.091	0.178	ns	0.013	0.037	-	\uparrow	\uparrow
PC 18:0_20:3	GPL	0.017	0.001	0.018	0.002	0.042	0.004	ns	0.033	0.029	-	\uparrow	\uparrow
LPC 22:1	GPL	2.406	0.116	3.013	0.271	4.445	0.283	ns	0.048	ns	-	\uparrow	-
LPC 20:2	GPL	5.535	0.375	6.571	0.508	9.153	0.345	ns	0.047	ns	-	\uparrow	-
PE 36:2	GPL	1.672	0.816	0.890	0.329	2.106	0.343	ns	0.033	ns	-	\uparrow	-
PC 11:0_11:0	GPL	0.037	0.007	0.044	0.005	0.021	0.001	ns	ns	0.034	-	-	\downarrow
PC 8:0_29:0	GPL	41.185	6.344	40.37 4	2.019	28.620	0.628	ns	ns	0.024	-	-	\downarrow

PC O-18:0_17:0	GPL	4.040	0.506	4.493	0.062	2.788	0.217	ns	ns	0.028	-	-	\downarrow	
PC O-34:0	GPL	1.800	0.415	2.186	0.069	1.176	0.099	ns	ns	0.018	-	-	\downarrow	
LPC O-16:0	GPL	0.050	0.014	0.126	0.006	0.052	0.006	ns	ns	0.020	-	-	\downarrow	
PE 16:0_18:0	GPL	0.826	0.073	0.779	0.019	0.547	0.026	ns	ns	0.023	-	-	\downarrow	
PC 10:0_34:4	GPL	0.901	0.115	0.805	0.060	0.471	0.031	ns	ns	0.037	-	-	\downarrow	
PC 15:0_18:1	GPL	0.053	0.008	0.041	0.002	0.017	4E-04	ns	0.021	0.002	-	\downarrow	\downarrow	
PC 16:0_20:1	GPL	1.586	0.332	1.902	0.119	1.082	0.108	ns	ns	0.046	-	-	\downarrow	
PC 16:1_18:2	GPL	0.416	0.073	0.443	0.021	0.261	0.013	ns	ns	0.018	-	-	\downarrow	
PC 17:0_16:2	GPL	0.087	0.024	0.098	0.007	0.061	0.003	ns	ns	0.039	-	-	\downarrow	
PC 17:0_20:4	GPL	0.122	0.023	0.100	0.008	0.057	0.003	ns	ns	0.028	-	-	\downarrow	
PC 24:3_24:3	GPL	0.294	0.044	0.190	0.012	0.100	0.011	ns	ns	0.037	-	-	\downarrow	
PC 36:1	GPL	33.686	6.058	35.55 3	2.168	13.379	1.348	ns	ns	0.013	-	-	\downarrow	
PC 38:3	GPL	2.009	0.166	2.025	0.164	1.196	0.073	ns	ns	0.043	-	-	\downarrow	
PC 38:4	GPL	11.379	1.807	8.046	0.233	6.534	0.064	ns	ns	0.023	-	-	\downarrow	
PC 42:4	GPL	0.100	0.039	0.163	0.010	0.099	0.008	ns	ns	0.043	-	-	\downarrow	
PC 44:3	GPL	15.039	1.962	16.95 1	1.351	9.443	0.918	ns	ns	0.048	-	-	\downarrow	
PC 44:5	GPL	21.835	4.008	20.90 3	1.439	10.653	0.756	ns	ns	0.021	-	-	\downarrow	
PC 9:0_34:4	GPL	10.486	1.226	8.675	0.354	6.682	0.121	ns	ns	0.028	-	-	\downarrow	
PC O-17:0_22:6	GPL	4.818	0.486	4.386	0.192	2.760	0.194	ns	ns	0.031	-	-	\downarrow	
PC O-38:1	GPL	0.339	0.216	0.984	0.136	0.118	0.009	ns	ns	0.006	-	-	\downarrow	
PC O-38:5	GPL	3.329	0.449	3.011	0.185	1.919	0.111	ns	ns	0.035	-	-	\downarrow	
PC O-40:4	GPL	25.115	3.384	20.31 3	1.386	12.673	0.629	ns	ns	0.032	-	-	\downarrow	
PC O-40:5	GPL	9.707	1.007	10.07 7	0.621	7.303	0.196	ns	ns	0.045	-	-	\downarrow	
PE 15:0_18:1(d7)(is)	GPL	2.987	1.547	3.190	0.236	1.310	0.069	ns	ns	0.008	-	-	\downarrow	
PE 16:0_16:1	GPL	2.707	0.607	2.532	0.161	1.682	0.079	ns	ns	0.039	-	-	\downarrow	
PE 18:0_24:3	GPL	32.669	6.015	30.14 7	1.347	20.126	0.990	ns	ns	0.027	-	-	\downarrow	

PE 18:1/18:1	GPL	31.668	6.464	23.93 1	2.104	9.700	0.619	ns	ns	0.012	-	-	\downarrow	
PE 18:1_22:6	GPL	36.951	5.142	36.56 2	1.626	27.337	1.077	ns	ns	0.044	-	-	\downarrow	
PE O-16:1_22:1	GPL	0.067	0.005	0.138	0.009	0.077	0.004	ns	ns	0.019	-	-	\downarrow	
PE O-17:1_22:5	GPL	0.120	0.020	0.152	0.011	0.091	0.002	ns	ns	0.025	-	-	\downarrow	
PE O-18:3_20:4	GPL	0.054	0.047	0.157	0.012	0.015	0.006	ns	ns	0.018	-	-	\downarrow	
PE O-34:1	GPL	0.219	0.023	0.435	0.028	0.253	0.020	ns	ns	0.034	-	-	\downarrow	
PE O-36:3	GPL	0.071	0.018	0.075	0.003	0.039	0.002	ns	ns	0.008	-	-	\downarrow	
PE O-38:5	GPL	7.215	1.033	7.574	0.608	4.236	0.286	ns	ns	0.032	-	-	\downarrow	
LPE 22:1	GPL	0.634	0.103	0.725	0.061	0.056	0.030	ns	ns	0.024	-	-	\downarrow	
LPE 26:1	GPL	1.275	0.257	1.306	0.049	0.686	0.038	ns	ns	0.010	-	-	\downarrow	
PG 14:0_18:1	GPL	1.217	0.174	1.036	0.084	0.620	0.011	ns	ns	0.027	-	-	\downarrow	
PG 16:1/16:1	GPL	7.362	1.732	5.918	0.586	2.992	0.251	ns	ns	0.034	-	-	\downarrow	
PG 16:1_20:4	GPL	11.685	1.822	8.506	0.145	5.934	0.306	ns	ns	0.023	-	-	\downarrow	
PG 16:2_18:1	GPL	0.302	0.046	0.217	0.007	0.154	0.004	ns	ns	0.012	-	-	\downarrow	
LPI 20:1	GPL	0.073	0.015	0.087	0.006	0.042	0.005	ns	ns	0.037	-	-	\downarrow	
CL 34:2_36:3	GPL	0.763	0.163	0.925	0.106	0.367	0.033	ns	ns	0.026	-	-	\downarrow	
PC 10:0_17:0	GPL	1.008	0.167	1.117	0.067	1.702	0.083	ns	ns	0.036	-	-	\uparrow	
PC O-15:0	GPL	0.090	0.011	0.078	0.004	0.114	0.006	ns	ns	0.036	-	-	\uparrow	
PC O-26:0	GPL	5.971	1.268	4.755	0.281	7.334	0.202	ns	ns	0.024	-	-	\uparrow	
PC 18:0_20:4	GPL	0.015	0.001	0.011	3E-04	0.015	0.001	ns	ns	0.026	-	-	\uparrow	
PC 18:0_22:4	GPL	0.068	0.009	0.044	0.002	0.075	0.003	ns	ns	0.008	-	-	\uparrow	
PC 18:1/18:1	GPL	0.137	0.026	0.154	0.009	0.224	0.008	ns	ns	0.034	-	-	\uparrow	
PC 18:1_26:1	GPL	0.096	0.011	0.088	0.007	0.152	0.007	ns	ns	0.029	-	-	\uparrow	
PC 18:5_26:6	GPL	1.393	0.278	1.561	0.061	2.376	0.101	ns	ns	0.018	-	-	\uparrow	
PC 21:0_22:1	GPL	0.154	0.012	0.142	0.007	0.227	0.008	ns	ns	0.017	-	-	\uparrow	
PC 40:4	GPL	0.042	0.012	0.028	0.003	0.060	0.002	ns	ns	0.014	-	-	\uparrow	
LPC 18:1	GPL	0.107	0.016	0.170	0.011	0.303	0.029	ns	ns	0.042	-	-	\uparrow	
LPC 19:1	GPL	0.908	0.143	0.877	0.039	1.335	0.068	ns	ns	0.027	-	-	\uparrow	

LPC 22:4	GPL	0.157	0.017	0.186	0.008	0.241	0.008	ns	ns	0.041	-	-	\uparrow	
PE 18:1_26:0	GPL	1.239	0.232	1.199	0.141	2.752	0.189	ns	ns	0.024	-	-	\uparrow	
PE O-18:2_16:1	GPL	0.166	0.049	0.160	0.010	0.363	0.042	ns	ns	0.027	-	-	\uparrow	
PE O-38:7	GPL	0.808	0.091	1.020	0.087	2.930	0.466	ns	ns	0.034	-	-	\uparrow	
PE O-44:2	GPL	9.382	1.659	8.058	0.531	12.481	0.483	ns	ns	0.029	-	-	\uparrow	
LPE O-18:1	GPL	0.050	0.003	0.048	0.003	0.114	0.013	ns	ns	0.028	-	-	\uparrow	
LNAPE 17:1/N-16:0	GPL	0.585	0.091	0.342	0.012	0.656	0.076	ns	ns	0.043	-	-	\uparrow	
LNAPE 17:1/N-24:0	GPL	0.056	0.014	0.038	0.003	0.063	0.004	ns	ns	0.047	-	-	\uparrow	
LNAPE 18:1/N-18:0	GPL	0.236	0.046	0.174	0.013	0.324	0.026	ns	ns	0.029	-	-	\uparrow	
PG 16:2_18:2	GPL	1.007	0.117	0.889	0.050	2.906	0.349	ns	ns	0.012	-	-	\uparrow	
PG 17:1_16:2	GPL	1.298	0.078	0.855	0.042	1.697	0.152	ns	ns	0.024	-	-	\uparrow	
PI 17:0_18:1	GPL	0.301	0.062	0.216	0.006	0.280	0.007	ns	ns	0.021	-	-	\uparrow	
PI 40:7	GPL	1.069	0.121	1.125	0.041	1.508	0.076	ns	ns	0.049	-	-	\uparrow	
PS 34:1	GPL	0.216	0.026	0.185	0.011	0.367	0.040	ns	ns	0.034	-	-	\uparrow	
PG 20:1_22:6	GPL	0.872	0.101	0.644	0.028	1.517	0.152	ns	ns	0.017	-	-	\uparrow	
HexCer 14:2;20/27:0	SL	1.005	0.059	0.974	0.041	0.535	0.011	ns	0.013	0.004	-	\downarrow	\downarrow	
SM 13:0;20/21:1	SL	10.571	0.498	6.332	0.248	4.950	0.201	ns	0.011	ns	-	\downarrow	-	
Cer 18:1;O2/24:0	SL	0.408	0.125	0.059	0.002	0.053	0.004	ns	0.043	ns	-	\downarrow	-	
Hex3Cer 42:1;20	SL	8.361	0.603	6.857	0.593	4.170	0.269	ns	0.043	ns	-	\downarrow	-	
SM 36:0;O2	SL	0.002	4E-04	0.016	0.005	0.016	0.003	ns	0.043	ns	-	\uparrow	-	
Hex3Cer 42:0;20	SL	1.054	0.493	1.309	0.067	0.129	0.009	ns	ns	2Ens04	-	-	\downarrow	
SM 23:0;20/17:0	SL	0.804	0.089	0.479	0.024	1.307	0.235	ns	ns	0.035	-	-	\downarrow	
Cer 17:0;20/15:1	SL	0.190	0.019	0.220	0.016	0.117	0.010	ns	ns	0.034	-	-	\downarrow	
Cer 18:1;20/24:0	SL	0.670	0.137	1.059	0.058	0.381	0.073	ns	ns	0.036	-	-	\downarrow	
Cer 18:2;20/25:0	SL	0.049	0.006	0.057	0.007	0.008	0.003	ns	ns	0.028	-	-	\downarrow	
Cer 18:2;O2/24:0	SL	0.338	0.023	0.548	0.030	0.315	0.025	ns	ns	0.031	-	-	\downarrow	
Hex3Cer 32:1;20	SL	9.341	1.419	8.556	0.318	3.828	0.366	ns	ns	0.014	-	-	\downarrow	
Hex3Cer 34:2;20	SL	10.855	1.600	13.80 6	0.305	8.763	0.537	ns	ns	0.021	-	-	\downarrow	

Cer 34:0;O2	SL	0.642	0.401	0.082	0.041	0.827	0.170	ns	ns	0.034	-	-	↑
SM 14:0;20/28:0	SL	0.935	0.136	0.661	0.038	2.509	0.486	ns	ns	0.024	-	-	\uparrow
SM 32:0;O2	SL	11.215	1.935	8.699	0.967	20.716	1.178	ns	ns	0.018	-	-	\uparrow
SM 20:1;20/13:1	SL	5.903	0.631	5.097	0.542	12.384	0.993	ns	ns	0.021	-	-	\uparrow
SM 20:1;20/21:1	SL	5.540	1.399	5.926	0.868	22.477	2.997	ns	ns	0.028	-	-	\uparrow
SM 34:1;O2	SL	0.800	0.099	0.592	0.019	0.987	0.064	ns	ns	0.024	-	-	\uparrow
CE 18:2	STL	0.018	0.002	0.016	0.001	0.029	0.001	ns	ns	0.024	-	-	\uparrow

Mean and SEM of the relative levels of lipids in untreated TNBC cells (CT = control), cells treated with palbociclib (palbo) and StPGA-SS-palbociclib (StPGA-SS-palbo), adjusted p-values (FDR = false discovery rate) of the comparisons and direction of lipid changes after each treatment over the control and of StPGA-SS-palbociclib over free palbociclib (StPGA-SS-palbo*). Data analysis used a FDR test (n = 4).* BMP = bis(monoacylglycerol)phosphate; CE = cholesterol ester; Cer = ceramide; CL = cardiolipin; DG = Diacylglyceride; FA = fatty acyl; FAHFA = fatty acyl ester of hydroxy fatty acid; GL = glycerolipid; GPL = glycerophospholipid; HBMP = hemiBis(monoacylglycero)phosphate; HexCer = hexosylceramide; LNAPE = lyso-N-acyl-phosphatidylethanolamine; LPC = lyso-phosphatidylcholine; LPE = lyso-phosphatidylethanolamine; LPG = lyso-phosphatidylglycerol; LPI = Lyso-phosphatidylinositol; MGDG = monogalactosyldiacylglycerol; ns = not statistically significant; PC = phosphatidylcholine; PE = phosphatidylethanolamine; PG = Phosphatidylglycerol; PI = Phosphatidylinositol; PS = phosphatidylserine; SL = sphingolipid; SM = sphingomyelin; STL = sterol lipid; TG = triglyceride.

Supporting Information 3.11. ¹³C-glucose MS fluxomics optimization

		M+	0	M-	1	M+	2	M+	-3	M+	4	M+	5	M+	6
Metabolite	Time (min)	Mean	SEM	Mean	SEM	Mean	SEM	Mean	SEM	Mean	SEM	Mean	SEM	Mean	SEM
	15	69.42	2.08	0.09	0.05	22.55	1.26	4.56	0.40	0.70	0.11	2.63	0.32	0.04	0.01
Cituata	60	61.94	1.23	0.59	0.02	25.81	0.91	6.04	0.11	2.13	0.08	3.31	0.19	0.17	0.01
Citrate	120	55.18	2.68	1.25	0.05	28.71	1.11	6.98	0.47	3.39	0.45	4.17	0.61	0.32	0.07
	180	54.57	2.54	1.48	0.14	28.73	1.16	7.10	0.71	3.60	0.56	4.20	0.56	0.32	0.09
	15 vs. 60	ns ^s	*	0.0	06	ns	;	ns	5	0.0	03	ns	5	0.00	01
p-value	60 vs. 120	ns		0.0	01	ns	i	ns	S	0.0	4	ns	5	ns	
	120 vs. 180	ns	i .	n:	S	ns	i	ns	5	ns	i	ns	5	ns	i .
	15	14.49	0.43	0.09	0.09	0.31	0.07	19.08	2.85	0.73	0.20	1.58	0.06	63.73	2.47
F-1,6-BP	60	14.74	0.48	0.12	0.06	0.42	0.02	17.33	2.44	0.66	0.26	1.63	0.18	65.11	2.15
1-1,0-01	120	16.79	2.15	0.02	0.02	0.29	0.09	18.63	2.68	1.08	0.32	1.57	0.05	61.64	2.36
	180	18.71	1.26	0.00	0.00	0.46	0.17	18.57	3.59	0.51	0.22	1.72	0.12	60.03	4.46
	15 vs. 60	ns		n:	S	ns	i	ns	S	ns	;	ns	5	ns	i
p-value	60 vs. 120	ns		n:	S	ns	i	ns	5	ns	i	ns	5	ns	i
	120 vs. 180	ns	i	n:	s	ns	i	ns	5	ns	i	ns	i	ns	i
	15	86.79	0.60	0.21	0.11	3.37	0.07	9.25	0.71	0.37	0.07				
Fumarate	60	80.15	0.40	1.21	0.21	7.36	0.30	10.51	0.17	0.76	0.14				
ramarace	120	75.33	1.76	1.77	0.15	9.45	0.51	12.27	1.38	1.18	0.17				
	180	75.45	2.50	2.18	0.13	9.59	1.05	11.60	1.05	1.18	0.32				
	15 vs. 60	0.02	24	0.0	04	0.00	01	0.0	01	0.0	28				
p-value	60 vs. 120	ns		0.0	17	0.0	3	ns	5	ns	i				
	120 vs. 180	ns	i	n:	S	ns	;	ns	S	ns	;				
α-KG	15	93.10	0.60	0.24	0.23	5.44	0.44	0.59	0.15	0.38	0.11	0.24	0.02		
u Ko	60	85.76	0.54	1.03	0.34	10.23	0.19	1.47	0.06	0.92	0.07	0.59	0.05		

	120	79.12	1.52	1.27	0.18	14.30	0.91	2.43	0.14	1.76	0.23	1.11	0.16	1	
	180	78.64	2.63	1.55	0.02	14.08	1.58	2.83	0.41	1.88	0.38	1.01	0.26		
	15 vs. 60	ns		ns	5	0.0	1	0.00	02	0.0	16	0.0	14		
p-value	60 vs. 120	ns	i	ns	5	0.02	26	0.00	06	0.03	32	0.0	39		
	120 vs. 180	ns		ns	5	ns	;	ns	S	ns	;	ns	s		

Mean and SEM of the isotopic distribution of 13 C-labeled metabolites of untreated TNBC cells incubated with 13 C-glucose for various times (15, 60, 120, and 180 min) and p-values of the comparison's times. Data analysis used a T-test (n = 3). * α -KG = α -ketoglutarate; F-1,6-BP = Fructose-1,6-biphosphate; ns = not statistically significant.

Supporting Information 3.12. ¹³C-glutamne MS fluxomics optimization

		M+	-0	M	+1	M+	-2	M+	-3	M+	-4	M+	-5	M+	-6
Metabolite	Time (min)	Mean	SEM	Mean	SEM	Mean	SEM	Mean	SEM	Mean	SEM	Mean	SEM	Mean	SEM
Clutamata	180	28.87	1.91	2.77	0.17	3.02	0.20	13.13	0.15	0.00	0.00	52.20	2.32		
Glutamate	360	26.90	2.67	3.26	0.13	3.47	0.11	13.16	0.22	0.00	0.00	53.22	2.67		
p-value	180 vs. 360	ns	*	n	S	ns	i	ns	5	ns	5	ns	3		
- 1/6	180	33.35	4.23	2.59	0.14	3.16	0.18	11.87	0.18	0.00	0.00	49.03	4.38		
α-KG	360	32.68	2.53	3.06	0.11	3.41	0.11	12.04	0.25	0.00	0.00	48.80	2.33		
p-value	180 vs. 360	ns	5	n:	S	ns	;	ns	5	ns	5	ns	5		
Cussiants	180	35.78	3.12	3.96	0.12	13.30	0.42	0.02	0.02	46.95	3.00				
Succinate	360	33.55	2.11	4.48	0.19	13.66	0.47	0.03	0.03	48.28	1.86				
p-value	180 vs. 360	ns	5	n:	S	ns	i	ns	5	ns	5				
E	180	43.02	2.14	3.87	0.20	10.84	0.33	5.99	0.05	36.27	2.49				
Fumarate	360	40.52	3.12	4.42	0.31	11.62	0.22	6.96	0.82	36.47	2.50				
p-value	180 vs. 360	ns	5	n:	S	ns	i	ns	5	ns	5				
Nalata	180	43.30	2.32	3.39	0.06	10.51	0.21	6.18	0.09	36.62	2.25				
Malate	360	39.98	2.58	4.08	0.09	11.02	0.12	7.00	0.58	37.92	2.08				
p-value	180 vs. 360	ns	5	n:	s	ns	;	ns	5	ns	5				
Citrate	180	49.88	2.19	3.35	0.11	8.19	0.18	6.04	0.06	25.71	1.87	6.53	0.24	0.3	0.05

	360	47.29	2.34	3.92	0.03	8.78	0.18	6.52	0.37	26.72	1.69	6.38	0.27	0.397	0.05
p-value	180 vs. 360	0.0	41	n	S	n	s	ns	5	ns	5	ns	S	ns	5

Mean and SEM of the isotopic distribution of 13 C-labeled metabolites of untreated TNBC cells incubated with 13 C-glutamine for various times (180 and 360 min) and p-values of the labeling time comparison. Data analysis used a T-test (n = 3). * α -KG = α -ketoglutarate; ns = not statistically significant

Supporting Information 3.13. ¹³C-glucose MS fluxomics analysis

		M+0	M+1	M+2	M+3	M+4	M+5	M+6	M+7	M+8	M+9	M+10	M+11	M+12	M+13	M+14	M+15
		Mean SEM	Mean SEM	Mean SEM	Mean SEM	Mean SEM	Mean SEM	Mean SEM	Mean SEM	Mean SEM	Mean SEM	Mean SEM	Mean SEM	Mean SEM	Mean SEM	Mean SEM	Mean SEM
	С	16.79 2.15	0.02 0.02	0.29 0.09	18.63 2.68	1.08 0.32	1.57 0.05	61.64 2.36									
F-1,6-BP	Р	25.74 4.18	0.30 0.16	0.73 0.23	14.83 3.09	1.18 0.20	1.26 0.48	55.95 1.42									
	PSP	43.41 5.14	0.98 0.47	0.93 0.47	10.21 1.18	1.54 0.38	2.76 0.65	40.16 5.54									
	C vs. P	ns	ns	ns	ns	ns	ns	ns									
p-value	C vs. PSP	0.009	ns	ns	0.045	ns	ns	0.024									
	P vs. PSP	ns	ns	ns	ns		ns	ns									
	С	52.63 2.51	0.12 0.12	4.69 1.18	42.57 2.54												
G-3-P	Р	51.13 1.47	0.31 0.16	2.96 0.55	45.59 2.02												
	PSP	50.99 2.64	0.36 0.36	6.31 1.10	42.35 2.71												
	C vs. P	ns	ns	ns	ns												
p-value	C vs. PSP	ns	ns	ns	ns												
	P vs. PSP	ns	ns	ns	ns												
	С	45.17 3.39	0.09 0.09	1.95 0.37	2.94 0.70	0.58 0.07	1.00 0.29	43.89 3.02	0.00 0.00	1.67 0.68	0.29 0.07	0.07 0.07	1.19 0.21	0.13 0.07	0.80 0.20	0.07 0.04	0.18 0.03
UDP-NAG	Р	25.89 2.84	0.85 0.62	2.46 0.39	4.57 0.04	0.93 0.48	1.91 0.70	58.19 3.25	0.00 0.00	1.84 0.19	0.15 0.13	0.39 0.13	1.31 0.23	0.07 0.04	1.02 0.20	0.10 0.06	0.33 0.09
	PSP	35.66 0.90	0.00 0.00	1.98 0.34	4.61 0.92	1.12 0.68	3.13 1.21	46.47 1.43	0.00 0.00	1.61 0.78	0.56 0.16	0.47 0.10	2.35 0.38	0.33 0.07	0.53 0.11	0.26 0.16	0.91 0.01
	C vs. P	0.012	ns	ns	ns	ns	ns	0.032	ns	ns	ns	ns	ns	ns	ns	ns	ns
p-value	C vs. PSP	ns	ns	ns	ns	ns	ns	ns	ns	ns	ns	0.029	ns	ns	ns	ns	4E-05
	P vs. PSP	0.031	ns	ns	ns	ns	ns	0.030	ns	ns	ns	ns	ns	0.032	0.036	ns	0.003
	С	50.58 2.24	0.21 0.12	0.97 0.19	19.60 0.27	0.14 0.14	1.42 0.19	10.25 1.40	0.50 0.02	2.71 0.14	9.73 0.72	0.23 0.17	3.66 0.36				
NANeur	Р	51.95 1.45	0.12 0.12	0.56 0.13	17.13 0.39	0.23 0.15	1.15 0.16	11.05 0.05	0.61 0.17	3.26 0.09	10.78 0.54	0.26 0.01	2.92 0.38				
	PSP	74.23 0.99	0.11 0.06	0.37 0.07	9.39 0.45	0.15 0.02	0.48 0.11	7.24 0.84	0.35 0.09	1.85 0.27	4.53 0.45	0.12 0.08	1.18 0.18				
	C vs. P	ns	ns	ns	0.006	ns	ns	ns	ns	0.028	ns	ns	ns				
p-value	C vs. PSP	0.001	ns	0.041	4E-05	ns	0.012	ns	ns	0.048	0.004	ns	0.004				
	P vs. PSP	2E-04	ns	ns	2E-04	ns	0.026	0.010	ns	0.008	0.001	ns	0.014				

1	С	55.18 2.68	1.25 0.05	28.71 1.11	6.98 0.47	3.39 0.45	4.17 0.61	0.32 0.07							
6															
Citrate	P	56.46 1.41	1.94 0.04		8.15 0.24			0.40 0.03							
	PSP	62.79 0.93	1.85 0.12	22.47 1.02	6.12 0.44	3.18 0.28	3.30 0.29	0.29 0.03							
	C vs. P	ns	3E-04	ns	ns	ns	ns	ns							
p-value	C vs. PSP	ns	0.011	0.014	ns	ns	ns	ns							
	P vs. PSP	0.020	ns	ns	0.016	0.036	ns	ns							
	С	79.12 1.52	1.27 0.18	14.30 0.91	2.43 0.14	1.76 0.23	1.11 0.16								
α-KG	Р	71.03 1.68	2.41 0.23	18.16 1.00	3.94 0.07	2.83 0.29	1.63 0.17								
	PSP	76.64 3.31	2.18 0.45	14.06 1.72	3.67 0.73	2.06 0.28	1.39 0.27								
	C vs. P	0.023	0.018	0.046	0.001	0.044	ns								
p-value	C vs. PSP	ns	ns	ns	ns	ns	ns								
	P vs. PSP	ns	ns	ns	ns	ns	ns								
	С	46.62 13.85	1.13 0.44	6.88 1.21	6.96 1.65	1.27 0.44	36.14 10.44	0.00 0.00	0.05 0.05	0.26 0.18	0.49 0.25	0.22 0.20			
IMP	Р	73.18 4.61	0.07 0.05	2.32 0.53	2.97 0.18	3.32 1.27	16.14 2.51	0.21 0.15	0.62 0.51	0.69 0.34	0.18 0.10	0.29 0.22			
	PSP	72.36 3.87	1.12 1.12	2.28 0.63	3.58 0.53	1.80 1.14		0.26 0.26	1.18 0.45	0.52 0.29	2.47 0.59	0.37 0.23			
	C vs. P	ns	ns	0.026	ns	ns	ns	ns	ns	ns	ns	ns			
p-value	C vs. PSP	ns	ns	0.028	ns	ns	ns	ns	ns	ns	0.037	ns			
p value											0.019				
	P vs. PSP	ns	ns	ns	ns	ns	ns	ns	ns	ns		ns			
	С	71.17 1.54	0.25 0.25	4.38 0.44	3.84 0.49	1.22 0.08	18.64 1.22	0.16 0.10	0.00 0.00	0.06 0.06	0.28 0.11	0.01 0.00			
AMP	Р	83.42 2.05	0.00 0.00	2.26 0.46	2.15 0.44		11.18 1.13		3E-03 3E-3	0.05 0.03	0.09 0.04	0.03 0.01			
	PSP	86.62 1.31	0.13 0.13	1.82 0.23	1.67 0.34	0.85 0.16	8.76 0.72	0.00 0.00	0.01 0.01	0.01 0.01	0.13 0.03	0.01 0.01			
	C vs. P	0.009	ns	0.030	ns	ns	0.011	ns	ns	ns	ns	ns			
p-value	C vs. PSP	0.002	ns	0.007	0.022	ns	0.002	ns	ns	ns	ns	ns			
	P vs. PSP	ns	ns	ns	ns	ns	ns	ns	ns	ns	ns	ns			
	С	67.17 0.80	1.54 0.12	4.37 0.37	4.26 0.42	1.22 0.10	21.38 1.22	0.01 0.01	0.04 0.02	0.00 0.00	0.00 0.00	0.01 3E-3			
ADP	Р	79.18 2.27	1.59 0.12	2.76 0.42	2.42 0.45	0.83 0.18	13.20 1.29	0.02 3E- 03	3E-3 3E-3	0.00 0.00	0.00 0.00	0.01 0.01			
	PSP	83.14 1.40	1.68 0.17	2.11 0.18	1.89 0.18	0.87 0.19	10.23 0.72	0.03 0.01	0.01 0.01	0.04 0.01	0.00 0.00	3E-03 3E-3			
p-value	C vs. P	0.008	ns	0.044	0.041	ns	0.010	ns	ns	ns	ns	ns			

	C vs. PSP	0.001	ns	0.005	0.007	ns	0.001	ns	ns	0.038	ns	ns					
	P vs. PSP	ns	ns	ns	ns	ns	ns	ns	ns	ns	ns	ns					
	С	67.13 0.89	1.06 0.10	5.61 0.31	4.02 0.32	1.36 0.10	20.42 1.22	0.00 0.00	0.35 0.02	0.01 0.01	0.01 0.00	0.01 3E-3					
ATP	Р	78.53 2.29	1.13 0.18	4.13 0.41	2.34 0.38	0.99 0.16	12.63 1.23	0.00 0.00	0.22 0.01	0.01 0.00	0.01 3E- 03	0.01 3E-3					
	PSP	82.13 0.65	1.15 0.31	3.67 0.20	1.80 0.21	0.92 0.14	9.77 0.44	0.12 0.02	0.23 0.04	0.02 0.00	0.03 0.01	0.14 0.03					
	C vs. P	0.010	ns	0.044	0.028	ns	0.011	ns	0.008	ns	ns	ns					
p-value	C vs. PSP	2E-04	ns	0.006	0.004	ns	0.001	ns	0.042	ns	0.026	0.019					
	P vs. PSP	ns	ns	ns	ns	ns	ns	ns	ns	ns	0.025	0.019					
	С	71.57 0.78	0.61 0.50	4.25 0.39	2.01 0.18	0.64 0.14	11.13 1.08	0.27 0.25	1.19 0.05	0.72 0.22	0.39 0.20	0.92 0.57	0.42 0.17	0.33 0.30	3.96 0.80	0.56 0.17	1.03 0.44
ADP-rib	Р	66.50 3.01	2.03 0.71	2.37 0.71	3.52 1.01	0.32 0.28	8.05 1.35	0.59 0.35	1.55 0.29	0.57 0.03	0.71 0.37	0.54 0.27	0.92 0.18	0.00 0.00	6.93 0.48	2.43 1.15	2.97 1.74
	PSP	38.64 7.63	3.59 1.82	1.78 1.52	3.14 0.67	0.56 0.20	7.81 2.04	0.32 0.03	2.15 0.64	0.74 0.06	0.99 0.23	0.50 0.18	1.43 0.56	0.09 0.09	8.50 1.03	0.45 0.45	29.32 9.52
	C vs. P	ns	ns	ns	ns	ns	ns	ns	ns	ns	ns	ns	ns	ns	0.033	ns	0.041
p-value	C vs. PSP	0.013	ns	ns	ns	ns	ns	ns	ns	ns	ns	ns	ns	ns	0.025	ns	ns
	P vs. PSP	0.027	ns	ns	ns	ns	ns	ns	ns	ns	ns	ns	ns	ns	ns	ns	ns
	С	64.10 3.63	0.52 0.28	4.72 0.50	3.98 0.42	3.80 1.27	20.11 1.78	0.02 0.02	1.69 0.80	0.17 0.15	0.29 0.13	0.59 0.36					
GMP	Р	81.28 1.20	0.03 0.03	2.85 0.30	2.17 0.37	1.38 0.18	10.77 0.57	0.20 0.10	0.52 0.16	0.24 0.06	0.47 0.30	0.09 0.07					
	PSP	82.96 0.86	0.65 0.65	2.09 0.42	1.92 0.25	1.12 0.25	9.54 0.55	0.94 0.34	0.33 0.14	0.00 0.00	0.34 0.10	0.12 0.06					
	C vs. P	0.011	ns	0.033	0.032	ns	0.008	ns	ns	ns	ns	ns					
p-value	C vs. PSP	0.007	ns	0.016	0.014	ns	0.005	ns	ns	ns	ns	ns					
	P vs. PSP	ns	ns	ns	ns	ns	ns	ns	ns	ns	ns	ns					
	С	69.10 1.21	0.00 0.00	3.99 0.20	4.36 0.49	1.23 0.12	20.82 1.46	0.08 0.08	0.13 0.07	0.04 0.02	0.00 0.00	0.23 0.05					
GDP	Р	80.90 1.20	0.07 0.07	2.36 0.33	2.22 0.26	0.94 0.14	12.87 0.45	0.01 0.01	0.04 0.04	0.03 0.02	3E-3 3E-3	0.55 0.11					
	PSP	81.45 1.59	0.26 0.26	2.16 0.19	1.75 0.18	0.71 0.08	9.76 0.91	0.18 0.08	0.02 0.02	0.01 0.01	0.00 0.00	3.69 1.87					
	C vs. P	0.002	ns	0.013	0.018	ns	0.006	ns	ns	ns	ns	ns					
p-value	C vs. PSP	0.004	ns	0.003	0.007	0.022	0.003	ns	ns	ns	ns	ns					
	P vs. PSP	ns	ns	ns	ns	ns	0.038	ns	ns	ns	ns	ns					
GTP	С	65.96 0.88	0.19 0.06	5.85 0.15	3.97 0.44	1.50 0.15	21.15 1.37	0.44 0.13	0.67 0.06	0.10 0.07	0.06 0.01	0.12 0.05					
GIF	Р	77.84 1.36	0.45 0.16	5.15 0.05	2.07 0.44	0.87 0.13	12.20 1.10	0.48 0.13	0.50 0.05	0.12 0.03	0.09 0.03	0.23 0.11					

	PSP	76.92 2.54	1.35 0.34	4.03 0.10	2.09 0.42	1.75 0.08	8.62 0.82	1.27 0.49	1.08 0.26	1.08 0.18	0.38 0.14	1.42 0.53			
	C vs. P	0.002	ns	0.012	0.037	0.035	0.007	ns	ns	ns	ns	ns			
p-value	C vs. PSP	0.015	0.027	0.001	0.036	ns	0.001	ns	ns	0.007	ns	ns			
	P vs. PSP	0.024	ns	0.001	ns	0.005	ns	ns	ns	0.006	ns	ns			
	С	93.44 0.13	0.00 0.00	0.65 0.10	0.85 0.14	0.28 0.11	3.54 0.35	0.36 0.07	0.54 0.07	0.24 0.05	0.10 0.05				
UDP	Р	95.09 0.73	0.00 0.00	0.46 0.13	0.53 0.21	0.29 0.07	2.66 0.22	0.24 0.05	0.31 0.04	0.28 0.07	0.14 0.06				
	PSP	91.39 0.94	0.00 0.00	0.83 0.07	0.94 0.15	0.26 0.10	4.97 0.61	0.19 0.05	0.73 0.03	0.23 0.02	0.46 0.10				
	C vs. P	ns	ns	ns	ns	ns	ns	ns	0.044	ns	ns				
p-value	C vs. PSP	ns	ns	ns	ns	ns	ns	ns	ns	ns	0.033				
	P vs. PSP	0.036	ns	ns	ns	ns	0.023	ns	0.002	ns	ns				
	С	93.51 0.20	0.00 0.00	0.95 0.07	0.89 0.08	0.23 0.08	3.34 0.10	0.27 0.10	0.31 0.10	0.40 0.09	0.11 0.04				
UMP	Р	95.72 0.75	0.00 0.00	0.42 0.10	0.46 0.10	0.33 0.10	2.38 0.37	0.22 0.05	0.30 0.05	0.14 0.03	0.03 0.01				
	PSP	91.21 2.09	0.36 0.34	1.03 0.12	0.82 0.43	0.33 0.08	4.45 0.66	0.33 0.16	0.91 0.32	0.25 0.12	0.31 0.22				
	C vs. P	0.047	ns	0.013	0.030	ns	ns	ns	ns	0.049	ns				
p-value	C vs. PSP	ns	ns	ns	ns	ns	ns	ns	ns	ns	ns				
	P vs. PSP	ns	ns	0.019	ns										
	С	95.12 1.52	0.00 0.00	2.58 0.93	0.55 0.32	0.19 0.06	0.62 0.27	0.00 0.00	0.73 0.08	0.07 0.02	0.13 0.04				
СТР	Р	87.44 2.04	0.00 0.00	10.50 2.18	0.21 0.11	0.07 0.04	0.36 0.12	0.05 0.03	1.02 0.41	0.21 0.06	0.15 0.03				
	PSP	58.36 2.51	0.00 0.00	36.11 1.80	0.55 0.55	0.22 0.22	0.50 0.07	0.45 0.30	3.08 0.44	0.47 0.25	0.26 0.02				
	C vs. P	0.040	ns	0.029	ns										
p-value	C vs. PSP	2E-04	ns	8E-05	ns	ns	ns	ns	0.006	ns	ns				
	P vs. PSP	0.001	ns	0.001	ns	ns	ns	ns	0.027	ns	0.039			11 . 11	

Mean and SEM of the mass isotopomer distribution of ¹³C-labeled metabolites of untreated TNBC cells (C = control) and cells treated with palbociclib (P) and StPGA-SS-palbociclib (PSP) and incubated with ¹³C-glucose for 120 min, and p-values of the comparison (each treatment over the control and of StPGA-SS-palbociclib over free palbociclib). Data analysis used a T-test (n = 3).

Supporting Information 3.14. ¹³C-glutamineMS fluxomics analysis

		M-	+0	M	+1	M+	2	M	+3	M	+4	M	+5	M-	+6	M	-7	M+	-8	M-	-9	M+:	10
		Mean	SEM	Mean	SEM	Mean	SEM	Mean	SEM	Mean	SEM	Mean	SEM	Mean	SEM	Mean	SEM	Mean	SEM	Mean	SEM	Mean	SEM
	С	28.87	1.91	2.77	0.17	3.02	0.20	13.13	0.15	0.00	0.00	52.20	2.32										
Glutamate	Р	56.47	0.95	2.94	0.14	2.88	0.06	9.41	0.20	0.01	0.01	28.29	0.67										
	PSP	46.30	1.02	3.14	0.14	3.37	0.17	11.37	0.09	0.00	0.00	35.81	1.10										
	C vs. P	2E-	04	n	s	ns		1E-	04	n	S	0.0	01										
p-value	C vs. PSP	1E-	03	n	s	ns		0.0	01	n	S	0.0	03										
	P vs. PSP	0.0	02	n:	s	0.04	19	0.0	01	n	s	0.0	04										
	С	33.35	4.23	2.59	0.14	3.16	0.18	11.87	0.18	0.000	0.000	49.030	4.378										
α-KG	Р	58.14	0.95	2.44	0.12	2.90	0.10	8.93	0.17	0.000	0.000	27.583	0.663										
	PSP	47.82	0.48	2.87	0.10	3.51	0.18	10.92	0.27	0.000	0.000	34.877	0.762										
	C vs. P	0.0	05	n	s	ns		3E-	04	n	S	0.0	80										
p-value	C vs. PSP	0.0	27	n	s	ns	;	0.0	43	n	S	0.0	33										
	P vs. PSP	0.0	01	n:	s	0.04	11	0.0	03	n	s	0.0	02										
	С	35.78	3.12	3.96	0.12	13.30	0.42	0.02	0.02	46.95	3.00												
Succinate	Р	62.67	1.74	3.50	0.28	9.19	0.46	0.02	0.02	24.62	1.03												
	PSP	52.34	1.41	4.22	0.24	11.48	0.53	0.09	0.05	31.86	0.95												
	C vs. P	0.0	02	n	s	0.00	03	n	S	0.0	02												
p-value	C vs. PSP	0.0	80	n	s	ns		n	S	0.0	09												
	P vs. PSP	0.0	10	n	s	0.03	31	n	S	0.0	07												
	С	43.02	2.14	3.87	0.20	10.84	0.33	5.99	0.05	36.27	2.49												
Fumarate	Р	71.24	0.42	3.13	0.14	6.99	0.05	2.97	0.11	15.66	0.50												
	PSP	62.18	0.61	3.38	0.29	8.68	0.09	3.47	0.26	22.29	0.60												
p-value	C vs. P	2E-	05	0.0	39	3E-0	04	2E-	05	0.0	01												
p-value	C vs. PSP	0.0	01	n	S	0.00	03	0.0	01	0.0	05								ļ				

	P vs. PSP	3E-04	ns	9E-05	ns	0.001				
	С	43.30 2.32	3.39 0.06	10.51 0.21	6.18 0.09	36.62 2.25				
Malate	Р	70.97 0.41	2.79 0.04	6.71 0.08	2.92 0.09	16.61 0.40				
	PSP	62.27 0.73	3.32 0.07	8.40 0.08	3.46 0.13	22.55 0.64				
	C vs. P	3E-04	0.001	7E-05	1E-05	0.001				
p-value	C vs. PSP	0.001	ns	0.001	7E-05	0.004				
	P vs. PSP	5E-04	0.003	1E-04	0.028	0.001				
	С	49.88 2.19	3.35 0.11	8.19 0.18	6.04 0.06	25.71 1.87	6.53 0.24	0.300 0.052		
Citrate	Р	73.57 0.63	2.54 0.08	5.17 0.15	3.34 0.01	11.51 0.38	3.80 0.08	0.070 0.010		
	PSP	65.61 0.74	3.20 0.06	6.87 0.09	3.90 0.12	16.38 0.41	3.86 0.16	0.177 0.012		
	C vs. P	0.001	0.004	2E-04	2E-06	0.002	5E-04	0.012		
p-value	C vs. PSP	0.002	ns	0.003	1E-04	0.008	0.001	ns		
	P vs. PSP	0.001	0.003	0.001	0.011	0.001	ns	0.002		
	С	49.73 2.14	3.51 0.15	8.32 0.18	6.59 0.12	24.64 1.82	6.86 0.36	0.35 0.05		
Aconitate	Р	73.19 0.50	2.96 0.10	5.40 0.21	3.53 0.08	10.91 0.16	3.92 0.07	0.09 0.01		
	PSP	65.39 0.91	3.27 0.04	6.94 0.18	4.41 0.14	15.67 0.49	4.13 0.17	0.20 0.05		
	C vs. P	4E-04	0.039	4E-04	3E-05	0.002	0.001	0.007		
p-value	C vs. PSP	0.003	ns	0.005	3E-04	0.009	0.002	ns		
	P vs. PSP	0.002	0.043	0.005	0.005	0.001	ns	ns		
	С	42.26 2.79	3.54 0.25	10.62 0.06	6.21 0.06	37.37 2.90				
Aspartate	Р	71.75 0.55	2.68 0.21	6.83 0.54	3.13 0.05	15.62 0.49				
	PSP	62.10 1.37	3.20 0.09	8.57 0.33	4.02 0.33	22.10 0.80				
	C vs. P	0.001	ns	0.003	3E-06	0.002				
p-value	C vs. PSP	0.003	ns	0.004	0.003	0.007				
	P vs. PSP	0.003	ns	ns	ns	0.002				
	С	87.46 2.36	0.60 0.08	9.35 1.90	2.58 0.78					
Pyruvate	Р	95.11 0.67	0.55 0.18	3.17 1.05	1.16 0.24					
	PSP	89.21 1.48	0.66 0.31	8.04 2.03	2.09 0.33					

	C vs. P	0.0)35	n	ıs	0.0	46	n	S														
p-value	C vs. PSP	r	ıs	n	S	n	S	n	S														
	P vs. PSP	0.0)22	n	S	n	S	n	S														
	С	98.24	0.19	1.00	0.28	0.06	0.04	0.07	0.04	0.04	0.00	0.03	0.02	0.24	0.08	0.22	0.08	0.04	0.01	0.02	0.01	0.05	0.01
Guanosine	Р	95.74	0.58	3.23	0.40	0.40	0.14	0.16	0.03	0.05	0.04	0.01	0.01	0.19	0.06	0.12	0.03	0.03	0.01	0.02	0.00	0.03	0.01
	PSP	96.47	1.70	2.90	1.67	0.04	0.03	0.10	0.02	0.07	0.03	0.03	0.02	0.10	0.01	0.21	0.03	0.03	0.02	0.02	0.02	0.04	0.00
	C vs. P	0.0)15	0.0	10	n	s	n	S	n	S	n	S	n	S	n	s	n	S	n	s	n	s
p-value	C vs. PSP	r	ıs	n	S	n	s	n	s	n	S	n	S	n	s	n	s	n	s	n	s	n	s
	P vs. PSP	r	ıs	n	S	n	S	n	S	n	S	n	S	n	S	n	S	n	S	n	S	n	S

Mean and SEM of the mass isotopomer distribution of ¹³C-labeled metabolites of untreated TNBC cells (C = control) and cells treated with palbociclib (P) and StPGA-SS-palbociclib (PSP) and incubated with ¹³C-glutamine for 180 min, and p-values of the comparison (each treatment over the control and of StPGA-SS-palbociclib over free palbociclib). Data analysis used a T-test (n = 3).

CHAPTER IV

Supporting Information 4.1. NMR signal assignment of the whole-cell and mitochondrial fractions obtained from breast tumors

W	/hole-cell		Mit	ochondria	
Metabolite	Right limit (ppm)	Left limit (ppm)	Metabolite	Right limit (ppm)	Left limit (ppm)
Isoleucine	0.926	0.947	Isoleucine	0.9262	0.9501
Isoleucine + leucine	0.948	0.960	Isoleucine + leucine	0.9502	0.9598
Leucine	0.960	0.981	Leucine	0.9599	0.9809
Valine	0.982	1.004	Valine	0.9821	1.0038
Isoleucine	1.004	1.023	Isoleucine	1.0039	1.0233
Valine	1.033	1.057	Valine	1.0347	1.0552
Isoleucine	1.260	1.295			
Lactate	1.317	1.348	Lactate	1.3178	1.3428
Lysine	1.453	1.466			
Alanine	1.468	1.496	Alanine	1.4677	1.4958
Lysine	1.496	1.553	Lysine	1.6989	1.7586
Arginine	1.628	1.660	Arginine	1.6281	1.6602
Leucine	1.662	1.699	Leucine	1.6616	1.6991
Lysine	1.852	1.914	Lysine	1.8865	1.9138
Acetate	1.914	1.925	Acetate	1.9139	1.925
Lysine + arginine	1.925	1.968	Lysine + arginine	1.9251	1.9678
Glutamate (ov*)	2.022	2.091	Glutamate (ov)	2.0217	2.091
Glutamine+glutamate	2.098	2.137	Glutamine + glutamate	2.0982	2.137
Methionine	2.137	2.144	Methionine	2.1374	2.1438
Glutathione (ov)	2.169	2.192	Glutathione (ov)	2.1693	2.1916
Glutamate	2.311	2.389	Glutamate	2.3385	2.3797
Glutamate	2.396	2.403			
Succinate	2.403	2.410	Succinate	2.4026	2.4098
Glutamine	2.416	2.480	Glutamine	2.4159	2.4799
Glutathione	2.525	2.530	Glutathione	2.5251	2.53
Citrate	2.531	2.539	Citrate	2.5311	2.5386
Glutathione	2.539	2.554			
Citrate	2.555	2.561			
Glutathione	2.564	2.603			
Methionine	2.631	2.651	Methionine	2.6284	2.6323
Aspartate	2.694	2.699	Aspartate	2.694	2.6994
Dimethylamine	2.723	2.730	Dimethylamine	2.7326	2.7398
Aspartate	2.804	2.813	Aspartate	2.8042	2.8127
Asparagine	2.824	2.829	Asparagine	2.8478	2.8692
Asparagine	2.847	2.876			
Lysine	3.014	3.035	Lysine	3.0142	3.035
Creatine	3.035	3.042	Creatine	3.0356	3.0456
Phosphocreatine	3.042	3.046			
Choline	3.199	3.212	Choline	3.199	3.2095
Phosphocholine	3.219	3.228	Phosphocholine	3.2183	3.2279

I		1			ı
GPC*	3.230	3.237	GPC*	3.2276	3.2364
Taurine	3.242	3.276	Taurine	3.2419	3.2759
Myo-inositol	3.279	3.301	Myo-inositol	3.279	3.3011
Taurine	3.402	3.442	Taurine	3.4071	3.4125
Glucose (ov)	3.446	3.511	Glucose (ov)	3.413	3.4483
Choline (ov)	3.511	3.537	Lactate	4.0872	4.1236
Myo-inositol (ov)	3.540	3.554			
Phosphocholine	3.585	3.606	Phosphocholine	4.1856	4.1927
Myo-inositol (ov)	3.610	3.619			
Myo-inositol	3.624	3.632			
Creatine	3.927	3.938			
Phosphocreatine	3.948	3.956			
Lactate	4.092	4.140			
Phosphocholine	4.155	4.190			
Threonine	4.249	4.261			
Threonine	4.261	4.271			
GPC*	4.319	4.342			
UDP-der*	4.342	4.370			
Ascorbate	4.508	4.521	Ascorbate	4.5097	4.5182
Glucose ov	4.639	4.646	Glucose (ov)	4.6385	4.6579
Ribose	4.920	4.946			
Glucose	5.238	5.246	Glucose	5.2244	5.2474
UDP-der*	5.610	5.638	UDP-der*	5.6112	5.6353
Uracil	5.793	5.824	Uracil	5.7963	5.8156
Uridine	5.891	5.926	Uridine	5.8912	5.9262
UDP-der*	5.982	6.011			
Fumarate	6.512	6.531	Fumarate	6.5173	6.5231
Tyrosine	6.886	6.917	Tyrosine	6.8921	6.9122
Histidine	7.041	7.088			
Tyrosine	7.181	7.213	Tyrosine	7.1875	7.213
Tryptophan	7.213	7.222	Tryptophan	7.3035	7.31684
Tryptophan	7.270	7.314	Phenylalanine + Tryptophan	7.3169	7.3329
Phenylalanine	7.317	7.349	Phenylalanine	7.3346	7.3447
Phenylalanine	7.360	7.400	Phenylalanine	7.3634	7.396
Phenylalanine	7.412	7.452	Phenylalanine	7.4151	7.4492
Uracil	7.526	7.535	Uracil	7.5279	7.5463
Tryptophan	7.536	7.541			
Uracil	7.541	7.549			
Tryptophan	7.549	7.557			
Niacinamide	7.584	7.616			
Tryptophan	7.727	7.753			
Histidine	7.761	7.803			
Uridine	7.860	7.868	Uridine	7.8612	7.8674
Inosine	8.228	8.240			
Niacinamide	8.240	8.268			
Adenosine	8.334	8.349			
Nucleotides	8.354	8.368			
•		i,			!

Nucleotides	8.376	8.392			
Formate	8.451	8.467	Formate	8.4554	8.4639
Niacinamide	8.698	8.733			
Niacinamide	8.930	8.956			

^{*}GPC = glycerophosphocholine; ov = overlapping; UDP-der = uridine diphosphate derivative

Supporting Information 4.2. NMR signal assignment of the whole-cell and mitochondrial fractions obtained from liver.

,	Whole-cell		M	itochondria	
Metabolite	Right limit (ppm)	Left limit (ppm)	Metabolite	Right limit (ppm)	Left limit (ppm)
Isoleucine	0.926	0.947	Isoleucine	0.926	0.947
Isoleucine + leucine	0.948	0.960	Isoleucine + leucine	0.948	0.960
Leucine	0.960	0.981	Leucine	0.960	0.981
Valine	0.982	1.004	Valine	0.982	1.004
Isoleucine	1.004	1.023	Isoleucine	1.004	1.023
Valine	1.033	1.057	Valine	1.033	1.057
Isoleucine	1.260	1.295			
Lactate	1.317	1.348	Lactate	1.320	1.342
			Lysine	1.403	1.452
Alanine	1.482	1.496	Alanine	1.483	1.494
Lysine	1.496	1.553	Lysine	1.496	1.553
Arginine	1.590	1.661			
Leucine	1.662	1.699	Leucine	1.660	1.700
			Leucine	1.759	1.777
			Ornithine	1.792	1.872
Lysine	1.852	1.914	Lysine	1.873	1.915
Acetate	1.914	1.925	Acetate	1.915	1.924
Glutamate (ov*)	2.022	2.091	Glutamate (ov)	2.022	2.079
Glutamine + glutamate	2.098	2.137	Glutamine + glutamate	2.100	2.137
Methionine	2.137	2.144	Methionine	2.136	2.150
Glutathione (ov)	2.144	2.155	Glutathione (ov)	2.151	2.192
Glutathione	2.156	2.193			
Methionine	2.195	2.244	Methionine	2.193	2.238
Glutamate	2.311	2.389	Glutamate	2.338	2.377
Succinate	2.403	2.410	Succinate	2.404	2.408
Glutamine	2.416	2.480	Glutamine	2.434	2.479
Glutathione	2.515	2.609	Glutathione	2.543	2.582
Methionine	2.631	2.651	Methionine	2.631	2.666
Aspartate	2.694	2.699			
Dimethylamine	2.723	2.730	Dimethylamine	2.735	2.741
Aspartate	2.804	2.813			
Asparagine (ov)	2.829	2.852	Asparagine (ov)	2.822	2.834
Asparagine	2.856	2.885	Asparagine	2.835	2.871
Glutathione	2.913	2.985			
			Asparagine	2.927	2.981
Lysine	3.014	3.035	Lysine	3.013	3.043

Creatine	3.037	3.042	Creatine	3.043	3.047
Creatine	3.037	3.042	Ornithine	3.054	3.047
			Phenyalanine	3.101	3.150
Phosphocreatine	3.043	3.049	Therryalarine	5.101	3.130
Choline	3.199	3.212	Choline	3.200	3.207
Phosphocholine	3.219	3.226	Phosphocholine	3.219	3.226
GPC*	3.213	3.237	GPC*	3.226	3.235
Glucose (ov)	3.237	3.266	Glucose (ov)	3.243	3.263
Taurine (ov)	3.244	3.265	Giucose (ov)	3.243	3.203
Maltose (ov)	3.244	3.203	Maltose (ov)	3.264	3.273
Taurine	3.272	3.271	iviaitose (ov)	3.204	3.273
Maltose	3.272	3.301	Maltose	3.276	3.300
Glucose	3.385	3.395	Glucose + maltose	3.386	3.449
Glucose	3.451	3.515	Glucose + maitose	5.300	3.449
Glucose	3.522	3.546			
Glucose	3.884	3.899			
Choline					
	4.054	4.085	Lastata	4.007	4 121
Lactate	4.092	4.140	Lactate	4.087	4.121
Phosphocholine	4.155	4.190			
Threonine	4.254	4.264			
Threonine	4.264	4.276			
GPC*	4.319	4.342			
UDP-der*	4.342	4.370			
Ascorbate	4.503	4.523			
Glutathione	4.561	4.598		4.620	
Glucose	4.639	4.650	Glucose	4.638	4.644
Maltose	4.664	4.673	Glucose + maltose	4.650	4.657
Ribose	4.920	4.946	Maltose	4.662	4.671
Maltose	5.408	5.421	Glucose	5.227	5.244
UDP-NAG*	5.443	5.472			
UDP-der*	5.609	5.621	UDP-der*	5.610	5.637
Uracil	5.793	5.824	Uracil	5.796	5.816
Uridine	5.891	5.926	Uridine	5.893	5.926
UDP-der	5.973	6.016			
Inosine	6.087	6.113	Inosine	6.092	6.118
Nucleotides	6.113	6.130			
Nucleotides	6.131	6.144			
Nucleotides	6.144	6.187			
Fumarate	6.512	6.531	Fumarate	6.518	6.523
Tyrosine	6.886	6.917	Tyrosine	6.891	6.912
Histidine	7.062	7.095	Histidine	7.052	7.063
Tyrosine	7.181	7.213	Tyrosine	7.187	7.209
Tryptophan	7.213	7.222			
Tryptophan	7.270	7.314	Tryptophan	7.282	7.324
Phenylalanine	7.317	7.349	Phenylalanine	7.324	7.345
Phenylalanine	7.360	7.400	Phenylalanine	7.363	7.397
Phenylalanine	7.412	7.452	Phenylalanine	7.415	7.451
Uracil	7.526	7.535	Uracil	7.533	7.555

Tryptophan	7.536	7.541			
Uracil	7.541	7.549			
Tryptophan	7.549	7.557			
Niacinamide	7.584	7.616	Niacinamide	7.586	7.615
Tryptophan	7.727	7.753	Tryptophan	7.729	7.755
			Histidine	7.770	7.788
Uridine	7.862	7.870	Uridine	7.861	7.871
Uridine (ov)	7.876	7.884	Uridine (ov)	7.871	7.875
			Uridine	7.873	7.884
Inosine + IMP*	8.231	8.240	Inosine + IMP*	8.229	8.239
Niacinamide	8.240	8.268	Niacinamide	8.238	8.265
AMP*	8.266	8.277			
Inosine	8.337	8.353	Inosine	8.338	8.349
Nucleotides	8.358	8.376			
Nucleotides	8.376	8.396	Adenosine	8.379	8.389
Formate	8.451	8.467	Formate	8.455	8.463
			IMP*	8.554	8.570
AMP*	8.589	8.620	AMP*	8.586	8.597
Niacinamide	8.698	8.733	Niacinamide	8.708	8.728
Niacinamide	8.930	8.956	Niacinamide	8.931	8.955

^{*}AMP = adenosine monophosphate; IMP = inosine monophosphate; ov = overlapping; UDP-der = uridine diphosphate derivative

Supporting Information 4.3. NMR signal assignment of the mitochondrial fractions obtained from lungs.

\	Whole-cell		M	itochondria	
Metabolite	Right limit (ppm)	Left limit (ppm)	Metabolite	Right limit (ppm)	Left limit (ppm)
Isoleucine	0.926	0.933	Isoleucine	0.926	0.934
Isoleucine	0.939	0.947	Isoleucine	0.940	0.946
Isoleucine + leucine	0.948	0.960	Isoleucine + leucine	0.951	0.959
Leucine	0.960	0.981	Leucine	0.960	0.981
Valine	0.982	1.004	Valine	0.982	1.004
Isoleucine	1.004	1.023	Isoleucine	1.005	1.024
Valine	1.033	1.057	Valine	1.035	1.055
Isoleucine	1.260	1.295			
Lactate	1.317	1.348	Lactate	1.317	1.342
Lysine	1.453	1.466			
Alanine	1.468	1.496	Alanine	1.475	1.492
Lysine	1.496	1.553			
Arginine	1.628	1.660			
Leucine	1.662	1.699			
Lysine	1.873	1.914	Lysine	1.852	1.913
Acetate	1.914	1.925	Acetate	1.913	1.924
Glutamate (ov*)	2.022	2.091	Glutamate (ov)	2.045	2.091
Glutamine+glutamate	2.098	2.137	Glutamine + glutamate	2.101	2.138
Methionine	2.137	2.144	Methionine	2.137	2.144
			Glutathione	2.156	2.191

			Acetone	2.232	2.238
Glutamate	2.311	2.389	Glutamate (ov)	2.339	2.352
Glutamate	2.396	2.403	Glutamate	2.352	2.370
			Glutamate (ov)	2.370	2.376
Succinate	2.403	2.410	Succinate	2.402	2.409
Glutamine (ov)	2.416	2.479	Glutamine (ov)	2.416	2.479
Glutathione	2.519	2.530	Glutathione	2.518	2.533
Citrate	2.531	2.539	Citrate	2.533	2.539
Glutathione	2.539	2.554	Sitt at 2	2.555	2.555
Citrate	2.555	2.561	Citrate	2.559	2.564
Glutathione	2.564	2.603	Citrate	2.555	2.504
Methionine	2.639	2.651			
Aspartate	2.694	2.699			
Dimethylamine	2.723	2.731	Dimethylamine	2.734	2.740
•	2.723	2.731	Dimetriylarilile	2.734	2.740
Aspartate					
Asparagine	2.840	2.871			
Asparagine 	2.924	2.944		2.042	2 222
Lysine	3.014	3.035	Lysine	3.012	3.033
Creatine	3.035	3.043	Creatine	3.036	3.046
Phosphocreatine	3.043	3.050			
Choline	3.199	3.212	Choline	3.200	3.210
Phosphocholine	3.212	3.218	Phosphocholine	3.219	3.227
GPC*	3.228	3.237	Glucose	3.227	3.235
Taurine	3.242	3.276	Glucose	3.243	3.252
Myo-inositol	3.279	3.301	Glucose	3.256	3.264
Taurine	3.402	3.442			
Phosphocholine	3.585	3.606			
Creatine	3.927	3.938			
Phosphocreatine	3.948	3.954			
Lactate	4.092	4.140	Lactate	4.087	4.121
Threonine	4.226	4.278			
GPC*	4.319	4.342			
UDP-der*	4.342	4.370			
Ascorbate	4.508	4.521	Ascorbate	4.508	4.515
			Glucose	4.636	4.660
Glucose	5.238	5.246	Glucose	5.225	5.243
UDP-NAG*	5.442	5.467			
UDP-der*	5.610	5.638	UDP-der*	5.612	5.637
UDP-der*	5.645	5.672			
Uracil	5.793	5.824			
UDP-der*	5.982	6.011			
Fumarate	6.512	6.531	Fumarate	6.518	6.523
Tyrosine	6.886	6.917	Tyrosine	6.892	6.913
Histidine	7.041	7.069			
Tyrosine	7.181	7.213	Tyrosine	7.188	7.208
,	7.101				
Tryptophan	7.213	7.222			
•		7.222 7.314	Tryptophan	7.271	7.295

Phenylalanine	7.360	7.400			
Phenylalanine	7.412	7.452	Phenylalanine	7.415	7.451
Uracil	7.526	7.535			
Tryptophan	7.536	7.541			
Uracil	7.541	7.549			
Tryptophan	7.549	7.557			
Niacinamide	7.584	7.616	Niacinamide	7.583	7.614
Tryptophan	7.727	7.753			
Inosine	8.228	8.240	Inosine	8.334	8.345
Niacinamide	8.240	8.268			
Adenosine	8.334	8.349			
Nucleotides	8.354	8.368			
Nucleotides	8.376	8.392			
Formate	8.451	8.467	Formate	8.455	8.464
Inosine	8.574	8.588			
Niacinamide	8.698	8.733	Niacinamide	8.707	8.726
Niacinamide	8.930	8.956	Niacinamide	8.937	8.948

^{*}GPC = glycerophosphocholine; ov = overlapping; UDP-der = uridine diphosphate derivative; UDP-NAG = uridine diphosphate N-acetylglucosamine

Supporting Information 4.4. NMR signal assignment of the mitochondrial fractions obtained from kidneys

V	Whole-cell			Mitochondria				
Metabolite	Right limit (ppm)	Left limit (ppm)	Metabolite	Right limit (ppm)	Left limit (ppm)			
Isoleucine	0.9262	0.9338	Isoleucine	0.9262	0.9338			
Isoleucine + leucine	0.9478	0.9598	Isoleucine + leucine	0.9478	0.9598			
Leucine	0.9599	0.9809	Leucine	0.9599	0.9809			
Valine	0.9821	1.0038	Valine	0.9821	1.0038			
Isoleucine	1.0039	1.0233	Isoleucine	1.0039	1.0233			
Valine	1.0325	1.0571	Valine	1.0325	1.0571			
Isoleucine	1.2598	1.2945						
Lactate	1.3173	1.3484	Lactate	1.3196	1.3415			
Lysine	1.4529	1.466						
Alanine	1.4677	1.4958	Alanine	1.4652	1.4952			
Lysine	1.496	1.5533	Lysine	1.4953	1.5433			
Arginine	1.6281	1.6602	Arginine + Leucine	1.6284	1.6992			
Leucine	1.6616	1.6991	•					
Lysine	1.8515	1.9138	Lysine + arginine	1.8673	1.9134			
Acetate	1.9139	1.925	Acetate	1.9150	1.9234			
Lysine + arginine	1.9251	1.9678	Lysine + arginine	1.9235	1.9667			
Glutamate (ov*)	2.0217	2.091	Glutamate (ov)	2.0224	2.0916			
Glutamine+glutamate	2.0982	2.137	Glutamine + glutamate	2.0906	2.1368			
Methionine	2.1374	2.1438	Methionine	2.1369	2.144			
Glutathione (ov)	2.229	2.584	Glutathione (ov)	2.169	2.1916			
			Valine	2.2424	2.3036			
Glutamate	2.3112	2.4025	Glutamate	2.3232	2.3768			
Succinate	2.4026	2.4098	Succinate	2.403	2.4081			
Glutamine (ov)	2.4159	2.4714	Glutamine (ov)	2.4234	2.4771			

I			1		
Glutamine	2.4715	2.4792			
Citrate	2.553	2.5589			
Glutathione	2.5845	2.6026			
Methionine	2.6308	2.6506	Methionine	2.6287	2.6537
Aspartate + methionine	2.6511	2.6935	Aspartate + methionine	2.6553	2.6964
Aspartate	2.694	2.6994			
Dimethylamine	2.7229	2.7304	Dimethylamine	2.7218	2.7278
Aspartate	2.8055	2.8139	Aspartate	2.8055	2.8102
Aspartate + asparagine	2.8227	2.8347	Aspartate + asparagine	2.8202	2.8341
Aspartate	2.8349	2.84			
Asparagine	2.8401	2.4875	Asparagine	2.8337	2.8695
Asparagine	2.8508	2.8758	Asparagine	2.9294	2.9442
Asparagine	2.9329	2.9753	Asparagine	2.958	2.9724
Lysine	3.0142	3.035	Lysine	3.0113	3.0342
Creatine	3.0351	3.0434	Creatine	3.0354	3.0471
Phosphocreatine	3.0441	3.0495			
Choline	3.199	3.2116	Choline	3.1997	3.2084
Phosphocholine	3.219	3.2279	Phosphocholine	3.2181	3.2269
GPC*	3.228	3.2335	GPC*	3.227	3.2335
Taurine (ov)	3.2419	3.2759	Taurine	3.2432	3.263
			Betaine	3.2642	3.272
Myo-inositol	3.279	3.3011	Myo-inositol	3.2758	3.2978
Taurine	3.4023	3.4415	Glucose (ov)	3.4077	3.4494
Phosphocholine	3.5849	3.6062			
Myo-inositol	3.6242	3.6315			
Betaine	3.8976	3.908			
Creatine	3.9274	3.9381			
Phosphocreatine	3.9486	3.9553			
Lactate	4	4.1395	Lactate	4.0871	4.11
Phosphocholine	4.1545	4.1895			
Threonine	4.2492	4.2607	Threonine	4.2488	4.2662
Threonine	4.2608	42,706			
GPC*	4.3194	4.3416			
UDP-der*	4.3417	4.3704			
Ascorbate	4.5084	4.5214			
Ribose	4.9204	4.9464	Ribose	4.9238	4.9414
Glucose	5.2378	5.2445	Glucose	5.2233	5.2454
UDP-der*	5.6099	5.6376	UDP-der*	5.611	5.6365
Uracil	5.7928	5.8236	Uracil	5.7963	5.8149
Uridine	5.8912	5.9282	Uridine	5.8932	5.8989
UDP-der*	5.9816	6.0111	UDP-der*	5.9065	5.9244
Inosine	6.0871	6.1128	Inosine	6.0949	6.1116
Fumarate	6.5121	6.5305	Fumarate	6.517	6.5236
Tyrosine	6.8861	6.917	Tyrosine	6.8879	6.9131
Histidine	7.0591	7.0749	Histidine	7.0512	7.0626
Tyrosine	7.1814	7.2133	Tyrosine	7.1874	7.2109
Tryptophan	7.2127	7.2218			

Tryptophan	7.2701	7.3139	Tryptophan	7.2721	7.3137
Phenylalanine	7.3167	7.3487	Phenylalanine	7.316	7.3451
Phenylalanine	7.3602	7.3995	Phenylalanine	7.3634	7.3972
Phenylalanine	7.4121	7.452	Phenylalanine	7.4152	7.4517
Uracil	7.5275	7.5346	Uracil	7.5285	7.5347
Tryptophan	7.5347	7.54	Tryptophan	7.5348	7.5414
Uracil	7.5402	7.5471	Uracil	7.5415	7.5474
Tryptophan	7.5472	7.5576	Tryptophan	7.5478	7.5566
Niacinamide	7.5842	7.6155	Niacinamide	7.5842	7.6155
Tryptophan	7.7269	7.7529	Tryptophan	7.7293	7.7543
Histidine	7.7836	7.8064	Histidine (ov)	7.7687	7.7809
Uridine	7.8595	7.8849	Uridine (ov)	7.8618	7.8725
			Uridine	7.8748	7.8832
Inosine + IMP*	8.2284	8.2401	Inosine + IMP*	8.2307	8.2357
Niacinamide	8.2402	8.2679	Niacinamide	8.2407	8.2647
AMP*	8.2741	8.2822			
Inosine	8.334	8.3491	Inosine	8.3379	8.3448
Nucleotides	8.354	8.3737			
Formate	8.4514	8.467	Formate	8.4551	8.4632
IMP*	8.5688	8.582	IMP*	8.5688	8.582
Niacinamide	8.6983	8.7331	Niacinamide	8.7091	8.726
Niacinamide	8.93	8.9562	Niacinamide	8.9371	8.9485

^{*}AMP = adenosine monophosphate; GPC = glycerophosphocholine; IMP = inosine monophosphate; ov = overlapping; UDP-der = uridine diphosphate derivative

Supporting Information 4.5. NMR signal assignment of the mitochondrial fractions obtained from brain.

Whole-cell			Mitochondria				
Metabolite	tabolite Right limit Left limit Metabolite (ppm) (ppm)		t Right limit (ppm)		Left limit (ppm)		
Isoleucine	0.9262	0.9466	Isoleucine	0.9279	0.9387		
Isoleucine + leucine	0.9478	0.9598	Isoleucine + leucine	0.9392	0.946		
Leucine	0.9599	0.9809	Leucine	0.9497	0.9804		
Valine	0.9821	1.0038	Valine	0.9821	1.0038		
Isoleucine	1.0039	1.0233	Isoleucine	1.0039	1.0233		
Valine	1.0325	1.0571	Valine	1.0352	1.0557		
Isoleucine	1.2598	1.2945					
Lactate	1.3173	1.3484	Lactate	1.3169	1.3449		
Alanine	1.4816	1.4956	Alanine	1.4836	1.4925		
Lysine	1.496	1.5533	Lysine (ov)	1.4956	1.5698		
Arginine	1.5896	1.6608	Arginine + leucine	1.6243	1.6874		
Leucine	1.6616	1.6991					
Lysine	1.8515	1.8679	Lysine	1.7001	1.7687		
4-aminobutyrate	1.8753	1.9119	4-aminobutyrate	1.8767	1.9119		
Acetate+ 4- aminobutyrate	1.9139	1.925	Acetate + 4- aminobutyrate	1.9139	1.9235		
4-aminobutyrate	1.9258	1.9372	4-aminobutyrate	1.9258	1.9347		
N-acetylaspartate	2.0121	2.0284	N-acetylaspartate	2.0171	2.0274		
Glutamate (ov*)	2.0324	2.091	Glutamate (ov) 2.0281		2.0905		

Glutamine+glutamate	2.0982	2.1515	Glutamine + glutamate	2.0982	2.1512
Glutathione	2.0982	2.1933	Glutathione	2.0982	2.1312
4-aminobutyrate	2.1337	2.1933	4-aminobutyrate	2.1317	2.3195
Glutamate	2.3359	2.3799	Glutamate	2.3359	2.3799
Succinate	2.4026	2.4098	Succinate	2.4026	2.4098
Glutamine	2.4020	2.4806	Glutamine	2.4020	2.4656
Giutailille	2.4255	2.4000	N-acetylaspartate	2.4233	2.4030
Glutathione	2.5276	2.6126	Glutathione	2.5293	2.6073
Giatatrilone	2.3270	2.0120	Aspartate	2.6278	2.6373
Aspartate	2.6623	2.6693	Aspartate	2.6614	2.6673
N-acetylaspartate	2.6855	2.6915	N-acetylaspartate	2.6846	2.6909
Aspartate	2.6903	2.6998	Aspartate (ov)	2.691	2.6968
N-acetylaspartate (ov)	2.7008	2.7186	N-acetylaspartate	2.7008	2.7186
	2.8056	2.7186	, · ·	2.8056	2.7186
Aspartate Asparate		2.8341	Aspartate		2.8412
Asparagine	2.8193 2.8559	2.8756	Asparate	2.8303 2.8485	2.8714
Asparagine	2.0339	2.0730	Asparagine	2.8798	2.9024
Glutathione	2.9024	2.9966	Asparagine Glutathione		2.9024
		3.0348		2.9107	3.0346
4-aminobutyrate Creatine	2.9997 3.0352	3.0348	4-aminobutyrate Creatine	2.9997 3.0347	3.0346
Phosphocreatine	3.0352	3.0435	Creatine	3.0347	3.045
Choline	3.199	3.2116	Choline	3.199	3.21
	3.219	3.2261			3.2278
Phosphocholine GPC* (ov)	3.219	3.2352	Phosphocholine GPC*	3.2175 3.2279	3.2278
Taurine	3.2425	3.2637	Taurine	3.2425	3.2637
Myo-inositol	3.2638	3.2677	Myo-inositol	3.2638	3.2677
Taurine	3.2678	3.276	Taurine	3.2678	3.2077
Myo-inositol	3.276	3.3009	Myo-inositol	3.2078	3.3009
iviyo-mositor	3.270	3.3003	Taurine	3.4067	3.4348
Choline	3.5076	3.516	Taurille	3.4007	3.4340
Myo-inositol	3.6043	3.6335	Myo-inositol	3.606	3.629
Ascorbate	3.721	3.7382	Wiyo-inositor	3.000	3.023
Creatine	3.9251	3.9402	Creatine	3.9291	3.9348
Phosphocreatine	3.9433	3.9568	Creatine	3.3231	3.3340
Myo-inositol	4.0493	4.0766			
Choline	4.0741	4.0908			
Lactate	4.0919	4.1348	Lactate	4.0864	4.121
Phosphocholine	4.1422	4.1348	Luctuic	1.0004	7.121
Threonine	4.2536	4.1893	Threonine	4.2698	4.3105
Ascorbate	4.5032	4.5231	Ascorbate	4.5073	4.5103
Glutathione	4.5553	4.5975	Glutathione	4.5545	4.5155
Saturnone		1.5575	Glucose	4.6383	4.6571
			Glucose	5.2279	5.2418
UDP-der*	5.6081	5.6354	UDP-der*	5.6104	5.6373
Uracil	5.7928	5.8236	35. dei	3.3101	3.3373
Uridine	5.89	5.9264	Uridine	5.89	5.9264
UDP-der*	5.9611	6.0085	UDP-der*	5.9611	6.0085
Inosine	6.0871	6.1128	Inosine	6.0932	6.1132
l mosnic	2.0071	3.1120	111031110	3.0332	3.1132

Nucleotides	6.1133	6.1443	Nucleotides	6.1133	6.155
Nucleotides	6.1439	6.1867			
Fumarate	6.5121	6.5305	Fumarate	6.5121	6.5282
Tyrosine	6.8861	6.917	Tyrosine	6.8907	6.9132
Histidine	7.053	7.0743	Histidine	7.0533	7.0633
Tyrosine	7.1814	7.2133	Tyrosine	7.1869	7.209
Tryptophan	7.2127	7.2218			
Tryptophan	7.2701	7.3139	Tryptophan	7.2723	7.3144
Phenylalanine	7.3167	7.3487	Phenylalanine	7.3179	7.3455
Phenylalanine	7.3602	7.3995	Phenylalanine	7.3602	7.3995
Phenylalanine	7.4121	7.452	Phenylalanine	7.4121	7.452
Uracil	7.5255	7.5353	Uracil	7.5255	7.5353
Tryptophan	7.536	7.541	Tryptophan	7.536	7.541
Uracil	7.5412	7.5492	Uracil	7.5412	7.5492
Tryptophan	7.5493	7.5567	Tryptophan	7.5493	7.5567
Nicotinurate	7.5842	7.6155	Nicotinurate	7.5848	7.6155
Tryptophan	7.7269	7.7529			
Uridine	7.8595	7.8703	Uridine	7.8628	7.8679
N-acetylaspartate (ov)	7.8857	7.9228	N-acetylaspartate	7.8828	7.9184
Inosine + IMP*	8.2284	8.2401	Inosine + IMP*	8.2293	8.239
Nicotinurate	8.2402	8.2679	Nicotinurate	8.2399	8.2653
AMP*	8.2657	8.2767			
Inosine	8.3369	8.353	Inosine	8.3385	8.3447
Nucleotides	8.3582	8.3757			
Nucleotides	8.3757	8.3963			
Formate	8.4514	8.467	Formate	8.4559	8.4619
Inosine	8.5726	8.584			
AMP*	8.6087	8.6244	AMP*	8.6143	8.6228
Nicotinurate	8.6983	8.7331	Nicotinurate	8.7082	8.726
Nicotinurate	8.93	8.9562	Nicotinurate	8.9385	8.9484

^{*}AMP = adenosine monophosphate; GPC = glycerophosphocholine; IMP = inosine monophosphate; ov = overlapping; UDP-der = uridine diphosphate derivative

Supporting Information 4.6. Comparative analysis of mitochondria and whole-cell metabolomic profiles in breast tumor

	Mitochondria		Whole-cell		Mito vs. Whole-cell	
Metabolite	Mean	SD	Mean	SD	VIP value	P-value
Lactate	32.582	5.583	186.153	4.501	6.400	2E-08
Alanine	12.777	1.956	22.541	2.032	1.592	0.001
Lysine	0.000	0.000	3.138	0.950	-	2E-04
Arginine	0.000	0.000	0.404	0.024	-	2E-08
Leucine	0.000	0.000	2.390	0.526	-	4E-05
Unknown 1	6.474	2.653	0.050	0.000	1.279	0.006
Lysine + arginine	0.589	0.928	3.942	0.787	-	0.002
Glutamate (ov*)	16.250	8.850	25.133	1.955	1.509	-
Glutamate	22.718	10.164	34.784	2.717	1.823	-
Glutamine	2.923	1.801	5.683	0.664	-	0.047

Glutathione	0.032	0.052	0.272	0.078	-	0.002
Citrate	0.230	0.109	0.975	0.261	-	0.001
Methionine	0.409	0.144	2.057	0.078	-	2E-06
Aspartate	0.000	0.000	0.285	0.025	-	2E-07
Dimethylamine	0.490	0.117	0.096	0.039	-	0.002
Aspartate	0.059	0.053	0.258	0.033	-	0.001
Asparagine	0.144	0.165	0.635	0.040	-	0.003
Creatine	8.083	3.754	20.117	7.238	1.677	0.019
Phosphocreatine	0.000	0.000	3.952	0.921	1.017	5E-05
Choline	33.451	13.249	23.749	4.890	1.713	-
Phosphocholine	23.088	10.297	28.916	2.671	1.412	-
Taurine	41.669	1.988	60.387	7.147	2.170	0.001
Myo-inositol	3.601	1.755	7.130	1.059	-	0.021
Taurine	6.542	1.353	57.209	7.293	3.668	4E-06
Glucose + taurine	80.377	10.253	9.538	1.613	4.330	3E-05
Lactate	38.004	14.325	48.791	2.074	1.825	-
Phosphocholine	10.433	4.386	6.216	0.547	1.104	-
Threonine	0.000	0.000	1.036	0.029	-	2E-10
Threonine	0.000	0.000	0.616	0.071	-	9E-07
Ascorbate	0.083	0.289	0.965	0.195	-	0.004
Glucose (ov*)	17.344	13.702	1.416	0.117	1.825	-
Glucose	5.245	7.752	0.721	0.164	1.285	-
UDP-der*	2.048	0.773	0.119	0.051	-	0.006
Uracil	0.551	0.429	1.607	0.267	-	0.009
Fumarate	0.209	0.084	0.443	0.206	-	0.059
Tyrosine	0.966	0.378	1.954	0.555	-	0.023
Tryptophan	0.000	0.000	0.151	0.035	-	5E-05
Tryptophan	0.000	0.000	0.127	0.033	-	9E-05
Niacinamide	0.000	0.000	0.594	0.051	-	2E-07
Tryptophan	0.000	0.000	0.280	0.075	-	1E-04
Histidine	0.000	0.000	0.675	0.143	-	3E-05
Inosine + IMP*	0.000	0.000	0.211	0.157	-	0.019
Niacinamide	0.000	0.000	0.613	0.077	-	1E-06
Inosine	0.000	0.000	0.179	0.155	-	0.034
Nucleotides	0.000	0.000	0.045	0.010	-	5E-05
Nucleotides	0.000	0.000	0.058	0.015	-	9E-05
Niacinamide	0.000	0.000	0.520	0.060	-	9E-07
Niacinamide	0.000	0.000	0.501	0.057		8E-07

Data analysis used an OPLS-DA model to obtain the VIP values and a T-test to obtain the p-values (n = 3-5).

Supporting Information 4.7. Comparative analysis of mitochondria and whole-cell metabolomic profiles in lung

	Mitochondria		Whole-cell		Mito vs. Whole-cell	
Metabolite	Mean	SD	Mean	SD	VIP value	P-value
Leucine	7.824	2.890	4.631	0.225	1.044	-
Valine	4.160	0.760	2.819	0.194	-	0.027

^{*}IMP=inosine monophosphate; ov = overlapping; UDP-der=uridine diphosphate derivative

1	i		i		İ	i
Lactate	39.048	10.054	41.244	9.451	1.637	-
Alanine	15.113	3.268	10.852	2.543	1.133	-
Leucine	0.000	0.000	1.180	0.467	-	0.001
Leucine + lysine	11.915	9.631	7.698	0.849	1.327	-
Unknown 1	14.592	3.226	0.050	8E-18	2.511	3E-04
Glutamate (ov*)	2.958	0.941	12.505	9.275	1.950	-
Glutathione	9.708	4.596	8.145	3.519	1.168	-
Acetone	4.647	1.564	0.050	0.000	1.410	0.002
Glutamate	6.715	0.548	19.547	12.208	2.236	0.047
Succinate	1.163	0.316	0.407	0.139	-	0.009
Glutamine (ov*)	3.568	1.010	5.665	1.093	-	0.033
Glutathione	0.255	0.185	0.653	0.200	-	0.028
Citrate	0.307	0.119	0.954	0.250	-	0.002
Glutathione	0.000	0.000	1.470	0.750	-	0.004
Glutathione	0.000	0.000	1.048	0.596	-	0.006
Aspartate	0.000	0.000	0.122	0.041	-	4E-04
Aspartate	0.000	0.000	0.379	0.165	-	0.002
Asparagine	0.000	0.000	0.346	0.267	-	0.022
Asparagine	0.000	0.000	0.396	0.328	-	0.029
Glutathione (ov*)	0.000	0.000	1.500	1.415	-	0.046
Creatine	7.036	1.401	4.104	0.352	1.037	0.014
Phosphocreatine	0.000	0.000	0.939	0.147	-	5E-06
Choline	41.654	13.509	18.766	9.805	2.989	0.045
Phosphocholine	0.000	0.000	2.315	1.556	-	0.012
Lactate	47.544	9.133	12.109	2.131	3.780	0.001
Ascorbate	0.561	0.231	2.069	0.213	-	1E-04
Glucose	17.119	11.854	8.565	6.097	1.298	-
Glucose	4.063	1.173	1.682	1.160	-	0.032
UDP-der*	1.863	0.499	0.213	0.025	-	0.001
Uracil	0.000	0.000	0.746	0.677	-	0.040
Uridine	0.000	0.000	0.199	0.171	-	0.033
Histidine	0.000	0.000	0.306	0.048	-	5E-06
Tryptophan	0.621	0.239	1.606	0.280	-	0.002
Tryptophan	0.000	0.000	0.085	0.023	-	1E-04
Uracil	0.000	0.000	0.356	0.319	-	0.038
Tryptophan	0.000	0.000	0.074	0.018	-	8E-05
Unknown 2	0.571	0.381	2.683	0.810	-	0.002
Inosine	0.000	0.000	0.095	0.019	-	2E-05
Niacinamide	0.000	0.000	0.540	0.099	-	1E-05
Nucleotides	0.000	0.000	0.023	0.008	-	0.001
Nucleotides	0.000	0.000	0.020	0.011	-	0.006
Tryptophan Uracil Tryptophan Unknown 2 Inosine Niacinamide Nucleotides	0.000 0.000 0.000 0.571 0.000 0.000	0.000 0.000 0.000 0.381 0.000 0.000	0.085 0.356 0.074 2.683 0.095 0.540 0.023	0.023 0.319 0.018 0.810 0.019 0.099 0.008		1E-04 0.038 8E-05 0.002 2E-05 1E-05 0.001

Data analysis used an OPLS-DA model to obtain the VIP values and a T-test to obtain the p-values (n = 3-5). *ov = overlapping; UDP-der=uridine diphosphate derivative

Supporting Information 4.8. Comparative analysis of mitochondria and whole-cell metabolomic profiles in liver

Mitochondria	Whole-cell	Mito vs. Whole-cell
--------------	------------	---------------------

Metabolite	Mean	SD	Mean	SD	VIP value	P-value
Isoleucine + leucine	8.827	4.104	1.351	0.102	1.861	0.022
Leucine	20.641	9.352	3.069	0.270	2.881	0.020
Valine	10.008	4.659	1.801	0.163	1.944	0.026
Isoleucine	3.723	2.023	0.894	0.082	1.124	-
Valine	8.451	3.905	1.553	0.096	1.794	0.025
Lysine	6.113	2.688	1.243	0.118	1.492	0.023
Methionine	6.083	2.316	1.527	0.291	1.433	0.017
Glutathione + methionine	6.032	2.195	9.835	1.180	1.328	0.035
Glutamate	5.790	2.518	3.402	0.593	1.069	-
Succinate	0.029	0.021	0.149	0.080	-	0.016
Glutathione	2.114	1.630	9.707	1.622	1.919	0.001
Methionine	3.760	1.723	0.470	0.111	1.126	0.019
Aspartate	0.000	0.000	0.084	0.063	-	0.020
Asparagine	0.898	0.371	0.230	0.206	-	0.003
Lysine	9.824	4.013	1.263	0.167	1.965	0.012
Phosphocreatine	1.243	0.444	0.405	0.112	-	0.021
Ornithine	3.945	1.633	0.717	0.306	1.158	0.017
Choline	0.657	0.643	2.154	0.322	-	0.010
Phosphocholine	11.309	3.007	3.701	0.777	1.855	0.006
Glycerophosphocholine	25.733	6.751	7.851	1.669	2.953	0.005
Glucose (ov)	23.936	11.755	37.942	6.412	2.497	-
Maltose (overlapping)	25.208	3.634	11.276	1.510	2.523	0.001
Taurine	0.050	0E+00	4.929	0.375	1.474	7E-08
Maltose	21.182	20.774	11.344	2.813	2.293	-
Lactate	42.629	25.175	9.518	0.748	3.802	-
Threonine (ov*)	0.000	0.000	0.366	0.129	-	0.001
Threonine	0.000	0.000	0.256	0.081	-	3E-04
Threonine	0.000	0.000	0.184	0.095	-	0.004
Threonine (ov*)	0.000	0.000	0.077	0.072	-	0.045
Ascorbate	0.000	0.000	0.561	0.233	-	0.001
Glutathione	0.000	0.000	1.315	0.179	-	2E-06
Glucose + maltose	21.200	10.584	12.629	0.794	1.734	-
Maltose	23.461	19.987	2.887	0.754	2.798	-
Glucose	25.114	17.303	26.683	1.270	1.776	-
UDP-NAG*	0.000	0.000	0.244	0.166	-	0.013
UDP-der*	2.235	0.740	0.009	0.039	1.010	0.002
UDP-der*	0.000	0.000	0.476	0.271	-	0.006
Nucleotides	0.000	0.000	0.039	0.014	-	0.001
Nucleotides	0.000	0.000	0.077	0.034	-	0.002
Tyrosine	2.382	1.236	0.587	0.042	-	0.051
Phenylalanine	2.965	1.357	0.620	0.044	1.018	0.027
Phenylalanine	2.802	1.363	0.565	0.042	-	0.033
Tryptophan	0.000	0.000	0.014	0.008	-	0.006
Uracil	0.000	0.000	0.087	0.024	-	1E-04
Tryptophan	0.000	0.000	0.075	0.072	-	0.050
Nucleotides	0.000	0.000	0.004	0.002	-	0.002

Data analysis used an OPLS-DA model to obtain the VIP values and a T-test to obtain the p-values (n = 3-5). *ov = overlapping; UDP-der=uridine diphosphate derivative; UDP-NAG= uridine diphosphate N-acetylglucosamine

Supporting Information 4.9. Comparative analysis of mitochondria and whole-cell metabolomic profiles in kidney.

	Mitochondria		Whol	e-cell	Mito vs. Whole-cell		
Metabolite	Mean	SD	Mean	SD	VIP value	P-value	
Isoleucine + leucine	8.779	1.244	4.370	0.361	1.158	0.001	
Leucine	20.356	2.757	9.642	1.113	1.818	0.001	
Valine	11.878	1.466	6.028	0.507	1.345	0.001	
Isoleucine	5.739	0.853	3.103	0.239	-	0.002	
Valine	10.774	1.268	5.359	0.659	1.298	0.001	
Lactate	19.751	2.944	95.777	33.801	4.902	0.002	
Alanine	21.608	1.821	16.779	3.604	1.159	0.041	
Lysine	1.477	1.455	3.715	0.498	-	0.046	
Leucine + lysine + arginine	19.010	3.110	14.258	1.424	1.079	0.051	
Unknown 1	1.802	0.388	0.000	0.000	-	2E-04	
Lysine + arginine	10.600	1.308	7.150	0.494	-	0.005	
Glutamate (ov*)	12.092	3.608	22.913	2.910	1.810	0.005	
Glutamine + glutamate	10.197	2.233	14.764	1.030	1.119	0.017	
Glutamine + glutamate	3.905	0.577	5.610	0.496	-	0.005	
Glutathione (ov*)	2.548	0.504	1.247	0.172	-	0.006	
Valine	1.723	0.629	3.401	0.563	-	0.009	
Glutamate	18.555	3.829	36.515	3.496	2.368	0.001	
Succinate	0.152	0.110	0.769	0.063	-	1E-04	
Glutamine (ov*)	2.652	0.957	6.757	0.531	1.128	0.001	
Glutathione (ov*)	0.000	0.000	0.567	0.437	-	0.022	
Citrate	0.000	0.000	0.106	0.053	-	0.003	
Glutathione (ov*)	0.000	0.000	0.324	0.214	-	0.011	
Methionine	4.136	0.423	2.528	0.342	-	0.001	
Dimethylamine	0.111	0.017	0.206	0.061	-	0.014	
Aspartate + asparagine	1.456	0.225	0.999	0.221	-	0.031	
Lysine	8.576	0.939	4.509	0.198	1.126	4E-04	
Phosphocreatine	0.000	0.000	1.569	0.248	-	5E-06	
Choline	8.110	1.113	59.442	13.312	4.018	1E-04	
Phosphocholine	10.387	2.072	20.246	4.059	1.736	0.003	
Glycerophosphocholine	10.312	2.060	14.559	1.342	1.091	0.020	
Taurine	24.176	11.267	86.644	8.890	4.437	2E-04	
Myo-inositol	7.032	2.051	12.999	1.723	1.329	0.006	
Lactate	22.681	10.083	28.409	9.495	1.252	-	
Unknown 2	6.168	1.601	2.770	3.282	1.018	-	
Threonine	5.496	1.680	0.452	1.008	1.209	0.004	
Ribose	7.574	15.308	35.238	59.765	3.491	-	
UDP-der*	1.344	0.360	0.428	0.657	-	0.040	
Uracil	0.328	0.077	1.231	0.489	-	0.005	
Uridine	0.288	0.071	0.827	0.472	-	0.038	
Inosine	0.141	0.157	1.108	0.388	-	0.002	

Fumarate	0.209	0.061	0.525	0.133	-	0.003
Tyrosine	2.292	0.276	1.702	0.265	-	0.025
Histidine	0.882	0.093	0.540	0.068	-	0.002
Tyrosine	2.973	0.383	2.036	0.318	-	0.012
Phenylalanine	4.128	0.499	1.851	0.281	-	4E-04
Phenylalanine	1.244	0.328	0.770	0.104	-	0.056
Phenylalanine	2.956	0.473	1.538	0.207	-	0.003
Uracil	0.105	0.024	0.461	0.108	-	3E-04
Uracil	0.112	0.049	0.467	0.120	-	0.001
Tryptophan	0.075	0.039	0.147	0.011	-	0.024
Niacinamide	0.225	0.097	1.279	0.197	-	5E-05
Unknown 3	2.605	0.789	6.503	0.674	1.105	4E-04
Inosine + IMP*	0.110	0.053	0.910	0.275	-	0.001
Niacinamide	0.112	0.058	1.209	0.173	-	1E-05
AMP*	0.000	0.000	0.021	0.007	-	0.001
Inosine	0.193	0.086	1.011	0.356	-	0.002
Nucleotides	0.000	0.000	0.075	0.012	-	7E-06
IMP*	0.000	0.000	0.024	0.013	-	0.006
Niacinamide	0.210	0.162	1.087	0.158	-	3E-04
Niacinamide	0.272	0.119	0.972	0.136		3E-04

Data analysis used an OPLS-DA model to obtain the VIP values and a T-test to obtain the p-values (n = 3-5).

Supporting Information 4.10. Comparative analysis of mitochondria and whole-cell metabolomic profiles in brain

	Mitochondria		Whole-cell		Mito vs. W	/hole-cell
Metabolite	Mean	SD	Mean	SD	VIP value	P-value
Isoleucine	0.027	0.013	1.153	0.645	-	0.006
Isoleucine (ov*)	0.023	0.008	1.182	0.420	-	0.001
Leucine	0.233	0.047	2.395	0.555	-	9E-05
Valine	0.081	0.017	1.117	0.195	-	2E-05
Isoleucine	0.040	0.010	0.573	0.098	-	1E-05
Valine	0.073	0.010	0.914	0.159	-	2E-05
Lactate	1.480	0.432	86.118	4.327	4.326	7E-09
Alanine (ov*)	0.256	0.067	3.084	0.562	-	2E-05
Alanine	0.207	0.047	2.713	0.152	-	3E-08
Lysine (ov*)	0.070	0.067	0.392	0.275	-	0.039
Lysine	0.101	0.082	3.582	1.673	-	0.003
Lysine	0.000	0.000	0.345	0.253	-	0.018
4-aminobutyrate	1.925	0.614	17.123	0.758	1.831	7E-08
Acetate + 4-aminobutyrate	1.263	0.265	16.012	3.146	1.791	3E-05
4-aminobutyrate	0.189	0.055	2.268	0.353	-	1E-05
N-acetylaspartate	3.050	0.718	26.964	4.345	2.290	0.017
Glutamate (ov*)	1.429	0.420	22.375	2.336	2.155	8E-07
Glutamine + glutamate	1.079	0.406	34.454	3.178	2.721	3E-07
Glutathione	0.687	0.255	7.408	0.348	1.217	6E-08

^{*}AMP=adenosine monophosphate; IMP=inosine monophosphate; ov = overlapping; UDP-der=uridine diphosphate derivative

ſ	Ì		Ì	ĺ	Ī	
4-aminobutyrate	2.444	0.930	20.310	0.848	1.988	8E-05
Glutamate	1.966	0.515	33.239	4.391	2.636	2E-06
Succinate	0.061	0.028	0.880	0.126	-	6E-06
Glutamine	0.097	0.112	21.791	1.300	2.190	2E-07
N-acetylaspartate	1.131	0.333	10.701	1.312	1.447	3E-06
Glutathione	0.701	0.395	7.087	0.758	1.181	4E-06
Aspartate	0.048	0.016	0.245	0.118	-	0.008
Aspartate	0.055	0.036	1.069	0.110	-	1E-06
Asparate + N-acetylaspartate	0.907	0.240	8.724	0.475	1.314	6E-08
N-acetylaspartate	0.338	0.086	2.643	0.264	-	1E-06
Aspartate (ov*)	0.081	0.037	1.588	0.205	-	3E-06
N-acetylaspartate	0.489	0.130	4.580	0.579	-	4E-06
Aspartate	0.074	0.029	1.187	0.131	-	0.003
Asparate	0.125	0.036	1.515	0.129	-	2E-05
Glutathione	0.395	0.221	4.561	2.414	-	0.007
4-aminobutyrate	2.413	0.903	20.022	1.808	1.954	1E-06
Creatine	5.364	1.367	49.135	4.626	3.117	8E-07
Phosphocreatine	0.000	0.000	4.829	1.530	1.009	3E-04
Choline	1.777	0.365	17.333	2.169	1.857	4E-05
Phosphocholine	3.031	0.617	16.094	4.660	1.673	2E-07
Glycerophosphocholine	1.234	0.290	9.796	0.852	1.376	7E-07
Taurine	2.698	0.725	25.541	4.481	2.242	2E-05
Myo-inositol	0.311	0.078	3.827	0.323	-	3E-07
Taurine	0.979	0.305	10.190	1.926	1.424	3E-05
Myo-inositol	1.121	0.275	12.475	0.332	1.584	3E-09
Taurine	3.880	0.932	34.673	7.368	2.600	0.003
Lactate	1.291	0.313	22.372	1.279	2.158	3E-08
Threonine	0.162	0.092	4.385	1.236	-	0.001
UDP-der*	0.268	0.055	1.445	0.442	-	0.001
Uridine	0.019	0.015	0.440	0.113	-	0.001
UDP-der*	0.014	0.015	0.594	0.114	-	2E-05
Nucleotides	0.014	0.013	0.372	0.025	-	2E-07
Nucleotides	0.000	0.000	0.162	0.118	-	0.017
Fumarate	0.032	0.007	0.318	0.133	-	0.002
Tyrosine	0.032	0.005	0.487	0.048	-	5E-07
Histidine	0.011	0.006	0.232	0.022	-	7E-06
Tyrosine	0.039	0.006	0.604	0.045	-	1E-07
Tryptophan	0.009	0.010	0.149	0.003	-	4E-07
Phenylalanine	0.037	0.025	0.653	0.084	-	4E-06
Phenylalanine	0.004	0.005	0.258	0.029	-	1E-06
Phenylalanine	0.026	0.009	0.508	0.061	-	2E-06
Uracil	0.001	0.001	0.104	0.022	-	4E-05
Tryptophan	0.002	0.001	0.048	0.012	-	1E-04
Uracil	0.001	0.001	0.155	0.074	-	0.003
Nicotinurate	0.011	0.018	0.825	0.172	-	3E-05
Uridine	0.011	0.008	0.220	0.086	-	0.012
Uridine sol	0.023	0.008	0.651	0.069	-	7E-07
N-acetylaspartate	0.017	0.021	1.673	0.678	-	0.001

Inosine + IMP*	0.079	0.025	1.647	0.340	-	5E-06
Nicotinurate	0.004	0.007	0.791	0.030	-	2E-09
Inosine	0.107	0.027	1.955	0.456	-	0.001
Nucleotides	0.000	0.000	0.062	0.025	-	0.001
Nucleotides	0.000	0.000	0.034	0.010	-	2E-04
AMP*	0.009	0.004	0.032	0.026	-	0.011
Nicotinurate	0.010	0.011	0.567	0.069	-	0.029
Nicotinurate	0.011	0.010	0.517	0.069	-	3E-06

Data analysis used an OPLS-DA model to obtain the VIP values and a T-test to obtain the p-values (n = 3-5).

Supporting Information 4.11. Comparative analysis of mitochondrial metabolomic profiles from healthy vs. metastatic lungs

	Healthy		Metas	static	Healthy vs. Metastatic		
Metabolite	Mean	SEM	Mean	SEM	P-value	VIP	
Choline	22.045	2.042	35.238	1.673	0.002	2.773	
Lactate	17.432	1.731	25.759	2.031	0.024	2.185	
Glucose	6.906	0.373	12.562	0.896	0.001	2.013	
Glutamate	2.459	0.390	6.031	0.808	0.007	1.698	
Phosphocholine	9.742	0.417	16.478	1.445	0.004	2.248	
Alanine	7.138	0.460	10.285	1.151	0.053	1.552	
Creatine	2.511	0.364	4.952	0.222	0.001	1.264	

Data analysis used an OPLS-DA model to obtain the VIP values and a T-test to obtain the p-values (n = 3-5)

^{*}AMP=adenosine monophosphate; IMP=inosine monophosphate; ov = overlapping; UDP-der=uridine diphosphate derivative

ANNEX II

PUBLICATIONS



pubs.acs.org/ac Article

NMR-Based Mitochondria Metabolomic Profiling: A New Approach To Reveal Cancer-Associated Alterations

Inés Domingo-Ortí, Patricia Ferrer-Torres, Ana Armiñán, María J. Vicent,* Antonio Pineda-Lucena,* and Martina Palomino-Schätzlein*



Cite This: https://doi.org/10.1021/acs.analchem.3c02432



ACCESS

III Metrics & More

Article Recommendations

Supporting Information

ABSTRACT: Studying metabolism may assist in understanding the relationship between normal and dysfunctional mitochondrial activity and various diseases, such as neurodegenerative, cardiovascular, autoimmune, psychiatric, and cancer. Nuclear magnetic resonance-based metabolomics represents a powerful method to characterize the chemical content of complex samples and has been successfully applied to studying a range of conditions. However, an optimized methodology is lacking for analyzing isolated organelles, such as mitochondria. In this study, we report the development of a protocol to metabolically profile mitochondria from healthy, tumoral, and metastatic tissues. Encouragingly, this approach provided quantitative information about up to 45 metabolites in one comprehensive and robust analysis. Our results revealed significant differences between whole-cell and mitochondrial metabolites, which supports a more refined approach to metabolic analysis. We applied our optimized methodology to investigate aggressive and metastatic breast cancer in mouse tissues, discovering that lung mitochondria

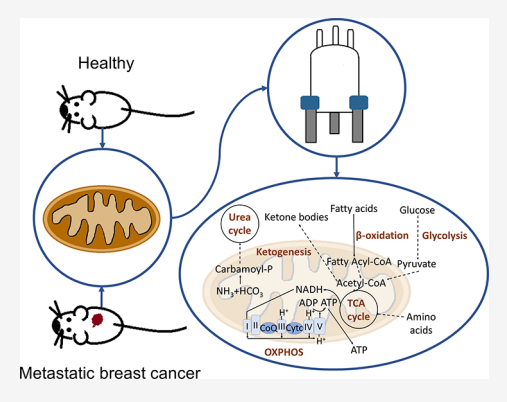


exhibit an altered metabolic fingerprint. Specific amino acids, organic acids, and lipids showed significant increases in levels when compared with mitochondria from healthy tissues. Our optimized methodology could promote a better understanding of the molecular mechanisms underlying breast cancer aggressiveness and mitochondrial-related diseases and support the optimization of new advanced therapies.

Mitochondria play critical roles in various cellular processes, including oxidative phosphorylation (OX-PHOS), fatty acid oxidation, the urea and Krebs cycles, gluconeogenesis, and ketogenesis. While ATP generation represents the primary function of mitochondria, they also provide building blocks for cell replication, control redox balance, participate in apoptosis, and function as a signaling platform. Normal cellular physiological function requires critical control of mitochondrial-associated activities; furthermore, mitochondrial dysfunction can prompt the onset of diverse pathological processes, including neurodegenerative, cardiovascular, autoimmune, and psychiatric diseases, and notably, cancer.

Cancer cells obtain energy through anaerobic glycolysis due to low oxygen levels, which impairs mitochondrial respiration and increases cell acidity due to increased lactate production (the "Warburg effect"). A higher mitochondrial membrane potential, reflecting the altered functional status of mitochondria, also characterizes tumorigenic development. Mitochondrial dysfunction induced by genetic alterations also triggers alterations to tumor cell energy production mechanisms (from OXPHOS to glycolysis), thus contributing to cancer progression. In this context, mitochondrial metabolism supports cancer cell adaptation, which promotes metastasis.

Furthermore, altered mitochondrial content supports additional facets of cancer aggressiveness.⁶

A deeper understanding of disease-associated molecular mechanisms may help to develop better therapeutic approaches for aggressive metastatic cancers. In this context, developing specific methods to study mitochondrial metabolism may detect disease-associated alterations to inform on these mechanisms. Metabolomic profiling provides a comprehensive quantitative analysis of metabolic pathway end products in biological systems, providing valuable information on the biochemical processes at play. Metabolomic analysis generally uses biofluids but also cell and tissue samples. Significantly, data from these latter matrices reflect changes occurring at the origin of the disorder and provide relevant information regarding associated mechanisms.

Received: June 5, 2023
Revised: October 13, 2023
Accepted: October 16, 2023



Whole-tissue metabolomics has been widely applied in biomedical research for the diagnosis of pathological processes, 15 the discovery of early disease biomarkers, 16 optimization of therapies for various pathologies, 17,18 the study of different disease rates between populations, 19 and identification of tumor characteristics and progression markers.²⁰ However, we lack protocols that support the metabolomic profiling of organelles, such as mitochondria. A more in-depth understanding of mitochondrial metabolomics could capture dynamic changes missed by "bulk" whole-cell profiling.²¹ A more targeted approach could also represent a valuable tool in mitochondria-related disease research, helping to evaluate novel drugs (particularly those targeting mitochondria) and supporting the early identification of biomarkers in diseases with a known mitochondrial impact (e.g., Alzheimer's disease, Parkinson's disease, and diabetes²).

While current mass spectrometry (MS)-based methods²² for quantifying the metabolite content of isolated mitochondria are very sensitive and suitable for the study of targeted metabolic changes,²³ the relatively complex sample preparation and analysis currently employed typically involve several steps, which involves a relatively high degree of difficulty.²² As an alternative/complementary strategy for mitochondrial metabolomics, we sought to develop a more straightforward, robust, nontargeted approach that generates a general mitochondrial metabolic fingerprint. We now describe the development of an optimized protocol for the metabolomic analysis of mitochondria isolated from healthy, tumoral, and metastatic tissues using nuclear magnetic resonance (NMR) spectroscopy.

■ EXPERIMENTAL SECTION

Materials and Reagents. Bovine serum albumin (BSA) and Trizma hydrochloride (Tris-HCl) were purchased from Sigma-Aldrich (St. Louis, USA). D-mannitol and sucrose were purchased from Merck Millipore (Burlington, USA). Deuterium oxide (D₂O) and 3-(trimethylsilyl) propionic acid d4 sodium salt (TSP) were obtained from Eurisotop (Tewksbury, USA). Monobasic sodium phosphate (NaH₂PO₄) was acquired from Acros Organics (Geel, Belgium). Milli-Q water was used for all experiments (Millipore; Burlington, USA). Radio-Immunoprecipitation Assay (RIPA) buffer was prepared by the authors. Immunodeficient NOD/SCID mice (NOD.CB17-Prkdc^{scid}/NCrHsd) were obtained from Envigo Laboratories Inc. Additional information about the biological material is provided in Supporting Information 1.

A 15 mL Dounce tissue homogenizer and Ultraturrax dispersing machine were purchased from Wheaton (Millville, USA) and IKA (Staufen, Germany), respectively. 3K centrifugal filters were acquired from Merck Millipore (Burlington, USA). NMR tubes (5 mm) and NMR tube caps (5 mm) for SampleJet were obtained from Deutero (Kastellaun, Germany) and Bruker (Billerica, USA), respectively.

Isolating Mitochondria from Tissues. The isolation procedure was performed at 4 °C to preserve mitochondria and avoid significant metabolic alterations (Supporting Information 2A). Organs were removed from storage at -80 °C and kept on ice. After weighing each sample, the tissues were homogenized in Buffer 1 (220 mM mannitol, 70 mM sucrose, 10 mM Tris-HCl solution, and 0.5 mg/mL BSA in Milli-Q water, pH 7.4) using a Dounce or Ultraturrax homogenizer. The homogenization of soft tissues was performed using two volumes (1:2, tissue/buffer) of Buffer 1

and 70 strokes with a Dounce homogenizer. The homogenate was diluted to obtain a 10% (v/v) homogenate solution. Due to its fibrous nature, the breast tumor tissue was homogenized in 20 volumes (1:20, tissue/buffer) of Buffer 1 with the Ultraturrax homogenizer used at 12,000 rpm for precisely 10 s. Supporting Information 3 describes various parameters, including tissue type, amount of tissue used, the homogenizer used, and the number of scans and duration of the NMR experiment.

Each homogenate was centrifuged at 560g for 15 min at 4 °C. Next, the supernatant containing mitochondria, cytosol, and membranes was transferred to a new tube, while the nuclear pellet was stored at -80 °C for further experiments. Critical step: As the nuclear pellet can easily become resuspended in the supernatant, sudden movements should be avoided and the supernatant should be collected carefully. The supernatant was then centrifuged at 7000g for 15 min at 4 °C. An aliquot (1 mL) of the supernatant (cytosol and membranes) was stored at -80 °C for further experiments. The mitochondrial pellet was then washed twice with Buffer 1 (volume approximately equal to the weight of the initial tissue) and centrifuged at 7000g for 15 min at 4 °C. Mitochondrial pellets were then weighed and stored at -80 °C.

The isolation of mitochondria was confirmed by Western blotting. Mitochondrial pellets were resuspended in RIPA buffer (25 μ L/10 mg; 150 mM NaCl, 50 mM Tris Base, 1% SDS, 0.5% sodium deoxycholate, and 1% NP40, pH 8) containing a protease inhibitor cocktail (25×). Cytosolic samples were prepared by adding 10 μ L of a protease inhibitor cocktail (25×) to 250 μ L of the cytosolic fraction. After vortexing, the samples were centrifuged at 13,200 rpm for 15 min at 4 °C, and the supernatant was kept for protein quantification via the Bradford Assay. Protein extract (20 μ g) was used to assess the expression of mitochondrial and cytosolic markers. Supporting Information 4 reports the primary and secondary antibodies used.

Metabolite Extraction and NMR Sample Preparation. The extraction of metabolites from mitochondria employed the following protocol (Supporting Information 2B). Frozen mitochondrial pellets were placed on ice and allowed to thaw for 5 min. Then, 700 μL of Buffer 2 [20 mM Na₂HPO₄ and 20 μM 3-(trimethylsilyl)propionic-2,2,3,3-d₄ acid sodium salt solution (TSP; used as an internal standard for NMR analysis) in D₂O, pH 7.4] was added, and the suspension was homogenized with a vortex, resuspended with a pipet, and subjected to ultrasound by submerging the tubes in an ultrasonic bath for 5 min. Samples were placed in liquid nitrogen for 1 min to break cell membranes and then allowed to thaw in a temperate water bath. This step was repeated two more times (three cycles in total). The suspension was centrifuged at 10,000g for 15 min at 4 °C, and the supernatant was transferred to 1.5 mL tubes.

Before NMR analysis, samples were passed through a 3 kDa centrifugal filter. The filter was washed three times with 400 μL of Milli-Q water and once with 400 μL of D2O by centrifuging at 14,000g for 15 min at room temperature. Samples were then filtered by centrifugation at 14,000g for 40 min at 4 °C. Critical step: If the filter becomes clogged, then transfer the sample to a fresh, washed filter. Finally, 550 μL of the samples was transferred to a 5 mm NMR tube.

Metabolite extraction using whole cells was performed using the same method. Buffer 2 (700 μ L) was added to the tissue to

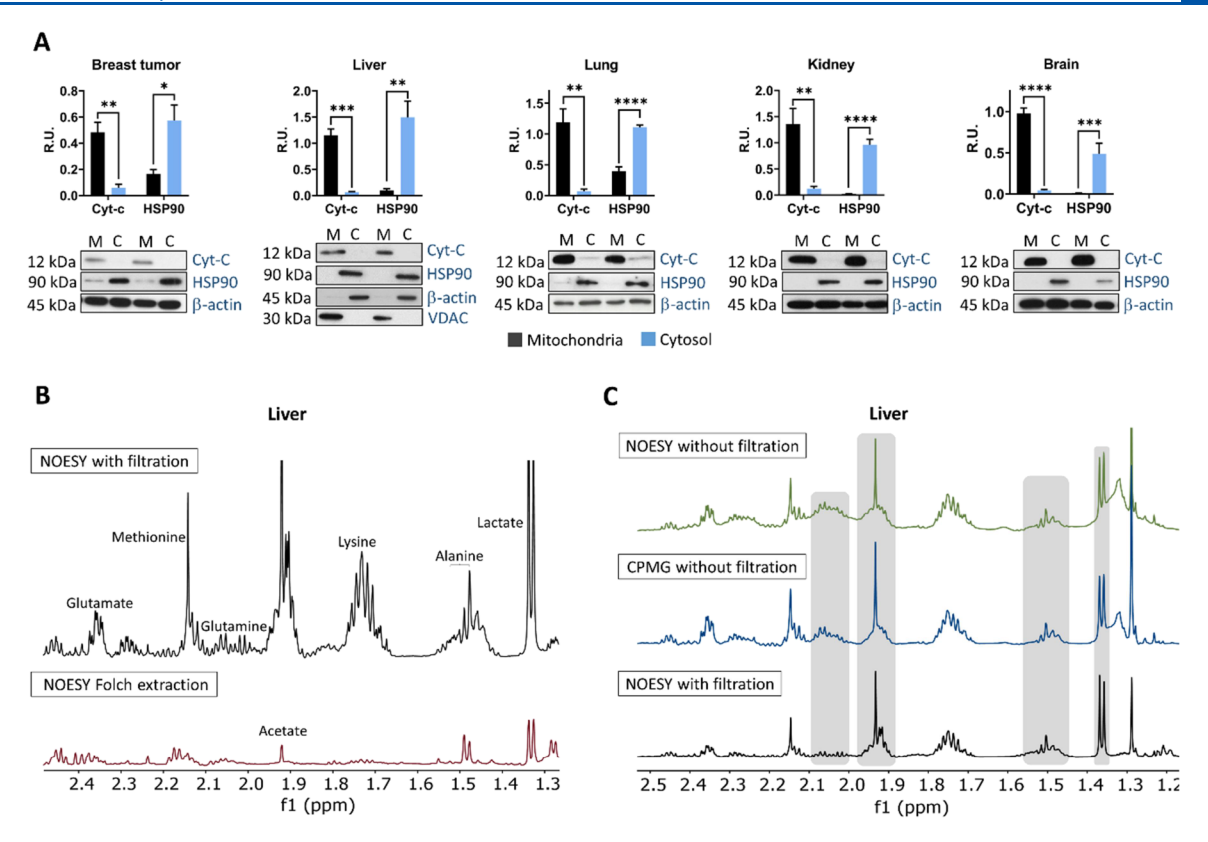


Figure 1. (A) Representative western blots and protein quantitation confirming mitochondrial isolation from tissues. Protein quantification was performed by densitometry analysis (average \pm SEM ($n \ge$)). Cytochrome-c: mitochondrial marker; HSP90: cytosolic marker; β -actin; and VDAC: loading controls. M: mitochondria; C: cytosol. (B) Aliphatic region of the H NMR spectra of liver mitochondria obtained by the "NOESY with filtration" and the "NOESY Folch extraction" metabolite extraction protocols. (C) Comparison of the NOESY spectra aliphatic region obtained with/without sample filtration compared to CPMG without filtration. Regions of the spectra experiencing the most significant changes are highlighted in gray.

perform the homogenization, and the metabolite extraction process was followed as before.

NMR Analysis. Samples were introduced into the NMR spectrometer (Bruker AVII-600 MHz equipped with a 5 mm TCI cryoprobe; see Supporting Information 2C), and the temperature was set to 27 $\,^{\circ}\text{C.}$ A reference standard sample (Bruker) containing 2 mM sucrose, 0.5 mM sodium trimethylsilylpropanesulfonate (DSS), and 2 mM NaN3 in H₂O/D₂O was first analyzed to ensure adequate spectral resolution and water suppression. ¹H 1D NOESY (Nuclear Overhauser Effect Spectroscopy) NMR spectra were acquired with corresponding scans for each tissue type (see Supporting Information 3 for mitochondrial samples and Supporting Information 6 for whole-cell samples). The following settings were applied to obtain good-quality spectra: 64,000 data points were digitalized over a spectral width of 30 ppm for optimal baseline correction, a 4 s relaxation delay was used between FID (free induction decay) readings and a water presaturation pulse of 25 Hz was applied to minimize the water signal. The FID values were multiplied by an exponential function with a 0.5 Hz line broadening factor.

Spectra Processing and Data Analysis. The acquired NMR spectra were processed by using Mestrenova 14.0.0 before data integration. The spectra were referenced to the internal standard (TSP), and the phase was corrected manually to obtain the spectra signals in pure absorption mode. The baseline was corrected by using a manual optimization of the Whittaker smoother correction.

An assignment table for each tissue type was prepared based on information available regarding the metabolomic profile of the total tissue (liver, 24 brain, 25 lung, 26 kidney, 24 breast tissue 24), as well as the Human Metabolome database 27 and the commercial Chenomx software (Chenomx Inc. Edmonton, Canada) (see Supporting Information 7). The integration templates were copied into a text file (example in Supporting Information 8), and the signals were integrated using the "Predefined sum" calculation method in MestreNova software by uploading the text file. Signal integrals were saved as 1D Integral Series (.txt) and opened in Excel.

For metabolomic analysis, the integral values were normalized to their total area by dividing each integral value by the sum of all integrals in the sample. This approach preserves the relative intensities of each sample peak. Signals stemming from the isolation buffer were excluded from data normalization To perform an absolute quantitative comparison of different procedures, we integrated a series of NMR signals corresponding to selected metabolites and quantified the integrals relative to the internal ERETIC signal to obtain absolute quantification. The ERETIC signal was previously calibrated with a prepared mixture sample of representative metabolites of known concentration.

Statistical analyses followed standard methods for multivariate and univariate analysis of metabolomic data. Unsupervised PCA (principal component analysis) and supervised OPLS-DA (orthogonal partial least-squares discriminant analysis) models were obtained using the SIMCA-P 16 software. Univariate analysis and ANOVA (One-Way

Analysis of Variance) were carried out using Excel and the MetaboAnalyst 5.0 web-based platform.²⁹

RESULTS

Optimizing the NMR Analysis of Mitochondrial Metabolites. Creating a mitochondrial metabolic profile involves three steps (Supporting Information 2): (A) isolation of the mitochondrial fraction from tissues, (B) extraction of metabolites from the mitochondrial fraction, and (C) relative quantification of metabolites by NMR. These steps can be carried out sequentially in a single day or over several days by freezing the samples in between steps.

The procedure used for mitochondrial isolation from tissues depends on the final aim of the study and the grade of purity and activity of the isolated mitochondria required. 30,31 We selected tissue homogenization followed by differential centrifugation as the most suitable method for mitochondria isolation from tissues to support the robust and reproducible acquisition of metabolomic profiles.³¹ The simplicity and high recovery rate make this approach commonplace in organelle isolation protocols, with extensive applications in tissues such as the liver, ^{31,32} heart, ³² musculoskeletal, ³² brain, ³² kidney, ³³ and testes. ³³ Generally, two standard methods are available for tissue homogenization-manual Dounce or automatic Ultraturrax approaches. We compared metabolite recovery using both homogenization methods for all tissues; only the tumor samples displayed a higher intensity in some NMR signals (e.g., acetate, creatine, and choline derivatives) after homogenization with Ultraturrax compared to Dounce (Supporting Information 9), probably due to its more compact nature (given the fibrous, muscular type of tissue). Therefore, we employed Ultraturrax homogenization for tumor samples and Dounce homogenization for all other samples (Supporting Information 3).

We confirmed the isolation of mitochondria by Western blotting analysis of the mitochondrial and cytosolic fractions isolated from each tissue (Figure 1A). We used cytochrome-c and heat shock protein 9 (HSP90) antibodies as mitochondrial and cytosolic markers, respectively, and β -actin or VDAC as loading controls (Supporting Information 4); in liver samples, we used β -actin for the cytosolic fractions and VDAC for the mitochondrial samples, due to the absence of β -actin in the mitochondria of healthy liver (Tan2006). For all organs, we observed a significantly higher level of mitochondrial marker expression in mitochondrial fractions than in cytosolic fractions, thereby confirming the presence of mitochondria. The cytosolic fractions presented comparatively low levels of cytochrome-c, further confirming the isolation of mitochondria from the cytosol (Figure 1A). A quantitative analysis of several replicates of the western blots showed higher enrichment levels for brain, kidney, and liver samples (92-99%), while the enrichment was slightly lower for tumor and lung samples (75%) (Supporting Information 5).

After organelle isolation, we explored the choice of a metabolite extraction protocol. Analysis of intact mitochondria by high-resolution magic-angle spinning NMR provides lower resolution and sensitivity than a ¹H NOESY of a mitochondrial extract,³⁴ crucial parameters when working with small sample amounts (such as mitochondrial fractions, in our case). To our knowledge, no study has reported the specific optimization of a protocol for extracting mitochondrial metabolites; however, some protocols have been established for analyzing limited-quantity samples.³⁵ The commonly used Folch extraction

method involves adding a chloroform/methanol/water mixture to simultaneously extract aqueous and hydrophobic metabolites;³⁶ however, alternative methods that avoid organic solvents may represent a more optimal choice for the analysis of small-quantity samples. The use of NMR buffer (Buffer 2) in place of organic solvents has been used in combination with sonication³⁷ or quenching in liquid nitrogen³⁸ to avoid metabolite loss during solvent evaporation. Moreover, sonication alone or combined with final sample ultrafiltration provides better-quality spectra than the Folch method.³⁸ Given these data, we chose to resuspend mitochondrial extracts in an NMR buffer (Buffer 2), quench them in liquid nitrogen, and then carry out centrifugal ultrafiltration to extract the metabolites for the present study. We also introduced 3 kDa centrifugal filters to eliminate broad protein signals during centrifugal ultrafiltration.

We first compared metabolite extraction carried out using two methods, namely, the optimized ("NOESY with filtration") and the traditional extraction ("NOESY Folch extraction"), in liver and breast tumor mitochondria samples, which represent normal and diseased tissues, respectively (Figure 1B, Supporting Information 10). A comparison of the obtained NMR spectra demonstrated a significantly higher metabolite recovery when using the "NOESY with filtration" method. This was further confirmed via the absolute quantification of a series of selected metabolites (valine, lactate, glutamate, glucose, fumarate, tyrosine, histidine, and phenylalanine) over the entire spectral range at different concentration levels (Supporting Information 11).

Next, we evaluated the efficacy of our method to remove protein signals by comparing the obtained spectra with the NMR spectra resulting from a specific NMR experiment that filters out macromolecule signals (Carr-Purcell-Meiboom-Gil, CPMG method) from an unfiltered sample (Figure 1C). The CPMG method consists of a ¹H 1D NMR experiment using a relaxation filter that minimizes the intensity of broad signals.^{39,40} Therefore, we compared the CPMG analysis of unfiltered liver mitochondria samples ("CPMG without filtration") with NOESY analysis ("NOESY without filtration" and "NOESY with filtration") to choose the optimal method. The NOESY experiment without filtration showed broad protein signals, altering the baseline of the whole spectrum, while the CPMG analysis showed the partial deletion of these protein signals in specific spectral regions, leaving cleaner metabolite signals (Figure 1C). However, the NOESY experiment with filtration gave rise to better-quality spectra with further reduced protein signals, enabling the correct relative quantification of the metabolite signals. Additionally, the "CPMG with filtration" analysis resulted in signals with lower intensity compared to the "NOESY with filtration" analysis (Supporting Information 12 Therefore, metabolite relative quantification relied on acquiring a 1D ¹H spectrum with water suppression by presaturation⁴¹ and a short NOESY mixing time to improve phase and baseline. 42 Spectra from ¹H-NOESY experiments with the previous settings usually result in reproducible and quantitatively accurate data, which remains crucial for metabolomics analysis.⁴³

The optimized methodology for NMR analysis of mitochondria isolated from tissues consisted of tissue homogenization using Dounce or Ultraturrax for soft and hard tissues, respectively, followed by differential centrifugation to obtain the mitochondrial fraction. Metabolite extraction from mitochondria involved dissolving the extract in the NMR

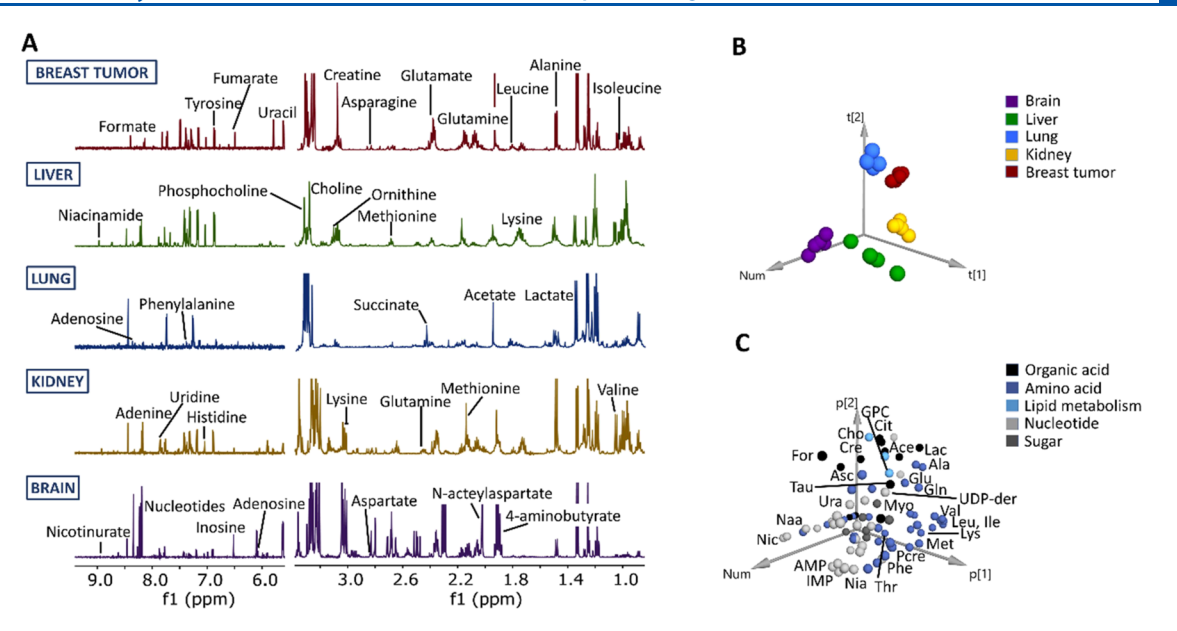


Figure 2. (A) Representative H-NOESY spectra from isolated mitochondria from healthy and tumorigenic tissues. The NMR region between 3.3 and 6 ppm corresponding to water and sucrose/mannitol signals present in Buffer 1 were removed to facilitate visual inspection. (B) PCA score plot of mitochondrial metabolomic profiles obtained from healthy and tumorigenic tissues. (C) PCA loading plot colored according to the metabolite chemical nature. Ace: acetate, Ala: alanine, AMP: adenosine monophosphate, Asc: ascorbate, Cre: creatine, Cho: choline, Cit: citrate, For: formate, Gln: glutamine, Glu: glutamate, GPC: glycerophosphocholine, Ile: isoleucine, IMP: inosine monophosphate, Lac: lactate, Leu: leucine, Lys: lysine, Met: methionine, Myo: myo-inositol, Naa: N-acetyl aspartate, Nia: niacinamide, Nic: nicotinurate, Phe: phenylalanine, PCre: phosphocreatine, Suc: succinate, Tau: taurine, Thr: threonine, UDP-der: UDP-derivative, Ura: uracil, Val: valine.

buffer, quenching the samples, and filtering the samples to eliminate broad protein signals. Finally, NMR analysis of mitochondria was carried out using a ¹H-NOESY experiment. The NMR spectra obtained from this procedure resulted in good-quality spectra, making this methodology suitable for studying metabolic alterations that occur in mitochondrial diseases.

Specific Mitochondrial Metabolomic Profile Characterizes Distinct Tissue Types. Using mitochondria isolation through differential centrifugation, buffer plus filtration metabolite extraction, and NOESY NMR on healthy (liver, lung, kidney, and brain) and breast tumor tissues from a mouse model allowed us to obtain distinct mitochondrial metabolic profiles. Figure 2A depicts the assigned ¹H-NOESY spectra of mitochondrial extracts isolated from the various tissue types under investigation. We adjusted the number of required scans for each experiment based on the weight of the mitochondrial extract obtained from each tissue (Supporting Information 3). After carefully analyzing all of the spectra, we identified 45 metabolites, including amino acids, organic acids, sugars, lipids, and nucleotides (Supporting Information 7). We observed high-quality spectra for breast tumors, kidney, and brain, and an excellent signal-to-noise ratio for the liver, perhaps due to the relatively high mitochondrial content of liver cells (1000– 4000 per cell).⁴⁴ The signal-to-noise ratio was a bit lower for the spectra of lung mitochondria, which may be due to the relatively low mass of this organ. 45

Further analysis of the spectra (Figure 2A) provided evidence of the specificity of certain mitochondrial metabolites in specific tissues. For example, we detected only ornithine and maltose in the liver, betaine in the kidney, acetone in the lung, and nicotinurate, *N*-acetyl aspartate, and 4-aminobutyrate in the brain (Figure 2A). We next performed a PCA on mice from three independent litters to evaluate potential differences in the composition of tissue-specific mitochondrial metab-

olomic profiles (Figure 2B). The resulting score plot demonstrated that samples from the same tissues tended to cluster together, confirming that the mitochondrial metabolomic profiles systematically differed between organs (Figure 2B). Interestingly, the lung exhibited some compositional similarity to breast tumors, while brain and liver samples differed from the remaining tissues.

The loading plot obtained from this analysis (Figure 2C) facilitated the identification of the mitochondrial metabolites that supported discrimination between tissues. Amino acids significantly contributed to the differentiation of liver and kidney samples, whereas nucleotides played a crucial role in discriminating brain tissue samples. Lipids and organic acids (such as lactate, citrate, and ascorbate) contributed to separating lung and breast tumor samples. We observed exceptionally high amounts of the organic acid succinate in lung samples, while breast tumor samples contained high amounts of creatine and acetate. Branched amino acids (such as valine, leucine, and isoleucine) and alanine characterized kidney and breast tumors, while brain samples displayed high levels of aspartate. The nonessential amino acids glutamine and glutamate also contributed to separating breast tumor samples.

Overall, the application of our optimized methodology to breast tumors, liver, lung, kidney, and brain tissues resulted in a specific metabolic profile of mitochondria due to the differential content of amino acids, organic acids, lipids, sugars, and nucleotides.

Mitochondrial Metabolomic Profiles Differ from Whole-Cell Metabolomic Profiles in Distinct Tissue Types. We next performed a similar analysis using total tissue samples to evaluate the differences between the mitochondrial profile and the profile of the whole cell (Supporting Information 13). PCA of whole-cell metabolomic profiles showed good separation between tissues (Supporting Information 13A), with breast tumor and kidney samples

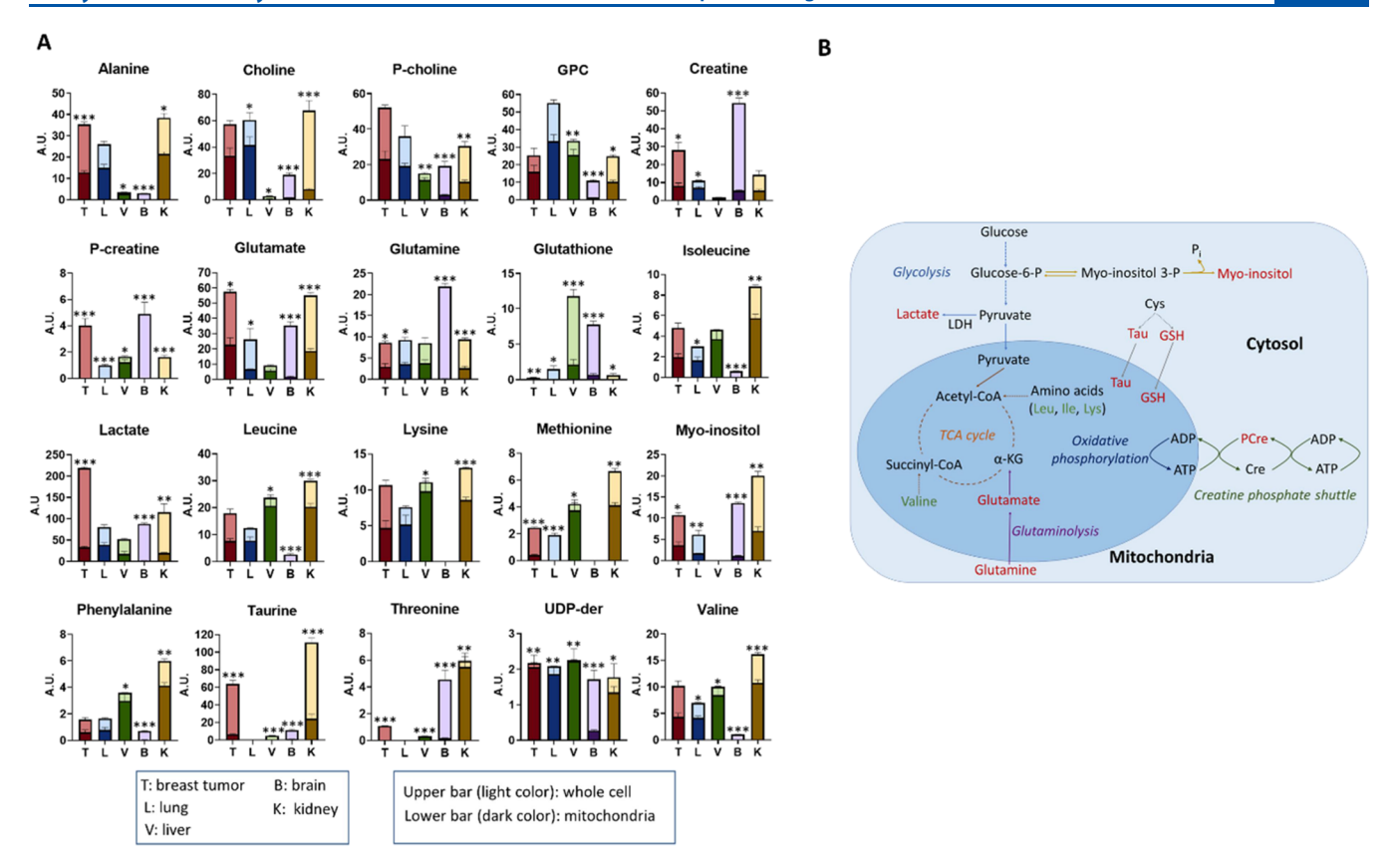


Figure 3. (A) Bar graphs corresponding to significantly altered metabolites from whole cells (top) and mitochondria (bottom) in healthy and tumorigenic tissues. Concentration values normalized to total intensity. Data represented as mean \pm SEM. *p < 0.05, **p < 0.01, ***p < 0.001. T: breast tumor; L: lung; V: liver; B: brain; K: kidney; P-choline: phosphocholine; GPC: glycerophosphocholine; P-creatine: phosphocreatine; UDP-der: UDP-derivative. (B) Summary of metabolic pathways in the mitochondria and cytosol and their interconnections. Mitochondrial metabolites in green are increased and in red are decreased. Glucose-6-P: glucose-6-phosphate, myo-inositol 3-P: myo-inositol 3-phosphate, LDH: lactate dehydrogenase, Cys: cysteine, Tau: taurine, GSH: glutathione, α -KG: α -ketoglutarate, Leu: leucine, Ile: isoleucine, Lys: lysine, ADP: adenosine monophosphate, ATP: adenosine triphosphate, Cre: creatine, PCre: phosphocreatine.

closer than compared to the PCA for mitochondrial metabolomic profiles. The loading plot of whole-cell samples showed similarities to the mitochondrial samples (Supporting Information 13B). Nucleotides again contributed to the separation of brain samples, while amino acids differentiated kidney and breast tumor samples from the remaining samples and the lung displayed high choline content. In contrast to mitochondrial analysis, several sugar metabolites, such as glucose, maltose, and ribose, separated liver samples from other tissues.

We performed a pairwise comparison (mitochondria vs. whole tissue; Figure 3A) for each different organ by first generating a validated discriminating OPLS-DA model and selecting metabolites with a variable importance plot (VIP) values >1, which were then subjected to univariate statistical analysis (Supporting Information 14). Figure 3A reports those metabolites displaying the most significant differences in intensity between isolated mitochondrial samples (bottomdark colored bar) and whole-tissue samples (upper-light colored bar). In general, isolated mitochondria contained elevated levels of glycerophosphocholine, valine, leucine, isoleucine, lysine, and UDP-derivatives and decreased levels of phosphocreatine, glutamate, glutamine, glutathione, lactate, myo-inositol, and taurine compared with the whole-cell samples (Figure 3A). These data agree with the distinct metabolic pathways that take place in mitochondria and the cytosol (Figure 3B). For example, amino acids can supply

tricarboxylic acid cycle intermediates in the mitochondria, ⁴⁶ while lactate, phosphocreatine, and myo-inositol are mainly located in the cytosol. ^{47–49} Metabolites such as glutathione and taurine are synthesized in the cytosol and move into the mitochondria using specific carrier molecules, ^{50,51} therefore their levels will change depending on the state of the cell.

Our analysis also supported the discovery that specific metabolites exhibit organ-specific changes. Tumor and brain samples possessed a higher proportion of most metabolites in whole cells than mitochondria, whereas lung and liver exhibited higher relative quantities of most metabolites in mitochondria (Figure 3A). Kidney samples displayed different tendencies in metabolite levels; for example, we observed higher amounts of choline, P-choline, taurine, glutamate, myoinositol, and lactate in whole cells but higher amounts of the amino acids alanine, isoleucine, leucine, lysine, methionine, phenylalanine, threonine, and valine and a UDP-derivative in mitochondria (Figure 3A). Whole-cell samples from breast tumors showed significantly increased levels of lactate and Pcholine compared to those of other organs (Figure 3A), which agrees with the metabolic reprogramming known to occur in tumor cells. Lactate levels tend to increase in tumor cells due to the Warburg effect, in which the final product of anaerobic glycolysis, pyruvate, becomes converted into lactate. 52 Additionally, choline metabolism also undergoes alterations in tumor cells, including breast cancer cells.

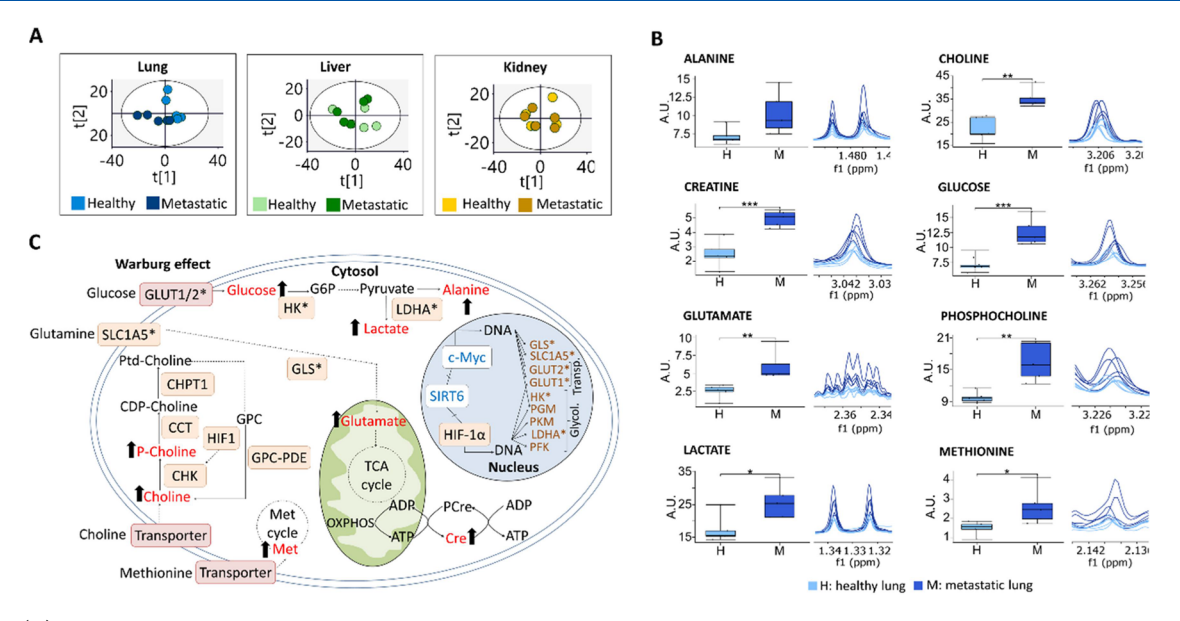


Figure 4. (A) PCA score plots of mitochondrial metabolite profiles of samples isolated from healthy and metastatic mouse models. (B) Mitochondrial metabolite signals and boxplots of relevant metabolites for group discrimination. Data represented as mean \pm SEM. *p < 0.05, **p < 0.01, ***p < 0.001. (C) Choline and glutamine metabolic pathways and the Warburg effect in cancer. GLS: glutaminase, SLC1A5: solute carrier family 1 member 5, GLUT1/2: glucose transporter 1/2, HIF1- α : hypoxia-inducible factor 1- α , HK: hexokinase, LDHA: lactate dehydrogenase A, CHK: choline kinase, GPC: glycerophosphocholine.

We also performed an ANOVA analysis on mitochondrial and whole-cell samples from all organs to obtain a more detailed description of any differences. The results demonstrated the alteration of 42 metabolites when comparing mitochondria isolated from distinct tissues but only 27 when performing the same analysis in whole-cell samples (Supporting Information 15).

Overall, these data confirm a significant contribution from organelle-specific metabolites and the relevance of the organelle-specific analysis.

Optimized Analysis of Mitochondrial Metabolic Profiles in Breast Cancer Models Distinguishes Metastatic Sites. We validated our mitochondrial metabolic profiling methodology by analyzing the impact of metastasis on mitochondrial metabolism in target and nontarget tissues using a mouse model of metastatic breast cancer. We induced MDA-MB-231-Luc tumors in five NOD/SCID mice, which we extracted after euthanizing them when tumors reached 1.0 cm³, approximately 42 days after inoculation. Previous work by our group revealed the complete invasion of the lungs at day 35, while the liver did not present signs of metastasis.⁵⁴ We compared the metabolic profiles of mitochondria isolated from a breast cancer-related metastatic site (lung) and nonmetastatic sites (liver and kidney) from healthy mice and breast cancer model mice (Figure 4, Supporting Information 16).

The PCA of mitochondria samples isolated from tissues from healthy and breast cancer model mice revealed robust discrimination between healthy and breast cancer model mice for the lungs (metastatic site), a slight discrimination in the liver (nonmetastatic site), and a lack of separation in the kidney (nonmetastatic site) (Figure 4A). The OPLS-DA model analysis of these data provided a similar outcome (Supporting Information 17), providing evidence for the significant impact of breast cancer metastasis on mitochondria in the lung. Notably, we failed to obtain an OPLS-DA model for liver and kidney mitochondria samples where metastasis

does not tend to occur in this model. This result agrees with a previous study reporting that MDA-MB-231-Luc tumors produce multiple organ metastases, especially in the lung and axillary lymph nodes. ⁵⁴ Overall, these data demonstrate the validity of the methodology for metabolic studies of mitochondria.

We conducted a univariate statistical analysis on mitochondrial metabolites displaying VIP values of >1 in the OPLS-DA model when comparing healthy and metastatic tissues (see Supporting Information 16). Figure 4B shows the boxplot of those mitochondrial metabolites exhibiting significant changes (p < 0.05) when comparing healthy and metastatic tissues and the corresponding NMR signal. Mitochondria from metastatic lung tissues had higher levels of eight metabolites when compared with healthy tissues (noted by black arrows in Figure 4C). Choline and phosphocholine, both exhibiting increased levels (known tumor-associated metabolic alterations⁵³), were found in metastatic lung mitochondria. The RAS (rat sarcoma) oncogenic signaling pathway and the oncogenic transcription factor HIF1 (hypoxia-inducible factor 1) regulate the expression of the CHK1 (checkpoint kinase 1) and CTL1 (choline transporter-like protein 1) choline metabolism-associated enzymes, and their upregulation increases the total choline intracellular concentration.⁵⁵ We also observed an increase in glucose and lactate in metastatic lung mitochondria, which correlates with the impact of the Warburg effect on cancer cells.⁵² Many cancers, including breast cancer, are characterized by elevated lactate concentrations that can be explained by altered glucose metabolism by different tumor suppressor genes and oncoproteins.⁵⁶ HIF1 upregulates the expression of the GLUT1 (glucose transporter 1) and GLUT2 (glucose transporter 2), and the HK2 (hexokinase 2) that initiates glycolysis.⁵⁶ Despite the relevance of glucose and lactate in tumor cell metabolism, metastatic liver mitochondria did not display alterations to these metabolites, which may reflect this tissue's lower degree of metastasis. Creatine, whose level increases in metastatic lung mitochondria, plays an

essential role in cancer cells by maintaining energy homeostasis. Furthermore, increased creatine kinase levels occur in distinct cancers.⁵⁷ Metastatic lung mitochondria also had increased levels of glutamate, alanine, and methionine, supporting the theory of dysregulated amino acid metabolism in cancer cells.⁵⁸ The increased levels of glutamate could also relate to tumor-associated increases in glutaminolysis,⁵⁹ which occurs when the MYC oncogene prompts the overexpression of the SLC1A5 (solute carrier family 1 member 5) glutamine transporter and upregulates the glutaminase enzyme (Figure 4C).

To further test the relevance of our method, we performed a similar comparison, assessing the whole cell rather than mitochondria (Supporting Information 17 and 18). Interestingly, in this analysis, we failed to detect alterations in alanine, lactate, phosphocholine, and methionine in the metastatic lung. Choline and glutamate showed the same trend in both wholecell and mitochondria of metastatic lung samples, while other metabolites (glycerophosphocholine, myo-inositol, leucine, lysine, and valine) displayed significant changes only in whole-cell analysis.

These findings support the hypothesis that mitochondrial and whole-cell metabolite analysis provides differing but complementary information, further evidence for the utility of organelle-specific analysis in exploring the mechanisms controlling metastasis.

CONCLUSIONS

In this work, we describe an optimized methodology to study the metabolomic profiles of mitochondria isolated from mouse tissues through NMR spectroscopy. The procedure involves (i) isolation of mitochondria through differential centrifugation, (ii) extraction of metabolites using an optimized protocol based on quenching, and (iii) NMR analysis. After confirming the presence of mitochondria in the isolated fractions by western blotting, we compared the metabolomic contents of whole cells and mitochondria in healthy and tumorigenic mouse tissues. This comparison provided evidence of significant changes in the levels of many metabolites; furthermore, we observed specific changes occurring in the mitochondria that were not observed in the whole-cell analysis. Our proposed methodology is relatively fast and straightforward, avoids solvent evaporation to prevent metabolite loss and degradation, and does not destroy samples, which allows further analysis with complementary analytical techniques (e.g., MS). Moreover, our methodology allows direct relative quantification of metabolite levels without a calibration curve. Overall, robust and reproducible metabolic data can be obtained in only a few hours.

Our methodology can also be applied to tissue samples obtained from animal models or human biopsies and could provide helpful information for clinical and preclinical research. Additionally, our methodology may find use in research projects focused on identifying biomarkers in diseases that impact mitochondrial metabolism, such as Alzheimer's disease, Parkinson's disease, or diabetes, using small muscle or fat biopsies before the manifestation of clinical symptoms.

Given the findings observed when comparing mitochondria isolated from tissues of healthy and metastatic breast cancer mouse models, we also hope that our methodology will play an essential role in cancer research. The increase in certain metabolite levels in lung mitochondria associated with tumorigenesis/metastasis suggests that components of the

associated metabolic pathways could serve as therapeutic targets. Therefore, mitochondria constitute promising targets for developing novel anticancer agents, and this method could also provide critical information regarding the impact of novel anticancer drugs on mitochondrial metabolism.

ASSOCIATED CONTENT

Solution Supporting Information

The Supporting Information is available free of charge at https://pubs.acs.org/doi/10.1021/acs.analchem.3c02432.

Detailed information on the biological material used, a schematic representation of the optimized protocol used for the NMR analysis of mitochondrial samples, NMR parameters used for the analysis of mitochondrial samples and for the whole-cell samples, primary and secondary antibodies used for the confirmation of mitochondrial isolation by western blotting, the values resulting from the western blotting quantification and the mitochondrial enrichment in the fractions obtained from the different tissues, the NMR signal assignment of the mitochondrial fractions obtained from each tissue, the integration template of the NMR signals used in MestreNova, ¹H NMR aliphatic regions from breast tumor mitochondria obtained with the Dounce and the Ultraturrax homogenizers, ¹H NMR aliphatic regions from breast tumor mitochondria obtained using the "NOESY with filtration" method and the "NOESY Folch extraction" method, the quantification of the NMR signals for the comparison of the metabolite extraction methods, comparison of the NOESY spectra obtained with the "NOESY with filtration" method and the CPMG with filtration method, PCA of the whole-cell metabolomic profiles of the different tissues including the 3D score plot and 3D loading plot, mean, SD, VIP values, and p-values for the comparative analysis of mitochondria and whole-cell metabolomic profiles from the different tissues, altered metabolites obtained from ANOVA analysis of mitochondria and whole-cell samples from the different tissues, mean, SD, VIP values, and p-values for the comparative analysis of the mitochondrial and whole-cell metabolomic profiles from healthy vs. metastatic tissues, and the statistical values of the OPLS-DA models obtained from the comparison between healthy and breast cancer mouse models (ZIP)

AUTHOR INFORMATION

Corresponding Authors

María J. Vicent — Centro de Investigación Príncipe Felipe, Polymer Therapeutics Laboratory and CIBERONC, Valencia 46012, Spain; orcid.org/0000-0001-7771-3373; Email: mjvicent@cipf.es

Antonio Pineda-Lucena — Drug Discovery Unit, Instituto de Investigación Sanitaria La Fe, Valencia 46026, Spain; Molecular Therapeutics Program, CIMA Universidad de Navarra, Pamplona 31008, Spain; Email: apinedal@ unav.es

Martina Palomino-Schätzlein — NMR Facility, Centro de Investigación Príncipe Felipe, Valencia 46012, Spain; ProtoQSAR, CEEI, Parque Tecnológico Valencia, Paterna 46980, Spain; ◎ orcid.org/0000-0001-7303-0743; Email: mpalomino@protogsar.com

Authors

Inés Domingo-Ortí — Centro de Investigación Príncipe Felipe, Polymer Therapeutics Laboratory and CIBERONC, Valencia 46012, Spain; NMR Facility, Centro de Investigación Príncipe Felipe, Valencia 46012, Spain; Drug Discovery Unit, Instituto de Investigación Sanitaria La Fe, Valencia 46026, Spain

Patricia Ferrer-Torres — NMR Facility, Centro de Investigación Príncipe Felipe, Valencia 46012, Spain; orcid.org/0000-0002-5075-4471

Ana Armiñán — Centro de Investigación Príncipe Felipe, Polymer Therapeutics Laboratory and CIBERONC, Valencia 46012, Spain

Complete contact information is available at: https://pubs.acs.org/10.1021/acs.analchem.3c02432

Author Contributions

M.J.V., A.P.L., and M.P.S. initiated, designed, funded, and supervised the study; I.D. performed most experiments; A.A. and P.F. contributed to experimental work and data analysis; I.D. and M.P.S. wrote the manuscript. I.D., M.J.V, A.P.L., and M.P.S revised and edited the manuscript. All authors discussed the results and approved the manuscript.

Notes

The authors declare no competing financial interest.

ACKNOWLEDGMENTS

We thank D. Charbonnier for support regarding animal tissues, Dr. Stuart P. Atkinson for his collaboration in manuscript preparation and English revision, the use of Biorender.com in Supporting Figure ², and funding from AECC Valencia, the Spanish Ministry of Science and Innovation (PID2019-108806RB-I00, SAF2017-89229-R), and the FPU grant to IDO ref: FPU19/03729. Part of the equipment employed in this work was funded by Generalitat Valenciana and cofinanced with FEDER funds (PO FEDER of Comunitat Valenciana 2014–2020).

REFERENCES

- (1) Duchen, M. R. Diabetes 2004, 53 (suppl. 1), S96-S102.
- (2) Murphy, E.; Ardehali, H.; Balaban, R. S.; DiLisa, F.; Dorn, G. W.; Kitsis, R. N.; Otsu, K.; Ping, P.; Rizzuto, R.; Sack, M. N.; Wallace, D.; Youle, R. J. Circ. Res. **2016**, 118 (12), 1960–1991.
- (3) Modica-Napolitano, J. S.; Singh, K. K. Mitochondrion 2004, 4 (5–6 spec. iss.), 755–762.
- (4) Scheid, A. D.; Beadnell, T. C.; Welch, D. R. Br. J. Cancer 2021, 124 (1), 124–135.
- (5) Zong, W.-X.; Rabinowitz, J. D.; White, E. Mol. Cell **2016**, 61 (5), 667–676
- (6) Simonnet, H.; Alazard, N.; Pfeiffer, K.; Gallou, C.; Béroud, C.; Demont, J.; Bouvier, R.; Schägger, H.; Godinot, C. *Carcinogenesis* **2002**, 23 (5), 759–768.
- (7) Nicholson, J. K.; Lindon, J. C.; Holmes, E. *Xenobiotica* **1999**, 29 (11), 1181–1189.
- (8) Miller, I. J.; Peters, S. R.; Overmyer, K. A.; Paulson, B. R.; Westphall, M. S.; Coon, J. J. *npj Digit. Med.* **2019**, 2 (1), 109.
- (9) Kok, M. G. M.; Nix, C.; Nys, G.; Fillet, M. Talanta **2019**, 197 (January), 49-58.
- (10) Gowda, G. A. N.; Shanaiah, N.; Cooper, A.; Maluccio, M.; Raftery, D. *Lipids* **2009**, *44* (6), 527–535.
- (11) Lima, A. R.; Pinto, J.; de Bastos, M. L.; Carvalho, M.; Guedes de Pinho, P. *Metabolomics* **2018**, *14* (7), 88.

- (12) Mirnezami, R.; Jiménez, B.; Li, J. V.; Kinross, J. M.; Veselkov, K.; Goldin, R. D.; Holmes, E.; Nicholson, J. K.; Darzi, A. *Ann. Surg.* **2014**, 259 (6), 1138–1149.
- (13) Wang, H.; Zhang, H.; Deng, P.; Liu, C.; Li, D.; Jie, H.; Zhang, H.; Zhou, Z.; Zhao, Y. L. BMC Cancer **2016**, 16 (1), 1–12.
- (14) Naz, S.; Moreira Dos Santos, D. C.; García, A.; Barbas, C. *Bioanalysis* **2014**, *6* (12), 1657–1677.
- (15) Domingo-Ortí, I.; Lamas-Domingo, R.; Ciudin, A.; Hernández, C.; Herance, J. R.; Palomino-Schätzlein, M.; Pineda-Lucena, A. *Aging* **2021**, *13* (4), 4850–4880.
- (16) Mayers, J. R.; Wu, C.; Clish, C. B.; Kraft, P.; Torrence, M. E.; Fiske, B. P.; Yuan, C.; Bao, Y.; Townsend, M. K.; Tworoger, S. S.; Davidson, S. M.; Papagiannakopoulos, T.; Yang, A.; Dayton, T. L.; Ogino, S.; Stampfer, M. J.; Giovannucci, E. L.; Qian, Z. R.; Rubinson, D. A.; Ma, J.; Sesso, H. D.; Gaziano, J. M.; Cochrane, B. B.; Liu, S.; Wactawski-Wende, J.; Manson, J. E.; Pollak, M. N.; Kimmelman, A. C.; Souza, A.; Pierce, K.; Wang, T. J.; Gerszten, R. E.; Fuchs, C. S.; Vander Heiden, M. G.; Wolpin, B. M. Nat. Med. 2014, 20 (10), 1193–1198.
- (17) Kaddurah-Daouk, R.; Kristal, B. S.; Weinshilboum, R. M. Annu. Rev. Pharmacol. Toxicol. 2008, 48, 653–683.
- (18) Armiñán, A.; Palomino-Schätzlein, M.; Deladriere, C.; Arroyo-Crespo, J. J.; Vicente-Ruiz, S.; Vicent, M. J.; Pineda-Lucena, A. *Biomaterials* **2018**, *162*, 144–153.
- (19) O'Keefe, S. J. D.; Li, J. V.; Lahti, L.; Ou, J.; Carbonero, F.; Mohammed, K.; Posma, J. M.; Kinross, J.; Wahl, E.; Ruder, E.; Vipperla, K.; Naidoo, V.; Mtshali, L.; Tims, S.; Puylaert, P. G. B.; Delany, J.; Krasinskas, A.; Benefiel, A. C.; Kaseb, H. O.; Newton, K.; Nicholson, J. K.; De Vos, W. M.; Gaskins, H. R.; Zoetendal, E. G. *Nat. Commun.* 2015, 6, 6342.
- (20) Chan, C. Y. E.; Koh, P. K.; Mal, M.; Cheah, P. Y.; Eu, K. W.; Backshall, A.; Cavill, R.; K, N. J.; C, K. H. J. Proteome Res. 2009, 8, 352–361.
- (21) Pan, D.; Lindau, C.; Lagies, S.; Wiedemann, N.; Kammerer, B. *Metabolomics* **2018**, *14* (5), 1–12.
- (22) Liu, X.; Xu, G. Anal. Chim. Acta 2018, 1037, 3-12.
- (23) Gravel, S.-P.; Andrzejewski, S.; Avizonis, D.; St-Pierre, J. *Metabolites* **2014**, *4* (2), 166–183.
- (24) Carneiro, T. J.; Araújo, R.; Vojtek, M.; Gonçalves-Monteiro, S.; Diniz, C.; de Carvalho, A. L. M. B.; Marques, M. P. M.; Gil, A. M. *Metabolites* **2019**, 9 (11), 1–17.
- (25) Glinskikh, A.; Snytnikova, O.; Zelentsova, E.; Borisova, M.; Tsentalovich, Y.; Akulov, A. *Molecules* **2021**, *26* (11), 3096.
- (26) Ling, Y. S.; Liang, H. J.; Chung, M. H.; Lin, M. H.; Lin, C. Y. Mol. Biosyst. **2014**, 10 (7), 1918–1931.
- (27) Wishart, D. S.; Guo, A. C.; Oler, E.; Wang, F.; Anjum, A.; Peters, H.; Dizon, R.; Sayeeda, Z.; Tian, S.; Lee, B. L.; Berjanskii, M.; Mah, R.; Yamamoto, M.; Jovel, J.; Torres-Calzada, C.; Hiebert-Giesbrecht, M.; Lui, V. W.; Varshavi, D.; Varshavi, D.; Allen, D.; Arndt, D.; Khetarpal, N.; Sivakumaran, A.; Harford, K.; Sanford, S.; Yee, K.; Cao, X.; Budinski, Z.; Liigand, J.; Zhang, L.; Zheng, J.; Mandal, R.; Karu, N.; Dambrova, M.; Schiöth, H. B.; Greiner, R.; Gautam, V. Nucleic Acids Res. 2022, 50 (D1), D622–D631.
- (28) Puchades-Carrasco, L.; Palomino-Schätzlein, M.; Pérez-Rambla, C.; Pineda-Lucena, A. *Brief. Bioinform.* **2016**, *17* (3), 541–552.
- (29) Pang, Z.; Chong, J.; Zhou, G.; De Lima Morais, D. A.; Chang, L.; Barrette, M.; Gauthier, C.; Jacques, P. É.; Li, S.; Xia, J. *Nucleic Acids Res.* **2021**, 49 (W1), W388–W396.
- (30) Barbieri, L.; Luchinat, E.; Banci, L. Biochim. Biophys. Acta Mol. Cell Res. 2014, 1843 (11), 2492–2496.
- (31) Go, Y. M.; Uppal, K.; Walker, D. I.; Tran, V.; Dury, L.; Strobel, F. H.; Baubichon-Cortay, H.; Pennell, K. D.; Roede, J. R.; Jones, D. P. *Methods Mol. Biol.* **2014**, *1198* (1), 43–73.
- (32) Franko, A.; Baris, O. R.; Bergschneider, E.; Von Toerne, C.; Hauck, S. M.; Aichler, M.; Walch, A. K.; Wurst, W.; Wiesner, R. J.; Johnston, I. C. D.; De Angelis, M. H. *PLoS One* **2013**, 8 (12), No. e82392.
- (33) Pallotti, F.; Lenaz, G. Methods Cell Biol. 2007, 80 (06), 3-44.

- (34) Gogiashvili, M.; Nowacki, J.; Hergenröder, R.; Hengstler, J. G.; Lambert, J.; Edlund, K. *Metabolites* **2019**, *9* (2), 19.
- (35) Mason, S.; Terburgh, K.; Louw, R. Metabolomics 2018, 14 (6), 74.
- (36) Folch, J.; Lees, M.; Sloane Stanley, G. J. Biol. Chem. 1957, 226 (1), 497–509.
- (37) Matheus, N.; Hansen, S.; Rozet, E.; Peixoto, P.; Maquoi, E.; Lambert, V.; Noël, A.; Frédérich, M.; Mottet, D.; De Tullio, P. *Phytochem. Anal.* **2014**, 25 (4), 342–349.
- (38) Gómez-Archila, L. G.; Palomino-Schätzlein, M.; Zapata-Builes, W.; Galeano, E. *PLoS One* **2021**, *16*, 1–20.
- (39) Meiboom, S.; Gill, D. Rev. Sci. Instrum. 1958, 29 (8), 688-691.
- (40) Carr, H. Y.; Purcell, E. M. Phys. Rev. 1954, 94 (3), 630-638.
- (41) Price, W. S. Water Signal Suppression in NMR Spectroscopy, 1999; vol 38. DOI: DOI: 10.1016/S0066-4103(08)60040-X.
- (42) Emwas, A. H.; Saccenti, E.; Gao, X.; McKay, R. T.; dos Santos, V. A. P. M.; Roy, R.; Wishart, D. S. *Metabolomics* **2018**, *14* (3), 1–23.
- (43) Emwas, A. H.; Roy, R.; McKay, R. T.; Tenori, L.; Saccenti, E.; Nagana Gowda, G. A.; Raftery, D.; Alahmari, F.; Jaremko, L.; Jaremko, M.; Wishart, D. S. *Metabolites* **2019**, *9* (7), 123.
- (44) Degli Esposti, D.; Hamelin, J.; Bosselut, N.; Saffroy, R.; Sebagh, M.; Pommier, A.; Martel, C.; Lemoine, A. *Biochem. Res. Int.* **2012**, 2012, No. 387626.
- (45) Bitar, A.; Lisbona, A.; Thedrez, P.; Sai Maurel, C.; Le Forestier, D.; Barbet, J.; Bardies, M. *Phys. Med. Biol.* **2007**, *52* (4), 1013–1025.
- (46) Martínez-Reyes, I.; Chandel, N. S. Nat. Commun. 2020, 11 (1), 1–11.
- (47) Schlattner, U.; Tokarska-Schlattner, M.; Wallimann, T. Biochim. Biophys. Acta, Mol. Basis Dis. 2006, 1762 (2), 164–180.
- (48) Croze, M. L.; Soulage, C. O. Biochimic 2013, 95 (10), 1811–1827.
- (49) Adeva-Andany, M.; López-Ojén, M.; Funcasta-Calderón, R.; Ameneiros-Rodríguez, E.; Donapetry-García, C.; Vila-Altesor, M.; Rodríguez-Seijas, J. *Mitochondrion* **2014**, *17*, 76–100.
- (50) Marí, M.; Morales, A.; Colell, A.; García-Ruiz, C.; Fernández-Checa, J. C. Antioxidants Redox Signal. 2009, 11 (11), 2685–2700.
- (51) Hansen, S. H.; Andersen, M. L.; Cornett, C.; Gradinaru, R.; Grunnet, N. J. Biomed. Sci. 2010, 17 (supp. 1), 1–8.
- (52) Warburg, O.; Wind, F.; Negelein, E. Br. Med. J. 1927, 8 (6), 519-530.
- (53) Glunde, K.; Penet, M. F.; Jiang, L.; Jacobs, M. A.; Bhujwalla, Z. M. Expert Rev. Mol. Diagn. 2015, 15 (6), 735–747.
- (54) Arroyo-Crespo, J. J.; Armiñán, A.; Charbonnier, D.; Deladriere, C.; Palomino-Schätzlein, M.; Lamas-Domingo, R.; Forteza, J.; Pineda-Lucena, A.; Vicent, M. J. *Int. J. Cancer* **2019**, *145* (8), 2267–2281.
- (55) Sonkar, Kanchan; Ayyappan, Vinay; Tressler, Caitlin M.; Adelaja, Oluwatobi; Cai, Ruoquing; Menglin Cheng, K. G. NMR Biomed. **2019**, 32 (10), No. e4112.
- (56) Hay, N. Nat. Rev. Cancer 2016, 16 (10), 635-649.
- (57) Kazak, L.; Cohen, P. Nat. Rev. Endocrinol. **2020**, 16 (8), 421–436.
- (58) Lieu, E. L.; Nguyen, T.; Rhyne, S.; Kim, J. *Exp. Mol. Med.* **2020**, 52 (1), 15–30.
- (59) Altman, B. J.; Stine, Z. E.; Dang, C. V. Nat. Rev. Cancer 2016, 16 (10), 619-634.